

A groundswell of scientists
running for Congress p. 860

A blood test for
cancer p. 868 & 870

Preempting epidemics via a
Global Virome Project p. 872

Science

\$15
23 FEBRUARY 2018

SCIENCE MAGAZINE

AAAS

MINDS AT WORK

Oldest dated cave art points to Neandertal
symbolic behavior pp. 852 & 912

CONTENTS

23 FEBRUARY 2018 • VOLUME 359 • ISSUE 6378



Scientists dive into politics

NEWS

IN BRIEF

848 News at a glance

IN DEPTH

852 EUROPE'S FIRST ARTISTS WERE NEANDERTALS

Spanish cave paintings date to before modern humans arrived in region

By T. Appenzeller

► REPORT P. 912; PODCAST

853 WORMS LIVING IN YOUR VEINS? SEVENTEEN VOLUNTEERS SAID 'OK'

A controversial study infects people with schistosomiasis to speed up drug and vaccine development *By K. Kupferschmidt*

854 BRINGING AN IRANIAN OASIS BACK FROM THE DEAD

Water crisis and rising air pollution are stoking regional tensions *By R. Stone*

856 BIOLOGIST UNVEILS CHINA'S FIRST PRIVATE RESEARCH UNIVERSITY

Venture aims to fill gap in higher education landscape *By D. Normile*

857 OCEAN ARRAY ALTERS VIEW OF ATLANTIC CONVEYOR

First data from subpolar moorings show surprising current strengths east of Greenland *By K. Kornei*

858 'EXTINCT' CARIBBEANS HAVE LIVING DESCENDANTS

Ancient DNA from Taino woman shows kinship to modern genomes *By L. Wade*

FEATURE

860 JUST ADD SCIENCE

Scientists hit the campaign trail in hopes of making Congress work better *By J. Mervis*

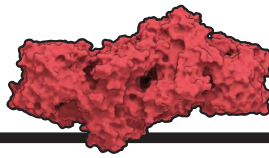
862 FIRST UP: TEXAS

By J. Mervis



869

Helping plants fix nitrogen



INSIGHTS

PERSPECTIVES

864 KEEPING WATCH ON THE OCEAN

Monitoring of fisheries fleets provides crucial data for sustainable use of ocean resources *By E. Poloczanska*

► REPORT P. 904

866 CANCER DETECTION: SEEKING SIGNALS IN BLOOD

Combining gene mutations and protein biomarkers for earlier detection and localization

By M. Kalinich and D. A. Haber

► REPORT P. 926

868 UNNATURALLY AGLOW WITH A BRIGHT INNER LIGHT

A bioluminescent system enables imaging single cells deep inside small animals *By Y. Nasu and R. E. Campbell*

► REPORT P. 935

869 TOWARD NITROGEN-FIXING PLANTS

A concerted research effort could yield engineered plants that can directly fix nitrogen *By A. Good*

871 BORON COMPOUNDS TACKLE DINITROGEN

A borylene compound can match transition metals by activating the strong N₂ bond

By D. L. J. Broere and P. L. Holland

► REPORT P. 896

POLICY FORUM

872 THE GLOBAL VIROME PROJECT

Expanded viral discovery can improve mitigation *By D. Carroll et al.*

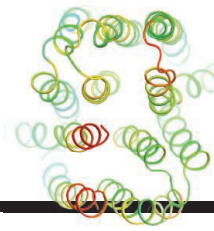
BOOKS ET AL.

875 EARTHQUAKE OR ATOMIC BOMB?

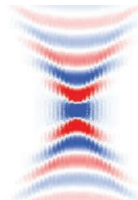
A seismologist reflects on his role in the contentious politics of nuclear weapon test bans *By A. Saperstein*

876 REASON (AND SCIENCE) FOR HOPE

An optimistic treatise celebrates the enlightened thinking that has made us happier, healthier, and safer than ever *By M. Shermer*



915

Clearing drugs
from cells

892

Extending excitation
lifetimes**LETTERS****877 BIOCONTROL OF INVASIVE CARP:
RISKS ABOUND**By *J. Marshall* et al.**877 WATERBIRDS TARGETED IN
IRAN'S WETLANDS**By *J. Parchizadeh* and *S. T. Williams***878 SHIFTING SANDS COULD BRING
INVASIVE SPECIES**By *R. A. Everett* et al.**877 NEXTGEN VOICES: SUBMIT NOW
THE PERFECT POSTDOC****RESEARCH****IN BRIEF****880** From *Science* and other journals**RESEARCH ARTICLE****883 CELL BIOLOGY**BAK/BAX macropores facilitate mitochondrial herniation and mtDNA efflux during apoptosis *K. McArthur* et al.
RESEARCH ARTICLE SUMMARY: FOR FULL TEXT: [dx.doi.org/10.1126/science.aoa6047](https://doi.org/10.1126/science.aoa6047)**REPORTS****OPTICS****884** Soliton microcomb range measurement
M.-G. Suh and *K. J. Vahala***887** Ultrafast optical ranging using microresonator soliton frequency combs *P. Trocha* et al.**892 METASURFACES**Infrared hyperbolic metasurface based on nanostructured van der Waals materials *P. Li* et al.**896 INORGANIC CHEMISTRY**Nitrogen fixation and reduction at boron *M.-A. Légaré* et al.
► PERSPECTIVE P. 871**900 PALEOCEANOGRAPHY**Breakup of last glacial deep stratification in the South Pacific
C. Basak et al.**904 FISHERIES**Tracking the global footprint of fisheries *D. A. Kroodsma* et al.

► PERSPECTIVE P. 864

908 OCEAN ACIDIFICATIONCoral reefs will transition to net dissolving before end of century
B. D. Eyre et al.**912 PALEOANTHROPOLOGY**U-Th dating of carbonate crusts reveals Neandertal origin of Iberian cave art
D. L. Hoffmann et al.

► NEWS STORY P. 852

915 STRUCTURAL BIOLOGYMolecular structure of human P-glycoprotein in the ATP-bound, outward-facing conformation
Y. Kim and *J. Chen***920 ORGANOID**Patient-derived organoids model treatment response of metastatic gastrointestinal cancers
G. Vlachogiannis et al.**926 CANCER**Detection and localization of surgically resectable cancers with a multi-analyte blood test *J. D. Cohen* et al.

► PERSPECTIVE P. 866

930 PROTEIN EVOLUTIONStructural principles that enable oligomeric small heat-shock protein paralogs to evolve distinct functions
G. K. A. Hochberg et al.**935 IMAGING**Single-cell bioluminescence imaging of deep tissue in freely moving animals
S. Iwano et al.

► PERSPECTIVE P. 868; VIDEO

940 MOLECULAR BIOLOGYStructures of human PRC2 with its cofactors AEBP2 and JARID2
V. Kasinath et al.**DEPARTMENTS****847 EDITORIAL**

Science matters for the census

By *Robert M. Groves* and *Steven H. Murdoch***950 WORKING LIFE**

Independent but not alone

By *Nicole Forrester***ON THE COVER**

A painting in La Pasiega cave in Cantabria, Spain. Carbonate crusts on top of paintings were dated with the U-Th method to provide minimum ages for the underlying art. The scalariform (ladder shape) composed of vertical and horizontal red lines (center left) is at least 64,000 years old. This is one of three cave paintings in Spain shown to be of Neandertal origin. See pages 852 and 912 and a related paper in *Science Advances* (10.1126/sciadv.aar5255). Photo: *C. D. Standish, A. W. G. Pike, and D. L. Hoffmann*

Science Staff	846
AAAS News & Notes	879
New Products	945
Science Careers	946

Editor-in-Chief Jeremy Berg

Executive Editor Monica M. Bradford News Editor Tim Appenzeller

Deputy Editors Lisa D. Chong, Andrew M. Sugden(UK), Valda J. Vinson, Jake S. Yeston

Research and Insights

DEPUTY EDITOR, EMERITUS Barbara R. Jasny SR. EDITORS Gemma Alderton(UK), Caroline Ash(UK), Julia Fahrenkamp-Uppenkamp(UK), Pamela J. Hines, Stella M. Hurtley(UK), Paula A. Kiberstis, Marc S. Lavine(Canada), Steve Mao, Ian S. Osborne(UK), Beverly A. Purnell, L. Bryan Ray, H. Jesse Smith, Jelena Stajic, Peter Stern(UK), Phillip D. Szuromi, Sacha Vignieri, Brad Wible, Laura M. Zahn ASSOCIATE EDITORS Michael A. Funk, Brent Grocholski, Priscilla N. Kelly, Seth Thomas Scanlon(UK), Keith T. Smith(UK) ASSOCIATE BOOK REVIEW EDITOR Valerie B. Thompson LETTERS EDITOR Jennifer Sills LEAD CONTENT PRODUCTION EDITORS Harry Jach, Lauren Kmec CONTENT PRODUCTION EDITORS Amelia Beyna, Jeffrey E. Cook, Amber Esplin, Chris Filatree, Cynthia Howe, Catherine Wolner SR. EDITORIAL COORDINATORS Carolyn Kyle, Beverly Shields EDITORIAL COORDINATORS Aneera Dobbins, Joi S. Granger, Jeffrey Hearn, Lisa Johnson, Maryrose Madrid, Scott Miller, Jerry Richardson, Anita Wynn PUBLICATIONS ASSISTANTS Ope Martins, Nida Masiulis, Dona Mathieu, Hilary Stewart(UK), Alana Warrie, Alice Whaley(UK), Brian White EXECUTIVE ASSISTANT Jessica Slater ADMINISTRATIVE SUPPORT Janet Clements(UK), Lizanne Newton(UK)

News

NEWS MANAGING EDITOR John Travis INTERNATIONAL EDITOR Richard Stone DEPUTY NEWS EDITORS Elizabeth Culotta, Martin Enserink(Europe), David Grimm, Eric Hand, David Malakoff, Leslie Roberts SR. CORRESPONDENTS Daniel Clery(UK), Jeffrey Mervis, Elizabeth Pennisi ASSOCIATE EDITORS Jeffrey Brainard, Catherine Matacic NEWS WRITERS Adrian Cho, Jon Cohen, Jennifer Couzin-Frankel, Jocelyn Kaiser, Kelly Servick, Robert F. Service, Erik Stokstad(Cambridge, UK), Paul Voosen, Meredith Wadman INTERNS Roni Dengler, Katie Langin, Matt Warren CONTRIBUTING CORRESPONDENTS John Bohannon, Warren Cornwall, Ann Gibbons, Mara Hvistendahl, Sam Kean, Eli Kintisch, Kai Kupferschmidt(Berlin), Andrew Lawler, Mitch Leslie, Eliot Marshall, Virginia Morell, Dennis Normile(Shanghai), Charles Piller, Tania Rabesandratana(London), Emily Underwood, Gretchen Vogel(Berlin), Lizzie Wade(Mexico City) CAREERS Donisha Adams, Rachel Bernstein(Editor), Maggie Kuo COPY EDITORS Dorie Chevlen, Julia Cole (Senior Copy Editor), Cyra Master (Copy Chief) ADMINISTRATIVE SUPPORT Meagan Weiland

Executive Publisher Rush D. Holt

Publisher Bill Moran Chief Digital Media Officer Josh Freeman

DIRECTOR, BUSINESS STRATEGY AND PORTFOLIO MANAGEMENT Sarah Whalen DIRECTOR, PRODUCT AND CUSTOM PUBLISHING Will Schweitzer MANAGER, PRODUCT DEVELOPMENT Hannah Heckner BUSINESS SYSTEMS AND FINANCIAL ANALYSIS DIRECTOR Randy Yi DIRECTOR, BUSINESS OPERATIONS & ANALYST Eric Knott SENIOR SYSTEMS ANALYST Nicole Mehmedovich SENIOR BUSINESS ANALYST Cory Lipman MANAGER, BUSINESS OPERATIONS Jessica Tierney BUSINESS ANALYSTS Meron Kebede, Sandy Kim, Jourdan Stewart FINANCIAL ANALYST Julian Iriarte ADVERTISING SYSTEM ADMINISTRATOR Tina Burks SALES COORDINATOR Shirley Young DIRECTOR, COPYRIGHT, LICENSING, SPECIAL PROJECTS Emilie David DIGITAL PRODUCT ASSOCIATE Michael Hardesty RIGHTS & PERMISSIONS ASSOCIATE Elizabeth Sandler RIGHTS, CONTRACTS, AND LICENSING ASSOCIATE Lili Catlett RIGHTS & PERMISSIONS ASSISTANT Alexander Lee

MARKETING MANAGER, PUBLISHING Shawana Arnold MARKETING ASSOCIATE Steven Goodman SENIOR ART ASSOCIATES Paula Fry ART ASSOCIATE Kim Huynh

INTERIM DIRECTOR, INSTITUTIONAL LICENSING Iquo Edim ASSOCIATE DIRECTOR, RESEARCH & DEVELOPMENT Elisabeth Leonard SENIOR INSTITUTIONAL LICENSING MANAGER Ryan Rexroth INSTITUTIONAL LICENSING MANAGERS Marco Castellan, Chris Murawski SENIOR OPERATIONS ANALYST Liana Guz MANAGER, AGENT RELATIONS & CUSTOMER SUCCESS Judy Lillibrige

WEB TECHNOLOGIES TECHNICAL DIRECTOR David Levy TECHNICAL MANAGER Chris Coleman PORTFOLIO MANAGER Trista Smith PROJECT MANAGER Tara Kiley, Dean Robbins DEVELOPERS Elissa Heller, Ryan Jensen, Brandon Morrison

DIGITAL MEDIA DIRECTOR OF ANALYTICS Enrique Gonzales SR. MULTIMEDIA PRODUCER Sarah Crespi MANAGING DIGITAL PRODUCER Kara Estelle-Powers PRODUCER Liana Birke VIDEO PRODUCERS Chris Burns, Nguyễn Khôi Nguyễn DIGITAL SOCIAL MEDIA PRODUCER Brice Russ

DIGITAL/PRINT STRATEGY MANAGER Jason Hillman QUALITY TECHNICAL MANAGER Marcus Spiegler DIGITAL PRODUCTION MANAGER Lisa Stanford ASSISTANT MANAGER DIGITAL/PRINT Rebecca Doshi SENIOR CONTENT SPECIALISTS Steve Forrester, Antoinette Hodal, Lori Murphy, Anthony Rosen CONTENT SPECIALISTS Jacob Hedrick, Kimberly Oster

DESIGN DIRECTOR Beth Rakouskas DESIGN MANAGING EDITOR Marcy Atarod SENIOR DESIGNER Chrystal Smith DESIGNER Christina Aycock GRAPHICS MANAGING EDITOR Alberto Cuadra GRAPHICS EDITOR Nirja Desai SENIOR SCIENTIFIC ILLUSTRATORS Valerie Altounian, Chris Bickel, Katharine Sutliff SCIENTIFIC ILLUSTRATOR Alice Kitterman INTERACTIVE GRAPHICS EDITOR Jia You SENIOR GRAPHICS SPECIALISTS Holly Bishop, Nathalie Cary PHOTOGRAPHY MANAGING EDITOR William Douthitt PHOTO EDITOR Emily Petersen IMAGE RIGHTS AND FINANCIAL MANAGER Jessica Adams

SENIOR EDITOR, CUSTOM PUBLISHING Sean Sanders: 202-326-6430 ASSISTANT EDITOR, CUSTOM PUBLISHING Jackie Oberst: 202-326-6463 ASSOCIATE DIRECTOR, BUSINESS DEVELOPMENT Justin Sawyers: 202-326-7061 science_advertising@aaas.org ADVERTISING PRODUCTION OPERATIONS MANAGER Deborah Tompkins SR. PRODUCTION SPECIALIST/GRAPHIC DESIGNER Amy Hardcastle SR. TRAFFIC ASSOCIATE Christine Hall DIRECTOR OF BUSINESS DEVELOPMENT AND ACADEMIC PUBLISHING RELATIONS, ASIA Xiaoying Chu: +86-131 6136 3212, xchu@aaas.org COLLABORATION/CUSTOM PUBLICATIONS/JAPAN Adarsh Sandhu +81532-81-5142 asandhu@aaas.org EAST COAST/E. CANADA Laurie Faraday: 508-747-9395, FAX 617-507-8189 WEST COAST/W. CANADA Lynne Stickrod: 415-931-9782, FAX 415-520-6940 MIDWEST Jeffrey Dembksi: 847-498-4520 x3005, Steven Loerch: 847-498-4520 x3006 UK EUROPE/ASIA Roger Goncalves: TEL/FAX +41 43 243 1358 JAPAN Kaoru Sasaki (Tokyo): +81 (3) 6459 4174 kasaki@aaas.org

GLOBAL SALES DIRECTOR ADVERTISING AND CUSTOM PUBLISHING Tracy Holmes: +44 (0) 1223 326525 CLASSIFIED advertise@sciencecareers.org SALES MANAGER, U.S., CANADA AND LATIN AMERICA SCIENCE CAREERS Claudia Paulsen-Young: 202-326-6577/ EUROPE/ROW SALES Sarah Lelarge SALES ADMIN ASSISTANT Kelly Grace +44 (0) 1223 326528 JAPAN Miyuki Tani(Osaka): +81 (6) 6202 6272 mtani@aaas.org CHINA/TAIWAN Xiaoying Chu: +86-131 6136 3212, xchu@aaas.org GLOBAL MARKETING MANAGER Allison Pritchard DIGITAL MARKETING ASSOCIATE Aimee Aponte

AAAS BOARD OF DIRECTORS, CHAIR Barbara A. Schaal PRESIDENT Susan Hockfield PRESIDENT-ELECT Margaret A. Hamburg CHIEF EXECUTIVE OFFICER Rush D. Holt BOARD Cynthia M. Beall, May R. Berenbaum, Carlos J. Bustamante, Kaye Husbands Fealing, Stephen P.A. Fodor, S. James Gates, Jr., Michael S. Gazzaniga, Laura H. Greene, Mercedes Pascual

SUBSCRIPTION SERVICES For change of address, missing issues, new orders and renewals, and payment questions: 866-434-AAAS (2227) or 202-326-6417, FAX 202-842-1065. Mailing addresses: AAAS, P.O. Box 96178, Washington, DC 20090-6178 or AAAS Member Services, 1200 New York Avenue, NW, Washington, DC 20005

INSTITUTIONAL SITE LICENSES 202-326-6730 REPRINTS: Author Inquiries 800-635-7181 COMMERCIAL INQUIRIES 803-359-4578 PERMISSIONS 202-326-6765, permissions@aaas.org AAAS Member Central Support 866-434-2227 www.aaas.org/membercentral.

Science serves as a forum for discussion of important issues related to the advancement of science by publishing material on which a consensus has been reached as well as including the presentation of minority or conflicting points of view. Accordingly, all articles published in Science—including editorials, news and comment, and book reviews—are signed and reflect the individual views of the authors and not official points of view adopted by AAAS or the institutions with which the authors are affiliated.

INFORMATION FOR AUTHORS See www.sciencemag.org/authors/science-information-authors

BOARD OF REVIEWING EDITORS

(Statistics board members indicated with \$)

Adriano Aguzzi, *University of Zurich*
Takuzo Aida, *University of Tokyo*
Leslie Aiello, *Werner-Green Foundation*
Judith Allen, *University of Manchester*
Sebastian Amigorena, *Institut Curie*
Meinrat O. Andreie, *Max Planck Inst. Mainz*
Paola Arlotta, *Harvard U.*
Johan Auwerx, *EPFL*
David Awshalom, *U. of Chicago*
Clare Baker, *U. of Cambridge*
Nenad Ban, *ETH Zürich*
Franz Bauer, *Pontificia Universidad Católica de Chile*
Ray H. Baughman, *U. of Texas at Dallas*
Carlo Beenakker, *Leiden U.*
Kamran Behnia, *ESPCI*
Yasmine Belkaid, *NIAID, NIH*
Philip Benfey, *Duke U.*
Gabriele Berger, *WIB*
Bradley Bernstein, *Massachusetts General Hospital*
Peer Bork, *EMBL*
Chris Bowler, *École Normale Supérieure*
Ian Boyd, *U. of St. Andrews*
Emily Brodsky, *U. of California, Santa Cruz*
Ron Brookmeyer, *U. of California, Los Angeles (S)*
Christian Büchel, *UKE Hamburg*
Dennis Burton, *The Scripps Res. Inst.*
Carter Tribley Butts, *U. of California, Irvine*
Gyorgy Buzsaki, *New York School of Medicine*
Blanch Capel, *Duke U.*
Mats Carlsson, *U. of Oslo*
Ib Chorkendorff, *Denmark TU*
James J. Collins, *MIT*
Robert Cook-Deegan, *Arizona State U.*
Lisa Cousens, *Oregon Health & Science U.*
Anne Cowan, *Walter & Eliza Hall Inst.*
Roberta Croce, *U. of Amsterdam*
Janet Currie, *Princeton U.*
Jeff L. Dangl, *U. of North Carolina*
Tom Daniel, *U. of Washington*
Chiara Darao, *Caltech*
Nicolas Dauphas, *U. of Chicago*
Frans de Waal, *Emory U.*
Stanislas Dehaene, *Collège de France*
Robert Desimone, *MIT*
Claude Desplan, *New York U.*
Sandra Diaz, *Universidad Nacional de Córdoba*
Dennis Discher, *U. of Pennsylvania*
Gerald W. Dorn II, *Washington U. in St. Louis*
Jennifer A. Doudna, *U. of California, Berkeley*
Bruce Dunn, *U. of California, Los Angeles*
William Dunphy, *Caltech*
Christopher Dye, *WHO*
Todd Ehlers, *U. of Tübingen*
Jennifer Elisseeff, *Johns Hopkins U.*
Tim Elston, *U. of North Carolina at Chapel Hill*
Barry Everitt, *U. of Cambridge*
Vanessa Ezenwa, *U. of Georgia*
Ernst Fehr, *U. of Zürich*
Anne C. Ferguson-Smith, *U. of Cambridge*
Michael Feuer, *The George Washington U.*
Toren Finkel, *NHBLI NIH*
Kate Fitzgerald, *U. of Massachusetts*
Peter Fratzl, *Max Planck Inst. Potsdam*
Elaine Fuchs, *Rockefeller U.*
Eileen Furlong, *EMBL*
Jay Gallagher, *U. of Wisconsin*
Daniel Geschwind, *U. of California, Los Angeles*
Karl-Heinz Glassmeier, *TU Braunschweig*
Ramon Gonzalez, *Rice U.*
Elizabeth Grove, *U. of Chicago*
Nicolas Gruber, *ETH Zürich*
Kip Guy, *U. of Kentucky College of Pharmacy*
Taekjip Ha, *Johns Hopkins U.*
Christian Haass, *Ludwig Maximilians U.*
Sharon Hammes-Schiffer, *U. of Illinois at Urbana-Champaign*
Wolf-Dietrich Hardt, *ETH Zürich*
Michael Hasselmo, *Boston U.*
Martin Heimann, *Max Planck Inst. Jena*
Yki Heliariutta, *U. of Cambridge*
Janet G. Hering, *Swiss Fed. Inst. of Aquatic Sciences & Technology*
Kai-Uwe Hinrichs, *U. of Bremen*
David Hochschild, *U. of Cambridge*
Lora Hooper, *UT Southwestern Medical Ctr. at Dallas*
Fred Hughson, *Princeton U.*
Randall Hulet, *Rice U.*
Auke Ijspeert, *EPFL*
Stephen Jackson, *UGS Southwest Climate Science Ctr.*
Seema Jayachandran, *Northwestern U.*
Kai Johnson, *EPFL*
Peter Jonas, *Inst. of Science & Technology Austria*
Matt Kaeberlein, *U. of Washington*
William Kaelin Jr., *Dana-Farber Cancer Inst.*
Daniel Kammen, *U. of California, Berkeley*
Abby Kavner, *U. of California, Los Angeles*
Hitoshi Kawai, *U. of Tokyo*
Masashi Kasai, *U. of Tokyo*
V. Naray Kim, *Seoul Nat. U.*
Robert Kingston, *Harvard Medical School*
Etienne Koechlin, *École Normale Supérieure*
Alexander Kolodkin, *Johns Hopkins U.*
Thomas Langer, *U. of Cologne*
Mitchell A. Lazar, *U. of Pennsylvania*
David Lazer, *Harvard U.*
Thomas Lecuit, *IBDM*
Virginia Lee, *U. of Pennsylvania*
Stanley Lemon, *U. of North Carolina at Chapel Hill*
Ottoline Leyser, *U. of Cambridge*
Wendell Lim, *U. of California, San Francisco*
Marcia C. Linn, *U. of California, Berkeley*
Jianguo Liu, *Michigan State U.*
Luis Liz-Marzán, *CIC biomaGUNE*
Jonathan Losos, *Harvard U.*
Ke Lu, *Chinese Acad. of Sciences*
Christian Lüscher, *U. of Geneva*
Laura Machesky, *King's College Research Beatson Inst.*
Anne Magurran, *U. of St. Andrews*
Oscar Marin, *King's College London*
Charles Marshall, *U. of California, Berkeley*
Christopher Marx, *U. of Idaho*
C. Robertson McClung, *Dartmouth College*
Rodrigo Medellín, *U. of Mexico*
Graham Medley, *London School of Hygiene & Tropical Med.*
Jane Memmott, *U. of Bristol*
Tom Misteli, *NCI, NIH*
Yasushi Miyashita, *U. of Tokyo*
Mary Ann Moran, *U. of Georgia*
Richard Morris, *U. of Edinburgh*
Alison Motsinger-Reif, *NC State U. (S)*
Daniel Neumark, *U. of California, Berkeley*
Kitty Nijmeijer, *U. of Eindhoven*
Helga Nowotny, *Austrian Council*
Rachel O'Reilly, *U. of Warwick*
Joe Orenstein, *U. of California, Berkeley & Lawrence Berkeley Nat. Lab.*
Harry Orr, *U. of Minnesota*
Pilar Ossorio, *U. of Wisconsin*
Andrew Oswald, *U. of Warwick*
Isabella Pagan, *Istituto Nazionale di Astrofisica*
Margaret Palmer, *U. of Maryland*
Steve Palumbi, *Stanford U.*
Jane Parker, *Max Planck Inst. Cologne*
Giovanni Parmigiani, *Dana-Farber Cancer Inst. (S)*
John H. J. Petrin, *Memorial Sloan Kettering Cancer Center*
Samuel Pfaff, *Salk Inst. for Biological Studies*
Kathrin Plath, *U. of California, Los Angeles*
Martin Plenio, *Ulm U.*
Albert Polman, *FOM Institute for AMOLF*
Elvira Polozanska, *Alfred-Wegener-Inst.*
Philippe Poulin, *CNRS*
Jonathan Pritchard, *Stanford U.*
David Randall, *Colorado State U.*
Sarah Reisman, *Caltech*
Félix A. Rey, *Institut Pasteur*
Trevor Robbins, *U. of Cambridge*
Amy Rosenzweig, *Northwestern U.*
Mike Ryan, *U. of Texas at Austin*
Mitinori Saitou, *Kyoto U.*
Shimon Sakaguchi, *Osaka U.*
Miquel Salmeron, *Lawrence Berkeley National Lab*
Jürgen Sandkuhler, *Medical U. of Vienna*
Alexander Schier, *Harvard U.*
Wolfram Schlenker, *Columbia U.*
Susannah Scott, *U. of California, Santa Barbara*
Vladimir Shalaev, *Purdue U.*
Beth Shapiro, *U. of California, Santa Cruz*
Jay Shendure, *U. of Washington*
Brian Shoichet, *U. of California, San Francisco*
Robert Siliciano, *Johns Hopkins School of Medicine*
Uri Simonsohn, *U. of Pennsylvania*
Alison Smith, *Johns Innes Centre*
Richard Smith, *U. of North Carolina at Chapel Hill (S)*
Mark Smyth, *QIMR Berghofer*
Pam Soltis, *U. of Florida*
John Speakman, *U. of Aberdeen*
Allan C. Spradling, *Carnegie Institution for Science*
Eric Steig, *U. of Washington*
Paula Stephan, *Georgia State U. & Nat. Bureau of Economic Res.*
V. S. Subrahmanian, *U. of Maryland*
Ira Tabas, *Columbia U.*
Sarah Teichmann, *U. of Cambridge*
Shubha Tole, *Inst. of Fundamental Research*
Wim van der Putten, *Netherlands Inst. of Ecology*
Bert Vogelstein, *Johns Hopkins U.*
David Wallach, *Weizmann Inst. of Science*
Jane-Ling Wang, *U. of California, Davis (S)*
David Waxman, *Fudan U.*
Jonathan Weissman, *U. of California, San Francisco*
Chris Wikle, *U. of Missouri (S)*
Terrie Williams, *U. of California, Santa Cruz*
Ian A. Wilson, *The Scripps Res. Inst. (S)*
Timothy D. Wilson, *U. of Virginia*
Yu Xie, *Princeton U.*
Jan Zaanen, *Leiden U.*
Kenneth Zaret, *U. of Pennsylvania School of Medicine*
Jonathan Zehr, *U. of California, Santa Cruz*
Len Zon, *Boston Children's Hospital*
Maria Zuber, *MIT*

Science matters for the census

In 1787, James Madison conceived of a scientific method to distribute political power in the United States. He proposed a decennial census of population to ensure that the membership of the House of Representatives would reflect the pattern of growth of the fledgling nation. From that first census emerged a whole system of social and economic measurement serving the country. As the 2020 U.S. census approaches, the science in the census—and the value of the census for science—can easily be threatened by politics.

How does the census matter for science? For most of the policy implications of the biomedical sciences, the census provides the benchmark information. Cancer registries produce their epidemiological importance when they are matched to population distributions. When the higher mortality of middle-aged whites was discovered, its value was discerned only by comparing death counts to the population totals in different age groups. Assessing the harmful impacts of toxic waste in water systems and patterns of water scarcity rests on population distributions. Because the social sciences explicitly focus on human behavior, their studies cannot proceed very far without a decennial census. It is unrivaled in revealing the variation in racial, cultural, ethnic, and age groups at the most granular level possible. Social scientists can track the emergence of new groups at very fine geographical detail, including congressional jurisdictions, place boundaries, and numerous other jurisdictional boundaries.

However, just as the census matters for science, so too does science matter for the census. The scientific method requires objectivity in gathering data, devotion to explicit standards for findings, commitment to wide dissemination of results, and norms of self-criticism regarding conclusions. Many of these principles are foundational to the decennial census. Objective measurements, tested through years of randomized

experiments, are key. Whenever possible, data-collection methods attempt to remove bias in responses due to nonobjective influences. Unusual effort is made to attain full participation so as to reduce self-selection biases. Documentation of data processing permits external critique. Formal estimation of the errors remaining in the collected data is presented, subjecting the census to open critique. Scores of evaluation studies are conducted post-census to provide insight into the weaknesses of the census. All of this self-criticism is freely distributed to the public.

Mistaking the decennial census as only an act of politics, solely useful for updating the distribution of political power, threatens the scientific basis of its credibility. The scientific components of the census should not be undermined by the last-minute addition of untested questions (as is currently proposed by the U.S. Department of Justice), a lack of public-communication campaigns that aid the participation of newly arrived residents (which arises from insufficient funding), or attempts to politicize the act of census taking.

Census data are used by scientists to draw representative samples for social and medical research and analyses and by the business sector to identify areas with different levels of demand for goods and services. It permits forecasts of residential displacement, rural to urban migration, social and political cleavages, and other features of the society and the economy. In the United States, the census is the only event in which everyone is asked to participate. In that sense, it is a national ceremony, renewing the population picture and providing objective evidence for the growth of subgroups. Although the constitutional origin of the U.S. census was explicitly political, the process has been protected from political interference and propelled forward by allegiance to scientific norms. Let's keep it that way.

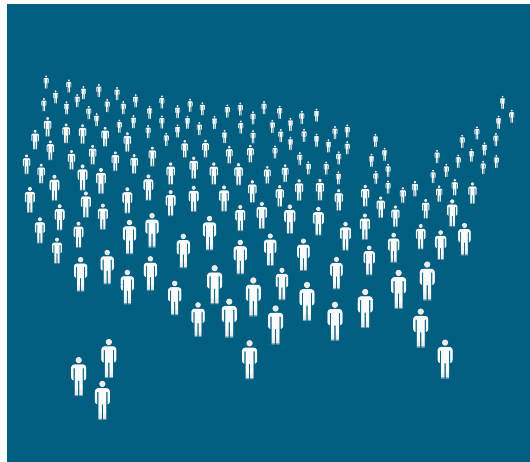
—Robert M. Groves and Steven H. Murdock



Robert M. Groves is the Gerald Campbell, S.J. Professor, Department of Mathematics and Statistics and Department of Sociology, and is provost at Georgetown University, Washington, DC, USA. He is a former director of the Census Bureau. bgroves@georgetown.edu



Steven H. Murdock is the Allyn R. and Gladys M. Cline Professor in Sociology, Rice University, Houston, TX, USA, and is a former director of the Census Bureau. steve.h.murdock@rice.edu



“...the science in the census...can easily be threatened by politics.”

“We’re in the science business ... and so I will have our agency certainly working in this field.”

U.S. Health and Human Services (HHS) Secretary Alex Azar, saying HHS will support research on gun violence, after a gunman murdered 17 people at a Florida high school.

IN BRIEF

Edited by **Jeffrey Brainard**

PUBLIC HEALTH

Brain ailment found in envoys to Cuba



Some diplomats working in the U.S. Embassy in Havana suffered neurological symptoms.

U.S. diplomats who fell ill in Cuba are victims of a newly identified neurological syndrome, according to brain researchers at the University of Pennsylvania (UPenn) who conducted brain scans and cognitive tests on 21 of the afflicted. But the team, which described its results last week in *The Journal of the American Medical Association*, was unable to shed light on the malady's mysterious cause. From late 2016 through August 2017, as many as 24 U.S. government personnel reported symptoms ranging from vertigo and sleeplessness to cognitive impairment. Fueling speculation about a sonic weapon, many described hearing loud sounds and feeling pressure in their ears before the onset of symptoms. Douglas Smith, director of UPenn's Center for Brain Injury and Repair, says it's "premature" to conclude that the diplomats were deliberately targeted in any way. But Smith and his colleagues believe an unidentified exposure triggered a "constellation" of neurological symptoms consistent with a concussion. Some neuroscientists argue that stress experienced by the diplomats is the likeliest explanation. But the UPenn group is convinced that the cases are a disease cluster.

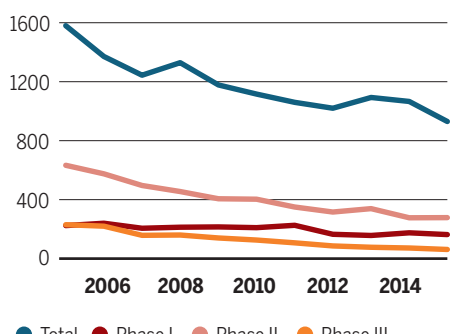
Why astronomers don't publish

SPACE SCIENCE | Researchers get quite creative when explaining why they haven't published results several years after using the world's top telescopes, a recent study has shown. The most common excuse: We need more time. Staff at the European Southern Observatory (ESO), based in Garching, Germany, were concerned that up to 50% of teams didn't publish after several years. Observatory staff identified researchers on 1278 projects who used ESO's telescopes between 2006 and 2013 but hadn't published by April 2016. They sent the project teams a questionnaire offering options to explain their lack of output. More than half of the teams selected reasons including: They actually had published and the papers were missed, they didn't get the quality or quantity of data expected, they didn't have the resources to process the data, or the results were inconclusive. The most common response, cited by 24% of respondents, was, "I am still working on the data." The good news? ESO estimates that 75% of teams will eventually publish, given the pace to date—but it is also reviewing its selection processes for teams applying for telescope time.

A squeeze on clinical trials

BIOMEDICINE | An analysis finds a troubling decline in the number of clinical trials funded by the U.S. National Institutes of Health (NIH) over a decade when the agency's budget stayed flat. NIH funded 1580 trials in 2005, but by 2015 that figure had dropped 41% to 930. The drop was

Number of NIH-funded clinical trials





The Tesla Roadster and its mannequin driver "Starman" began a long orbit.

Orbiting SpaceX Roadster is unlikely to crash to Earth

Spacex CEO Elon Musk scored a publicity coup by launching his Tesla Roadster into an orbit around the sun on 6 February aboard the company's inaugural Falcon Heavy rocket. Researchers have since calculated there's a very slim chance, 6% in the next million years, that the space-traveling sports car will make a fiery return to Earth by burning up in the atmosphere. The Roadster is now heading beyond the

orbit of Mars, and an orbital dynamics team led by Hanno Rein of the University of Toronto in Canada decided to map out the car's future path. It will repeatedly cross the orbits of Mars, Earth, and Venus, with many close encounters. These will slightly alter the car's trajectory, making its path impossible to precisely predict in the long term. But the team was able to calculate probabilities of collisions, including a 2.5% chance of hitting Venus.

sharpest for phase II and III studies, which are mid- and late-stage tests of therapies, according to the study of clinicaltrials.gov data published on 1 February in *Clinical Trials*. NIH-funded trials are important because they often evaluate drugs and treatments that companies don't view as potentially profitable and because the researchers are expected to be impartial, say the authors at the Johns Hopkins University Bloomberg School of Public Health in Baltimore, Maryland. NIH officials attribute the changes to the rising costs of clinical trials during a time when the agency's buying power fell 20%. But NIH received large budget increases the past 2 years, which could mean a future uptick in trials.

Concussion blood test approved

MEDICAL TESTING | The U.S. Food and Drug Administration (FDA) on 14 February approved the first blood test to help evaluate whether an adult has suffered a concussion. It promises to reduce the number of computerized tomography (CT) scans physicians order for these patients. Today, athletes, soldiers, and others with concussion symptoms are routinely given a CT scan, but no signs of brain tissue damage are found in about 90% of cases. By using the blood test, which predicts with 99.6% accuracy when no signs of brain damage will be found on a CT scan, doctors can avoid prescribing unnecessary scans,

which are expensive and expose people to significant levels of radiation. The blood test, developed by Banyan Biomarkers Inc., based in San Diego, California, detects two proteins that are released into the blood after traumatic brain injury. FDA evaluated data from a multicenter clinical study of 1947 individual blood samples from adults with suspected traumatic brain injury and reviewed the product's performance by comparing blood test results with CT scans. The U.S. Department of Defense provided more than \$100 million to support the test's development.

Patent fight over cattle DNA

AGRICULTURAL GENETICS | In a case reminiscent of the ultimately thwarted attempt to patent human genes linked to breast cancer, a legal war is brewing in Australia over a sweeping bid by a U.S. consortium to patent methods for identifying desirable bovine traits such as extra fat deposits and a faster growth rate. If granted, the patent would threaten the ability of Australia's cattle business to improve its stock, harming its international competitiveness, according to industry group Meat and Livestock Australia (MLA). The group is challenging the patent sought by Cargill USA, an agricultural company based in Minneapolis, Minnesota, and Branhaven LLC, a genetic technology investment firm. On 9 February, MLA won a minor victory

BRAIN RHYTHMS

The rap on consciousness

After previously rhyming on evolution and climate, science-themed rap artist Baba Brinkman brings his latest show, *Rap Guide to Consciousness*, to New York City's SoHo Playhouse in March and April, following performances in London and Edinburgh. His new lyrics draw on cognitive neuroscience and philosophy.

"Real Recognize Real" considers the idea that consciousness evolved from physical processes.

It took a billion years to make a brain and connect it up

*Eighty billion neurons in a network
Each with 7000 synaptic connectors
A minimum of 50 trillion intersections
Such a pretty materialistic picture*

"Can't Stop" ponders whether humans have free will—and whether it really matters in the end.

*If every decision is made in a part of my brain that's invisible to me
That's "will," but with a subliminal origin,
I'm not thinkin' it's too "free"
But if not me, who was it that chose to bust the rhyme?
And if the clock was reset,
I bet I could not have done otherwise*



Using drones, scientists obtained a more accurate count of these fake plastic terns than human observers did.

when a federal court judge in Melbourne, Australia, upheld aspects of MLA's complaint but allowed the consortium to amend the patent application.

Drones excel at counting wildlife

WILDLIFE CONSERVATION | Scientists pitted humans against drones in an epic test of birdwatching—and the drones came out on top. Seasoned birdwatchers were asked to count thousands of fake plastic terns spread out on a beach in south Australia, from a distance typical for

birdwatching. At the same time, scientists flew a drone overhead to take pictures. People with little birdwatching experience were asked to count the birds in the photos—and they were considerably better than the experts on the ground. So was an algorithm trained to identify the birds. Writing last month in *Methods in Ecology and Evolution*, Jarrod Hodgson at the University of Adelaide in Australia and his colleagues said drones could save ecologists time in the field and allow them to survey wildlife populations without disturbing sensitive breeding sites.

THREE Qs

E. O. Wilson wants to save rare Florida tree

Government officials, conservationists, and researchers—including renowned Harvard University biologist Edward O. Wilson—will gather next week in Bristol, Florida, to discuss the fate of the Florida torreya (*Torreya taxifolia*). Also known as stinking cedar, it is considered by many to be the most endangered tree species in the world. A deadly fungus has killed all but about 1000 trees, most of which grow along a 56-kilometer stretch of Florida's Apalachicola River, and the pathogen has already infected the remaining trees. *Science* caught up with Wilson, who has been called “the father of biodiversity,” on the eve of his trip to the meeting.

Q: When did you first find out the Florida torreya was in trouble?

A: In July 1957. I was collecting ants up and down the Florida peninsula and panhandle. At Torreya State Park, we got a lot of good stuff. But we noticed that this marvelous endemic [tree] from the ice age was wilted. So, this is how it began, and now it's on its last legs.

Q: What makes this tree and region special to you?

A: It's where I come from, where I spent my boyhood. Not exactly there, but an area like that. I go to somewhere on the Gulf Coast several times a year, as I've been active in doing research to propose a new national

park in the Mobile-Tensaw River delta [in Alabama] and to promote the setting up of a biodiversity corridor [that] would stretch from somewhere around Tallahassee and along the Gulf Coast as far as Louisiana. The Apalachicola River might be part of that.

Q: Can this tree be saved?

A: There is an out. The torreya has become a reasonably popular ornamental, and it's being widely distributed. And in the return of the American chestnut, where there seemed to be no hope after it went completely extinct—therein lies the story of what could happen to the torreya. I'd like to see the torreya become a symbol and an issue that people are interested in.

Early origins for land plants

EVOLUTION | The oldest known fossils of land plants are 420 million years old, but pond scum first made landfall almost 100 million years earlier, researchers have now estimated. That conclusion, reported this week in the *Proceedings of the National Academy of Sciences*, suggests plants may have had a greater role in the diversification of early animals than previously thought. Using previous genetic-based “molecular clock” approaches, scientists could only approximate the date when freshwater green algae first colonized land; uncertainties about how the terrestrial plant family tree branched early in its evolutionary history prevented more precise estimates. Now, by using a mix of computational approaches for analyzing molecular clock data and estimating plant ages under different evolutionary scenarios, paleobiologist Philip Donoghue from the University of Bristol in the United Kingdom and his colleagues found that plants made landfall about 500 million years ago—during the Cambrian period, when the development of multicellular animal species took off. “The study has important global implications, because we know early plants cooled the climate and increased the oxygen level in the Earth’s atmosphere,” conditions that supported terrestrial animal life, says Tim Lenton, an earth system scientist at the University of Exeter in the United Kingdom.

New tool tracks trial results

CLINICAL RESEARCH | Researchers this week launched a new online tool to hold clinical trial sponsors accountable for publishing results from their studies.

FDAAA TrialsTracker, developed by a team at the University of Oxford in the United Kingdom and described in a 16 February paper on the preprint server bioRxiv, pulls information from the U.S. National Library of Medicine's database clinicaltrials.gov and determines which of the listed trials are due to report results under the Food and Drug Administration Amendments Act of 2007. A federal rule that took effect in January 2017 expanded and clarified that law, which requires sponsors to report a study's results within 12 months of completion. As *Science* went to press, more than 90% of the 114 listed trials were in compliance.

Polish logging suffers legal blow

FOREST CONSERVATION | A major environmental conflict—the logging of a primeval forest in Poland—may be nearing an end. A legal opinion developed for the European Court of Justice declared this week that controversial logging by the country's Forest Service is illegal. The court is expected to back the legal opinion, developed by the court's advocate general, Yves Bot, when it issues a final ruling, possibly next month. Poland's minister of the environment indicated he will accept the court's final ruling. The Białowieża Forest in eastern Poland is a UNESCO World Heritage site and the largest remnant of a forest that once covered lowland Europe. In 2016, Polish authorities approved a tripling of logging, saying that it was necessary to fight an outbreak of spruce bark beetles. Scientists argued that the logging would cause more harm than good. Environmental groups filed a complaint with the European Commission, which took the case to the court, charging that Poland was in violation of EU laws to protect habitat and birds (*Science*, 8 December 2017, p. 1240). Bot's opinion agrees, also noting that Poland had not adequately assessed the impact of the logging.



Białowieża Forest, the subject of a court case over logging, hosts a diverse array of plants and wildlife.

2018 AAAS MEETING

A spotlight on research and policy

Some 7000 attendees, sponsors, and reporters traveled to Austin for the annual meeting of AAAS, which publishes *Science*. Some highlights are below.

Infants primed for visual language

Babies are as primed to learn a visual language as they are a spoken one. Rain Bosworth, a psychologist at the University of California, San Diego, tracked the eye movements of 6-month-olds and 1-year-olds as they observed a hand "fingerspelling"—spelling out words with individually signed letters. She and colleagues found that the 6-month-old babies, who had never seen sign language before, favored cleanly formed letters, whereas the 12-month-olds did not show a preference. That and other evidence suggest a critical developmental window for babies to pick up visual languages, similar to the window for acquiring a spoken language documented by previous research. As 95% of deaf children are born to hearing parents, they are at risk for developmental delays because they need exposure to sign language early on, the scientists say.



Deaf children may have a critical developmental window during which they can pick up sign language.

Trust in scientists remains high

Amid political turmoil over science, many researchers worry that Americans have lost faith in them. But since 1979, surveys have shown that roughly seven in 10 Americans believe the effects of scientific research are more positive than negative for society. Communications expert John Besley of Michigan State University in East Lansing talked with attendees about trust in science. Afterward, *Science* asked Besley whether he expects that trust to decline. "There's no evidence there to suggest that," he said. "If anything, I'm amazed how stable Americans' views about science have been over the last 10 or 20 years. It's interesting, too, because other things haven't been stable. Trust in the medical community has come down over time, interest in environmental pollution has come down over time, and worry about various technologies has gone up. Given how positively people view science and scientists, stability is a good thing."

Biden plugs cancer 'moonshot'

In a forceful speech, former U.S. Vice President Joe Biden called for building the cancer moonshot he started while in office, an effort to accelerate progress in cancer research and treatment. "It's the one way to convince the American people that we can embark on so many other astonishing efforts that are within our capacity to handle," he said. Biden touted signs of progress but also called on scientists to focus cancer research on patient health rather than professional advancement. A proprietary culture of medicine gets in the way of sharing data that could lead to better diagnosis and cures, he said. "Writ large, you scientists don't share well." Biden also criticized President Donald Trump's administration and other national leaders for denying scientific findings and issued a passionate call to double or even triple federal science funding.



ARCHAEOLOGY

Europe's first artists were Neandertals

Spanish cave paintings date to before modern humans arrived in region

By Tim Appenzeller

For once, the fractious scientists who study the Neandertals agree about something: that a study on p. 912 has dropped a bombshell on their field, by presenting the most persuasive case yet that our vanished cousins had the cognitive capacity to create art. Once seen as brute cavemen, Neandertals have gained stature as examples of sophisticated technology and behavior have turned up in their former territory across Europe. But few researchers imagined them engaging in one of the most haunting practices in human prehistory: creating paintings—vehicles for symbolic expression—in the darkness of caves.

Now, archaeologists may have to accept that Neandertals were the original cave artists. A team of dating experts and archaeologists reports that simple creations—the outline of a hand, an array of lines, and a painted cave formation—from three caves in Spain all date to more than 64,800 years ago, at least 20,000 years before modern humans reached Europe. Shells from a fourth Spanish cave, pigment-stained and pierced as if for use as body ornaments, are even older, a team including several of the same researchers reports in a second paper, in *Science Advances*. Some researchers had already attributed the shells to Neandertals, but the new dates leave little doubt.

The shells amount to only a handful and might have been perforated naturally, causing some researchers to question their significance. Not so the paintings. “Most of my colleagues are going to be stunned,” says Jean-Jacques Hublin of the Max Planck Institute (MPI) for Evolutionary Anthropology in Leipzig, Germany, who was not involved in either study. “People saw cave painting as a major gap between Neandertals and modern humans. This discovery reduces the distance.”

Just how much is the question. João Zilhão of the University of Barcelona in Spain, an author of both papers, has spent years pressing the case that Neandertals were the mental equals of modern humans, and he sees the newly dated paintings and shells as full vindication. “I’d like to see the expression on some faces as they read the papers,” he says. Hublin, who accepts that Neandertals were cognitively sophisticated but believes their cultural achievements fell short of modern humans, is impatient with what he sees as Zilhão’s absolutism. “What is the goal—to say that Neandertals were just like modern humans? That is a very far stretch.”

And some researchers, trying to absorb findings that fly in the face of their long-time view of Neandertals, aren’t sure what to think. “I find [it] incredibly challenging,” says Shannon McPherron of MPI, whose own work has cast doubt on claims that Neandertals buried their dead or made systematic use

of fire. The new dates, he says, have “shattered my model of Neandertal behavior.”

With rare exceptions, cave art could not be directly dated until recently, making it hard to challenge the assumption that the artists were modern humans. For one thing, most cave paintings lack organic residues that can be dated by the radioactive decay of carbon isotopes. But in the early 2000s, scientists devised an alternative dating strategy based on the thin layer of calcite that can form when groundwater seeps down a cave wall and across a painting. The water contains a smattering of uranium atoms that decay into a distinctive isotope of thorium, which accumulates in the calcite over millennia. Grind a few flecks of calcite off a cave painting, measure the ratio of uranium and thorium isotopes, and you can read out the age of the calcite. The underlying painting must be at least that old—and could be much older.

It’s not easy, says MPI’s Dirk Hoffmann, who was among the first to apply uranium-thorium dating to cave paintings and is the first author of both papers. “The challenge is to find these calcites. You need a wall where you occasionally have a little water coming in that deposits calcite without damaging the painting.” Then comes the “nerve-wracking” task of scraping off the calcite without marring the pigment, and the painstaking analysis of a sample of few milligrams. Hoffmann and his colleagues applied the technique to

In Spain's La Pasiega Cave, a set of lines (center) painted by Neandertals was embellished by later artists.

cave art across Italy, France, Portugal, and Spain. Most of the dates fell within the European reign of modern humans, which began 40,000 to 45,000 years ago. But in the three cases described in *Science*, the paintings are far too old to have been made by them.

"To me the biggest question is how good is the dating," says Harold Dibble of the University of Pennsylvania, who has long challenged claims of sophisticated Neandertal behavior. But others see little reason for doubt. Multiple samples from each painting yielded consistent results, and in several cases Hoffmann and his colleagues analyzed scrapings from increasing depths in the calcite layer. The dates grew older as they approached the pigment, adding credibility. "I am confident that the [uranium-thorium] dates are correct," says Rainer Grün, an expert in the technique at Griffith University in Nathan, Australia, who did not take part in the work.

Zilhão predicts that other cave paintings will prove equally ancient, if not more so. "This is just scratching the surface of an entirely new world." He cites two other finds as evidence of a long Neandertal tradition of art and ritual. One is a pair of corral-shaped structures, the larger one more than 6 meters across, assembled from broken stalagmites and scorched by fire, found by cavers more than 300 meters deep in Bruniquel Cave in France. In 2016, a French-led team reported in *Nature* that the structures were built some 175,000 years ago—presumably by Neandertals, perhaps for ritual purposes. And then there are the colored shells from Cueva de los Aviones, a sea cave in southern Spain, where Hoffmann's uranium-thorium dating of a calcite crust covering the objects has just yielded an age of more than 115,000 years.

But was this Neandertal artistic creativity equivalent to the art and symbolism practiced by modern humans? At sites across Africa, our direct ancestors were making shell beads and etching abstract designs into egg shells and minerals 80,000 years ago and more. Neandertal achievements were fully comparable, Zilhão insists, and to suggest otherwise implies a double standard.

Hublin disagrees. The startling new dates for the paintings "show that Neandertals had the same potential as modern humans in a number of domains," he acknowledges. But he and others see differences in cognition and culture that even the new research does not erase. And Hublin notes that soon after their arrival in Europe, "modern humans replaced [Neandertals], and there are reasons."

Like the gap between these two kinds of humans, the rift among Neandertal experts has narrowed. But it has not yet closed. ■

INFECTIOUS DISEASES

Worms living in your veins? Seventeen volunteers said 'OK'

A controversial study infects people with schistosomiasis to speed up drug and vaccine development

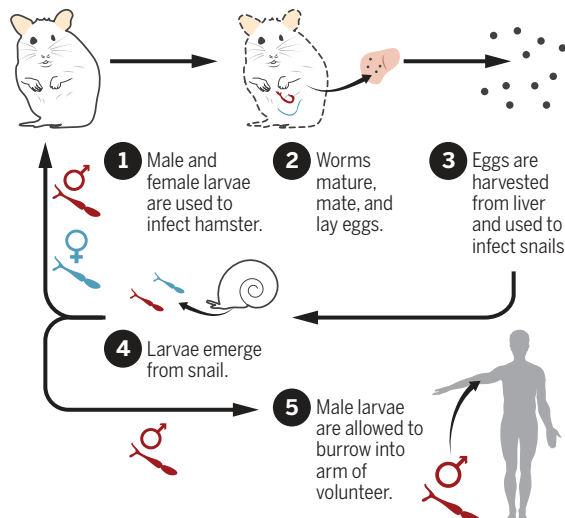
By Kai Kupferschmidt, in Leiden, the Netherlands

At 12:05 p.m. on a Thursday in February, a lab technician takes a six-well plate containing a solitary red snail and places it in a heated water bath under a strong light. The light and warmth signal hundreds of tiny larval parasites to stream out of the mollusk. Now, the clock starts ticking for Meta Roestenberg, an infectious disease physician here at Leiden University Medical Center. She has about 4 hours to launch a unique, controversial experiment in which she will let the parasites burrow into the arms of four healthy volunteers. If she waits too long, the larvae start to die.

Roestenberg and her colleagues are infecting people with *Schistosoma mansoni*, one of five tiny waterborne worm species that cause schistosomiasis, a disease that sickens millions of people in Africa, the Middle East, and Latin America and kills thousands each year. There is no schistosomiasis vaccine and only one old, inadequate drug, praziquantel, to treat it.

Parasites to the people

Researchers have long grown *Schistosoma mansoni* in the lab, using hamsters. Now, they are also infecting humans with the parasitic worms.



Infecting humans could help speed up the development of new interventions. Roestenberg has designed the experiment to prevent the parasites from reproducing, and she says the risk to volunteers is extremely low.

But not low enough, some scientists argue, because there is no guarantee that subjects will get rid of their parasites when the study is over. "I would not volunteer for this study and if I had a son or daughter who wanted to volunteer, I would recommend against it," says Daniel Colley, a schistosomiasis researcher at the University of Georgia in Athens.

At 1:05 p.m., the technician takes the plate out of the bath. The larvae are ready to be harvested. Viewed under a microscope, they move around frantically, like minipropellers. Another technician removes one drop, dilutes it, adds iodine to kill the parasites, and counts them. That allows the researchers to calculate how many are left in the well: 574. They need only 80 today, 20 per volunteer.

A snail population in an African lake could shed millions of these larvae into the water on

a single day, each equipped with a chemical sensor that lets it home in on humans entering the water. After penetrating the skin, they migrate to the liver, where they mature and mate. Male-female couples stay together and move to blood vessels in the bowel, where they can reside for years, shedding hundreds of eggs a day. Most eggs end up in urine and feces, and if they make their way back into the lake they may infect fresh snails. But some get trapped in the liver, kidneys, or spleen, causing damage and leading to pain, blood loss, malnutrition, and sometimes death.

Researchers in this same lab recreated the parasite's life cycle decades ago, with hamsters taking the place of

humans. That allowed them to produce and study *S. mansoni*. Now, Roestenberg wants to bring humans back into the mix. Field trials, especially of vaccines, are hugely expensive and complex, and the risk of failure is considerable. A controlled infection study can act as a gatekeeper, she says: "It gives you an indication whether something can work in humans or not."

Studies in which people are purposely infected with malaria, cholera, and flu are on the rise (*Science*, 20 May 2016, p. 882), but they haven't been done with schistosomiasis, in part because damage from the *S. mansoni* eggs can be irreversible. The goal of the current study, which began in early 2017, is to find out whether Roestenberg's infection model is safe; if so, she hopes to test a vaccine later this year.

At 1:35 p.m., Roestenberg walks to the room where the volunteers will be infected. She opens a transparent plastic container that contains epinephrine, antihistamines, and corticosteroids. "This is the emergency box," she says—in case a subject has a strong allergic reaction. None of the 13 volunteers infected so far has, although one who was infected with 30 larvae developed a strong fever. In another precaution, the volunteers have been tested to rule out risk factors



In nature, male and female *Schistosoma mansoni* worms pair up within the host.

such as HIV infection and pregnancy. In nature, people become infected with both male and female parasites, but Roestenberg uses only males, so there will be no eggs and thus, she says, no symptoms. And when the study ends in 12 weeks, the volunteers will be given praziquantel to cure them.

That drug, Colley emphasizes, is "not terribly effective." But Roestenberg says that even if it fails, volunteers needn't worry. "The ethics board asked me: 'If one worm survives even after multiple treatments, what will happen to that person?' And I said: 'They'll probably live to be 100.'" The board gave her its blessing. Colley agrees

the risk is low, but still, *S. mansoni* has an average life span of 5 to 10 years. "That is a long time to have something as ugly as a schistosome living in your blood vessels, putting out excrement and things."

At 2:15 p.m., Roestenberg huddles in a small meeting room with three colleagues. The worms are not drugs, but they need to be released for use just like an experimental drug would be. The scientists check numbers on some documents against data on a computer screen, then they sign a form. The experiment can begin.

Twenty minutes later, back in the infection room, the volunteers stretch out their arms so that a little metal cylinder, a few centimeters in diameter, can be taped to their skin. Carefully, an assistant pipettes a few drops of water, containing exactly 20 parasites, into each cylinder. The volunteers are nervous, but they say they are motivated. "I like the fact that the study is related to vaccines, because I've worked in that field before," says one, a young scientist. The woman next to him says she comes from East Africa and knows the disease firsthand. They will also be paid €1000 for their time.

Once infected, the volunteers will return to the lab every week so the research team can test their blood for a molecule called CAA, which the worms regurgitate from their stomachs. CAA's presence will indicate that the worms are still alive; in future trials, its absence might mean that a vaccine or drug has worked.

Some schistosomiasis scientists agree that the potential benefits justify the minimal risks. "My hope is that it would hugely accelerate identification of worthwhile candidate vaccines," says Alison Elliott of the London School of Hygiene & Tropical Medicine, who works at a joint Ugandan and U.K. research unit in Entebbe. She is interested in establishing the model there; people in Uganda, a country badly affected by schistosomiasis, might react differently to a vaccine if they were exposed to the worms in childhood, she explains. At a recent stakeholders' meeting, "Ethics and regulatory colleagues were very supportive of taking discussions of the model forward, and community representatives are already keen for the opportunity to volunteer!" Elliott added in an email.

"It's itching a little bit," one of the Leiden volunteers says 5 minutes into the exposure. After half an hour, when the infested water is removed from the volunteers' forearms, red spots reveal where the parasites have entered their new hosts. Then, close to 4 p.m., the clock stops ticking; the volunteers head home and Roestenberg and her colleagues go out for a coffee. ■

ENVIRONMENT

Bringing an Iranian oasis back from the dead

Water crisis and rising air pollution are stoking regional tensions

By Richard Stone, in Zabol, Iran

Sun-bleached skiffs lie in a jumble along the barren southern shore of Hamoun-e Puzak, a former lake. In the afternoon heat, Fata Morgana cliffs shimmer on the horizon. The boats aren't much use these days. Hamoun-e Puzak and two sister lakes are now seas of sand, and the marshes they supported have withered away.

"People would fish here. Children would swim here. No more," says Nayyerah Pourmollae, who heads the environment department of Sistan and Baluchestan province in southeastern Iran. The Hamoun wetlands, which once encompassed as much as 5800 square kilometers along Iran's border with Afghanistan and supported settlements stretching back 5 millennia, "are an ecological catastrophe," she says. On the Iranian side, villages are emptying. Winds in what has become a dust bowl ravage crops and sweep up pesticide residues and other pollutants. And a haven for migratory birds and other wildlife is vanishing.

But now, after years of bickering about which country is to blame, Iran and Afghanistan are discussing solutions.

Since 2014, the United Nations Development Programme (UNDP) has been crafting a restoration plan that would require Afghanistan to help restore the flow of the Helmand, the main river feeding the former wetlands, and Iran to overhaul its water management. And last month, experts from the two nations met in Paris for a workshop on transboundary water issues. The bilateral efforts hearten water researchers. As dire as the situation has become, "The Hamouns can be saved," says Farhad Yazdandoost, an expert on water resources management at Khajeh Nasir Toosi University of Technology in Tehran.

Water woes plague Iran. Precipitation is sparse in most areas and unreliable, but some of the worst scourges are self-inflicted. Hundreds of thousands of illegal



wells nationwide are depleting aquifers, for example, and scores of major dams are diverting water for irrigation. In one high-stakes initiative, the government is trying to save Lake Urmia, which covered about 5200 square kilometers at its peak but has largely evaporated (*Science*, 4 September 2015, p. 1044). The decline of the Hamouns, which lie in a poor border region beset by drug smugglers, has occurred out of the spotlight. Yet it threatens people and ecosystems on both sides of the border, making it “one of the biggest human security challenges we face in south or west Asia,” says Ahmad Abrishamchi, a water expert at Sharif University of Technology in Tehran.

The vulnerable hydrology of the Hamoun oasis was its undoing. Snowmelt in the Hindu Kush mountains of Afghanistan feeds the Helmand, which flows into Hamoun-e Puzak. From there, water would spill into the other two lakes (see map, right). The result was an expansive way station for flamingos and other migratory birds and a home for otters, deer, and leopards. The delta would expand and contract seasonally; in springtime, water would circulate back into Afghanistan.

But that was decades ago. In the early 1950s, Afghanistan built Kajaki Dam on the Helmand, upstream of Kandahar. The Helmand’s flow tapered, but the Hamoun oasis held on until Afghanistan dug irrigation canals in the 1990s, Iranian officials say. “Virtually everything depends on what happens upstream in Afghanistan,” Yazdandoost says.

“I don’t buy that,” says Sher Jan Ahmadzai, a water expert and director of the Center for Afghanistan Studies at the University of Nebraska in Omaha. He says there has been virtually no development on the Afghan side of the border in the past 40 years. Ahmadzai and Afghan officials place the blame squarely on Iran’s own water management, including diversions from the Helmand to supply four

reservoirs—the Chah-nimeh—filled in the 1990s and 2000s to store freshwater for the provincial capital, Zahedan, and other towns.

Either way, these days the Helmand in Iran is dry, apart from water pulses that arrive between February and April, says Reza Mirshekar, an ecologist with the province’s environment department. Last October, when *Science* visited Jarike Dam, where the Helmand crosses into Iran, not a drop of water was present in a riverbed choked with

A sea of sand

The three Hamoun lakes dried up more than a decade ago, taking an entire wetland ecosystem with them.



yellow sand and fringed with scraggly tamarisk. Jarike was built in the 1960s to control springtime flooding, Mirshekar says. Now, the rusting structure is an anachronism. “The last flood was 30 years ago,” he says.

Dwindling water resources have left the area on the knife-edge of sustainability. Clusters of blue-and-white-checked water towers, replenished primarily by water from other regions, stand guard over many villages in Iran’s Sistan region. Cities such as Zahedan and Zabol rely on the Chah-nimeh. “If these

dry up, everyone here will have to migrate,” Pourmollae says. The situation is even more dire on the Afghan side of the border, where most people now rely on water trucked over from Iran, Ahmadzai says.

The retreat of the Hamoun lakes and wetlands—a process that accelerated in the late 1990s until the surface water largely vanished in 2004—has compounded the crisis. Fierce winds blow from May to September, sweeping up toxic dust. In 2016, Zabol had the highest levels of fine particulates of any city anywhere, according to the World Health Organization—an annual mean of 217 micrograms per cubic meter of the smallest particles, called PM2.5. That surpasses notoriously polluted cities such as Beijing and New Delhi.

The restoration plan UNDP is developing with input from Iran and Afghanistan would ensure that less water is diverted from the Helmand for agriculture; channel some water from the Chah-nimeh reservoirs to the Hamouns during the dry months; and, in both countries, encourage a switch to less thirsty crops and widely implement drip irrigation. Afghanistan’s government is ready to work with Iran on a solution, Ahmadzai says.

Negotiating the details and funding will take years, Ahmadzai predicts. Yet Soroosh Sorooshian, a water expert at the University of California, Irvine, is convinced that the Hamouns are not a lost cause. “Experience has shown that water bodies that have dwindled to nothing can bounce back,” he says. “It might take decades, but there is still hope.”

In an abandoned village west of Zabol, near a former lake shore, single-story domed houses of beige brick are half buried in sand. Outside the home of one of the last remaining families, a young girl corrals a little lamb almost as big as she is and cradles it like a baby. Her family is hopeful despite the devastation, Mirshekar says. “They are waiting for the water to come back.” ■



HIGHER EDUCATION

Biologist unveils China's first private research university

Venture aims to fill gap in higher education landscape

By Dennis Normile, in Hangzhou, China

Shi Yigong has never shied away from risky career moves. In 2008, the structural biologist turned down a \$10 million grant from the Howard Hughes Medical Institute in Chevy Chase, Maryland, for his work on programmed cell death and relinquished an endowed chair at Princeton University to relocate to Beijing, because, he says, he felt he could “play a much more important role in a rapidly transforming country.” His latest move may be even more audacious: Shi, 50, has resigned as a vice president of one of China’s premier institutions, Tsinghua University in Beijing, to launch a small university here in southeastern China, near Hangzhou’s scenic West Lake.

“It’s time for China to experiment with something new and exciting in higher education,” Shi says. Westlake University, which Shi is pitching as the nation’s first private research university, will focus on natural sciences, medical sciences, and engineering. By the end of the month, formal approval from China’s education ministry is expected, Shi says, and construction will begin in March.

Observers say Westlake could become a beacon on China’s higher education landscape. In contrast to public universities, which answer to government bureaucrats and are struggling to educate burgeoning ranks of undergraduates, Westlake is intended to be nimble, and focused on research.



Shi Yigong thinks private research universities can drive innovation.

“Westlake University has a golden opportunity,” providing it can attract top-shelf faculty and maintain its autonomy, says Gerard Postiglione, a higher education specialist at the University of Hong Kong (HKU) in China. “China needs to develop a viable model for a private research university that can drive economic restructuring,” he says, as the nation looks to home-grown innovations to ease the economy’s reliance on low-end manufacturing.

In 1995, China had just over 1000 universities and colleges and fewer than 6 million students. By 2016, the numbers had swelled to nearly 2600 institutions with close to 30 million students, and enrollment is expected to climb higher as a growing percentage of

high school graduates pursues higher education. So far, the expansion has not undercut China’s top universities, Postiglione says. Government programs that concentrated resources on top-tier schools “really led China’s universities to world-class status.”

But Shi believes Westlake will show that private research universities could be a valuable source of innovation. China has 400 or so private universities focusing on undergraduate education, but “their contribution to society and to science and technology is way below what they could be doing,” he says.

In March 2015, he and six colleagues outlined their vision for Westlake in a letter to Chinese President Xi Jinping. After a nod of approval from “top Chinese leadership,” Shi says, the group lined up support from

An artist's rendition of Westlake University. Campus construction is due to begin next month.

Hangzhou and Zhejiang province, which provided land and promised to build the campus and contribute to research expenses for the first 5 years. Philanthropists have pledged \$400 million to the Westlake Education Foundation, an endowment that will cover the university’s operating expenses.

Unlike public universities in China, which have government officials as their overlords, Westlake will be governed by a board of directors. That will give it more flexibility than China’s public universities have in selecting top officers, staffing departments, and setting strategic directions, Postiglione says. “Private universities tend to be more nimble.”

Shi, who wouldn’t say whether he will maintain a lab at Tsinghua while serving as Westlake’s first president, aims to make the new university small and elite. He anticipates that in about 10 years, Westlake will have a student body of 5000, including graduate students—the size of Princeton—and a faculty of 300, similar to that of the California Institute of Technology in Pasadena. The goal, Shi says, is “to educate the next generation of the brightest students to serve the nation and the world.”

Theoretical physicist Li Jian, Shi’s first recruit, says he shares that “bigger purpose.” Joining Westlake’s faculty is a “once in a lifetime” opportunity, says Li, who earned his Ph.D. at HKU and did postdocs in Switzerland and at Princeton. Shi (who did his own graduate work in the lab of Jeremy Berg, *Science*’s editor-in-chief) says Westlake is hiring without regard to nationality and will match salaries, benefits, and support packages offered elsewhere. So far, however, all of the 30-plus faculty members are Chinese.

One gap in Westlake’s plan is an absence of nonscience courses. Emphasizing science and engineering “can produce people who know formulas, but innovation comes from scientists who have some background in the humanities and social sciences,” Postiglione says. Shi says Westlake will add those departments “perhaps in 5 to 10 years.”

Another concern is whether Westlake can maintain its autonomy. The Communist Party might insist that Westlake follow a “socialist orientation” and require the courses on Marxism and Communist Party thought that all university students in China are obliged to take, says Huang Futa, a higher education expert at Hiroshima University in Japan. Shi says he is prepared for that. Westlake “must be principally guided by the central government and the Communist Party,” he says. If anyone presumes that will be an impediment to making Westlake a world class university, he says, “we will prove them wrong.” ■

OCEANOGRAPHY

Ocean array alters view of Atlantic conveyor

First data from subpolar moorings show surprising current strengths east of Greenland

By Katherine Kornei, in Portland, Oregon

Oceanographers have put a stethoscope on the coursing circulatory system of the Atlantic Ocean, and they have found a skittish pulse that's surprisingly strong in the waters east of Greenland—discoveries that should improve climate models.

The powerful currents known as the Atlantic meridional overturning circulation (AMOC) are an engine in Earth's climate. The AMOC's shallower limbs—which include the Gulf Stream—move warm water from the tropics northward, warming Western Europe. In the north, the waters cool and sink, forming deeper limbs that transport the cold water back south—and sequester anthropogenic carbon in the process. This overturning is why the AMOC is sometimes called the Atlantic conveyor belt.

Last week, at the American Geophysical Union's Ocean Sciences meeting here, scientists presented the first data from an array of instruments moored in the subpolar North Atlantic. The observations reveal unexpected eddies and strong variability in the AMOC currents. They also show that the currents east of Greenland contribute the most to the total AMOC flow. Climate models, on the other hand, have emphasized the currents west of Greenland in the Labrador Sea. "We're showing the shortcomings of climate models," says Susan Lozier, a physical oceanographer at Duke University in Durham, North Carolina, who leads the \$35 million, seven-nation project known as the Overturning in the Subpolar North Atlantic Program (OSNAP).

Four years ago, researchers began placing OSNAP's 53 moorings, studded with sensors to measure temperature, salinity, and current flow, in the waters between Labrador and Scotland. The moorings, galvanized steel wires as thick as a pinkie, are anchored to the ocean floor and tugged vertically by submerged floats. Some moorings are short, designed to measure deep currents near the ocean floor, while others rise nearly to the surface. Since 2004, researchers have gathered data from another array, at 26°N,

stretching from Florida to Africa. But OSNAP is the first to monitor the circulation farther north, where a critical aspect of the overturning occurs. It's here in the frigid Nordic Seas that water masses become cold and dense, sinking in streams that snake along the basin bottom, eventually turning southward and reaching the subtropics in about a decade.

It is thought that the formation of this so-called "deep water" helps drive the AMOC, but the first 21 months of data from OSNAP aren't conclusive. Both of the recorded winters were unusually cold and created similarly large amounts of deep water, but the strength of the AMOC whipsawed wildly between 8 and 25 sverdrups, a unit of flow roughly

between 2014 and 2017, researchers deployed 135 neutrally buoyant glass tubes, each roughly 2 meters long, at depths between 1800 and 2800 meters near the southern tip of Greenland. About half of the floats have now surfaced and relayed records of their daily positions to satellites passing overhead, says Amy Bower, a physical oceanographer at the Woods Hole Oceanographic Institution in Massachusetts and an OSNAP principal investigator.

Bower and her team were surprised to find that several floats had been caught off the tip of Greenland in kilometer-scale eddies that were previously known to exist only much farther north. These "eggbeaters,"

Bower says, may be stirring up and fragmenting the ribbons of deep water that wind around Greenland.

OSNAP's ability to ground truth earlier assumptions has climate scientists eager to get their hands on the new data, says Steve Yeager, who works on AMOC simulations at the National Center for Atmospheric Research in Boulder, Colorado. "It provides a really critical benchmark for models."

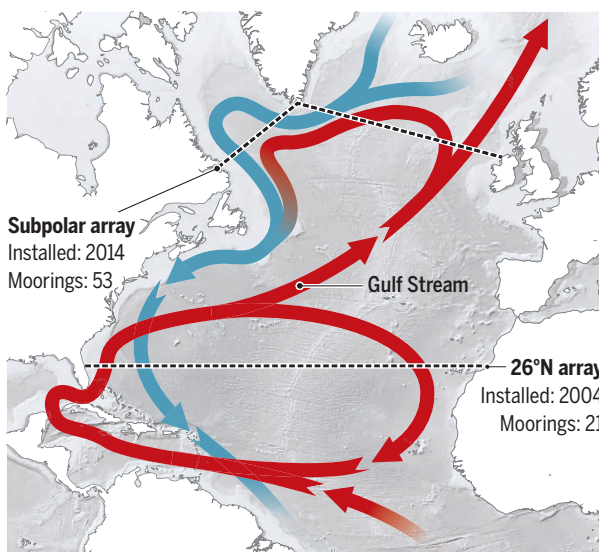
At the meeting, researchers working with the 21 moorings of the 26°N array also released their latest findings, which include measurements through February 2017. They show that the AMOC has weakened by about 15% compared with its 2004–08 level. Some climate models have raised the specter of a sudden shutdown of the AMOC—the apocalyptic scenario, leading to a frozen Europe, depicted in the 2004 movie *The Day After Tomorrow*—and the possibility is also supported by evidence from the geological

past. But the decline in the AMOC hasn't persisted long enough yet to be a cause for concern, says David Smeed, a physical oceanographer at the National Oceanography Centre in Southampton, U.K.

The overall trend of the AMOC will become clearer with time. This summer, researchers on the *R/V Neil Armstrong* will pull up OSNAP moorings and retrieve readings recorded from 2016–18. ■

In circulation

Arrays monitor circulating currents in the Atlantic Ocean, in which warm shallow waters move north (red), while cold deep waters move south (blue).



equivalent to the total flow of all the world's rivers. However, this variability was on such short timescales—months—that it might not be linked to the deep-water formation at all, Lozier says. "We need more winters."

Another reason to study the AMOC in the subpolar North Atlantic is that the rugged ocean floor in this region carves the current pathways up into tortuous tributaries, unlike the relatively smooth flows at 26°N. OSNAP's stationary moorings cannot trace these meandering pathways, so the array is supplemented by drifting floats. Be-

GENETICS

'Extinct' Caribbeans have living descendants

Ancient DNA from Taino woman shows kinship to modern genomes

By Lizzie Wade

Jorge Estevez grew up in the Dominican Republic and New York City hearing stories about his native Caribbean ancestors from his mother and grandmother. But when he told his teachers that he is Taino, an indigenous Caribbean, they said that was impossible. "According to Spanish accounts, we went extinct 30 years after [European] contact," says Estevez, an expert on Taino cultures at the Smithsonian Institution's National Museum of the American Indian, who is based in New York City.

Many scientists and historians continue to believe the Taino were wiped out by disease, slavery, and other brutal consequences of European colonization without passing down any genes to people in the Caribbean today. But a new genetic study of a 1000-year-old skeleton from the Bahamas shows that at least one modern Caribbean population is related to the region's precontact indigenous people, offering direct molecular evidence against the idea of Taino "extinction."

"These indigenous communities were written out of history," says Jada Benn Torres, a genetic anthropologist at Vanderbilt University in Nashville who studies the Caribbean's population history and has worked with native groups on several islands. "They are adamant about their continuous existence, that they've always been [on these islands]," she says. "So to see it reflected in the ancient DNA, it's great."

The skeletal remains come from a site called Preacher's Cave on Eleuthera, an island in the Bahamas. Archaeologists began excavating there in the early 2000s to probe the Bahamas' first European arrivals: Puritans who took refuge in the cave after a shipwreck. As they dug, they also found older artifacts associated with the island's precontact indigenous culture, including a handful of well-preserved burials.

At the time, Hannes Schroeder, an ancient DNA researcher at the Natural History Museum of Denmark and the University of Copenhagen, was on the lookout for skeletons from the Caribbean he could test for

DNA—even though he knew success was a long shot. DNA deteriorates faster in hot, humid environments than it does in cold, dry ones. Hunting for ancient DNA in the Caribbean "was uncharted waters," he says. He tested teeth from five of the Preacher's Cave burials, and in the end just one had DNA intact enough to sequence. But by the standards of ancient DNA from the tropics, that tooth was a bonanza.

It belonged to a woman who lived about 1000 years ago, according to radiocarbon dating. Schroeder's team sequenced each nucleotide base of her genome an average of 12.4 times, providing the most complete genetic picture of a precontact Taino individual to date, they report this week in the *Proceed-*

about 2500 years ago, the woman's ancestors migrated from the northern coast of South America into the Caribbean, rather than reaching the islands via the Yucatán Peninsula or Florida. It seems that once people arrived, they didn't stay put. Archaeologists know that ceramics and other goods were traded between islands, indicating frequent trips. Moreover, the Taino woman's genome doesn't contain long repetitive sequences characteristic of inbred populations. Her community, therefore, was likely spread out across many islands and not confined to 500-square-kilometer Eleuthera. "It looks like an interconnected network of people exchanging goods, services, and genes," says William Schaffer, a bioarchaeologist at Phoenix College who helped excavate the remains in Preacher's Cave.

Genetic studies of modern populations have found that many people from Puerto Rico, Cuba, and several other Caribbean islands carry significant indigenous ancestry, in addition to genes inherited from European and African populations. Still, it's possible that these living people descend not from the Taino, but rather from other Native Americans who, like many Africans, were forcibly brought to the islands as slaves. But when Schroeder compared the genomes of modern Puerto Ricans to the ancient Taino woman's genome, he concluded that they descend in part from an indigenous popula-

tion closely related to hers. "It's almost like the ancient Taino individual they're looking at is the cousin of the ancestors of people from Puerto Rico," Nieves-Colón says. Growing up in Puerto Rico, she, like Estevez, was always told that the Taino died out. "You know what? These people didn't disappear. In fact, they're still here. They're in us."

Estevez, who founded the cultural organization Higuayagua Taino of the Caribbean, didn't need an ancient DNA study to tell him who he is. Thanks to his family's oral history and cultural practices, he says, he has always had a strong connection to his indigenous ancestry. But he hopes the new study will convince skeptics that Taino people are alive and kicking. "It's another nail in the extinction coffin," he says. ■



Jorge Estevez (left) and other Higuayagua Taino members dance in New York City.

ings of the National Academy of Sciences. "It's a feat of working with tropical samples," says Maria Nieves-Colón, a geneticist who studies ancient and modern Caribbean populations at the National Laboratory of Genomics for Biodiversity in Irapuato, Mexico, and at Arizona State University in Tempe.

The Taino woman's DNA shores up archaeological evidence about her ancestors and her culture. When Schroeder's team compared her genome to those of other Native American groups, they found she was most closely related to speakers of Arawakan languages in northern South America. Early Caribbean ceramics and tools are strikingly similar to ones found in excavations there, archaeologists have long argued.

The two lines of evidence suggest that

JUST ADD SCIENCE

Scientists hit the campaign trail in hopes of making Congress work better



By **Jeffrey Mervis**

Last month, Randy Wadkins prepared for the spring semester at the University of Mississippi by reviewing his notes for the advanced chemistry course he has taught for many years. Then the professor of biochemistry, who grew up near the university's Oxford campus and received his Ph.D. there, forced himself to step outside his comfort zone: He flew to Washington, D.C., where he asked strangers for money.

Wadkins is running for U.S. Congress, and his fundraiser took place in a neighborhood restaurant just a few kilometers from where he would like to be working come January 2019. Wadkins warmed up his small but enthusiastic audience with a story about picking peas as a child every Saturday on his grandparents' farm to supplement his family's meager pantry. It reflects his "I'm just an ordinary person like you" message to Democrats in Mississippi's first congressional district, who on 5 June will choose a standard bearer to oppose the Republican incumbent in November.

The candidate voiced his anger about the state of U.S. politics with the young professionals, who shared his distaste for the policies of President Donald Trump and the Republican majority in Congress. A dysfunctional and hyperpartisan House of Representatives, he told them, might work better if more of its 435 members were scientists like himself. Then came his pitch: "I'm here to help make that happen, and the first step is by taking your money."

Wadkins, who studies biomolecular structures to better understand cancer and how to treat it, is part of what some commentators are calling a historic groundswell of candidates with backgrounds in science, technology, engineering, and mathematics (STEM). At the federal level, at least 60 science candidates are bidding for seats in Congress, according to 314 Action, a D.C.-based nonprofit advocacy group formed 2 years ago to encourage scientists to engage in politics. The candidates—mostly first-timers running for House seats—include a physicist who spent 2 decades at a prominent national laboratory, a clinical oncologist at a top-rated cancer center, a former chemistry professor at a 4-year state college, a geologist trying to document every aspect of a tiny piece of the Mojave Desert, and a postdoctoral bioengineering fellow. Some 200 people with STEM backgrounds are also running for state legislative seats, 314 Action estimates, with a similar number vying for school board and other local- and county-level positions.

Almost all are Democrats energized by what they regard as a rising antiscience sentiment pervading Washington, D.C. “I’m afraid we’re entering a dark era, with science, reason, and education under attack,” Wadkins told his supporters. “And I think members with scientific training can help prevent that.”

But first, science candidates must win their races. Most face long odds. For starters, voters may be impressed by a candidate’s scientific credentials, but such background is rarely a decisive factor when they go to the polls. In addition, most of this year’s STEM candidates are political novices who are starting out far behind their opponents when it comes to knowing how to run a professional campaign.

The demographics of the district can also be a huge barrier. Even a well-funded and well-run campaign probably won’t be enough for a first-time Democratic candidate to win in a traditionally Republican district.

Initially, the biggest challenge for most science candidates is raising money. Those running for a House seat should expect to spend at least \$4 million in the general election, experts say, and that figure could be much higher in urban areas with costly media markets. A primary race traditionally costs much less, although this year some candidates have already raised more than \$1 million with their primaries still months away.

But politicos say the usual rules might not apply this year. Democratic leaders are hoping for a wave election, one in which they can flip enough Republican seats to gain control of the House and, if things go especially well, the Senate. And scientific expertise may be more important than usual, muses Kyle Kondik, managing editor of Sabato’s Crystal Ball, a widely read election tip sheet run by Larry Sabato, a political scientist at the University of Virginia in Charlottesville.

“Voters are often looking for something that they don’t have now,” says Kondik, who is based in Washington, D.C. “And to the extent that the Trump administration is seen as anti-intellectual, a candidate with a scientific or medical background may seem like an attractive alternative.”

The first big test for this cohort of science candidates comes on 6 March, when Texas holds the nation’s first primary elections. Several candidates are running to

become Democratic nominees in that Lone Star state’s House districts (see sidebar, p. 862). Primaries in other states stretch into September, and then there are only 2 months before the nationwide general election on 6 November.

WADKINS LIKES HIS CHANCES in his Mississippi primary, where to date only one other person has thrown their hat into the ring. (The filing deadline is 1 March.) But Wadkins knows that even if he wins his party’s nomination, he’ll face a steep climb in trying to unseat Representative Trent Kelly (R). Trump won the district by 33 points over Democrat Hillary Clinton in the 2016 presidential race, and Kelly beat his Democratic challenger by an even bigger margin.

For the moment, however, Wadkins is focused on getting his message out: Kelly



Biochemist and congressional candidate Randy Wadkins meets voters in Columbus, Mississippi.

has been all too willing to fall in line behind Trump and Republican leaders, and voters need someone who will fight for their interests. Doing so takes money—a precious commodity in his district.

“I’m a Democrat running in one of the poorest districts in the poorest state in the nation,” he says. So, Wadkins has cast a wider net, with a fundraiser last fall in Silicon Valley—organized by a colleague who spent a year at Stanford University in Palo Alto, California—as well as the January event in the nation’s capital.

Wadkins is no stranger to Washington, D.C. In 2015, he took a sabbatical year to work as a congressional science fellow for Representative Steve Cohen (D-TN) on health care issues. (The program is managed by AAAS, which publishes *Science*.)

Although there were no high rollers in the crowd, which included several other

former fellows, Wadkins was pleased to net \$3000. That amount, added to the \$55,000 he’d raised by that point, has been enough to fuel a campaign that competes for attention with his academic duties. But it is an order of magnitude less than many other candidates around the country have amassed.

The lawyers, executives, and career politicians who typically seek federal office often enjoy long-cultivated and extensive networks of wealthy donors who fuel their campaigns. Scientists generally lack such networks. And once they reach out to their natural constituency, they quickly discover that the average scientist isn’t rich, isn’t used to contributing to a candidate, and isn’t politically active.

“Most academics don’t make a lot of money,” says Molly Sheehan, a bioengineering postdoctoral researcher at the University of Pennsylvania. She’s running as a Democrat in the seventh congressional district of Pennsylvania, an open seat in suburban Philadelphia.

“They also aren’t like lawyers, who view their political donations as a business expense and are willing to shell out \$1000,” adds Sheehan, who as of 31 December 2017 had raised about \$35,000 and loaned herself \$170,000. “Academic scientists think that \$100 is a big deal.”

Phil Janowicz, a former chemistry professor at California State University in Fullerton who is seeking the Democratic nomination

for the 39th congressional district in southern California, typically spends mornings with political activists, in hopes of winning their backing. In the evenings and on weekends he’s knocking on doors and attending small gatherings to introduce himself to voters in a district that leans Republican, but went for Clinton in 2016. But the rest of his time is devoted to fundraising. “I wake up thinking about raising money, and I go to sleep thinking about raising money,” says Janowicz, who runs an education consulting business with his wife out of his home. “I will spend about 8 hours a day, 6 days a week, raising money.”

Those efforts had generated \$160,000 by the end of December 2017, and Janowicz has loaned his campaign an equal amount. That has allowed him to hire a full-time campaign manager and even open a small office—a luxury for some candidates.

First up: Texas

This year's race to control the U.S. Congress kicks off with a 6 March primary election in Texas, and scientists are among the contenders.

In the seventh congressional district on Houston's affluent west side, clinical oncologist Jason Westin is one of four candidates seen as having a good shot at the Democratic nomination for a seat in the House of Representatives. In November, the winner will oppose Republican incumbent John Culberson, who heads a House subcommittee that sets budgets for science agencies including NASA and the National Science Foundation. Culberson has coasted to victory since his first race in 2000. But the district's voters preferred Democrat Hillary Clinton in the 2016 presidential race, and Democrats believe a strong candidate could beat him.

In the 21st congressional district in central Texas, the retirement of Representative Lamar Smith, the Republican chairman of the House science committee, has set off a feeding frenzy. Eighteen candidates are vying for a chance to retain Republican control of a district that stretches from southern Austin to northern San Antonio.

Four Democrats are hoping an anti-Republican wave election could allow one of them to capture the open seat. In the mix are Joseph Kopser, an Army veteran and entrepreneur with an engineering degree, and Mary Wilson, a former mathematics professor turned minister.

In a third contest, Jon Powell, a retired geologist, is seeking the Democratic nomination in southeastern Texas's 36th district, now represented by Republican Brian Babin. But Powell is a decided underdog: He badly trails his Democratic challenger in raising money, and the eventual nominee will face long odds, as the district is one of the most Republican in the nation. —Jeffrey Mervis

One science candidate who appears to have mastered the art of fundraising is Joseph Kopser, a 20-year Army veteran and entrepreneur with an engineering degree from the U.S. Military Academy at West Point in New York. He is running as a Democrat in Texas's 21st congressional district, a Republican stronghold in the central part of the state.

Kopser had amassed \$678,000 by the end of December 2017, far outpacing any of his three primary opponents. In fact, Kopser claims that his fundraising prowess pushed the Republican incumbent, Representative Lamar Smith, chairman of the House science committee, into deciding last fall not to seek a 17th term. (Smith's official statement said simply that "this seems like a good time" to retire.)

The size of a candidate's war chest is an imperfect metric of their viability, notes election pundit Kondik. That's especially true for primary elections, he says, which attract voters who are likely to be paying attention already. Instead of expensive ads aimed at swaying undecided voters, primaries require an army of volunteers trying to boost turnout among those already on your side. Still, Kondik notes dryly, "Every candidate would rather have more money than less."

Beyond Money, Candidates need a message that, ideally, both distinguishes them from their primary opponents and positions them for the general election. For those with science backgrounds, that message usually includes references to their training in analyzing large amounts of data, their adherence to evidence in weighing the issues, and their conviction that science and technology are essential to the country's future.

"I'm a father of three, a cancer doctor, and an award-winning researcher from MD Anderson [Cancer Center], and I deal with facts every day in my job" is how Jason Westin recently introduced himself at a candidates' forum on climate change in Houston, Texas. Westin, who until recently ran clinical trials testing treatments for lymphoma, is running in a crowded field for the Democratic nomination in a House district—the seventh—that includes Houston's affluent west side. The winner will challenge the veteran Republican incumbent, John Culberson.

That potential matchup gives Westin another rhetorical target. "My first commercial describes how I will stand up to Trump and the Republican Congress against their attacks on science," he says. "When I'm in

Congress I'll use facts and science to fight back for us."

Such words are sure to resonate with the research community. But there is little evidence that a candidate's views on science influence how people vote. Savvy candidates must find a way to apply their scientific knowledge to issues—the economy, health care, immigration, national security, and such social issues as abortion and same-sex marriage—that voters do care about, says political scientist Norm Ornstein, a resident scholar at the American Enterprise Institute in Washington, D.C. Along the way, he adds, they need to avoid talking down to voters and coming across as know-it-alls.

Kopser, for one, appears to be taking such advice to heart. In remarks and campaign materials, he emphasizes his military and business experience and focuses on top-tier issues such as health care and jobs. Kopser, who founded and

sold a transit company focused on optimizing urban commuting, also calls himself a "clean energy warrior" and highlights the need to address climate change. But the campaign is careful to talk about climate in ways it hopes will resonate with different blocs of voters, says Ian Rivera, Kopser's campaign manager.

"When we're in downtown Austin, we talk about rising sea levels ... and other broad environmental impacts," he explains—a topic important to urban, liberal audiences. With veterans, climate becomes "a question of national security. ... We talk about how changing climate patterns dried up crops in eastern Syria," helping fuel the rise of the Islamic State group. In rural Gillespie County, climate is "a pocketbook issue" because peach farmers there "are selling North Carolina peaches at their farmers' markets because the [Texas] winter never got cold enough to kill the pests."

Money does allow a candidate to use paid advertising to amplify key talking points. Westin, for example, is using excerpts from a short campaign video for 30-second ads on CNN. "It's not possible to knock on 700,000 doors," he explains. "And CNN is a rich target. Our polling shows that most voters don't really know any of us."

Candidates with fewer resources, however, are pursuing less expensive ways of getting out their message. Their efforts include large doses of door knocking and community events, and heavy use of social media such as Facebook and Twitter.

"I think I can reach people through social media," says Jess Phoenix, a geologist



Chemist Phil Janowicz (top middle) and geologist Jess Phoenix (bottom left) are running for U.S. House seats in two districts near Los Angeles, California. Physicist Elaine DiMasi (bottom right) hopes to represent Long Island, New York.

running in a strong Democratic field for the chance to oust Republican Steve Knight from the 25th congressional district in California, which covers the northern suburbs of Los Angeles. Political groups gave her a lot of advice on how to structure her campaign, she says, but “it wasn’t working for me because it all relies on having an extensive donor network of rich people. ... I want to have my campaign funded by regular people. If that means I have to do things on a shoestring budget, I will.”

Phoenix has already applied that bare-bones approach to a research project she and her husband launched 5 years ago. Dubbed Blueprint Earth, its goal is to catalog everything from soil microbes to clouds in a 1-square-kilometer patch of the Mojave Desert. But she acknowledges that running for Congress has required a whole new level of social media presence.

Patrick Madden, a professor of computer science at the State University of New York in Binghamton, thinks he has found a way to help Phoenix and other scientists amplify their reach on social media. Madden, a Democrat, found himself with some unexpected free time last fall after he dropped his bid to represent New York’s 22nd congressional district to make way for another candidate backed by the party. He’s used it to develop a website, activeresist.com, that allows science-based candidates to promote two or three news stories each day.

In essence, Madden says, his software is a twist on the same techniques that Russian operatives and others have used to spread fake news and try to influence elections through social media. But instead of bots pushing content into users’ newsfeeds, the retweets and likes will come from real people, including voters in their districts.

NO MATTER how effective social media might be at reaching voters, it can’t replace the blood, sweat, tears, and face time that a candidate must put in. And for many science candidates, that has meant abandoning or dramatically reducing their professional activities to take up politics.

Last summer, for example, physicist Elaine DiMasi gave up a tenured position at the Department of Energy’s Brookhaven National Laboratory in Upton, New York, to run in the first congressional district of New York on Long Island. (As a federal employee she couldn’t do both.) That was a gamble, as election handicappers say she is a long shot in her bid to win the Democratic nomination and take on two-term incumbent Representative Lee Zeldin (R).

DiMasi works on deciphering the structures of biological materials using Brookhaven’s National Synchrotron Light Source. It requires persistence and attention to detail, traits that have also proved useful as a candidate. “Politics is about showing up,” DiMasi says. “I would go into a room of influential people, and the first three times I showed up they didn’t care. But on the fourth time, they’d say, ‘Oh good, Elaine’s here.’ A scientist might well wonder: ‘What did I do differently?’ I simply offered myself.”

Such persistent networking is part of the interpersonal skills—she calls them the “politics part of a campaign”—that are separate from the nuts and bolts of running for office. And it doesn’t come naturally. “You can only learn it from experience,” she says.

In Texas, cancer researcher Westin hasn’t totally quit his state-funded job. Instead, he handed off his clinical trials to colleagues and reduced his clinical hours to 1 day a week. He did so, he says, to make sure that nobody could argue that “the state of Texas was paying me to run for office.” The schedule has left him 6 days a week to campaign.

On 6 March, Westin will find out whether that was enough. Regardless of whether he and others succeed, however, those who want the science community to become more active in politics see this year’s campaigns as a wonderful opportunity for scientists to apply their skills and experience in a new realm. “We’re part of a profound experiment,” DiMasi says, “and I love that.” ■

S SCIENCEMAG.ORG/NEWS

Go online for full coverage of the 2018 elections.

INSIGHTS



PERSPECTIVES

FISHERIES

Keeping watch on the ocean

Monitoring of fisheries fleets provides crucial data for sustainable use of ocean resources

By Elvira Poloczanska

Coastal and high-seas fisheries make a crucial contribution to global food security (1), but the vast distances of open waters and limitations of observing systems have precluded a high-resolution global view of fishing activity (2). Monitoring of fisheries has traditionally relied on region- and fleet-specific electronic vessel-monitoring systems, log books, and

on-board observers; access to these data is often constrained. Ship positioning data from automatic ship identification systems (AISs), designed to track and monitor specific vessel movements, is providing a surge of information on ocean fisheries. On page 904 of this issue, Kroodsma *et al.* (3) report tracking industrial fishing from 2011 to 2016 by processing 22 billion AIS messages. They show that more than 55% of the ocean area is fished. Global patterns of fishing are sensitive to culture and political events and are partially insulated from short-term environmental variation.

Alfred Wegener Institute, Integrative Ecophysiology, Bremerhaven, Germany. Email: elvira.poloczanska@awi.de

AIS was developed for collision avoidance. Since 2005, its use has been mandated by the International Maritime Organization for most seagoing vessels of 300 gross tonnage and above and for all passenger ships irrespective of size. Emerging applications of AIS data include fleet and cargo tracking, national fishing fleet monitoring, and maritime security (2, 4). For example, AIS data is yielding information on maritime trade routes and shipping corridors and on trade flows for decision-making (5), enabling assessments of the contribution of ship exhaust emissions to air pollution (6), and allowing



A commercial fleet fishes for herring in Sitka Sound, Alaska. Real-time information on global fishing activity could guide sustainable ocean management.

reduced fishing activity in the exclusive economic zones of many island states—information relevant to conservation planning. The availability of oceanographic data has driven the development of dynamic ocean management approaches, which use near real-time data to guide marine spatial management (10). The near real-time tracking of shipping and fishing vessels with AIS can provide critical information on the spatial and temporal distribution of resource users.

Extreme events, such as anomalous warm periods and storms, and rising temperatures in the ocean are affecting the distribution and abundance of marine organisms and redistributing fisheries resources (11). Biodiversity models project a large-scale rearrangement of fish stocks over the coming decades, with decreases in fisheries production in tropical regions (12). High-seas fisheries governance has the potential to reduce the risks from climate change—for example, through international cooperation and the closure of high-seas areas to fishing (11, 12).

Understanding the responses of fishing fleets to cultural, economic, and political drivers, such as regulatory policies, will inform efforts to tackle marine global challenges such as threats to biodiversity from climate change and human use. It will also help to effectively manage the ocean to “conserve and sustainably use the oceans, seas, and marine resources for sustainable development” (United Nations Sustainable Development Goal 14). High-resolution and real-time information on fishing activity data from AIS provides crucial information with which to tackle the multiple objectives of marine resource use and conservation. ■

evaluation of the exposure of marine mammals and fish to underwater acoustic noise from shipping (7, 8).

Kroodsma *et al.* used AIS data from 2012 to 2016 to elucidate the spatial and temporal fluctuations of global fishing activities. They generated labeled tracks of more than 70,000 identified fishing vessels by training convolutional neural networks to identify vessel types and fishing activity from AIS; these are tasks that would take a fisheries expert ~200 years working full time to accomplish (3). Mapping effort over space and time reveals how cultural activities influence fishing activities. The analysis reveals the human face of fishing; for example, latitudinal drops in fishing activity are associated with the Christmas vacation in European and North American fisheries and the Chinese New Year for Chinese vessels. A reduction in activity at weekends is evident in European and North American fisheries effort but less so in Chinese vessels.

Political influences are also evident, such as the annual moratoria for Chinese vessels.

Climatic variations can influence the location and abundance of fish stocks and their accessibility to fishing fleets. For example, an abrupt warming in the Western Indian Ocean in 1997 to 1998 changed the tuna distribution; as a result, many fishing fleets shifted to the eastern Indian basin (9). Kroodsma *et al.* explored the relationships of fishing activity to the elevated sea surface temperatures in the Indian and Pacific Oceans in 2015, the result of a positive Indian Ocean Dipole Mode Index and a large El Niño event. As their analysis shows, longline fishing in the Indian Ocean concentrates between the 16° and 19° isotherms and shifted 70 to 90 km south in July 2015 compared with the preceding and following years. They report that the influence of the large El Niño event was evident in shifts of fishing effort across all fleets in the equatorial Pacific. Kroodsma *et al.* also found

REFERENCES

1. Food and Agricultural Organization of the United Nations (FAO), *The State of World Fisheries and Aquaculture 2016. Contributing to Food Security and Nutrition for All* (FAO, 2016).
2. D.J. McCauley *et al.*, *Science* **351**, 1148 (2016).
3. D.A. Kroodsma *et al.*, *Science* **359**, 904 (2018).
4. M.D. Robards *et al.*, *Bull. Mar. Sci.* **92**, 75 (2016).
5. H.Y. Jia, O.D. Lampe, V. Solteszova, S.P. Strandenes, *Marit. Econ. Logist.* **19**, 619 (2017).
6. L. Johansson, J. P. Jalkanen, J. Kukkonen, *Atmos. Environ.* **167**, 403 (2017).
7. L.T. Hatch, C.W. Clark, S.M. Van Parijs, A.S. Frankel, D.W. Ponirakis, *Conserv. Biol.* **26**, 983 (2012).
8. J.A. Stanley, S.M. Van Parijs, L.T. Hatch, *Sci. Rep.* **7**, 14633 (2017).
9. F. Ménard, F. Marsac, E. Bellier, B. Cazelles, *Fish. Oceanogr.* **16**, 95 (2007).
10. A. Hobday *et al.*, *Stanford Environ. Law J.* **33**, 125 (2014).
11. O. Hoegh-Guldberg *et al.*, in *Climate Change 2014: Impacts, Adaptation, and Vulnerability. Part B: Regional Aspects. Contribution of Working Group II to the Fifth Assessment Report of the Intergovernmental Panel on Climate Change*, V.R. Barros *et al.*, Eds. (Cambridge Univ. Press, 2014), pp. 1655–1731.
12. W.W.L. Cheung *et al.*, *Fish Fish.* **18**, 254 (2017).

10.1126/science.aar7613

CANCER

Cancer detection: Seeking signals in blood

Combining gene mutations and protein biomarkers for earlier detection and localization

By Mark Kalinich^{1,2} and Daniel A. Haber^{1,2}

Most cancers are detected when they cause symptoms that lead to medical evaluation. Unfortunately, in too many cases this results in diagnosis of cancers that are locally invasive or already metastatic and hence no longer curable with surgical resection or radiation treatment. Medical therapies, which might be curative in the setting of minimal tumor burden, typically provide more limited benefit in more advanced cancers, given the emergence of drug resistance (1). On page 926 of this issue, Cohen *et al.* (2) describe a strategy for early cancer detection, CancerSEEK, aimed at screening for multiple different cancers within the general population. This study challenges current assumptions in the field of blood-based biomarkers and sets the stage for the next generation of cancer screening initiatives.

Given the potential curative advantage of earlier diagnosis and treatment, why have so many cancer screening approaches failed? In the past, efforts at screening healthy populations for cancer have relied on tests that were insufficiently specific. For example, most men with rising serum prostate-specific antigen (PSA) do not have prostate cancer but instead have benign prostatic enlargement. However, where accurate tests exist, there have been dramatic improvements in cancer outcomes (3). For example, advanced cervical cancer has virtually disappeared in countries where Pap screening is the standard of care; although less reliable, mammography and screening colonoscopy are recommended for early detection of breast and colon cancers in individuals above ages 40 to 45 and 50, respectively, and screening heavy smokers by use of low-dose chest computed tomography (CT) scans reduces deaths from lung cancer (4). However, these tests are imperfect, and cost-effectiveness for broad deployment remains a challenge, particularly because a multitude of false-positive test results may lead to extensive diagnostic evaluations and unnecessary medical in-

terventions. Unfortunately, for the majority of cancers no effective early screening tests are available.

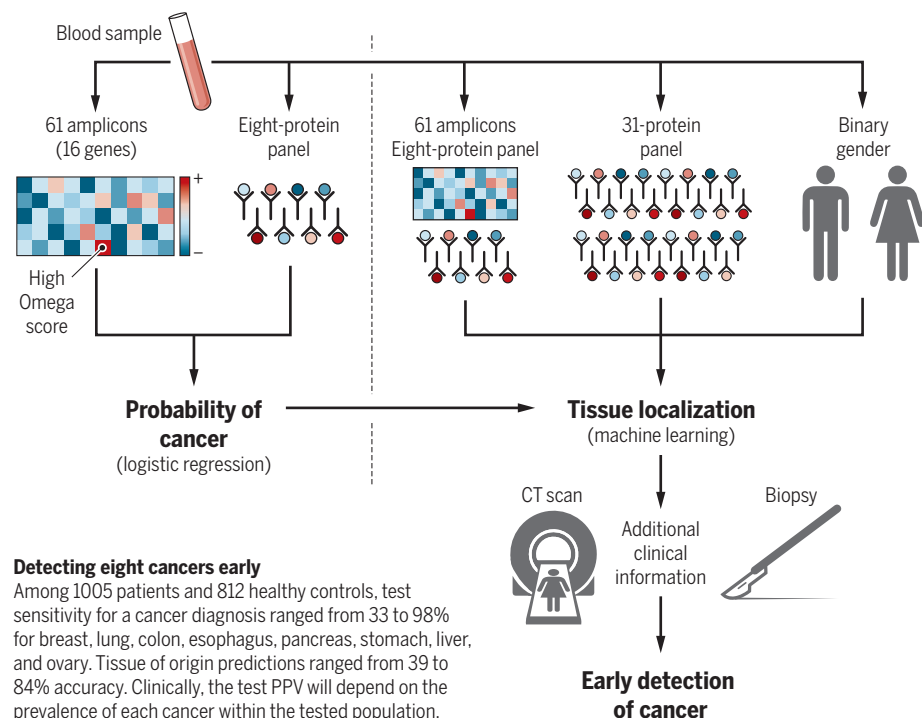
It is in this setting that emerging molecular analyses of blood specimens, so-called “liquid biopsies,” are poised to revolutionize cancer screening (5). Circulating cell-free DNA (cfDNA) in the blood consists of small fragments of DNA that are approximately 150 nucleotides in length. cfDNA is primarily derived from normal tissues, but a small fraction may be derived from tumor cells in individuals who have cancer. This circulating tumor DNA (ctDNA) may be identified by the presence of characteristic mutations in cancer genes or by variations in chromosome copy numbers (6). Recent studies have established the reliability of ctDNA genotyping for monitoring treatment response and identifying drug resistance mechanisms in patients with advanced cancer (7, 8). However, the much

lower amount of ctDNA in the plasma of patients who have a localized tumor poses a challenge for early cancer screening, as does the absence of knowledge about which mutation to look for. Furthermore, some background mutations detectable in the blood may arise from nonmalignant proliferation of blood cells in older individuals, a phenomenon called clonal hematopoiesis of indeterminate potential (CHIP) (9). Importantly, cancer gene mutations alone are insufficient to identify the tissue of origin for a given cancer signal in the blood because similar mutations are present in multiple different cancers. Thus, a tissue-agnostic blood-based screening test has limited clinical utility, unless accompanied by insight into which organ should be investigated for follow-up.

Cohen *et al.* sought to combine ctDNA sequencing of cancer genes with quantitation of tumor-associated serum protein

How the CancerSEEK algorithm works

Plasma-based sequencing of 16 cancer genes generates an Omega score that is combined with eight cancer-associated serum proteins to derive a probability for having any of eight different types of cancer. A machine learning algorithm then integrates these data with 31 additional serum proteins and patient gender to predict the tissue of origin.



¹Massachusetts General Hospital Cancer Center, Harvard Medical School, Boston, MA 02467, USA. ²Howard Hughes Medical Institute, Bethesda, MD 20815, USA.
Email: dhaber@mgh.harvard.edu

markers, deriving a probabilistic algorithm for the presence of cancer and for the tissue of origin. After estimating the minimal number of recurrent cancer gene mutations required for a robust signal in eight different cancer types, Cohen *et al.* assigned an Omega score to condense the entirety of the ctDNA sequencing data into a single number, based on the most predictive mutation identified. Added to the Omega score are levels for eight cancer-associated serum proteins, which are combined by the CancerSEEK algorithm into a single probability of the sample having come from an individual with cancer (see the figure). Of the 1005 patients studied with operable cancers, the test sensitivity ranged from 33 to 98%, depending on the cancer type, with a test specificity in healthy blood donors greater than 99%. In patients correctly identified as having some type of cancer, a further algorithm that incorporates the Omega score and the initial eight protein panel, as well as measurements of an additional 31 proteins and the patient's gender, correctly localizes the tumor to one of two top predicted anatomic sites in 83% of patients.

Among the key discoveries in this study is that a relatively small panel of cancer genes sequenced repeatedly to extreme depth to find rare alleles, with the pool of templates divided into multiple fractions in order to enhance signal detection, is sufficient to provide information for many different types of cancer. Compared with other efforts that use large-scale ctDNA sequencing (10), this approach will have greatly reduced cost. Also, by combining multiple protein biomarkers with ctDNA genotyping, the devised algorithm can implicate candidate tissues of origin, information unavailable from mutational data alone.

There are a number of important caveats. The predictive value of any diagnostic test relies on the prevalence of the disease within the tested population. For instance, in testing apparently healthy individuals within the general population, the prevalence of all eight cancers can be conservatively estimated as 1% of people over age 64 (11). Hence, in this setting even a test that is 99% sensitive and 99% specific will yield a positive predictive value (PPV) of only 50% (half of all test positives will be a false-positive result). Similarly, a positive CancerSEEK test result would be predicted to have a PPV of 40 to 45% for a person having any of the eight different cancers (2). Although the model was not designed to screen for individual cancer types, breaking down the aggregate PPV into its individual component cancers

would result in further reduction in PPV, particularly for rare cancers. Because PPVs improve with higher disease prevalence, application of any cancer screening test to subpopulations with increased genetic or environmental risk factors (for example, carriers of familial breast cancer susceptibility mutations, heavy smokers at risk for lung cancer, or patients with liver cirrhosis predisposed to hepatocellular carcinoma) would of course increase the likelihood of true-positive results.

A well-documented challenge in early cancer detection studies is that patient populations at increased risk for cancer may also have precancerous or inflammatory conditions resulting in baseline elevation of serum protein biomarkers, a confounding factor that is not well recapitulated in the healthy control population used to build the CancerSEEK test. Al-

invasion, and their cure rate is unknown. As the authors acknowledge, diagnosing cancers before clinical symptoms trigger an initial diagnostic procedure will require detection of even lower levels of signal, and prospective studies of patients whose cancer is first detected through blood-based screening will be required to determine real-world performance and whether such early screening can lead to improved cure rates. In addition, as the authors suggest, by coupling an initial blood-based screening test with secondary high-specificity confirmatory tests, it may be possible to achieve PPVs that would enable large-scale clinical implementation.

Undoubtedly, effective screening for early invasive cancers represents the best hope for reducing cancer mortality and morbidity. The conceptual advances and the practical feasibility of the CancerSEEK

assay constitute an important milestone toward the application of early cancer detection. Most importantly, the ongoing development of cost-effective and accurate blood-based cancer screening strategies is poised to revolutionize clinical cancer care, bringing with it new emphasis on genetic and environmental risk stratification so as to tailor application of screening tests; minimally invasive imaging, biopsy, and molecular characterization of early tumors that are discovered and might be either indolent or invasive; and deployment of increasingly effective therapeutic options to stages of cancer for which they have curative potential. The vision of effective earlier cancer detection and intervention warrants validation in appropriate populations through large-scale clinical trials that are likely to radically change the way we diagnose and treat cancer. ■

“...effective screening for early invasive cancers represents the best hope for reducing cancer mortality and morbidity.”

though the relative contributions of ctDNA genotyping versus serum protein markers varies among the individual cancers analyzed by Cohen *et al.*, the integration of these potentially orthogonal markers into the CancerSEEK algorithm is likely to strengthen its accuracy when trained on clinically relevant populations. Extending from this study, future research may combine multiple blood-based analytes, including massive ctDNA sequencing for mutations (10), high-throughput screening for chromosome copy number variation (12), scoring for tissue-specific DNA methylation patterns (13), serum-based multi-protein mass spectrometric quantitation (14), and digital quantitation of lineage-specific RNA from circulating tumor cells (15). Each of these blood-based assays may provide optimal capabilities for the detection of specific cancer types within at-risk patient populations, and as elegantly demonstrated by Cohen *et al.*, combinations of tests may be optimal to enable both high-sensitivity detection and identification of the tissue of origin.

The ultimate goal of cancer screening is to diagnose invasive cancers early, while they are still curable. All the patients studied by Cohen *et al.* had been diagnosed as part of standard clinical evaluation and were candidates for surgical resection of their tumors, but many already had local

REFERENCES

1. D. A. Haber, N. S. Gray, J. Baselga, *Cell* **145**, 19 (2011).
2. J. D. Cohen, *Science* **359**, 926 (2018).
3. R. A. Smith *et al.*, *CA Cancer J. Clin.* **67**, 100 (2017).
4. National Lung Screening Trial Research Team *et al.*, *N. Engl. J. Med.* **365**, 395 (2011).
5. A. Bardelli, K. Pantel, *Cancer Cell* **31**, 172 (2017).
6. J. C. M. Wan *et al.*, *Nat. Rev. Cancer* **17**, 223 (2017).
7. S. J. Dawson *et al.*, *N. Engl. J. Med.* **368**, 1199 (2013).
8. L. Goyal *et al.*, *Cancer Discov.* **7**, 252 (2017).
9. S. Jaiswal *et al.*, *N. Engl. J. Med.* **371**, 2488 (2014).
10. A. M. Aravanis, M. Lee, R. D. Klausner, *Cell* **168**, 571 (2017).
11. Surveillance, Epidemiology, and End Results (SEER) Program; <https://seer.cancer.gov>.
12. V. A. Adalsteinsson *et al.*, *Nat. Commun.* **8**, 1324 (2017).
13. M. W. Snyder, M. Kircher, A. J. Hill, R. M. Daza, J. Shendure, *Cell* **164**, 57 (2016).
14. P. E. Geyer, L. M. Holdt, D. Teupser, M. Mann, *Mol. Syst. Biol.* **13**, 942 (2017).
15. M. Kalinich *et al.*, *Proc. Natl. Acad. Sci. U.S.A.* **114**, 1123 (2017).

10.1126/science.aas9102

IMAGING

Unnaturally aglow with a bright inner light

A bioluminescent system enables imaging single cells deep inside small animals

By Yusuke Nasu and Robert E. Campbell

Bioluminescent insects, fungi, and sea creatures must have seemed mysterious and supernatural to the people of antiquity. It was not until the late 19th century that science began to displace the magic by demonstrating that bioluminescence in insects, such as the firefly (*Photinus pyralis*), is a chemical reaction that requires a protein (a luciferase) and substrates [adenosine triphosphate (ATP), O₂, and a luciferin, d-luciferin] (1). Understanding of the biochemical mechanisms of bioluminescence has grown over the past century, as has appreciation of its widespread prevalence in nature. Since cloning the gene for firefly luciferase (2), researchers have sought to exploit this molecular lightbulb for bioanalysis applications and bioluminescence imaging (BLI) in model animals (3). On page 935 of this issue, Iwano *et al.* (4) report the development of a luciferase-luciferin pair that, due to its brightness and red-colored glow, opens the door to a range of biomedical applications, such as detection of single cells deep within tissue, that were not previously feasible with BLI.

Transplantation of bioluminescence from firefly into mouse is the essential first step toward achieving BLI, but this process is associated with several challenges. Delivery of the foreign gene is the least of these, as viral delivery and other expression methods are now routine. Much more pressing are the challenges that arise from the opacity of mice and their lack of the biosynthetic machinery to make d-luciferin. The first of these challenges is partially surmountable because mice are only mostly opaque. Visible light does travel some distance through mammalian tissue, with more red-shifted light traveling farther. When firefly luciferase acts on its normal d-luciferin substrate, it produces yellow-green light with a peak wavelength of 560 nm (5). Previous efforts to produce red-shifted lucif-

erases led to variants with peak bioluminescence at ~620 nm (6), which is similar to a red-shifted d-luciferin-dependent luciferase from the railroad worm (*Phrixothrix hirtus*) (7). These wavelengths of light are on the edge of the near-infrared optical window (~650 to 950 nm), where tissue is most transparent to light (although still mostly opaque).

Lack of endogenous d-luciferin is overcome by administering this molecule to the mouse, typically by injection. Once injected, the substrate permeates through the tissue and, upon encountering luciferase, is consumed

peak emission at a wavelength of 675 nm and has much higher affinity for firefly luciferase than d-luciferin, but it is consumed more slowly. Most important, the hydrochloride salt of AkaLumine (AkaLumine-HCl) permeates particularly well through tissue and reaches the brain when orally administered.

As the forces of natural evolution have optimized luciferase to preferentially act on d-luciferin, Iwano *et al.* performed directed evolution of firefly luciferase to improve its activity toward AkaLumine. A population of luciferase variants was created by random

gene mutation, imaged in bacterial colonies sprayed with AkaLumine, and the brightest variant was picked to be the parent of the next generation. Twenty-one generations later, Iwano *et al.* arrived at a highly optimized variant with peak emission at 650 nm, designated Akaluc. The 28 amino acid substitutions in this enzyme made it faster and more thermally stable and enabled it to accumulate at high concentrations in cells without causing toxicity. Altogether, these properties make it ~40-fold brighter than firefly luciferase in cultured cells when combined with AkaLumine.

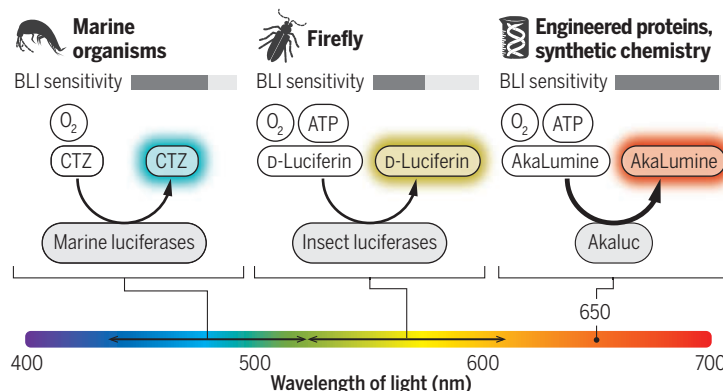
For small-animal BLI, the combination of Akaluc and

AkaLumine-HCl (AkaBLI) provides an unnatural luciferase-luciferin pair that, by design, has red-shifted emission and facile tissue penetration. Iwano *et al.* demonstrate that these combined benefits result in 100- to 1000-fold brighter in vivo bioluminescence than the combination of firefly luciferase and d-luciferin. These improvements enable detection of a single cell lodged in a capillary of a lung in mice. Tissue opacity notwithstanding, this is analogous to spotting the glow of a single firefly in the volume of a school gym.

Iwano *et al.* demonstrate the AkaBLI technology is a substantial upgrade from firefly luciferase with d-luciferin. However, to be the best available luciferase system, AkaBLI must also outperform marine-organism-derived luciferases that use coelenterazine (CTZ) as their luciferin and require O₂ but not ATP. This includes *Renilla* sea pansy luciferase (10) and crustacean luciferases such as NanoLuc

Luciferase-luciferin bioluminescent pairs

Akaluc, an engineered firefly luciferase, is optimized to use an unnatural luciferin, AkaLumine. The Akaluc system (AkaBLI) enables bioluminescence imaging (BLI) with unprecedented sensitivity *in vivo*, unlike marine luciferases, which are mainly used *in vitro*.



with concomitant generation of photons. The faster luciferase consumes d-luciferin, the brighter the bioluminescent signal, but the faster it will decay due to decreasing substrate concentration. A more elegant solution would be insertion of the d-luciferin biosynthetic machinery into the mouse genome, but this has yet to be achieved.

Because the luciferin must be exogenously administered, it does not necessarily have to be the natural, species-specific luciferase substrate. Just as synthetic organic chemistry is used to create drug analogs with superior efficacy and bioavailability, so too can a luciferin be modified for improved bioluminescence. Key improvements in a luciferase substrate could include an inherently red-shifted emission wavelength and improved distribution through tissue. Indeed, a substrate with these favorable properties, AkaLumine, has been developed (4, 8, 9). AkaLumine provides

(11, 12). Such luciferases have been supplanting firefly luciferase for many applications in recent years. Similar to the efforts of Iwano *et al.*, much effort has been expended on optimizing these luciferase-luciferin pairs. In one recent example, Yeh *et al.* (13) optimized NanoLuc for enhanced bioluminescence with a synthetic analog of CTZ. This system is reported to be ~80-fold brighter than firefly luciferase with d-luciferin in vitro and ~60-fold brighter when cells and substrate were injected under the skin of a mouse.

Iwano *et al.* make a compelling case that the exceptional in vitro brightness of CTZ-dependent luciferases has led the scientific community somewhat astray. While acknowledging the brightness of such luciferases in vitro, they demonstrate that CTZ-type substrates suffer from inadequate biodistribution and spontaneous oxidation and bioluminescence in vivo. This luciferase-independent bioluminescence contributes to a brightening of the background and diminishes the sensitivity of BLI. d-luciferin-type substrates, which require both ATP and O₂ as cosubstrates, are much less likely to undergo luciferase-independent oxidation than CTZ-type substrates, which require only O₂ as a cosubstrate. It remains to be seen whether the community of researchers working on CTZ-dependent luciferases can develop substrates that combine resistance to in vivo oxidation, red-shifted emission, and improved biodistribution, including blood-brain barrier permeability.

AkaBLI is a substantial leap forward for small-animal BLI. This technology will allow a range of in vivo applications, including monitoring neuronal-activity-dependent gene expression, following tumor growth and metastasis, tracking immune cell migration, monitoring stem cell fate, and assessing the efficiency of gene delivery and editing technologies. A future version, engineered for Ca²⁺-responsive bioluminescence (14), could be a powerful tool for real-time imaging of neuronal activity in freely behaving animals. ■

REFERENCES

1. V. Pieribone, D. F. Gruber, *Aglow in the Dark: The Revolutionary Science of Biofluorescence* (Harvard Univ. Press, Cambridge, MA, 2005).
2. J. R. de Wet *et al.*, *Proc. Natl. Acad. Sci. U.S.A.* **82**, 7870 (1985).
3. C. M. Rathbun, J. A. Prescher, *Biochemistry* **56**, 5178 (2017).
4. S. Iwano *et al.*, *Science* **359**, 935 (2018).
5. H. H. Seliger, W. D. McElroy, *Arch. Biochem. Biophys.* **88**, 136 (1960).
6. B. R. Branchini *et al.*, *Anal. Biochem.* **396**, 290 (2010).
7. V. R. Viviani *et al.*, *Biochemistry* **38**, 8271 (1999).
8. S. Iwano *et al.*, *Tetrahedron* **69**, 3847 (2013).
9. T. Kuchimaru *et al.*, *Nat. Commun.* **7**, 11856 (2016).
10. W. W. Lorenz *et al.*, *Proc. Natl. Acad. Sci. U.S.A.* **88**, 4438 (1991).
11. S. Inouye *et al.*, *FEBS Lett.* **481**, 19 (2000).
12. M. P. Hall *et al.*, *ACS Chem. Biol.* **7**, 1848 (2012).
13. H.-W. Yeh *et al.*, *Nat. Methods* **14**, 971 (2017).
14. K. Suzuki *et al.*, *Nat. Commun.* **7**, 13718 (2016).

10.1126/science.aas9159



PLANT SCIENCE

Toward nitrogen-fixing plants

A concerted research effort could yield engineered plants that can directly fix nitrogen

By Allen Good

Nitrogen is the main nutrient that limits crop yield. Biologically reactive nitrogen is therefore routinely supplied to crops as synthetic nitrogen fertilizer. In the developed world, the extensive use of synthetic fertilizer in agriculture has substantial financial and environmental costs (1). By contrast, in the developing world, the lack of fertilizer causes low crop yields, resulting in hunger and malnutrition. Many of these problems could be avoided if plants could be engineered to fix nitrogen directly from air.

One hundred years ago, Burrill and Hansen asked whether symbiosis is possible between nonlegume plants and the bacteria that produce nitrogen-fixing nodules on the roots of legumes (2). This approach involves creating the capacity for nonlegumes to form a tight symbiotic relationship with nitrogen-fixing bacteria.

The advent of DNA technologies in the 1970s led to a second approach: introducing nitrogen-fixation genes directly into a plant. However, this dream remains unrealized (3, 4). Here, we look at the current status and future of engineering nitrogen-

fixing cereal plants by directly introducing the genes required to make a functional nitrogenase in a plant.

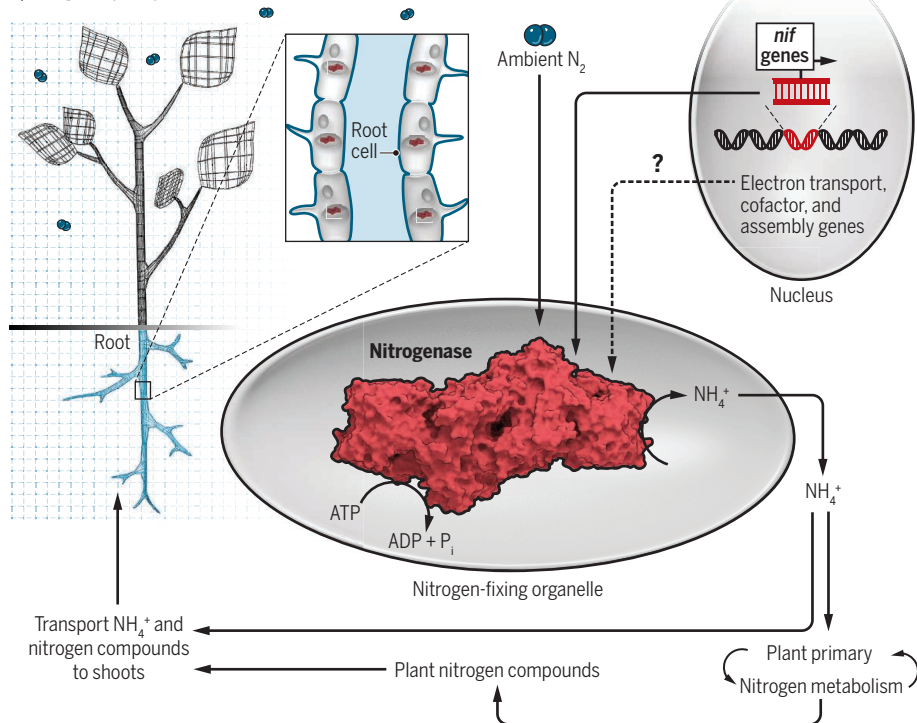
Biological nitrogen fixation is catalyzed by nitrogenase, a complex and extremely oxygen-sensitive enzyme that requires multiple genes for its assembly (5). The best studied nitrogenase, molybdenum (Mo) nitrogenase, consists of an iron (Fe) protein (NifH) and a MoFe protein (NifDK) (5). The minimum genetic requirements for nitrogenase activity depend on the nitrogenase; the minimum genes required for the Mo nitrogenase in *Escherichia coli* include genes encoding the Fe and MoFe proteins (*nifH*, *D*, and *K*), a chaperone for correct folding of one of the structural components (*nifM*), electron-transfer proteins (*nifF* and *J*), and cofactor assembly proteins (3, 6).

López-Torrejón *et al.* introduced *nifH* and *nifM* genes from the nitrogen-fixing bacterium *Azotobacter vinelandii* into the nuclear genome of the yeast *Saccharomyces cerevisiae*, which they used as a model eukaryote (7). NifH and NifM coexpression in aerobically grown yeast produced active nitrogenase Fe protein, even without the presence of the Nif-specific iron-sulfur (Fe-S) cluster assembly proteins (NifS and NifU). This result showed that mitochondria can protect the oxygen-labile Fe protein and that the native mitochondrial Fe-S cluster assembly machinery can success-

Department of Biological Sciences, University of Alberta, Edmonton, Alberta T6G 2E9, Canada.
Email: allen.good@ualberta.ca

Putative nitrogen-fixing plant

Efforts are under way to introduce bacterial *nif* genes into plants, thereby enabling them to fix nitrogen from the air. The use of such plants as crops would reduce the need for fertilizer. ADP, adenosine diphosphate; P_i , inorganic phosphate.



fully assemble and insert the Fe-S clusters required for Fe protein function.

Progress has also been made in introducing nitrogenase genes into plants. Ivleva *et al.* (8) introduced the *nifH* and *nifM* genes into the tobacco chloroplast genome and demonstrated that the transgenic plants produced detectable Fe protein activity. Burén *et al.* (9) expressed a synthetic version of NifB from the thermophilic methanogen *Methanocaldococcus infernus* in tobacco and found that it accumulated as a soluble protein. Allen *et al.* (10) showed that tobacco plants can transiently express several different nitrogenase proteins targeted to the mitochondria. Yang *et al.* (11) have also shown that plant-sourced electron transport chains can replace bacterial electron-transfer components, in a model system.

These studies prove that scientists can dissect the function of different nitrogenase genes in their host species and in model bacteria, yeast, and plants. Engineered plants can make the most oxygen-labile component of nitrogenase, the Fe protein, in different organelles, and this component is functional when combined with bacterially produced MoFe protein *in vitro* (7).

However, several scientific challenges must be overcome before we can make a nitrogen-fixing plant (see the figure). For example, it remains unclear what the minimum number of *nif* genes necessary for production of a

functional plant-hosted nitrogenase is, where to target such genes in plants (chloroplast or mitochondria), and what the optimal expression levels of the various genes necessary for producing a robust nitrogenase are. Nitrogenase uses large amounts of adenosine triphosphate (ATP), but the theoretical energy requirement for nitrogen fixation is almost identical to that required for nitrate assimilation (12). Furthermore, in legumes, attempts to estimate energy requirements for biological nitrogen fixation by growing legumes with or without nitrate have generally indicated little or no difference in growth (except for the initial period of nodule establishment) (12). The product of nitrogen fixation, ammonium (see the figure), can be toxic to plants; however, plants have ammonium transporters available to move ammonium from the mitochondrion into the cytoplasm and subsequently load it into the xylem. A plant that is fixing nitrogen at a sufficient rate to produce amounts of ammonium that are toxic to the plant would, in some ways, represent an interesting success of this research.

Once transgenic plants have been developed that exhibit nitrogenase activity in the laboratory, there will be substantial challenges to moving the technology to the field, not least of which might be achieving the public acceptance of a genetically modified plant. Not all challenges can be predicted, but the best way forward would include

reaching a consensus among researchers as to the model plant systems to be used for development of nitrogen-fixing plants. Useful model dicot plants could include tobacco (the classic model) and a nonlegume oilseed such as *Brassica napus*, which is already a transgenic crop; rice and wheat would be logical cereal crops.

The economic benefits of biological nitrogen fixation by plants could be substantial. Globally, over \$100 billion per year is spent on fertilizers, and the environmental costs are even greater. In the United States alone, the cost of farm-associated nitrogen pollution has been estimated to be \$157 billion annually (13). Fertilizer use also contributes to climate change. The Intergovernmental Panel on Climate Change (IPCC) estimates that 1% of the nitrogen fertilizer is lost in the form of NO_x . This translates into a CO_2 equivalent of 300 million metric tons (MMT), at a current value of \$4.5 billion annually (14). A nitrogen-fixing plant would not only reduce the costs of food production but would, in theory, address many of the environmental costs. Yet, current international funding for this research is likely between \$5 million and \$10 million annually—a tiny fraction of the money spent on fertilizers.

With adequate funding, it should be possible within the next decade or so to create a transgenic plant that can fix nitrogen at biologically significant rates. However, the real challenge will be to demonstrate that a plant can fix significant amounts of nitrogen, consistently, in the field. Given the present understanding of the biochemical basis of nitrogen fixation and its genetic determinants, as well as technical advances in plant transformation and organelar targeting, and a concerted research effort, the dream of a nitrogen-fixing crop plant in the field could be achieved within the next several decades. ■

REFERENCES AND NOTES

1. J. N. Galloway *et al.*, *Science* **320**, 889 (2008).
2. T. J. Burrell, R. Hansen, *III. Agric. Exp. Stn. Bull.* **202**, 115 (1917).
3. E. J. Vicente, D. R. Dean, *Proc. Natl. Acad. Sci. U.S.A.* **114**, 3009 (2017).
4. P. H. Beatty, A. G. Good, *Science* **333**, 416 (2011).
5. L. C. Seefeldt *et al.*, *Annu. Rev. Biochem.* **78**, 701 (2009).
6. J. Yang *et al.*, *Proc. Natl. Acad. Sci. U.S.A.* **111**, E3718 (2014).
7. G. López-Torrejón *et al.*, *Nat. Commun.* **7**, 11426 (2016).
8. N. B. Ivleva *et al.*, *PLOS ONE* **11**, e0160951 (2016).
9. S. Burén *et al.*, *Front. Plant Sci.* **8**, 1567 (2017).
10. R. S. Allen *et al.*, *Front. Plant Sci.* **8**, 287 (2017).
11. J. Yang *et al.*, *Proc. Natl. Acad. Sci. U.S.A.* **114**, E2460 (2017).
12. I. R. Kennedy, Y.-T. Tchan, *Plant Soil* **141**, 93 (1992).
13. D. J. Sloboda *et al.*, *Environ. Res. Lett.* **10**, 025006 (2015).
14. Based on the current value of CO_2 on the California carbon exchange of \$15 per ton. IPCC; 1% = 1 MMT = 300 MMT carbon equivalents. At a current cost of \$15 per MT, this is equivalent to \$4.5 billion annually.

ACKNOWLEDGMENTS

Thanks to P. Beatty, D. Dean, R. Dixon, L. Rubio, and Y. Wang for support and editorial advice.

Boron compounds tackle dinitrogen

A borylene compound can match transition metals by activating the strong N₂ bond

By Daniël L. J. Broere¹ and Patrick L. Holland²

The high stability of elemental nitrogen (N₂) is reflected in the name that Lavoisier coined for the element that makes up the seemingly inert component of the atmosphere, *azote*, meaning “no life.” Ironically, chemical processes that convert this robust molecule into ammonia (NH₃) are essential to keep the billions of people on our planet alive. Both the industrial Haber-Bosch process and natural nitrogenase enzymes use iron (Fe) to catalyze this challenging chemical transformation. Transition metals (M) weaken or break the strong triple bond (N≡N) by donating electrons from their atomic d orbitals into the antibonding π orbitals of N₂. Main-group elements such as boron (B) lack accessible d orbitals, so their ability to weaken N₂ would seem to be very limited. However, on page 896 of this issue, Légaré *et al.* (1) show that modification of the electronic environment of the B atom can enable N₂ binding and reduction at a B center.

The efforts of synthetic chemists over many decades have shown that complex ions of many metals can interact with N₂.

More specifically, the right combination of empty and filled d orbitals on the metal can accept electrons from N₂, and simultaneously weaken the N≡N bond through π -backdonation, which moves electron density from the metal into antibonding orbitals of N₂ (see the left panel of the figure). Légaré *et al.* used a borylene compound, which is a monovalent B atom with a lone pair of electrons, to bind N₂ (see the middle panel of the figure). Although most boron compounds have B in the +3 oxidation state, borylenes formally have the +1 oxidation state, making them very electron-rich.

In 2011, Bertrand and co-workers (2) demonstrated that these intrinsically reactive boron(I) species can be isolated by binding cyclic (alkyl)(amino)carbenes (CAACs), which stabilize the extra electrons on B. These borylenes mimic transition metals by binding carbon monoxide (CO) (3) and releasing it upon irradiation with light (4, 5). Because CO binding typically depends on π -backdonation, this finding suggested that borylenes might also bind N₂, albeit by using different orbitals than transition metals do. Recent work demonstrated binding of N₂ to an unstabilized borylene under matrix conditions at 10 K (6). However, even at these extremely low temperatures, which are used to observe the most reactive and unstable molecules, N₂ binding was very weak.

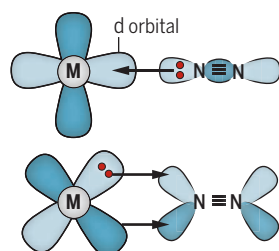
Légaré *et al.* show how to make a reactive borylene that can bind N₂ to form an adduct

that is stable enough to isolate (see the right panel of the figure). The resulting product consists of an N₂ fragment bound by two borylenes. In contrast to the linear M-N-N-M units typically found in transition-metal complexes, the B-N-N-B unit has a zigzag structure, which makes the product somewhat resemble an organic azo compound (C-N=N-C). However, quantum-mechanical calculations imply an electronic structure in which the borylene accepts electron density from N₂ with simultaneous π -backdonation from its filled p orbital. As a result, the N≡N bond is reduced to a bond order of ~1.5 in the borylene adduct. Although there is not yet evidence for the reversibility of N₂ binding, the bound N₂ molecule can be further reduced with potassium and protonated to generate a borahydrazine, which has a N-N single bond and new N-H bonds.

The work by Légaré *et al.* presents a remarkable example of an isolated compound in which a nonmetal can bind and reduce N₂, and underlines the potential of main-group elements for small-molecule activation. It also raises the question: What is next for borylenes? Classical steps in transition-metal catalysis involve two-electron redox changes on the metal center. However, the borylenes described by Légaré *et al.* readily undergo one-electron redox changes. Binding of cooperative (7) or redox-active (8) ligands to a borylene could assist in facilitating multielectron transformations, a strategy that has met with recent success in complexes of first-row transition metals that perform one-electron redox chemistry (9). The work by Légaré *et al.* also could lead to pathways to use borylenes for the conversion of N₂ into amines and other N-containing organic compounds with Earth-abundant boron catalysts. ■

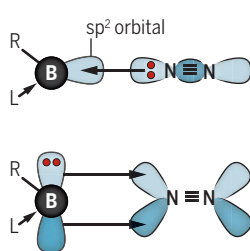
Binding N₂ at boron

Transition metals (M) bind N₂ by accepting and donating electron density using d orbitals. Légaré *et al.* now show that borylenes (B) can bind N₂ using p orbitals.



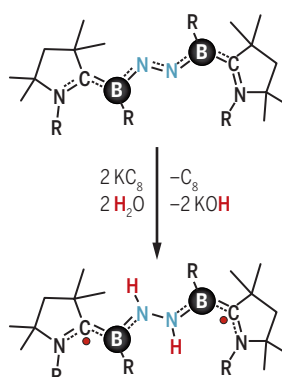
Metal N₂ complex

Empty d orbital accepts electron density from N₂ and filled d orbital donates electron density into N₂ (π -backdonation).



Borylene N₂ complex

Empty sp² orbital accepts electron density from N₂, and filled p orbital donates electron density into N₂ (π -backdonation).



Reduction of bound N₂

After reduction and protonation, N₂ forms borahydrazine (R represents an aryl group).

REFERENCES

- M.-A. Légaré *et al.*, *Science* **359**, 896 (2018).
- R. Kirjo, B. Donnadieu, M. A. Celik, G. Frenking, G. Bertrand, *Science* **333**, 610 (2011).
- F. Dahcheh, D. Martin, D. W. Stephan, G. Bertrand, *Angew. Chem. Int. Ed.* **53**, 13159 (2014).
- H. Braunschweig *et al.*, *Nature* **522**, 327 (2015).
- H. Braunschweig *et al.*, *J. Am. Chem. Soc.* **139**, 1802 (2017).
- K. Edel, M. Krieg, D. Grote, H. F. Bettinger, *J. Am. Chem. Soc.* **139**, 15151 (2017).
- J. R. Khusnutdinova, D. Milstein, *Angew. Chem. Int. Ed.* **54**, 12236 (2015).
- P. J. Chirik, K. Wieghardt, *Science* **327**, 794 (2010).
- J. I. van der Vlugt, *Eur. J. Inorg. Chem.* **3**, 363 (2012).

10.1126/science.aar7395



INFECTIOUS DISEASES

The Global Virome Project

Expanded viral discovery can improve mitigation

By Dennis Carroll, Peter Daszak, Nathan D. Wolfe, George F. Gao, Carlos M. Morel, Subhash Morzaria, Ariel Pablos-Méndez, Oyewale Tomori, Jonna A. K. Mazet

Outbreaks of novel and deadly viruses highlight global vulnerability to emerging diseases, with many having massive health and economic impacts. Our adaptive toolkit—based largely on vaccines and therapeutics—is often ineffective because countermeasure development can be outpaced by the speed of novel viral emergence and spread. Following each outbreak, the public health community laments a lack of prescience, but after decades of reacting to each event with little focus on mitigation, we remain only marginally better protected against the next epidemic. Our ability to mitigate disease emergence is undermined by our poor understanding of the diversity and ecology of viral threats, and of the drivers of their emergence. We describe a Global Virome Project (GVP) aimed to launch in 2018 that will help identify the bulk of this viral threat and provide timely data for public health interventions against future pandemics.

Nearly all recent pandemics have a viral etiology with animal origins, and with their intrinsic capacity for interspecies transmission, viral zoonoses are prime candidates for

causing the next great pandemic (1, 2). However, if these viruses are our enemy, we do not yet know our enemy very well. Around 263 viruses from 25 viral families are known to infect humans (3) (see the figure), and given the rate of discovery following identification of the first human virus (yellow fever virus in 1901), it is likely many more will emerge in the future (4). We estimate, from analysis of recent viral discovery data (5), that ~1.67 million yet-to-be-discovered viral species from key zoonotic viral families exist in mammal and bird hosts—the most important reservoirs for viral zoonoses (supplementary text).

By analyzing all known viral-host relationships (3, 6), the history of viral zoonoses (7), and patterns of viral emergence (1), we can reasonably expect that between 631,000 and 827,000 of these unknown viruses have zoonotic potential (supplementary text). We have no readily available technological countermeasures to these as-yet-undiscovered viruses. Furthermore, the rate of zoonotic viral spillover into people is accelerating, mirroring the expansion of our global footprint and travel networks (1, 8), leading to a nonlinear rise in pandemic risk and an exponential growth in their economic impacts (8).

PROMISING PILOT, CHALLENGING SCALE

Since 2009, the U.S. Agency for International Development (USAID) has conducted a large-scale pilot project, spanning more than 35 countries over 8 years at a cost of around \$170 million, to evaluate the feasibility of preemptively mitigating pandemic threats.

Scientists prepare to collect a blood sample from a *Rousettus* sp. fruit bat in Thailand to test for novel viruses. The Global Virome Project aims to identify and characterize the majority of currently unknown viruses in key wildlife groups, including rodents, nonhuman primates, and bats.

Other previous studies had begun to conduct targeted viral discovery in wildlife (9), and develop mitigation strategies for the emergence of avian flu, for example. However, the USAID Emerging Pandemic Threats (EPT) PREDICT project is the first global-scale coordinated program designed to conduct viral discovery in wildlife reservoir hosts, and characterize ecological and socioeconomic factors that drive their risk of spillover, to mitigate their emergence in people (10).

Working with local partners and governments, wildlife and domestic animals and at-risk human populations in geographic hotspots of disease emergence (1) are sampled, and viral discovery conducted. A strategy to identify which novel viruses are most at risk of spillover has been developed (11), and further work is conducted on these to characterize them prior to, or in the early stages of, spillover. Metadata on the ecology of wildlife-livestock-human transmission interfaces, and on human behavioral patterns in communities, are concurrently analyzed so that strategies to reduce spillover can be developed (supplementary text). To date, EPT PREDICT has discovered more than 1000 viruses from viral families that contain zoonoses, including viruses involved in recent outbreaks (12), and others of ongoing public health concern (13). The focus of EPT PREDICT on capacity building, infrastructure support, training, and epidemiological analysis differs substantially from the GVP's emphasis on large-scale sampling and viral discovery. However, to discover the bulk of the projected remaining 1.67 million unknown viruses in animal reservoirs and characterize the majority of 631,000 to 827,000 viruses of highest zoonotic potential requires overcoming some challenges of scale.

The first challenge is cost. To estimate this, we analyzed data on field sampling and laboratory expenditures for viral discovery from (5, 10), and estimates of unknown viral diversity in mammalian and avian hosts (supplementary text). We estimate that discovery of all viral threats and characterization of their risk for spillover, using currently available technologies and protocols, would be extremely costly at over \$7 billion (supplementary text). However, previous work shows that viral discovery rates are vastly higher in the early stages of a sampling program, and that discovering the last few, rare, viruses is extremely costly and time-consuming owing to the number of samples required to find

The list of author affiliations is provided in the supplementary materials. Email: daszak@ecohealthalliance.org

them (5) (supplementary text). We used data on rates of viral discovery (5) to estimate that the substantial majority of the viral diversity from our target zoonotic reservoirs could be discovered, characterized, and assessed for viral ecology within a 10-year time frame for ~\$1.2 billion (16% of total costs for 71% of the virome, considering some fixed costs) (fig. S1). Those viruses remaining undiscovered will, by the nature of sampling bias toward more common host species, represent the rarest viruses with least opportunity for spillover, and therefore reduced public health risk. Their discovery would require exponentially greater sampling effort and funding that could be better spent on countermeasures for the more likely threats (supplementary text).

Stakeholders from Asia, Africa, the Americas, and Europe, spanning industry, academia, intergovernmental agencies, non-governmental organizations (NGOs), and the private sector, began meeting in 2016 to design a framework for the governance, management, technical operation, and scope of the GVP. Key efforts include developing finance streams; establishing a transparent, equitable implementation strategy; designing data- and sample-sharing protocols; developing laboratory and metadata platforms; targeting of host taxa and sampling sites; analyzing return on investment; forming collaborative field and laboratory networks; developing risk characterization frameworks for viruses discovered; designing a strategy to assess and mitigate risk behaviors that facilitate viral emergence; and planning in-country capacity building for sustainable threat mitigation. Funding has been identified to support an initial administrative hub, and fieldwork is planned to begin in the first two countries, China and Thailand, during 2018.

With outputs intended to serve the global public good, the GVP is developing a transparent and equitable strategy to share data, viral samples, and their likely products, including benefits derived from future development of medical countermeasures. These build on the Nagoya Protocol to the Convention on Biological Diversity and the Pandemic Influenza Preparedness Framework, negotiated by the World Health Organization (WHO). The international collaborative nature and global ownership of the project should help leverage funding from diverse international donors, including government agencies focused on national virome projects or on international development projects in other countries, and private-sector philanthropic donors focused on technology and big science.

The diversity of tasks required to conduct the GVP should reduce the potential for it to divert funds from current public health programs. For example, discrete work streams on

targeted sampling of wildlife, on bioinformatics, and on behavioral risk analysis fall within the focus of current scientific research programs in a range of donor agencies. Governments and corporations with specific remits and geographic responsibilities have been approached to finance subprojects relevant to their sectors (e.g., capacity development, surveillance of specific taxa, geographically focused activities, medical countermeasure development, training, surveillance, and technological platforms). In addition, leaders in China and a number of countries have begun developing national virome projects as part of the GVP, leveraging current research funding to include GVP sites.

Technological challenges include safe field sampling in remote locations and cost-effic-

“...the GVP goals...improve capacity to detect, diagnose, and discover viruses in vulnerable populations...”

tive laboratory platforms that can be standardized in low-income settings. To achieve these goals, existing national, regional, and international networks will need to be enhanced and expanded within standardized sampling and testing frameworks. Existing networks of field biologists from environment ministries, academic institutions, and conservation and health NGOs may assist in surveillance. National science and technology agencies, regional One Health platforms, transboundary disease surveillance networks, Institut Pasteur laboratories, WHO, United Nations Food and Agricultural Organization, and the World Organization for Animal Health collaborating, and reference centers and viral discovery laboratories, including USAID EPT PREDICT, are currently involved in planning these activities around a decade-long sampling and testing time frame. A monitoring and evaluation strategy is being developed based on analysis of viral discovery rates against predicted viral diversity, to identify when to halt surveillance and testing as the GVP progresses. Stakeholders will also tackle the challenge of how to decide when enough potentially dangerous viruses have been discovered in a host species or region to call for action to reduce underlying drivers of emergence (e.g., hunting and trading of a wildlife reservoir).

Laboratory platforms developed by USAID EPT PREDICT have proven capacity to identify novel viruses and are relatively inexpensive and reliable, being based on polymerase chain reaction using degenerate

primers that target a range of viral families of known zoonotic potential. However, scaling up to a full global virome project will require discovery of three orders of magnitude more viruses in a similar time frame. Technological solutions will be needed to increase the speed and efficiency, and reduce the cost, of sequence generation. These will likely include next-generation sequencing and other unbiased approaches to identify evolutionarily distinct viral clades.

A key challenge is how to assess the potential for novel viruses to infect people or become pandemic (14). The EPT PREDICT project (11) and others (2, 6) have developed preliminary zoonotic risk characterization frameworks based on viral and host traits and the ecological and demographic characteristics of the sampling site. These approaches will be used in the GVP to triage novel viruses for further characterization to assess their zoonotic capacity (supplementary text). In vitro receptor binding analyses coupled with in vivo models have proven useful in this capacity for some viral families [e.g., coronaviruses (13)]. Although this is not yet feasible for all potentially zoonotic viral clades, applying these techniques to a larger viral data set as the GVP progresses will allow validation of risk frameworks and may increase our capacity to predict zoonotic potential. However, advancing these goals will require new collaboration among lab virologists, epidemiologists, and modelers, innovative approaches to field-testing the boundaries of virus-host relationships, and support across agencies that often fund separate virology, public health, evolutionary biology, and biodiversity modeling initiatives.

INVESTMENTS, RETURNS

The cost of the GVP represents a sizable investment and, even if a large number of potential zoonoses are discovered, only a minority is likely to have the potential to cause large-scale outbreaks and mortality in people (1, 2, 7). However, given the high cost of single epidemic events, data produced by the GVP may provide substantial return on investment by enhancing diagnostic capacity in the early stages of a new disease outbreak or by rapidly identifying spillover hosts, for example. Recent analysis of the exponentially rising economic damages from increasing rates of zoonotic disease emergence suggests that strategies to mitigate pandemics would provide a 10:1 return on investment (1, 8). Even small reductions in the estimated costs of a future influenza pandemic (hundreds of billions of dollars) or of the previous SARS (severe acute respiratory syndrome) epidemic (\$10 billion to \$30 billion) could be substantial. The goal of the GVP is to improve efficiency in the face of these increasing viral

spillover rates by enhancing (not replacing) current pandemic surveillance, prevention, and control strategies. If we were to invest only in surveillance for known pathogens (our current business-as-usual strategy), our calculations suggest we would protect ourselves against less than 0.1% of those viruses that could conceivably infect people, even using the lower bounds of our uncertainty for our viral estimates (i.e., 263 viruses known from humans out of 263,824 unknown potential zoonoses; supplementary text).

The potential benefits of the GVP may be enhanced to maximize public health benefits (supplementary text) by (i) optimizing sampling to target species most likely to harbor “missing zoonoses” (6), or to target emerging disease hotspot regions most likely to propagate major disease outbreaks (1); (ii) using human and livestock syndromic surveillance to identify regions for wildlife sampling proximal to repeated outbreaks of severe influenza-like-illnesses, fevers of unknown origin, encephalitides, livestock “abortion storms,” and other potential emerging disease events; (iii) initially targeting RNA viruses, which caused 94% of the zoonoses documented from 1990 to 2010; and (iv) fostering economies of scale and adoption of technological innovation as the GVP ramps up. This includes use of laboratories that can facilitate regional sample processing, development of centralized bioinformatics platforms, and improved logistics for sample collection and transport. We also expect the cost of testing and sequencing to decrease as technology is enhanced, much as the development of next-generation sequencing reduced genetic sequencing costs by up to four orders of magnitude in a decade.

The accelerated pace of viral discovery under the GVP will make the virological, phylogenetic, and modeling approaches used in pandemic preparedness more data-rich, and likely more effective. For example, having the sequence data for thousands, rather than a few, viruses from a single family could extend vaccine, therapeutic, or drug development to a wider range of targets, leading to broad-spectrum vaccines and other countermeasures. Identification of novel viruses may be useful to programs like the Coalition for Epidemic Preparedness Innovations (CEPI) in assessing the breadth of action of candidate vaccines and therapeutics, and in expanding their efficacy. More broad-scale prevention approaches could provide immediate return on investment prior to vaccine and countermeasure development, which would require substantial investment and time. For example, metadata on viral reservoir host identity, geography, seasonality, proximity to people, and drivers of emergence will refine our mechanistic understanding of spillover

and enhance published models of emerging infectious diseases risk (1, 6). Identification of novel viruses in hunted, traded, or farmed wildlife species could be used to enhance biosecurity in markets and farming systems, reducing public health risk, increasing food security, and assisting in conservation of hunted species. The presence of hosts harboring high-risk novel viruses in proximity to human populations may allow targeted follow-up to examine evidence of spillover and design intervention strategies (supplementary text). Ultimately, the benefits of the GVP may include enhancing our understanding of viral biology, such as drivers of competition or cooperation among viruses within hosts, genomic underpinnings of host-virus coevolution, processes underlying deep evolution of viral clades, and the identification of novel viral groups (15).

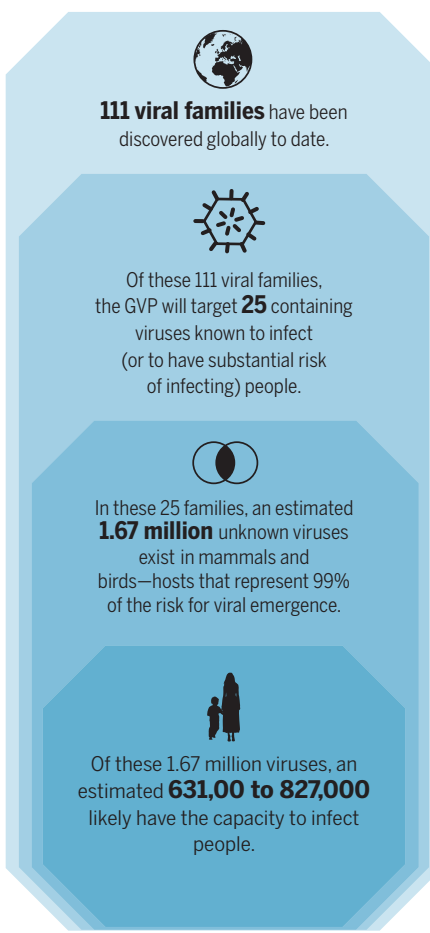
The regions targeted by the GVP are largely highly biodiverse, rapidly developing countries in the tropics, which often have low

capacity to deal with public health crises (1). The expanded laboratory capacity, field sampling, and data generation intrinsic to the GVP goals will therefore improve capacity to detect, diagnose, and discover viruses in vulnerable populations within regions most critical to preventing future pandemics. This enhanced capacity may also help improve diagnosis and control for endemic diseases, as well as the portion of the virome that remains undiscovered.

The Human Genome Project in the 1980s catalyzed technological innovation that dramatically shortened the time and cost for its completion, and ushered in the era of personalized genomics and precision medicine. The GVP will likely accelerate development of pathogen discovery technology, diagnostic tests, and science-based mitigation strategies, which may also provide unexpected benefits. Like the Human Genome Project, the GVP will provide a wealth of publicly accessible data, potentially leading to discoveries that are hard to anticipate, perhaps viruses that cause cancers and chronic physiological, mental health, or behavioral disorders. It will provide orders-of-magnitude more information about future threats to global health and biosecurity, improve our ability to identify vulnerable populations, and enable us to more precisely target mitigation and control measures to foster an era of global pandemic prevention. ■

GVP targeting strategy

The project will capitalize on economies of scale in viral testing, systematically sampling mammals and birds to identify currently unknown, potentially zoonotic viruses that they carry.



REFERENCES AND NOTES

1. K.E. Jones *et al.*, *Nature* **451**, 990 (2008).
2. J.L. Geoghegan, A.M. Senior, F. Di Giallonardo, E.C. Holmes, *Proc. Natl. Acad. Sci. U.S.A.* **113**, 4170 (2016).
3. A.M. King, M.J. Adams, E.B. Carstens, E.J. Lefkowitz, *Virus Taxonomy: Classification and Nomenclature of Viruses: Ninth Report of the International Committee on Taxonomy of Viruses* (Elsevier, Philadelphia, 2012).
4. M. Woolhouse, F. Scott, Z. Hudson, R. Howey, M. Chase-Topping, *Philos. Trans. R. Soc. Lond. B Biol. Sci.* **367**, 2864 (2012).
5. S.J. Anthony *et al.*, *mBio* **4**, e00598-13 (2013).
6. K.J. Olival *et al.*, *Nature* **546**, 646 (2017).
7. N.D. Wolfe, C.P. Duranvan, J. Diamond, *Nature* **447**, 279 (2007).
8. J. Pike, T.L. Bogich, S. Elwood, D.C. Finnoff, P. Daszak, *Proc. Natl. Acad. Sci. U.S.A.* **111**, 18519 (2014).
9. J.F. Drexler *et al.*, *Nat. Commun.* **3**, 796 (2012).
10. data.predict.global
11. S.S. Morse *et al.*, *Lancet* **380**, 1956 (2012).
12. G. Grard *et al.*, *PLOS Pathogens* **8**, e1002924 (2012).
13. X.-Y. Ge *et al.*, *Nature* **503**, 535 (2013).
14. J.L. Geoghegan, E.C. Holmes, *Open Biol.* **7**, 170189 (2017).
15. C.X. Li *et al.*, *eLife* **4**, e05378 (2015).

ACKNOWLEDGMENTS

P.D., N.D.W., and J.A.K.M. are funded by USAID EPT PREDICT. We acknowledge S.J. Anthony, C.J. Chrisman, Y. Feferholtz, T. Goldstein, C.K. Johnson, D. Nabarro, K.J. Olival, N. Ross, E. Rubin, R. Waldman, B. Watson, C. Zambrana-Torrelio, attendees of the Rockefeller Foundation–funded Bellagio Center Global Virome Project Workshop August 2016 (www.globalviromeproject.org/about/), members of the GVP Core Group and Steering Committee, and co-leads of the GVP Working Groups for their help refining the concept and this manuscript.

SUPPLEMENTARY MATERIALS

www.scienmag.org/content/359/6378/872/suppl/DC1



NUCLEAR WEAPONS

Earthquake or atomic bomb?

A seismologist reflects on his role in the contentious politics of nuclear weapon test bans

By Alvin Saperstein

At a time when a considerable fraction of the population is adamant in their refusal to apply science to public policy, it is helpful to look back to a similar scenario that played out during the Cold War. In *Silencing the Bomb*, geophysicist Lynn Sykes tells the story of the efforts of a group of scientists who sought to halt the worldwide testing of nuclear weapons throughout the mid- to late 20th century. The book further shows how individuals who were committed to the development and procurement of nuclear weapons during this period used secrecy, denial, and falsification of science to thwart the desires of the American public, the majority of whom, many polls revealed, were in favor of banning nuclear testing.

That some headway was ultimately made in the form of the Comprehensive Nuclear-Test-Ban Treaty (CTBT) is due to the efforts of many people, including Sykes himself. International attempts to control or ban nuclear weapons depend on the verification of test bans. Detection of underground

nuclear explosions depends on the science of seismology, of which Sykes has long been a very distinguished practitioner.

The book starts with the author's brief description of what it was like to be a scientific participant in the 1974 negotiations that led to the Threshold Test Ban Treaty, an agreement that prohibits the testing of nuclear devices having a yield exceeding

150 kilotons. The American delegation, he recalls, was under continuous surveillance, as became obvious when one member of the party asked the Moscow hosts what to do if he got lost on the way to or from the opera. ("Do not worry" was their only reply.)

In the chapters that follow, Sykes offers a concise history of the development and deployment of nuclear weapons, summarizes the international attempts to control nuclear explosion tests made between 1955 and 1963,

and describes the practice known as "decoupling," in which nuclear explosions are muffled from seismic detection by conducting them in large underground cavities.

Much of the remainder of the book is dedicated to describing the international negotiations, congressional hearings, and politics that have surrounded efforts to institute a partial or complete ban on nuclear testing. At the 1972 CTBT Senate hearings,



Silencing the Bomb
One Scientist's Quest to Halt Nuclear Testing
Lynn R. Sykes
Columbia University Press, 2017. 303 pp.

The reviewer is professor emeritus of physics, Wayne State University, Detroit, MI 48202, USA. Email: a_saperstein@wayne.edu

A military parade in Pyongyang, North Korea, on 8 February underscores present-day nuclear tensions.

Sykes himself testified about the general concurrence among civilian seismologists that future substantial nuclear tests would be reliably detected. (Later reports from the National Academies would conclude that no useful knowledge could be obtained from nuclear explosions too small to be detected, meaning that there would be no benefit to cheating test bans.) Nevertheless, the hearing did not compel Congress to enter into negotiations to secure a full test ban treaty.

The book concludes with estimates of the number and sizes of nuclear weapons currently possessed by the major powers and a discussion of the possible consequences of accidental nuclear weapon deployment and deliberate nuclear war, including nuclear winter. Sykes's conclusion, with which this reviewer strongly agrees, is that "[t]he probability per year of a nuclear exchange may be low, but if it happens, the consequences will be catastrophic."

Despite the risks, universal support for ending nuclear weapons research remains elusive. Yet Sykes continues to advocate for test bans, writing "[g]etting the public and governments to deal with rare but catastrophic events is difficult but very necessary."

Although the book is not intended for a technical audience, it would have benefited from a more detailed discussion of the terms used to describe seismic events, as well as their relation to the yields of suspected nuclear explosions. Many readers may likewise struggle to understand how scientists distinguish explosions from earthquakes. For example, in chapter 7, Sykes alludes to the superiority of Love waves over Rayleigh waves in distinguishing between earthquakes and underground explosions, without explaining what these two types of wave are or what makes the former preferable.

The book also discusses how those opposed to test bans tend to overestimate the size of Soviet nuclear test explosions, without describing how these errors come about. Without this information, some readers—particularly those who are disinclined to agree with Sykes's commitment to banning nuclear testing—may find it easy to dismiss his arguments.

To conclude, although lacking in scientific detail, *Silencing the Bomb* gives a good overview of the domestic politics that have surrounded nuclear test bans since their inception. This account will be useful to both technically inclined and lay audiences. ■

SCIENCE AND SOCIETY

Reason (and science) for hope

An optimistic treatise celebrates the enlightened thinking that has made us happier, healthier, and safer than ever

By Michael Shermer

For most of us, it is easier to imagine the world going to hell in a handbasket than it is to picture a rosy future. We can readily conjure up incremental improvements such as increased Internet bandwidth, improved automobile navigation systems, or another year added to our average life span. But what really gets our imaginations roiling are images of nuclear Armageddon, robots run amok, and terrorists in trucks mowing down pedestrians. The reason for this asymmetry is an evolved feature of human cognition called the negativity bias, a phenomenon explored in depth by the Harvard psychologist and linguist Steven Pinker in his magisterial new book, *Enlightenment Now*.

This new book is an estimable sequel to Pinker's *The Better Angels of Our Nature*, which Bill Gates called "the most inspiring book I've ever read." This is not hyperbole. *Enlightenment Now* is the most uplifting work of science I've ever read.

Pinker begins with the Enlightenment because the scientists and scholars who drove that movement took the methods developed in the Scientific Revolution and applied them to solving problems in all fields of knowledge. "Dare to know" was Immanuel Kant's oft-quoted one-line summary of the age he helped launch, and with knowledge comes power over nature, starting with the second law of thermodynamics, which Pinker fingers as the cause of our natural-born pessimism.

In the world in which our ancestors evolved the cognition and emotions that we inherited, entropy dictated that there were more ways for things to go bad than good. Thus, our modern psychology is tuned to a world that was more dangerous than it is today, he argues. Because our ancestors' survival depended on vigilantly scanning for negative stimuli, good experiences (e.g., a pain-free day) often go unnoticed, as we attempt to respond to the failures that could spell the end of our existence. But instead of interpreting accidents, plagues, famine, and disease as the wrath of angry gods,

vengeful demons, or bewitching women like our medieval ancestors did, we enlightened thinkers now know that's just entropy taking its course.

In 75 charts and graphs and thousands of statistics, Pinker documents how we have systematically applied knowledge to problems in order to propel ourselves to unimaginable levels of progress. Since the Enlightenment, he reveals, more people live longer, healthier, happier, and more meaningful lives filled with enriching works of art, music, literature, science, technology, and medicine. This is not to mention improvements to food, drink, clothes, transportation, and houses, nor the ever-increasing ease of international travel or instant access to much of the world's knowledge that many of us enjoy today.

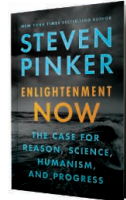
Exceptions are no counter to Pinker's massive data set. Follow the trend lines, not the headlines, he urges. For example, although military engagements make the news daily, "[w]ar between countries is obsolescent, and war within countries is absent from five-sixths of the world's surface." "In most times and places, homicides kill far more people than wars," he adds, "and homicide rates have been falling as well."

We're not just less likely to fall victim to an intentional death. On the whole, we are safer than ever. "Over the course of the 20th century, Americans became 96 percent less likely to be killed in a car accident,

Enlightenment Now

The Case for Reason, Science, Humanism, and Progress

Steven Pinker
Viking, 2018. 576 pp.



88 percent less likely to be mowed down on the sidewalk, 99 percent less likely to die in a plane crash, 59 percent less likely to fall to their deaths, 92 percent less likely to die by fire, 90 percent less likely to drown, 92 percent less likely to be asphyxiated, and 95 percent less likely to be killed on the job."

Each area of improvement has specific causes that Pinker carefully identifies, but he attributes our overall progress to "Enlightenment humanism," a secular worldview that values science and reason over superstition and dogma. It is a heroic journey, Pinker concludes with rhetorical flair: "We are born into a pitiless universe, facing steep odds against life-enabling order and in constant jeopardy of falling apart." Nevertheless, "human nature has also been blessed with resources that open a space for a kind of redemption. We are endowed with the power to combine ideas recursively, to have thoughts about our thoughts. We have an instinct for language, allowing us to share the fruits of our experience and ingenuity. We are deepened with the capacity for sympathy—for pity, imagination, compassion, commiseration."

This is our story, not vouchsafed to any one tribe but "to any sentient creature with the power of reason and the urge to persist in its being." With this fact, there is reason (and science) for hope. ■

10.1126/science.aar8093

PODCAST

A Wilder Time
Notes from a Geologist at the Edge of the Greenland Ice
William E. Glassley
Bellevue Literary Press, 2018.
224 pp.

Greenland's rapidly melting ice sheet may earn more press today, but the bedrock below—filled with tantalizing clues about Earth's early history—has captured the imagination of geologists for decades. This week on the *Science* podcast, William Glassley reflects on his firsthand experience conducting research in remote regions of the island's pristine wilderness. scienmag.org/podcasts

The reviewer is the publisher of *Skeptic* magazine, a presidential fellow at Chapman University, and the author of *Heavens on Earth: The Scientific Search for the Afterlife, Immortality, and Utopia*. Email: mshermer@skeptic.com



Clouds obscure a mountain range above the Kaiser Franz Josef Fjord in northeast Greenland.



The Australian government is grappling with ways to control carp.

Edited by Jennifer Sills

Biocontrol of invasive carp: Risks abound

Introduced common carp (*Cyprinus carpio*) infest many Australian waterways and dominate their ecosystems (1). To reduce carp numbers and aid native species recovery, the Australian Government has proposed the release of cyprinid herpesvirus 3 (CyHV-3; koi herpesvirus) (2). This virus, presumed to be absent from Australia, can devastate farmed carp (3, 4). Because of its economic impact, the World Organization for Animal Health requires notification when the virus is identified (5). Safety concerns have been raised over the release of CyHV-3, including potential infection of threatened native fish and environmental damage due to decomposing carp (4, 6). However, our knowledge of CyHV-3 pathogenesis, carp biology, and Australian river ecology suggests that a more likely problem is low efficacy.

Resistance-conferring genetic polymorphisms have been described in carp (7). CyHV-3 virulence also shows strong environmental dependence: Disease develops at 16° to 28°C, whereas temperatures above 30°C block infection and lead to immunity (8). Infected carp seek out warm water refuges, which are abundant in Australian rivers (9). The high fecundity of carp may then allow rapid repopulation of any depleted waterways by immune or genetically resistant individuals. Moreover, there is little published evidence that Australian carp are currently free of the virus: Genetic analysis indicates that CyHV-3 was infecting carp elsewhere before their introduction into Australia, and the lack of recorded CyHV-3-associated mass carp deaths in Australia may simply reflect a lack of environmental cofactors. Of note,

CyHV-3 monitoring in Japanese rivers since 2004, when there was mass carp death in Lake Biwa, has shown a continued high prevalence of infection without obvious ill-effects (10).

Before a costly and irreversible large-scale CyHV-3 release, further assessments should provide convincing evidence that the virus is not already present in Australia and that, through contained, small-scale field trials, it can achieve sustainable reductions in free-living Australian carp populations without harming native ecosystems. We also support development of alternative approaches, such as release of daughterless fish, for long-term control of invasive carp populations (11).

Jonathan Marshall,^{1,2} Andrew J. Davison,³ R. Keller Kopf,⁴ Maxime Boutier,⁵ Philip Stevenson,⁶ Alain Vanderplasschen^{5*}

¹Queensland Department of Environment and Science, Water Planning Ecology, Brisbane, QLD 4001, Australia. ²Australian Rivers Institute, Griffith University, Nathan, QLD 4111, Australia. ³MRC-University of Glasgow Centre for Virus Research, Glasgow, G61 1QH, UK. ⁴Institute for Land, Water, and Society, Charles Sturt University, Albury, NSW 2640, Australia. ⁵Department of Parasitic and Infectious Diseases, University of Liège, Liège, B-4000, Belgium. ⁶School of Chemistry and Molecular Biosciences, University of Queensland, St. Lucia, QLD 4072, Australia.

*Corresponding author.
Email: a.vdplasschen@uliege.be

REFERENCES

1. R. K. Kopf *et al.*, *Nat. Ecol. Evol.* **1**, 172 (2017).
2. Australian Government, Department of Agriculture and Water Resources, National Carp Control Plan (www.agriculture.gov.au/pests-diseases-weeds/pest-animals-and-weeds/national-carp-control-plan).
3. M. Boutier *et al.*, *Adv. Virus Res.* **93**, 161 (2015).
4. K. A. McColl *et al.*, *J. Fish. Dis.* **40**, 1141 (2017).
5. World Organisation for Animal Health, "OIE-Listed diseases, infections and infestations in force in 2018" (www.oie.int/en/animal-health-in-the-world/oie-listed-diseases-2018/).
6. J. Lighten, C. van Oosterhout, *Nat. Ecol. Evol.* **1**, 87 (2017).
7. K. L. Rakus *et al.*, *Fish Shellfish Immunol.* **26**, 737 (2009).
8. A. Ronen *et al.*, *Vaccine* **21**, 4677 (2003).
9. K. Rakus *et al.*, *Cell Host Microbe* **21**, 244 (2017).
10. K. Uchii *et al.*, *FEMS Microbiol. Ecol.* **87**, 536 (2014).
11. R. Thresher *et al.*, *Nat. Biotech.* **32**, 424 (2014).

10.1126/science.aar7827

Waterbirds targeted in Iran's wetlands

Millions of migratory birds arrive each autumn at Fereydunkenar International Wetland (FIW) in Iran due to its rich ecosystem (1). FIW comprises 5427 ha located in the southern Caspian Sea and includes Fereydunkenar, Sorkhrud, and Azbaran lagoons, which are designated as Wetlands of International Importance in the Ramsar Convention on Wetlands (2). However, an estimated 3000 of these birds are currently being killed daily by local hunters in FIW (3) to sell at the local market, facilitated by the recent adoption of more efficient type of net (1).

This could have catastrophic effects on the species that depend on this ecosystem. For example, the last remaining individual of the western population of the Critically Endangered Siberian crane (*Grus leucogeranus*) (4) winters in the FIW each year, where it is not protected (5). Of the three Siberian cranes that entered FIW in 2007, two were killed (6).

Despite the global importance of the FIW to Critically Endangered species, Iran's Department of the Environment has thus been unable to curb the illegal activities that threaten this ecosystem. Armed locals show a great deal of resistance to wildlife rangers in the FIW when they attempt to enforce existing laws to curtail hunting (7). To bring poaching under control, the Iranian government should increase police presence and enforcement in the area and introduce new national legislation to control trade in endangered species at local markets. In addition, the international community (particularly the UN Convention on Biological Diversity) should pressure Iran to enforce such laws by imposing fines on the government if migratory birds are killed.

Finally, experience has shown the

effectiveness of engaging with local communities to gain support for conservation efforts. Iranian authorities have used this strategy to address poaching of the critically endangered Asiatic cheetah *Acinonyx jubatus venaticus*, which only lives in Iran (8). To raise awareness in local communities, the Department of the Environment developed educational programs, held training workshops, and distributed literature highlighting the value of the Asiatic cheetah (9). As a result, the rate of cheetah mortality by local people reduced substantially (10). As in the case of the cheetah, if local communities realize the importance of these migratory birds, they will likely work to conserve them.

Jamshid Parchizadeh¹ and Samuel T. Williams²

¹Tehran City, Tehran Province, Iran. ²Department of Zoology, School of Mathematical and Natural Sciences, University of Venda, Thohoyandou, South Africa.

*Corresponding author.

Email: jamshid.parchizadeh@gmail.com

REFERENCES

- France 24, "Iran's wetlands: a 'real massacre' for migratory birds," *The Observers* (2015); <http://observers.france24.com/en/20150120-iran-wetlands-migrating-birds-hunters>.
- M. Ahmadpour *et al.*, *Environ. Monit. Assess.* **188**, 666 (2016).
- "Daily kill of 3000 birds in Fereydunknar," *Mehr News Agency* (2017); www.mehrnews.com/news/4168294/ [in Farsi].
- IUCN Red List of Threatened Species, *Leucogeranus leucogeranus* ([www.iucnredlist.org/details/22692053/0](http://iucnredlist.org/details/22692053/0)).
- "Last western Siberian crane 'Omid' lands in Iran," *Mehr News Agency* (2017); www.mehrnews.com/news/129694/ [in Farsi].
- "Fears of extinction for West Siberian cranes due to cruel hunting in Iran and Pakistan," *The Siberian Times* (2015); <http://siberiantimes.com/ecology/casestudy/features/f0139-fears-of-extinction-for-west-siberian-cranes-due-to-cruel-hunting-in-iran-and-pakistan>.
- "The beginning of the massacre of migratory birds in Fereydunknar," *Young Journalists Club* (2017); www.yjc.ir/fa/news/5378457 [in Farsi].
- J. Parchizadeh, S.T. Williams, *Nature* **552**, 31 (2017).
- UNDP Iran, "Conservation of Asiatic Cheetah Project (CACP)-Phase II" (2017); www.undp.org/content/iran/en/home/operations/projects/environment_and_sustainable_development/conservation-of-asiatic-cheetah-cACP-phase-II.html.
- A.R. Jourabchian, M.S. Farhadinia, "Final report on

conservation of the Asiatic cheetah, its natural habitats, and associated biota in Iran" (Project Number IRA/00/G35, GEF/UNDP/DoE, Tehran, Iran 2008) [Farsi with English summary].

10.1126/science.aar8560

Shifting sands could bring invasive species

In their Letter "Greenland: Build an economy on sand" (17 November 2017, p. 879), M. Bendixen *et al.* suggest that Greenland develop a sand export industry. Bendixen *et al.* caution that implementation of sand extraction methods must minimize adverse impacts on local environments, but they do not touch on the potential for a substantial consequence of a new export trade: the introduction of non-native invasive organisms to Greenland.

In the Perspective that prompted Bendixen *et al.*'s Letter ("A looming tragedy of the sand commons," 8 September 2017, p. 970), A. Torres *et al.* discuss the need to evaluate the full spectrum of environmental impacts and cascading effects of extractive sand mining, including the transfer of invasive species, to minimize unintended consequences. The delivery of non-native biota deserves particular attention when initiating new or expanded export/import industries serviced by maritime transportation. Shifts in export of bulk commodities like sand may be especially potent as a source of new invasions.

Commercial ships that move bulk cargo often discharge large volumes of foreign-sourced ballast water and organisms to exporting ports (1) and carry biofouling organisms on their underwater surfaces (2). As a result, shipping is a leading source of coastal invasions worldwide (3). Port infrastructure and development may also facilitate invasions (4). Although vessels are increasingly subject to regulations to reduce shipborne invasions, the efficacy of these

measures remains unknown (5). Hence, the potential effect of large increases in maritime activity on invasion dynamics at high northern latitudes is a growing concern (6).

These concerns should not prevent new or increasing maritime trade. However, particularly when wholly new infrastructure may be required, all stakeholders should collaborate to develop and implement innovative and comprehensive invasion prevention strategies.

Richard A. Everett^{1*} and A. Whitman Miller²

Gregory M. Ruiz²

¹United States Coast Guard, Environmental Standards Division (CG-OES-3), Washington, DC 20593, USA. ²Smithsonian Environmental Research Center, Edgewater, MD 21037, USA.

*Corresponding author.

Email: richard.a.everett@uscg.mil

†The views expressed herein are those of the author and are not to be construed as official or reflecting the views of the Commandant or of the U.S. Coast Guard.

REFERENCES

- E. Verling *et al.*, *Proc. R. Soc. B* **272**, 1249 (2005).
- D. Minchin, S. Gollasch, *Biofouling* **19**, 111 (2003).
- G.M. Ruiz *et al.*, *Aquat. Ecosyst. Health Manag.* **18**, 299 (2015).
- K.A. Dafforn, *Manag. Biol. Invasions* **8**, 153 (2017).
- K. Carney *et al.*, *PLOS One* **12**, e0172468 (2017).
- A. Ricciardi *et al.*, *Trends Ecol. Evol.* **32**, 464 (2017).

10.1126/science.aar7741

TECHNICAL COMMENT ABSTRACTS

Comment on "The whole-soil carbon flux in response to warming"

Jing Xiao, Fangjian Yu, Wanying Zhu, Chenchao Xu, Kaihang Zhang, Yiqi Luo, James M. Tiedje, Jizhong Zhou, Lei Cheng

In a compelling study, Hicks Pries *et al.* (Reports, 31 March 2017, p. 1420) showed that 4°C warming significantly enhanced soil CO₂ production in the 1-meter soil profile, with all soil depths displaying similar temperature sensitivity (Q₁₀). We argue that some caveats can be identified in their experimental approach and analysis, and that these critically undermine their conclusions and hence their claim that the strength of feedback between the whole-soil carbon and climate has been underestimated in terrestrial models.

Full text: dx.doi.org/10.1126/science.aoa0218

Response to Comment on "The whole-soil carbon flux in response to warming"

Caitlin E. Hicks Pries, C. Castanha, R. Porras, Claire Phillips, M. S. Torn

Temperature records and model predictions demonstrate that deep soils warm at the same rate as surface soils, contrary to Xiao *et al.*'s assertions. In response to Xiao *et al.*'s critique of our Q₁₀ analysis, we present the results with all data points included, which show Q₁₀ values of >2 throughout the soil profile, indicating that all soil depths responded to warming.

Full text: dx.doi.org/10.1126/science.aoa0457

NEXTGEN VOICES: SUBMIT NOW

The perfect postdoc

Add your voice to Science! Our new NextGen VOICES survey is now open:

What is the purpose of a postdoc? To address this question, write a job advertisement for the ideal postdoc position. Describe the responsibilities and benefits of the job as well as the skills a qualified candidate should have.

To submit, go to <http://sciedmag.org/nextgen-voices>

Deadline for submissions is 2 March. A selection of the best responses will be published in the 6 April issue of Science. Submissions should be 100 words or less. Anonymous submissions will not be considered.

New AAAS president emphasizes science as public service

Margaret Hamburg's humanitarian impulses started early

By Michaela Jarvis

Very early on, Margaret Hamburg learned two important lessons about science. Her mother, a noted psychiatrist who was the first African American woman to be admitted to Vassar College and to graduate from the Yale University School of Medicine, had persevered through a difficult childhood after her surgeon father died and Jim Crow laws prevented her family from inheriting his property. Hamburg's father, the son of Jewish immigrants who had escaped pogroms in Europe, was the first in his family to earn an advanced degree and went on to become the chair of the Stanford University psychiatry department. Growing up on the Stanford campus, Hamburg learned that science could be not only the pathway toward a rewarding and interesting life but also an invaluable tool for making the world a better place.

"Both my parents are unusually big thinkers, who were committed to the world of service and using knowledge to improve the condition of others," Hamburg said in an interview this month, just before she was due to start a 1-year term as president of AAAS.

Hamburg followed her parents into medicine and into public service. After attending Harvard Medical School, she did neuroscience research at Rockefeller University, studied neuropharmacology at the National Institute of Mental Health, and conducted HIV/AIDS research policy and research at the National Institute of Allergy and Infectious Diseases. Early in her career, at age 36, Hamburg became New York City's health commissioner, where she worked to improve services for women and children, combat HIV infection, prevent the spread of tuberculosis, and initiate a bioterrorism preparedness program. In 1997, President Bill Clinton named her assistant secretary for planning and evaluation in the Department of Health and Human Services. She then spent about 8 years at the nonprofit Nuclear Threat Initiative as founding vice president for biological programs and senior scientist. For 6 years, she served as the commissioner of the U.S. Food and Drug Administration, a difficult post from which she often emerged with praise from factions on both sides of contentious issues. Since 2015, she has served as the foreign secretary of the National Academy of Medicine.

Speaking about her current tenure as AAAS president—a position her father, David Hamburg, held in 1984—Hamburg said that now is the most important time ever for science to fulfill its role in providing innovations that will help solve the world's biggest problems, such as disease, poverty, food and water shortages, climate change, and security. Solving such problems, Hamburg said, will require cooperation across international borders and across the many scientific disciplines represented by AAAS.

"None of the challenges that we face in our modern world," she said, "fit neatly into one area of expertise, one government agency, or one domain of work. Nor can we work in isolation within our national borders."

Hamburg sees AAAS as critical to helping expand scientific collaboration between countries and regions, both to solve the major problems requiring international solutions and to leverage that collaboration to improve global diplomatic relations. Hamburg called the work of the AAAS Center for Science Diplomacy, which marks its 10th anniversary this year, an important program that "especially now deserves attention."

Over the course of her career, Hamburg acquired much cross-disciplinary experience handling real-world competing interests,

while at the same time bringing scientific rigor to the decision-making. "I have learned to listen carefully to pull together different parts of my experience with new things I'm exposed to, to take a synthetic approach to problem solving," she said.

Such synthesis is also necessary, Hamburg said, to narrow the gap between scientists and nonscientists, a gap that can be associated with today's "tendency to discount experts" and even the inadequate funding of science.

"I would like to better understand the increasing skepticism about science," she said. "It concerns and surprises me on many levels. I think it is important that we as the science community, led by AAAS, are getting out and learning, talking to people, trying to make sure that we are not a closed community, but one that is truly engaging the wider public."

While Hamburg came of age in an era when conferences, journal articles, and the occasional educational television show were the main science communication methods, she said that she advocates taking up the most cutting-edge tools available. "We need to embed science in the most updated media modalities and find more exciting and engaging ways to communicate science," she said.

Meanwhile, ongoing improvement of science education, as well as broadening the reach of science education—by expanding "pathways to science" such as science camps, special programs, and role modeling in students' own communities—are key to "helping people embrace and become aware of the importance of science," Hamburg said.

Quoting AAAS CEO Rush Holt, Hamburg said that at this point in history, AAAS must come out strongly as a "force for science"—and that she is ready to lend her own might to that.

"I care passionately about science," she said, "and what it can offer if we harness it to improve the lives of people and make a difference in our world."



Margaret Hamburg

RESEARCH

How oligomeric proteins
keep in step as they diversify

Hochberg et al., p. 930



IN SCIENCE JOURNALS

Edited by Stella Hurtley



The closing of leaf stomata can be coordinated from leaf to leaf.

PLANT BIOLOGY

Sending a canopy-wide message

Although not all leaves in the canopy of a plant may be exposed to light at the same time, it is beneficial to coordinate the closure of the pores (stomata) in the leaves to prevent desiccation. Devireddy *et al.* showed in *Arabidopsis thaliana* plants that a wave of reactive oxygen species and Ca^{2+} enabled leaves experiencing light stress to trigger stomatal closure in leaves not exposed to light. Stomatal closure required abscisic acid in light-stressed leaves and jasmonic acid in nonexposed leaves. This coordinated and dynamic response may enable plants to acclimate to light stress. —WW

Sci. Signal. **11**, eaam9514 (2018).

IMAGING

Improved spy tactics for single cells

Bioluminescence imaging is a tremendous asset to medical research, providing a way to monitor living cells noninvasively

within their natural environments. Advances in imaging methods allow researchers to measure tumor growth, visualize developmental processes, and track cell-cell interactions. Yet technical limitations exist, and it is difficult to image deep tissues

or detect low cell numbers *in vivo*. Iwano *et al.* designed a bioluminescence imaging system that produces brighter emission by up to a factor of 1000 compared with conventional technology (see the Perspective by Nasu and Campbell).

Individual tumor cells were successfully visualized in the lungs of mice. Small numbers of striatal neurons were detected in the brains of naturally behaving marmosets. The ability of the substrate to cross the blood-brain barrier should provide important opportunities for neuroscience research. —PNK

Science, this issue p. 935; see also p. 868

INFECTIOUS DISEASES

Memories of exposure

Protective memory B cell responses are shaped through multiple mechanisms, including clonal selection of naïve B cells and affinity maturation. Memory B cell responses are considered critical to the development of a successful malaria vaccine—a goal that has remained remarkably elusive. Murugan *et al.* characterized memory B cell responses to the *Plasmodium falciparum* circumsporozoite (PfCSP) protein in human volunteers immunized with sporozoites. Repeated immunization induced potent responses to the immunodominant PfCSP NANP repeat by the clonal selection of naïve and preexisting memory B cell precursors; B cell responses were less influenced by affinity maturation. —CNF

Sci. Immunol. **3**, eaap8029 (2018).

ORGANOIDS

Cancer organoids to model therapy response

Cancer organoids are miniature, three-dimensional cell culture models that can be made from

primary patient tumors and studied in the laboratory. Vlachogiannis *et al.* asked whether such “tumor-in-a-dish” approaches can be used to predict drug responses in the clinic. They generated a live organoid biobank from patients with metastatic gastrointestinal cancer who had previously been enrolled in phase I or II clinical trials. This allowed the authors to compare organoid drug responses with how the patient actually responded in the clinic. Encouragingly, the organoids had similar molecular profiles to those of the patient tumor, reinforcing their value as a platform for drug screening and development. —PNK

Science, this issue p. 920

OCEAN ACIDIFICATION

Acid reef-flux

The uptake of anthropogenic carbon dioxide from the atmosphere is reducing the pH of the oceans. Ocean acidification means that calcium carbonate—the material with which coral reefs are built—will be more difficult for organisms to generate and will dissolve more quickly. Eyre *et al.* report that some reefs are already experiencing net sediment dissolution. Worryingly, the rates of loss will increase as ocean acidification intensifies. —HJS

Science, this issue p. 908

PALEOANTHROPOLOGY

Neandertal cave art

It has been suggested that Neandertals, as well as modern humans, may have painted caves. Hoffmann *et al.* used uranium-thorium dating of carbonate crusts to show that cave paintings from three different sites in Spain must be older than 64,000 years. These paintings are the oldest dated cave paintings in the world. Importantly, they predate the arrival of modern humans in Europe by at least 20,000 years, which suggests that they must be of Neandertal

origin. The cave art comprises mainly red and black paintings and includes representations of various animals, linear signs, geometric shapes, hand stencils, and handprints. Thus, Neandertals possessed a much richer symbolic behavior than previously assumed. —AMS

Science, this issue p. 912

FUNGAL INFECTIONS

Iron in the fire

Although transplantation is a life-saving therapy, patients receiving new organs are at serious risk for invasive, potentially fatal infections. *Aspergillus fumigatus* is a particularly common and troublesome fungal pathogen, but its ability to invade transplant tissues is poorly understood. To evaluate this property, Hsu *et al.* infected transplants in mice. Bleeding, caused by damage to small vessels in grafted airways, led to increased tissue iron, a known growth factor for *Aspergillus*. Thus, therapies in development that block iron and protect blood vessels may extend the life of organ recipients. —OMS

Sci. Transl. Med. **10**, eaag2616 (2018).

OPTICS

Miniaturized optical ranging and tracking

Light detection and ranging systems are used in many engineering and environmental sensing applications. Their relatively large size and cost, however, tend to be prohibitive for general use in autonomous vehicles and drones. Suh and Vahala and Trocha *et al.* show that optical frequency combs generated by microresonator devices can be used for precision ranging and the tracking of fast-moving objects. The compact size of the microresonators could broaden the scope for widespread applications, providing a platform for miniaturized laser ranging systems suitable for photonic integration. —ISO

Science, this issue p. 884, p. 887

IN OTHER JOURNALS

Edited by Sacha Vignieri and Jesse Smith

Illustration of the Chinese low-Earth-orbiting satellite, Micius



QUANTUM OPTICS

Quantum-secure satellite communication

The distribution of secret quantum keys between interested parties is a critical requirement to establish secure and unbreakable communication links. Liao *et al.* demonstrate quantum key distribution between the Chinese low-Earth-orbiting satellite Micius and ground stations located in China and Austria. Once the quantum keys have been distributed, a secure communication channel can be established between the stations, some 7600 kilometers apart. The link is robust enough that information and images can be transmitted, as well as allowing a quantum-secured video conference call to be held between the Chinese and Austrian Academies of Sciences. A network of satellites could establish a worldwide quantum-secure internet. —ISO

Phys. Rev. Lett. **120**, 030501 (2018).

STEM CELLS

Cholesterol and stem cell proliferation

Cells require basic building components such as nucleotides, amino acids, and lipids. The lipid cholesterol regulates

specific signaling pathways for proper cell function. Wang *et al.* report an additional role, one that affects the critical balance between proliferation and differentiation. When the phospholipid-remodeling enzyme Lpcat3 is inhibited, cholesterol



BIOGEOGRAPHY

Different responses to climate change in mountain plants

In a warming climate, the distributions of plant species inhabiting mountain slopes tend to move uphill. However, species abundance may also change, leading to altered dynamics in the plant communities. Rumpf *et al.*, in a study of nearly 200 mountain species in the European Alps, recorded trends toward increased local abundance in the majority of species. In particular, plants from lower elevations tended to increase in abundance as their upper range limits shifted uphill, whereas those from higher elevations showed the opposite trend. Thus, higher-elevation species are more likely to lose out through the combined effects of climate change and competition. —AMS

Proc. Natl. Acad. Sci. 10.1073/pnas.1713936115 (2018).

Climate-driven changes in abundance could increase competition between high- and low-altitude plant species.

biosynthesis increases, with resultant intestinal stem cell proliferation. This increase in cell number is normalized if cholesterol synthesis is blocked pharmacologically. Similarly, crypt organoid growth increased with cholesterol levels, and loss of Lpcat3 enhances tumor formation. This work reveals a critical role for phospholipid remodeling and cholesterol metabolism in intestinal stem cell homeostasis and cancer development. —BAP

Cell Stem Cell 10.1016/j.stem.2017.12.017 (2018).

BIOMEDICINE

How endothelial cells change identity

The development of healthy heart valves during mammalian embryogenesis requires that endothelial cells morph into a distinct cell type. When this identity change, called endothelial-to-mesenchymal transition (EndoMT), occurs inappropriately in adults, it can lead to disorders such as atherosclerosis, organ fibrosis, and pulmonary hypertension. To investigate the mechanisms regulating EndoMT, Xiong *et al.*

studied cultured endothelial cells and mice deficient in a certain metabolic enzyme. They discovered that loss of endothelial fatty acid oxidation promotes EndoMT, most likely through changes in intracellular acetyl coenzyme A levels. These results suggest that therapies aimed at increasing fatty acid oxidation, including several drugs that already exist for other purposes, could potentially be used to treat disorders caused by aberrant EndoMT. —PAK

Mol. Cell 69, 689 (2018).

NEUROSCIENCE

Tackling the mechanisms behind depression

The anaesthetic drug ketamine also has a rapid antidepressant effect. Although ketamine is known to block *N*-methyl-D-aspartate (NMDA) receptors, its exact target—which brain region and which cell groups—has remained elusive. Yang *et al.* found that neuronal burst firing in a single brain region called the lateral habenula drove robust depressive-like behaviors. These behaviors could be rapidly blocked by local ketamine infusion. Instead of acting on GABAergic neurons as

previously suggested, ketamine blocked glutamatergic neurons in the “anti-reward center” lateral habenula to disinhibit downstream dopaminergic and serotonergic neurons. Lateral habenula bursting strongly required the synergistic action of NMDA receptors and voltage-sensitive T-type calcium channels. The latter may therefore be another promising target for the development of new rapid-acting antidepressants. —PRS

Nature 10.1038/nature25509 (2018).

PHYSICS

A stringy magnet

In one-dimensional antiferromagnetic materials, the neighboring spins align opposite to each other, but if the material is put in a strong enough magnetic field, the spins will eventually all point in the direction of the field. In intermediate fields, according to a long-standing prediction, strings of spins pointing opposite to the magnetic field will form. Wang *et al.* observed these so-called Bethe strings in the compound $\text{SrCo}_2\text{V}_2\text{O}_8$ by using terahertz spectroscopy in magnetic fields

up to 30 T. By comparing with calculations, the researchers were able to identify the signatures of two- and three-string states in the spectra. —JS

Nature 554, 219 (2018).

CLIMATE CHANGE

The shape of things to come

A widespread and intense heat wave struck western and central Europe in June 2017, ranking as one of the most intense mega-heat waves since 1948. Like similar episodes in 2003 and 2010, it affected a wide area and displayed exceptional intensity. What set it apart from those events, however, is how early in the year it occurred. Sánchez-Benítez *et al.* analyzed its characteristics and attributed its occurrence to the formation of an intense subtropical ridge like those more typically occurring in July and August. They conclude that this episode could be a good example of what the future may bring, with high-summer mega-heat waves occurring earlier in the year. —HJS

Geophys. Res. Lett.

10.1002/2018GL077253 (2018).

ALSO IN SCIENCE JOURNALS

Edited by Stella Hurtley

CELL BIOLOGY

The great escape

Mitochondrial DNA (mtDNA) is a potent damage-associated molecular pattern that, if it reaches the cytoplasm or extracellular milieu, triggers innate immune pathways. mtDNA signaling has been implicated in a wide range of diseases; however, the mechanisms of mtDNA release are unclear, and the process has not been observed in real time thus far. McArthur *et al.* used live-cell lattice light-sheet microscopy to look at mtDNA release during intrinsic apoptosis. Activation of the pro-death proteins BAK and BAX resulted in the formation of large macro-pores in the mitochondrial outer membrane. These massive holes caused the inner mitochondrial membrane to balloon out into the cytoplasm, resulting in mitochondrial herniation. This process allowed the contents of the mitochondrial matrix, including mtDNA, to escape into the cytoplasm. —SMH

Science, this issue p. 883

PALEOCEANOGRAPHY

CO₂ escaped from the deep

Why did the concentration of atmospheric carbon dioxide rise so much and so quickly during the last deglaciation? Evidence has begun to accumulate suggesting that old, carbon-rich water accumulated at depth in the Southern Ocean, which then released its charge when Southern Ocean stratification broke down as the climate there warmed. Basak *et al.* present measurements of neodymium isotopes that clearly show that the deepwater column of the glacial southern South Pacific was stratified, just as would be necessary for the accumulation of old, carbon-rich water. Their data also show that North Atlantic processes were not the dominant control on Southern

Ocean water-mass structure during that interval, as has been thought. —HJS

Science, this issue p. 900

INORGANIC CHEMISTRY

Boron learns to give back to nitrogen

Although diatomic nitrogen is famously inert, a variety of transition metals can bind to it through a process termed backbonding. As the nitrogen weakly shares its own electrons, some electrons from the metal reach back out to it. Nonmetals would not seem to have the capacity for this type of bonding, but now Légaré *et al.* show that conventionally electron-deficient boron can be coaxed into it (see the Perspective by Broere and Holland). The authors treated boron-based precursors with potassium under a nitrogen atmosphere to produce several compounds with sandwiched dinitrogen between two boron centers in reduced motifs reminiscent of metal complexes. —JSY

Science, this issue p. 896;
see also p. 871

METASURFACES

Patterning a hyperbolic metasurface

Structured metasurfaces potentially enable the control of the propagation direction of excitations on the material's surface. However, the high losses associated with the materials used to date has led to relatively short lifetimes for the excitations. Li *et al.* patterned a subwavelength grating into a layer of hexagonal boron nitride (hBN) and found that the lifetime and propagation length of the excitations could be much longer. Direct imaging of the polariton excitations illustrates that hBN can be a viable platform for nanophotonic circuits. —ISO

Science, this issue p. 892

FISHERIES

More than half the fish in the sea

As the human population has grown in recent decades, our dependence on ocean-supplied protein has rapidly increased. Kroodsma *et al.* took advantage of the automatic identification system installed on all industrial fishing vessels to map and quantify fishing efforts across the world (see the Perspective by Poloczanska). More than half of the world's oceans are subject to industrial-scale harvest, spanning an area four times that covered by terrestrial agriculture. Furthermore, fishing efforts seem not to depend on economic or environmental drivers, but rather social and political schedules. Thus, more active measures will likely be needed to ensure sustainable use of ocean resources. —SNV

Science, this issue p. 904;
see also p. 864

CANCER

SEEK and you may find cancer earlier

Many cancers can be cured by surgery and/or systemic therapies when detected before they have metastasized. This clinical reality, coupled with the growing appreciation that cancer's rapid genetic evolution limits its response to drugs, have fueled interest in methodologies for earlier detection of the disease. Cohen *et al.* developed a noninvasive blood test, called CancerSEEK that can detect eight common human cancer types (see the Perspective by Kalinich and Haber). The test assesses eight circulating protein biomarkers and tumor-specific mutations in circulating DNA. In a study of 1000 patients previously diagnosed with cancer and 850 healthy control individuals, CancerSEEK detected cancer with a sensitivity of 69 to 98%

(depending on cancer type) and 99% specificity. —PAK

Science, this issue p. 926;
see also p. 866

PROTEIN EVOLUTION

Putting distance between protein relatives

Many proteins form complexes to function. When the gene for a self-assembling protein duplicates, it might be expected that the related proteins (paralogs) would retain interfaces that would allow coassembly. Hochberg *et al.* show that the majority of paralogs that oligomerize in fact self-assemble. These paralogs have more diverse functions than those that coassemble, implying that maintaining coassembly would constrain evolution of new function. The authors experimentally investigated how two oligomeric small heat-shock protein paralogs avoid coassembly and found that flexibility at regions outside of the interaction interfaces played a key role. —VV

Science, this issue p. 930

MOLECULAR BIOLOGY

Complete architecture of PRC2

Polycomb repressive complex 2 (PRC2) methylates lysine 27 in histone H3 to achieve gene silencing. Kasinath *et al.* report multiple structures of complete human PRC2 with its four core subunits (EZH2, EED, SUZ12, and RBAP48) and two cofactors (AEBP2 and JARID2) in different active states. These structures describe the molecular mimicry of H3 tails by AEBP2 and JARID2 to regulate PRC2 activity and reveal the organizational role of SUZ12 in maintaining the integrity and stability of the complex. —SYM

Science, this issue p. 940

STRUCTURAL BIOLOGY**A path to multidrug resistance**

Permeability glycoprotein (PgP) uses the energy from adenosine triphosphate (ATP) hydrolysis to transport substrates out of the cell. Many of its substrates are drugs, so it plays an important role in drug resistance. Structures in the inward-facing conformation have been determined for mouse, yeast, and algal PgP. Kim and Chen present the cryo-electron microscopy structure of human PgP in an outward-facing conformation. Two ATP molecules are bound between two nucleotide-binding domains. The substrate-binding site, located in the transmembrane domain, is open to the outside of the cell, but compressed, and no substrate is bound. This suggests that ATP binding, rather than ATP hydrolysis, promotes the transition to the outward-facing conformation and substrate release. —VV

Science, this issue p. 915

PLANT SCIENCE**Can scientists create nitrogen-fixing plants?**

Globally, more than \$100 billion is spent each year on nitrogen fertilizers, which also cause substantial environmental damage. In a Perspective, Good highlights recent research into creating plants that can directly fix nitrogen from the air. Laboratory studies have shown that genes required for nitrogen fixation can be introduced into plants and that these engineered plants can make a key part of the nitrogen-fixing enzyme nitrogenase. However, no plant has been shown to fix nitrogen directly. Given recent technical advances, a concerted research effort focused on a specific set of suitable model plants could quickly make considerable progress toward this goal. But even once such a plant has been made, substantial hurdles remain in translating this research to the field. —JFU

Science, this issue p. 869

RESEARCH ARTICLE SUMMARY

CELL BIOLOGY

BAK/BAX macropores facilitate mitochondrial herniation and mtDNA efflux during apoptosis

Kate McArthur,* Lachlan W. Whitehead, John M. Heddleston, Lucy Li, Benjamin S. Padman, Viola Oorschot, Niall D. Geoghegan, Stephane Chappaz, Sophia Davidson, Hui San Chin, Rachael M. Lane, Marija Dramicanin, Tahnee L. Saunders, Canby Sugiana, Romina Lessene, Laura D. Osellame, Teng-Leong Chew, Grant Dewson, Michael Lazarou, Georg Ramm, Guillaume Lessene, Michael T. Ryan, Kelly L. Rogers, Mark F. van Delft, Benjamin T. Kile*

INTRODUCTION: There has been an explosion of interest in the role of cell death pathways and damage-associated molecular pattern (DAMP) signaling in shaping inflammatory and immune responses. Mitochondria are central to the intrinsic apoptosis pathway, the classical form of programmed cell death. Several mitochondrial constituents have been implicated as DAMPs, including mitochondrial DNA (mtDNA). Recent work has shown that activation of intrinsic BAK and BAX-mediated apoptosis results in mtDNA-dependent triggering of the innate immune cGAS/STING pathway, resulting in type I interferon production by dying cells. The apoptotic caspase cascade normally functions to suppress this mtDNA-induced cGAS/STING signaling, rendering apoptosis “immunologically silent.”

RATIONALE: It is thought that during apoptosis, mtDNA is released into the cytoplasm. In addition to apoptosis, loss of mtDNA from the matrix has been associated with conditions including HIV and dengue infection, calcium overload, irradiation, or inflammatory diseases such as systemic lupus erythematosus or rheumatoid arthritis. However, mtDNA escape from the mitochondria has not been documented in real time.

RESULTS: Using a combination of live-cell lattice light-sheet microscopy, 3D structured illumination microscopy, correlative light electron microscopy, and electron cryotomography, we found that after BAK/BAX activation and cytochrome c loss, the mitochondrial net-

work broke down and large BAK/BAX pores appeared in the outer membrane. These BAK/BAX macropores allowed the inner membrane an outlet through which it herniated, carrying with it mitochondrial matrix components, including the mitochondrial genome. A subset of the herniated inner membranes lost their integrity, allowing mtDNA to be exposed to the cytoplasm.

CONCLUSION: An extensive literature suggests that mtDNA is found outside the mitochondria—and, indeed, outside the cell—in a wide range of circumstances. Our study provides a mechanistic description of its release from the mitochondria. mtDNA release from mitochondria during apoptosis occurs irrespective of caspase activity, but in normal cells, caspases attenuate the subsequent cGAS/STING-mediated

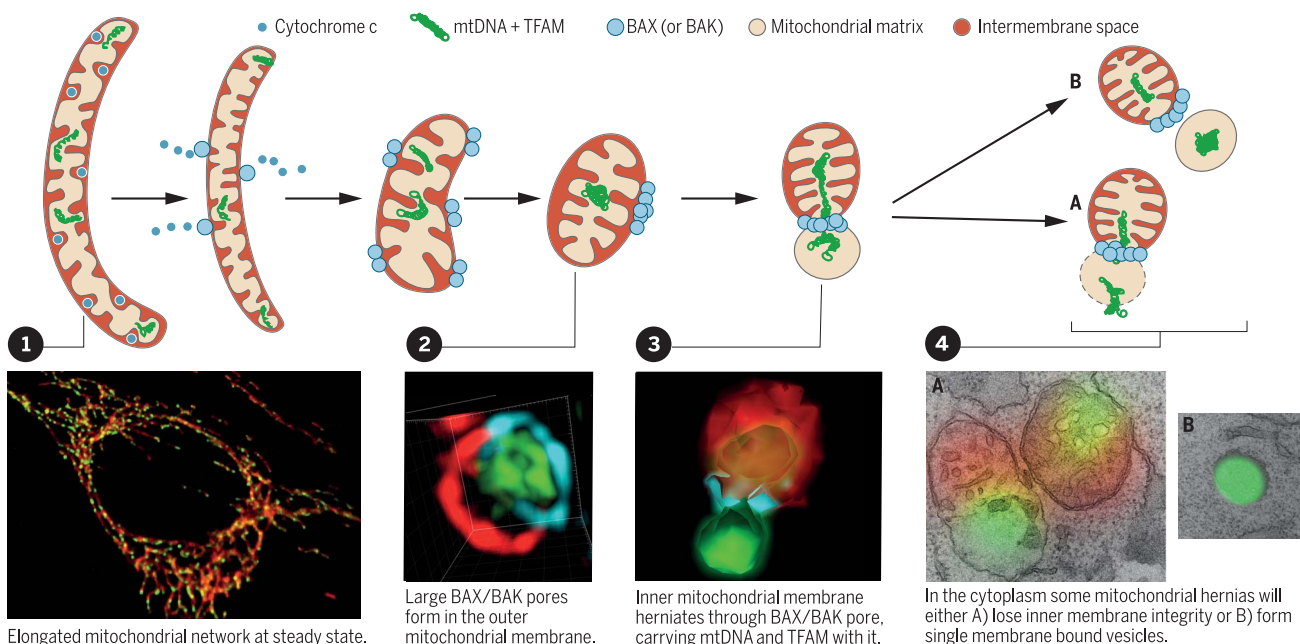
interferon response by driving rapid cellular collapse and clearance. Mitochondrial herniation might represent a general mechanism of mtDNA escape.

In addition to BAK and BAX oligomerization, there may be alternative triggers—for example, other pore-forming proteins (host- or pathogen-derived) or mitochondrial stresses—that lead to the occurrence of this phenomenon. ■

The list of author affiliations is available in the full article online.

*Corresponding author. Email: kate.mcARTHUR@monash.edu (K.M.); benjamin.kile@monash.edu (B.T.K.)
Cite this article as K. McArthur et al., *Science* **359**, eaao6047 (2018). DOI: 10.1126/science.aao6047

Schematic of apoptotic mitochondrial herniation. Inset images show the key stages as captured by lattice light-sheet microscopy, structured illumination microscopy, and correlative light and electron microscopy.



RESEARCH ARTICLE

CELL BIOLOGY

BAK/BAX macropores facilitate mitochondrial herniation and mtDNA efflux during apoptosis

Kate McArthur,^{1,2,3*} Lachlan W. Whitehead,^{1,2} John M. Heddleston,⁴ Lucy Li,¹ Benjamin S. Padman,⁵ Viola Oorschot,⁶ Niall D. Geoghegan,^{1,2} Stephane Chappaz,^{1,2,3} Sophia Davidson,¹ Hui San Chin,¹ Rachael M. Lane,³ Marija Dramicanin,^{1,2} Tahnee L. Saunders,³ Canny Sugiana,³ Romina Lessene,^{1,2} Laura D. Osellame,⁵ Teng-Leong Chew,⁴ Grant Dewson,^{1,2} Michael Lazarou,⁵ Georg Ramm,^{5,6} Guillaume Lessene,^{1,2,7} Michael T. Ryan,⁵ Kelly L. Rogers,^{1,2} Mark F. van Delft,^{1,2} Benjamin T. Kile^{1,2,3*}

Mitochondrial apoptosis is mediated by BAK and BAX, two proteins that induce mitochondrial outer membrane permeabilization, leading to cytochrome c release and activation of apoptotic caspases. In the absence of active caspases, mitochondrial DNA (mtDNA) triggers the innate immune cGAS/STING pathway, causing dying cells to secrete type I interferon. How cGAS gains access to mtDNA remains unclear. We used live-cell lattice light-sheet microscopy to examine the mitochondrial network in mouse embryonic fibroblasts. We found that after BAK/BAX activation and cytochrome c loss, the mitochondrial network broke down and large BAK/BAX pores appeared in the outer membrane. These BAK/BAX macropores allowed the inner mitochondrial membrane to herniate into the cytosol, carrying with it mitochondrial matrix components, including the mitochondrial genome. Apoptotic caspases did not prevent herniation but dismantled the dying cell to suppress mtDNA-induced innate immune signaling.

The mitochondrial, or intrinsic, apoptosis pathway is governed by the interplay among members of the BCL-2 family of proteins, which mediate mitochondrial integrity (1, 2). At steady state, pro-survival BCL-2 members (e.g., MCL-1 and BCL-X_L) restrain the activity of pro-death BAK and BAX. In response to developmental cues and stress signals, pro-survival activity is overwhelmed, permitting BAK and BAX activation. BAK and BAX oligomerize in the mitochondrial outer membrane, causing its permeabilization and the release of apoptogenic factors, of which the best characterized is cytochrome c (3, 4). Cytoplasmic cytochrome c forms part of the apoptosome complex, which successively activates caspase-9 and the apoptotic effector caspases, caspase-3 and caspase-7. Together, these proteases efficiently cleave a multitude of

substrates within the cell to accelerate its demise (5).

Apoptosis, unlike other forms of cell death such as necroptosis or pyroptosis, is generally thought to be an immunologically silent process, thereby providing a mechanism for cell clearance and tissue homeostasis that does not provoke a potentially damaging inflammatory or immune response. Immunological silence requires a functional apoptotic caspase cascade (6, 7). Genetic ablation or pharmacological inhibition of the caspase cascade during BAK/BAX-mediated apoptosis results in the production of the potent antiviral cytokine interferon- β (IFN- β). This is the result of mitochondrial DNA (mtDNA) triggering the activation of the cGAS/STING (cyclic guanosine monophosphate/adenosine monophosphate synthase/stimulator of interferon genes) signaling pathway, a cytosolic component of the cell's innate immune system designed to detect pathogen-derived DNA. In the absence of active caspases, mtDNA is recognized as a damage-associated molecular pattern (DAMP), and the dying cell behaves as if it were virally infected.

How cGAS gains access to the mitochondrial genome during apoptosis remains unknown, but the fact that mtDNA is enriched in cGAS immunoprecipitates from cells undergoing caspase-inhibited apoptosis suggests that the two do interact (6). The simplest explanation is that mtDNA is released into the cytoplasm. Multiple

studies have found evidence of mtDNA release from damaged mitochondria. mtDNA fragments are seen in the cytoplasmic fractions of cells induced to undergo death by calcium overload or irradiation, which has been ascribed to opening of the so-called mitochondrial permeability transition pore (MPTP) (8, 9). Cytosolic mtDNA fragments are also found in cells experiencing mitochondrial stress (10) or inflammasome activation (11); however, the mechanism of mtDNA release in these settings is not clear. It has been postulated that apoptosis is a key upstream requirement, because overexpression of BCL-2 attenuated downstream mtDNA-induced NLRP3 activation (11). Despite this finding and those in the earlier reports (6, 7), the notion that BAK and BAX might directly mediate mtDNA efflux remains controversial (12). Furthermore, although it is generally accepted that mtDNA would activate DNA sensors upon its release into the cytoplasm, mtDNA release itself has not been demonstrated in real time (13).

mtDNA is released from apoptotic mitochondria

To establish whether mtDNA is released into the cytosol during intrinsic apoptosis, we imaged immortalized mouse embryonic fibroblasts (MEFs) with live-cell lattice light-sheet microscopy (LLSM) (14). Wild-type MEFs are dependent on the pro-survival proteins MCL-1 and BCL-X_L for survival. MEFs lacking MCL-1 undergo BAK/BAX-dependent apoptosis in response to the BH3 mimetic drug ABT-737, a potent inhibitor of BCL-X_L and BCL-2 (15, 16) (Fig. 1A). To visualize mitochondria, we stably transduced *Mcl1*^{-/-} MEFs with a vector encoding the mitochondrial outer-membrane protein TOMM20 bearing a HaloTag (TOMM20-Halo), which fluoresces upon addition of the cell-permeant HaloTag-specific dye JaneliaFluor-646 (17). mtDNA was detected by coexpression of the mtDNA-binding protein TFAM (transcription factor A, mitochondrial), which was tagged with the green fluorescent protein (GFP) variant mNeonGreen (18) (Fig. 1B). At steady state, mitochondria formed an elaborate network, throughout which individual mtDNA nucleoids were evenly distributed (Fig. 1C). Upon addition of ABT-737, this network underwent an almost immediate dissolution, breaking down within several minutes of the onset of apoptosis (Fig. 1D). Coincident with this process, TFAM-positive nucleoids coalesced within mitochondria. As mitochondria condensed into discrete globular structures, we observed nucleoids being released into the cytoplasm (Movie 1). This phenomenon was remarkably consistent in its form and kinetics. Moreover, it occurred in both the presence and absence of the pan-caspase inhibitor QVD-OPh (19). When apoptotic cells were co-incubated with QVD-OPh, they remained attached to the coverslip, allowing continuous imaging for up to 1 hour. In contrast, without caspase inhibition, cells rapidly contracted and detached from the coverslip immediately after nucleoid release (Fig. 1E and Movie 2).

¹Walter and Eliza Hall Institute of Medical Research, Parkville, Victoria, Australia. ²Department of Medical Biology, University of Melbourne, Parkville, Victoria, Australia. ³Anatomy and Developmental Biology, Monash Biomedicine Discovery Institute, Monash University, Melbourne, Victoria, Australia.

⁴Advanced Imaging Center, Howard Hughes Medical Institute, Janelia Research Campus, Ashburn, VA, USA. ⁵Biochemistry and Molecular Biology, Monash Biomedicine Discovery Institute, Monash University, Melbourne, Victoria, Australia.

⁶Monash Ramaciotti Centre for Cryo Electron Microscopy, Monash University, Melbourne, Victoria, Australia. ⁷Department of Pharmacology and Therapeutics, University of Melbourne, Parkville, Victoria, Australia.

*Corresponding author. Email: kate.mcarthur@monash.edu (K.M.); benjamin.kile@monash.edu (B.T.K.)

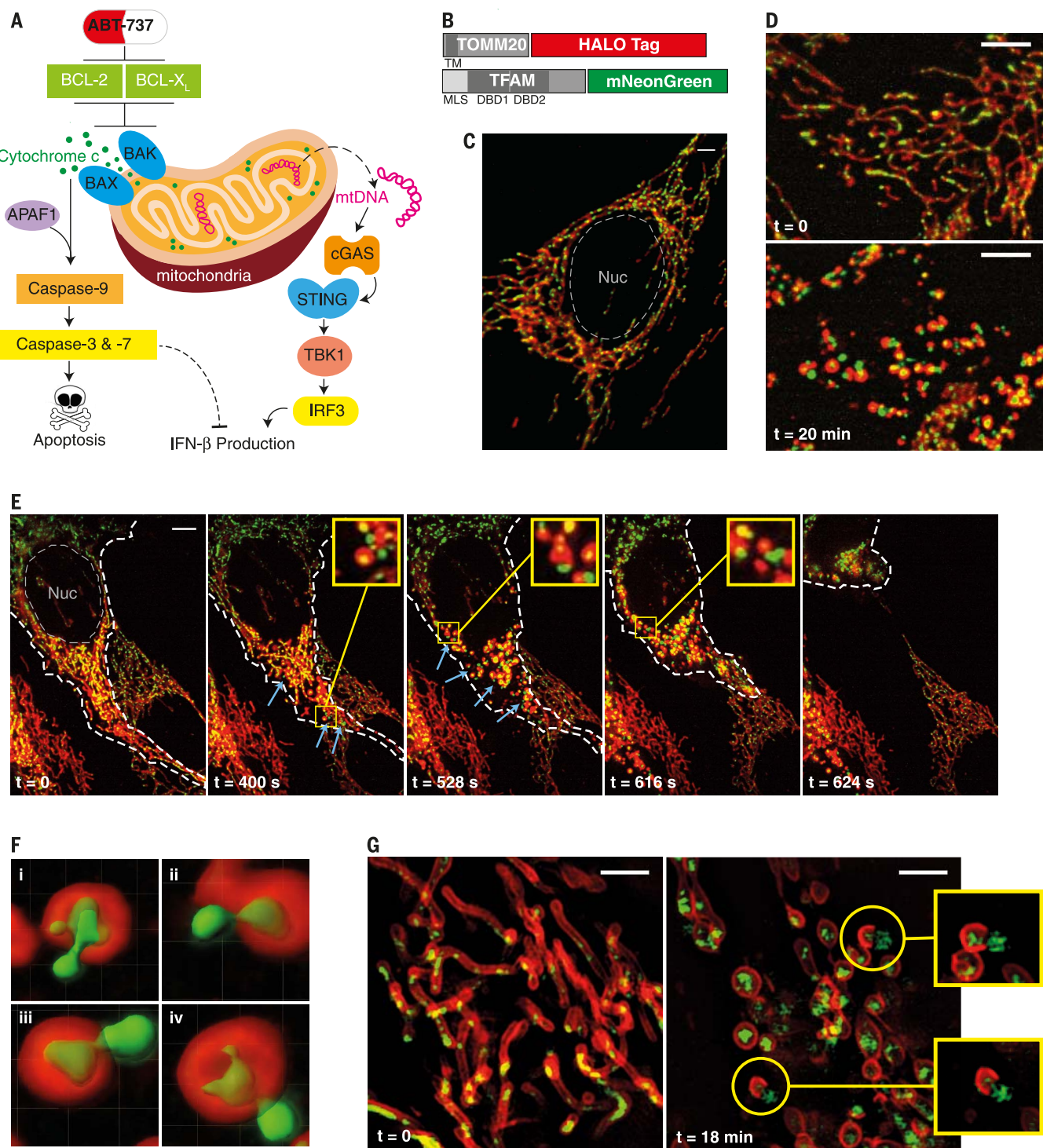


Fig. 1. mtDNA is released from apoptotic mitochondria. (A) Apoptotic interferon production pathway. APAF1, apoptotic protease activating factor 1; TBK1, TANK binding kinase 1; IRF3, interferon regulatory factor 3. (B) Fluorescent fusion proteins used to visualize mitochondria (TOMM20-Halo) and mtDNA (TFAM-mNeonGreen). TM, transmembrane domain; MLS, mitochondrial localization sequence; DBD1 and DBD2, DNA binding domain-1 and -2. (C) Typical staining of mitochondrial network in *Mcl1*^{-/-} MEFs at steady state, as imaged by LLSM, showing mitochondria (red, TOMM20-Halo) and mtDNA (green, TFAM-mNeonGreen). (D) Still snapshots of nucleoid efflux before and 20 min after ABT-737 (500 nM) + QVD-OPh (20 μ M) treatment, as imaged by LLSM (see Movie 1). (E) Snapshots from LLSM of

Mcl1^{-/-} MEFs undergoing apoptosis with active caspase cascades; elapsed time after ABT-737 (500 nM) treatment is indicated (see Movie 2). The cell is outlined by a dashed white line. Blue arrows highlight nucleoid externalization events. (F) Multiple examples [(i) to (iv)] of single mitochondria undergoing nucleoid efflux from LLSM movies in (D), displayed using 3D surface reconstructions overlaid upon original data with Imaris software. (For 3D surface reconstructions of the full time lapse, see Movie 3.) (G) 3D-SIM imaging of nucleoid externalization under the same conditions as (D) (see Movie 4). Insets show mitochondria during nucleoid efflux. Scale bars, 5 μ m [(C) to (E)], 2 μ m (G). Data in (D), (E), and (G) are representative of at least three independent experiments.

Three-dimensional (3D) surface reconstruction revealed that nucleoid release occurred from a single site on mitochondrial fragments. TFAM-positive nucleoids formed barbell-shaped structures during the release process, suggesting physical constriction at the mitochondrial surface (Fig. 1F and Movie 3). Intriguingly, nucleoids remained in close proximity to the mitochondria from which they had exited. These patterns of constriction through single exit points were confirmed in more detail by live 3D structured illumination microscopy (3D-SIM), which clearly demonstrated nucleoid release from mitochondria with a “cup-like” appearance (Fig. 1G and Movie 4). Similar results were obtained in human HeLa cells incubated with a combination of ABT-737 and the MCL-1 inhibitor S63845 (20) (fig. S1A), or in MEFs when mtDNA was visualized with the DNA dye PicoGreen (21) (fig. S1B). Given the propensity of the latter to photobleach, we focused on the TFAM mtDNA reporter system for further investigation.

Cytochrome c loss precedes mtDNA efflux

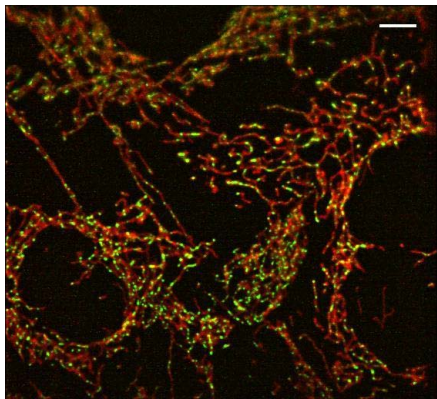
To understand the temporal relationship between mtDNA release and other events during mitochondrial apoptosis, we used LLSM to image MEFs coexpressing TOMM20-Halo, TFAM-Tomato, and cytochrome c-GFP (Fig. 2A and Movie 5). Upon treatment with ABT-737 and QVD-OPh, cytochrome c loss from mitochondria was clearly evident. Consistent with previous reports (22–26), it occurred rapidly in a wave-like fashion across the mitochondrial network, over a period of 30 to 90 s. Cytochrome c efflux preceded mitochondrial network dissolution and subsequent mtDNA release, the kinetics of which were quantified using custom automated FIJI

(27) scripts (Fig. 2, B to D, and fig. S2, A and B). This combination of visual and quantitative analysis clearly identified BAK/BAX-mediated cytochrome c release as the first event, with mitochondrial morphological rearrangement and mtDNA efflux occurring consecutively thereafter. The relative timing of each event was remarkably consistent between individual cells and across independent experiments (Fig. 2E). To further confirm that loss of cytochrome c precedes nucleoid release, we conducted a kinetic analysis in which cells were treated, fractionated, and immunoblotted to observe the timing of cytochrome c and TFAM appearance in the cytosol of apoptotic cells. Full release of cytochrome c was observed as early as 0.5 to 1 hour (Fig. 2F). TFAM was detected in the cytosol after 4 and 6 hours [as was another matrix component, dihydrolipoamide dehydrogenase (DLD)]—time points at which IFN- β was present in supernatants (Fig. 2G).

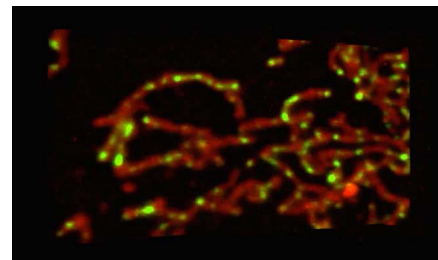
Mitochondrial dynamics and mtDNA release

To maintain a healthy network, mitochondria continuously undergo fission and fusion (28–31).

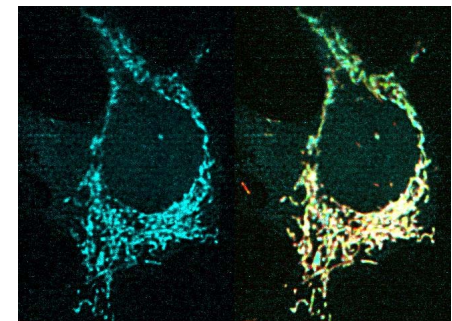
Downloaded from <http://science.sciencemag.org/> on February 22, 2018



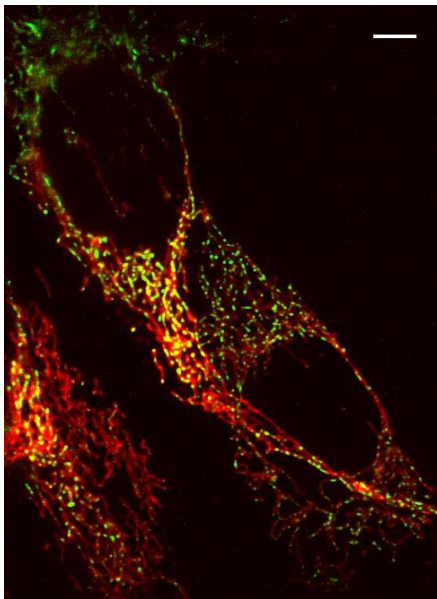
Movie 1. Lattice light-sheet imaging of mitochondria (red, TOMM20-Halo) and mtDNA (green, TFAM-mNeonGreen) from *Mcl1*^{-/-} MEFs undergoing apoptosis induced by ABT-737 and QVD-OPh. Images were captured at a rate of one 3D volume every 8 s.



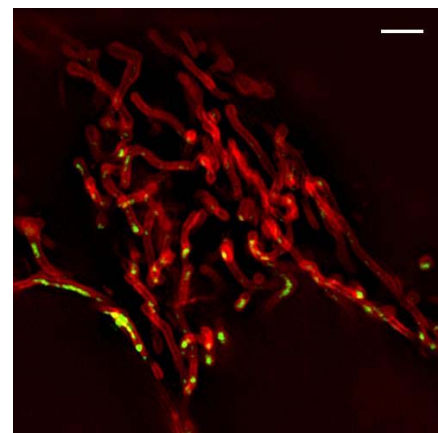
Movie 3. 3D surface reconstruction generation (red, mitochondria; green, mtDNA nucleoids) using Imaris software, which highlights mtDNA release events in Movie 1.



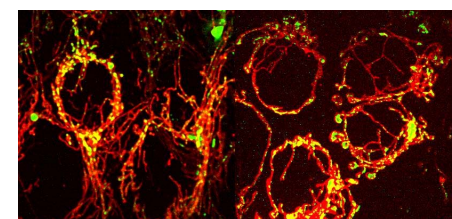
Movie 5. Lattice light-sheet imaging of mitochondria (red, TOMM20-Halo), mtDNA (green, TFAM-mNeonGreen), and cytochrome c (blue) from *Mcl1*^{-/-} MEFs undergoing apoptosis induced by ABT-737 and QVD-OPh. Images were captured at a rate of one 3D volume every 13 s.



Movie 2. Lattice light-sheet imaging of mitochondria (red, TOMM20-Halo) and mtDNA (green, TFAM-mNeonGreen) from *Mcl1*^{-/-} MEFs undergoing apoptosis with active caspases induced by ABT-737 treatment alone. Images were captured at a rate of one 3D volume every 8 s.



Movie 4. 3D SIM imaging of mitochondria (red, TOMM20-Halo) and mtDNA (green, TFAM-mNeonGreen) from *Mcl1*^{-/-} MEFs undergoing apoptosis induced by ABT-737 and QVD-OPh. Images were captured at a rate of one 3D volume every 60 s.



Movie 6. Lattice light-sheet imaging of mitochondria (red, TOMM20-Halo) and mtDNA (green, TFAM-mNeonGreen) from DRP1-deficient MEFs undergoing apoptosis induced by ABT-737 and QVD-OPh. Left: *Mcl1*^{CRISPR-/-}*Drp1*^{-/-} MEFs derived from *Drp1* knockout mice. Right: *Mcl1*^{-/-}*Drp1*^{CRISPR-/-} MEFs generated by CRISPR/Cas9 targeting of *Drp1*. Images were captured at a rate of one 3D volume every 13 s.

In mammals, the former is mediated by dynamin-related protein-1 (DRP1) (32, 33), the latter by optic atrophy protein-1 (OPA1) and mitofusin-1 and -2 (MFN1 and MFN2) (34, 35). Mitochondrial fragmentation during apoptosis has been widely documented (36–39), and a large body of evidence suggests that the response to various apoptotic stimuli is altered when fission or fusion are inhibited (40–43) [reviewed in (44)]. However, the precise requirement for fission (in particular) in mitochondrial apoptosis and its temporal relationship to cytochrome c release remains controversial (45–47).

To establish whether fission and/or fusion facilitate apoptotic mtDNA release, we generated *Drp1*^{−/−} *Mcl1*^{−/−}, *Opa1*^{−/−} *Mcl1*^{−/−}, and *Mfn1*^{−/−} *Mfn2*^{−/−} *Mcl1*^{−/−} MEFs and imaged these cells by LLSM. Consistent with their established role in fusion (48–50), loss of either OPA1 or MFN1/

MFN2 resulted in hyperfragmented mitochondria at steady state (fig. S3A). *Opa1*^{−/−} *Mcl1*^{−/−} and *Mfn1*^{−/−} *Mfn2*^{−/−} *Mcl1*^{−/−} cells exhibited a modest increase in sensitivity to ABT-737, readily undergoing cytochrome c release and nucleoid efflux in response to ABT-737 (Fig. 3, A to D, and fig. S3, B to D). In contrast, and as previously reported (51, 52), fission-deficient *Drp1*^{−/−} cells at steady state exhibited a hyperfused mitochondrial network (fig. S3A). The behavior of this network, upon induction of BAK/BAX-mediated apoptosis, was cell line-dependent. In MEFs derived from knockout mice, marked mitochondrial rearrangement was observed, but it was incomplete, with mitochondria exhibiting a “beads-on-a-string” appearance and only a limited number releasing mtDNA (Fig. 3, E and F, fig. S3F, and Movie 6). Strikingly, mtDNA release was observed only from discrete globular mitochondria,

of which there were fewer in the absence of DRP1. In contrast, when we induced apoptosis in independently derived CRISPR/Cas9 *Drp1*-targeted MEF subclones (deletion confirmed by imaging and immunoblot; fig. S3H), mitochondrial network breakdown was equivalent to that seen in wild-type counterparts (Fig. 3E and Movie 6). However, regardless of the disparities in mitochondrial dynamics, in all DRP1-deficient lines tested, we observed robust cGAS-dependent IFN-β secretion during caspase-inhibited apoptosis (fig. S3, E and G). Thus, loss of DRP1 does not prevent mtDNA-induced DAMP signaling.

mtDNA is released through BAK/BAX foci

We thus revisited the proposed involvement of the MPTP in facilitating this process (8). The exact nature and composition of the MPTP remains controversial; currently, it is defined by the

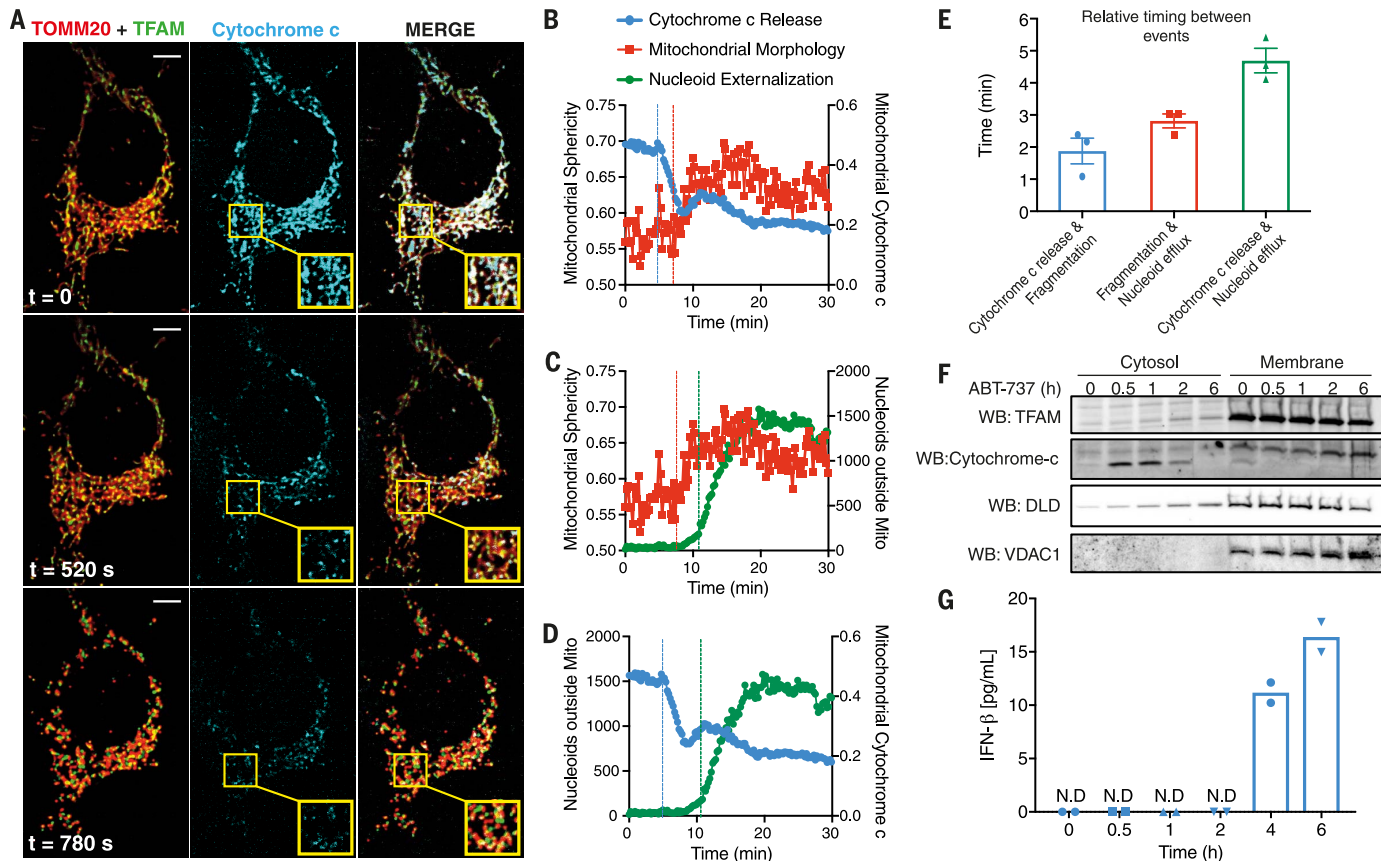


Fig. 2. Cytochrome c loss precedes mtDNA efflux. (A) Snapshots from LLSM imaging of *Mcl1*^{−/−} MEFs expressing TOMM20-Halo (stained with JF-646) (red), TFAM-tdTomato (green), and cytochrome c-GFP (blue), with cytochrome c loss and externalized nucleoids apparent 520 s and 780 s, respectively, after ABT-737 (500 nM) + QVD-OPh (20 μM) treatment (see Movie 5). Scale bars, 5 μm. (B to D) Kinetic quantitation of LLSM imaging in (A), representative of three independent experiments, depicting the relative timing between mitochondrial fragmentation and cytochrome c loss (B), mitochondrial fragmentation and nucleoid externalization (C), and cytochrome c loss and nucleoid externalization (D). Dashed vertical lines indicate the time at which each event begins, as determined visually from time-lapse movies. Parameters used to quantitate events are mitochondrial sphericity (reflective of morphology changes; values range between 0 = linear and 1 = sphere), area of cytochrome c signal inside mitochondria (pixels) relative to mitochondrial area (pixels) (reflective of cytochrome c loss to the cytoplasm), and number of mtDNA nucleoids outside mitochondria.

(E) Graphical representation of relative timing between the initiation of each event (cytochrome c loss, mitochondrial fragmentation, and externalized nucleoids) across three separate imaging experiments. Data are means ± SEM. (F) Western blots of cytosolic (left) and membrane (right) fractions of *Mcl1*^{−/−} MEFs pretreated with QVD-OPh (50 μM) followed by ABT-737 (1 μM) at the indicated times. DLD, dihydrolipoamide dehydrogenase (matrix protein); VDAC1, voltage-dependent anion-selective channel 1 (OMM protein). (G) IFN-β in culture supernatants from *Mcl1*^{−/−} MEFs in (F) collected immediately before fractionation. Blots and data in (F) and (G) are representative of two or three independent experiments. N.D., not detected.

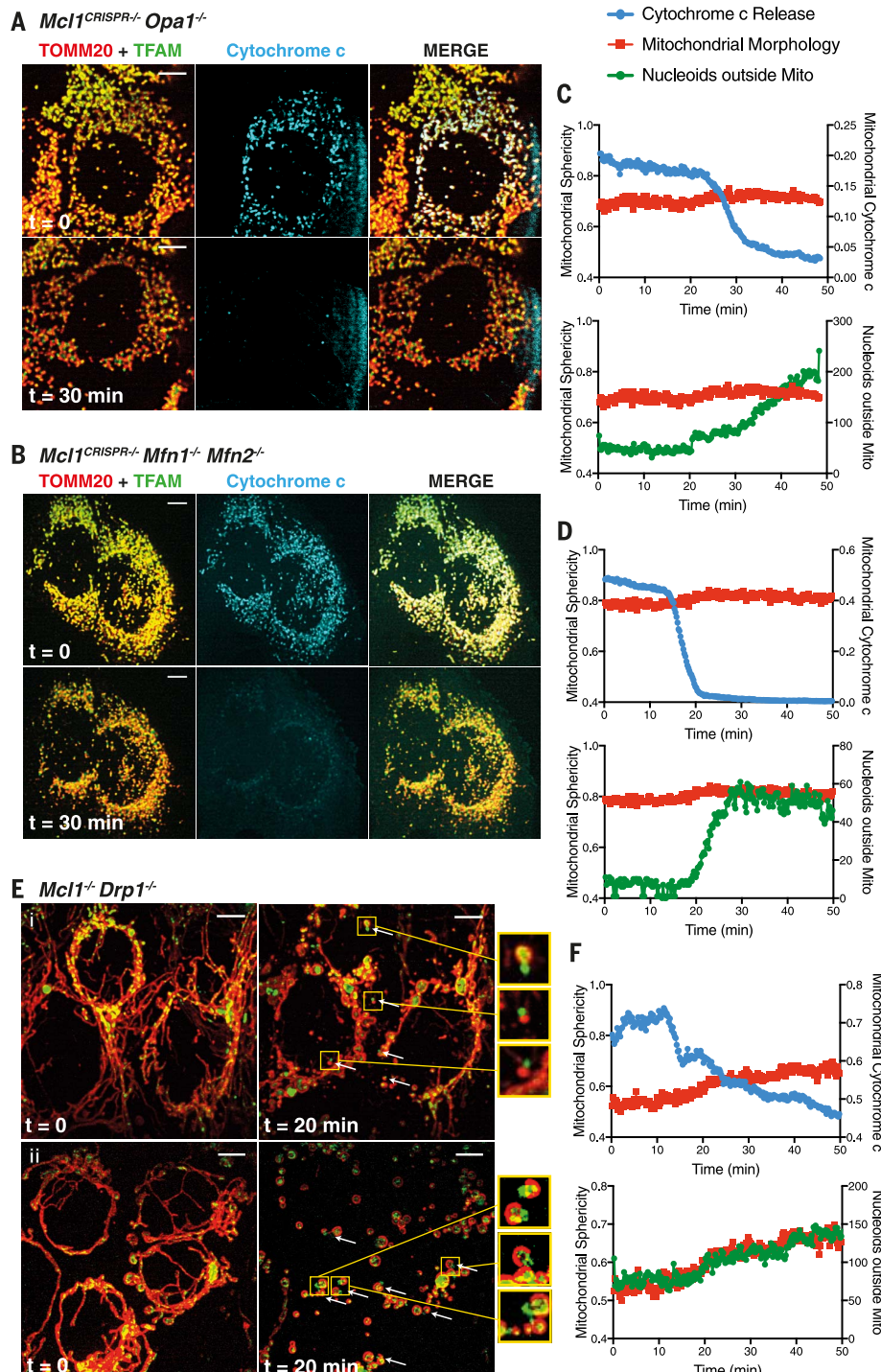
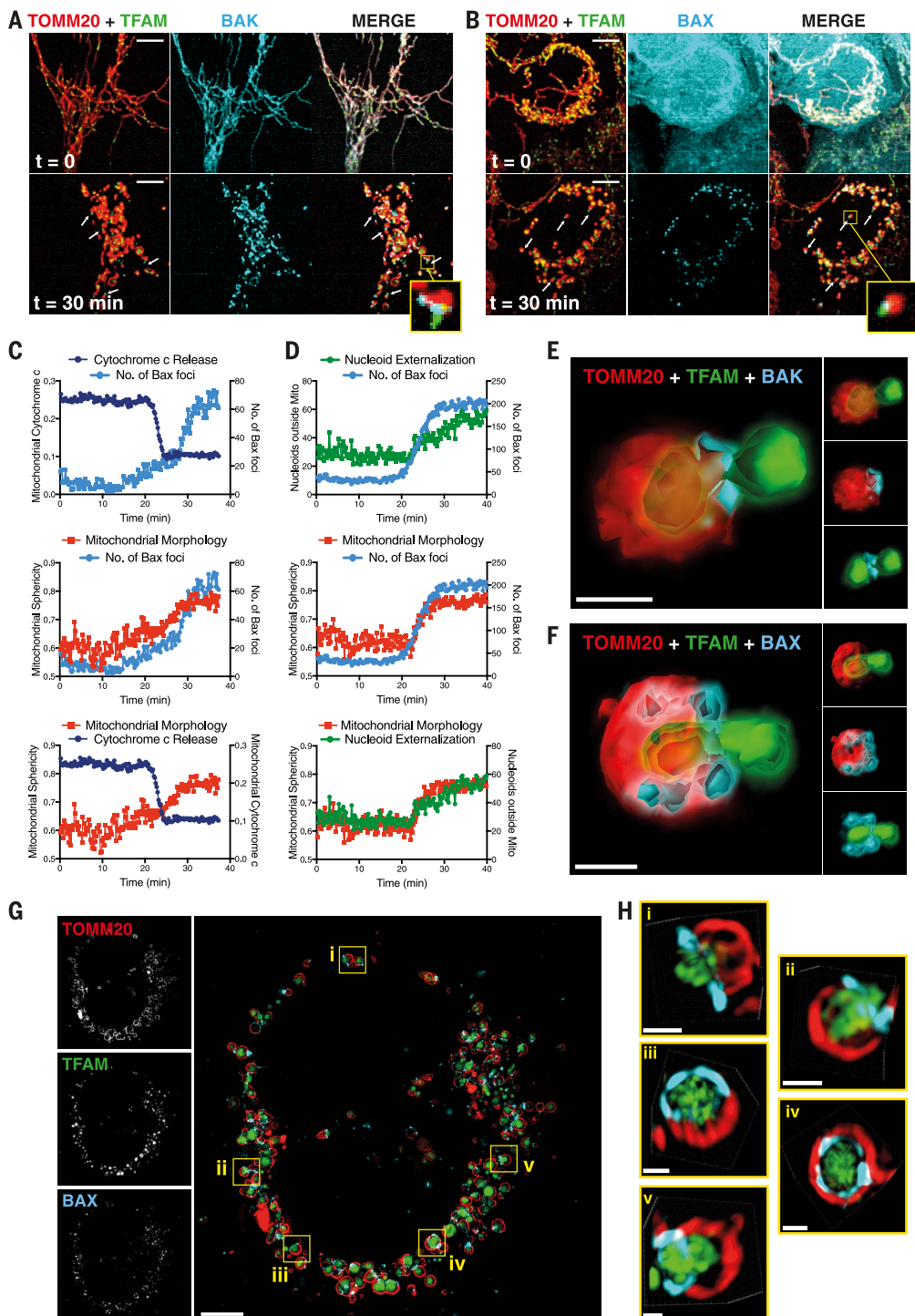


Fig. 3. Breakdown of mitochondrial network and mtDNA release during apoptosis does not require DRP1 or the mitochondrial fusion machinery. (A and B) Apoptotic mtDNA release from fusion-deficient *Mcl1*^{-/-} *Opa1*^{-/-} MEFs (A) and *Mcl1*^{-/-} *Mfn1*^{-/-} *Mfn2*^{-/-} MEFs (B) 30 min after ABT-737 (500 nM) + QVD-OPh (20 μ M) treatment, as imaged by LLSM. (C and D) Kinetic quantitation of (A) and (B), respectively. (E) Two examples of mitochondrial fragmentation during apoptosis in MCL1/DRP1-deficient MEFs 20 min after ABT-737 (1 μ M) + QVD-OPh (20 μ M) treatment, as imaged by LLSM. Top: *Mcl1*^{CRISPR-/-} *Drp1*^{-/-} MEFs derived from *Drp1* knockout mice. Bottom: *Mcl1*^{-/-} *Drp1*^{CRISPR-/-} MEFs generated by CRISPR/Cas9 targeting of *Drp1*. mtDNA release events are highlighted by white arrows (see Movie 6). Scale bars in (A), (B), and (E), 5 μ m. (F) Kinetic quantitation of apoptotic mtDNA release from fission-deficient *Mcl1*^{-/-} *DRP1*^{-/-} MEFs, showing the relative timing of mitochondrial fragmentation, cytochrome c loss, and nucleoid externalization. All images and graphs are representative of three independent experiments.

ability of the drug cyclosporin A (CsA) to block its opening (53, 54). When we pretreated MEFs with CsA and then induced apoptosis, we saw identical patterns and amounts of nucleoid efflux (fig. S4, A and B). This indicated that apoptotic mtDNA efflux does not require MPTP opening. To assess mitochondrial membrane potential during herniation, we stained cells with the membrane potential dye TMRM and imaged them via LLSM. When treated with ABT-737 and QVD-OPh, all mitochondria rapidly lost TMRM staining (fig. S2, C and D). This occurred before mitochondrial morphology rearrangement and mtDNA release. In contrast, treatment of cells with the uncoupling agents actinomycin A and oligomycin A (A/O) triggered a drastic loss of TMRM staining but did not lead to mitochondrial morphology changes or mtDNA release (fig. S2, C and D). Accordingly, A/O treatment did not induce IFN- β production from MEFs (fig. S2E). Thus, although mitochondria lose membrane potential during caspase-inhibited apoptosis, loss of potential in itself does not trigger mtDNA release. We therefore considered the possibility that BAK and BAX directly facilitate this process.

It is well established that activation of BAK and BAX leads to their oligomerization in the outer mitochondrial membrane (OMM) and its subsequent permeabilization (40, 55–58). However, they are not thought to rupture the inner mitochondrial membrane (IMM) (59). We thus examined the localization of BAK and BAX during mtDNA release. LLSM imaging of *Bak*^{-/-} *Bax*^{-/-} *Mcl1*^{-/-} MEFs reconstituted with a tagged variant of BAK (BAK-mRuby2), in addition to TOMM20-Halo and TFAM-mNeonGreen, revealed uniform BAK staining across the mitochondria. Upon induction of apoptosis, BAK became concentrated in bright foci in the OMM (Fig. 4A). In cells reconstituted with a tagged variant of BAX (BAX-mRuby2), BAX staining was ubiquitous at steady state, consistent with its reported cytoplasmic location. In response to ABT-737, BAX was very clearly recruited to, and also formed bright foci in, fragmented mitochondria (Fig. 4B and Movie 7). In both cases, these large aggregates of BAK or BAX—which were similar in scale and topology to those previously described using stimulated emission depletion microscopy or single-molecule localization microscopy (60, 61)—appeared 4 to 8 min after cytochrome c loss (Fig. 4C, top), concurrent with mitochondrial morphology changes and nucleoid release (Fig. 4D, middle and bottom). Given that cytochrome c release precedes fragmentation and mtDNA efflux (Fig. 2), this suggests that cytochrome c must exit from BAK or BAX pores too small to be resolved by LLSM. This idea is consistent with a model (62) whereby only a small amount of BAX is required for mitochondrial outer membrane permeabilization (MOMP) and the majority is recruited after cytochrome c release has taken place. mtDNA release was observed only after large BAK/BAX foci had appeared, and these BAK/BAX foci were present at the same location from which mtDNA was released (Fig. 4, A and B, white arrows). 3D visualization clearly showed BAK and BAX encircling the point of

Fig. 4. mtDNA is released from BAK/BAX foci. (A and B) Representative snapshots from LLSM imaging of *Mcl1*^{-/-} *Bak*^{-/-} *Bax*^{-/-} MEFs overexpressing TOMM20-Halo (red), TFAM-mNeonGreen (green), and reexpressing mRuby2-BAK (A) or mRuby2-BAX (B) (blue), before and after mtDNA release 30 min after ABT-737 (10 μ M) + QVD-OPh (20 μ M) treatment (see Movie 7). Scale bars, 5 μ m. **(C)** Kinetic quantitation of the appearance of BAX foci with respect to cytochrome c release and fragmentation of mitochondria events (mitochondrial sphericity measurement) from LLSM imaging of *Mcl1*^{-/-} *Bak*^{-/-} *Bax*^{-/-} MEFs expressing TOMM20-Halo, mRuby2-BAX, and cytochrome c-GFP. **(D)** Kinetic quantitation of the appearance of BAX foci with respect to nucleoid externalization and mitochondrial fragmentation events from LLSM imaging of *Mcl1*^{-/-} *Bak*^{-/-} *Bax*^{-/-} MEFs expressing TOMM20-Halo, mRuby2-BAX, and TFAM-mNeonGreen. Data in (C) and (D) are representative of three independent experiments. **(E and F)** Single mitochondria undergoing nucleoid externalization from LLSM movies, displayed using 3D surface reconstructions overlaid upon original data with Imaris software. Scale bars, 500 nm. **(G)** 3D-SIM imaging of *Mcl1*^{-/-} *Bak*^{-/-} *Bax*^{-/-} MEFs expressing TOMM20-Halo (stained with JF-646), mScarlet-BAX, and TFAM-mNeonGreen, 90 min after ABT-737 (10 μ M) + QVD-OPh (20 μ M) treatment. Overview image is a maximum projection of the SIM reconstruction, with selected examples where clear BAX rings were evident [boxed and labeled (i) to (v)]. Image is representative of 20 images taken over the course of three independent experiments. Scale bar, 4 μ m. **(H)** 3D snapshots of single mitochondria undergoing nucleoid externalization from the SIM image in (G). Scale bars, 500 nm.



mtDNA constriction and exit from fragmented mitochondria (Fig. 4, E and F, and fig. S4, C and D). This was confirmed at higher resolution by 3D-SIM (Fig. 4, G and H, and fig. S4E).

mtDNA release is the result of IMM herniation

mtDNA nucleoids are located in the matrix of the mitochondria, insulated from the cytosol by two membranes, the inner and outer. Thus, our data raised the question of how mtDNA

might make its way from the matrix to the cytoplasm via an OMM pore. To address this, we examined the behavior of a fluorophore targeted to the space within the mitochondrial matrix (MMX-Tomato) expressed in *Mcl1*^{-/-} MEFs (fig. S5A). Upon treatment with ABT-737, MMX-Tomato exited the mitochondria in a manner similar to that of mtDNA: It was constricted during its release from a single discrete point, after which it remained in close proximity to the mitochondria, rather than dispersing throughout

the cytoplasm as we had anticipated (fig. S5B). This suggested the presence of an additional barrier restricting its egress to the cytoplasm. The obvious candidate for this was the IMM. We thus fluorescently labeled the IMM protein Distal Module Assembly Component-1 (63) (DMAC1-Tomato) and followed its localization during mtDNA release. LLSM imaging revealed that the majority of IMM remained localized with the OMM signal after mtDNA release (i.e., remained inside fragmented mitochondria) (fig. S5C).

Given that the resolution of LLSM is diffraction-limited (14), we again used higher-resolution live 3D-SIM and imaged cells expressing DMAC1-Tomato and TOMM20-Halo [stained with JF-546 (17) to visualize both mitochondrial membranes. These studies revealed ultrathin DMAC1-containing "blisters" encapsulating mtDNA external to the OMM (Fig. 5, A and B). This suggested that the IMM herniates through macropores formed by BAK and BAX. To examine this in more detail, we conducted immunogold transmission electron microscopy (TEM) and electron cryotomography (ECT) studies of ABT-737-treated *Mcl1*^{-/-} MEFs. For TEM, mtDNA was visualized by the expression of GFP-tagged TFAM and immunogold la-

belling via an antibody to GFP. The TEM images revealed multiple instances where the OMM had peeled away from the IMM (Fig. 5C, ii), and others where the OMM clearly terminated while the IMM continued, ballooning out and encapsulating the mtDNA-TFAM signal (Fig. 5C, iii and iv). ECT confirmed the mitochondrial herniation event (Fig. 5, D and E). The advantages of ECT are enhanced resolution, elimination of any potential for sectioning artifacts, and 3D visualization (Movie 8). Thus, these data indicate that as a consequence of BAK/BAX OMM permeabilization, mitochondria fragment and larger BAK/BAX foci assemble. The formation of these BAK/BAX macropores elicits IMM herniation.

Immunoprecipitation of cGAS from apoptotic cells enriches for mtDNA (6). In considering the mechanism by which this interaction occurs, we wondered whether cGAS might localize to herniated mitochondria, potentially translocating across the IMM. To establish whether cGAS localizes to mitochondrial hernias, we initially conducted LLSM studies of *Mcl1*^{-/-} *cGAS*^{CRISPR-/-} MEFs reconstituted with cGAS-GFP. At steady state, cGAS staining was diffuse throughout the cytoplasm. We added ABT-737 and imaged for 1 hour. Mitochondrial network breakdown and herniation occurred, but no change in cGAS localization was observed. To establish whether cGAS might localize to hernias at later time

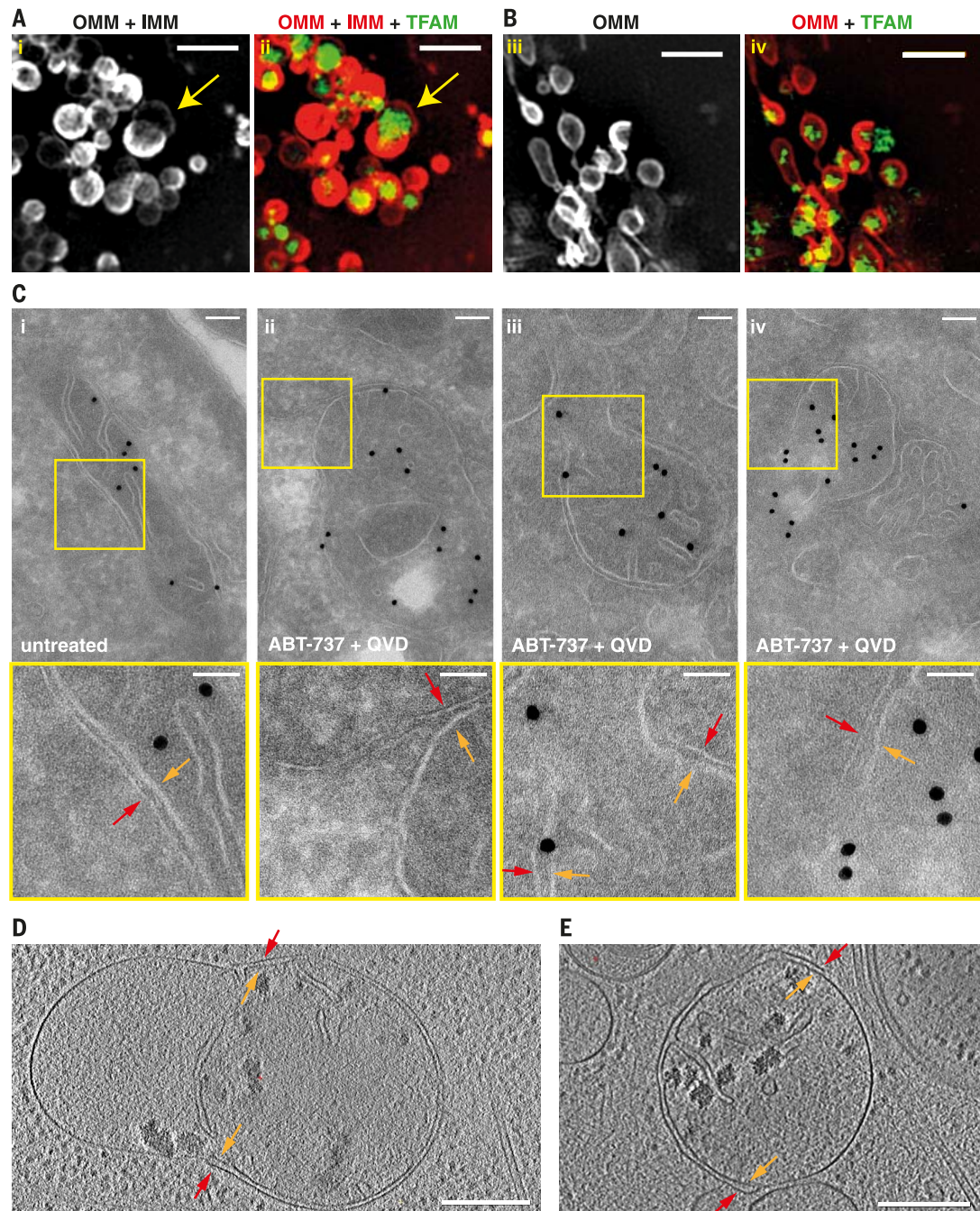


Fig. 5. mtDNA release occurs via inner mitochondrial membrane herniation. (A and B) 3D-SIM imaging of *Mcl1*^{-/-} MEFs expressing TOMM20-Halo (stained with JF-546) and TFAM-mNeonGreen, with additional DMAC1-Tomato [(i) and (ii)], representative of three independent experiments. For ease of comparison, 3D-SIM images from Fig. 1G (where only the OMM and mtDNA were stained) are included in (B). Joint IMM and OMM staining [(i), or red in (ii)] shows thin membrane (yellow arrows) encapsulating mtDNA [TFAM, green, (ii)] that is not present when OMM is stained alone [compare with (iii) and (iv)]. Scale bars, 2 μ m. (C) Electron microscopy imaging of untreated (i) or apoptotic mitochondria [(ii), (iii), and (iv)] immunogold-labeled for anti-GFP-TFAM to visualize location of mtDNA (black spots). Insets are annotated with arrows to mark areas where IMM (orange) and OMM (red) are clearly shown together [(i), untreated], peeling away from one another (ii), or during herniation where OMM clearly stops [(iii) and (iv)]. Scale bars, 100 nm (main images), 50 nm (insets). (D and E) ECT images of apoptotic mitochondria 90 min after ABT-737 (1 μ M) + QVD-OPh (20 μ M) treatment. Tomographic 10-nm slices are shown; arrows mark areas where OMM (red) clearly stops while IMM (orange) continues. Scale bars, 250 nm. See also Movie 8.

points, we conducted a 6-hour time course and imaged cells by confocal microscopy. At 4 and 6 hours after the induction of apoptosis, despite the presence of IFN- β in supernatants (indicative of cGAS activation), no discernible change in the pattern of cGAS staining was apparent (fig. S6, A and B).

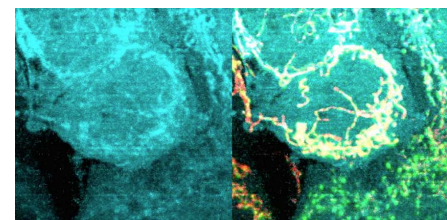
Given that cGAS did not appear within intact hernias or accumulate at their surface, we postulated that a loss of IMM integrity might facilitate mtDNA access to cGAS or vice versa. We

used correlative light and electron microscopy (CLEM) to enable the overlay of fluorescent signals and mitochondrial ultrastructure. *Mcl1*^{-/-} MEFs expressing TOMM20-Halo and TFAM-mNeonGreen were fixed 90 min after ABT-737 and QVD-OPh treatment, a time at which the majority of mitochondria had undergone herniation. These cells were subjected to confocal and electron microscopy, and the two images were correlated after acquisition (Fig. 6, A and B, and fig. S6D). Consistent with our immunogold TEM

and ECT studies (Fig. 5, C to E, and fig. S6C), we observed many instances where the OMM had dissipated, with TFAM staining aligning to the IMM-bound structures (Fig. 6C). CLEM revealed instances where IMM integrity had been lost (Fig. 6, D and E, black arrows), although this was in a minority of mitochondrial hernias. The fact that this was in the minority of mitochondria is in line with the limited translocation of TFAM to the cytosolic fraction of apoptotic cells that we had observed by immunoblot (Fig. 2F). In rare cases, TFAM-positive, single membrane-bound structures were observed, some in close proximity to herniated mitochondria (Fig. 6E, red arrow) and some apparently isolated (Fig. 6F, red arrow).

Discussion

We have shown that BAK/BAX activation initiates a series of events that culminate in mtDNA release. Breakdown of the mitochondrial network follows BAK/BAX-mediated MOMP and cytochrome c efflux, and coincides with the formation of BAK/BAX foci large enough to be detected by LLSM. These BAK/BAX macropores allow the tightly packed IMM an outlet through which it herniates, carrying with it mitochondrial matrix components, including the mitochondrial genome. Although the elegant nature of the herniation event initially suggested a highly regulated process, we postulate that it is



Movie 7. Lattice light-sheet imaging of mitochondria (red, TOMM20-Halo), mtDNA (green, TFAM-mNeonGreen), and BAX (blue) from *Mcl1*^{-/-} *Bak*^{-/-} *Bax*^{-/-} MEFs overexpressing BAX-mRuby2 and undergoing apoptosis induced by ABT-737 and QVD-OPh. Images were captured at a rate of one 3D volume every 13 s.



Movie 8. Reconstructed cryo-tomogram of an apoptotic herniating mitochondria (from Fig. 5E) moving through the z axis.

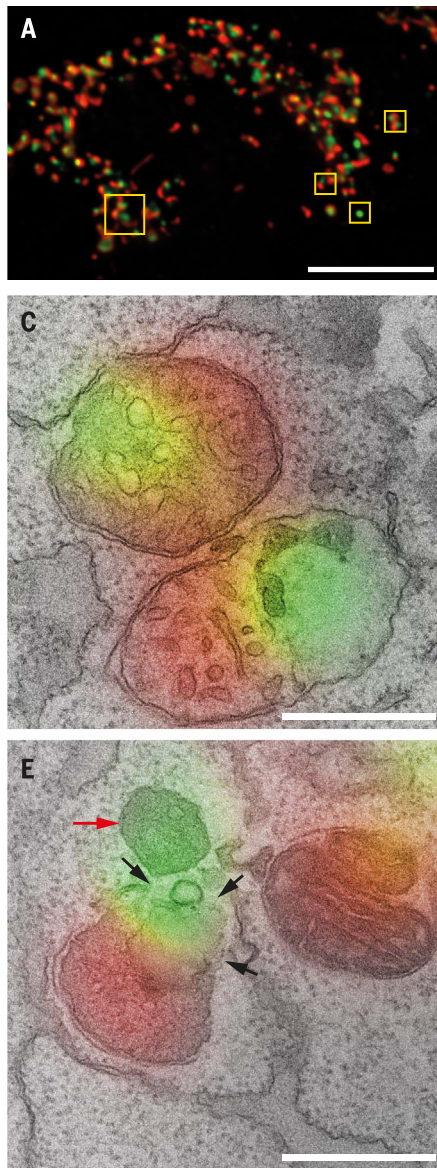


Fig. 6. Correlative light and electron microscopy of apoptotic mitochondrial herniation.

(A) Confocal light microscopy imaging of *Mcl1*^{-/-} MEFs expressing TOMM20-Halo (stained with JF-546) (red) and TFAM-mNeonGreen (green), fixed 90 min after ABT-737 (1 μ M) + QVD-OPh (20 μ M) treatment. (B) TEM imaging of the same cells as in (A). Scale bars, 10 μ m. (C to F) Selected examples from (A) and (B) at higher resolution, displaying a light microscopy image overlaid on an aligned electron microscopy image. The example shown in (C) is representative of the majority of herniation events observed; those in (D) and (E), where there is evidence of IMM breakdown, were less frequent. The image in (F) is representative of the few observed examples of TFAM-positive, single-membrane walled structures. Scale bars, 500 nm.

simply the physical result of massive holes forming in the mitochondrial outer membrane (i.e., collateral damage). Upon exposure to the cytoplasm, IMM hernias lose integrity, facilitating the recognition of mtDNA by cGAS. Dissipation of the IMM appears to occur in a limited number of mitochondria, but enough mtDNA reaches the cytosol to initiate a robust cGAS/STING pathway response. This is consistent with recent reports highlighting the profound sensitivity of cGAS to cytosolic TFAM-bound DNA (64).

The requirement for mitochondrial fission in apoptotic cell death is controversial. Several studies suggest that it is essential, because DRP1 inhibition or deletion reportedly delays cytochrome c release and cell death [reviewed in (45, 65)]. In contrast, others have concluded that because DRP1 inhibition does not confer a level of protection equivalent to that of BCL-X_L overexpression, fission and mitochondrial apoptosis are independent processes (66). Our data support the latter view. The absence of DRP1 resulted in mitochondrial network hyperfusion in both the original knockout mouse-derived MEFs and the newly generated CRISPR-targeted clones, but it did not inhibit apoptotic mitochondrial network breakdown and herniation in the CRISPR lines. We suggest that, given the profound OMM damage induced by BAK and BAX, apoptotic breakdown is not a facsimile of normal mitochondrial fission. Recent work indicates that the endoplasmic reticulum contacts mitochondria near nucleoids engaged in replication, thereby marking points of mitochondrial division (67, 68). It will be interesting to see how these mechanisms might influence mitochondrial collapse during apoptosis. Even though the impairment of mitochondrial network breakdown that was apparent during apoptosis in the *Drp1* knockout MEF cell line is likely artifactual, this system does suggest that in any setting where fragmentation is compromised, the frequency of mitochondrial herniation events will be correspondingly reduced.

Our work provides a mechanistic description of mtDNA release from mitochondria during apoptosis. It occurs irrespective of caspase activity, but in normal cells, caspases attenuate the subsequent cGAS/STING-mediated antiviral response by driving rapid cellular collapse and clearance. Previous reports have shown that genetic ablation of the apoptotic caspase cascade in vivo—at least in the hematopoietic system—results in mtDNA-dependent IFN production (6, 7). We thus contend that IMM herniation is a common event in normal physiology and that it occurs in any cell whose homeostatic turnover is governed by BAK and BAX. An extensive literature suggests that mtDNA is found outside the mitochondria—and, indeed, outside the cell—in a wide range of circumstances (13, 69). This raises the question of whether BAK/BAX-mediated mtDNA release represents a source of circulating mtDNA at steady state, or in any of the conditions where increased levels of extracellular mtDNA have been implicated in disease pathology.

It is unclear whether IMM herniation represents a general mechanism of mtDNA escape.

In addition to BAK and BAX oligomerization there may be alternative triggers, for example, other pore-forming proteins (host- or pathogen-derived) or mitochondrial stresses. Indeed, whether and how herniation may be triggered during HIV or dengue infection, calcium overload, irradiation, or during inflammatory diseases such as systemic lupus erythematosus or rheumatoid arthritis—all conditions that have been associated with loss of mtDNA from the matrix (13, 69, 70)—remains to be established. In some of these conditions cytoplasmic mtDNA is thought to be the pathological trigger, while in others, it is extracellular mtDNA. Our findings demonstrate that herniation is one route to the former. It may, in some circumstances, also contribute to generation of the latter (fig. S6E). The TFAM-positive single membrane bound structures observed in the cytoplasm of apoptotic cells suggest that hernias may bud off, and as such, represent an additional class of mitochondrial-derived vesicles (71).

Materials and methods

Cell culture

MEFs were derived from mice on a C57BL/6 background or backcrossed for more than 10 generations and prepared from embryonic day 13–14 embryos. After removal of the head, thoracic cavity, and fetal liver, a single-cell suspension was prepared in Dulbecco's modified Eagle's (DME) medium (GIBCO, ThermoFisher 11965092) supplemented with 4 mM L-glutamine, glucose (4.5 g/liter), and 10% heat-inactivated fetal bovine serum (FBS; Sigma 12003C) and cultured at 37°C, 5% CO₂ on tissue culture plates coated with 0.1% gelatin. Immortalization of MEFs was performed by transfection (Amaxa Nucleofector) of an expression plasmid encoding the SV40 T antigen (gift from D. C. S. Huang). Immortalized MEF lines were routinely maintained at 37°C, 5% CO₂ in DME-KELSO medium [prepared in-house from DMEM (GIBCO 31600083) supplemented with 40 mM sodium bicarbonate, 1 mM HEPES, 0.0135 mM folic acid, 0.24 mM L-asparagine, 0.55 mM L-arginine, 1× Pen/Strep, and 22.2 mM D-glucose] supplemented with 10% heat-inactivated FBS, penicillin/streptomycin (Pen/Strep) (Sigma P0781, 10 µl/ml), and 100 µM L-asparagine (Sigma A4159). HeLa cells were maintained at 37°C, 5% CO₂ in DME medium supplemented with 10% heat-inactivated FBS and Pen/Strep. mtDNA depletion and assessment of mtDNA content was carried out as described (6). *Drp1*^{−/−}, *Opa1*^{−/−}, and *Mfn1*^{−/−} *Mfn2*^{−/−} MEF lines were a gift from M. Ryan. To generate knockout MEFs, we used transient CRISPR/Cas9-mediated gene targeting. Targeting guide sequences were designed using Benchling software, cloned into the px458 vector (containing Cas9 and GFP marker) [gift from F. Zhang (72): Addgene plasmid 48138] and were transfected into MEFs using Fugene 6 (Roche) at a 3:1 ratio. GFP-positive cells were sorted by flow cytometry (InFlux) and clones derived from single cells were expanded. The targeted gene locus was sequenced and clones bearing indels predicted to disrupt gene function on both alleles were selected for further experimentation.

Additionally, *Mcl1*^{CRISPR−/−} clones were functionally tested by assessing their sensitivity to ABT-737 and immunoblotted for protein expression. *Drp1*^{CRISPR−/−} clones were generated as described (72) on a *Mcl1*^{−/−} *Bak*^{−/−} *Bax*^{−/−} background, reexpressing fluorescently tagged BAX, and clones were selected based on mitochondrial and peroxisomal morphology (assessed by confocal imaging) and immunoblot of protein expression. The targeting guide sequences were as follows: *Mcl1*#1, GATCATCTCGCGTACTTGC; *Mcl1*#2, GGAGCAGGCGACCGGCTCCA; cGAS#1, GATTCTTGTAGCTCAATCCTG; cGAS#2, GAAATTCAAAAGATTCCACG; *Drp1*, GCAGGACGTCTAACACAG.

Constructs and reagents

Imaging constructs were generated using PCR amplification of sequences encoding the fluorescent proteins mNeonGreen (Allele Biotechnology), pBabe (LTR)-cytochrome c-GFP [gift from D. Green (25): Addgene plasmid 41183], pTRIP-CMV-GFP-FLAG-cGAS [gift from N. Manel (73): Addgene plasmid 86675], mRuby2-NT-C1 [gift from M. Davidson (74): Addgene plasmid 54561], pCytTERM-mScarlet-N1 [gift from D. Gadella (75): Addgene plasmid 85066] mCherry, tdTomato [gift from D. C. S. Huang], or the HaloTag (Promega). These were cloned into an MSCV-IRES-hygromycin or MSCV-IRES-puromycin construct (a hygromycin/puromycin selectable retroviral vector) such that they were fused either N-terminally to BAK or BAX (murine coding sequences, gifts from D. Huang) or C-terminally to the matrix targeting sequence from OTC, DMAC1 (gift from M. Ryan), TFAM (OriGene NM_009360), or TOMM20 (GenScript synthesis NM_014765.2) sequences. MEF lines stably expressing fluorescent fusion proteins were prepared as follows: Expression plasmids were transiently transfected into Phoenix ecotropic packaging cells using Fugene 6 (Roche). Viral supernatants were collected 48 hours later and used to infect MEFs by spin infection. Cell populations expressing the fluorescent fusion proteins were sorted by flow cytometry (InFlux). Drug treatments used throughout the study include QVD-OPh (MedKoo Biosciences 1135695-98-5, MP Biomedicals 03OPH109, or made in-house by R. Lessene), ABT-737 (Active Biochemicals A-1002), S63845 (SYNthesis MedChem), cyclosporin A (Sigma 30024), antimycin A (Sigma A8674, CAS:1397-94-0), and oligomycin A (Selleck S1478, CAS:579-13-5).

Viability assay

Cell viability was quantified by CellTiterGlo (Promega G7570) or flow cytometric analysis of cells excluding propidium iodide (Sigma P4864, 5 µg/ml).

ELISA

IFN-β protein was measured using the VeriKine-HS Mouse Interferon Beta ELISA (PBL Assay Science 42410) as per manufacturer's instructions.

Subcellular fractionation and immunoblotting

Cells were grown overnight in 10-cm dishes, pretreated with QVD-OPh (50 µM) for 30 min,

then treated with ABT-737 (1 μ M) for times as indicated. Culture supernatants were retrieved for analysis of IFN- β by ELISA, and cells were trypsinized and fractionated into cytosol and mitochondria-enriched heavy membrane fractions by incubating in 0.025% w/v digitonin (Biosynth) in 20 mM Hepes KOH pH 7.5, 93 mM sucrose, 100 mM KCl, 2.5 mM MgCl₂ for 10 min on ice. Cytosol and heavy membrane fractions were separated by centrifugation at 13,000g for 5 min at 4°C, before analysis on reducing SDS-PAGE, transfer to nitrocellulose membrane, and immunoblotting for TFAM (ab131607, Abcam), cytochrome c (556433, BD Biosciences), DLD [sc-365977 (G-2), Santa Cruz Biotechnologies], and VDAC1 (MABN504, Merck).

Confocal microscopy

For imaging of cells at steady state, cells were plated in 8-well chamber slides (iBidi 80826) and incubated with PicoGreen dye (InvivoGen, 3 μ l/ml) in serum-free medium for 1 hour at 37°C, and Mitotracker Red-FM dye (InvivoGen, 1 μ M) for 30 min (added halfway through PicoGreen staining). For imaging of apoptotic cells, cells were plated in 8-well chamber slides (iBidi 80826) and incubated with drug treatments at 37°C for indicated times, after which media was replaced with 2% paraformaldehyde (Electron Microscopy Sciences 15710). Cells were left to fix for 15 min, before three washes in phosphate-buffered saline (PBS), and incubated at room temperature for 40 min in permeabilization/blocking buffer of 0.1% Tween (Sigma P1379), 3% goat serum (Life Technologies 501972). Cells were then incubated overnight at 4°C with primary antibodies anti-TOMM20 (Santa Cruz Biotech sc-11415) and anti-DNA (ProGen AC-30-10) in blocking buffer, washed twice, then incubated for 1 hour in secondary antibodies [goat anti-rabbit AF647 (Life Technologies A21245) and goat anti-mouse AF488 (Life Technologies A11001)]. In both cases, wells were then washed in PBS, before phenol red-free medium was added and cells imaged on the Zeiss LSM 780 confocal microscope using a 63 \times /1.4 Plan Apo objective. Images shown are maximum-intensity projections from Z-stacks.

Lattice light-sheet microscopy

The lattice light-sheet microscopes used in these experiments are housed in the Advanced Imaging Center (AIC) at the Howard Hughes Medical Institute Janelia Research Campus, or the Walter & Eliza Hall Institute of Medical Research. The systems were configured and operated as described (14). For all experiments, MEFs were grown on 5-mm round glass coverslips (Warner Instruments CS-5R). All drug treatments were done after sample mounting in the imaging/media chamber, with the exception of PicoGreen (Invitrogen, ThermoFisher P7581) or TMRM (Sigma T5428) staining and CsA pretreatments, which were done 30 min before sample mounting. During imaging, cells were maintained in Leibovitz's L-15 medium (GIBCO, ThermoFisher 21083027) supplemented with 10% FBS, 25 mM HEPES (GIBCO, ThermoFisher 15630080), Pen/Strep

(Sigma P0781, 10 μ l/ml), 100 μ M L-asparagine (Sigma A4159), and 20 μ M TROLOX (Santa Cruz 53188-07-1). Samples were illuminated by lattice light-sheet using 488-nm, 560-nm, or 641-nm diode lasers (MPB Communications) through an excitation objective (Special Optics, 0.65 NA, 3.74-mm WD) at 70 to 75%, 40 to 80%, and 60 to 100% AOTF transmittance (respectively) and 90 mW, 75 mW, and 100 mW initial box power (respectively) for the Janelia system, or 10 to 25%, 15 to 35%, and 10 to 25% AOTF transmittance (respectively) and 30 to 60 mW, 50 to 100 mW, and 50 to 100 mW initial box power (respectively) for the WEHI system. The lattice light-sheet was illuminated at the back aperture of the excitation objective through an annular mask of 0.44 inner NA and 0.55 outer NA. Fluorescent emission was collected by detection objective (Nikon, CFI Apo LWD 25XW, 1.1 NA) and detected by sCMOS cameras (Hamamatsu Orca Flash 4.0 v2). Acquired data were deskewed as described (14) and deconvolved using an iterative Richardson-Lucy algorithm. Point-spread functions for deconvolution were experimentally measured using 200-nm TetraSpeck beads adhered to 5-mm glass coverslips (Invitrogen T7280) for each excitation wavelength.

Live 3D structure illumination microscopy

Live, two-color, 3D-SIM images were captured on a custom-built structured illumination microscope housed in the Advanced Imaging Center (AIC) at the Howard Hughes Medical Institute, Janelia Research Campus. This platform consists of a Zeiss AxioObserver inverted microscope platform with a motorized stage and Zeiss 100 \times /1.46 NA oil immersion objective. Laser excitation was achieved with 488-nm and 561-nm lasers using an acousto-optical modulator, which is synchronized with a spatial light modulator for fast dual color switching at each optical plane as described (76). Cells were maintained at 37°C, 5% CO₂ in Leibovitz's L-15 medium (GIBCO, ThermoFisher 21083027) supplemented with 10% FBS, 25 mM HEPES (GIBCO, ThermoFisher 15630080), Pen/Strep (Sigma P0781, 10 μ l/ml), 100 μ M L-asparagine (Sigma A4159), and 20 μ M TROLOX (Santa Cruz 53188-07-1). All drug treatments were done after sample mounting in the imaging/media chamber. 512 \times 512 images of each channel were collected serially on two separate sCMOS cameras (Hamamatsu Flash 4.0) and camera exposures were typically set at 10 or 20 ms. The step size was set at 150 nm, and z-thicknesses of 1.35 to 2.85 μ m were captured at each time point. The reconstruction of the data was performed using a custom-written program and all chromatic alignments were performed after acquisition.

Live, three-color, 3D-SIM imaging was performed on the OMX-SR system (GE Healthcare). This platform consists of an Olympus 60 \times 1.42 NA oil immersion lens and three PCO.edge sCMOS cameras. Laser excitation was achieved with 488-nm, 561-nm, and 642-nm lasers. During imaging, cells were maintained at 25°C, 5% CO₂ in Fluorobrite DMEM medium (GIBCO, ThermoFisher A1896701) supplemented with 10% FBS, 25 mM

HEPES (GIBCO, ThermoFisher 15630080, Pen/Strep (Sigma P0781, 10 μ l/ml), 100 μ M L-asparagine (Sigma A4159) and 20 μ M TROLOX (Santa Cruz 53188-07-1). 512 \times 512 images were captured with camera exposures kept below 10 ms. The step size was set at 125 nm, and volumes varied between 1.0 and 2.5 μ m for each time point. The reconstruction and chromatic alignment of data was performed using SoftWorx (GE Healthcare) with a Wiener filter set at 0.005. For all experiments, MEFs were grown on 23-mm round glass coverslips (Warner Instruments). All SIM data, including raw and reconstructed images, were subjected to SIMcheck FIJI Plugin (77) to ensure that image quality was within acceptable standards.

Immunogold transmission electron microscopy

Fixation and embedding procedures were carried out as described (78). Sections were cut on a Leica FC7-UC7. Immunolabeling was done with goat anti-GFP/biotin (Rockland 600-106-215) and rabbit anti-biotin (Rockland, 100-4198) followed by incubation with protein-A-Gold 15 nm (Department of Cell Biology, University Medical Center, Utrecht). High-resolution EM images were taken on a Hitachi H-7500 TEM and a FEI Tecnai T12 TEM.

Correlative light and electron microscopy

Mcl^{-/-} MEFs expressing TOMM20-Halo and TFAM-mNeonGreen were grown overnight in a 35 mm 500-grid plastic-bottomed μ -Dish (Ibidi, Germany). After treatment with QVD-OPh (20 μ M) and ABT-737 (1 μ M), cells were stained with CellMask Deep Red Plasma Membrane stain (ThermoFisher, 2.5 μ g/ml) and JaneliaFluor-646 HaloTag-specific dye (17) (50 nm) for 30 min at 37°C and 5% CO₂, then fixed using prewarmed phosphate-buffered 4% paraformaldehyde at 37°C for 1 hour. The fixed sample was imaged on an inverted Leica SP8 confocal laser scanning microscope equipped with an 40 \times /1.10 objective (water immersion, HC PLAPO, CS2; Leica Microsystems) using an HyD Hybrid Detector (Leica Biosystems) through the Leica Application Suite X (LASX v2.0.1). The optical data (35 nm lateral pixel resolution; 200 nm axial voxel resolution) was deconvolved for subsequent alignment (fast classic maximum likelihood estimation; 10 signal-to-noise ratio; 40 iterations; 0.05 quality threshold) using Huygens Professional (v15.10; Scientific Volume Imaging). After optical image acquisition, the sample was post-fixed overnight with 2.5% glutaraldehyde in 0.1 M sodium cacodylate buffer at 4°C, rinsed twice with 0.1 M sodium cacodylate, then osmicated with ferricyanide-reduced osmium tetroxide (1% (w/v) OsO₄, 1.5% (w/v) K₃[Fe(CN)₆], 0.065 M cacodylate buffer) for 2 hours at 4°C, and thoroughly rinsed five times using MilliQ water. All subsequent stages were microwave assisted using a BioWave Pro microwave system (Pelco). The sample was en bloc stained with 2% (w/v) aqueous uranyl acetate using three microwave duty cycles (120 s on, 120 s off) at 100 W under vacuum, then rinsed five times with MilliQ water. Microwave-assisted

dehydration was performed at atmospheric pressure using 150 W for 40 s per stage of a graduated series of ethanol (50%, 70%, 90%, 100%, 100%) and propylene oxide (100%, 100%), and microwave-assisted resin infiltration was performed under vacuum at 250 W for 180 s per stage using a graduated series of Procure-Araldite (25%, 50%, 75%, 100%, 100%) in propylene oxide, before resin polymerization at 60°C for 48 hours. The target depth within the target cell was then relocated within the resin block, using the procedure outlined in (79). The resin block was trimmed, then sectioned using Ultracut UCT ultramicrotome (Leica) equipped with a 45° diamond knife (Diatome) to cut serial sections (average thickness 78 nm) for collection on nine separate 300-mesh hex thin-bar copper grids. Grids containing the sections closest to the target z-planes (1000 nm to 1600 nm depth into resin block) were stained at room temperature using 2% (w/v) aqueous uranyl acetate (10 min) and Reynolds lead citrate (3 min). A 27-image TEM montage of the target cell was manually acquired using a Tecnai T12 TEM operated at 120 kV. The image montage was corrected for EM lens distortion and stitched by linear blending using the appropriate plugins in FIJI (FIJI Is Just ImageJ) (27, 80, 81). Within GIMP (GNU Image Manipulation Program, version 2.8.2), the distortion-corrected TEM montage was aligned with the deconvolved optical data using filopodia, the nucleus, and other intrinsic features as anchor points. All subsequent TEM data were aligned directly to this canonical alignment. Correlated fluorescence data were obtained by scaling and aligning TEM images to the TEM montage, extracting the aligned region from the fluorescence channels, then performing the reverse operations with bicubic interpolation.

Electron cryotomography

Cells were grown overnight on 200 mesh Quantifoil gold grids, stimulated for 90 min with ABT-737 (1 μM) + QVD-OPh (20 μM), and cryo-fixed in liquid ethane using a Vitrobot Mark IV. Continuous cryo-tomograms from -60° to 60° were recorded on a Titan Krios at a magnification of 19,500 using the Volta phase plate, an energy filter, and a K2 Summit camera at a dose of about 90 electrons per angstrom. Reconstruction was done using the IMOD Tomography package. Tomographic slices of 10-nm thickness are shown.

Data analysis

All image data were analyzed using the FIJI distribution of ImageJ (27). The segmentation of mitochondria and TFAM signal was performed using the WEKA Trainable Segmentation plugin. Segmentation was trained on representative frames of five images from different data sets, then applied to all frames of all data sets. All resultant segmentation was then also validated visually. Mitochondrial morphology was measured using FIJI's in-built morphology measures. Cytochrome c release was measured by calculating the area (pixels) of signal above background, within the segmented mitochondria signal, which was set manually at a level that was consistent

between all data sets and accurately matched the behavior that was qualitatively observed. This was then graphed relative to mitochondrial area (i.e., cytochrome c area/mito area) to ensure that changes in cytochrome c area were not artifacts of changing mitochondrial morphology. For nucleoid release measurements, the TFAM signal was segmented, thresholded, and masked with the inverse of the segmented mitochondria signal, thereby ensuring that only signal from TFAM outside the mitochondria would be measured. BAX aggregation was quantified by segmenting and counting all regions of BAX signal above a set size and intensity limit as they appeared over time. For all manual adjustments, threshold values were set using representative frames and validated against additional frames (from later time points) before application to the entire time course. Once threshold values had been set and validated, all measurements were then automated across all independent experiments and time points.

Code availability

Custom scripts automating the combinations of FIJI in-built plugins/filters used for analysis are available as supplementary files (code files S1 and S2).

REFERENCES AND NOTES

1. R. J. Youle, A. Strasser, The BCL-2 protein family: Opposing activities that mediate cell death. *Nat. Rev. Mol. Cell Biol.* **9**, 47–59 (2008). doi: 10.1038/nrm2308; pmid: 18097445
2. P. E. Czabotar, G. Lessene, A. Strasser, J. M. Adams, Control of apoptosis by the BCL-2 protein family: Implications for physiology and therapy. *Nat. Rev. Mol. Cell Biol.* **15**, 49–63 (2014). doi: 10.1038/nrm3722; pmid: 24355989
3. R. M. Kluck, E. Bossy-Wetzel, D. R. Green, D. D. Newmeyer, The release of cytochrome c from mitochondria: A primary site for Bcl-2 regulation of apoptosis. *Science* **275**, 1132–1136 (1997). doi: 10.1126/science.275.5303.1132; pmid: 9027315
4. J. Yang et al., Prevention of apoptosis by Bcl-2: Release of cytochrome c from mitochondria blocked. *Science* **275**, 1129–1132 (1997). doi: 10.1126/science.275.5303.1129; pmid: 9027314
5. O. Julien, J. A. Wells, Caspases and their substrates. *Cell Death Differ.* **24**, 1380–1389 (2017). doi: 10.1038/cdd.2017.44; pmid: 28498362
6. M. J. White et al., Apoptotic caspases suppress mtDNA-induced STING-mediated type I IFN production. *Cell* **159**, 1549–1562 (2014). doi: 10.1016/j.cell.2014.11.036; pmid: 25525874
7. A. Rongvaux et al., Apoptotic caspases prevent the induction of type I interferons by mitochondrial DNA. *Cell* **159**, 1563–1577 (2014). doi: 10.1016/j.cell.2014.11.037; pmid: 25525875
8. M. Patrushev et al., Mitochondrial permeability transition triggers the release of mtDNA fragments. *Cell. Mol. Life Sci.* **61**, 3100–3103 (2004). doi: 10.1007/s0018-004-4424-1; pmid: 15538781
9. M. Patrushev et al., Release of mitochondrial DNA fragments from brain mitochondria of irradiated mice. *Mitochondrion* **6**, 43–47 (2006). doi: 10.1016/j.mito.2005.12.001; pmid: 16413832
10. A. P. West et al., Mitochondrial DNA stress primes the antiviral innate immune response. *Nature* **520**, 553–557 (2015). doi: 10.1038/nature14156; pmid: 25642965
11. K. Shimada et al., Oxidized mitochondrial DNA activates the NLRP3 inflammasome during apoptosis. *Immunity* **36**, 401–414 (2012). doi: 10.1016/j.jimmuni.2012.01.009; pmid: 22342844
12. T.-D. Kaneganti, M. Kundu, D. R. Green, Innate immune recognition of mtDNA—an undercover signal? *Cell Metab.* **21**, 793–794 (2015). doi: 10.1016/j.cmet.2015.05.019; pmid: 26039443
13. A. P. West, G. S. Shadel, Mitochondrial DNA in innate immune responses and inflammatory pathology. *Nat. Rev. Immunol.* **17**, 363–375 (2017). doi: 10.1038/nri.2017.21; pmid: 28393922
14. B.-C. Chen et al., Lattice light-sheet microscopy: Imaging molecules to embryos at high spatiotemporal resolution. *Science* **346**, 1257998–1257998 (2014). doi: 10.1126/science.1257998; pmid: 25342811
15. T. Oltersdorff et al., An inhibitor of Bcl-2 family proteins induces regression of solid tumours. *Nature* **435**, 677–681 (2005). doi: 10.1038/nature03579; pmid: 15902208
16. M. F. van Delft et al., The BH3 mimetic ABT-737 targets selective Bcl-2 proteins and efficiently induces apoptosis via Bak/Bax if Mcl-1 is neutralized. *Cancer Cell* **10**, 389–399 (2006). doi: 10.1016/j.ccr.2006.08.027; pmid: 17097561
17. J. B. Grimm et al., A general method to improve fluorophores for live-cell and single-molecule microscopy. *Nat. Methods* **12**, 244–250 (2015). doi: 10.1016/j.ccr.2006.08.027; pmid: 17097561
18. N. C. Shaner et al., A bright monomeric green fluorescent protein derived from *Branchiostoma lanceolatum*. *Nat. Methods* **10**, 407–409 (2013). doi: 10.1038/nmeth.2413; pmid: 23524392
19. T. M. Caserta, A. N. Smith, A. D. Gultice, M. A. Reedy, T. L. Brown, Q-VD-OPh, a broad spectrum caspase inhibitor with potent antiapoptotic properties. *Apoptosis* **8**, 345–352 (2003). doi: 10.1023/A:1024116916932; pmid: 12815277
20. A. Kotschy et al., The MCL1 inhibitor S63845 is tolerable and effective in diverse cancer models. *Nature* **538**, 477–482 (2016). doi: 10.1038/nature19830; pmid: 27760111
21. N. Ashley, D. Harris, J. Poulton, Detection of mitochondrial DNA depletion in living human cells using PicoGreen staining. *Exp. Cell Res.* **303**, 432–446 (2005). doi: 10.1016/j.yexcr.2004.10.013; pmid: 15652355
22. P. D. Bholia, A. L. Mattheyses, S. M. Simon, Spatial and temporal dynamics of mitochondrial membrane permeability waves during apoptosis. *Biophys. J.* **97**, 2222–2231 (2009). doi: 10.1016/j.bpj.2009.07.056; pmid: 19843454
23. M. Rehm et al., Dynamics of outer mitochondrial membrane permeabilization during apoptosis. *Cell Death Differ.* **16**, 613–623 (2009). doi: 10.1038/cdd.2008.187; pmid: 19136937
24. M. Rehm, H. Düssmann, J. H. M. Prehn, Real-time single cell analysis of Smac/DIABLO release during apoptosis. *J. Cell Biol.* **162**, 1031–1043 (2003). doi: 10.1083/jcb.200303123; pmid: 12975347
25. J. C. Goldstein, N. J. Waterhouse, P. Juin, G. I. Evan, D. R. Green, The coordinate release of cytochrome c during apoptosis is rapid, complete and kinetically invariant. *Nat. Cell Biol.* **2**, 156–162 (2000). doi: 10.1038/35004029; pmid: 10707086
26. L. Larigue et al., An intracellular wave of cytochrome c propagates and precedes Bax redistribution during apoptosis. *J. Cell Sci.* **121**, 3515–3523 (2008). doi: 10.1242/jcs.029587; pmid: 18840646
27. J. Schindelin et al., Fiji: An open-source platform for biological-image analysis. *Nat. Methods* **9**, 676–682 (2012). doi: 10.1038/nmeth.2019; pmid: 22743772
28. B. Westermann, Mitochondrial fusion and fission in cell life and death. *Nat. Rev. Mol. Cell Biol.* **11**, 872–884 (2010). doi: 10.1038/nrm3013; pmid: 21102612
29. R. J. Youle, A. M. van der Bliek, Mitochondrial fission, fusion, and stress. *Science* **337**, 1062–1065 (2012). doi: 10.1126/science.1219855; pmid: 22936770
30. L. Pernas, L. Scorrano, Mito-morphosis: Mitochondrial fusion, fission, and cristae remodeling as key mediators of cellular function. *Annu. Rev. Physiol.* **78**, 505–531 (2016). doi: 10.1146/annurev-physiol-021115-105011; pmid: 22666705
31. J. R. Friedman, J. Numari, Mitochondrial form and function. *Nature* **505**, 335–343 (2014). doi: 10.1038/nature12985; pmid: 24429632
32. E. Smirnova, L. Gripasic, D. L. Shurland, A. M. van der Bliek, Dynamin-related protein Drp1 is required for mitochondrial division in mammalian cells. *Mol. Biol. Cell* **12**, 2245–2256 (2001). doi: 10.1091/mbc.12.8.2245; pmid: 11514614
33. J. Prudent, H. M. McBride, Mitochondrial dynamics: ER actin tightens the Drp1 noose. *Curr. Biol.* **26**, R207–R209 (2016). doi: 10.1016/j.cub.2016.01.009; pmid: 26954442
34. N. Ishihara, Y. Eura, K. Mihara, Mitofusin 1 and 2 play distinct roles in mitochondrial fusion reactions via GTPase activity. *J. Cell Sci.* **117**, 6535–6546 (2004). doi: 10.1242/jcs.01565; pmid: 15572413
35. S. Cipolat, O. Martins de Brito, B. Dal Zilio, L. Scorrano, OPA1 requires mitofusin 1 to promote mitochondrial fusion. *Proc. Natl. Acad. Sci. U.S.A.* **101**, 15927–15932 (2004). doi: 10.1073/pnas.0407043101; pmid: 15509649
36. I. Martinou et al., The release of cytochrome c from mitochondria during apoptosis of NGF-deprived sympathetic neurons is a reversible event. *J. Cell Biol.* **144**, 883–889 (1999). doi: 10.1083/jcb.144.5.883; pmid: 10085288

37. S. Frank *et al.*, The role of dynamin-related protein 1, a mediator of mitochondrial fission, in apoptosis. *Dev. Cell* **1**, 515–525 (2001). doi: [10.1016/S1534-5807\(01\)00055-7](https://doi.org/10.1016/S1534-5807(01)00055-7); pmid: [11703942](https://pubmed.ncbi.nlm.nih.gov/11703942/)

38. M. Karbowski *et al.*, Quantitation of mitochondrial dynamics by photolabeling of individual organelles shows that mitochondrial fusion is blocked during the Bax activation phase of apoptosis. *J. Cell Biol.* **164**, 493–499 (2004). doi: [10.1083/jcb.200309082](https://doi.org/10.1083/jcb.200309082); pmid: [14769861](https://pubmed.ncbi.nlm.nih.gov/14769861/)

39. C. Sheridan, P. Delivani, S. P. Cullen, S. J. Martin, Bax- or Bak-induced mitochondrial fission can be uncoupled from cytochrome C release. *Mol. Cell* **31**, 570–585 (2008). doi: [10.1016/j.molcel.2008.08.002](https://doi.org/10.1016/j.molcel.2008.08.002); pmid: [18722181](https://pubmed.ncbi.nlm.nih.gov/18722181/)

40. M. Karbowski *et al.*, Spatial and temporal association of Bax with mitochondrial fission sites, Drp1, and Mfn2 during apoptosis. *J. Cell Biol.* **159**, 931–938 (2002). doi: [10.1083/jcb.200209124](https://doi.org/10.1083/jcb.200209124); pmid: [12499352](https://pubmed.ncbi.nlm.nih.gov/12499352/)

41. S. Wasik, R. Zunino, H. M. McBride, Bax/Bak promote remodeling of DRP1 and its stable association with mitochondria during apoptotic cell death. *J. Cell Biol.* **177**, 439–450 (2007). doi: [10.1083/jcb.200610042](https://doi.org/10.1083/jcb.200610042); pmid: [17470634](https://pubmed.ncbi.nlm.nih.gov/17470634/)

42. S. Montessuit *et al.*, Membrane remodeling induced by the dynamin-related protein Drp1 stimulates Bax oligomerization. *Cell* **142**, 889–901 (2010). doi: [10.1016/j.cell.2010.08.017](https://doi.org/10.1016/j.cell.2010.08.017); pmid: [20850011](https://pubmed.ncbi.nlm.nih.gov/20850011/)

43. H. Otera, N. Miyata, O. Kuge, K. Miura, Drp1-dependent mitochondrial fission via MID49/51 is essential for apoptotic cristae remodeling. *J. Cell Biol.* **212**, 531–544 (2016). doi: [10.1083/jcb.201508099](https://doi.org/10.1083/jcb.201508099); pmid: [26903540](https://pubmed.ncbi.nlm.nih.gov/26903540/)

44. D.-F. Suen, K. L. Norris, R. J. Youle, Mitochondrial dynamics and apoptosis. *Genes Dev.* **22**, 1577–1590 (2008). doi: [10.1101/gad.1658508](https://doi.org/10.1101/gad.1658508); pmid: [18559474](https://pubmed.ncbi.nlm.nih.gov/18559474/)

45. J. C. Martinou, R. J. Youle, Which came first, the cytochrome c release or the mitochondrial fission? *Cell Death Differ.* **13**, 1291–1295 (2006). doi: [10.1038/sj.cdd.4401985](https://doi.org/10.1038/sj.cdd.4401985); pmid: [16763618](https://pubmed.ncbi.nlm.nih.gov/16763618/)

46. L. A. Gillies, T. Kuwana, Apoptosis regulation at the mitochondrial outer membrane. *J. Cell. Biochem.* **115**, 632–640 (2014). doi: [10.1002/jcb.24709](https://doi.org/10.1002/jcb.24709); pmid: [24453042](https://pubmed.ncbi.nlm.nih.gov/24453042/)

47. B. Oettinghaus *et al.*, DRP1-dependent apoptotic mitochondrial fission occurs independently of BAX, BAK and APAF1 to amplify cell death by BID and oxidative stress. *Biochim. Biophys. Acta* **1857**, 1267–1276 (2016). doi: [10.1016/j.bbabi.2016.03.016](https://doi.org/10.1016/j.bbabi.2016.03.016); pmid: [26997499](https://pubmed.ncbi.nlm.nih.gov/26997499/)

48. A. Olichon *et al.*, Loss of OPA1 perturbs the mitochondrial inner membrane structure and integrity, leading to cytochrome c release and apoptosis. *J. Biol. Chem.* **278**, 7743–7746 (2003). doi: [10.1074/jbc.C200677200](https://doi.org/10.1074/jbc.C200677200); pmid: [12509422](https://pubmed.ncbi.nlm.nih.gov/12509422/)

49. R. Sugioka, S. Shimizu, Y. Tsujimoto, Fzo1, a protein involved in mitochondrial fusion, inhibits apoptosis. *J. Biol. Chem.* **279**, 52726–52734 (2004). doi: [10.1074/jbc.M408910200](https://doi.org/10.1074/jbc.M408910200); pmid: [15459195](https://pubmed.ncbi.nlm.nih.gov/15459195/)

50. D. Arnoult, A. Grodet, Y.-J. Lee, J. Estaquier, C. Blackstone, Release of OPA1 during apoptosis participates in the rapid and complete release of cytochrome c and subsequent mitochondrial fragmentation. *J. Biol. Chem.* **280**, 35742–35750 (2005). doi: [10.1074/jbc.M505970200](https://doi.org/10.1074/jbc.M505970200); pmid: [16115883](https://pubmed.ncbi.nlm.nih.gov/16115883/)

51. N. Ishihara *et al.*, Mitochondrial fission factor Drp1 is essential for embryonic development and synapse formation in mice. *Nat. Cell Biol.* **11**, 958–966 (2009). doi: [10.1038/ncb1907](https://doi.org/10.1038/ncb1907); pmid: [19578372](https://pubmed.ncbi.nlm.nih.gov/19578372/)

52. J. Wakabayashi *et al.*, The dynamin-related GTPase Drp1 is required for embryonic and brain development in mice. *J. Cell Biol.* **186**, 805–816 (2009). doi: [10.1083/jcb.200903065](https://doi.org/10.1083/jcb.200903065); pmid: [19752021](https://pubmed.ncbi.nlm.nih.gov/19752021/)

53. C. P. Baines *et al.*, Loss of cyclophilin D reveals a critical role for mitochondrial permeability transition in cell death. *Nature* **434**, 658–662 (2005). doi: [10.1038/nature03434](https://doi.org/10.1038/nature03434); pmid: [15800627](https://pubmed.ncbi.nlm.nih.gov/15800627/)

54. V. Petronilli, A. Nicolli, P. Costantini, R. Colonna, P. Bernardi, Regulation of the permeability transition pore, a voltage-dependent mitochondrial channel inhibited by cyclosporin A. *Biochim. Biophys. Acta* **1187**, 255–259 (1994). doi: [10.1016/0006-2789\(94\)90122-8](https://doi.org/10.1016/0006-2789(94)90122-8); pmid: [7521212](https://pubmed.ncbi.nlm.nih.gov/7521212/)

55. K. G. Wolter *et al.*, Movement of Bax from the cytosol to mitochondria during apoptosis. *J. Cell Biol.* **139**, 1281–1292 (1997). doi: [10.1083/jcb.139.5.1281](https://doi.org/10.1083/jcb.139.5.1281); pmid: [9382873](https://pubmed.ncbi.nlm.nih.gov/9382873/)

56. A. Nechushtan, C. L. Smith, I. Lamensdorf, S. H. Yoon, R. J. Youle, Bax and Bak coalesce into novel mitochondria-associated clusters during apoptosis. *J. Cell Biol.* **153**, 1265–1276 (2001). doi: [10.1083/jcb.153.6.1265](https://doi.org/10.1083/jcb.153.6.1265); pmid: [11402069](https://pubmed.ncbi.nlm.nih.gov/11402069/)

57. S. S. Smaili, Y. T. Hsu, K. M. Sanders, R. T. Russell, R. J. Youle, Bax translocation to mitochondria subsequent to a rapid loss of mitochondrial membrane potential. *Cell Death Differ.* **8**, 909–920 (2001). doi: [10.1038/sj.cdd.4400889](https://doi.org/10.1038/sj.cdd.4400889); pmid: [11526446](https://pubmed.ncbi.nlm.nih.gov/11526446/)

58. G. Dewson, R. M. Kluck, Mechanisms by which Bak and Bax permeabilise mitochondria during apoptosis. *J. Cell Sci.* **122**, 2801–2808 (2009). doi: [10.1242/jcs.038166](https://doi.org/10.1242/jcs.038166); pmid: [19795525](https://pubmed.ncbi.nlm.nih.gov/19795525/)

59. S. W. G. Tait, D. R. Green, Mitochondria and cell death: Outer membrane permeabilization and beyond. *Nat. Rev. Mol. Cell Biol.* **11**, 621–632 (2010). doi: [10.15252/embj.201592789](https://doi.org/10.15252/embj.201592789); pmid: [26783364](https://pubmed.ncbi.nlm.nih.gov/26783364/)

60. L. Große *et al.*, Bax assembles into large ring-like structures remodeling the mitochondrial outer membrane in apoptosis. *EMBO J.* **35**, 402–413 (2016). doi: [10.15252/embj.201592789](https://doi.org/10.15252/embj.201592789); pmid: [26783364](https://pubmed.ncbi.nlm.nih.gov/26783364/)

61. R. Salvador-Gallego *et al.*, Bax assembly into rings and arcs in apoptotic mitochondria is linked to membrane pores. *EMBO J.* **35**, 389–401 (2016). doi: [10.15252/embj.201593384](https://doi.org/10.15252/embj.201593384); pmid: [26783362](https://pubmed.ncbi.nlm.nih.gov/26783362/)

62. R. Düssmann *et al.*, Single-cell quantification of Bax activation and mathematical modelling suggest pore formation on minimal mitochondrial Bax accumulation. *Cell Death Differ.* **17**, 278–290 (2010). doi: [10.1038/cdd.2009.123](https://doi.org/10.1038/cdd.2009.123); pmid: [19745831](https://pubmed.ncbi.nlm.nih.gov/19745831/)

63. D. A. Stroud *et al.*, Accessory subunits are integral for assembly and function of human mitochondrial complex I. *Nature* **538**, 123–126 (2016). doi: [10.1038/nature19754](https://doi.org/10.1038/nature19754); pmid: [27626371](https://pubmed.ncbi.nlm.nih.gov/27626371/)

64. L. Andreeva *et al.*, cGAS senses long and HMGB/TFAM-bound U-turn DNA by forming protein-DNA ladders. *Nature* **549**, 394–398 (2017). doi: [10.1038/nature23890](https://doi.org/10.1038/nature23890); pmid: [28902841](https://pubmed.ncbi.nlm.nih.gov/28902841/)

65. R. J. Youle, M. Karbowski, Mitochondrial fission in apoptosis. *Nat. Rev. Mol. Cell Biol.* **6**, 657–663 (2005). doi: [10.1038/nrm1697](https://doi.org/10.1038/nrm1697); pmid: [16025099](https://pubmed.ncbi.nlm.nih.gov/16025099/)

66. P. A. Parone *et al.*, Inhibiting the mitochondrial fission machinery does not prevent Bax/Bak-dependent apoptosis. *Mol. Cell. Biol.* **26**, 7397–7408 (2006). doi: [10.1128/MCB.02282-05](https://doi.org/10.1128/MCB.02282-05); pmid: [17015472](https://pubmed.ncbi.nlm.nih.gov/17015472/)

67. J. R. Friedman *et al.*, ER tubules mark sites of mitochondrial division. *Science* **334**, 358–362 (2011). doi: [10.1126/science.1207385](https://doi.org/10.1126/science.1207385); pmid: [21885730](https://pubmed.ncbi.nlm.nih.gov/21885730/)

68. S. C. Lewis, L. F. Uchiyama, J. Nunnari, ER-mitochondria contacts couple mtDNA synthesis with mitochondrial division in human cells. *Science* **353**, aaf5549 (2016). doi: [10.1126/science.aaf5549](https://doi.org/10.1126/science.aaf5549); pmid: [27418514](https://pubmed.ncbi.nlm.nih.gov/27418514/)

69. R. K. Boyapati, A. Tamborska, D. A. Dorward, G.-T. Ho, Advances in the understanding of mitochondrial DNA as a pathogenic factor in inflammatory diseases. *F1000 Res.* **6**, 169 (2017). doi: [10.12688/f1000research.10397.1](https://doi.org/10.12688/f1000research.10397.1); pmid: [28299196](https://pubmed.ncbi.nlm.nih.gov/28299196/)

70. S. Aguirre *et al.*, Dengue virus NS2B protein targets cGAS for degradation and prevents mitochondrial DNA sensing during infection. *Nat. Microbiol.* **2**, 17037 (2017). doi: [10.1038/nmicrobiol.2017.37](https://doi.org/10.1038/nmicrobiol.2017.37); pmid: [28346446](https://pubmed.ncbi.nlm.nih.gov/28346446/)

71. A. Sugiura, G.-L. McLelland, E. A. Fon, H. M. McBride, A new pathway for mitochondrial quality control: Mitochondrial-derived vesicles. *EMBO J.* **33**, 2142–2156 (2014). doi: [10.15252/embj.201488104](https://doi.org/10.15252/embj.201488104); pmid: [25107473](https://pubmed.ncbi.nlm.nih.gov/25107473/)

72. F. A. Ran *et al.*, Genome engineering using the CRISPR-Cas9 system. *Nat. Protoc.* **8**, 2281–2308 (2013). doi: [10.1038/nprot.2013.143](https://doi.org/10.1038/nprot.2013.143); pmid: [24157548](https://pubmed.ncbi.nlm.nih.gov/24157548/)

73. M. Raab *et al.*, ESCRT III repairs nuclear envelope ruptures during cell migration to limit DNA damage and cell death. *Science* **352**, 359–362 (2016). doi: [10.1126/science.aad7611](https://doi.org/10.1126/science.aad7611); pmid: [27013426](https://pubmed.ncbi.nlm.nih.gov/27013426/)

74. A. J. Lam *et al.*, Improving FRET dynamic range with bright green and red fluorescent proteins. *Nat. Methods* **9**, 1005–1012 (2012). doi: [10.1038/nmeth.2171](https://doi.org/10.1038/nmeth.2171); pmid: [22961245](https://pubmed.ncbi.nlm.nih.gov/22961245/)

75. D. S. Bindels *et al.*, mScarlet: A bright monomeric red fluorescent protein for cellular imaging. *Nat. Methods* **14**, 53–56 (2017). doi: [10.1038/nmeth.4074](https://doi.org/10.1038/nmeth.4074); pmid: [27869816](https://pubmed.ncbi.nlm.nih.gov/27869816/)

76. R. Fiolka, L. Shao, E. H. Rego, M. W. Davidson, M. G. L. Gustafsson, Time-lapse two-color 3D imaging of live cells with doubled resolution using structured illumination. *Proc. Natl. Acad. Sci. U.S.A.* **109**, 5311–5315 (2012). doi: [10.1073/pnas.1119262109](https://doi.org/10.1073/pnas.1119262109); pmid: [22431626](https://pubmed.ncbi.nlm.nih.gov/22431626/)

77. G. Ball *et al.*, SIMcheck: A toolbox for successful super-resolution structured illumination microscopy. *Sci. Rep.* **5**, 15915 (2015). doi: [10.1038/srep15915](https://doi.org/10.1038/srep15915); pmid: [26525406](https://pubmed.ncbi.nlm.nih.gov/26525406/)

78. J. W. Slot, H. J. Geuze, Cryosectioning and immunolabeling. *Nat. Protoc.* **2**, 2480–2491 (2007). doi: [10.1038/nprot.2007.365](https://doi.org/10.1038/nprot.2007.365); pmid: [17947990](https://pubmed.ncbi.nlm.nih.gov/17947990/)

79. B. S. Padman, M. Bach, G. Ramm, An improved procedure for subcellular spatial alignment during live-cell CLEM. *PLOS ONE* **9**, e95967 (2014). doi: [10.1371/journal.pone.0095967](https://doi.org/10.1371/journal.pone.0095967); pmid: [24755651](https://pubmed.ncbi.nlm.nih.gov/24755651/)

80. S. Preibisch, S. Saalfeld, P. Tomancak, Globally optimal stitching of tiled 3D microscopic image acquisitions. *Bioinformatics* **25**, 1463–1465 (2009). doi: [10.1093/bioinformatics/btp184](https://doi.org/10.1093/bioinformatics/btp184); pmid: [19346324](https://pubmed.ncbi.nlm.nih.gov/19346324/)

81. V. Kayng, B. Fischer, E. Müller, J. M. Buhmann, Fully automatic stitching and distortion correction of transmission electron microscope images. *J. Struct. Biol.* **171**, 163–173 (2010). doi: [10.1016/j.jsb.2010.04.012](https://doi.org/10.1016/j.jsb.2010.04.012); pmid: [20450977](https://pubmed.ncbi.nlm.nih.gov/20450977/)

ACKNOWLEDGMENTS

We thank A. Taylor, L. Shao, F. Babayekhorasani, and S. Khuon for microscopy assistance; B. Howden for personnel support; C. De Nardo for administrative support; and D. C. S. Huang and F. Kraus for providing constructs and cell lines. **Funding:** Supported by an Australian Federal Government Postgraduate Award (K.M.); Project Grants (1077750, 1106471, 1078924, 1083077), Program Grants (1016647, 1113577, 1113133), Fellowships (1063008, B.T.K.; 1110789, G.L.), an ARC Future Fellowship (160100063, M.L.), an ARC Discovery Grant (DP16012176, M.T.R.), and an Independent Research Institutes Infrastructure Support Scheme Grant (361646) from the Australian National Health and Medical Research Council (NHMRC); the Australian Cancer Research Fund; and a Victorian State Government Operational Infrastructure Support Grant. The Advanced Imaging Center at Janelia Research Campus is jointly supported by the Howard Hughes Medical Institute and the Gordon and Betty Moore Foundation. The Monash Ramaciotti Centre for Cryo-Electron Microscopy is supported by the Ramaciotti Foundation (CDI1/1958) and the Australian Research Council (LE120100090 and LE100100165). **Author contributions:** K.M., J.M.H., N.D.G., L.L., and K.L.R. performed LLSM and 3D-SIM microscopy experiments. K.M. and S.D. performed confocal microscopy experiments. V.O. and G.R. performed EM experiments; B.S.P. performed CLEM experiment. L.W., K.M., B.T.K., M.L., N.D.G., S.C., and M.D. analyzed data. K.M., T.L.S., C.S., L.L., G.D., and R.M.L. performed cell culture and related experiments. L.D.O., R.L., M.T.R., and H.S.C. provided reagents. B.T.K., K.M., and M.F.V.D. conceived the project and planned experiments. M.F.V.D., M.T.R., G.D., K.L.R., G.L., T.L.C., J.M.H., S.C., G.R., and M.L. contributed insightful discussions. K.M. and B.T.K. wrote the manuscript, and all authors contributed to its revision. **Competing interests:** All authors declare no competing interests. **Data and materials availability:** All data and custom analysis scripts are available in the manuscript or the supplementary materials.

SUPPLEMENTARY MATERIALS

www.science.org/content/359/6378/eaao6047/suppl/DC1
Figs. S1 to S6
Code Files S1 and S2

8 August 2017; accepted 24 January 2018
10.1126/science.aao6047

REPORT

OPTICS

Soliton microcomb range measurement

Myoung-Gyun Suh and Kerry J. Vahala*

Laser-based range measurement systems are important in many application areas, including autonomous vehicles, robotics, manufacturing, formation flying of satellites, and basic science. Coherent laser ranging systems using dual-frequency combs provide an unprecedented combination of long range, high precision, and fast update rate. We report dual-comb distance measurement using chip-based soliton microcombs. A single pump laser was used to generate dual-frequency combs within a single microresonator as counterpropagating solitons. We demonstrated time-of-flight measurement with 200-nanometer precision at an averaging time of 500 milliseconds within a range ambiguity of 16 millimeters. Measurements at distances up to 25 meters with much lower precision were also performed. Our chip-based source is an important step toward miniature dual-comb laser ranging systems that are suitable for photonic integration.

The invention of the optical frequency comb has had a major impact on light detection and ranging (LIDAR) systems. In addition to providing a highly accurate frequency calibration source in methods such as multiwavelength interferometry (1) and frequency-modulated continuous-wave laser interferometry (2), frequency combs have enabled a new method called dual-comb LIDAR (3). In this method, two frequency combs having slightly different repetition rates are phase-locked. Their combined output pulse streams then provide a LIDAR source with subnanometer precision and range ambiguity many orders beyond the pulse-to-pulse separation distance of each comb. Besides mode-locked lasers, electro-optic modulation combs have also been used in the related field of tomography (4). The development of miniature frequency combs [microcombs (5–14)] suggests that chip-integrated dual-comb LIDAR systems may be possible. A recent advancement in microcombs is the realization of soliton mode locking (15–19), which provides phase-locked femtosecond pulses with gigahertz to terahertz repetition rates. Soliton microcombs are being studied in several frequency comb applications, including optical frequency synthesis (20), optical communications (21), and dual-comb spectroscopy (22–24). We demonstrate time-of-flight distance measurement using a chip-based dual-soliton source. Beyond the demonstration of microcomb LIDAR, the two soliton streams are cogenerated as counterpropagating solitons within a single resonator (25). This simplifies the system by eliminating the need for two resonators and two pump lasers while also improving mutual coherence between the two combs. Although a close examination of

systematics and other issues is not presented, the work establishes the feasibility of soliton microcombs as well as the cogeneration method for LIDAR applications.

By pumping a resonance of a silica wedge resonator (26) along the clockwise (CW) and counterclockwise (CCW) directions, we generated counterpropagating solitons with average power of ~1 mW (Fig. 1A). The two pumps were derived from a single 1550-nm fiber laser; after a 50/50 fiber splitter, their frequencies were controlled using acousto-optic modulators (AOMs). A feedback loop with 20-kHz bandwidth (27) fixes the frequency detuning of one pump relative to the cavity resonant frequency, while the second pump frequency can be independently tuned using an AOM. Chiral symmetry breaking (28, 29) was observed but did not prevent counterpropagating soliton generation (30). Typical optical spectra of the CW and CCW solitons (Fig. 1, B and C) show the characteristic hyperbolic-secant-square spectral envelope (the green dashed curve in Fig. 1B is a fit using a soliton pulse width of 200 fs).

Fast photodetection (bandwidth 50 GHz) of the dual pulse streams as measured on an electrical spectrum analyzer (ESA) shows that the repetition frequency (f_{rep}) is approximately 9.36 GHz (Fig. 1D). A zoom-in of the electrical spectrum near f_{rep} (Fig. 1D, inset) resolves the two distinct repetition frequencies of the CW/CCW solitons. Note that the intersoliton beat notes are >40 dB lower than the repetition frequency signals and are below the electrical noise level. The repetition frequency difference (Δf_{rep}) between CW and CCW solitons is adjusted by using the AOMs to tune the frequency difference of the two pump lasers (Δf_{pump}). This repetition rate control results from the Raman-induced soliton self-frequency shift (25), such that Δf_{rep} increases with increasing Δf_{pump} (Fig. 1E). The maximum $\Delta f_{\text{rep}} \sim 20$ kHz

is limited by the maximum $\Delta f_{\text{pump}} \sim 3$ MHz, which is set by the 3-dB frequency shift range of the AOM. Within the tunable range of Δf_{rep} , we also observed phase locking of the CW and CCW solitons and their relative repetition rates by injection locking through the backscattered light (25). However, the relative stability of unlocked solitons was sufficient for the time-of-flight distance measurement.

The generated CW/CCW soliton streams were coupled in opposing directions toward the LIDAR setup, with the CW soliton stream output through a gradient-index collimator toward the target mirror (Fig. 1A). A fiber delay line (physical path length ~15 m) was added before the collimator to increase the effective target distance. The CW soliton stream reflected from the target was combined with the reference CW soliton stream via a circulator and 50/50 coupler. Finally, the CW soliton stream carrying the distance information (green and orange dashed arrows) was combined with the CCW soliton stream (blue dashed arrow) to generate the periodic interference (interferogram) of the dual-soliton pulse streams. Figure 2A shows a portion of the measured interferogram as displayed by the oscilloscope. The period of the interferogram is set by the difference of the CW and CCW soliton repetition rates. The interferogram is recorded for a total of 2 s with a sampling time of 250 ns; however, only a 5-ms portion of the overall span is shown. A zoomed-in view of the interferogram (Fig. 2B) shows the reference peaks and target peaks within two periods of 176 μ s, corresponding to $\Delta f_{\text{rep}} \sim 5.685$ kHz. The temporal location of the peaks in the electrical pulse stream is determined by Hilbert-transforming the interferogram. The time interval between a reference peak and a target peak is then calculated for each period and converted to the distance scale. The drift of Δf_{rep} is adaptively corrected in the data (30, 31). Figure 2C plots this distance versus time where the time increment in the plot is the interferogram period (176 μ s). The averaged target distance is 4.637429 mm and the range ambiguity is 16 mm (one-half of the pulse-to-pulse distance separation at a soliton repetition rate of 9.36 GHz). The right panel of Fig. 2C shows a single time period of the Hilbert-transformed interferogram near 1 s in the measurement (vertical dashed line in left panel). The inset of the right panel gives the zoomed-in target intensity peak and shows a full-width, half-maximum pulse width of ~1.45 μ s. The Allan deviation of the distance time series is calculated at averaging times ranging from 352 μ s to 667 ms (Fig. 3). Fitting to the plot gives $\sigma \sim 10$ μ m (T_{update}/T) $^{1/2}$, where $T_{\text{update}} \sim 176$ μ s is the update time and T is the averaging time. Near an averaging time of 500 ms, a precision of 200 nm is achieved (30).

The distance measurement shown in Fig. 2C has a range ambiguity of 16 mm. To greatly extend this range ambiguity, we performed a similar distance measurement after manually swapping the roles of two soliton streams. In principle, this could be implemented using an integrated optical switch. The Vernier effect resulting from the difference in the soliton repetition rates can then

T. J. Watson Laboratory of Applied Physics, California Institute of Technology, Pasadena, CA 91125, USA.

*Corresponding author. Email: vahala@caltech.edu

be used to resolve the range ambiguity (3). Figure 4 shows a zoom-in view of the two distance measurements where R_{CW} (red) and R_{CCW} (blue) are the measured distances when the CW soliton and the CCW soliton are used for ranging. The average distance difference, $\Delta R = \text{mean}(R_{\text{CW}}) - \text{mean}(R_{\text{CCW}})$, between the two measurements is $16.02 \mu\text{m}$. Considering the Vernier effect (3), the ambiguity-resolved distance is $R' = \Delta R(f_{\text{rep}}^{\text{CCW}}/\Delta f_{\text{rep}}) + R_{\text{CW}} \approx$

$26.3729 \pm 0.466 \text{ m}$, with a new range ambiguity of $\sim 26 \text{ km}$. This measured distance is in good agreement with the optical path length of the target ($\sim 26.815 \text{ m}$), including fiber delay, as measured using an optical time-domain reflectometer. The uncertainty ($\pm 0.466 \text{ m}$) in this partially ambiguity-resolved measurement results from the original 200-nm precision multiplied by $\sqrt{2}f_{\text{rep}}/\Delta f_{\text{rep}}$. If this uncertainty were below the

pulse-to-pulse range ambiguity, which would require a precision of $(c\Delta f_{\text{rep}})/(2\sqrt{2}f_{\text{rep}}^2)$ (6.88 nm in this experiment), then a nanometer-scale precision would be possible in the fully ambiguity-resolved case (3). In addition to the time-of-flight measurement, complementary interferometric measurement using phase-locked CW/CCW solitons could improve the precision. Finally, increasing Δf_{rep} would improve the precision by

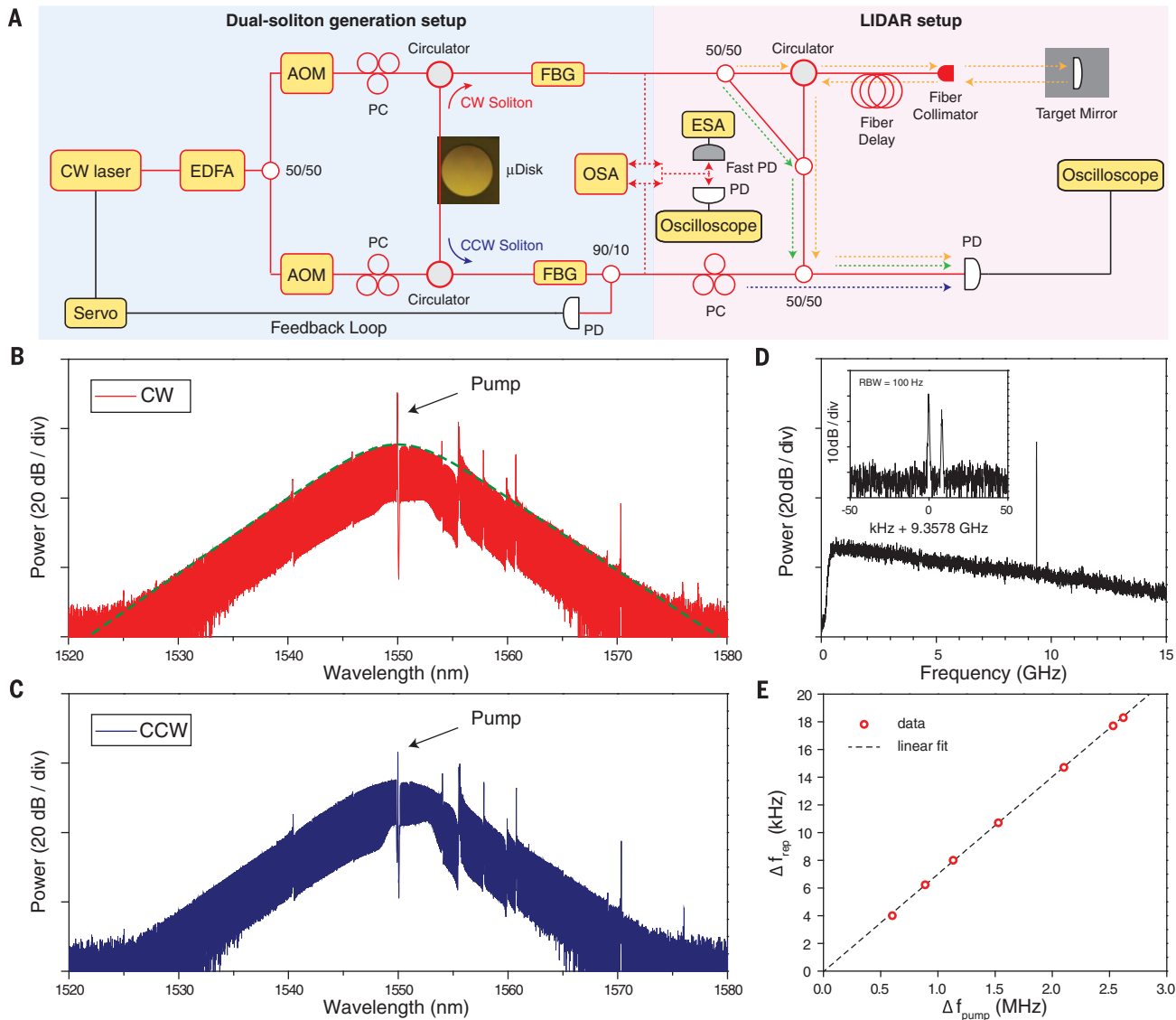


Fig. 1. Experimental setup for dual-soliton generation and ranging measurement.

measurement. (A) The dual-soliton generation setup (left) and LIDAR setup (right). A fiber laser at 1550 nm is amplified by an erbium-doped fiber amplifier (EDFA) and split using a 50/50 coupler to pump the resonator in two directions. In each path, an acousto-optic modulator (AOM) tunes the pump frequency and modulates the pump power for soliton triggering. The pump light is polarization-controlled (PC) and evanescently coupled into the microresonator by means of a fiber taper. Solitons are stabilized and the pump laser frequency locked to the resonator by a servo feedback loop using the photodetected (PD) CCW soliton power (27). A fiber Bragg grating (FBG) filter is used to attenuate the transmitted pump power. An optical spectrum analyzer (OSA) and electrical spectrum analyzer (ESA) are used to analyze the dual-soliton

source. For distance detection, the CW soliton stream is split into two paths: the reference path (green dashed arrow) and the target path (orange dashed arrow). In the data, the distance difference between the target and reference paths is divided by 2. The CW soliton streams of both paths are combined with the CCW soliton stream (blue dashed arrow) and photodetected to generate the interferogram. (B and C) Typical optical spectra of the CW solitons (B) and CCW solitons (C) with hyperbolic-secant-square fit [green dashed curve in (B)]. Attenuated pump laser lines are also indicated. (D) Electrical spectrum of the photodetected solitons showing the approximate repetition frequency $f_{\text{rep}} \sim 9.36 \text{ GHz}$. Inset: Zoom-in of the spectrum showing the resolved CW/CCW repetition rates. (E) Measured repetition frequency difference Δf_{rep} versus pump frequency difference Δf_{pump} .

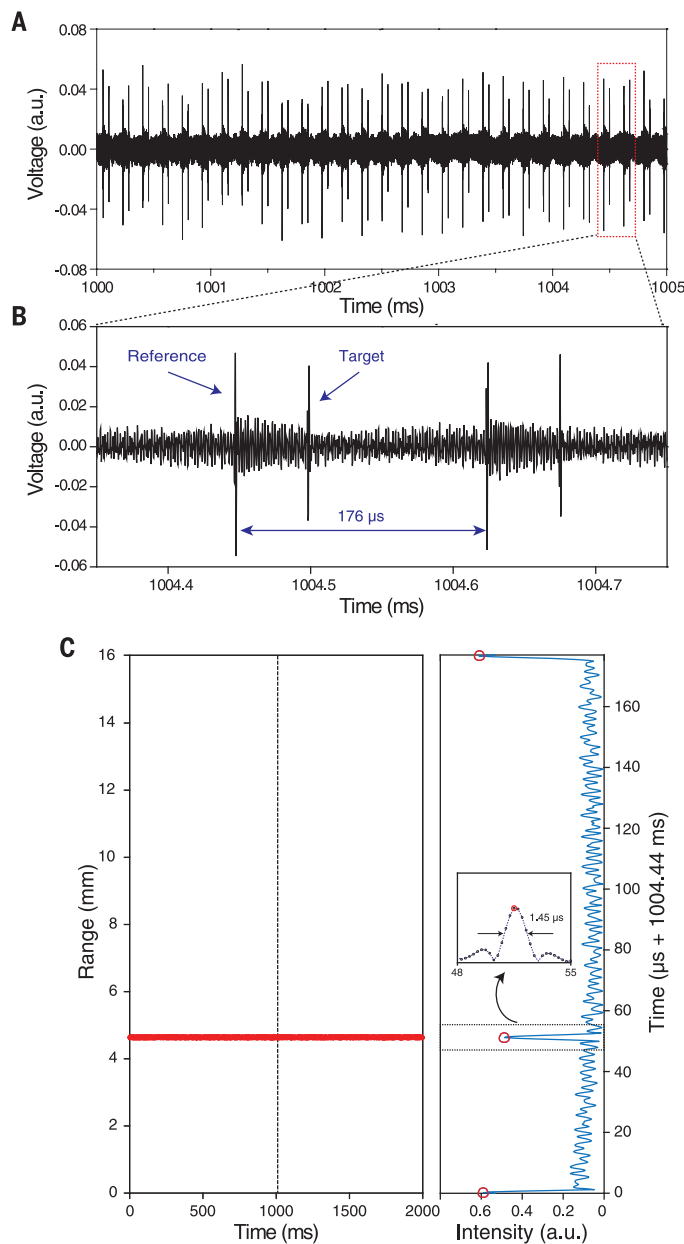


Fig. 2. Distance measurement. (A) Typical interferogram containing range information. (B) Zoom-in of the interferogram over two time periods. The reference peaks and target peaks are shown; the time period is approximately 176 μ s. (C) Left: The measured distance between the reference peak and target peak is plotted versus time. The range ambiguity in this measurement is 16 mm. Right: The electrical intensity trace (blue) and peaks (red circles) for a data trace near 1 s (dashed vertical line in left panel). Inset: Zoom-in of the target intensity peak showing the electrical pulse width of 1.45 μ s.

allowing greater averaging of distance data within a given time interval. Achieving the larger range measurements in free space would require optical amplification; in the case of outdoor ranging (32), the precision will also be limited by environmental perturbation (33).

The update time of $\sim 176 \mu$ s and the range ambiguity of ~ 26 km are determined by $\Delta f_{\text{rep}} =$

5.685 kHz, which can be tuned by changing Δf_{pump} . The tunable range and absolute value of Δf_{rep} can be further increased by using a smaller-diameter resonator and generating CW/CCW solitons from two different mode families (30). The tunability of Δf_{rep} is useful in that the LIDAR system can be adjusted to provide an optimal update time and range ambiguity according to the

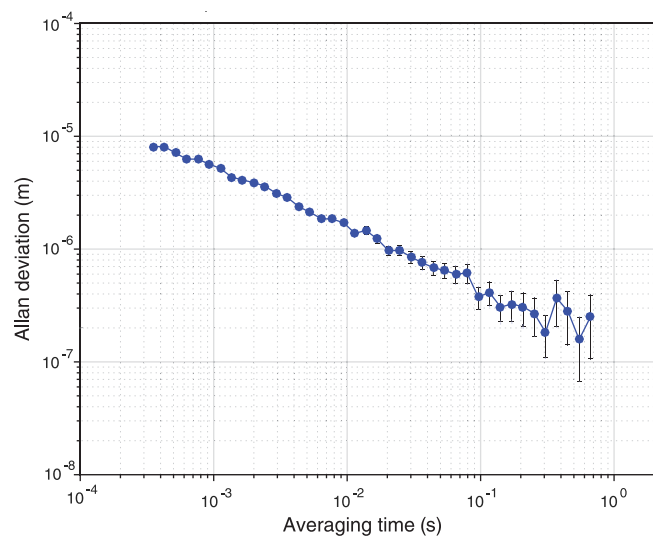


Fig. 3. Precision of distance measurement versus averaging time. Allan deviation is calculated from the 2-s time series (Fig. 2C) of measured distance (i.e., reference peak to signal peak); 200-nm precision is achieved near an averaging time of 500 ms. Error range is calculated from the Allan deviation divided by the square root of sample size.

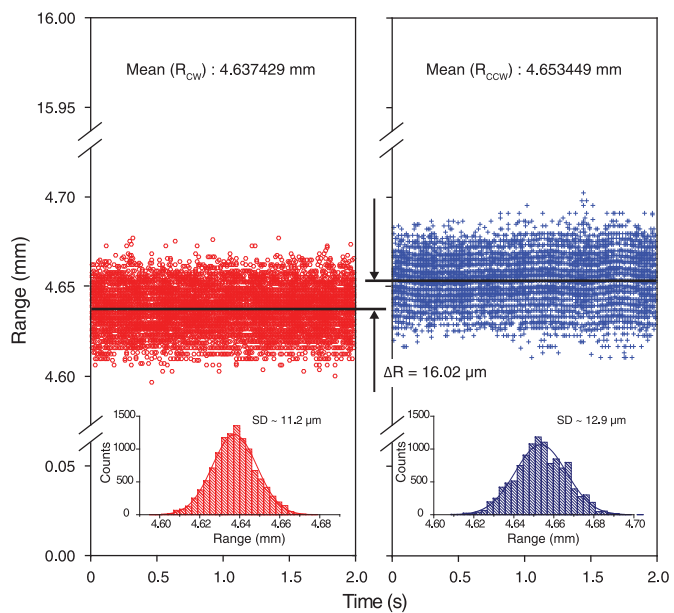


Fig. 4. Resolving range ambiguity. R_{CW} (red) and R_{CCW} (blue) are range data versus time, using the CW and CCW solitons to probe the target. The distance difference [$\Delta R = \text{mean}(R_{\text{CW}}) - \text{mean}(R_{\text{CCW}})$] between the two measurements is 16.02 μ m and is used to determine the absolute range (see text). Data in red are from Fig. 2C. Insets: Histograms of the two range measurements for one measurement frame, along with the Gaussian fitting curves with standard deviation (SD) values. Standard deviation improves with averaging time as per Fig. 3.

application. For example, in applications requiring faster update rates, increasing Δf_{rep} improves the update time while reducing the range ambiguity. Our demonstration of a soliton dual-comb LIDAR system using a single, chip-based micro-resonator pumped by a single laser is a step toward miniaturization of dual-comb ranging systems. Other chip-based components are required

in a full system. Along these lines, there is remarkable progress on realization of microcomb systems (20). Moreover, a waveguide-integrated structure comparable in performance to that used in this work has recently been demonstrated (34). Finally, we note other soliton microcomb range measurement work (35) that was reported while we were preparing this manuscript.

REFERENCES AND NOTES

- Y. Salvadé, N. Schuhler, S. Lévéque, S. Le Floch, *Appl. Opt.* **47**, 2715–2720 (2008).
- E. Baumann *et al.*, *Opt. Lett.* **38**, 2026–2028 (2013).
- I. Coddington, W. Swann, L. Nenadovic, N. Newbury, *Nat. Photonics* **3**, 351–356 (2009).
- S.-J. Lee, B. Widjatmoko, M. Kourogi, M. Ohtsu, *Jpn. J. Appl. Phys.* **40**, L878–L880 (2001).
- P. Del'Haye *et al.*, *Nature* **450**, 1214–1217 (2007).
- T. J. Kippenberg, R. Holzwarth, S. A. Diddams, *Science* **332**, 555–559 (2011).
- I. S. Grudinin, N. Yu, L. Maleki, *Opt. Lett.* **34**, 878–880 (2009).
- S. B. Papp, S. A. Diddams, *Phys. Rev. A* **84**, 053833 (2011).
- Y. Okawachi *et al.*, *Opt. Lett.* **36**, 3398–3400 (2011).
- J. Li, H. Lee, T. Chen, K. J. Vahala, *Phys. Rev. Lett.* **109**, 233901 (2012).
- B. Hausmann, I. Bulu, V. Venkataraman, P. Deotare, M. Lončar, *Nat. Photonics* **8**, 369–374 (2014).
- L. Razzari *et al.*, *Nat. Photonics* **4**, 41–45 (2010).
- F. Ferdous *et al.*, *Nat. Photonics* **5**, 770–776 (2011).
- H. Jung, C. Xiong, K. Y. Fong, X. Zhang, H. X. Tang, *Opt. Lett.* **38**, 2810–2813 (2013).
- T. Herr *et al.*, *Nat. Photonics* **8**, 145–152 (2014).
- X. Yi, Q.-F. Yang, K. Y. Yang, M.-G. Suh, K. Vahala, *Optica* **2**, 1078 (2015).
- V. Brasch *et al.*, *Science* **351**, 357–360 (2016).
- P.-H. Wang *et al.*, *Opt. Express* **24**, 10890–10897 (2016).
- C. Joshi *et al.*, *Opt. Lett.* **41**, 2565–2568 (2016).
- D. T. Spencer *et al.*, arXiv:1708.05228 (2017).
- P. Marin-Palomo *et al.*, *Nature* **546**, 274–279 (2017).
- M.-G. Suh, Q.-F. Yang, K. Y. Yang, X. Yi, K. J. Vahala, *Science* **354**, 600–603 (2016).
- A. Dutt *et al.*, arXiv:1611.07673 (2016).
- N. G. Pavlov *et al.*, *Opt. Lett.* **42**, 514–517 (2017).
- Q.-F. Yang, X. Yi, K. Y. Yang, K. Vahala, *Nat. Photonics* **11**, 560–564 (2017).
- H. Lee *et al.*, *Nat. Photonics* **6**, 369–373 (2012).
- X. Yi, Q.-F. Yang, K. Y. Yang, K. Vahala, *Opt. Lett.* **41**, 2037–2040 (2016).
- Q.-T. Cao *et al.*, *Phys. Rev. Lett.* **118**, 033901 (2017).
- L. Del Bino, J. M. Silver, S. L. Stebbings, P. Del'Haye, *Sci. Rep.* **7**, 43142 (2017).
- See supplementary materials.
- T.-A. Liu, N. R. Newbury, I. Coddington, *Opt. Express* **19**, 18501–18509 (2011).
- J. Lee, Y.-J. Kim, K. Lee, S. Lee, S.-W. Kim, *Nat. Photonics* **4**, 716–720 (2010).
- N. Bobroff, *Meas. Sci. Technol.* **4**, 907–926 (1993).
- K. Y. Yang *et al.*, arXiv:1702.05076 (2017).
- P. Trocha *et al.*, arXiv:1707.05969 (2017).

ACKNOWLEDGMENTS

We thank N. Newbury, X. Yi, and Q. Yang for helpful discussions and feedback on this manuscript. Supported by the Defense Advanced Research Projects Agency under the SCOUT (contract no. W911NF-16-1-0548) program, the Air Force Office of Scientific Research, and the Kavli Nanoscience Institute.

SUPPLEMENTARY MATERIALS

www.sciencemag.org/content/359/6378/884/suppl/DC1
Supplementary Text
Fig. S1
Reference (36)

26 June 2017; accepted 11 January 2018
10.1126/science.aaol1968

OPTICS

Ultrafast optical ranging using microresonator soliton frequency combs

P. Trocha,^{1,*} M. Karpov,^{2,*} D. Ganin,^{1,*} M. H. P. Pfeiffer,² A. Kordts,² S. Wolf,¹ J. Krockenberger,¹ P. Marin-Palomo,¹ C. Weimann,^{1,†} S. Randel,^{1,3} W. Freude,^{1,3} T. J. Kippenberg,^{2,‡} C. Koos^{1,3,‡}

Light detection and ranging is widely used in science and industry. Over the past decade, optical frequency combs were shown to offer advantages in optical ranging, enabling fast distance acquisition with high accuracy. Driven by emerging high-volume applications such as industrial sensing, drone navigation, or autonomous driving, there is now a growing demand for compact ranging systems. Here, we show that soliton Kerr comb generation in integrated silicon nitride microresonators provides a route to high-performance chip-scale ranging systems. We demonstrate dual-comb distance measurements with Allan deviations down to 12 nanometers at averaging times of 13 microseconds along with ultrafast ranging at acquisition rates of 100 megahertz, allowing for in-flight sampling of gun projectiles moving at 150 meters per second. Combining integrated soliton-comb ranging systems with chip-scale nanophotonic phased arrays could enable compact ultrafast ranging systems for emerging mass applications.

Laser-based light detection and ranging (LIDAR) is a key technology in industrial and scientific metrology, offering high-precision, long-range, and fast acquisition (1, 2). LIDAR systems have found their way into a wide variety of applications, comprising, for example, industrial process monitoring, autonomous driving, satellite formation flying, or drone navigation. When it comes to fast and accurate ranging over extended distances, optical frequency combs (3) have been demonstrated to exhibit characteristic advantages, exploiting time-of-flight (TOF) schemes (4), interferometric approaches (5), or combinations thereof (6). In early experiments (4), mode-locked fiber lasers were used for TOF ranging, thereby primarily exploiting the stability of the repetition rate. Regarding interferometric schemes, optical frequency combs were exploited to stabilize the frequency interval between continuous-wave (CW) lasers used in synthetic-wavelength interferometry (5, 7). Dual-comb schemes, which rely on multiheterodyne detection by coherent superposition of a pair of slightly detuned frequency combs (8), allow combining of TOF measurements with optical interferometry, thereby simultaneously exploiting the radio-frequency coherence of the pulse train and the optical coherence of the individ-

ual comb tones (6). More recently, comb-based schemes have been demonstrated as a viable path to high-speed sampling with acquisition times down to 500 ns (9).

However, besides accuracy and acquisition speed, footprint is becoming increasingly important for LIDAR systems. On the technology side, recent advances in photonic integration show that large-scale nanophotonic phased arrays (10, 11) open a promising path toward ultra-compact systems for rapid high-resolution beam steering. To harness the full potential of these approaches, the optical phased arrays need to be complemented by LIDAR engines that combine high precision with ultrafast acquisition and that are amenable to chip-scale integration. Existing dual-comb LIDAR concepts cannot fulfill these requirements because they rely either on cavity-stabilized mode-locked fiber lasers (6) or on spectral broadening of initially narrow-band seed combs (9), which typically require delicate fiber-based dispersion management schemes, usually in combination with intermediate amplifiers.

Here, we show that dissipative Kerr soliton (DKS) states (12, 13) in microresonator-based optical frequency combs (14, 15) provide a route to integrated LIDAR systems that combine sub-wavelength accuracy and unprecedented acquisition speed with scalable fabrication, robust implementation, and compact form factors. DKSs are solutions of a driven, damped, and detuned nonlinear Schrödinger equation, often referred to as a Lugiato-Lefever equation (16). Such ultra-short temporal solitons can circulate continuously in the cavity, relying on a double balance of dispersion and nonlinearity as well as parametric gain and cavity loss (13). In the frequency

domain, DKS pulse trains correspond to optical frequency combs, which combine large bandwidths and smooth spectral envelopes with free spectral ranges in the range from tens of gigahertz to a few terahertz. Microresonator-based DKSs have recently been used in low-noise microwave generation (17), frequency metrology (18), dual-comb spectroscopy (19), coherent communications (20), and optical frequency synthesis (21). In our demonstrations, we exploit DKS combs for synthetic-wavelength interferometry with massively parallel multiheterodyne detection. Our scheme is based on a pair of free-running comb generators and does not require phase locking of the combs to each other. The large optical bandwidth of more than 11 THz leads to highly precise distance measurements with Allan deviations reaching 12 nm at an averaging time of 14 μ s, whereas the large free spectral range (FSR) enables high-speed measurements at rates of up to 100 MHz. We prove the viability of our technique by sampling the naturally scattering surface of air-gum projectiles on the fly, achieving lateral spatial resolutions of more than 2 μ m for object speeds of more than 150 m/s.

For DKS comb generation, we use a pair of CW-pumped silicon nitride (Si_3N_4) microring resonators on separate chips (22–24). The devices (Fig. 1A) are fabricated using the photonic Damascene process (25), which enables crack-free fabrication of high-quality (Q) microresonators ($Q > 1$ million) with large waveguide dimensions (1.65 by 0.85 μ m). DKS comb generation is achieved by sweeping the pump laser frequency from the effectively blue-detuned to a defined point in the effectively red-detuned regime of a selected cavity resonance, where the microresonator system supports soliton formation (13) (Fig. 1B). Once the laser scan stops, typically a multisoliton state is generated. By next applying the backward frequency tuning technique (26), a single-soliton state corresponding to an optical frequency comb with a spectrally smooth squared hyperbolic secant (sech^2) shape envelope (Fig. 1C) is achieved in a deterministic manner. A more detailed description of the experimental setup and of the microresonator devices can be found in (27).

The experimental setup used for dual-comb ranging is depicted in Fig. 2A. For multiheterodyne detection, we use two Kerr comb generators with slightly different free spectral ranges of $\omega_{\text{S},r}/2\pi = 95.842$ GHz and $\omega_{\text{LO},r}/2\pi = 95.746$ GHz, respectively. To demonstrate that our concept does not require phase locking of the DKS combs, we used a pair of free-running CW lasers to pump the microresonators and compensate for the stochastic phase drifts by digital signal processing (27). The pump light for the signal and the Local oscillator (LO) comb is amplified by erbium-doped fiber amplifiers (EDFA) to power levels of 3.5 and 2.6 W, respectively, and then coupled to the microresonator chips with a coupling efficiency of ~60% per facet. The resulting combs feature overall power levels of 4.3 and 2.5 mW and are amplified by a pair of C+L-band (1530 to

¹Institute of Photonics and Quantum Electronics (IPQ), Karlsruhe Institute of Technology (KIT), 76131 Karlsruhe, Germany. ²Laboratory of Photonics and Quantum Measurements (LPQM), École Polytechnique Fédérale de Lausanne (EPFL), CH-1015 Lausanne, Switzerland. ³Institute of Microstructure Technology (IMT), Karlsruhe Institute of Technology, 76131 Karlsruhe, Germany.

*These authors contributed equally to this work. [†]Present address: Corporate Research and Technology, Carl Zeiss AG, Oberkochen, Germany. [‡]Corresponding author. Email: tobias.kippenberg@epfl.ch (T.J.K.); christian.koos@kit.edu (C.K.)

1565 nm and 1565 to 1625 nm) EDFA to 450 mW to improve the measurement accuracy. A spectrum of an amplified comb is shown in Fig. 2C. The gain bandwidth of the EDFA limits the number of usable lines to about 115, which is sufficient for our experiments.

For distance measurements, the signal comb is split by a fiber-based 50:50 coupler, and one part is routed to the target and back to a balanced measurement photodetector (meas. PD), while the other part is directly sent to the balanced reference detector (ref. PD); see Fig. 2A. Measurement and reference PDs feature bandwidths of 43 GHz. Similarly, the LO comb is split into two portions, which are routed to the measurement PD and the reference PD for multiheterodyne detection. The resulting baseband signal contains discrete beat notes, which are recorded by a 33-GHz real-time sampling oscilloscope and separated by means of a numerically calculated Fourier transform. The distance to the target is extracted from the phase of the baseband beat notes. Data processing and evaluation are performed offline; see (27) for details of the underlying algorithms.

Figure 2B shows the Fourier transform of a recorded baseband signal, revealing the various beat notes between the signal and LO comb lines. The spacing of the beat notes is given by the difference of the line spacing of the LO and the signal comb and amounts to $\Delta f_r = \Delta\omega_r/2\pi = 96.4$ MHz, thereby dictating a minimum possible acquisition time of $T_{\min} = 1/\Delta f_r = 10.4$ ns and a maximum possible distance acquisition rate of 96.4 MHz.

For a thorough stability and precision analysis of our dual-comb scheme, we measure the distance to a static mirror and evaluate the Allan deviation. The entire measurement contains a series of $\sim 1.1 \times 10^6$ individual data points taken at an acquisition time of 10.4 ns per point, leading to a total duration of ~ 12 ms. The extracted Allan deviation is plotted in Fig. 2D. At an averaging time of 10.4 ns, the Allan deviation amounts to 284 nm, and it decreases to 12 nm for an averaging time of 13 μ s. At small averaging times, the Allan deviation decreases with increasing averaging time, as expected for dominating white noise such as shot noise or amplified spontaneous emission (ASE) originating from the EDFA. For larger averaging times, the Allan deviation increases, which we attribute to thermal drift of the fibers and to mechanical vibrations at acoustic frequencies. The current measurement accuracy is hence only limited by a nonideal implementation of the system. Further improvements are possible by reducing the ASE noise floor of the EDFA and by avoiding thermal drift and mechanical vibrations. Fundamentally, the measurement accuracy is only limited by inevitable shot noise and possibly by additional ASE noise of ideal EDFA. For comb powers of 10 mW, this would allow for measurement accuracies of better than 10 nm at the highest acquisition rate of 100 MHz; see (27) for details.

Besides the Allan deviation, we also estimated the accuracy of our technique by measuring variable distances to a target that is moved over a

full ambiguity distance $L_{\text{amb}} = \frac{c}{2\Delta\omega_r/2\pi}$ (Fig. 2E). In this experiment, the target mirror is stepped in increments of 50 μ m using a feedback-stabilized stage with a positioning accuracy of more than 50 nm. To reduce the impact of fiber drift, the distance measurement is continuously switched between the movable target mirror and a static calibration mirror in quick succession, taking between 6500 and 9500 measurements with the full acquisition rate of ~ 96 MHz on each mirror; see (27). From these measurements, we extract the distance to the target mirror and the associated standard deviation; see (27) for details. In the upper part of Fig. 2E, the measured distance is plotted as a function of the distance set by the translation stage. Measured distances exceeding the ambiguity distance of $L_{\text{amb}} = 1.56$ mm are unwrapped manually. The bottom part of Fig. 2E shows the residual deviations of the measured positions from the set positions along with the respective standard deviations indicated as error bars. Importantly, no cyclic error is observed throughout the ambiguity distance. We determine the accuracy of our measurement to 188 nm, defined as the standard deviation of the residuals, which are of the same order of magnitude as the 50-nm positioning accuracy of the stage specified by the manufacturer. In this measurement, the refractive index of air is considered according to Ciddor's formula for ambient

laboratory conditions. The measured 188-nm standard deviation of the residuals is still dominated by drift and acoustic vibrations of the measurement setup rather than by the measurement system itself, despite compensation via the static calibration mirror. This can be inferred from the fact that the standard deviation of 188 nm is still much larger than the intrinsic system-related errors of 5 nm that should be expected for the averaging time of 100 μ s; see (27) for a more detailed discussion.

To validate the reproducibility of our system and to benchmark the results with respect to existing techniques, we measured the profile of a quickly rotating disk with grooves of different depths on its surface (see Fig. 3A). In this experiment, the measurement beam is focused to the surface near the edge of the disk, which rotates at a frequency of about 600 Hz, thus resulting in an edge velocity of 160 m/s. The distance acquisition rate in this experiment amounts to 96.5 MHz, limited by the spectral spacing of $\Delta\omega_r/2\pi$ of the beat notes in the baseband photocurrent but not by the acquisition speed of our oscilloscopes. The resulting profiles are shown in Fig. 3B for two measurements, which were taken independently from one another during different round trips of the disc. Measurement points close to the edges of the grooves may suffer from strong scattering and low power levels,

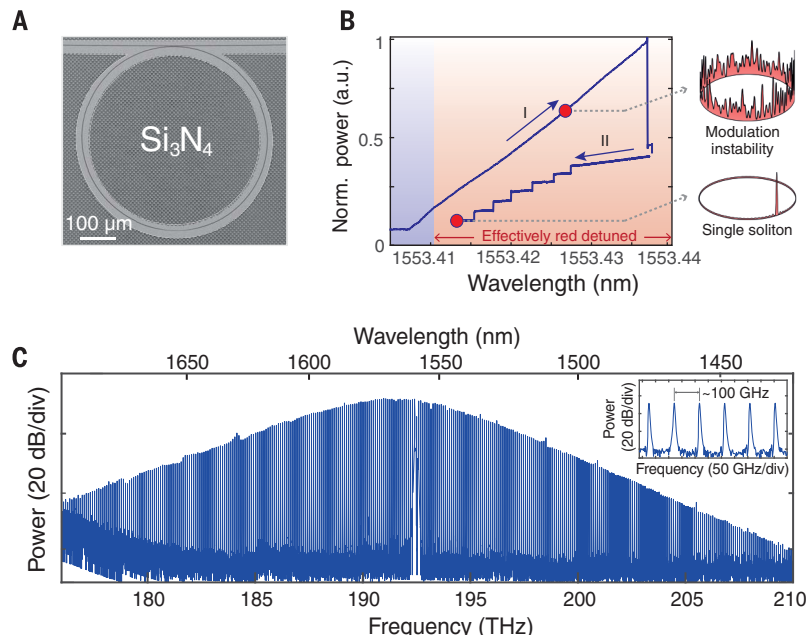


Fig. 1. Dissipative Kerr soliton (DKS) generation in silicon nitride (Si_3N_4) microresonators. (A) Scanning electron microscopy image of a silicon nitride microresonator with a radius of 240 μ m. The checkerboard pattern results from the photonic Damascene fabrication process (25). (B) Visualization of the backward tuning technique. The pump laser wavelength is changed from an effective blue-detuned state, thereby increasing the intracavity power and giving rise to modulation instability (arrow I). Eventually, the intracavity field switches from this chaotic state into a multisoliton state when the laser tuning is stopped. From there on, the laser wavelength is tuned toward lower wavelengths, decreasing the number of solitons until a single-soliton state is reached. The decreasing number of solitons is visible by the decreasing steps of the intracavity power (arrow II). (C) Spectrum of a DKS optical frequency comb with zoom-in. The spectrum combines large bandwidth and a smooth spectral envelope and features a line spacing of ~ 100 GHz.

which lead to unreliable distance information. Using the fit error of the linear phase characteristic as a quality criterion, our technique allows identification of such nonusable measurement points and allows automatically discarding them from the data; see (27) for details. The raw data of both measurements was further subject to vibrations of the disk arising from the driving engine. These vibrations have been removed by fitting a polynomial to the top surface of the disk and by using it for correction of the overall measurement data. In a first experiment, we analyze the reproducibility of the technique by a detailed comparison of the results obtained from the two measurements (see Fig. 3B, Inset 1). The measured profiles exhibit good agreement regarding macroscopic features such as the groove depth, as well as microscopic features such as surface texture and a decrease of depth toward the edge of the groove. Deviations are attributed to the fact that the two measurements have been taken independently and might hence not have sampled the exact same line across the groove. In addition, we benchmark our technique by comparing the obtained profile of a single groove

with a profile obtained from an industrial optical coordinate-measuring machine (CMM, Werth VideoCheck HA) (Fig. 3B, Inset 2). Both profiles are in good agreement, with some minor deviations that we again attribute to slightly different measurement positions along the analyzed groove.

Ultrafast ranging is demonstrated by measuring the profile of a flying air-gun bullet that is shot through the focus of the measurement beam (see Fig. 3C). The projectile moves at a speed of 150 m/s (Mach 0.47), which, together with the acquisition rate of 96.2 MHz, results in a lateral distance of 1.6 μ m between neighboring sampling points on the surface of the bullet. The full profile of the projectile is taken during a single shot and depicted in red in Fig. 3D along with a reference measurement obtained from the static bullet using a swept-source optical coherence tomography system (dark blue). For better comparison, the two profiles were rotated and an actual speed of the bullet of 149 m/s was estimated for best agreement. Both curves clearly coincide and reproduce the shape of the fired projectile. Missing data points in the dual-DKS-

comb measurement at the tip of the projectile are caused by low power levels of the back-coupled signal, which is inevitable for such steep surfaces in combination with the limited numerical aperture of the lens used for collecting the backscattered light. As before, these measurement points have been discarded from the data based on a large fit error of the linear phase characteristic (27). An image of the projectile after recovery from the backstop exhibits a strong corrugation of the bullet toward its back (Fig. 3E). This leads to deviations of the measured profiles in Fig. 3D toward the right-hand side, since the strongly corrugated surface of the projectile in this area has very likely been sampled at two different positions.

To make dual-DKS-comb ranging a viable option for practical applications, the limited ambiguity distance of 1.56 mm must be overcome. This can be achieved, for example, by switching the role of the LO comb and the measurement comb (6) or by sending the LO comb also to the target while evaluating not only the difference signal of the balanced photodetectors but also the sum (28). Using such techniques,

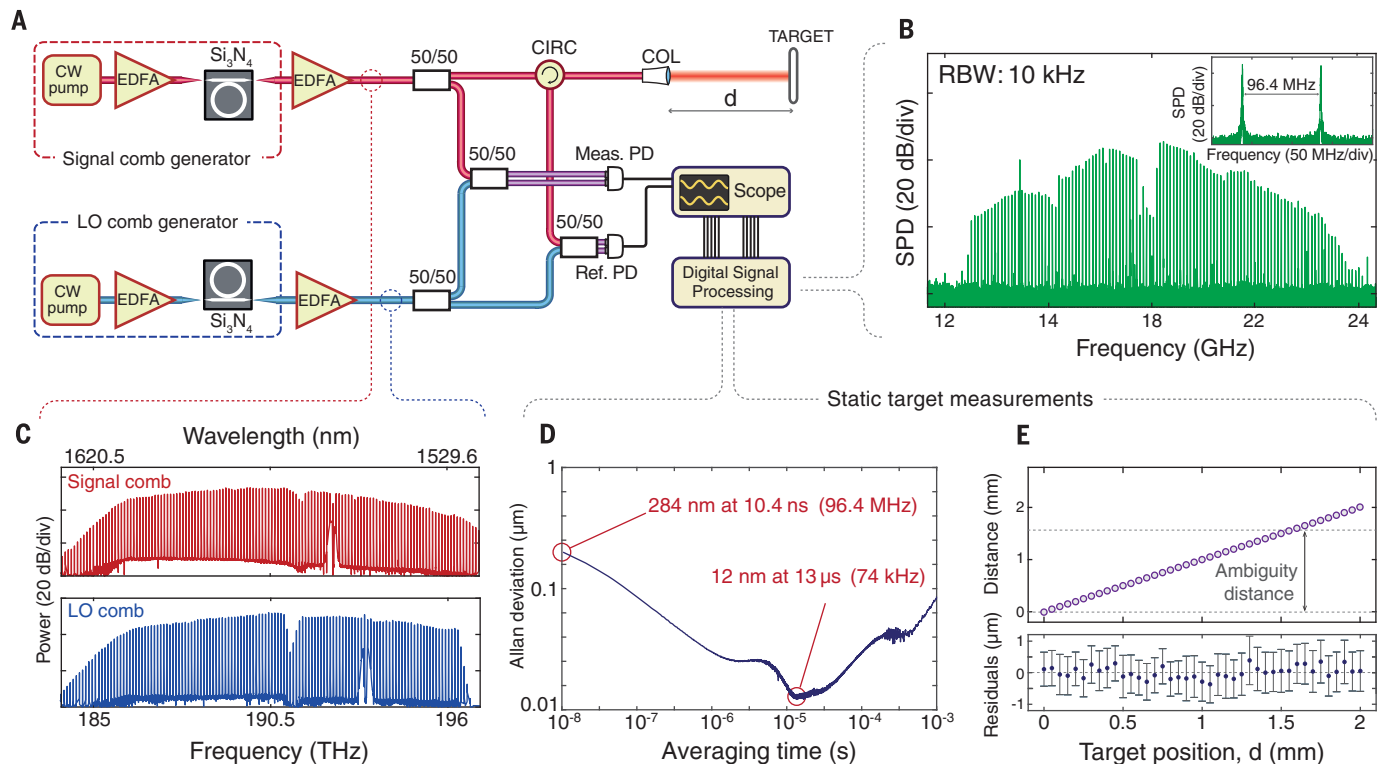


Fig. 2. Experimental demonstration and performance characterization.

tion. (A) Experimental setup. DKS combs are generated by a pair of silicon nitride (Si_3N_4) microresonators, which are pumped by free-running CW lasers and EDFA. After suppressing residual pump light by fiber Bragg gratings (not shown), the combs are amplified by another pair of EDFA. The signal comb (red) is split, and one part is routed to the target and back to a balanced measurement photodetector (Meas. PD) by optical fibers, an optical circulator (CIRC), and a collimator (COL), while the other part is directly sent to the balanced reference detector (Ref. PD). Similarly, the LO comb is split into two portions, which are routed to the measurement PD and the reference PD for multiheterodyne detection. The resulting baseband beat

signals are recorded by a 33-GHz real-time sampling oscilloscope. Digital signal processing is performed offline. (B) Numerically calculated Fourier transform of a recorded time-domain signal. (C) Optical spectra of the signal comb (red) and the local oscillator comb (blue) after amplification. (D) Allan deviation of measured distances as a function of averaging time. The increase toward longer averaging times is attributed to drifts and to mechanical vibrations of the fibers that lead to the target (27). (E) (Top) Scan of measured position versus set position in steps of 50 μ m over the full ambiguity distance (marked by dashed lines). (Bottom) Residual deviations ("residuals") between measured and set positions, with standard deviations as error bars.

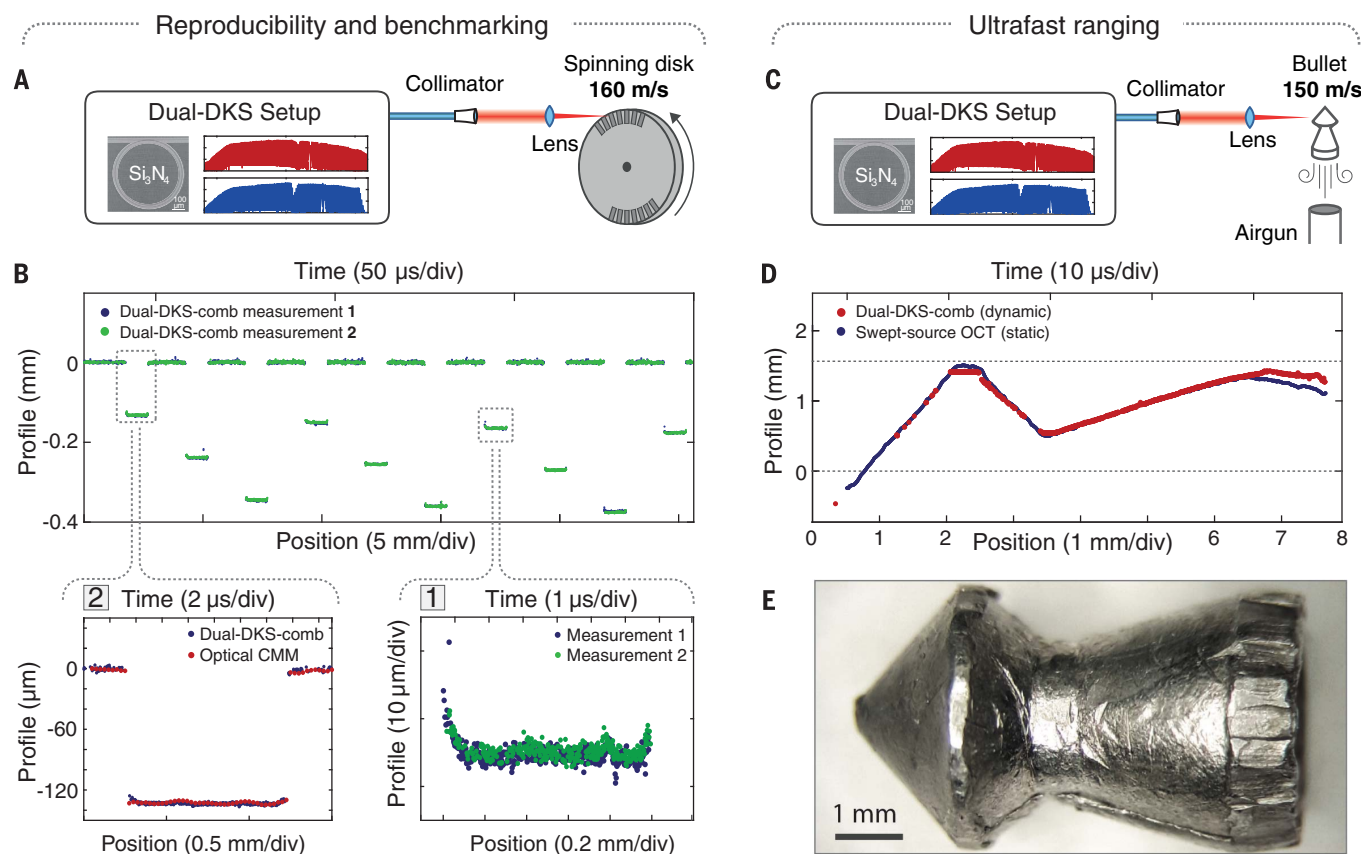


Fig. 3. Reproducibility, benchmarking, and ultrafast ranging demonstration. **(A)** Setup for reproducibility and benchmarking experiments. The measurement beam is focused on the surface of a spinning disk with grooves of different depths. **(B)** Measured surface profile of the disk as a function of position (bottom scale) and time (top scale). The plot contains two independent measurements depicted in blue and green. (Inset 1) Reproducibility demonstration by detailed comparison of the two independent measurements plotted in (B). The measured profiles exhibit good agreement regarding both macroscopic features, such as the groove depth, and microscopic features. (Inset 2) Benchmarking of the high-speed dual-DKS-comb measurement to the results obtained from an industrial optical CMM. **(C)** Setup of ultrafast ranging experiment. **(D)** Measured profile of the projectile obtained from single-shot in-flight dual-DKS-comb measurement (red), along with a swept-source optical coherence tomography (OCT) profile scan that was recorded on the static projectile after recovery from the backstop. The deviations toward the back end of the projectile are attributed to strong corrugations in this area; see (E). **(E)** Image of the projectile after recovery from the backstop.

and microscopic features. (Inset 2) Benchmarking of the high-speed dual-DKS-comb measurement to the results obtained from an industrial optical CMM. (C) Setup of ultrafast ranging experiment. (D) Measured profile of the projectile obtained from single-shot in-flight dual-DKS-comb measurement (red), along with a swept-source optical coherence tomography (OCT) profile scan that was recorded on the static projectile after recovery from the backstop. The deviations toward the back end of the projectile are attributed to strong corrugations in this area; see (E). (E) Image of the projectile after recovery from the backstop.

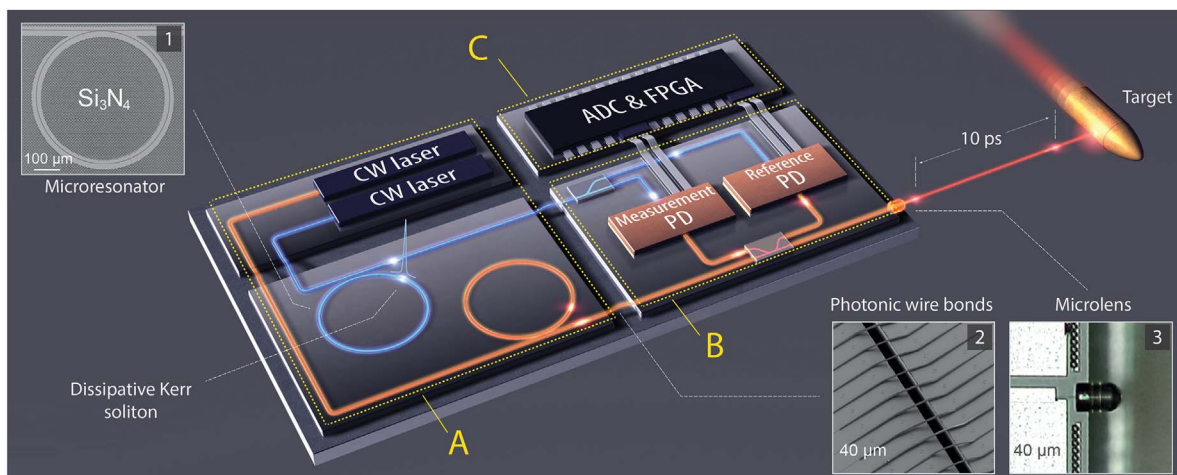


Fig. 4. Artist's view of a dual-comb chip-scale LIDAR engine. The system consists of a dual-frequency comb source (A), a photonic integrated circuit (PIC) for transmission and detection of the LIDAR signal (30) (B), and data acquisition and signal processing electronics (C). The system is realized as a photonic multichip assembly that combines the

distinct advantages of different photonic integration platforms. The insets show various technologies that could be used to realize the envisioned LIDAR engine. (Inset 1) Si_3N_4 microresonator for comb generation (24, 25). (Inset 2) Photonic wire bonds for chip-chip connections (29). (Inset 3) Facet-attached microlens for collimation of the emitted free-space beam (31).

high-precision ranging over extended distances should be possible, only limited by coherence lengths of the individual comb lines, which amount to several kilometers. The high acquisition rate allows tracking continuous movements of objects at any practical speed, with an ambiguity limit of \sim 145,000 m/s.

Our experiments demonstrate the viability of chip-scale DKS comb generators to act as optical sources for high-performance ranging systems and are a key step toward fully integrated chip-scale LIDAR engines, as illustrated as an artist's view in Fig. 4. In this vision, the LIDAR system is realized as a photonic multichip assembly, in which all photonic integrated circuits are connected by photonic wire bonds (Fig. 4, Inset 2) (29). The comb generators are pumped by integrated CW lasers, and a dedicated optical chip is used to transmit and receive the optical signals (30). The receiver is equipped with a chip-attached microlens that collimates the emitted light toward the target (Fig. 4, Inset 3) (31). The electrical signals generated by the photodetectors are sampled by analog-to-digital converters (ADC) and further evaluated by digital signal processing in powerful field-programmable gate arrays (FPGA) or application-specific integrated circuits. Free-running pump lasers greatly simplify the implementation in comparison with configurations where two comb generators are simultaneously pumped by a single light source. Although most of the technological building blocks for realizing this vision have already been demonstrated, one of the remaining key challenges is to reduce the power levels required for DKS generation to typical output power levels of state-of-the-art diode lasers. This requires silicon nitride microresonators with higher quality factors that can be achieved by optimizing the waveguide geometry and the fabrication processes. We expect that such optimizations will allow increasing the Q-factor by about one order of magnitude, thus reducing the pump power

requirements by two orders of magnitude. Alternatively, other integration platforms, such as silicon oxide or AlGaAs, can be used, permitting comb generation with only a few milliwatts of pump power (32). These power levels are realistically achievable with integrated pump laser diodes. Based on these findings, we believe that DKS-based dual-comb LIDAR could have a transformative impact on all major application fields that require compact LIDAR systems and high-precision ranging, in particular when combined with large-scale nanophotonic phased arrays (10, 11). Acquisition rates of hundreds of megahertz could enable ultrafast three-dimensional imaging with megapixel resolution and update rates of hundreds of frames per second.

REFERENCES AND NOTES

1. M.-C. Amann, T. M. Bosch, M. Lescure, R. A. Myllyla, M. Rioux, *Opt. Eng.* **40**, 1330700 (2001).
2. G. Berkovic, E. Shafir, *Adv. Opt. Photonics* **4**, 441 (2012).
3. T. Udem, R. Holzwarth, T. W. Hänsch, *Nature* **416**, 233–237 (2002).
4. K. Minoshima, H. Matsumoto, *Appl. Opt.* **39**, 5512–5517 (2000).
5. N. Schuhler, Y. Salvadé, S. Lévéque, R. Dändliker, R. Holzwarth, *Opt. Lett.* **31**, 3101–3103 (2006).
6. I. Coddington, W. C. Swann, L. Nenadovic, N. R. Newbury, *Nat. Photonics* **3**, 351–356 (2009).
7. Y.-S. Jang *et al.*, *Sci. Rep.* **6**, 31770 (2016).
8. F. Keilmann, C. Gohle, R. Holzwarth, *Opt. Lett.* **29**, 1542–1544 (2004).
9. V. Ataie *et al.*, *Optical Fiber Communication Conference/National Fiber Optic Engineers Conference 2013* (2013), p. OTh3D.2.
10. J. Sun, E. Timurdogan, A. Yaacobi, E. S. Hosseini, M. R. Watts, *Nature* **493**, 195–199 (2013).
11. J. C. Hulme *et al.*, *Opt. Express* **23**, 5861–5874 (2015).
12. N. Akhmediev, A. Ankiewicz, *Dissipative Solitons: Lecture Notes in Physics* (Springer, Berlin Heidelberg, 2005).
13. T. Herr *et al.*, *Nat. Photonics* **8**, 145–152 (2013).
14. P. Del'Haye *et al.*, *Nature* **450**, 1214 (2007).
15. T. J. Kippenberg, R. Holzwarth, S. A. Diddams, *Science* **332**, 555 (2011).
16. L. A. Lugiato, R. Lefever, *Phys. Rev. Lett.* **58**, 2209–2211 (1987).
17. W. Liang *et al.*, *Nat. Commun.* **6**, 7957 (2015).
18. J. D. Jost *et al.*, *Optica* **2**, 706 (2015).
19. M.-G. Suh, Q.-F. Yang, K. Y. Yang, X. Yi, K. J. Vahala, *Science* **354**, 600–603 (2016).
20. P. Marin-Palomo *et al.*, *Nature* **546**, 274–279 (2017).
21. D. T. Spencer *et al.*, arXiv:1708.05228 (2017).
22. J. S. Levy *et al.*, *Nature Photonics* **4**, 37 (2010).
23. D. Moss, R. Morandotti, L. Gaeta, M. Lipson *Nat. Photon.* **7**, 597 (2013).
24. V. Brasch *et al.*, *Science* **351**, 357–360 (2016).
25. M. H. P. Pfeiffer *et al.*, *Optica* **3**, 20 (2016).
26. H. Guo *et al.*, *Nat. Phys.* **13**, 94–102 (2017).
27. Materials and methods are available as supplementary materials.
28. C. Koos, C. Weimann, J. Leuthold, Multiscale distance measurement with frequency combs, U.S. Patent 20150070685 (2013).
29. N. Lindenmann *et al.*, *Opt. Express* **20**, 17667–17677 (2012).
30. C. Weimann, M. Lauermann, F. Hoeller, W. Freud, C. Koos, *Optics Express* **25**, 30091 (2017).
31. P.-I. Dietrich *et al.*, arXiv:1802.00051 [physics.app-ph] (2018).
32. M. Pu, L. Ottaviano, E. Semenova, K. Yvind, *Optica* **3**, 823–826 (2016).

ACKNOWLEDGMENTS

This work was supported by the Deutsche Forschungsgemeinschaft (DFG) through the Collaborative Research Center "Wave Phenomena: Analysis and Numerics" (CRC 1173, project B3 "Frequency combs"), by the European Research Council (ERC Starting Grant EnTeraPIC, number 280145), by the European Union project BigPipes, by the Alfried Krupp von Bohlen und Halbach Foundation, by the Karlsruhe School of Optics and Photonics (KSOP), and by the Helmholtz International Research School for Teratonics (HIRST). D.G. is supported by the Horizon 2020 Research and Innovation Program under the Marie Skłodowska-Curie grant agreement no. 642890 (TheLink). P.M.-P. is supported by the Erasmus Mundus doctorate program Europhotonics (grant number 159224-1-2009-1-FR-ERA MUNDUS-EMJD). SiN₄ devices were fabricated and grown in the Center of MicroNanoTechnology (CMI) at EPFL. EPFL acknowledges support by the U.S. Air Force Office of Scientific Research, Air Force Material Command, USAF, number FA9550-15-1-0099. This work is supported by the European Space Technology Centre with ESA contract no. 4000116145/16/NL/MH/GM. This work was supported by funding from the Swiss National Science Foundation under grant agreement no. 161573 (precoR). The data sets are available through Zenodo at <https://doi.org/10.5281/zenodo.1116280>.

SUPPLEMENTARY MATERIALS

www.sciencemag.org/content/359/6378/887/suppl/DC1

Materials and Methods

Figs. S1 to S6

Table S1

References (33–36)

17 July 2017; accepted 11 January 2018
10.1126/science.aaq3924

METASURFACES

Infrared hyperbolic metasurface based on nanostructured van der Waals materials

Peining Li,¹ Irene Dolado,¹ Francisco Javier Alfaro-Mozaz,¹ Fèlix Casanova,^{1,2} Luis E. Hueso,^{1,2} Song Liu,³ James H. Edgar,³ Alexey Y. Nikitin,^{2,4} Saül Vélez,^{1*} Rainer Hillenbrand^{2,5†}

Metasurfaces with strongly anisotropic optical properties can support deep subwavelength-scale confined electromagnetic waves (polaritons), which promise opportunities for controlling light in photonic and optoelectronic applications. We developed a mid-infrared hyperbolic metasurface by nanostructuring a thin layer of hexagonal boron nitride that supports deep subwavelength-scale phonon polaritons that propagate with in-plane hyperbolic dispersion. By applying an infrared nanoimaging technique, we visualize the concave (anomalous) wavefronts of a diverging polariton beam, which represent a landmark feature of hyperbolic polaritons. The results illustrate how near-field microscopy can be applied to reveal the exotic wavefronts of polaritons in anisotropic materials and demonstrate that nanostructured van der Waals materials can form a highly variable and compact platform for hyperbolic infrared metasurface devices and circuits.

Optical metasurfaces are thin layers with engineered optical properties (described by the effective permittivities in the two lateral directions), which are obtained by lateral structuring of the layers (1–3). Applications include flat lenses, high-efficiency holograms, generation of optical vortex beams, and manipulation of the polarization state of light (1–5). With metallic metasurfaces, one can also control the properties of surface plasmon polaritons (SPPs, electromagnetic waves arising from the coupling of light with charge oscillations in the metasurface) propagating along the metasurface. The near-field enhancement and confinement provided by SPPs are other effective means for controlling the phase and polarization of transmitted light, or the thermal radiation emitted from the metasurface (2, 3). Metasurfaces can also be used to control the properties of SPPs in nanophotonic circuits and devices for applications such as unidirectional excitation of SPPs, modulation of SPPs, or two-dimensional (2D) spin optics (2, 6, 7).

Recently, hyperbolic metasurfaces (HMSs) were predicted, which are uniaxial metasurfaces where the two effective in-plane permittivities $\epsilon_{\text{eff},x}$ and $\epsilon_{\text{eff},y}$ have opposite signs (2, 6). In such materials, the SPPs exhibit a hyperbolic in-plane dispersion, i.e., the isofrequency surface in wave vector space describes open hyperboloids (2, 6, 8–13).

Consequently, the polaritons on HMSs possess an extremely anisotropic in-plane propagation (i.e., different wave vectors in different lateral directions). This behavior leads to remarkable photonic phenomena. For example, the wavefronts of a diverging polariton beam emitted by a pointlike source can exhibit a concave curvature (6, 8), in stark contrast to the convex wavefronts in isotropic materials. Further, the large wave vectors (limited only by the inverse of the structure size) yield a diverging, anomalously large photonic density of states, which can be appreciably larger than that of isotropic SPPs (2, 8). Such polariton properties promise intriguing applications, including planar hyperlenses (2, 8), diffraction-free polariton propagation (6, 13), engineering of polariton wavefronts (6), 2D topological transitions (8), and super-Coulombic optical interactions (10).

HMSs could be created artificially by lateral structuring of thin layers of an isotropic material (2, 6, 13). Alternatively, 2D materials with natural in-plane anisotropy, e.g., black phosphorous, could represent a natural class of HMSs (14–16). However, only a few experimental studies at microwave (11, 12) and visible frequencies (13) have been reported so far, demonstrating only weakly confined SPPs on structured metal surfaces. Artificial HMSs at mid-infrared and terahertz frequencies (corresponding to energies of molecular vibrations and thermal emission and absorption) have not been realized yet, and visualization of the diverging concave wavefronts of deeply subwavelength-scale confined in-plane hyperbolic polaritons on either artificial or natural HMSs has been elusive.

Here we propose, design, and fabricate a mid-infrared HMS by lateral structuring of thin layers of the polar van der Waals (vdW) material hex-

agonal boron nitride (hBN). In contrast to metal layers, they support strongly volume-confined phonon polaritons (quasiparticles formed by the coupling of light with lattice vibrations) with notably low losses, thus representing a suitable basis for mid-infrared HMSs.

The material hBN is a polar vdW (layered) crystal, thus possessing a uniaxial permittivity (17–23). It has a mid-infrared Reststrahlen band from 1395 to 1630 cm^{−1} (24), where the in-plane permittivity is negative and isotropic, $\epsilon_{\text{hBN},x} = \epsilon_{\text{hBN},y} = \epsilon_{\text{hBN},\perp} < 0$, and the out-of-plane permittivity is positive, $\epsilon_{\text{hBN},z} = \epsilon_{\text{hBN},\parallel} > 0$. As a result, the phonon polaritons in natural hBN exhibit an out-of-plane hyperbolic dispersion, whereas the in-plane dispersion is isotropic (17–23). The isotropic (radial) propagation of the conventional hyperbolic phonon polaritons (HPhPs) in a natural hBN layer is illustrated with numerical simulations (Fig. 1, A to D), where a dipole above the hBN layer essentially launches the fundamental slab mode M0 (17–19). To turn the hBN layer into an in-plane HMS, a grating structure is patterned, consisting of hBN ribbons of width w that are separated by air gaps of width g (Fig. 1E). Because of the anisotropic permittivity of hBN, however, the hBN grating represents a biaxial layer exhibiting three different effective permittivities ($\epsilon_{\text{eff},x} \neq \epsilon_{\text{eff},y} \neq \epsilon_{\text{eff},z}$), in contrast to uniaxial metal gratings where $\epsilon_{\text{eff},x} \neq \epsilon_{\text{eff},y} = \epsilon_{\text{eff},z}$ (which can be considered as canonical HMS structures at visible frequencies). These designed biaxial layers can support highly confined polaritons with in-plane hyperbolic dispersion. They could be considered as Dyakonov polaritons (25), which are similar to Dyakonov waves on biaxial dielectric materials (26).

We first applied effective medium theory (25) to determine the parameters required for the grating to function as an HMS. The effective permittivities were calculated as a function of ribbon and gap widths, w and g (figs. S1 and S2), according to

$$\epsilon_{\text{eff},x} = 1 / \left[\frac{1 - \xi}{\epsilon_{\text{hBN},\perp}} + \xi \right] \quad (1)$$

$$\epsilon_{\text{eff},y} = \epsilon_{\text{hBN},\perp} (1 - \xi) + \xi \quad (2)$$

$$\epsilon_{\text{eff},z} = \epsilon_{\text{hBN},\parallel} (1 - \xi) + \xi \quad (3)$$

where $\xi = g/(w + g)$ is the so-called filling factor. We find that the condition for well-pronounced in-plane hyperbolic dispersion, $-10 < \text{Re}(\epsilon_{\text{eff},y})/\text{Re}(\epsilon_{\text{eff},x}) < 0$, can be fulfilled in the frequency range 1400 to 1500 cm^{−1} for filling factors in the order of $\xi = 0.5$. For example, at a frequency $\omega = 1425 \text{ cm}^{-1}$ ($\epsilon_{\text{hBN},\perp} = -22.2 + 0.9i$ and $\epsilon_{\text{hBN},\parallel} = 2.6$), we obtain $\epsilon_{\text{eff},x} = 3.7$, $\epsilon_{\text{eff},y} = -15.2 + 0.6i$, and $\epsilon_{\text{eff},z} = 2.1$ for $w = 70 \text{ nm}$ and $g = 30 \text{ nm}$, which corresponds to a grating structure that can be fabricated by electron beam lithography and etching. Note that the same effective in-plane permittivities for a metal grating [$\text{Re}(\epsilon_{\text{metal}}) <$

¹CIC nanoGUNE, 20018 Donostia-San Sebastián, Spain.

²IKERBASQUE, Basque Foundation for Science, 48013 Bilbao, Spain. ³Department of Chemical Engineering, Kansas State University, Manhattan, KS 66506, USA. ⁴Donostia International Physics Center (DIPC), 20018 Donostia-San Sebastián, Spain.

⁵CIC nanoGUNE and Universidad del País Vasco-Euskal Herriko Unibertsitatea, 20018 Donostia-San Sebastián, Spain.

*Present address: Department of Materials, ETH Zürich, 8093 Zürich, Switzerland.

†Corresponding author. Email: r.hillenbrand@nanogune.eu

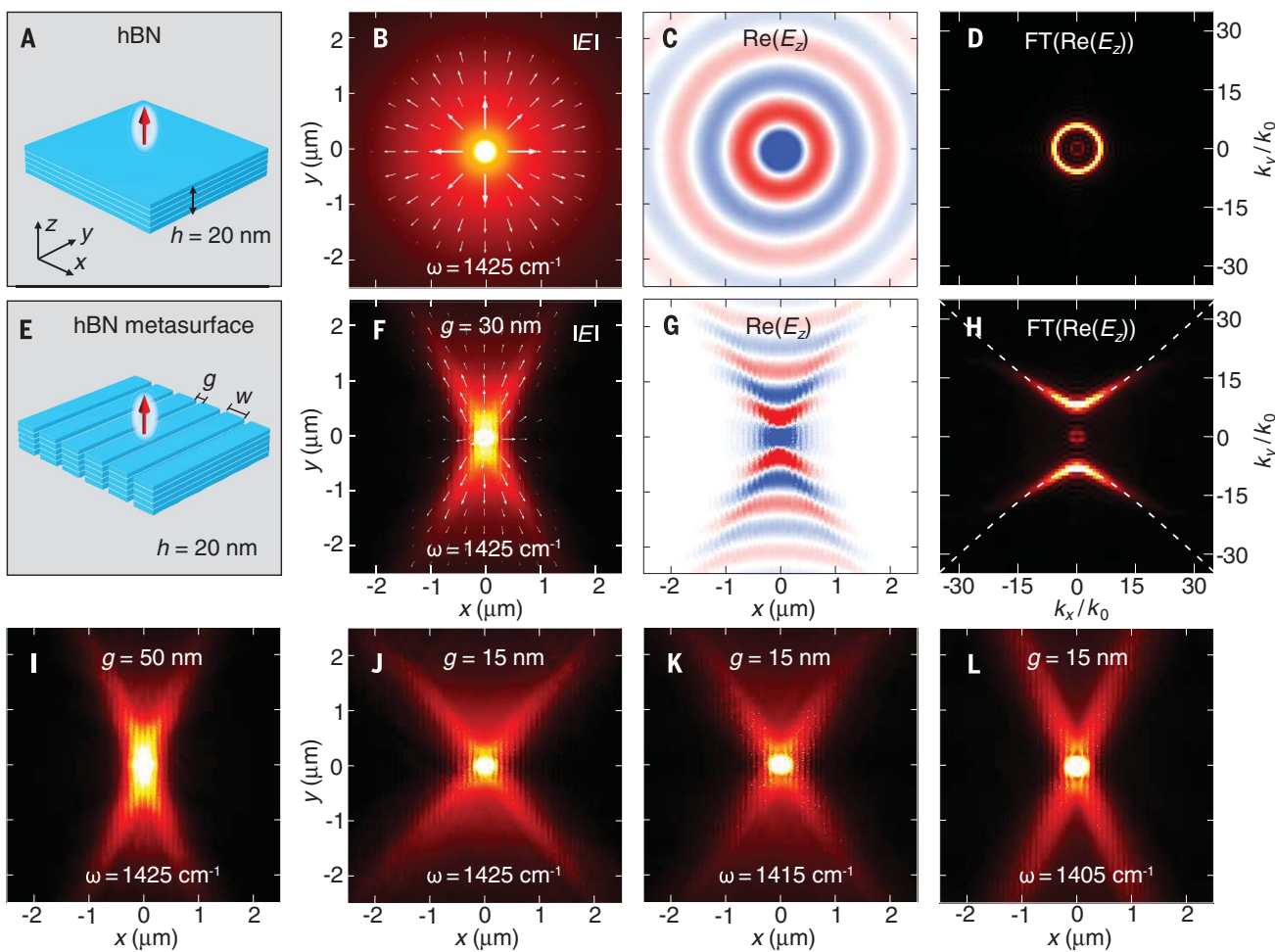


Fig. 1. Dipole-launching of hBN phonon polaritons. (A) Schematic of dipole launching of phonon polaritons on a 20-nm-thick hBN flake. h , height. (B) Simulated magnitude of the near-field distribution above the hBN flake, $|E|$. (C) Simulated real part of the near-field distribution above the hBN flake, $\text{Re}(E_z)$. (D) Absolute value of the Fourier transform (FT) of panel (C). k_x and k_y are normalized to the photon wave vector k_0 . (E) Schematic of dipole launching of phonon polaritons on a 20-nm-thick hBN HMS (ribbon width $w = 70$ nm; gap width $g = 30$ nm). (F) Simulated

magnitude of the near-field distribution above the hBN HMS, $|E|$. (G) Simulated real part of the near-field distribution above the hBN HMS, $\text{Re}(E_z)$. (H) Absolute value of the FT of panel (G). The features revealed by the FT of the dipole-launched polaritons can be well fitted by a hyperbolic curve (white dashed lines). (I to L) Simulated magnitude of the near-field distributions for HMSs with different gap sizes and operation frequencies. The grating period $w + g$ is fixed to 100 nm in all simulations. The white arrows in (B) and (F) display the simulated power flow.

-1000 at mid-infrared frequencies] would require 100-nm-wide ribbons separated by less than 1-nm-wide gaps (fig. S1), thus strongly challenging their fabrication. Alternatively, one could use doped semiconductors and (isotropic) polar crystals, where the permittivities in the mid-infrared and terahertz spectral range are similar to that of hBN (27, 28). However, the losses in doped semiconductors are typically larger than those in hBN. Phonon polaritons in polar crystals such as SiC exhibit low losses similar to hBN, but thin layers are difficult to grow without defects, which increase losses (27, 28). Thus, hBN represents a promising material for the experimental realization of grating-based HMSs, owing to the easy preparation of high-quality single-crystalline thin layers.

To verify the HMS design parameters, we carried out numerical simulations (see supplementary materials, note S3) of dipole-launched

polaritons on a 20-nm-thick hBN grating, using $w = 70$ nm, $g = 30$ nm, and bulk hBN permittivities at $\omega = 1425 \text{ cm}^{-1}$ (Fig. 1, F and G). The typical hyperbolic polariton rays can be seen in the intensity image (Fig. 1F), whereas the real part of the electric field distribution reveals the concave polariton wavefronts (Fig. 1G). The formation of these wavefronts arises from an interference phenomenon of polaritons that propagate with a direction-dependent wavelength (determined by the hyperbolic isofrequency curves) at a given frequency. Fourier transform (FT) of Fig. 1G corroborates the polaritons' in-plane hyperbolic dispersion and large wave vectors (deep subwavelength-scale confinement) thus showing that the biaxial grating structure functions as a HMS (Fig. 1H). We repeated the numerical simulation of dipole-launched polaritons on a 20-nm-thick biaxial layer with the corresponding effective permittivities (fig. S3). Excellent quantitative

agreement is found with the simulated near-field distribution above the grating structure.

The numerical simulations also show that the wave vector (and thus the confinement) of the hyperbolic metasurface phonon polaritons (HMS-PhPs) is increased compared to that of the conventional HPhPs on the natural hBN layer (compare Fig. 1H with 1D). They further demonstrate that the HMS-PhP propagation depends on frequency (Fig. 1, J to L) and that it can be tuned by varying the structure size (Fig. 1, F, I, and J).

For an experimental demonstration of our proposed metasurface, we etched a 5 μm -by-5 μm grating (schematic in Fig. 2A and topography image in Fig. 2B) into a 20-nm-thick exfoliated flake of isotopically enriched (29–31) low-loss hBN (see supplementary materials, note S1). The ribbon and slit widths are 75 and 25 nm, respectively (fig. S4). Near-field polariton interferometry was used to show that the grating

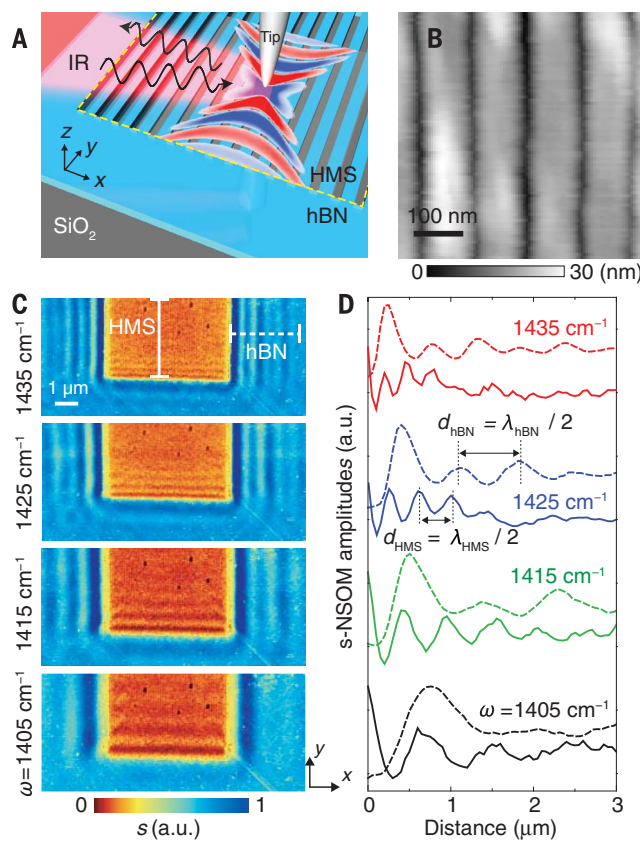


Fig. 2. Polariton-interferometry imaging of phonon polaritons on a 20-nm-thick hBN HMS.

(A) Schematic of the near-field polariton interferometry experiment. IR, infrared. (B) Topography image of the hBN HMS (nominal grating parameters are $w \approx 75$ nm and $g \approx 25$ nm; see also fig. S4). (C) Near-field images (amplitude signal s) recorded at four different frequencies. a.u., arbitrary units. (D) s-NSOM amplitude profiles along the solid (vertical) and dashed (horizontal) white lines in (C). (E) Illustration of the polariton interferometry contrast mechanism. The tip launches phonon polaritons on the HMS (indicated by simulated near fields). The polaritons with wave vector parallel to the grating reflect at the lower horizontal boundary (indicated by the black arrow) and interfere with the local field underneath the tip. Tip-launched polaritons propagating in other directions cannot be probed by the tip. The orange dashed lines mark the boundaries of the HMS. (F and G) Experimental (squares) and numerically calculated (solid lines) wave vectors of phonon polaritons on the unpatterned flake and the HMS, respectively. The line colors indicate the frequency ω according to (D).

supports polaritons (17, 18). The metallic tip of a scattering-type near-field scanning optical microscope (s-NSOM), acting as an infrared antenna, concentrates an illuminating infrared beam to a nanoscale spot at the tip apex, which serves as a point source to launch polaritons on the sample (Fig. 2A). The tip-launched polaritons reflect at sample discontinuities (such as edges and defects), propagate back to the tip, and interfere with the local field below the tip. Recording the tip-scattered field (amplitude signal s in our case; see supplementary materials, note S2) as a function of the tip position yields images that exhibit interference fringes of $\lambda_p/2$ spacing, where λ_p is the polariton wavelength (17, 18).

Figure 2C shows the polariton interferometry images of our sample measured at four different frequencies. On both the grating (HMS) and the surrounding (unpatterned) hBN flake, polariton

fringes are observed. On the grating, we see fringes only parallel to the horizontal HMS boundary, which could be explained by a close-to-zero reflection at the left and right boundaries of the grating, or, more interestingly, by the absence of polariton propagation in the x direction (horizontal), the latter being consistent with hyperbolic polariton dispersion. We further observe a nearly twofold-reduced fringe spacing on the grating, d_{HMS} , compared to that of the unpatterned flake, d_{hBN} (see line profiles in Fig. 2D), indicating superior polaritonic-field confinement on the grating. For further analysis (see also fig. S5), we compare in Fig. 2, F and G, the experimental polariton wave vectors $k = 2\pi/\lambda_p = \pi/d$ (squares) with isofrequency curves of the calculated polariton wave vectors (solid lines). The calculation predicts a hyperbolic isofrequency curve for the grating polaritons, where the wave vector in the y direction is increased

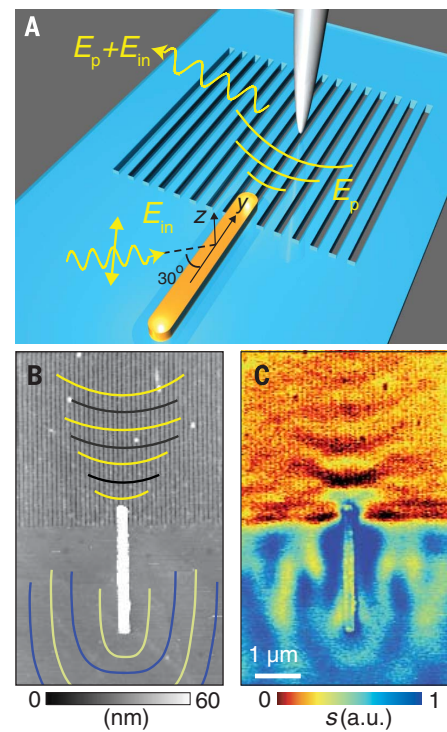


Fig. 3. Wavefront imaging of antenna-launched HMS-PhPs. (A) Schematic of the experiment. (B) Topography image. The lines illustrate wavefronts of HMS-PhPs on the HMS (yellow and black) or phonon polaritons on the unpatterned flake (yellow and blue). (C) Near-field image recorded at $\omega = 1430$ cm $^{-1}$, clearly revealing concave wavefronts of HMS-PhPs emerging from the rod's upper extremity.

by nearly a factor of two, which quantitatively matches our experimental observation well. Although the polariton confinement increases on the HMS, the calculated relative propagation length [often used as figure of merit (FOM) = k/γ , with k and γ being the real and imaginary parts of the complex wave vector K (17, 31)] and polariton lifetime remain nearly the same (fig. S6). Experimentally, however, the FOM and lifetime on the metasurface are reduced by more than 35% as compared to that of polaritons on the unpatterned flake, which we attribute to polariton losses caused by fabrication imperfections leading, for example, to polariton scattering (figs. S7 and S8).

The near-field images provide experimental indication that the hBN grating functions as an in-plane HMS. However, they do not reveal anomalous (concave) wavefronts such as the ones observed in Fig. 1. This can be understood by considering that only the polaritons propagating perpendicular to the metasurface boundary are back-reflected to the tip and thus recorded (Fig. 2E). The anomalous wavefronts are the result of interference of hyperbolic polaritons propagating in all allowed directions. To obtain real-space images of the anomalous wavefronts, we performed near-field imaging of

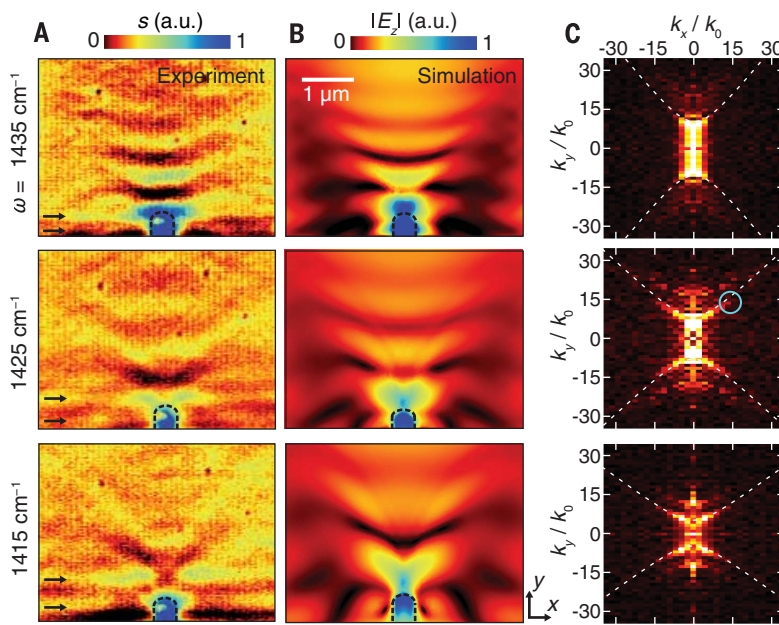


Fig. 4. Frequency dependence of HMS-PhP wavefronts. (A and B) Experimental and calculated near-field distribution of HMS-PhPs launched by the antenna at three different frequencies. Black arrows in (A) indicate the fringes of polaritons launched by the tip and reflected at the boundary between the HMS and the unpatterned flake. Black dashed lines indicate the extremity of the gold rod. (C) Absolute value of the FT of the images shown in (A). White dashed lines represent the numerically calculated isofrequency curves of antenna-launched HMS-PhPs. The features in the gap between the hyperbolic isofrequency curves correspond to the FT of the antenna fields that are not coupled to polaritons (32), analogous to the central circular feature in the FT of the dipole-launched HMS-PhPs (Fig. 1H). The light-blue circle at $\omega = 1425 \text{ cm}^{-1}$ marks a pixel whose value is still above the noise floor. The largest polariton wave vectors thus amount to about $k = (k_x^2 + k_y^2)^{0.5} = [(15k_0)^2 + (15k_0)^2]^{0.5} > 20k_0$.

HMS polaritons emerging from a nanoscale confined source located directly on the sample.

For nanoimaging of the polariton wavefronts, we used antenna-based polariton launching (32). A gold rod acting as an infrared antenna was fabricated on top of the sample studied in Fig. 2 (schematic in Fig. 3A and topography image in Fig. 3B). Illumination with p-polarized infrared light excites the antenna, yielding nanoscale concentrated fields at the rod extremities, which launch polaritons on either the metasurface or the unpatterned flake (upper and bottom parts of Fig. 3, B and C, respectively). The polariton field propagating away from the antenna, E_p , interferes with the illuminating field, E_{in} , yielding interference fringes on the sample (illustrated by solid lines in Fig. 3B) (19). This pattern is mapped by recording the field scattered by the metal tip of the s-NSOM while the sample is scanned. Because E_{in} is constant (i.e., independent of sample position), the interference pattern observed in the amplitude image directly uncovers the spatial distribution of the polariton field E_p and thus the polariton wavefronts [note that retardation in first-order approximation can be neglected owing to the much shorter polariton wavelength compared to the illuminating photon wavelength (19)].

Figure 3C shows a near-field image of the antenna on the hBN sample at $\omega = 1430 \text{ cm}^{-1}$.

In the lower part of the image, we clearly observe the conventional (convex) polariton fringes, which are caused by antenna-launched HPhPs on the unpatterned hBN layer (see also fig. S9). The upper part of the image, in notable contrast, exhibits anomalous polariton fringes emerging from the rod's upper extremity. They clearly reveal the concave wavefronts of a diverging polariton beam on the hBN grating. The image thus provides clear experimental visualization of in-plane hyperbolic polaritons and thus verifies that the grating functions as a HMS. By varying the illumination frequency, the anomalous polariton wavefronts can be tuned (Fig. 4A) from smoothly concave [nearly diffraction-free polariton propagation (6)] at $\omega = 1435 \text{ cm}^{-1}$ to a wedge-like shape at $\omega = 1415 \text{ cm}^{-1}$. We corroborate the experimental near-field images with the numerical simulations shown in Fig. 4B, which indeed show an excellent agreement, particularly regarding the fringe spacing and curvatures.

For simplicity, we did not include the metallic tip into the calculations, which in the experiment launches polaritons simultaneously with the gold antenna. Analogous to Fig. 2, the tip-launched polaritons reflect at the boundary between the hBN grating and the unpatterned hBN flake, yielding horizontal fringes in the experimental near-field images (marked by arrows in Fig. 4A) that are not seen in the simulated

images (Fig. 4B). Note that the tip-launched polaritons are weakly reflected at the gold antenna and thus are not producing disturbing interference with the antenna-launched polaritons. The weak polariton reflection at metal structures on top of hBN samples is consistent with former observations and could be explained by the hyperbolic polaritons propagating through the hBN underneath the metal structure (19). For further details on tip-launched versus antenna-launched polaritons, see also fig. S10.

To determine the in-plane HMS-PhP wave vectors, we performed a FT of the experimental near-field images of Fig. 4A (fig. S11). The FTs are shown in Fig. 4C (see also fig. S13), clearly revealing hyperbolic features. They exhibit an excellent agreement with the numerically calculated hyperbolic dispersions of HMS-PhPs (white dashed lines; see supplementary materials, note S3), thus further corroborating that the real-space images in Fig. 4A reveal the wavefronts of in-plane hyperbolic polaritons. Figure 4C also verifies the large polariton wave vectors k achieved with our HMS [for example, $k = (k_x^2 + k_y^2)^{0.5} > 20k_0$ at $\omega = 1425 \text{ cm}^{-1}$, with k_0 being the photon wave vector], which are considerably larger than that of the SPPs on metal-based HMSs ($k < 3k_0$) (12, 13). In principle, the wave vectors predicted theoretically (Fig. 1H) and observed experimentally (Fig. 4C) could be larger, amounting up to $70k_0$, which is their theoretical limit given by the grating period. We explain the nonvisibility of such large wave vectors by the wave vector distribution of the near fields of the 250-nm-wide antenna, which exhibits dominantly small wave vectors below $28k_0$. For that reason, large wave vector polaritons on the HMS are only weakly excited and masked by small wave vector polaritons. To increase the excitation and relative weight of large wave vector HMS-PhPs, we suggest fabricating launching structures of smaller dimensions. Indeed, in numerical calculations, we can observe larger polariton wave vectors (and thus more pronounced polariton rays) by simply placing the polariton-launching dipole closer to the HMS surface (see fig. S12). We can also see a second (much weaker) hyperbolic feature at larger k values. We assign it to tip-launched polaritons that weakly reflect at the gold rod (fig. S13). Because of their weak reflection, they are barely recognized in the real-space images of Fig. 4A. More interestingly, the FTs of the near-field images verify that the opening angle θ of the hyperboloids decreases with increasing frequency (fig. S14). This has been predicted in numerous previous theoretical and numerical studies (6, 8) and now can be directly observed in experimental data.

Considering that fabrication of nanoscale gratings by electron beam lithography and etching is a widely applicable technique, we envision HMSs based on other vdW materials (MoS_2 , Bi_2Se_3 , etc.) or multilayer graphene samples, as well as on thin layers of polar crystals (SiC , quartz, etc.) or low-loss doped semiconductors (27, 28). Combinations of different materials could lead to HMSs covering the entire spectral range,

from mid-infrared to terahertz frequencies. The combined advantage of strong polariton-field confinement, anisotropic polariton propagation, tunability by geometry and electric gating, as well as the possibility of developing vdW heterostructures (33), could open exciting new possibilities for flatland infrared, thermal, and optoelectronic applications, such as infrared chemical sensing, planar hyperlensing (8, 18, 27), exotic optical coupling (10), and manipulation of near-field heat transfer (2, 8). Real-space wavefront nanoimaging of in-plane hyperbolic polaritons, as demonstrated in our work, will be an indispensable tool for verifying new design principles and for quality control.

REFERENCES AND NOTES

1. N. Yu *et al.*, *Science* **334**, 333–337 (2011).
2. A. V. Kildishev, A. Boltasseva, V. M. Shalaev, *Science* **339**, 1232009 (2013).
3. N. Yu, F. Capasso, *Nat. Mater.* **13**, 139–150 (2014).
4. X. Ni, N. K. Emani, A. V. Kildishev, A. Boltasseva, V. M. Shalaev, *Science* **335**, 427 (2012).
5. D. Lin, P. Fan, E. Hasman, M. L. Brongersma, *Science* **345**, 298–302 (2014).
6. Y. Liu, X. Zhang, *Appl. Phys. Lett.* **103**, 141101 (2013).
7. J. Lin *et al.*, *Science* **340**, 331–334 (2013).
8. J. S. Gomez-Diaz, A. Alù, *ACS Photonics* **3**, 2211–2224 (2016).
9. J. S. Gomez-Diaz, M. Tymchenko, A. Alù, *Phys. Rev. Lett.* **114**, 233901 (2015).
10. C. L. Cortes, Z. Jacob, *Nat. Commun.* **8**, 14144 (2017).
11. P. V. Kapitanova *et al.*, *Nat. Commun.* **5**, 3226 (2014).
12. Y. Yang *et al.*, *NPG Asia Mater.* **9**, e428 (2017).
13. A. A. High *et al.*, *Nature* **522**, 192–196 (2015).
14. D. N. Basov, M. M. Fogler, F. J. García de Abajo, *Science* **354**, aag1992 (2016).
15. T. Low *et al.*, *Nat. Mater.* **16**, 182–194 (2017).
16. A. Nemelentsau, T. Low, G. Hanson, *Phys. Rev. Lett.* **116**, 066804 (2016).
17. S. Dai *et al.*, *Science* **343**, 1125–1129 (2014).
18. S. Dai *et al.*, *Nat. Commun.* **6**, 6963 (2015).
19. E. Yoxall *et al.*, *Nat. Photonics* **9**, 674–678 (2015).
20. J. D. Caldwell *et al.*, *Nat. Commun.* **5**, 5221 (2014).
21. P. Li *et al.*, *Nat. Commun.* **6**, 7507 (2015).
22. Z. Sun, Á. Gutiérrez-Rubio, D. N. Basov, M. M. Fogler, *Nano Lett.* **15**, 4455–4460 (2015).
23. A. J. Giles *et al.*, *Nano Lett.* **16**, 3858–3865 (2016).
24. See supplementary materials.
25. Z. Jacob, E. E. Narimanov, *Appl. Phys. Lett.* **93**, 221109 (2008).
26. O. Takayama, D. Artigas, L. Torner, *Nat. Nanotechnol.* **9**, 419–424 (2014).
27. S. Law, V. Podolskiy, D. Wasserman, *Nanophotonics* **2**, 103–130 (2013).
28. A. Boltasseva, H. A. Atwater, *Science* **331**, 290–291 (2011).
29. T. B. Hoffman, B. Clubine, Y. Zhang, K. Snow, J. H. Edgar, *J. Cryst. Growth* **393**, 114–118 (2014).
30. J. H. Edgar *et al.*, *J. Cryst. Growth* **403**, 110–113 (2014).
31. A. J. Giles *et al.*, *Nat. Mater.* **17**, 134–139 (2017).
32. P. Alonso-González *et al.*, *Science* **344**, 1369–1373 (2014).
33. S. Dai *et al.*, *Nat. Nanotechnol.* **10**, 682–686 (2015).

ACKNOWLEDGMENTS

Funding: The authors acknowledge support from the European Commission under the Graphene Flagship (GrapheneCore1, grant

no. 696656), the Marie Skłodowska-Curie individual fellowship (SGPCM-705960), the Spanish Ministry of Economy, Industry, and Competitiveness (national projects MAT2015-65525-R, MAT2015-65159-R, FIS2014-60195-JIN, MAT2014-53432-C5-4-R, FIS2016-80174-P, MAT2017-88358-C3-3-R and the project MDM-2016-0618 of the Maria de Maeztu Units of Excellence Programme), the Basque government (PhD fellowship PRE-2016-1-0150), the Regional Council of Gipuzkoa (project no. 100/16), and the Department of Industry of the Basque Government (ELKARTEK project MICRO4FA). Further, support from the Materials Engineering and Processing program of the NSF, award number CMMI 1538127, and the II-VI Foundation is greatly appreciated.

Author contributions: P.L. and R.H. conceived the study. Sample fabrication was performed by I.D. and S.V., coordinated by S.V., and supervised by F.C. and L.E.H. P.L. performed the experiments and simulations. F.J.A.-M. and A.Y.N. contributed to the simulations. S.L. and J.H.E. grew the isotopically enriched boron nitride. R.H. coordinated and supervised the work. P.L. and R.H. wrote the manuscript with the input of all other co-authors.

Competing interests: R.H. is cofounder of and on the scientific advisory board of Neaspec GmbH, a company producing scattering-type near-field scanning optical microscope systems, such as the one used in this study. The remaining authors declare no competing financial interests. **Data and materials availability:** All data are available in the manuscript or the supplementary materials.

SUPPLEMENTARY MATERIALS

www.sciencemag.org/content/359/6378/892/suppl/DC1
Materials and Methods
Figs. S1 to S14
References (34–36)

11 October 2017; accepted 10 January 2018
10.1126/science.aaq1704

Nitrogen fixation and reduction at boron

Marc-André Légaré,^{1,2} Guillaume Bélanger-Chabot,^{1,2} Rian D. Dewhurst,^{1,2} Eileen Welz,³ Ivo Krummenacher,^{1,2} Bernd Engels,³ Holger Braunschweig^{1,2,*}

Currently, the only compounds known to support fixation and functionalization of dinitrogen (N_2) under nonmatrix conditions are based on metals. Here we present the observation of N_2 binding and reduction by a nonmetal, specifically a dicoordinate borylene. Depending on the reaction conditions under which potassium graphite is introduced as a reductant, N_2 binding to two borylene units results in either neutral (B_2N_2) or dianionic ($[B_2N_2]^{2-}$) products that can be interconverted by respective exposure to further reductant or to air. The ^{15}N isotopologues of the neutral and dianionic molecules were prepared with ^{15}N -labeled dinitrogen, allowing observation of the nitrogen nuclei by ^{15}N nuclear magnetic resonance spectroscopy. Protonation of the dianionic compound with distilled water furnishes a diradical product with a central hydrazido $B_2N_2H_2$ unit. All three products were characterized spectroscopically and crystallographically.

The element nitrogen is essential for life on Earth and makes up over three-quarters of the atmosphere by volume, yet its common elemental form (dinitrogen, N_2) is extremely stable and thus difficult to utilize. Nature overcomes this through the nitrogen-binding enzymes called nitrogenases (1, 2), whereas industry relies on the energy-intensive, transition-metal-catalyzed Haber-Bosch process (3, 4) to convert dinitrogen to ammonia for the production of fertilizer. In the century since the discovery of the Haber-Bosch process, a number of transition-metal (TM) species have been found to bind (and even functionalize) N_2 at low temperatures (5–14). The rare ability of certain transition-metal complexes to bind N_2 is attributed to their advantageous combination of unoccupied and occupied d orbitals, which are of appropriate energy and symmetry to synergically accept electron density from and backdonate to N_2 (Fig. 1A). The latter process, termed π backdonation, weakens the N-N bond while simultaneously strengthening the metal-nitrogen bond and is thus crucial in effective N_2 binding and activation. In contrast to transition metals, main-group compounds generally lack the combination of empty and filled orbitals required to form bonds of σ and π symmetry, respectively, and thus very few are able to provide π backbonding. Accordingly, N_2 binding by p-block compounds is currently restricted to a handful of highly reactive, most often strongly Lewis acidic, species generated in the gas phase or under matrix isolation conditions (15–18). Of the main-group elements, only the strongly reductive element lithium reacts with N_2 at room

temperature (albeit slowly) to give an isolable product, the binary nitride Li_3N (19).

Over the past decade, advances in the chemistry of low-valent, low-coordinate main-group elements have indicated that these compounds, often bearing reactive lone pairs of electrons as well as vacant orbitals at the same atom, effectively mimic transition metals in many reactions (20). Undoubtedly the most well-developed examples of these are the singlet carbenes ($:CR_2$), particularly the σ -donating and π -accepting carbenes developed by Bertrand and co-workers (21). The combination of filled and empty orbitals proximal in space and energy in these compounds has facilitated binding and activation of a number of challenging small molecules such as H_2 , NH_3 , and P_4 under mild conditions. Base-stabilized borylenes (22, 23), compounds containing a monovalent boron atom and one or two neutral donor groups ($:BRL_n$; $n = 1, 2$; R = anionic substituent; L = neutral donor; Fig. 1B), are a promising recent addition to the family of main-group metallomimetics. In 2014, Stephan and Bertrand reported the fixation of CO at the boron atom of a borylene-like allenic dicoordinate (RBL) species (Fig. 1B, ii and iii) (24), and we have subsequently detailed photolytic decarbonylation and donor exchange reactions (Fig. 1B, i to iii) at monovalent boron centers (25, 26)—all characteristic reactions of transition metals. Our observation of strong π -backbonding from boron to CO in a number of borylene complexes (Fig. 1B, i), which is also a bonding motif critical to end-on dinitrogen binding to metal centers (Fig. 1A), inspired us to test our borylene fragment as a scaffold to bind N_2 . The suitability of borylenes as candidates for N_2 binding is further underlined by a recent report of N_2 binding by the unstabilized borylene “ PhB ” under matrix conditions (18).

In previous work, we showed that borylene species [DurB(CO)(CAAC)] (3, Fig. 1C; Dur = 2,3,5,6-tetramethylphenyl; CAAC = 1-(2,6-

diisopropylphenyl)-3,3,5,5-tetramethylpyrrolidin-2-ylidene] undergoes photolytic decarbonylation to generate the transient dicoordinate borylene [DurB(CAAC)] (2), which could be trapped with Lewis bases (pyridine, isonitrile, N-heterocyclic carbene) or would undergo C-H activation in the absence of a base (26). However, similar attempts to bind N_2 to the boron atom by photodecarbonylation under a N_2 atmosphere provided only the previously reported C-H activation product 4.

During a search for a more convenient synthetic route to 3 {previously accessible only by addition of CAAC to transition-metal borylene complex [Fe(BDur)(CO)₃(PMe₃)₂] (26)}, we found that this compound could be prepared by reducing [(CAAC)BBr₂Dur] (1) with potassium graphite (KC₈) under an atmosphere of CO (Fig. 1C). Similarly, reduction of 1 under an argon atmosphere produced the aforementioned C-H activation product 4. These reactions again suggested the intermediacy of dicoordinate borylene species [DurB(CAAC)] (2, Fig. 1C)—but notably without photolytic conditions that could be detrimental to the formation of N_2 adducts—prompting us to attempt this reaction under an atmosphere of N_2 . To this end, toluene was added to a solid mixture of [(CAAC)BBr₂Dur] (1) and five equivalents of KC₈ at $-80^\circ C$ under 1 atm of dinitrogen, which led to an immediate change from colorless to fuchsia, a color not encountered in analogous reactions under either argon or CO. The resulting mixture was allowed to warm up to room temperature and after overnight reaction showed the presence of C-H activation product 4 by ^{11}B nuclear magnetic resonance (NMR) [δ_B ~70 and 86 parts per million (ppm), corresponding to two diastereoisomers (26)] and provided a very low yield of dark purple crystals of new compound 5 (Fig. 1C) with a substantially upfield-shifted ^{11}B NMR signal (δ_B 10.7 ppm).

A single-crystal x-ray diffraction study of these crystals showed them to comprise the dinitrogen bis(borylene) compound $\{[(CAAC)DurB]_2(\mu^2-N_2)\}$ (Fig. 1C and Fig. 2, top). The solid-state structure of 5 showed two [(CAAC)DurB] fragments bound through their boron atoms to a central N_2 unit. The two halves of the molecule are considerably different, with the B2-N2-N1 angle [146.1(2) $^\circ$] significantly closer to linearity than B1-N1-N2 [131.9(2) $^\circ$]. The B1-N1 [1.423(4) Å] and B2-N2 [1.403(5) Å] distances are equivalent within experimental uncertainty and are in the range of conventional B-N double bonds in aminoboranes (27). The N1-N2 bond length [1.248(4) Å] lies far closer to the range of N-N double bonds than single bonds in organic N-N compounds, as exemplified by azobenzene [$d(N=N)$: 1.247(2) Å] (28) and 1,2-diphenylhydrazine [$d(N-N)$: 1.394(7) Å] (29), respectively. However, the B1-N1-N2-B2 torsion angle [113.3(4) $^\circ$] is not consistent with double bonding between two sp^2 -hybridized nitrogen atoms. In contrast to 5, dinuclear TM complexes of N_2 predominantly contain linear MNMN axes (6–14), as the metals’ d orbitals allow overlap with the two orthogonal π orbitals of N_2 . Despite the nonlinear B-N-N-B unit in 5, the solid-state structure suggests that the B-N bonding in 5

¹Institute for Inorganic Chemistry, Julius-Maximilians-Universität Würzburg, Am Hubland, 97074 Würzburg, Germany.

²Institute for Sustainable Chemistry & Catalysis with Boron, Julius-Maximilians-Universität Würzburg, Am Hubland, 97074 Würzburg, Germany.

³Institute for Physical and Theoretical Chemistry, Julius-Maximilians-Universität Würzburg, Emil-Fischer-Strasse 42, 97074 Würzburg, Germany.

*Corresponding author. Email: h.braunschweig@uni-wuerzburg.de

resembles that of a TM-like (N_2 -to-M σ -donation and M-to- N_2 π -backbonding) coordination complex of N_2 rather than that of organic azo (i.e., C=N=N-C), hydrazido [C-N(H)-N(H)-C], or diimido (C=N-N=C) compounds. This is hinted at by the short B-C^{carbene} bonds [B1-C1: 1.528(5) Å; B2-C2: 1.541(4) Å], which suggest that the boron atoms have monovalent borylene character, to which the N_2 unit acts as a Lewis σ -donor and π -acceptor. Indeed, the formal boron-centered lone pairs of electrons appear to be delocalized between both the N_2 and CAAC ligands in π -backbonding interactions that are plausibly the key to the stability of the complex (22, 23). Metal-to- N_2

π -backdonation is also known to be an important factor in many transition-metal complexes of N_2 and to contribute to the weakening of the N_2 bond, critical for its functionalization (6–14). Accordingly, **5** is structurally similar to **3** but features slightly longer B-C^{carbene} bonds [**3**: 1.499(2) Å], suggesting that the N_2 fragment in **5** accepts a higher degree of backbonding from boron than does CO in **3**, thus decreasing the B-to-CAAC backdonation. The strong B-to- N_2 backbonding can also explain the long N-N bond in **5** when compared to many bridging, end-on-bound metal-dinitrogen complexes (14). The bend in the structure of **5** is not unexpected, however, as the

geometries of the suitable backbonding orbitals are different in the case of boron (p) than for TMs (d). Density functional theory (DFT) calculations (fig. S1 and table S1) accurately reproduced the solid-state geometry of **5** and allowed us to study the orbitals involved in the borylene- N_2 bonding. Kohn-Sham orbital analysis of this structure showed that the HOMO-1 consists of a combination of one of the N-N(π^*) orbitals, the boron p and the C-N^{carbene}(π^*) orbitals (fig. S1). This electronic pattern is typical for the sharing of boron's formal lone pair of electrons with both the CAAC and N_2 ligands. Computed Wiberg bond indices (WBIs) on this geometry are consistent

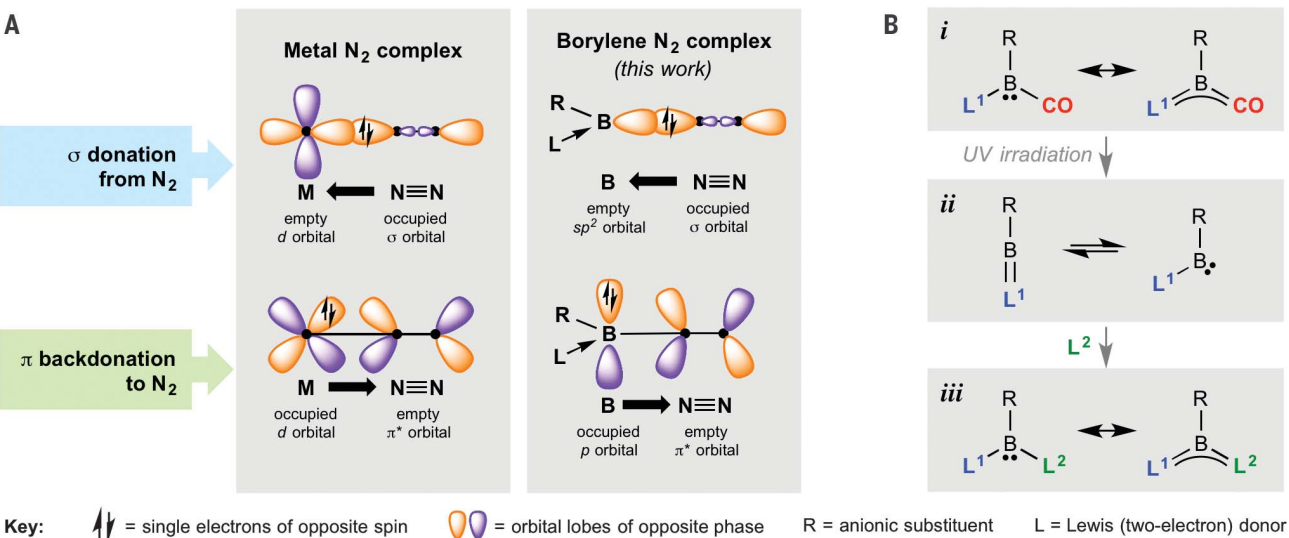


Fig. 1. Nitrogen binding motifs to transition metals and borylenes. (A) Simplified schematic of the bonding in well-known end-on-bound transition metal N_2 complexes (left) and prospective application to monovalent boron species (BRL) (right, this work). **(B)** Known photodecarbonylation and ligand

binding chemistry of tri- (*i* and *iii*) and dicoordinate (*ii*) borylene species. **(C)** Outcomes of various reduction reactions of dihaloborane adduct **1**, including generation of a transient dicoordinate borylene species (**2**) and its reaction with dinitrogen. Dip, 2,6-diisopropylphenyl; Dur, 2,3,5,6-tetramethylphenyl.

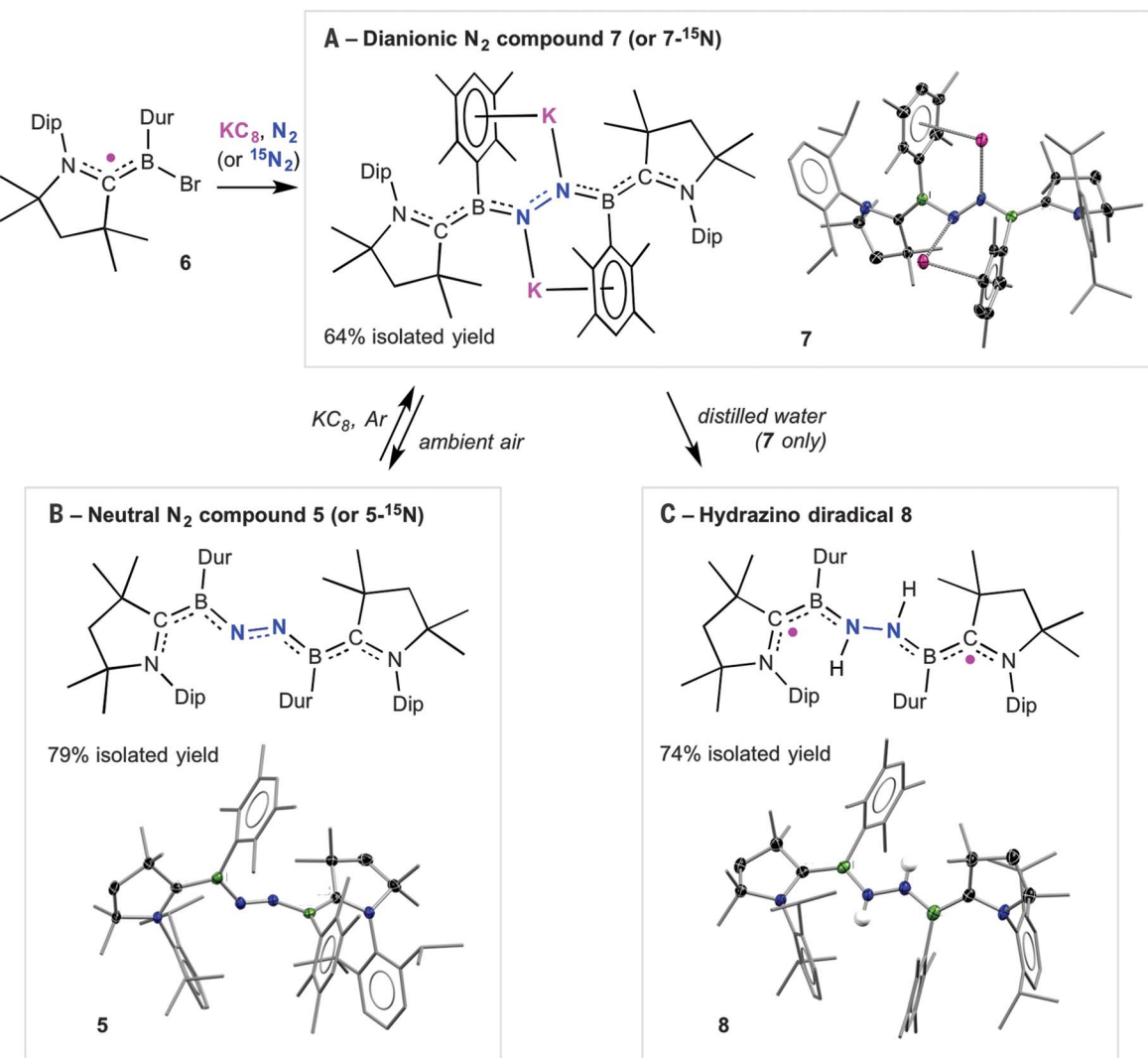


Fig. 2. Optimized syntheses and crystallographic characterization of borylene dinitrogen compounds. (A) Reduction of radical **6** to form dipotassium complex **7**. **(B)** Synthesis of **5** via reversible oxidation of **7** in

air. **(C)** Product (**8**) of the protonation of **7** in water. All ellipsoids are shown at the 50% probability level. Hydrogen atoms (except the nitrogen-bound hydrogens of **8**) and peripheral ellipsoids have been removed for clarity.

with strong B-N and N-N bonds with multiple-bond character (N1-N2: 1.51; B1-N1: 1.14; B2-N2: 1.30) (see table S1 for comparison with model compounds).

As evidenced by 1H NMR spectroscopy, **5** exists in solution as a mixture of two conformers that interconvert rapidly at room temperature (fig. S21). At $-38^\circ C$, the exchange is slow enough to allow the acquisition of well-resolved spectra (fig. S22). These show that both conformers are unsymmetrical, similar to the solid-state structure, with two distinct sets of CAAC and duryl resonances for each conformer. Unfortunately, however, the dinitrogen compound **5** could not be reproducibly separated from the borylene C-H activation product **4** owing to the low yield of **5** and the very similar solubilities of the compounds.

Given this complication, and the need for two borylene fragments to bind the dinitrogen in **5**, we reasoned that maximizing the concentration

of the borylene **2** in the reaction solution might lead to better selectivity to **5** and its isolation. We therefore sought to use the one-electron reduction product of **1**, the captodatively stabilized radical $[(CAAC)BBrDur]$ (**6**, Fig. 1C), as an advanced intermediate to rapidly generate borylene **2** by a simple one-electron reduction step. Radical **6**, the bromide analog of previously published radical $[(CAAC)BClDur]$ (30), was thus prepared and isolated by reduction of **1** with a 1.5-fold excess of KC_8 under argon (Fig. 1C; see supplementary materials for details). Subsequently, solid **6** was treated with 10 equivalents of KC_8 in toluene at $-80^\circ C$ under dinitrogen, and the solution turned an intense fuchsia, indicating the formation of **5**. The flask was then placed under 4 atm of dinitrogen and with stirring warmed to room temperature over ~ 20 min, during which time the initial fuchsia color gave way to deep blue. After 4 hours of reaction, a dark blue, highly sem-

sitive solid was isolated in good yield (64%) from this mixture and ascertained to be the dipotassium complex $\{[(CAAC)DurB]_2(\mu^2-N_2K_2)\}$ (**7**, Fig. 2), a product of two-electron reduction of dinitrogen compound **5**. Conveniently, in contrast to **5**, **7** can be separated from the side-product **4** and its presumed overreduction decomposition products by washing the solid with cold pentane. Complex **7** shows a ^{11}B NMR signal at δ_B 31.2 ppm, substantially downfield from that of neutral dinitrogen complex **5** (δ_B 10.7 ppm). Both solution-state 1H NMR spectroscopy and x-ray crystallography (Fig. 2) showed that **7** is a symmetrical species, in contrast to **5**. The solid-state structure of dipotassium compound **7** shows notably shorter B-C^{carbene} bonds [**7**: 1.470(4) Å] and longer B-N bonds [**7**: 1.484(4) Å] than neutral **5**. This is consistent with increased B-to-CAAC backbonding resulting from a lesser degree of B-to-N backbonding, to be expected with the population of

orbitals of the N_2 fragment concomitant with its reduction. The N-N bond is also slightly (4.5%) longer in **7** [1.304(3) Å] than in **5**. A similar, but smaller, difference was observed by Holland and co-workers between a (LFe=N=N=FeL) complex and its reduced dipotassium congener, the latter having a 2.8% longer N-N bond (37). Calculations indicate that the strength of the B-CAAC and B-N bonds mirrors the structural changes from **5** to **7** (WBI: B1-C1 = B2-C2 = 1.42; B1-N1 = B2-N2 = 0.87). The strength of the N-N bond, by contrast, does not change substantially (WBI: 1.65) and remains in the range of the strength for double bonds. The natural charges of the nitrogen atoms, however, become more negative from **5** (-0.358, -0.362) to **7** (-0.485), reflective of the reduction of the dinitrogen fragment. Similar negative charges appear on the C^{CAAC} atom of **7**, consistent with a rerouting of the boron backbonding from the N_2 fragment to the CAAC ligand. Although **7** can be reliably and reproducibly isolated, it decomposes rapidly when exposed to air, moisture, or protic compounds, especially when in solution.

Although we could not isolate pure samples of neutral dinitrogen compound **5** from the reduction of radical **6** under N_2 as it rapidly converts to **7**, we were gratified to observe that the product dipotassium complex **7** can be readily oxidized by ambient air to provide pure **5** in good yield (79%) as deep purple crystals (Fig. 2B). Compound **5** can also be quantitatively reduced back to its dipotassium complex **7** by treatment with KC_8 under argon. Alternatively, treating the dipotassium complex **7** with distilled water led to a turquoise solution showing no ^{11}B NMR signal, from which a turquoise solid was isolated in 74% yield. This compound was shown by single-crystal x-ray diffraction, electron paramagnetic resonance (EPR) spectroscopy, high-resolution mass spectrometry, and infrared spectroscopy (N-H band at $\nu = 3403 \text{ cm}^{-1}$; see Fig. 2C and figs. S35 to S37) to be the paramagnetic diradical diborohydrazine compound $\{[(\text{CAAC})\text{DurB}]_2(\mu^2\text{-N}_2\text{H}_2)\}$ (**8**, Fig. 2C, bottom). The EPR spectrum of a powder sample of **8** at 290 K (fig. S35) shows the typical signature of a triplet state, with a half-field signal at about $g = 4$ and zero-field splitting parameters of $|D/\hbar c| = 0.021 \text{ cm}^{-1}$ and $|E/\hbar c| = 0.00083 \text{ cm}^{-1}$. The solid-state structure of **8** also supports its description as a hydrazine complex. With a N-N bond length of 1.402(2) Å, **8** is the only compound of our series to bear a distinct N-N single bond. The B-N distances [1.435(4) and 1.417(4) Å] are in the range of double bonds, which explains the planar geometry of the N atoms and indicates that their nonbonding electron pairs

are donated to boron. Mirroring the conversion of the dinitrogen moiety to a hydrazido fragment, the computed WBI for the N-N is also the smallest of the series (1.13), which is consistent with the assignment of a single bond and similar to the parent hydrazine and diphenylhydrazine calculated as model compounds (1.04 and 1.02, respectively). The N atomic charges are also the most negative of the series (-0.581, -0.572). That hydrazino compound **8** is a diradical is unsurprising, given that stable radicals of the form $[(\text{CAAC})\text{BR}_2]^{\bullet}$ are known, of which the aforementioned radical **6** is an example (30).

As a final confirmation that the products reported herein arise from the fixation of dinitrogen, we prepared the ^{15}N isotopologues of the diamagnetic species **5** and **7** and characterized them by ^{15}N NMR spectroscopy. Dipotassium complex **7-¹⁵N** was synthesized in a similar manner to **7** by the reduction of **6** with ~10 equivalents of KC_8 under an atmosphere of $^{15}\text{N}_2$ (98% isotopic purity) and was isolated in 40% yield as a blue solid showing analogous ^{11}B and ^1H NMR spectra to **7**, and a broad singlet at 235 ppm in its ^{15}N NMR spectrum (fig. S42). High-resolution mass spectroscopy (HRMS) allowed determination of the exact empirical formula of **7-¹⁵N**, showing a molecular ion signal and isotopic distribution corresponding to replacement of two K^+ ions with H^+ ions (as also observed in the HRMS of its ^{14}N isotopologue **7**) and full ^{15}N enrichment (fig. S43). A C_6D_6 solution of **7-¹⁵N** was subsequently exposed to ambient air directly in the NMR tube to give quantitative conversion to **5-¹⁵N** as confirmed by ^{11}B and ^1H NMR and HRMS (fig. S47). Analogous to **5**, **5-¹⁵N** appears to be present in solution as a pair of unsymmetrical conformers. Consequently, its ^{15}N NMR spectrum of **5-¹⁵N** displayed four broad signals at $\delta = 58.8, 52.7, 46.7$, and 42.6 (fig. S46).

These results provide an important bridgehead for dinitrogen activation with elements of the p block, having the potential to lead to a range of nitrogen-containing molecules with exciting applications.

REFERENCES AND NOTES

- B. K. Burgess, D. J. Lowe, *Chem. Rev.* **96**, 2983–3012 (1996).
- B. M. Hoffman, D. Lukyanov, Z.-Y. Yang, D. R. Dean, L. C. Seefeldt, *Chem. Rev.* **114**, 4041–4062 (2014).
- Catalytic Ammonia Synthesis—Fundamentals and Practice, J. R. Jennings, Ed. (Springer Science+Business Media, New York, 1991).
- R. Schlögl, *Ammonia Synthesis*, in *Handbook of Homogeneous Catalysis*, G. Ertl, H. Knözinger, F. Schüth, J. Weitkamp, Eds. (Wiley, 2008).
- A. D. Allen, C. V. Senoff, *J. Chem. Soc. Chem. Commun.* 621–622 (1965).
- M. Hidai, Y. Mizobe, *Chem. Rev.* **95**, 1115–1133 (1995).
- B. A. MacKay, M. D. Fryzuk, *Chem. Rev.* **104**, 385–402 (2004).
- R. R. Schrock, *Acc. Chem. Res.* **38**, 955–962 (2005).
- N. Hazari, *Chem. Soc. Rev.* **39**, 4044–4056 (2010).
- M. D. Fryzuk, *Chem. Commun. (Camb.)* **49**, 4866–4868 (2013).
- H. Tanaka, Y. Nishibayashi, K. Yoshizawa, *Acc. Chem. Res.* **49**, 987–995 (2016).
- R. J. Burford, A. Yeo, M. D. Fryzuk, *Coord. Chem. Rev.* **334**, 84–99 (2017).
- G. P. Connor, P. L. Holland, *Catal. Today* **286**, 21–40 (2017).
- R. J. Burford, M. D. Fryzuk, *Nat. Rev. Chem.* **1**, 0026 (2017).
- G. Maier, H. P. Reisenauer, J. Henkelmann, C. Kliche, *Angew. Chem. Int. Ed.* **100**, 303 (1988).
- J. Jin *et al.*, *Angew. Chem. Int. Ed.* **55**, 2078–2082 (2016).
- M. Winkler, W. Sander, *J. Org. Chem.* **71**, 6357–6367 (2006).
- K. Edel, M. Krieg, D. Grote, H. F. Bettinger, *J. Am. Chem. Soc.* **139**, 15151–15159 (2017).
- N. N. Greenwood, *Chemistry of the Elements* (Butterworth-Heinemann, ed. 2, 1997).
- P. P. Power, *Nature* **463**, 171–177 (2010).
- D. Martin, M. Soleilhavoup, G. Bertrand, *Chem. Sci.* **2**, 389–399 (2011).
- R. Kirjo, B. Donnadieu, M. A. Celik, G. Frenking, G. Bertrand, *Science* **333**, 610–613 (2011).
- M. Soleilhavoup, G. Bertrand, *Angew. Chem. Int. Ed.* **56**, 10282–10292 (2017).
- F. Dahche, D. Martin, D. W. Stephan, G. Bertrand, *Angew. Chem. Int. Ed.* **53**, 13159–13163 (2014).
- H. Braunschweig *et al.*, *Nature* **522**, 327–330 (2015).
- H. Braunschweig *et al.*, *J. Am. Chem. Soc.* **139**, 1802–1805 (2017).
- K.-A. Østby, G. Gundersen, A. Haaland, H. Nøth, *Dalton Trans.* (13): 2284–2291 (2005).
- J. A. Bouwstra, A. Schouten, J. Kroon, *Acta Crystallogr. C* **39**, 1121–1123 (1983).
- D. C. Pestana, P. P. Power, *Inorg. Chem.* **30**, 528–535 (1991).
- P. Bissinger *et al.*, *Angew. Chem. Int. Ed.* **53**, 7360–7363 (2014).
- S. F. McWilliams *et al.*, *Inorg. Chem.* **55**, 2960–2968 (2016).

ACKNOWLEDGMENTS

This work was financially supported by the Deutsche Forschungsgemeinschaft under its Research Grants program (H.B.) and Research Training Group GRK2112 - Molecular Biradicals: Structure, Properties and Reactivity (B.E.). M.-A.L. thanks the National Sciences and Engineering Research Council of Canada for a postdoctoral fellowship. G.B.-C. thanks the Alexander von Humboldt Foundation for a postdoctoral fellowship. We thank R. Berermann for NMR experiments, K. Radacki for crystallographic insight, and C. Mahler for mass spectrometry. X-ray data are available free of charge from the Cambridge Crystallographic Data Centre under reference CCDC-1578524 (**5**), -1578525 (**1**), -1578526 (**8**), -1578527 (**6**), and -1578528 (**7**). Further spectroscopic, crystallographic, and computational data are included in the supplementary materials.

SUPPLEMENTARY MATERIALS

www.science.org/content/359/6378/896/suppl/DC1
Materials and Methods
Figs. S1 to S54
Tables S1 and S2
References (32–50)

9 October 2017; accepted 12 December 2017
10.1126/science.aao1684

PALEOCEANOGRAPHY

Breakup of last glacial deep stratification in the South Pacific

Chandranath Basak,^{1*}†‡ Henning Fröllje,^{1,2}‡ Frank Lamy,³ Rainer Gersonde,³ Verena Benz,³ Robert F. Anderson,⁴ Mario Molina-Kescher,⁵ Katharina Pahnke¹

Stratification of the deep Southern Ocean during the Last Glacial Maximum is thought to have facilitated carbon storage and subsequent release during the deglaciation as stratification broke down, contributing to atmospheric CO₂ rise. Here, we present neodymium isotope evidence from deep to abyssal waters in the South Pacific that confirms stratification of the deepwater column during the Last Glacial Maximum. The results indicate a glacial northward expansion of Ross Sea Bottom Water and a Southern Hemisphere climate trigger for the deglacial breakup of deep stratification. It highlights the important role of abyssal waters in sustaining a deep glacial carbon reservoir and Southern Hemisphere climate change as a prerequisite for the destabilization of the water column and hence the deglacial release of sequestered CO₂ through upwelling.

The Southern Ocean (SO) has long been recognized as a key player in regulating atmospheric CO₂ variations and hence global climate based on the tight coupling between Southern Hemisphere (SH) temperatures and atmospheric CO₂ concentrations (1). Nevertheless, the mechanisms involved are not fully understood. The most promising explanation includes changes of the biological pump and its interaction with ocean circulation in the SO, where CO₂ sequestration and release occur because of the production of new and upwelling of old deep waters (2–4). The SO therefore acts as a component of ocean-atmosphere interactions that is sensitive to changes in climate and the stability of the water column. Evidence exists for a stratified deep SO during the Last Glacial Maximum (LGM) (5, 6), which led to diminished gas exchange as compared with that of today and the presence of radiocarbon-depleted deep waters in the South Pacific (7) overlying better ventilated bottom waters (7–9). With the onset of SH warming during the last deglaciation, which was approximately coincident with Heinrich Stadial 1 (HS1), the SO water column became destratified and well mixed, releasing sequestered CO₂ to the atmosphere and contributing to the deglacial atmospheric CO₂ rise (4–7). The proposed destratification mechanisms include southward-shifting westerlies and enhanced upwelling (5),

as well as sea ice retreat, associated buoyancy flux changes, and increased mixing of northern and southern-sourced waters (10). Here, we show evidence for a sharp geochemical boundary between deep and bottom waters in the Pacific sector of the SO during the LGM. This deep stratification is defined by distinct neodymium (Nd) isotope signatures of the deep and abyssal waters during the LGM, in contrast to a homogeneous Nd isotopic composition of the deep to abyssal South Pacific today (11). We further suggest a role for SH climate in triggering the breakup of deep stratification, thus setting the stage for upwelling and release of sequestered carbon.

We used Nd isotopes (¹⁴³Nd/¹⁴⁴Nd, expressed as ε_{Nd}) from fossil fish teeth and debris and

planktic foraminifera from deep (3000 to 4000 m) to abyssal (>4000 m) water depths in the South Pacific in order to reconstruct the history of the deepwater column structure over the past 30,000 years (Fig. 1 and supplementary materials). The ε_{Nd} signature of modern Circumpolar Deep Water (CDW) (ε_{Nd} = -8 to -9) (12, 13) is largely determined by mixing between North Atlantic Deep Water (NADW) with ε_{Nd} = -13.5 near its source (13) and North Pacific Deep Water (NPDW) with ε_{Nd} = -3.5 (14), with additional contributions from Antarctic Bottom Water (AABW) with ε_{Nd} = -9 and -7 in the South Atlantic (12) and the South Pacific (11), respectively. It is well documented that end-member ε_{Nd} signatures of NPDW and NADW remained constant at least for the past 2 million years (15). Ross Sea Bottom Water (RSBW) acquires its ε_{Nd} from Antarctic shelf sediments. Because the Ross Sea shelf receives its sediments through glacier transport, a substantial change in the shelf sediment lithology would require a change in provenance and/or flow direction of the glaciers. Thus, we assume that the RSBW end member remained constant and that the observed seawater changes are related to water mass mixing. Previous studies suggest that glacial-interglacial and shorter-term ε_{Nd} changes of South Atlantic deep water were controlled by changes in NADW export (16–18). We present evidence from South Pacific deep (E11-2, PS75/073-2, PS75/056-1, and PS75/059-2; 3109 to 3613 m water depth) and abyssal (PS75/054-1; 4085 m water depth) (Fig. 1 and table S1) sediment cores that indicates instead a strong additional SH climate control on the development of the SO deepwater structure and ε_{Nd} composition over the past 30,000 years.

All cores have independent age models based on tuning benthic or planktic δ¹⁸O records to the

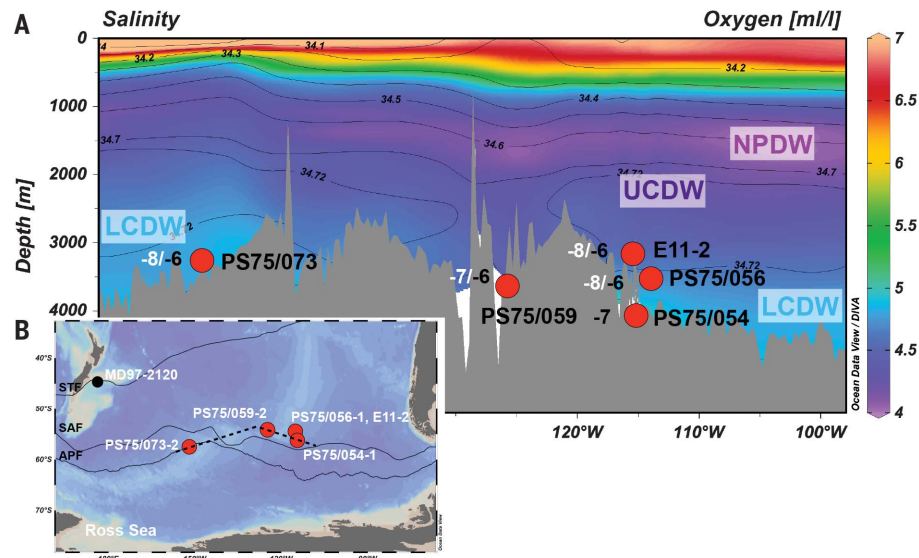
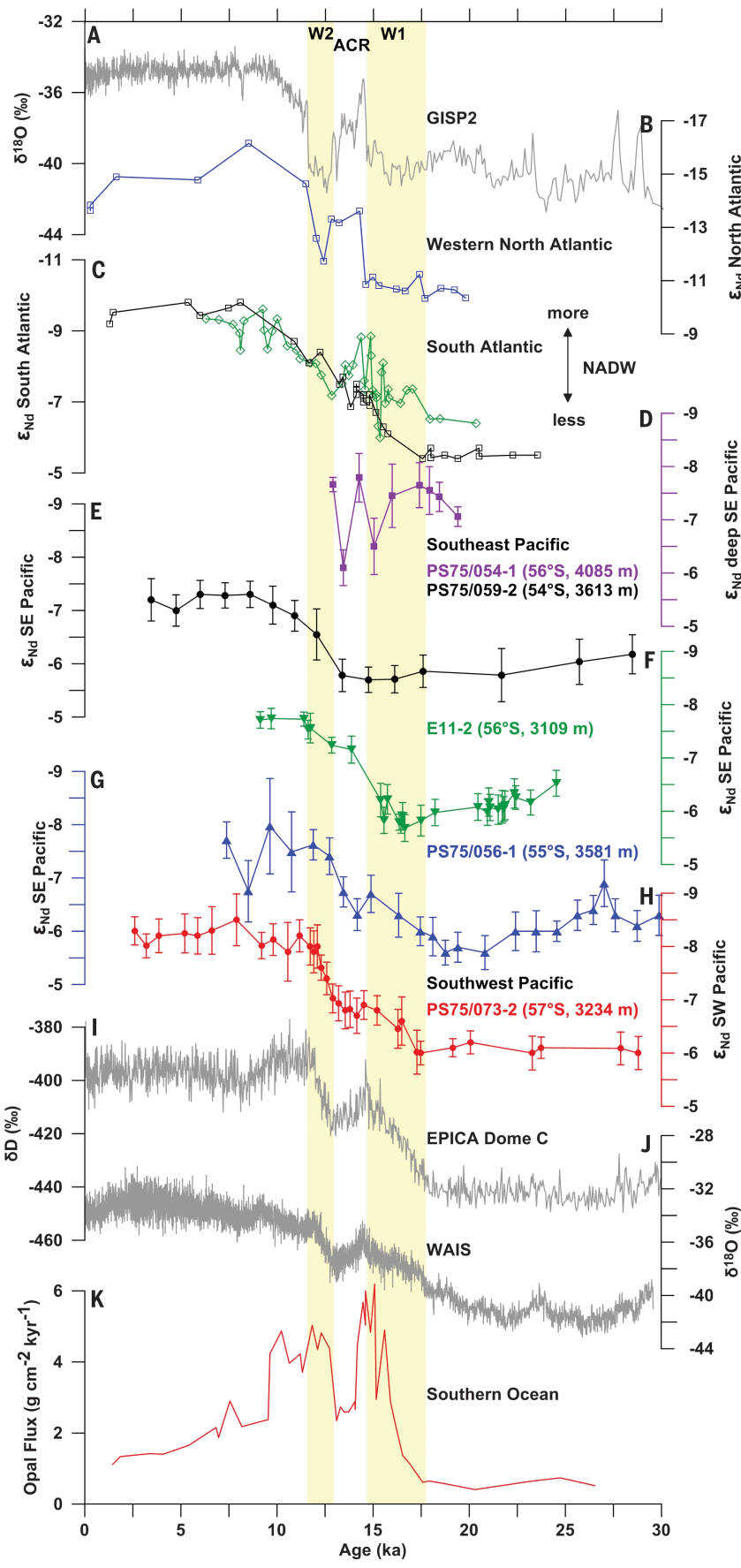


Fig. 1. Modern hydrography and core locations in the South Pacific. (A) Zonal section [along stippled line in (B)] of dissolved oxygen (color) (45) and salinity (contours) (46), with depth locations of studied cores, major deepwater masses, and modern (white) and LGM (black) ε_{Nd} values at each core site. (B) Core locations, including reference core MD97-2120, and major Antarctic fronts (47). APF, Antarctic Polar Front; SAF, Subantarctic Front; STF, Subtropical Front.

well-dated core MD97-2120 (19, 20), except for PS75/054-1, which is tied to PS75/056-1 by using x-ray fluorescence rubidium scans in both cores, a proxy for dust content (supplementary materials). The cores cover the depth range of modern lower to upper CDW (L/UCDW) and are therefore ideal for monitoring the deglacial evolution of the deep South Pacific water column structure (Fig. 1 and supplementary materials). Nd isotopes show late Holocene core-top values of -8.3 (PS75/073-2) and -7.2 to -7.7 (PS75/059-2, PS75/056-1, and E11-2), which is consistent with modern CDW, with slightly different contributions from NPDW and NADW related to the difference in depth and latitudinal position of the cores (Fig. 1 and fig. S3) (21). The deepest core (PS75/054-1) lacks Late Holocene sediments, but modern hydrography at the core site indicates the presence of LCDW (Fig. 1A and supplementary materials). This core is currently located close to the boundary of LCDW and RSBW (the South Pacific contribution to AABW). Considering that the temporal resolution of the core is low after HS1, with the observed changes only supported by individual data points, we restrict our discussion related to this core to the LGM and HS1.

During the LGM, the average ε_{Nd} at the deep sites was consistently at ~ -6 (Figs. 1A and 2, E to H), suggesting that one homogeneous water mass occupied the deep South Pacific. By contrast, at abyssal depth, a more negative ε_{Nd} of -7.5 ± 0.2 ($n = 5$) prevailed throughout the LGM and early deglaciation, suggesting reduced mixing between deep and abyssal waters and a northward expansion of RSBW ($\varepsilon_{\text{Nd}} = -7$) (Figs. 1A and 2D) (21). The deglaciation in the deep cores (PS75/056-1 and PS75/073-2) was marked by an ε_{Nd} decrease that started at the beginning of the first SH warming (W1) at ~ 18.8 and ~ 17.3 thousand years ago (ka ago), respectively (Fig. 3), which is coincident with HS1 in the Northern Hemisphere (NH) (Figs. 2 and 3) (21). A brief halt in the ε_{Nd} decrease in these cores occurred during the Antarctic Cold Reversal (ACR), and a second ε_{Nd} decrease was synchronous with the second SH warming starting at ~ 12.8 ka ago (W2) (Fig. 2). In the northernmost core PS75/059-2, LGM ε_{Nd} values of ~ -6 persisted until at least 13.4 ka ago, followed by an ε_{Nd} decrease

Fig. 2. Evolution of the SO water column structure, NADW formation, and climate over the past 30,000 years. (A) Greenland ice core $\delta^{18}\text{O}$ (48). (B) ε_{Nd} of western North Atlantic core GGC6 (22). (C) ε_{Nd} of South Atlantic cores RC11-83 (16) and MD07-3076 (17). (D to H) Fish teeth and planktic foraminifera ε_{Nd} of South Pacific cores (this study). Vertical error bars are propagated errors (supplementary materials). (I) European Project for Ice Coring in Antarctica (EPICA) Dome C ice core δD (49, 50). (J) West Antarctic Ice Sheet (WAIS) ice core $\delta^{18}\text{O}$ (51). (K) Opal fluxes from the South Atlantic (core TN057-13PC) representing SO upwelling (5). SH warming episodes W1 and W2 [after (21)] roughly correspond to NH cold phases HS1 and Younger Dryas.



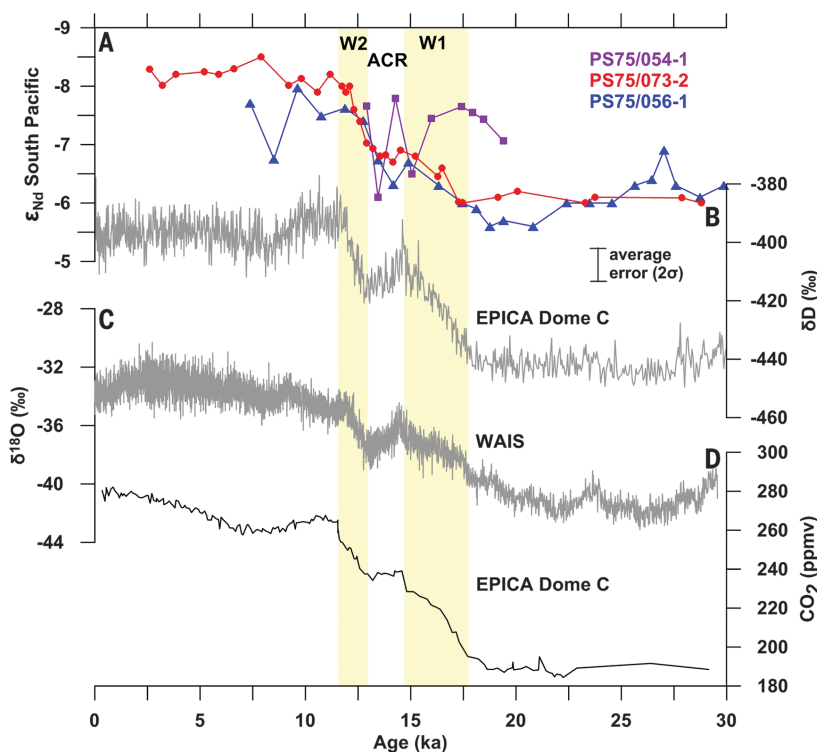


Fig. 3. Comparison of South Pacific ϵ_{Nd} time series and Antarctic climate over the past 30,000 years. (A) Downcore ϵ_{Nd} records from deep South Pacific cores. (B) EPICA Dome C ice core δD (49, 50). (C) $\delta^{18}\text{O}$ record of WAIS ice core (51). (D) Atmospheric CO_2 concentrations from EPICA Dome C ice core (49, 50, 52).

during W2 that coincided with the second ϵ_{Nd} decrease in the other cores. This difference in timing is real and cannot be explained by age model uncertainties (supplementary materials). Similarly, the first ϵ_{Nd} decrease in core E11-2 started at mid-W1, with some delay relative to the deeper cores; the difference in timing is, however, close to the age model uncertainty.

The homogeneous LGM deepwater ϵ_{Nd} of ~ 6 in the South Pacific is in line with a reduced incorporation of unradiogenic NADW into SO water masses. This may be explained by reduced formation and southward export of NADW during the LGM (22, 23). In addition, despite continuous formation of North Atlantic Component Water (NACW) (24, 25), a decoupling of the upper (northern sourced) and lower (southern sourced) circulation cells in the Atlantic during the LGM (10) would also have prevented an incorporation of the North Atlantic signal into the SO. The slightly more radiogenic glacial ϵ_{Nd} in the South Pacific ($\epsilon_{\text{Nd}} = -6$) relative to the South Atlantic ($\epsilon_{\text{Nd}} = -6.5$ to -7.3) (16, 18) results from the higher influence of radiogenic Pacific deep water and/or less direct influence of NADW in the Pacific. The most radiogenic glacial South Atlantic ϵ_{Nd} of -5.5 (17) has previously been related to higher Pacific influence in the central southwest Atlantic (24). The distinct abyssal South Pacific LGM ϵ_{Nd} of -7.5 (PS75/054) differs from glacial CDW ($\epsilon_{\text{Nd}} = -6$) and modern

NPDW ($\epsilon_{\text{Nd}} = -3.5$) (14) but is similar to modern RSBW ($\epsilon_{\text{Nd}} = -7 \pm 0.5$) (11).

Today, AABW is formed over the Antarctic shelves and spreads northward at abyssal depth. Outside the SO, abyssal water is largely represented by LCDW. For the LGM, it was suggested that AABW extended far into the North Atlantic as NADW shoaled (22, 23). That is, AABW changes have largely been explained on the basis of the dependent interplay between the upper and lower circulation cells in the Atlantic (16, 18, 22–24). The exclusive history of AABW, however, is relatively unstudied. The eastern South Pacific is located at the far end of the NADW flow path, and our cores should therefore document the history of RSBW and CDW without being masked by direct influence of fluctuating NADW contributions. Moreover, NPDW formation can be considered constant during both the LGM and the Holocene, although there are reports of increased NPDW formation during HS1 (26). Changes in NPDW can thus be excluded as a possible agent controlling South Pacific abyssal water ϵ_{Nd} during the LGM and Holocene. Our observed glacial abyssal ϵ_{Nd} of -7.5 together with the ϵ_{Nd} contrast to overlying deep waters ($\epsilon_{\text{Nd}} = -6$) therefore provide direct evidence for glacial northward expansion of RSBW and reduced mixing between the deep and bottom layer (Fig. 4). This is in line with previous suggestions of increased glacial presence of RSBW in the southwest Pacific (8)

and increased glacial formation and export of AABW into the Pacific (27).

The glacial deep stratification inferred from different ϵ_{Nd} above and below ~ 3500 to 4000 m water depth is consistent with salinity and density reconstructions that show a clear separation between very high-density bottom water at 3600 m and lower-density water at 3200 m in the SO (28, 29). This high density of SO bottom water during the LGM together with a reduced flow speed of the Antarctic Circumpolar Current (ACC) north of the Antarctic Polar Front (APF) (30) would have reduced diapycnal mixing at depths where mixing occurs today through interaction of abyssal current flow with bottom topography (31). A glacial northward expansion of extremely dense (29) RSBW and isolation from overlying deep water may have further stabilized the deep-water column in the South Pacific and hence facilitated efficient deepwater carbon storage (7, 17, 32).

The deglacial deepwater ϵ_{Nd} decrease during W1 (HS1) is a pervasive feature of SO deepwater records (Fig. 2, C and F to H) and has previously been associated with the resumption of NADW formation and incorporation of its unradiogenic ϵ_{Nd} into CDW (17, 18, 33). Yet, this initial ϵ_{Nd} decrease in all but one available record (18) from the SO predated NADW reinvigoration in the deep North Atlantic (Fig. 2) (22). That is, the observed SO-wide deglacial ϵ_{Nd} decrease cannot be explained by increased supply of unradiogenic NACW to the SO. The coincidence of the ubiquitous SO deepwater ϵ_{Nd} decrease with SH climate warming instead suggests a SH/SO control. The high density of RSBW is acquired through brine rejection during sea ice formation in cold climates. SH warming will reduce sea ice formation and thus brine rejection, leading to a decrease in bottom water density (28). A weakening of the density contrast between deep and bottom waters together with increasing ACC strength (30), and hence enhanced flow over bottom topography, would have been conducive to vertical mixing at depth (31). The resulting destratification of the deep SO would lead to the observed deepwater ϵ_{Nd} decrease, concurrent abyssal water ϵ_{Nd} increase, and trend toward a geochemically homogeneous deep to abyssal SO during mid-deglaciation as a result of upward mixing of less radiogenic RSBW/AABW (Figs. 2 and 4). The Ross and Weddell Seas are two main sites of modern AABW formation, and the bottom waters formed there have distinct ϵ_{Nd} signatures of -7 and -9 , respectively (11, 12). These distinct signatures can explain the observed differences in the deglacial ϵ_{Nd} amplitudes in the South Pacific and South Atlantic during W1 (LGM to 15 ka ago: $\sim 1 \epsilon_{\text{Nd}}$ and $\sim 2 \epsilon_{\text{Nd}}$ units, respectively) (Figs. 2C and 3) and the SO-wide early deglacial ϵ_{Nd} decrease. Additionally, increasing incorporation of NACW (or Glacial North Atlantic Intermediate Water above 2 km) (34) into SO deep waters through increased mixing between the upper (NACW-bearing) and lower [Southern Component Water (SCW)-bearing] circulation cells (10) could have also decreased

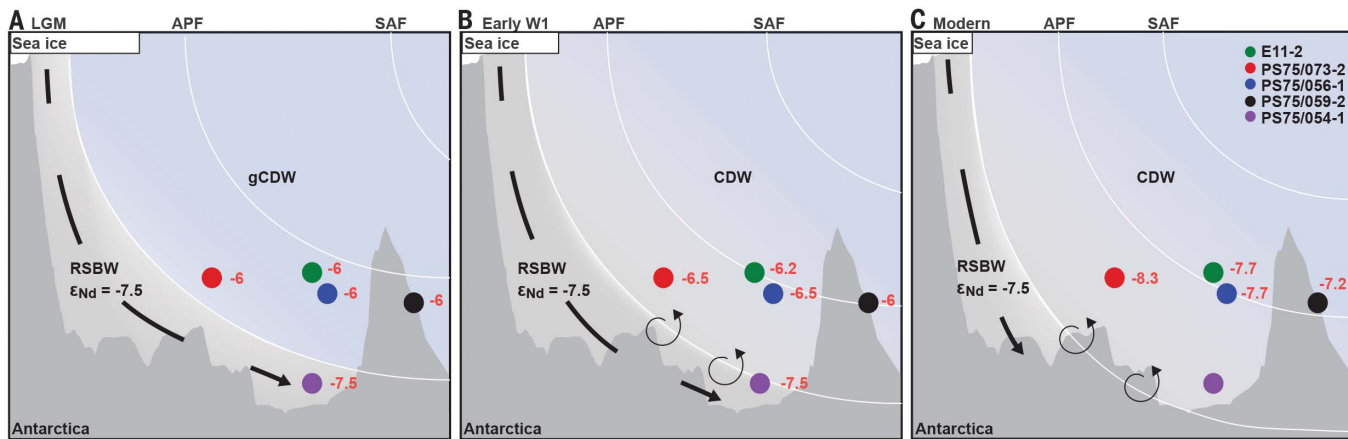


Fig. 4. Schematic illustration of the South Pacific water column structure for the LGM, deglaciation, and Holocene. (A) LGM: NADW input to SO strongly reduced/absent. RSBW ($\epsilon_{\text{Nd}} = -7.5$) extends further north than today and is isolated from overlying glacial CDW (gCDW) ($\epsilon_{\text{Nd}} = -6$). (B) Early deglacial: SO warming during W1 leads to destratification at depth and increased mixing of RSBW into CDW,

changing the CDW ϵ_{Nd} to ~ -6.5 . Atlantic contribution is still attenuated. Core PS75/059-2 is isolated from early deglacial SO processes. (C) Holocene and modern: Strengthening of the Atlantic Meridional Overturning Circulation and SO warming lead to incorporation of NADW into CDW (10), changing its ϵ_{Nd} signature to -8 . RSBW does not extend to deepest site (PS75/054-1).

the ϵ_{Nd} of CDW. However, given the physical constraint of the Drake Passage ($\sim 57^{\circ}$ to 61° S, sill depth ~ 2000 m), which prevents a meridional net geostrophic flow across this latitude band for waters shallower than the sill depth (35, 36), we consider this mechanism less important.

The delayed response to W1 in the northernmost core PS75/059-2 (at 12.1 ka ago) is robust and outside the age model uncertainty, whereas the smaller delay in the shallowest core E11-2 (change at 15.6 ka ago) is close to the age model uncertainty (supplementary materials). Under modern conditions, core PS75/059-2 exhibits stronger NPDW influence than the other core sites that are dominantly influenced by LCDW (Fig. 1) (11). The ϵ_{Nd} decrease seen in LCDW-influenced cores during W1 may hence not have affected PS75/059-2.

On the basis of reduced radiocarbon ventilation ages in the deep Cape Basin (41° S) (37) during the Bølling-Allerød (B-A; approximately at the same time as the ACR), Barker *et al.* (37) argued for strongly enhanced southward flow of NADW. A northern source of this well-ventilated water is, however, not confirmed by Nd isotope results and was instead suggested to indicate ventilation by SCW (17). Similarly, we see no evidence for increased incorporation of NACW into CDW during the ACR in the South Pacific, nor is this seen in any other independently dated SO ϵ_{Nd} record (Fig. 2) (17, 38). A change in the North Atlantic ϵ_{Nd} end member toward more radiogenic values exclusively during the B-A/ACR period that could explain the lacking ϵ_{Nd} decrease at this time is unlikely. Such an end member ϵ_{Nd} change would be at odds with existing ϵ_{Nd} records in the deep North Atlantic that show unradiogenic ϵ_{Nd} during the B-A (18, 22) along with evidence for the long-term stability of the North Atlantic ϵ_{Nd} end member (39, 40). Instead, ^{14}C -based evidence suggests that the deep North and South Atlantic were equally well ventilated during

the ACR (41), indicating that the SO cannot have been exclusively ventilated by NADW. We suggest that although the ACR was a time of active NADW formation, making it quite different from the LGM in the NH, the ACR boundary conditions in the SH were akin to glacials, albeit less pronounced. Thus, similar to glacials, NADW incorporation into the SO during the ACR would have been restricted in response to reduced mixing between the NACW and SCW cells in the Atlantic (10, 32). This may have been promoted by northward-shifted westerlies similar to those of the LGM (42) in response to southern cooling, hampering the southward pull of NADW (35). With the onset of W2, mixing between the cells increased because of SH warming and sea ice retreat (10), a southward shift of the westerlies, and resulting increase in NADW southward pull (43), leading to the final incorporation of NACW into CDW despite reduced NADW formation at this time (the Younger Dryas stadial) (22). That is, SH processes initialized the establishment of modern conditions with NACW being mixed into CDW, explaining the second ϵ_{Nd} decrease in the deep South Pacific.

Although a high-density contrast between deep and abyssal waters has been suggested on the basis of porewater chloride measurements (29), clear evidence of deep-abyssal stratification in the SO has been elusive. Our results show that RSBW expanded during the LGM, occupying the abyssal South Pacific to at least ~ 4000 m water depth, and was sharply separated from overlying deep water (Fig. 4). This may have further stabilized a stratified deep ocean, a scenario conducive to carbon accumulation in deep waters. The timing of W1 in the SH is well synchronized with deep-abyssal destratification indicated by a decrease in SO deepwater ϵ_{Nd} (trend toward ϵ_{Nd} homogenization) and also suggested on the basis of carbon isotopes (44). At the same time, a wind-

driven upwelling pulse occurred in the SO that was suggested to have released old carbon stored in the deep SO to the atmosphere (Fig. 2) (5). However, an additional prerequisite for the initial deglacial CO_2 release is the breakup of stratification in the deep-abyssal SO. Our data now provide evidence that this deep-abyssal destratification occurred in response to the initial deglacial SH warming. Thus, both deep vertical mixing and wind-driven upwelling were instrumental in the release of accumulated carbon from the deep SO to the atmosphere during Termination 1.

REFERENCES AND NOTES

1. F. Parrenin *et al.*, *Science* **339**, 1060–1063 (2013).
2. D. M. Sigman, E. A. Boyle, *Nature* **407**, 859–869 (2000).
3. D. M. Sigman, M. P. Hain, G. H. Haug, *Nature* **466**, 47–55 (2010).
4. A. Abelmann *et al.*, *Nat. Commun.* **6**, 8136 (2015).
5. R. F. Anderson *et al.*, *Science* **323**, 1443–1448 (2009).
6. A. Burke, L. F. Robinson, *Science* **335**, 557–561 (2012).
7. T. A. Ronge *et al.*, *Nat. Commun.* **7**, 11487 (2016).
8. I. N. McCave, L. Carter, I. R. Hall, *Quat. Sci. Rev.* **27**, 1886–1908 (2008).
9. E. L. Sikes, M. S. Cook, T. P. Guilderson, *Earth Planet. Sci. Lett.* **438**, 130–138 (2016).
10. R. Ferrari *et al.*, *Proc. Natl. Acad. Sci. U.S.A.* **111**, 8753–8758 (2014).
11. C. Basak, K. Pahnke, M. Frank, F. Lamy, R. Gersonne, *Earth Planet. Sci. Lett.* **419**, 211–221 (2015).
12. T. Stichel, M. Frank, J. Rickli, B. A. Haley, *Earth Planet. Sci. Lett.* **317–318**, 282–294 (2012).
13. F. Laca, C. Jeandel, *Geochim. Geophys. Geosyst.* **6**, Q12008 (2005).
14. H. Fröhliche *et al.*, *Geochim. Cosmochim. Acta* **189**, 110–131 (2016).
15. L. D. Pena, S. L. Goldstein, *Science* **345**, 318–322 (2014).
16. A. M. Piotrowski, S. L. Goldstein, S. R. Hemming, R. G. Fairbanks, *Earth Planet. Sci. Lett.* **225**, 205–220 (2004).
17. L. C. Skinner *et al.*, *Geology* **41**, 667–670 (2013).
18. J. Lippold *et al.*, *Earth Planet. Sci. Lett.* **445**, 68–78 (2016).
19. K. Pahnke, R. Zahn, H. Elderfield, M. Schulz, *Science* **301**, 948–952 (2003).
20. K. Pahnke, R. Zahn, *Science* **307**, 1741–1746 (2005).

21. G. Siani *et al.*, *Nat. Commun.* **4**, 2758 (2013).

22. N. L. Roberts, A. M. Piotrowski, J. F. McManus, L. D. Keigwin, *Science* **327**, 75–78 (2010).

23. W. B. Curry, D. W. Oppo, *Paleoceanography* **20**, PA1017 (2005).

24. J. N. W. Howe *et al.*, *Nat. Commun.* **7**, 11765 (2016).

25. L. D. Keigwin, S. A. Swift, *Proc. Natl. Acad. Sci. U.S.A.* **114**, 2831–2835 (2017).

26. J. W. B. Rae *et al.*, *Paleoceanography* **29**, 645–667 (2014).

27. I. R. Hall, I. N. McCave, N. J. Shackleton, G. P. Weedon, S. E. Harris, *Nature* **412**, 809–812 (2001).

28. J. F. Adkins, *Paleoceanography* **28**, 539–561 (2013).

29. J. F. Adkins, K. McIntyre, D. P. Schrag, *Science* **298**, 1769–1773 (2002).

30. F. Lamy *et al.*, *Proc. Natl. Acad. Sci. U.S.A.* **112**, 13496–13501 (2015).

31. M. Nikurashin, R. Ferrari, *Geophys. Res. Lett.* **40**, 3133–3137 (2013).

32. L. C. Skinner, S. Fallon, C. Waelbroeck, E. Michel, S. Barker, *Science* **328**, 1147–1151 (2010).

33. A. M. Piotrowski, S. L. Goldstein, S. R. Hemming, R. G. Fairbanks, *Science* **307**, 1933–1938 (2005).

34. J. Lynch-Stieglitz *et al.*, *Science* **316**, 66–69 (2007).

35. J. R. Toggweiler, B. Samuels, *Deep Sea Res. Part I Oceanogr. Res. Pap.* **42**, 477–500 (1995).

36. L. Talley, *Oceanography (Wash. D.C.)* **26**, 80–97 (2013).

37. S. Barker, G. Knorr, M. J. Vautravers, P. Diz, L. C. Skinner, *Nat. Geosci.* **3**, 567–571 (2010).

38. A. M. Piotrowski *et al.*, *Earth Planet. Sci. Lett.* **357–358**, 289–297 (2012).

39. T. van de Flierdt, L. F. Robinson, J. F. Adkins, S. R. Hemming, S. L. Goldstein, *Paleoceanography* **21**, PA4102 (2006).

40. G. L. Foster, D. Vance, J. Prytulak, *Geology* **35**, 37–40 (2007).

41. L. C. Skinner, C. Waelbroeck, A. E. Scrivner, S. J. Fallon, *Proc. Natl. Acad. Sci. U.S.A.* **111**, 5480–5484 (2014).

42. F. Lamy, D. Hebbeln, G. Wefer, *Quat. Res.* **51**, 83–93 (1999).

43. J. R. Toggweiler, J. L. Russell, S. R. Carlson, *Paleoceanography* **21**, PA2005 (2006).

44. E. L. Sikes, A. C. Elmore, K. A. Allen, M. S. Cook, T. P. Gilderson, *Earth Planet. Sci. Lett.* **456**, 87–97 (2016).

45. H. E. Garcia *et al.*, *World Ocean Atlas 2009*, NOAA Atlas No. NESDros. Inf. Serv. 70 (NOAA, 2010).

46. J. I. Antonov *et al.*, *World Ocean Atlas 2009*, NOAA Atlas No. NESDros. Inf. Serv. 69 (NOAA, 2010).

47. A. H. Orsi, T. Whitworth III, W. D. Nowlin Jr., *Deep Sea Res. Part I Oceanogr. Res. Pap.* **42**, 641–673 (1995).

48. P. Grootes, M. Stuiver, *J. Geophys. Res.* **102**, 26455–26470 (1997).

49. J. Jouzel *et al.*, *Science* **317**, 793–796 (2007).

50. D. Veres *et al.*, *Clim. Past* **9**, 1733–1748 (2013).

51. WAIS Divide Project Members, *Nature* **500**, 440–444 (2013).

52. E. Monnin *et al.*, *Science* **291**, 112–114 (2001).

ACKNOWLEDGMENTS

Data presented in this study are available in the supplementary materials and on Pangaea under <http://doi.pangaea.de/10.1594/PANGAEA.858969>. We thank the scientific party, captain, and crew of *R/V Polarstern* cruise ANT-XXVI/2. We thank M. Schulz and P. Böning from the Max Planck Research Group for Marine Isotope Geochemistry for help with labwork. We are grateful to J. Ullermann (Alfred Wegener Institute) for measuring benthic $\delta^{18}\text{O}$ data that we used for age model construction of cores PS75/059-2 and PS75/056-1. We also thank three anonymous reviewers for their thoughtful comments. Financial support for this study came from the National Science Foundation (NSF) under grant OCE-09-35115 to K.P., ICBM, and the Max Planck Institute for Marine Microbiology.

SUPPLEMENTARY MATERIALS

www.sciencemag.org/content/359/6378/900/suppl/DC1
 Materials and Methods
 Supplementary Text
 Figs. S1 to S5
 Tables S1 to S4
 References (53–91)

29 June 2017; accepted 10 January 2018
 10.1126/science.aoa2473

FISHERIES

Tracking the global footprint of fisheries

David A. Kroodsma,^{1*} Juan Mayorga,^{2,3} Timothy Hochberg,¹ Nathan A. Miller,⁴ Kristina Boerder,⁵ Francesco Ferretti,⁶ Alex Wilson,⁷ Bjorn Bergman,⁴ Timothy D. White,⁶ Barbara A. Block,⁶ Paul Woods,¹ Brian Sullivan,⁷ Christopher Costello,² Boris Worm⁵

Although fishing is one of the most widespread activities by which humans harvest natural resources, its global footprint is poorly understood and has never been directly quantified. We processed 22 billion automatic identification system messages and tracked >70,000 industrial fishing vessels from 2012 to 2016, creating a global dynamic footprint of fishing effort with spatial and temporal resolution two to three orders of magnitude higher than for previous data sets. Our data show that industrial fishing occurs in >55% of ocean area and has a spatial extent more than four times that of agriculture. We find that global patterns of fishing have surprisingly low sensitivity to short-term economic and environmental variation and a strong response to cultural and political events such as holidays and closures.

Agriculture, forestry, and fishing are the main activities by which humans appropriate the planet's primary production (1, 2) and reshape ecosystems worldwide (3). Recent advances in satellite-based observation have allowed high-resolution monitoring of forestry and agriculture, creating opportunities such as carbon management (4), agricultural forecasting (5), and biodiversity monitoring (6) on a global scale. In contrast, we lack a precise understanding

of the spatial and temporal footprint of fishing, limiting our ability to quantify the response of global fleets to changes in climate, policy, economics, and other drivers. Although fishing activities have been monitored for selected fleets using electronic vessel monitoring systems, logbooks, or onboard observers, these efforts have produced heterogeneous data that are neither publicly available nor global in scope. As a result, the global footprint of fishing activity, or "effort,"

could be inferred only from disaggregated catch data (7, 8).

Recent expansion of the automatic identification system (AIS) (9) presents an opportunity to fill this gap and quantify the behavior of global fleets down to individual vessels (10). Although AIS was originally designed to help prevent ship collisions by broadcasting to nearby vessels a ship's identity, position, speed, and turning angle every few seconds, these messages are also recorded by satellite- or land-based receivers. Whereas its usefulness as a tracking tool has been established locally (11–13), we use AIS to directly map global fishing activity.

We processed 22 billion global AIS positions from 2012 to 2016 and trained two convolutional neural networks (CNNs): one to identify vessel characteristics and a second to detect AIS positions indicative of fishing activity (fig. S1). The vessel characterization CNN was trained on 45,441 marine vessels (both fishing and nonfishing) that were matched to official fleet registries. The resulting model identifies six classes of fishing vessels and six classes of nonfishing vessels (tables S1 and S2) with 95% accuracy

¹Global Fishing Watch, Washington, DC 20036, USA. ²Bren School of Environmental Science and Management, University of California, Santa Barbara, CA 93106, USA.

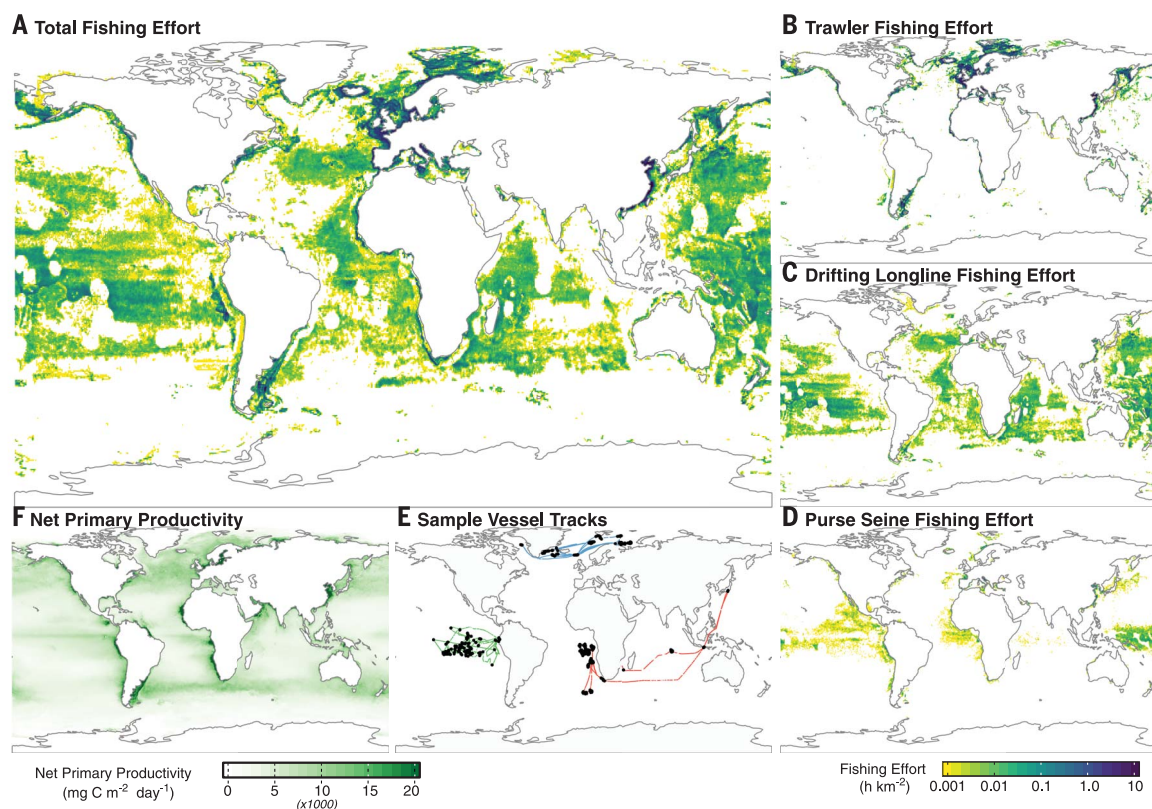
³Pristine Seas, National Geographic Society, Washington, DC 20036, USA. ⁴SkyTruth, Shepherdstown, WV 25443, USA.

⁵Department of Biology, Dalhousie University, Halifax, Nova Scotia B3H4R2, Canada. ⁶Department of Biology, Stanford University, CA 94305, USA. ⁷Google, Mountain View, CA 94043, USA.

*Corresponding author. Email: david@globalfishingwatch.org

Fig. 1. The spatial footprint of fishing.

(A to D) Total fishing effort [hours fished per square kilometer (h km^{-2})] in 2016 by all vessels with AIS systems (A), trawlers (B), drifting longliners (C), and purse seiners (D). (E) Examples of individual tracks of a trawler (blue), a longliner (red), and a purse seiner (green). Black symbols show fishing locations for these vessels, as detected by the neural network, and colored lines are AIS tracks. (F) Global patterns of average annual NPP [expressed as milligrams of carbon uptake per square meter per day ($\text{mg C m}^{-2} \text{ day}^{-1}$)] are shown for reference.



and performs well at predicting vessel length [R^2 (coefficient of determination) = 0.90], engine power ($R^2 = 0.83$), and gross tonnage ($R^2 = 0.77$) (fig. S2). The fishing detection model was trained on AIS data from 503 vessels and identified fishing activity with >90% accuracy (fig. S3 and table S3).

The resulting data set contains labeled tracks of more than 70,000 identified fishing vessels that are 6 to 146 m in length. We aggregated fishing effort by fishing hours (the time spent fishing) and by kilowatt-hours (kWh) (the estimated energy expended). This effort can be mapped at hour- and kilometer-level resolution, or two to three orders of magnitude higher than previous global maps of catch-derived effort (14, 15). Although the data set includes only a small proportion of the world's estimated 2.9 million motorized fishing vessels (16), it contains 50 to 75% of active vessels larger than 24 m (tables S4 and S5) and >75% of vessels larger than 36 m, the size at which most vessels are mandated by the International Maritime Organization to transmit AIS signals. We empirically estimate that vessels with AIS account for 50 to 70% of the total energy expended while fishing beyond 100 nautical miles from land (fig. S4). The fraction of fishing captured closer to shore varies strongly by region, largely on the basis of national AIS usage rates (tables S4 and S5). For pelagic ecosystems, we cross-referenced AIS data with effort data reported by regional fisheries management organizations (RFMOs) and found strongly positive relationships (fig. S5). Regional deviations from this relationship can help identify zones of poor satellite coverage, limited AIS usage, or potential misreporting of fishing effort to RFMOs.

Over the course of 1 year (2016), our data set captured 40 million hours of fishing activity by vessels that consumed 19 billion kWh of energy and covered a combined distance of more than 460 million km, equivalent to traveling to the Moon and back 600 times. The spatial footprint of fishing, as determined with AIS, is unevenly distributed across the globe (Fig. 1A). Global hot spots of fishing effort were seen in the northeast Atlantic (Europe) and northwest Pacific (China, Japan, and Russia) and in upwelling regions off South America and West Africa (Fig. 1A). Areas with minimal fishing effort included the Southern Ocean, parts of the northeast Pacific and central Atlantic, and the exclusive economic zones (EEZs) of many island states, forming conspicuous "holes" in the global effort map (Fig. 1A).

Dividing the ocean into an equal-area grid with 0.5° resolution at the equator, we observed fishing in 55% of cells in 2016. The total area fished is likely higher, as we did not observe some fishing effort in regions of poor satellite coverage or in EEZs with a low percentage of vessels using AIS (figs. S6 and S7 and table S6). If we generously assume that these regions are fully fished, we would calculate that 73% of the ocean was fished in 2016. There may also be some regions of the high seas with good satellite coverage where we are missing effort due to vessels not having AIS. However, given that AIS captures the

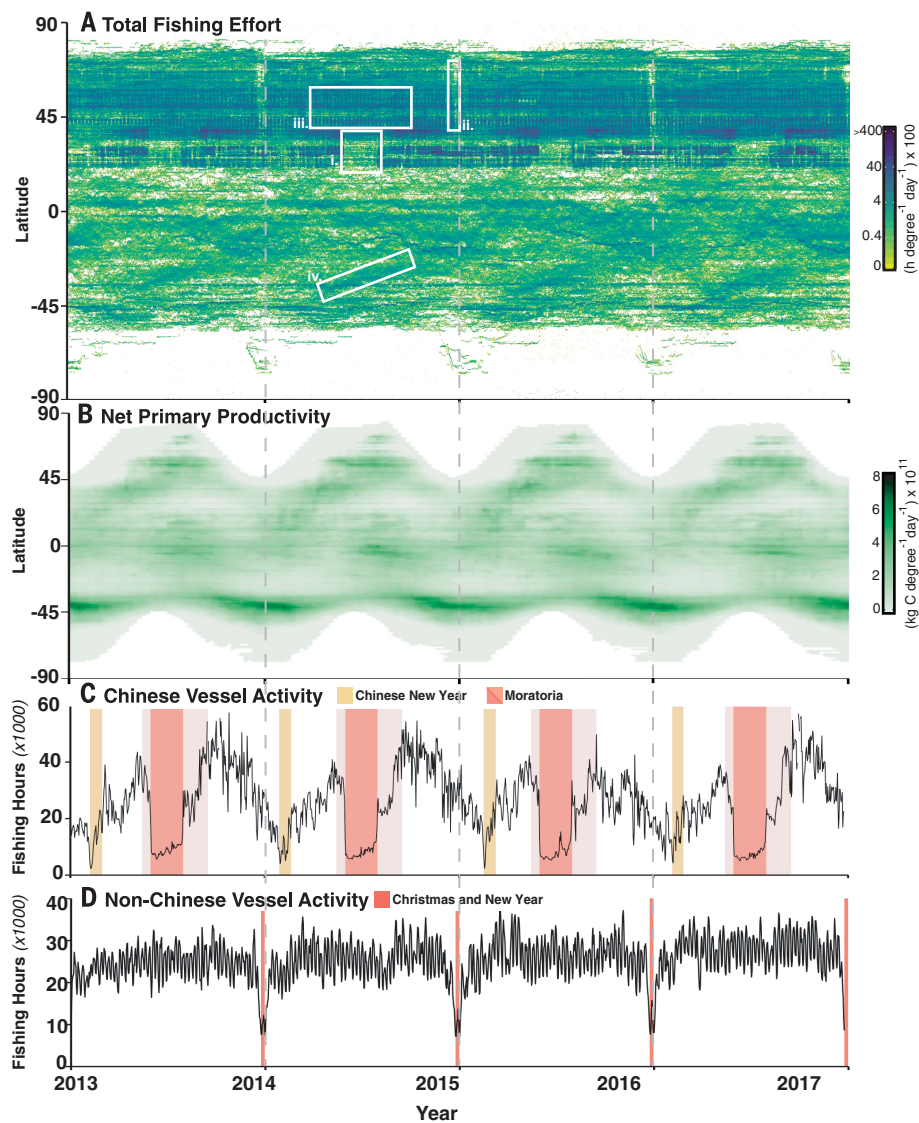


Fig. 2. The temporal footprint of fishing. Fishing hours by day and latitude (A) and seasonal patterns of marine net primary production (B). (C) Fishing hours per day for the Chinese fleet, with annual moratoria and the Chinese New Year highlighted. Light pink shading shows where some regions in the Chinese EEZ observe fishing moratoria, and dark pink shading shows where most of the Chinese EEZ is under moratorium. (D) In contrast, non-Chinese vessels show a strong weekly pattern and a drop in effort due to the Christmas holiday. Insets in (A) highlight periods of low effort around (i) annual fishing moratoria in Asian waters, (ii) Christmas in North America and Europe, and (iii) weekends, as well as (iv) a seasonal signal for longline fishing in the Southern Hemisphere (Fig. 3C).

majority of fishing effort in the high seas (fig. S4), this missing effort is unlikely to substantially affect our estimate. Previous work, based on ocean basin-scale landing data, estimated that >95% of the ocean may be fished when using a similar grid size (15). Though our estimate is lower, the percentage of the ocean fished is still much higher than the fraction of land used in agriculture or grazing (~34%) (17), covering more than 200 million km², compared with 50 million km² for agriculture.

This large spatial footprint varies by gear type and fleet. Longline fishing was the most widespread activity and was detected in 45% of

the ocean (Fig. 1B), followed by purse seining (17%) (Fig. 1C) and trawling (9.4%) (Fig. 1D). Different gear types had distinct latitudinal distributions, with trawling confined mostly to higher latitudes, purse seining concentrated in tropical regions, and longlining in between. Longliners had the greatest average trip length between anchorages (7100 km) and displayed transoceanic circumglobal movements, whereas purse seiners (average trip length, 750 km) and trawlers (average trip length, 510 km) were typically active on a more regional scale (Fig. 1E). Analyzing the spatial distribution of individual fleets, we found

that most nations fished predominantly within their own EEZ, with five flag states (China, Spain, Taiwan, Japan, and South Korea) accounting for more than 85% of observed fishing effort on the high seas (fig. S8).

The temporal footprint of fishing was surprisingly consistent through time (Fig. 2A). A large annual drop in mid-latitude effort coincides with annual fishery moratoria in China, a smaller drop at higher latitudes corresponds to the Christmas vacation in Europe and North America, and breaks in effort occur during the weekends for many Northern Hemisphere fisheries (Fig. 2A, insets). In stark contrast, temporal patterns of net primary productivity (NPP) present a seasonal “heartbeat” of biological activity (Fig. 2B) that is not

reflected by human activity at this scale (Fig. 2A). For non-Chinese vessels (Fig. 2D), the largest contributors to variations in the overall temporal footprint were the Christmas holiday and weekends, with the remaining seasonal variation explaining a small amount of the temporal footprint (fig. S9). In contrast, Chinese vessels show little weekly variation, and their yearly pattern is dominated by the Chinese New Year and the annual moratoria during the summer months (Fig. 2C). Although some fleets display seasonal movements (Fig. 3), the work week, holidays, and political closures are much more influential than natural cycles in determining the temporal footprint of fishing on a global scale. This pattern stands in stark contrast to agriculture, which is focused on

plants and nonmigratory herbivores tied to seasonal cycles of terrestrial primary production (18).

We further inspected how the spatial and temporal footprint of fishing responds to other environmental or economic drivers—namely, annual NPP, sea surface temperature (SST), and fuel prices. Annual NPP predicts fish catch from coastal ecosystems (19) but has not been analyzed as a predictor of effort across the global ocean. Using a general additive model that accounts for spatial autocorrelation, we found a highly significant but relatively weak relationship between fishing hours (Fig. 1A) and NPP (Fig. 1F) (slope = 0.58, $P < 0.001$), with only 1.7% of spatial deviance explained. This relationship was strongest for purse seiners [slope = 0.74,

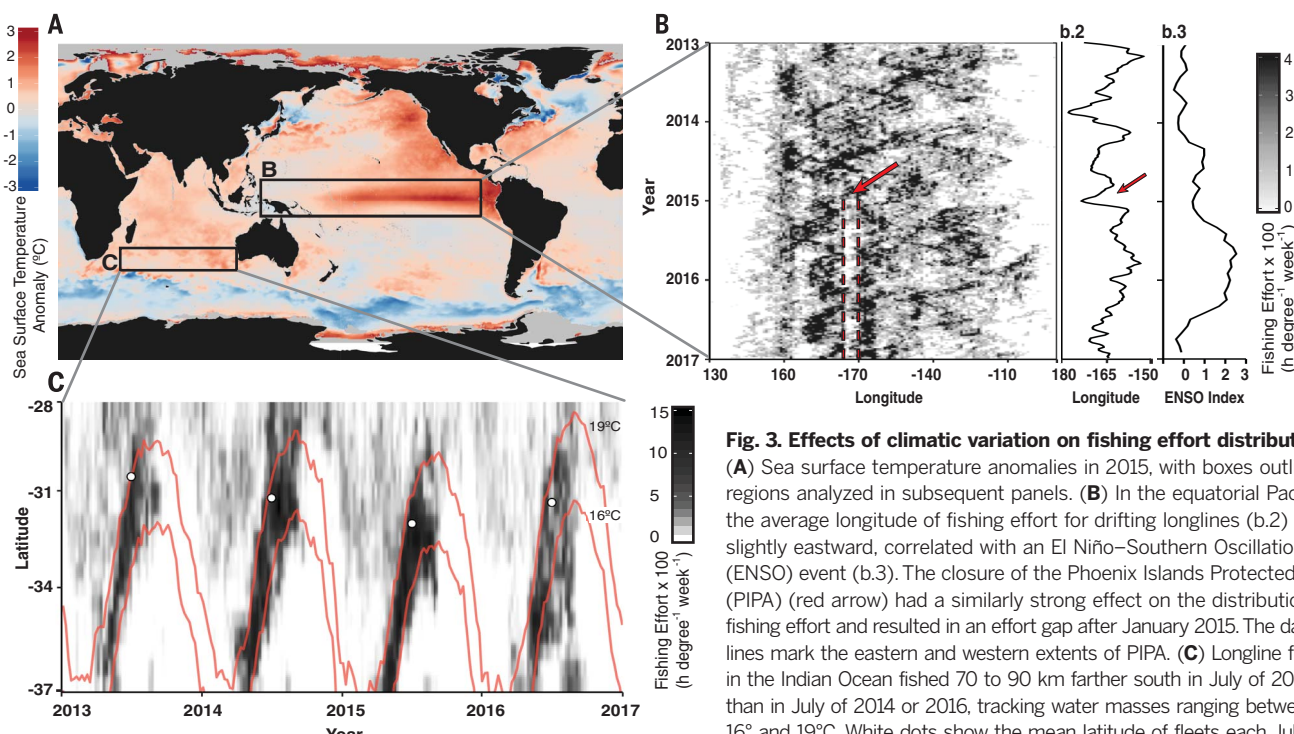


Fig. 3. Effects of climatic variation on fishing effort distribution.

(A) Sea surface temperature anomalies in 2015, with boxes outlining regions analyzed in subsequent panels. (B) In the equatorial Pacific, the average longitude of fishing effort for drifting longlines (b.2) shifts slightly eastward, correlated with an El Niño–Southern Oscillation (ENSO) event (b.3). The closure of the Phoenix Islands Protected Area (PIPA) (red arrow) had a similarly strong effect on the distribution of fishing effort and resulted in an effort gap after January 2015. The dashed lines mark the eastern and western extents of PIPA. (C) Longline fleets in the Indian Ocean fished 70 to 90 km farther south in July of 2015 than in July of 2014 or 2016, tracking water masses ranging between 16° and 19°C. White dots show the mean latitude of fleets each July.

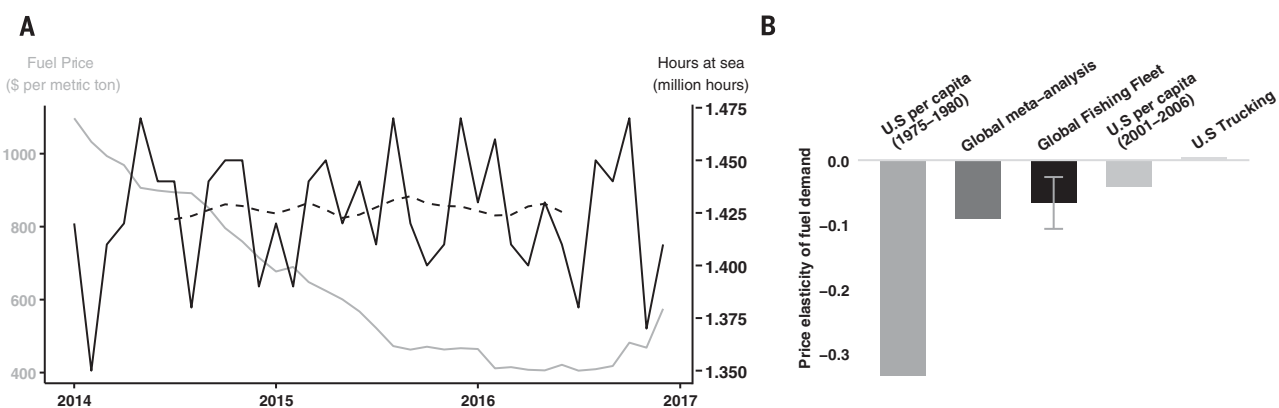


Fig. 4. Response to economic forcing. (A) Monthly averages of the global price of marine diesel oil (gray line) and total hours at sea by the global fishing fleet after removing seasonality (solid black line) reveal that a large decrease in fuel price from 2013 to 2016 corresponded to minimal change in

fishery activity (the dashed line corresponds to the trend component via additive decomposition). (B) The short-run price elasticity of fuel demand ($-0.06, P < 0.001$; error bar denotes 95% confidence interval) is comparable to those in other sectors.

$P < 0.001$, deviance explained (DE) = 2.5%] and trawlers (slope = 0.69, $P < 0.001$, DE = 2.1%), which are commonly found in highly productive coastal areas, and weakest for drifting longlines (slope = 0.37, $P < 0.001$, DE = 0.6%), which operate largely in medium- to low-productivity waters. Although these relationships may be strengthened by incorporating additional drivers and different scales, global fishing effort corresponds only loosely to NPP.

We further explored the response to elevated SST in 2015 (Fig. 3), when a positive Indian Ocean dipole mode index and an El Niño event warmed the Indian and Pacific Oceans, respectively (20). In the Indian Ocean, we found longline fishing concentrated between the 16° and 19°C isotherms [r (correlation coefficient) = 0.8 between average latitude of fishing effort and the 19°C isotherm]. Fishing effort in this region was an average of 70 to 90 km farther south in July of 2015 than in July of 2014 or 2016 (Fig. 3C). In the equatorial Pacific, previous studies have shown that regional warming during El Niño years correlates with a shift in the catch of skipjack tuna of up to 40° longitude (21). By analyzing effort across all fleets in the region, we find a more modest response. The total fleet shifts by ~3.5° per unit of the El Niño–Southern Oscillation (ENSO) index (second-order autoregression model, $P < 0.001$), with purse seiners responding more strongly than longlines. This shift corresponds to a movement of ~10° longitude of the average location of fishing effort over ~2 years (Fig. 3B, b.2). This shift, likely due to a strong El Niño, was similar in magnitude to the effect of a change in policy. When the Phoenix Islands Protected Area (PIPA) was closed to industrial fishing in 2015 (Fig. 3B), the average longitude of fishing effort moved by ~10° over a month as fleets recalibrated to new regulations (Fig. 3B, b.2).

Changes in fuel price may also drive variation in fishing effort, as fuel represents, on average, 24% of costs (22). Previous research regarding the effects of fuel price on the structure (23), economic performance (24), and behavior (25) of European fishing fleets suggests that, at a regional level, fishing fleets respond to fuel price. To measure elasticity globally, we built a monthly time series of the average price of marine diesel matched with tracking data for all fishing vessels active since 2014. The resulting sample includes 5933 vessels from 82 flag states (table S7). We found that a >50% drop in fuel price corresponded to a minimal change in fishing effort (measured as the time spent at sea) (Fig. 4 and table S8). These data suggest that the short-run price elasticity of fuel demand for the global fishing fleet is -0.061 ($P < 0.001$) (Fig. 4B), implying that a 10% increase in the price of fuel would correspond to a 0.6% decrease in global fishing activity. This elasticity is smaller than that implied by previous studies in fisheries but is comparable to those in

other commercial sectors (26–28) (Fig. 4B). It is possible that abundant fuel subsidies decouple fisheries from energy costs, masking the true price elasticity of fuel demand.

These results provide insight into the spatial and temporal footprint of global fishing fleets. Fishing vessels exhibit behavior with little natural analog, including circumglobal movement patterns and low sensitivity to energy costs or seasonal and short-term interannual oceanographic drivers. It appears that modern fishing is like other forms of mass production that are partially insulated from natural cycles and are instead shaped by policy and culture. The absolute footprint of fishing is much larger than those of other forms of food production, even though capture fisheries provide only 1.2% of global caloric production for human food consumption (29), ~34 kcal per capita per day (16). We also find that large regions of the ocean are not heavily fished, and these areas may offer opportunities for low-cost marine conservation. To further the understanding and monitoring of global fisheries, we are making daily high-resolution global rasters of effort publicly available. These data provide a powerful tool for improved global-scale ocean governance and are well positioned to help assess the effectiveness of existing management regimes while accelerating the development of novel dynamic management approaches (30) that respond in real time to changing ocean conditions, management issues, or conservation concerns.

REFERENCES AND NOTES

- H. Haberl *et al.*, *Proc. Natl. Acad. Sci. U.S.A.* **104**, 12942–12947 (2007).
- W. Swartz, E. Sala, S. Tracey, R. Watson, D. Pauly, *PLOS ONE* **5**, e15143 (2010).
- P. M. Vitousek, H. A. Mooney, J. Lubchenco, J. M. Melillo, *Science* **277**, 494–499 (1997).
- V. De Sy *et al.*, *Curr. Opin. Environ. Sustain.* **4**, 696–706 (2012).
- M. Burke, D. B. Lobell, *Proc. Natl. Acad. Sci. U.S.A.* **114**, 2189–2194 (2017).
- W. Turner *et al.*, *Trends Ecol. Evol.* **18**, 306–314 (2003).
- J. A. Anticamara, R. Watson, A. Gelchu, D. Pauly, *Fish. Res.* **107**, 131–136 (2011).
- R. A. Watson *et al.*, *Fish Fish.* **14**, 493–503 (2013).
- International Telecommunication Union (ITU), “Technical characteristics for an automatic identification system using time division multiple access in the VHF maritime mobile frequency band” (Recommendation ITU-R M.1371-5, ITU, 2014); www.itu.int/dms_pubrec/itu-r/rec/m/R-REC-M.1371-5-201402-!!PDF-E.pdf.
- D. J. McCauley *et al.*, *Science* **351**, 1148–1150 (2016).
- F. Natale, M. Gibin, A. Alessandri, M. Vespe, A. Paulrud, *PLOS ONE* **10**, e0130746 (2015).
- E. N. de Souza, K. Boerder, S. Matwin, B. Worm, *PLOS ONE* **11**, e0158248 (2016).
- T. D. White *et al.*, *Biol. Conserv.* **207**, 64–71 (2017).
- D. Pauly, D. Zeller, Eds., *Sea Around Us* concepts, design, and data (2015); www.seararoundus.org.
- R. A. Watson, *Sci. Data* **4**, 170039 (2017).
- Food and Agriculture Organization of the United Nations (FAO), *The State of World Fisheries and Aquaculture 2016* (FAO, 2016).
- J. A. Foley *et al.*, *Nature* **478**, 337–342 (2011).
- L. Guanter *et al.*, *Proc. Natl. Acad. Sci. U.S.A.* **111**, E1327–E1333 (2014).
- E. Chassot *et al.*, *Ecol. Lett.* **13**, 495–505 (2010).
- P. L. Barnard *et al.*, *Nat. Commun.* **8**, 14365 (2017).
- P. Lehodey, M. Bertignac, J. Hampton, A. Lewis, J. Picaut, *Nature* **389**, 715–718 (1997).
- World Bank, *The Sunken Billions Revisited: Progress and Challenges in Global Marine Fisheries* (World Bank, 2017).
- H. Stouter, K. Van Craeynest, A. Heene, X. Gellynick, H. Polet, “The effect of fuel price scenarios on Belgian fishing fleet dynamics,” paper presented at the International Council for the Exploration of the Sea (ICES) Annual Science Conference, Halifax, Canada, 22 to 26 September 2008 (CM 2007/M:04); www.vliz.be/imisdocs/publications/135276.pdf.
- A. Cheilaris, J. Guillen, D. Damalas, T. Barbas, *Mar. Policy* **40**, 18–24 (2013).
- D. J. Beare, M. Machiels, *ICES J. Mar. Sci.* **69**, 1064–1068 (2012).
- J. E. Hughes, C. R. Knittel, D. Sperling, “Evidence of a shift in the short-run price elasticity of gasoline demand” (Working paper 12530, National Bureau of Economic Research, 2006).
- J. J. Winebrake *et al.*, *Transp. Res. D* **38**, 166–177 (2015).
- T. Havranek, Z. Irsova, K. Janda, *Energy Econ.* **34**, 201–207 (2012).
- FAO, *FAO Statistical Pocketbook 2015* (FAO, 2016).
- R. Lewison *et al.*, *Bioscience* **65**, 486–498 (2015).

ACKNOWLEDGMENTS

E. Chassot and the Institut de Recherche Pour le Développement (IRD) and the Seychelles Fishing Authority (SFA) provided logbook data for verification. V. Manthos and C. Thomas of SkyTruth contributed to vessel labeling. E. Tuya, A. Arana, E. Mueller, and K. Wurster assisted with engineering for the AIS data pipeline. C. Bacon and K. Schwerin assisted with data processing, machine learning, and data labeling. K. Cutlip provided editorial advice. J.M. acknowledges the input and guidance of E. Sala. **Funding:** We gratefully acknowledge funding by the Leonardo DiCaprio Foundation, Adessium Foundation, Bloomberg Philanthropies, Marisla Foundation, The Waterloo Foundation, and the Wyss Foundation. Google provided cloud computing resources and technical guidance. Oceana provided support and development for Global Fishing Watch. C.C. and J.M. acknowledge support from the Waitt Family Foundation. B.W. and K.B. received support from Google Earth Engine, the Natural Sciences and Engineering Research Council of Canada, and a Transatlantic Ocean System Science and Technology scholarship to K.B. T.D.W. acknowledges support from the NSF Graduate Research Fellowship Program (grant DGE-114747). F.F. and B.A.B. acknowledge support from the Bertarelli Foundation. N.A.M. acknowledges support from the Walton Family Foundation. **Author contributions:** B.S., B.W., C.C., K.B., J.M., and D.A.K. conceived of the study. B.W. and D.A.K. wrote the manuscript with input from all authors. J.M. and C.C. calculated fuel elasticity. B.B., K.B., T.D.W., D.A.K., and J.M. curated labeled vessel information data. K.B. and B.B. led expert labeling of fishing effort. P.W. designed and managed the AIS data pipeline. A.W. and T.H. developed the CNN. N.A.M. and K.B. analyzed spatial distribution of fleets. F.F., T.D.W., and B.A.B. analyzed NPP and compared it with RFMO data. D.A.K. oversaw the project. N.A.M. and J.M. created the figures. T.H. carried out temporal analysis. **Competing interests:** None declared. **Data and materials availability:** The raw AIS data were obtained from ORBCOMM. Daily fishing effort, gridded at 0.01° by flag state and gear type, as well other data that supported figures and analyses, are available at globalfishingwatch.io. Underlying raw AIS data (i.e., individual vessel tracks) are publicly available from source data providers and may or may not require a fee to access, depending on user affiliation and terms of use. All (other) data needed to evaluate the conclusions in the paper are present in the paper or the supplementary materials.

SUPPLEMENTARY MATERIALS

www.science.org/content/359/6378/904/suppl/DC1
Materials and Methods
Figs. S1 to S9
Tables S1 to S8
References (31–46)
4 August 2017; accepted 17 January 2018
10.1126/science.aaq5646

OCEAN ACIDIFICATION

Coral reefs will transition to net dissolving before end of century

Bradley D. Eyre,^{1*} Tyler Cyronak,² Patrick Drupp,³ Eric Heinen De Carlo,³ Julian P. Sachs,⁴ Andreas J. Andersson²

Ocean acidification refers to the lowering of the ocean's pH due to the uptake of anthropogenic CO₂ from the atmosphere. Coral reef calcification is expected to decrease as the oceans become more acidic. Dissolving calcium carbonate (CaCO₃) sands could greatly exacerbate reef loss associated with reduced calcification but is presently poorly constrained. Here we show that CaCO₃ dissolution in reef sediments across five globally distributed sites is negatively correlated with the aragonite saturation state (Ω_{ar}) of overlying seawater and that CaCO₃ sediment dissolution is 10-fold more sensitive to ocean acidification than coral calcification. Consequently, reef sediments globally will transition from net precipitation to net dissolution when seawater Ω_{ar} reaches 2.92 ± 0.16 (expected circa 2050 CE). Notably, some reefs are already experiencing net sediment dissolution.

Coral reef structures are the accumulation of calcium carbonate (CaCO₃) from coral aragonite skeletons, red and green calcareous macroalgae, and other calcareous organisms such as bryozoans, echinoderms, and foraminifera. This structure provides the habitat for many species, promoting rich biological diversity and an associated myriad of ecosystem services to humans such as fisheries and tourism (1). There are two main pools of CaCO₃ in coral reefs: the framework (e.g., deposited CaCO₃ skeletons and living coral and other organisms) and permeable sediments (e.g., broken-down framework and any infaunal production) (2). For net accretion to occur at the whole-reef scale, CaCO₃ production (plus any external sediment supply) must be greater than the loss through physical, chemical, and biological erosion and transport and dissolution as follows (2):

$$\text{CaCO}_3 \text{ accretion} = \text{CaCO}_3 \text{ production} - \text{CaCO}_3 \text{ dissolution} - \text{physical loss of CaCO}_3 \quad (1)$$

Net ecosystem calcification (NEC), which refers to the chemical balance of CaCO₃ production and CaCO₃ dissolution, is typically inferred from changes in total alkalinity and does not include physical loss of CaCO₃.

Ocean acidification (OA) refers to the lowering of the ocean's pH due to the uptake of anthropogenic CO₂ from the atmosphere. When CO₂ from the atmosphere dissolves in seawater, it decreases the pH, the CO₃²⁻ concentration, and the CaCO₃ saturation state ($\Omega = [\text{Ca}^{2+}][\text{CO}_3^{2-}]/K_{\text{sp}}^*$ where K_{sp}^* is the stoichiometric ion concentra-

tion product at equilibrium) (3). Although OA-associated changes are expected to negatively affect the accretion of coral reefs (4), these future predictions are mostly based on the relationship between Ω and calcification rates of individual corals or coral reef communities [e.g., (5, 6); table S3] and NEC [e.g., (7); table S2]. However, the impact of OA on net coral reef accretion is also dependent on the poorly known effects of OA on the dissolution of permeable coral reef CaCO₃ sediments, which accumulate over thousands of years (8) and can be the major repository of CaCO₃ in modern coral reefs (9). Numerical modeling, laboratory, field, and mesocosm studies have found an increase in CaCO₃ sediment dissolution with decreasing Ω and pH (OA) (10, 11).

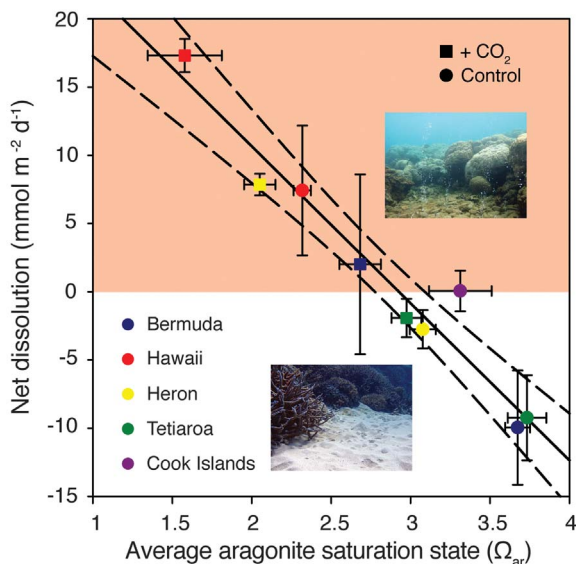
Notably, a number of studies have hypothesized that CaCO₃ dissolution may respond more rapidly to OA than coral calcification [e.g., (2, 12, 13)]. Supporting this hypothesis, a recent in situ study

found that CaCO₃ sediment dissolution increased by an order of magnitude more than calcification decreased, per unit decrease in Ω (14). However, the in situ CaCO₃ sediment dissolution measurements were only undertaken at one site on Heron Island, Australia, and it is unknown how applicable the findings are to coral reefs globally. For example, CaCO₃ sediment dissolution of different coral reefs may respond differently to OA because of differences in the present-day saturation state of the water column and differences in sediment properties such as mineralogy, porosity, permeability, grain size, organic carbon concentration, and metabolism, which in turn are controlled by factors such as light, depth, and hydrodynamics.

We measured CaCO₃ sediment dissolution using 57 individual in situ advective benthic chamber incubations at five reef locations in the Pacific and Atlantic Oceans (fig. S1). Incubations were undertaken over a diel light-dark cycle, and four of the reef incubations were run under control and end-of-century [high partial pressure of CO₂ ($p\text{CO}_2$), low pH] OA conditions. The five sites covered a range of initial water column CaCO₃ saturation states and sediment properties such as mineralogy, grain size, organic carbon concentration, and metabolism (table S1).

Our results show that CaCO₃ sediment dissolution across the five coral reefs is significantly and negatively correlated with average Ω_{ar} of the overlying seawater coefficient of determination [$r^2 = 0.49$, $P < 0.0001$, $n = 57$] (fig. S2). The increase in CaCO₃ sediment dissolution with decreasing seawater Ω_{ar} is consistent with other recent mesocosm and in situ studies from single locations (10, 11, 14). The seawater Ω_{ar} value of $\sim 2.92 \pm 0.16$ (x intercept) at which the sediments transition from net precipitating to net dissolving (Fig. 1) is well above the expected thermodynamic transition value for aragonite ($\Omega_{\text{ar}} = 1$) and saturation state of the average bulk Mg-calcite (13 to 15 mol % MgCO₃) found in most coral reefs (15). This can be explained by the interaction of

Fig. 1. Average CaCO₃ permeable sediment dissolution rates for each set of control (circles) and high $p\text{CO}_2$ (squares) treatments for each of the five reefs as a function of seawater average aragonite saturation state (Ω_{ar}) ($r^2 = 0.94$, $P < 0.0001$, $n = 9$; $y = -11.51x + 33.683$). No high- $p\text{CO}_2$ treatments were available for the Cook Islands. Error bars represent standard error. The sediments transition from net precipitating to net dissolving at a seawater Ω_{ar} value of $\sim 2.92 \pm 0.16$ ($\pm 95\%$ confidence interval). Data are in table S5. [Top photo by K. Fabricius, Australian Institute of Marine Science, and bottom photo by A. Andersson, Scripps Institution of Oceanography]



¹Centre for Coastal Biogeochemistry, School of Environment, Science and Engineering, Southern Cross University, Lismore, NSW 2480, Australia. ²Scripps Institution of Oceanography, University of California, San Diego, La Jolla, CA 92093-0244, USA. ³Department of Oceanography, University of Hawaii at Manoa, Honolulu, HI 96822, USA. ⁴School of Oceanography, University of Washington, Seattle, WA 98195, USA.

*Corresponding author Email: bradley.eyre@scu.edu.au

Fig. 2. Percent change in coral reef permeable sediment dissolution, coral calcification, and NEC per unit change in seawater aragonite saturation state (Ω_{ar}). The change is from a baseline Ω_{ar} of 3.5 and hence all lines intersect at $\Omega_{\text{ar}} = 3.5$ (100%). The thin lines are the individual measurements, and the thick line is the average. The length of line is the Ω_{ar} range over which the study was done. Coral calcification data are from (23). NEC data are from table S2.

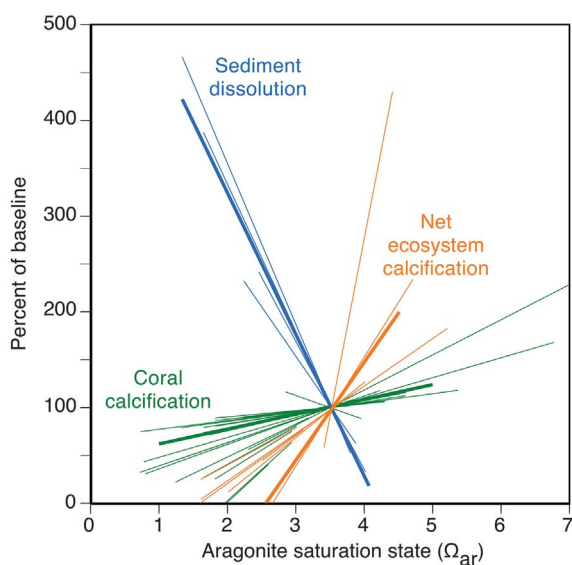
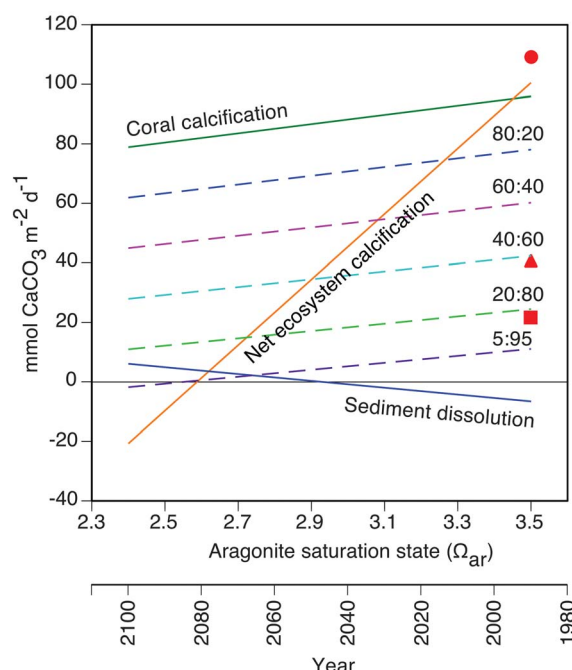


Fig. 3. Empirical model of coral reef permeable sediment dissolution, coral calcification, and NEC versus aragonite saturation state (Ω_{ar}) from reefs around the globe (solid lines).

The current (2010) global average Ω_{ar} of ocean water around reefs was set at 3.3 (37), and the average annual change in Ω_{ar} was set at -0.01 (18). Theoretical reefs with coral:sand covers of 80:20, 60:40, 40:60, 20:80, and 5:95% were also modeled (dashed lines). The red symbols are global estimates of NEC for full coral reefs (109.6 mmol $\text{CaCO}_3 \text{ m}^{-2} \text{ day}^{-1}$) (circle), an average of coral reefs and coral reef lagoons (41.1 mmol $\text{CaCO}_3 \text{ m}^{-2} \text{ day}^{-1}$) (triangle), and coral reef lagoons (21.9 mmol $\text{CaCO}_3 \text{ m}^{-2} \text{ day}^{-1}$) (square) (40).



bulk seawater saturation state and porewater metabolic processes (2). Much lower Ω_{ar} values are typically found in sediment porewater owing to the decomposition of organic matter and associated production of dissolved inorganic carbon (16). It has been hypothesized that organic matter decomposition decreases porewater Ω until it becomes undersaturated with respect to the most soluble bulk carbonate mineral phase present, which then starts to dissolve at a point called the carbonate critical threshold (CCT) (17). Further organic matter decomposition then drives carbonate sediment dissolution. However, in shallow carbonate sediments, there is a strong diel cycle in photosynthesis and respiration, and the daily-integrated sediment productivity/

respiration ratio can drive net dissolution or precipitation (2, 14). In our experiments, benthic chambers containing acidified seawater (with higher $p\text{CO}_2$ and lower Ω_{ar}) (fig. S1) were placed over carbonate sands to mimic late-21st century seawater chemistry, and this seawater was advected into the permeable carbonate sands and became the starting composition of porewater (2). Under such conditions, less organic matter decomposition is required to reach the CCT, leaving more respiratory CO_2 available to drive dissolution (17). That is, for the same amount of sediment respiration, more carbonate dissolution will occur when seawater with a lower Ω_{ar} is advected into the sediments. This hypothesis is supported by results of in situ sediment chamber

incubations under controlled and elevated $p\text{CO}_2$ conditions (10) but does not unequivocally demonstrate the underlying mechanism.

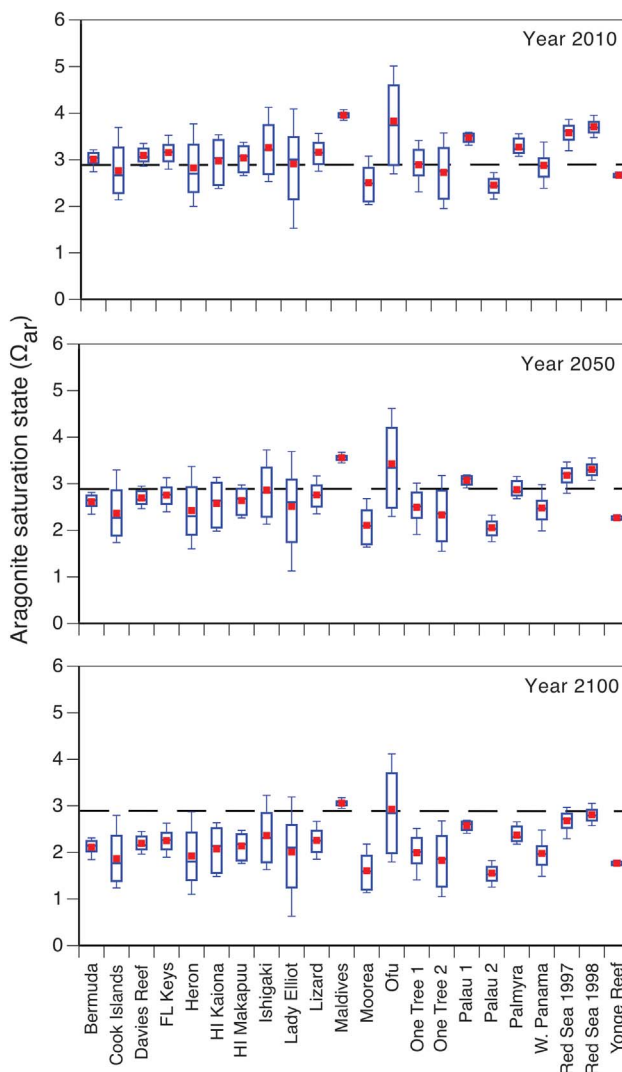
Average CaCO_3 sediment dissolution for each set of control and high- $p\text{CO}_2$ treatments at each of the five reef locations is also significantly and negatively correlated with average Ω_{ar} ($r^2 = 0.94$, $P < 0.001$, $n = 9$) (Fig. 1). Notably, there is no significant difference (Student's *t* test; $P < 0.01$) in benthic metabolism (production/respiration) between control and $p\text{CO}_2$ treatments at any of the reef sites (fig. S3), with increased dissolution only driven by changes in overlying seawater chemistry (i.e., OA conditions). Carbonate sediment dissolution at each of the four reefs has the same response to lowered seawater Ω_{ar} (increased seawater $p\text{CO}_2$), but the impact of OA on each reef is different owing to different starting conditions (Fig. 1). For example, carbonate sediments in Hawaii are already net dissolving and will be strongly net dissolving by the end of the century. In contrast, carbonate sediments at Tetiaroa are strongly net precipitating and will remain net precipitating at the end of the century. Carbonate sediments at Heron Island and Bermuda will both transition from net precipitating to net dissolving by the end of the century.

The transition of coral reef sands from net precipitating to net dissolving occurs when the seawater Ω_{ar} reaches 2.92 ± 0.16 (Fig. 1 and fig. S1). Hence, current reef seawater conditions control the impact that OA will have on the net carbonate accretion of coral reefs. The current seawater carbonate chemistry (e.g., pH, Ω_{ar}) of coral reefs is controlled by a combination of the open ocean source water and biogeochemical and hydrodynamic processes on the reef. There are latitudinal and regional variations in the open ocean Ω_{ar} with, for example, tropical reefs bathed in higher- Ω_{ar} water than higher-latitude reefs (18). The open ocean seawater composition is then modified by net ecosystem production (NEP – photosynthesis minus autotrophic and heterotrophic respiration) and NEC (19). Globally, it has been proposed that the average $p\text{CO}_2$ of coral reefs has increased 3.5 times faster than in the open ocean over the past 20 years, most likely due to increased terrestrial nutrient and organic matter inputs (20). For example, in Kaneohe Bay, Hawaii, the carbonate sediments are currently net dissolving because of low reef seawater Ω_{ar} (Fig. 1) associated with low- Ω_{ar} source water (7) and large inputs of terrestrial nutrients and organic matter (21, 22). In contrast, the carbonate sediments at Tetiaroa are strongly net precipitating because of high reef seawater Ω_{ar} (Fig. 1) associated with high- Ω_{ar} source water and most likely little to no terrestrial organic matter inputs. External inputs of organic matter are thus an important control on the dissolution and associated net accretion of coral reefs (2, 17).

CaCO_3 sediment dissolution across the five reefs is clearly very sensitive to OA with a 170% change per unit change in seawater Ω_{ar} (Figs. 1 and 2). This is an order of magnitude greater than predicted changes in coral calcification due to OA. For example, a recent meta-analysis

Fig. 4. Box plots of 2010, 2050, and 2100 Ω_{ar} for 22 reefs across the global oceans (details in table S4).

The dashed line at Ω_{ar} 2.92 shows when the reef sediments will transition to net dissolving. The 2010, 2050, and 2100 predictions were calculated with the average annual open ocean change in Ω_{ar} of -0.01 , but with average actual Ω_{ar} starting values for each reef for the year the data were collected. These calculations ignore the minor nonlinear behavior of Ω_{ar} in response to rising CO_2 over the range modeled. The box plot red square is the mean; the horizontal line in the box is the median; the upper and lower box are the 75 and 25 percentiles, respectively; and the top and bottom whiskers are the 90 and 10 percentiles, respectively.



of biologically mediated coral calcification only showed a 15% reduction per unit change in seawater Ω_{ar} (Fig. 2), or as low as a 10% reduction if only studies integrating light and dark calcification rates were considered (23). The change in CaCO_3 sediment dissolution per unit change in seawater Ω_{ar} across the individual reefs is also less variable than the response of coral calcification per unit change in seawater Ω_{ar} across the individual studies (Fig. 2). Differences in the response of carbonate sediment dissolution and coral calcification to OA most likely reflect differences in the biologically mediated process of calcification compared to the geochemically mediated process of dissolution.

Coral calcification has shown taxa-specific responses to OA (24) most likely due to differences in characteristics such as the percentage of skeletal tissue cover and the ability to regulate pH of calcifying fluids (25, 26). Observations that both near-shore and deep-sea calcifiers can live and calcify under thermodynamically unfa-

vorble conditions [$\Omega_{\text{ar}} < 1$; (27, 28)] suggest that seawater chemistry is only part of the equation and that organisms may have mechanisms and/or strategies to deal with the predicted changes in seawater carbonate chemistry and could potentially adapt to OA (5, 29). For example, given a sufficient supply of nutrition and energy, many calcifiers are less negatively affected by OA (30). In contrast to biologically mediated calcification, increasing CaCO_3 dissolution is mostly a geochemical response to changes in seawater chemistry and will increase according to thermodynamic and kinetic constraints (Fig. 3) (31, 32).

Future predictions of OA effects on coral reefs are often based on the relationship between average Ω_{ar} and NEC (see table S2). On average, there is a 102% change in NEC per unit change in seawater Ω_{ar} (Fig. 2), which is more sensitive than coral calcification (10 to 15%) but less sensitive than carbonate sediment dissolution (170%). The order-of-magnitude greater response of NEC compared to coral calcification could in part be

due to sediment dissolution being more sensitive to decreasing Ω_{ar} and therefore making an increasingly greater contribution to the decrease in NEC. In addition, other components of the coral reef benthic community such as crustose coralline algae and calcareous benthic macroalgae, which are also more sensitive to changes in Ω_{ar} than corals (33, 34), could also contribute to the greater response of NEC. Consistent with this is the stronger response and sensitivity of whole coral reef community calcification to changes in Ω_{ar} than that observed in studies of individual organisms [e.g., (12, 35, 36)]. The highly variable response of the NEC of individual reefs to changes in Ω_{ar} probably reflects variations in composition of benthic communities, combined with the variable response of individual benthic communities (i.e., sediments, corals, crustose coralline algae).

An understanding of the absolute changes in CaCO_3 production and dissolution (and physical loss) as the ocean acidifies is required to be able to predict the future evolution of coral reefs (see Eq. 1). We developed a simple model based on empirical relationships between average Ω_{ar} and NEC, coral calcification, and sediment dissolution from reefs around the globe (Fig. 1 and tables S2 and S3) and predicted future changes in the open ocean Ω_{ar} (18) to quantify changes in the CaCO_3 production of coral reefs (see materials and methods for a detailed description of the model). Under present-day average tropical ocean Ω_{ar} (33), coral reef sediments are net precipitating and coral calcification and NEC are positive (Fig. 3). However, the model shows there has already been on average a reduction in coral reef sediment precipitation from 18.1 to $4.3 \text{ mmol m}^{-2} \text{ day}^{-1}$, a reduction in NEC from 210.7 to $78.5 \text{ mmol m}^{-2} \text{ day}^{-1}$, and a reduction in coral calcification of 111.4 to $92.8 \text{ mmol m}^{-2} \text{ day}^{-1}$ since pre-industrial time when the average tropical ocean Ω_{ar} was ~ 4.5 (37). When the average tropical ocean Ω_{ar} reaches ~ 2.92 in ~ 2048 , coral reef sediments will become net dissolving (Fig. 3). By 2082, global average coral reef NEC will become negative (i.e., net dissolving; Fig. 3). By 2078 ($\Omega_{\text{ar}} = 2.62$), sediment dissolution will exceed the global average coral reef NEC (Fig. 3). For coral reefs with 5% coral cover and 95% sediment cover, probably a common future scenario with increasing coral cover loss, this transition to net dissolution will also occur in 2085 ($\Omega_{\text{ar}} = 2.55$) (Fig. 3).

The above model scenarios assumed a current average open ocean Ω_{ar} of 3.3 for coral reefs. However, an analysis of 22 coral reefs (see also table S1) shows a wide range of Ω_{ar} values, and therefore the timing of the transition to net dissolving will vary for individual reefs (Fig. 4). On average, four reefs already experience conditions that would promote net sediment dissolution, and by the end of the century, all but two reefs across the three ocean basins would on average experience sediment dissolution. The above model scenarios also assumed open ocean changes in Ω_{ar} , but the average seawater carbonate chemistry conditions of coral reefs may be appreciably different because of changes in reef biogeochemical processes and inputs of terrestrial nutrient and

organic matter (19, 20). One study suggests that the seawater $p\text{CO}_2$ on some reefs has increased up to 3.5 times faster than in the open ocean (20). Under this more rapid acidification scenario, coral reefs on average could transition to net sediment dissolution by the end of the decade (2020) ($\Omega_{\text{ar}} = 2.92$), and NEC will become negative by 2031 ($\Omega_{\text{ar}} = 2.58$). This study also has not included the effect of sea surface temperature increases on CaCO_3 sediment dissolution. Although initial studies show a nonadditive effect of increased temperature and lowered Ω_{ar} on CaCO_3 sediment dissolution (38), little is known about these combined stressors. Bleaching and coral mortality will also most likely accelerate the breakdown of coral reefs (39), making more sediment and organic matter available for dissolution.

A transition to net sediment dissolution will result in loss of material for building shallow reef habitats such as reef flats and lagoons and associated coral cays (2). However, it is unknown if the whole reef will erode once the sediments become net dissolving, as the corals will still calcify (Fig. 3), and the framework may still accrete. It is also unknown if reefs will experience catastrophic destruction once they become net eroding, or if they will slowly erode, driven by organic matter input and OA (17).

REFERENCES AND NOTES

- O. Hoegh-Guldberg, *Mar. Freshw. Res.* **50**, 839 (1999).
- B. D. Eyre, A. J. Andersson, T. Cyronak, *Nat. Clim. Chang.* **4**, 969–976 (2014).
- R. E. Zeebe, D. Wolf-Gladrow, *CO_2 in Seawater: Equilibrium, Kinetics, Isotopes* (Elsevier Oceanography Series, Amsterdam, 2001), vol. 65.
- O. Hoegh-Guldberg *et al.*, *Science* **318**, 1737–1742 (2007).
- J. M. Pandolfi, S. R. Connolly, D. J. Marshall, A. L. Cohen, *Science* **333**, 418–422 (2011).
- R. van Hooidonk, J. A. Maynard, D. Manzello, S. Planes, *Glob. Change Biol.* **20**, 103–112 (2014).
- B. T. Smith, E. Frankel, J. S. Jell, in *Reefs and Carbonate Platforms in the Pacific and Indian Oceans*, G. F. Camoin, P. J. Davies, Eds. (Blackwell, 2009), pp. 279–294.
- J. Gattuso, M. Frankignoulle, R. Wollast, *Annu. Rev. Ecol. Syst.* **29**, 405–434 (1998).
- T. Cyronak, I. R. Santos, B. D. Eyre, *Geophys. Res. Lett.* **40**, 4876–4881 (2013).
- S. Comeau, P. J. Edmunds, C. A. Lantz, R. C. Carpenter, *Sci. Rep.* **4**, 6681 (2014).
- A. J. Andersson *et al.*, *Biogeosciences* **6**, 1811–1823 (2009).
- J. Erez, S. Reynaud, J. Silverman, K. Schneider, D. Allemand, in *Coral Reefs: An Ecosystem in Transition*, Z. Dubinsky, N. Stambler, Eds. (Springer, 2011), pp. 151–176.
- T. Cyronak, B. D. Eyre, *Mar. Chem.* **183**, 1–12 (2016).
- J. W. Morse, A. J. Andersson, F. T. Mackenzie, *Geochim. Cosmochim. Acta* **70**, 5814–5830 (2006).
- J. W. Morse *et al.*, *Am. J. Sci.* **285**, 147–185 (1985).
- A. J. Andersson, *Front. Mar. Sci.* **2**, 52 (2015).
- N. R. Bates *et al.*, *Oceanography (Wash. D.C.)* **27**, 126–141 (2014).
- A. J. Andersson, K. L. Yeakel, N. R. Bates, S. J. de Putron, *Nat. Clim. Chang.* **4**, 56–61 (2014).
- T. Cyronak, K. G. Schulz, I. R. Santos, B. D. Eyre, *Geophys. Res. Lett.* **41**, 5538–5546 (2014).
- S. Ringuet, F. T. Mackenzie, *Estuaries* **28**, 327–337 (2005).
- P. S. Drupp, E. H. De Carlo, F. T. Mackenzie, *Mar. Chem.* **185**, 48–64 (2016).
- N. C. S. Chan, S. R. Connolly, *Glob. Change Biol.* **19**, 282–290 (2013).
- P. J. Edmunds, R. C. Carpenter, S. Comeau, *Oceanography (Wash. D.C.)* **26**, 149–152 (2013).
- M. McCulloch *et al.*, *Geochim. Cosmochim. Acta* **87**, 21–34 (2012).
- M. Wall *et al.*, *Sci. Rep.* **6**, 30688 (2016).
- R. E. Thresher, B. Tilbrook, S. Fallon, N. C. Wilson, J. Adkins, *Mar. Ecol. Prog. Ser.* **442**, 87–99 (2011).
- M. Lebrato *et al.*, *Global Biogeochem. Cycles* **30**, 1038–1053 (2016).
- M. Holcomb *et al.*, *Sci. Rep.* **4**, 5207 (2014).
- E. K. Towle, I. C. Enochs, C. Langdon, *PLOS ONE* **10**, e0123394 (2015).
- L. M. Walter, *Geochim. Cosmochim. Acta* **48**, 1059–1069 (1984).
- L. M. Walter, J. W. Morse, *Geochim. Cosmochim. Acta* **49**, 1503–1513 (1985).
- P. Jokiel *et al.*, *Coral Reefs* **27**, 473–483 (2008).
- I. B. Kuffner, A. J. Andersson, P. L. Jokiel, K. S. Rodgers, F. T. Mackenzie, *Nat. Geosci.* **1**, 114–117 (2008).
- K. Yates, R. Halley, *Estuaries Coasts* **29**, 24–39 (2006).
- S. G. Dove *et al.*, *Proc. Natl. Acad. Sci. U.S.A.* **110**, 15342–15347 (2013).
- L. Cao, K. Caldeira, *Geophys. Res. Lett.* **35**, L19609 (2008).
- D. Trnovsky, L. Stoltenberg, T. Cyronak, B. D. Eyre, *Front. Mar. Sci.* **3**, 211 (2016).
- T. P. Hughes *et al.*, *Nature* **543**, 373–377 (2017).
- J. D. Milliman, *Global Biogeochem. Cycles* **7**, 927–957 (1993).

ACKNOWLEDGMENTS

This work was funded by Australian Research Council Discovery Grants 110103638 (B.D.E.) and 150102092 (B.D.E. and A.J.A.), with contributions from NSF OCE 12-55042 (A.J.A.), Sea Grant N. NA140AR4170071 (E.H.D.C.), and James and Marsha Seeley and the Tetiaroa Society (J.P.S.). B.D.E. conceived the project and wrote the manuscript. T.C. contributed to the writing. B.D.E. and T.C. did the modeling. B.D.E., T.C., and A.J.A. did the data analysis. All authors contributed to the data collection, discussed the results, and commented on the manuscript. The data are provided in the supplementary materials. All authors declare no conflicting interests. I. Alexander and J. Rosentreter assisted with the figure preparation. K. Schulz reviewed a draft manuscript. We thank two anonymous reviewers for helpful comments. This is School of Ocean and Earth Sciences and Technology contribution 10270 and UNIHI-SEAGRANT-JC-15-23.

SUPPLEMENTARY MATERIALS

www.sciencemag.org/content/359/6378/908/suppl/DC1

Materials and Methods

Figs. S1 to S4

Tables S1 to S5

References (41–76)

14 June 2017; accepted 6 December 2017

10.1126/science.aaol1118

U-Th dating of carbonate crusts reveals Neandertal origin of Iberian cave art

D. L. Hoffmann,^{1*} C. D. Standish,^{2*} M. García-Díez,³ P. B. Pettitt,⁴ J. A. Milton,⁵ J. Zilhão,^{6,7,8} J. J. Alcolea-González,⁹ P. Cantalejo-Duarte,¹⁰ H. Collado,¹¹ R. de Balbín,⁹ M. Lorblanchet,¹² J. Ramos-Muñoz,¹³ G.-Ch. Weniger,^{14,15} A. W. G. Pike^{2†}

The extent and nature of symbolic behavior among Neandertals are obscure. Although evidence for Neandertal body ornamentation has been proposed, all cave painting has been attributed to modern humans. Here we present dating results for three sites in Spain that show that cave art emerged in Iberia substantially earlier than previously thought. Uranium-thorium (U-Th) dates on carbonate crusts overlying paintings provide minimum ages for a red linear motif in La Pasiega (Cantabria), a hand stencil in Maltravieso (Extremadura), and red-painted speleothems in Ardales (Andalucía). Collectively, these results show that cave art in Iberia is older than 64.8 thousand years (ka). This cave art is the earliest dated so far and predates, by at least 20 ka, the arrival of modern humans in Europe, which implies Neandertal authorship.

The origin of human symbolism is a central concern of modern paleoanthropology (1). For the European Middle Paleolithic and the African Middle Stone Age, symbolic behavior has been inferred from the use, presumably for body adornment, of mineral pigments, shell beads, eagle talons, and feathers (2–7). Cave and rock art constitutes particularly impressive and important evidence for symbolic behavior (8), but little is known about the chronology of its emergence, owing to difficulties in precise and accurate dating (9).

Claims for Neandertal authorship of cave art have been made (10, 11). However, ambiguities of indirect dating and uncertainty in distinguishing between natural and intentional modification

(12, 13) leave these claims unresolved. Recent technical developments enable the possibility of obtaining age constraints for cave art by U-Th dating of associated carbonate precipitates (14). This dating approach can provide robust age constraints while keeping the art intact. However, it is a destructive technique, in that a carbonate sample is required (albeit, a very small sample, typically <10 mg) and is taken not from the art itself but from the associated carbonates. The key condition is demonstrating an unambiguous stratigraphic relationship between the sample and the art whose age we wish to constrain. Dating of carbonate crusts formed on top of the art provides a minimum age (15). For art painted on top of carbonates (e.g., on flowstone walls, stalagmites, or stalactites), dating the underlying “canvas” provides a maximum age (15).

With this approach, the earliest results so far are for a hand stencil from Leang Timpuseng, Sulawesi (Indonesia), with a minimum age of 39.9 thousand years (ka) (16), and a red disc on the Panel of Hands in El Castillo, Cantabria (Spain), with a minimum age of 40.8 ka (17). Whereas the art in Sulawesi has been attributed to modern humans, the minimum age for the red disc in El Castillo relates to a point in time when it could be attributed to either Cantabria’s first modern humans or the region’s earlier Neandertal populations (18, 19).

Here we report U-Th dating results of carbonate formations associated with rock art in three

Spanish caves: La Pasiega (Cantabria), Maltravieso (Extremadura), and Doña Trinidad (or Ardales; Andalucía) (fig. S1) (20). Our criteria for sample selection and subsequent sampling strategy strictly followed previously described methods (14). The reliability of the U-Th dating results is controlled by quality criteria for the carbonate (14) as well as by the collection and analysis of multiple subsamples of a given crust.

La Pasiega is part of the Monte Castillo cave art complex, a World Heritage Site that also includes the caves of El Castillo, Las Chimeneas, and Las Monedas. Together, these caves show continued human occupation throughout the past 100 ka. At La Pasiega, the rock art comprises mainly red and black paintings, including groups of animals, linear signs, claviform signs, dots, and possible anthropomorphs (21). Maltravieso was episodically used by hominin groups during the past 180 ka (22); it contains an important set of red hand stencils (~60), which form part of a larger body of art that includes both geometric designs (e.g., dots and triangles) and painted and engraved figures (23). Ongoing excavations have shown that Ardales was occupied in the Middle and Upper Paleolithic. Its walls feature an impressive number (>1000) of paintings and engravings in a vast array of forms, including hand stencils and prints; numerous dots, discs, lines, and other geometric shapes; and figurative representations of animals, including horses, deer, and birds (24).

We obtained U-Th ages for 53 samples removed from 25 carbonate formations stratigraphically



Fig. 1. Red scalariform sign, panel 78 in hall XI of La Pasiega gallery C. This panel features the La Trampa pictorial group (21). (Inset) Crust sampled and analyzed for a minimum age (64.8 ka), which constrains the age of the red line. See (20) for details.

*These authors contributed equally to this work.

†Corresponding author. Email: a.w.pike@soton.ac.uk

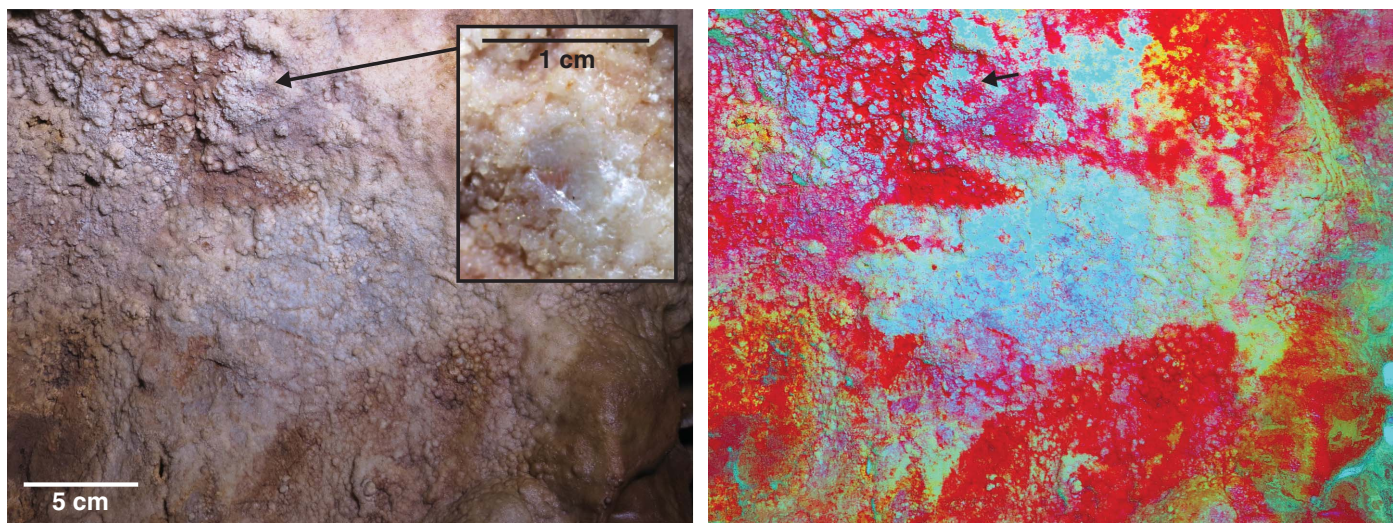


Fig. 2. Hand stencil GS3b in Maltravieso cave (minimum age 66.7 ka). (Left) Original photo. The inset shows where the overlying carbonate was sampled for MAL 13. (Right) Same picture after application of the DStretch software (25) (correlation LRE 15%, auto contrast) to enhance color contrast. See (20) for details.

related to paintings in these caves. The full details of our methods and data are described in the supplementary materials (20). Here we present and discuss the results that are most meaningful for the antiquity of the art.

In La Pasiega gallery C (fig. S2), a cauliflower-type carbonate formation on top of a red scalariform sign [panel 78 of hall XI (Fig. 1) (20)] yielded U-Th dates for three subsamples (outer, middle, and inner) that increase in age with depth—that is, toward the pigment layer. They provide a minimum age of 64.8 ka (sample PAS 34) (Table 1) (20) for the sign.

In Maltravieso (fig. S7), we dated samples from five locations on various carbonate formations overlying the same red hand stencil (motif GS3b) (Fig. 2) (20). Carbonate deposits almost completely obscure this hand stencil, making it difficult to see with the naked eye and challenging to record by conventional photography. Figure 2 therefore also shows a version of the photographic documentation after we used the DStretch software (25) to enhance the image. For subsamples in all locations, the expected depth-age consistency was confirmed. The oldest date provides a minimum age of 66.7 ka (MAL 13) (Table 1) (20) for the hand stencil.

In Ardales (fig. S9), we dated layers of five carbonate curtains from three areas of the cave (II-A, II-C, and III-C) that had been painted red. In three cases we were able to obtain both maximum and minimum ages by dating samples from immediately underneath the pigment and from carbonate that subsequently formed on top. These age pairs constrain one or more episodes of painting to between 48.7 ka and 45.3 ka ago (ARD 14 and 15), 45.5 ka and 38.6 ka ago (ARD 26 and 28), and 63.7 ka and 32.1 ka ago (ARD 6 and 8) (Table 1) (20). A further two samples yielded minimum ages of 65.5 ka (ARD 13) (Fig. 3), indicating an earlier episode of painting, and 46.9 ka (ARD 16), consistent with the other episodes (fig. S42) (20).

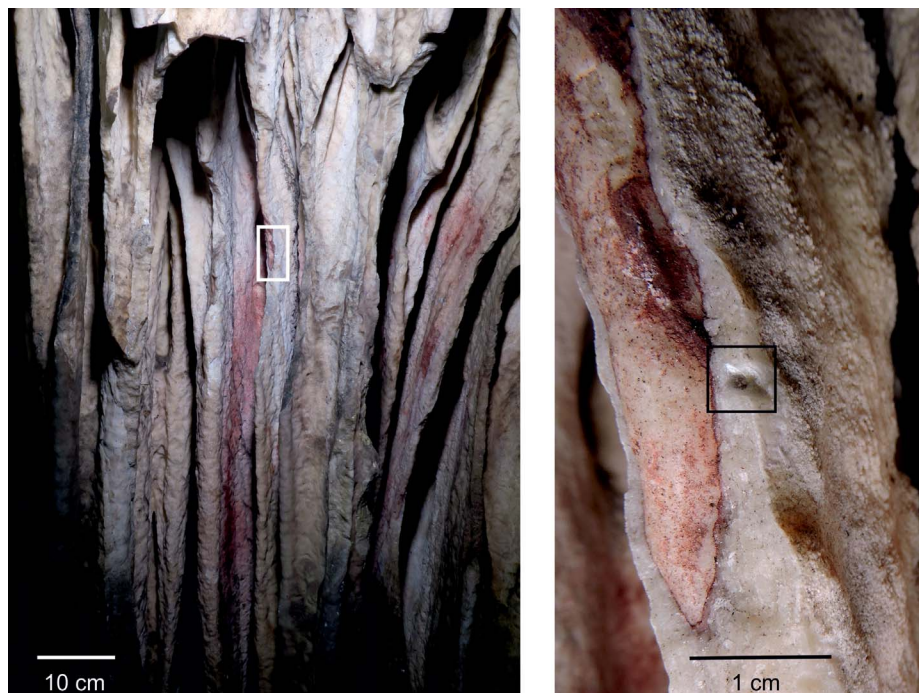


Fig. 3. Speleothem curtain 8 in section II-A-3 in Ardales cave with red pigment, painted before at least 65.5 ka ago. (Left) Series of curtains with red paint on top, partially covered with later speleothem growth. The white rectangle outlines the area shown at right. (Right) Detail of curtain 8. The black square indicates where carbonate, overlying the red paint, was sampled for ARD 13. See (20) for details.

Criteria for reliable minimum (or maximum) ages (14) were met by all samples. The oldest minimum ages from the three caves are consistent and, at 64.8 ka or older for each site, substantially predate the arrival of modern humans in Europe, which has been variously estimated at between 45 ka and 40 ka ago (26, 27). Our dating results show that cave art was being made at La Pasiega, Maltravieso, and Ardales

at least 20 ka before that. In this age range, Iberia was exclusively populated by Neandertals, as indicated by numerous diagnostic osteological remains, including articulated skeletons (28, 29). The implication is, therefore, that the artists were Neandertals.

All examples of early cave art dated thus far were created in red pigment, and comprise dots, lines, disks, and hand stencils (30). This is a

Table 1. U-Th results of samples discussed in the text. More details and additional results can be found in table S4 (20). All ratios are activity ratios. Analytical errors are at the 95% confidence level. Spl ID, sample identifier.

Spl ID	Site and description	^{238}U (ng/g)	$^{230}\text{Th}/^{232}\text{Th}$	$^{230}\text{Th}/^{238}\text{U}$ uncorrected	$^{234}\text{U}/^{238}\text{U}$ uncorrected	Age uncorrected (ka)	Age corrected (ka)
PAS 34a	Pasiega C, no. 78, cauliflower-type carbonate on top of red line of scalariform motif, minimum age	289.29 ± 9.06	32.82 ± 0.21	1.5149 ± 0.0106	3.7694 ± 0.0082	52.52 ± 0.47	51.56 ± 1.09
PAS 34b	As above	215.56 ± 7.43	28.28 ± 0.19	1.5453 ± 0.0121	3.6744 ± 0.0094	55.53 ± 0.56	54.36 ± 1.39
PAS 34c	As above	178.31 ± 8.31	7.25 ± 0.07	2.0348 ± 0.0213	3.4591 ± 0.0092	85.79 ± 1.28	79.66 ± 14.90
MAL 13	Maltravieso, cauliflower-type surface cleaning fraction	117.2 ± 1.99	12.47 ± 0.16	0.4639 ± 0.0068	1.1872 ± 0.0328	53.32 ± 2.30	41.68 ± 2.44
MAL 13A	As above	142.69 ± 3.39	37.50 ± 0.57	0.6067 ± 0.0123	1.2024 ± 0.0305	74.86 ± 3.78	70.08 ± 3.82
						or - 3.41	or - 3.37
ARD 6	Ardales, red paint on curtain formation, II-C-8, carbonate from underlying curtain, maximum age	511.42 ± 6.38	34.95 ± 0.14	0.4661 ± 0.0021	1.0459 ± 0.0021	64.09 ± 0.44	62.97 ± 0.69
ARD 8	Ardales, red paint on curtain formation, II-C-8, carbonate from overlying curtain, minimum age	297.21 ± 2.89	145.58 ± 1.06	0.2703 ± 0.0018	1.0477 ± 0.0024	32.51 ± 0.26	32.35 ± 0.27
ARD 13A	Ardales, red paint on curtain formation, II-A-3 curtain 8, minimum age	1229.61 ± 25.84	152.83 ± 1.14	0.3661 ± 0.0033	1.0385 ± 0.0033	47.33 ± 0.57	47.13 ± 0.56
						or - 0.56	or - 0.57
ARD 13B	As above	331.54 ± 13.53	42.59 ± 0.58	0.4878 ± 0.0073	1.0369 ± 0.0234	69.09 ± 2.93	68.13 ± 2.96
						or - 2.62	or - 2.62
ARD 14A	Ardales, red paint on curtain formation, II-A-3 curtain 6, carbonate from underlying curtain, maximum age	684.76 ± 13.29	395.03 ± 4.91	0.3683 ± 0.0063	1.0379 ± 0.0029	47.72 ± 1.05	47.64 ± 1.07
						or - 1.02	or - 1.03
ARD 15A	Ardales, red paint on curtain formation, II-A-3 curtain 6, carbonate from overlying curtain, minimum age	1696.03 ± 53.88	337.14 ± 3.63	0.3584 ± 0.0050	1.0374 ± 0.0025	46.15 ± 0.81	46.06 ± 0.81
						or - 0.82	or - 0.77
ARD 15B	As above	667.98 ± 37.85	152.07 ± 3.27	0.3467 ± 0.0110	1.0347 ± 0.0061	44.45 ± 1.79	44.25 ± 1.78
						or - 1.82	or - 1.77
ARD 16A	Ardales, red paint on curtain formation, II-A-3 curtain 5, carbonate from overlying curtain, minimum age	313.84 ± 5.88	58.92 ± 0.74	0.3317 ± 0.0044	1.0323 ± 0.0051	42.23 ± 0.74	41.75 ± 0.77
						or - 0.72	
ARD 16B	As above	250.2 ± 4.29	84.25 ± 0.84	0.3628 ± 0.0050	1.0314 ± 0.0051	47.23 ± 0.85	46.86 ± 0.85
						or - 0.83	or - 0.92
ARD 16C	As above	227.59 ± 28.55	56.70 ± 2.84	0.3690 ± 0.0213	1.0227 ± 0.0342	48.79 ± 4.26	48.23 ± 4.43
						or - 4.00	or - 4.10
ARD 26A	Ardales, red paint visible as a line on cross section of a broken curtain, between III-C-3 and III-C-2, carbonate from overlying curtain, minimum age	564.64 ± 13.56	1004.53 ± 20.81	0.3243 ± 0.0099	1.0502 ± 0.0203	40.20 ± 1.84	40.17 ± 1.73
						or - 1.69	or - 1.77
ARD 26B	As above	532.37 ± 14.02	985.93 ± 24.33	0.3258 ± 0.0112	1.0496 ± 0.0113	40.45 ± 1.82	40.42 ± 1.79
						or - 1.70	or - 1.78
ARD 28A	Ardales, red paint visible as a line on cross section of a broken curtain, between III-C-3 and III-C-2, carbonate from underlying curtain, maximum age	520.54 ± 8.11	4626.61 ± 188.57	0.3379 ± 0.0192	1.0458 ± 0.0124	42.48 ± 3.09	42.47 ± 3.07
						or - 2.91	or - 2.97

restricted and nonfigurative set of subjects and could represent the extension of Neandertal body art to the external world. Regardless of whether concentrations of color, dots, disks, and linear motifs can be conceived as symbolic, hand stencils (which, unlike positive hand prints, cannot

be created by accident) require a light source and previous selection and preparation of the coloring material—evidence of premeditated creation. Because a number of hand stencils seem to have been deliberately placed in relation to natural features in caves rather than randomly created

on accessible surfaces (31), it is difficult to see them as anything but meaningful symbols placed in meaningful places.

This cave painting activity constitutes a symbolic behavior by definition, and one that is deeply rooted. At Ardales, distinct episodes over

a period of more than 25 ka corroborate that we are not dealing with a one-off burst but with a long tradition that may well stretch back to the time of the annular construction found in Bruniquel cave, France (32), dated to 176.5 ± 2.1 ka ago. Dating results for the excavation site at Cueva de los Aviones, Spain (2), which place symbolic use of marine shells and mineral pigments by Neandertals at >115 ka ago (33), further support the antiquity of Neandertal symbolism.

Cave art such as that dated here exists in other caves of Western Europe and could potentially be of Neandertal origin as well. Red-painted draperies are found at Les Merveilles (France; panel VII) (34) and El Castillo (Spain), whereas hand stencils and linear symbols are ubiquitous and, when part of complex superimpositions, always form the base of pictorial stratigraphies. We therefore expect that cave art of Neandertal origin will eventually be revealed in other areas with Neandertal presence elsewhere in Europe. We also see no reason to exclude that the behavior will be equally ancient among coeval non-Neandertal populations of Africa and Asia.

The authorship of the so-called “transitional” techno-complexes of Europe, which, like the Châtelperronian, feature abundant pigments and objects of personal ornamentation, has long been the subject of debate (35, 36). Direct or indirect (via acculturation) assignment to modern humans has been based on an “impossible coincidence” argument—that is, the implausibility that Neandertals would independently evolve the behavior just at the time when modern humans were already in or at the gates of Europe. By showing that the Châtelperronian is but a late manifestation of a long-term indigenous tradi-

tion of Neandertal symbolic activity, our results bring closure to this debate.

REFERENCES AND NOTES

- C. Henshilwood, F. d'Errico, Eds., *Homo Symbolicus: The Dawn of Language, Imagination and Spirituality* (John Benjamins, 2011).
- J. Zilhão et al., *Proc. Natl. Acad. Sci. U.S.A.* **107**, 1023–1028 (2010).
- M. Peresani, I. Fiore, M. Gala, M. Romandini, A. Tagliacozzo, *Proc. Natl. Acad. Sci. U.S.A.* **108**, 3888–3893 (2011).
- D. Radovčić, A. O. Sršen, J. Radovčić, D. W. Frayer, *PLOS ONE* **10**, e0119802 (2015).
- C. S. Henshilwood, F. d'Errico, I. Watts, *J. Hum. Evol.* **57**, 27–47 (2009).
- C. S. Henshilwood et al., *Science* **334**, 219–222 (2011).
- F. d'Errico, C. Henshilwood, M. Vanhaeren, K. van Niekerk, *J. Hum. Evol.* **48**, 3–24 (2005).
- A. Leroi-Gourhan, B. Delluc, G. Delluc, *Préhistoire de l'Art Occidental* (Citadelles et Mazarin, 1995).
- P. Pettitt, A. Pike, *J. Archaeol. Method Theory* **14**, 27–47 (2007).
- J. C. Marquet, M. Lorblanchet, *Antiquity* **77**, 661–670 (2003).
- J. Rodríguez-Vidal et al., *Proc. Natl. Acad. Sci. U.S.A.* **111**, 13301–13306 (2014).
- P. Pettitt, *Before Farming* **2003**, 1–3 (2003).
- E. Camarós et al., *Quat. Int.* **435**, 237–246 (2017).
- D. L. Hoffmann, A. W. G. Pike, M. García-Díez, P. B. Pettitt, J. Zilhão, *Quat. Geochronol.* **36**, 104–119 (2016).
- Minimum ages are calculated by subtracting the 95% uncertainty from the mean; maximum ages are calculated by adding the 95% uncertainty to the mean.
- M. Aubert et al., *Nature* **514**, 223–227 (2014).
- A. W. G. Pike et al., *Science* **336**, 1409–1413 (2012).
- J. J. Hublin, *Quat. Sci. Rev.* **118**, 194–210 (2015).
- J. Zilhão, *Pyrenae* **37**, 7–84 (2006).
- See supplementary materials.
- H. Breuil, H. Obermaier, H. Alcalde del Río, *La Pasiega à Puent Viesgo (Santander, Espagne)* (Institut de Paléontologie Humaine, 1913).
- N. Barrero et al., in *O Paleolítico, Actas do IV Congreso de Arqueología Peninsular*, N. Bicho, Ed. (Universidade do Algarve, 2005), pp. 265–284.
- H. Collado, J. J. García, in *IFRAO 2013 Proceedings: American Indian Rock Art* (International Federation of Rock Art Organizations, 2013), vol. 40, pp. 383–440.
- P. Cantalejo et al., *La Cueva de Ardales: Arte Prehistórico y Ocupación en el Paleolítico Superior* (Diputación de Málaga, 2006).
- P. Clog, M. Díaz-Andreu, B. Larkman, *J. Archaeol. Sci.* **27**, 837–843 (2000).
- J. Zilhão, F. D'Errico, *J. World Prehist.* **13**, 1–68 (1999).
- T. Higham et al., *Nature* **512**, 306–309 (2014).
- M. J. Walker et al., *Proc. Natl. Acad. Sci. U.S.A.* **105**, 20631–20636 (2008).
- R. E. Wood et al., *Archaeometry* **55**, 148–158 (2013).
- M. García-Díez et al., *J. Anthropol. Sci.* **93**, 135–152 (2015).
- P. Pettitt, A. M. Castillejo, P. Arias, R. O. Peredo, R. Harrison, *Antiquity* **88**, 47–63 (2014).
- J. Jaubert et al., *Nature* **534**, 111–114 (2016).
- D. L. Hoffmann, D. E. Angelucci, V. Villaverde, J. Zapata, J. Zilhão, *Sci. Adv.* **4**, eaar5255 (2018).
- M. Lorblanchet, *Art Pariétal: Grottes Ornées du Quercy* (Edition Rouergue, 2010).
- P. Mellars, *Proc. Natl. Acad. Sci. U.S.A.* **107**, 20147–20148 (2010).
- F. Caron, F. d'Errico, P. Del Moral, F. Santos, J. Zilhão, *PLOS ONE* **6**, e21545 (2011).

ACKNOWLEDGMENTS

This research was financially supported by the Natural Environment Research Council (UK) (grant NE/K015184/1 to A.W.G.P.), the National Geographic Society (USA) (grant ECO603-12 to D.L.H.), the Max Planck Society (Germany), and a Royal Society Wolfson Research Merit Award (to A.W.G.P.). The work of M.G.-D. was supported by the Research Group IT622-13 of the Basque government. We thank the governments of Andalucía, Cantabria, and Extremadura for sampling permissions. We are grateful for fieldwork support by J. C. Aguilar, M. Batut, J. R. Bello, D. Garrido, R. Gutiérrez, and C. Hoffmann. The data described are presented in the supplementary materials. We dedicate this paper to the memory of José Antonio Lasheras.

SUPPLEMENTARY MATERIALS

www.sciencemag.org/content/359/6378/912/suppl/DC1
Materials and Methods
Supplementary Text
Figs. S1 to S42
Tables S1 to S4
References (37–51)

25 August 2017; accepted 1 December 2017
10.1126/science.aap7778

Cite as: Y. Kim and J. Chen, *Science* 10.1126/science.aar7389 (2018).

Molecular structure of human P-glycoprotein in the ATP-bound, outward-facing conformation

Youngjin Kim and Jue Chen*

Howard Hughes Medical Institute, The Rockefeller University, 1230 York Avenue, New York, NY 10065, USA.

*Corresponding author. Email: juechen@rockefeller.edu

The multidrug transporter P-glycoprotein is an ATP-binding cassette exporter responsible for clinical resistance to chemotherapy. P-glycoprotein extrudes toxic molecules and drugs from cells through ATP-powered conformational changes. Despite decades of effort, only the structures of the inward-facing conformation of P-glycoprotein are available. Here we present the structure of human P-glycoprotein in the outward-facing conformation, determined by electron cryo-microscopy at 3.4-Å resolution. The two nucleotide-binding domains form a closed dimer occluding two ATP molecules. The drug-binding cavity observed in the inward-facing structures is re-orientated toward the extracellular space and compressed to preclude substrate binding. This observation indicates that ATP binding, not hydrolysis, promotes substrate release. The structure evokes a model in which the dynamic nature of P-glycoprotein enables translocation of a large variety of substrates.

Cancer cells develop resistance to chemically diverse compounds, a phenomenon known as multidrug resistance (MDR). In order to improve the effectiveness of chemotherapy, many laboratories have searched for mechanisms that account for MDR. In 1973, Keld Danø demonstrated that the reduced drug accumulation in tumor cells was energy-dependent (1). In 1976, by labeling cell-surface carbohydrates, Juliano and Ling identified a glycoprotein enriched in colchicine-resistant cells but not in wild-type cells (2). The protein was named the Permeability(P)-glycoprotein" (Pgp) because it was thought to confer drug resistance by making the cellular membrane less permeable (3). Ten years later, the genes responsible for MDR in human, mouse, and hamster (named MDR genes) were cloned (4–6) and it was shown that the protein product of the *mdr1* gene was indeed Pgp (7).

Pgp is an ATP-binding cassette (ABC) transporter, using the energy from ATP hydrolysis to pump substrates across the membrane. It contains two transmembrane domains (TMDs) and two cytoplasmic nucleotide-binding domains (NBDs) (Fig. 1A). Pgp is expressed in many membrane "barriers" of the body, including the blood-brain barrier, gastrointestinal tract, kidney, liver, ovary, and the placenta (2, 8–11). Thus, the physiological function of Pgp is likely to protect sensitive tissues and the fetus from endogenous and exogenous toxicity (12). More than 300 compounds have been identified as potential substrates of Pgp (13, 14). Drug resistance mediated by Pgp depends on ATP hydrolysis (15–17), and the ATPase activity of Pgp is stimulated by the transported drugs (18–20). Vanadate trapping and photo-cleavage experiments showed that Pgp contains two active ATPase sites, but only one ATP is hydrolyzed at a time (21).

The molecular structures of Pgp in a transport cycle have been investigated using a variety of methods, including antibody binding (22), tryptophan fluorescence (23), luminescence (24), double electron-electron resonance (DEER) (25), electron microscopy (26, 27), and X-ray crystallography (28–31). Although the crystal structures of Pgp have been determined for the mouse (28, 29), *C. elegans* (30), and *Cyanidioschyzon merolae* (31) orthologs, all of these structures exhibit a similar conformation, in which the two NBDs are separated from each other and the translocation pathway is accessible from inside the cell (i.e., the inward-facing conformation). To reveal conformational changes that enable substrate translocation, we pursued the structure of human Pgp in an ATP-bound, outward-facing conformation.

Pgp contains two active ATPase sites, each comprising the Walker A/B motifs of one NBD and the LSGQQ motif of the other NBD. At each ATPase site, a highly conserved glutamate residue acts as the catalytic base for ATP hydrolysis. Mutating either catalytic glutamate severely reduces ATPase activity; concurrent mutations at both positions trap Pgp in an ATP-occluded form, likely with a closed-NBD dimer (32–34). Based on these data, we generated a mutant of Pgp in which both catalytic glutamates were replaced by glutamines (E556Q/E1201Q). Compared to the wild-type (*wt*) protein, whose ATPase activity increases as a function of ATP concentration and is stimulated by the substrate vinblastine, the E556Q/E1201Q mutant remains inactive over a large range of ATP and vinblastine concentrations (Fig. 1, B and C).

For cryo-EM studies, the mutant protein was incubated with 150 μM vinblastine and 10 mM Mg²⁺/ATP to promote ATP occlusion (32–34). A cryo-EM dataset consisting of

~1 million particles was collected and analyzed for structural homogeneity. Three-dimensional classification using Relion (35) showed that the majority of the particles exhibited an NBD-dimerized conformation (fig. S1). Refinement of the best class produced a map at 3.4 Å resolution (figs. S1 and S2), which enabled us to build a nearly complete model of Pgp except for the two termini and residues 81–104 and 631 to 694, which form an extracellular loop and intracellular linker, respectively (fig. S3).

The overall structure of human Pgp is substantially different from the previously determined inward-facing conformations (Fig. 1D). Instead of enclosing an internal cavity, the TM helices pack closely in the membrane inner leaflet. The two cytosolic NBDs make extensive contacts with each other, forming the typical “head-to-tail” dimer characteristic of ABC transporters (Fig. 2A). Two ATP molecules are bound at the dimer interface, interacting with the Walker A motif of one NBD, the ABC signature motif of the other NBD (Figs. 1D and 2). This structure, largely consistent with what is expected of an outward-facing conformation, also reveals several unanticipated features that advance our understanding of the transport cycle.

Biochemical studies have shown that mouse Pgp containing alanine substitutions of both catalytic glutamates occludes maximally a single ATP (32, 36). Nucleotide trapping by Vi or BeFx also occurs at only one of the two catalytic sites (37, 38). This suggests structural asymmetry of the two ATPase sites in the outward-facing conformation. However, the structures of the two NBDs are nearly identical (superposition of all 246 C α atoms in the NBDs yields a root-mean-square deviation (RMSD) of 0.5 Å) (fig. S4A). Furthermore, the cryo-EM densities for both ATPs are equally strong and the ATP molecules make very similar contacts with nearby residues (Fig. 2B and fig. S4B).

The conserved glutamine in the Q loop is one of the most-studied residues in Pgp (Q475 in NBD1 and Q1118 in NBD2). Mutating the Q loop in mouse and human Pgp reduced—and in the case of the double mutants abolished—both ATPase and drug transporter activity (42–45). Puzzlingly, though, linking the two TMDs together with a flexible cross-linker restores the ATPase activity of the double Q-to-A mutant (45). It is debated whether the function of the Q loop is to coordinate the Mg²⁺ ion for ATP hydrolysis, to communicate the chemistry at the ATPase sites to conformational changes in the TMDs, or to facilitate formation of the NBD-closed conformation (42–45). The structure of Pgp indicates that the Q loop is critically positioned to perform all three tasks (Fig. 2, A and C). In both NBDs, the Q loop is part of the interface between NBD and TMD, interacting with the coupling helices IH2 and IH4 (fig. S4C). They also contribute to the closed NBD-dimer interface by directly contacting the opposite NBD. Furthermore, Q475 and Q1118 reach into the ATP binding sites, coordinating the Mg²⁺ ions and the γ -phosphate of ATP making van der Waals contacts with the ABC Signature motif of the opposite NBD (Fig. 2, A and C). Substitutions of the Q loop Q may disturb the precise geometry of the ATPase site necessary for hydrolysis and destabilize the NBD dimer. Bringing the two TMDs closer could compensate for the latter effect, thus explaining why the cross-linker restores the activity of the double Q-to-A mutant (45).

The drug-binding cavity observed in the inward-facing structures is altered completely upon NBD dimerization (Fig. 3, A and B): Only a small opening is observed at the extracellular side of the membrane. Drug-binding residues, distributed on the surface of the inward-facing cavity, are reoriented toward the extracellular space. Although vinblastine was included in the sample at a concentration 5-fold higher than the apparent Km (Fig. 1B), no density corresponding to vinblastine was observed. This observation is consistent with biochemical data demonstrating that Pgp has a lower drug affinity in the presence of ATP (46–50). Recent experiments carried out in native membranes show that binding of the non-hydrolyzable ATP analog AMP-PMP is sufficient to induce drug release (51). Thus, it is likely that the cryo-EM structure represents a post-translocation state in which the substrate has already been released to the extracellular side of the membrane.

The extracellular segments of the TMDs have relatively less-defined EM densities and higher B factors (fig. S3 and Fig. 3C), indicating that these regions are flexible. Independently, DEER measurements of the outward-facing state showed that distances measured between pairs of residues in the extracellular side of the TMDs were distributed over a

broad range instead of a single population, indicating the presence of multiple conformations (25). As Pgp is a promiscuous transporter interacting with a large variety of compounds, the intrinsic flexibility of the extracellular segments enables prompt closure of the outward-facing cavity, thereby preventing reentry of the substrate or other compounds into the translocation pathway.

As illustrated in Fig. 4A, the structures of various Pgp orthologs determined in the absence of ATP have a similar inward-facing architecture. Transition from the inward- to the outward-facing conformation involves global movement of the two halves of the molecule as well as extensive local rearrangements of TM helices (Fig. 4). The two “crossing” helices in each TMD (TM 4-5 in TMD1 and TM 10-11 in TMD2) pivot inward, bringing the NBDs closer to each other (Fig. 4A). In addition, the extracellular regions of TM 7 and 8 pull away from TM 9-12, resulting in an outward-facing configuration (Fig. 4A).

A prominent local conformational change occurs in helices flanking the lateral opening to the membrane inner leaflet (Fig. 4B). In the inward-facing conformation, these helices are interrupted by flexible loops (Fig. 4B) (30, 31). Mutations of *Cyanidioschyzon merolae* Pgp (*cmPgp*) that changed a disordered loop in TM4 into a continuous helix also diminished transport activity (31), underscoring the functional importance of the helix breakers. In the crystal structure of *C. elegans* Pgp two maltoside detergent molecules are observed at the lateral opening (Fig. 4B), suggesting that these loops function as binding sites for substrates or flexible hinges to gate the drug-translocation pathway (31). In the outward-facing conformation, however, both TM4 and TM10 are continuous helices (Fig. 4, A and B). The continuity of these helices is important to completely close the intracellular gate upon NBD dimerization, avoiding potential leakage in the outward-facing state.

Another observation revealed in our analysis is that the NBD/TMD interfaces are largely unchanged during the switch from the inward- to outward-facing conformation (Fig. 4C). The NBD/TMD interface is important in transmitting conformational changes associated with ATP hydrolysis to substrate translocation. Multiple structures of the maltose importer show that the coupling helix rotates relative to the NBDs during a transport cycle (52). In contrast, the equivalent interfaces in Pgp (NBD1/IH4 and NBD2/IH2) are maintained in the two different conformations (Fig. 4C). Only small movements are observed for IH1 and IH3, as these regions engage additional contacts with the opposite NBD upon dimerization. Similarly, analysis of different inward-facing Pgp structures show that the NDB/TMD interface is largely unchanged (28), suggesting that the NBD and the intracellular helical region of TMD move as one concerted rigid body in the transport cycle.

The structure of the human Pgp determined in this study is stabilized by mutations that prevent ATP hydrolysis, which suggests it likely corresponds to a state that occurs after NBD dimerization but before ATP has been hydrolyzed. The observations that the drug-binding site is collapsed and the substrate is absent in this conformation suggest that substrate release occurs prior to ATP hydrolysis. Incorporating this information into the large body of data on Pgp, we hypothesize a model in which the unusually dynamic nature of Pgp enables unidirectional transport of a broad range of substrates (fig. S5). In a transport cycle, Pgp isomerizes between two basic states: an inward-facing state where NBDs are separated and an outward-facing state where NBDs are dimerized. In the inward-facing state, the two halves of Pgp pivot to modulate the drug-binding cavity, thereby enabling Pgp to recruit substrates of different sizes. Local conformational flexibility around the lateral gate further facilitates substrate entry from the inner leaflet of the membrane. Upon ATP binding, the transporter isomerizes to the outward-facing state and the drug-binding site is rearranged so that its affinity for the substrate is lower than in the inward-facing state. The outer leaflet regions of the TM helices are flexible, allowing substrate release and subsequent closure of the translocation pathway. In the outward-facing conformation two ATP molecules are bound to stabilize the NBD dimer. Subsequent ATP hydrolysis, which may occur at only one of the two catalytic sites stochastically (i.e., if two ATP molecules are required to hold the NBDs together), resets the transporter to the inward-facing state.

REFERENCES AND NOTES

1. K. Danø, Active outward transport of daunomycin in resistant Ehrlich ascites tumor cells. *Biochim. Biophys. Acta* **323**, 466–483 (1973). [doi:10.1016/0005-2736\(73\)90191-0](https://doi.org/10.1016/0005-2736(73)90191-0) [Medline](#)
2. R. L. Juliano, V. Ling, A surface glycoprotein modulating drug permeability in Chinese hamster ovary cell mutants. *Biochim. Biophys. Acta* **455**, 152–162 (1976). [doi:10.1016/0005-2736\(76\)90160-7](https://doi.org/10.1016/0005-2736(76)90160-7) [Medline](#)
3. M. M. Gottesman, V. Ling, The molecular basis of multidrug resistance in cancer: The early years of P-glycoprotein research. *FEBS Lett.* **580**, 998–1009 (2006). [doi:10.1016/j.febslet.2005.12.060](https://doi.org/10.1016/j.febslet.2005.12.060) [Medline](#)
4. I. B. Roninson, H. T. Abelson, D. E. Housman, N. Howell, A. Varshavsky, Amplification of specific DNA sequences correlates with multi-drug resistance in Chinese hamster cells. *Nature* **309**, 626–628 (1984). [doi:10.1038/309626a0](https://doi.org/10.1038/309626a0) [Medline](#)
5. I. B. Roninson, J. E. Chin, K. G. Choi, P. Gros, D. E. Housman, A. Fojo, D. W. Shen, M. M. Gottesman, I. Pastan, Isolation of human *mdr* DNA sequences amplified in multidrug-resistant KB carcinoma cells. *Proc. Natl. Acad. Sci. U.S.A.* **83**, 4538–4542 (1986). [doi:10.1073/pnas.83.12.4538](https://doi.org/10.1073/pnas.83.12.4538) [Medline](#)
6. D. W. Shen, A. Fojo, J. E. Chin, I. B. Roninson, N. Richert, I. Pastan, M. M. Gottesman, Human multidrug-resistant cell lines: Increased *mdr1* expression can precede gene amplification. *Science* **232**, 643–645 (1986). [doi:10.1126/science.3457471](https://doi.org/10.1126/science.3457471) [Medline](#)
7. K. Ueda, M. M. Cornwell, M. M. Gottesman, I. Pastan, I. B. Roninson, V. Ling, J. R. Riordan, The *mdr1* gene, responsible for multidrug-resistance, codes for P-glycoprotein. *Biochem. Biophys. Res. Commun.* **141**, 956–962 (1986). [doi:10.1016/S0006-291X\(86\)80136-X](https://doi.org/10.1016/S0006-291X(86)80136-X) [Medline](#)
8. F. Thiebaut, T. Tsuruo, H. Hamada, M. M. Gottesman, I. Pastan, M. C. Willingham, Cellular localization of the multidrug-resistance gene product P-glycoprotein in

normal human tissues. *Proc. Natl. Acad. Sci. U.S.A.* **84**, 7735–7738 (1987). [doi:10.1073/pnas.84.21.7735](https://doi.org/10.1073/pnas.84.21.7735) [Medline](#)

9. J. Lotsch, C. Skarke, I. Tegeder, G. Geisslinger, Drug interactions with patient-controlled analgesia. *Clin. Pharmacokinet.* **41**, 31–57 (2002). [doi:10.2165/00003088-200241010-00004](https://doi.org/10.2165/00003088-200241010-00004) [Medline](#)

10. N. Mizuno, T. Niwa, Y. Yotsumoto, Y. Sugiyama, Impact of drug transporter studies on drug discovery and development. *Pharmacol. Rev.* **55**, 425–461 (2003). [doi:10.1124/pr.55.3.1](https://doi.org/10.1124/pr.55.3.1) [Medline](#)

11. J. Sun, Z. G. He, G. Cheng, S. J. Wang, X. H. Hao, M. J. Zou, Multidrug resistance P-glycoprotein: Crucial significance in drug disposition and interaction. *Med. Sci. Monit.* **10**, RA5–RA14 (2004). [Medline](#)

12. A. H. Schinkel, J. J. M. Smit, O. van Tellingen, J. H. Beijnen, E. Wagenaar, L. van Deemter, C. A. A. M. Mol, M. A. van der Valk, E. C. Robanus-Maandag, H. P. J. te Riele, A. J. M. Berns, P. Borst, Disruption of the mouse *mdr1a* P-glycoprotein gene leads to a deficiency in the blood-brain barrier and to increased sensitivity to drugs. *Cell* **77**, 491–502 (1994). [doi:10.1016/0092-8674\(94\)90212-7](https://doi.org/10.1016/0092-8674(94)90212-7) [Medline](#)

13. Z. Wang, Y. Chen, H. Liang, A. Bender, R. C. Glen, A. Yan, P-glycoprotein substrate models using support vector machines based on a comprehensive data set. *J. Chem. Inf. Model.* **51**, 1447–1456 (2011). [doi:10.1021/ci2001583](https://doi.org/10.1021/ci2001583) [Medline](#)

14. L. Chen, Y. Li, H. Yu, L. Zhang, T. Hou, Computational models for predicting substrates or inhibitors of P-glycoprotein. *Drug Discov. Today* **17**, 343–351 (2012). [doi:10.1016/j.drudis.2011.11.003](https://doi.org/10.1016/j.drudis.2011.11.003) [Medline](#)

15. M. Azzaria, E. Schurr, P. Gros, Discrete mutations introduced in the predicted nucleotide-binding sites of the *mdr1* gene abolish its ability to confer multidrug resistance. *Mol. Cell. Biol.* **9**, 5289–5297 (1989). [doi:10.1128/MCB.9.12.5289](https://doi.org/10.1128/MCB.9.12.5289) [Medline](#)

16. H. Hamada, T. Tsuruo, Purification of the 170- to 180-kilodalton membrane glycoprotein associated with multidrug resistance. 170- to 180-kilodalton membrane glycoprotein is an ATPase. *J. Biol. Chem.* **263**, 1454–1458 (1988). [Medline](#)

17. H. Hamada, T. Tsuruo, Characterization of the ATPase activity of the M_r 170,000 to 180,000 membrane glycoprotein (P-glycoprotein) associated with multidrug resistance in K562/ADM cells. *Cancer Res.* **48**, 4926–4932 (1988). [Medline](#)

18. M. K. al-Shawi, A. E. Senior, Characterization of the adenosine triphosphatase activity of Chinese hamster P-glycoprotein. *J. Biol. Chem.* **268**, 4197–4206 (1993). [Medline](#)

19. S. V. Ambudkar, Drug-stimulatable ATPase activity in crude membranes of human *MDR1*-transfected mammalian cells. *Methods Enzymol.* **292**, 504–514 (1998). [doi:10.1016/S0076-6879\(98\)92039-0](https://doi.org/10.1016/S0076-6879(98)92039-0) [Medline](#)

20. B. Sarkadi, E. M. Price, R. C. Boucher, U. A. Germann, G. A. Scarborough, Expression of the human multidrug resistance cDNA in insect cells generates a high activity drug-stimulated membrane ATPase. *J. Biol. Chem.* **267**, 4854–4858 (1992). [Medline](#)

21. C. A. Hrycyna, M. Ramachandra, S. V. Ambudkar, Y. H. Ko, P. L. Pedersen, I. Pastan, M. M. Gottesman, Mechanism of action of human P-glycoprotein ATPase activity. Photochemical cleavage during a catalytic transition state using orthovanadate reveals cross-talk between the two ATP sites. *J. Biol. Chem.* **273**, 16631–16634 (1998). [doi:10.1074/jbc.273.27.16631](https://doi.org/10.1074/jbc.273.27.16631) [Medline](#)

22. E. B. Mechetner, B. Schott, B. S. Morse, W. D. Stein, T. Druley, K. A. Davis, T. Tsuruo, I. B. Roninson, P-glycoprotein function involves conformational transitions detectable by differential immunoreactivity. *Proc. Natl. Acad. Sci. U.S.A.* **94**, 12908–12913 (1997). [doi:10.1073/pnas.94.24.12908](https://doi.org/10.1073/pnas.94.24.12908) [Medline](#)

23. N. Sonveaux, C. Vigano, A. B. Shapiro, V. Ling, J. M. Ruysschaert, Ligand-mediated tertiary structure changes of reconstituted P-glycoprotein. A tryptophan fluorescence quenching analysis. *J. Biol. Chem.* **274**, 17649–17654 (1999). [doi:10.1074/jbc.274.25.17649](https://doi.org/10.1074/jbc.274.25.17649) [Medline](#)

24. M. E. Zoghbi, L. Mok, D. J. Swartz, A. Singh, G. A. Fendley, I. L. Urbatsch, G. A. Altenberg, Substrate-induced conformational changes in the nucleotide-binding domains of lipid bilayer-associated P-glycoprotein during ATP hydrolysis. *J. Biol. Chem.* **292**, 20412–20424 (2017). [doi:10.1074/jbc.M117.814186](https://doi.org/10.1074/jbc.M117.814186) [Medline](#)

25. B. Verhalen, R. Dastvan, S. Thangapandian, Y. Peskova, H. A. Koteiche, R. K. Nakamoto, E. Tajkhorshid, H. S. Mchaourab, Energy transduction and alternating access of the mammalian ABC transporter P-glycoprotein. *Nature* **543**, 738–741 (2017). [doi:10.1038/nature21414](https://doi.org/10.1038/nature21414) [Medline](#)

26. A. Moeller, S. C. Lee, H. Tao, J. A. Speir, G. Chang, I. L. Urbatsch, C. S. Potter, B. Carragher, Q. Zhang, Distinct conformational spectrum of homologous multidrug ABC transporters. *Structure* **23**, 450–460 (2015). [doi:10.1016/j.str.2014.12.013](https://doi.org/10.1016/j.str.2014.12.013) [Medline](#)

27. G. A. Frank, S. Shukla, P. Rao, M. J. Borgnia, A. Bartesaghi, A. Merk, A. Mobin, L. Esser, L. A. Earl, M. M. Gottesman, D. Xia, S. V. Ambudkar, S. Subramanian, Cryo-EM analysis of the conformational landscape of human P-glycoprotein (ABCB1) during its catalytic cycle. *Mol. Pharmacol.* **90**, 35–41 (2016). [doi:10.1124/mol.116.104190](https://doi.org/10.1124/mol.116.104190) [Medline](#)

28. L. Esser, F. Zhou, K. M. Pluchino, J. Shiloach, J. Ma, W. K. Tang, C. Gutierrez, A. Zhang, S. Shukla, J. P. Madigan, T. Zhou, P. D. Kwong, S. V. Ambudkar, M. M. Gottesman, D. Xia, Structures of the multidrug transporter P-glycoprotein reveal asymmetric ATP binding and the mechanism of polyspecificity. *J. Biol. Chem.* **292**, 446–461 (2017). [doi:10.1074/jbc.M116.755884](https://doi.org/10.1074/jbc.M116.755884) [Medline](#)

29. S. G. Aller, J. Yu, A. Ward, Y. Weng, S. Chittaboina, R. Zhuo, P. M. Harrell, Y. T. Trinh, Q. Zhang, I. L. Urbatsch, G. Chang, Structure of P-glycoprotein reveals a molecular basis for poly-specific drug binding. *Science* **323**, 1718–1722 (2009). [doi:10.1126/science.1168750](https://doi.org/10.1126/science.1168750) [Medline](#)

30. M. S. Jin, M. L. Oldham, Q. Zhang, J. Chen, Crystal structure of the multidrug transporter P-glycoprotein from *Caenorhabditis elegans*. *Nature* **490**, 566–569 (2012). [doi:10.1038/nature11448](https://doi.org/10.1038/nature11448) [Medline](#)

31. A. Kodan, T. Yamaguchi, T. Nakatsu, K. Sakiyama, C. J. Hipolito, A. Fujioka, R. Hirokane, K. Ikeguchi, B. Watanabe, J. Hiratake, Y. Kimura, H. Suga, K. Ueda, H. Kato, Structural basis for gating mechanisms of a eukaryotic P-glycoprotein homolog. *Proc. Natl. Acad. Sci. U.S.A.* **111**, 4049–4054 (2014). [doi:10.1073/pnas.1321562111](https://doi.org/10.1073/pnas.1321562111) [Medline](#)

32. G. Tomblin, L. A. Bartholomew, I. L. Urbatsch, A. E. Senior, Combined mutation of catalytic glutamate residues in the two nucleotide binding domains of P-glycoprotein generates a conformation that binds ATP and ADP tightly. *J. Biol. Chem.* **279**, 31212–31220 (2004). [doi:10.1074/jbc.M404689200](https://doi.org/10.1074/jbc.M404689200) [Medline](#)

33. G. Tomblin, A. Muharemagić, L. B. White, A. E. Senior, Involvement of the “occluded nucleotide conformation” of P-glycoprotein in the catalytic pathway. *Biochemistry* **44**, 12879–12886 (2005). [doi:10.1021/bi0509797](https://doi.org/10.1021/bi0509797) [Medline](#)

34. I. Carrier, P. Gros, Investigating the role of the invariant carboxylate residues E552 and E1197 in the catalytic activity of Abcb1a (mouse Mdr3). *FEBS J.* **275**, 3312–3324 (2008). [doi:10.1111/j.1742-4658.2008.06479.x](https://doi.org/10.1111/j.1742-4658.2008.06479.x) [Medline](#)

35. S. H. Scheres, RELION: Implementation of a Bayesian approach to cryo-EM structure determination. *J. Struct. Biol.* **180**, 519–530 (2012). [doi:10.1016/j.jsb.2012.09.006](https://doi.org/10.1016/j.jsb.2012.09.006) [Medline](#)

36. G. Tomblin, L. A. Bartholomew, G. A. Tyndall, K. Gim, I. L. Urbatsch, A. E. Senior, Properties of P-glycoprotein with mutations in the “catalytic carboxylate” glutamate residues. *J. Biol. Chem.* **279**, 46518–46526 (2004). [doi:10.1074/jbc.M408052200](https://doi.org/10.1074/jbc.M408052200) [Medline](#)

37. B. Sankaran, S. Bhagat, A. E. Senior, Inhibition of P-glycoprotein ATPase activity by beryllium fluoride. *Biochemistry* **36**, 6847–6853 (1997). [doi:10.1021/bi970034s](https://doi.org/10.1021/bi970034s) [Medline](#)

38. I. L. Urbatsch, B. Sankaran, J. Weber, A. E. Senior, P-glycoprotein is stably inhibited by vanadate-induced trapping of nucleotide at a single catalytic site. *J. Biol. Chem.* **270**, 19383–19390 (1995). [doi:10.1074/jbc.270.33.19383](https://doi.org/10.1074/jbc.270.33.19383) [Medline](#)

39. F. J. Sharom, X. Yu, J. W. Chu, C. A. Doige, Characterization of the ATPase activity of P-glycoprotein from multidrug-resistant Chinese hamster ovary cells. *Biochem. J.* **308**, 381–390 (1995). [doi:10.1042/bj3080381](https://doi.org/10.1042/bj3080381) [Medline](#)

40. S. V. Ambudkar, I. H. Lelong, J. Zhang, C. O. Cardarelli, M. M. Gottesman, I. Pastan, Partial purification and reconstitution of the human multidrug-resistance pump: Characterization of the drug-stimulatable ATP hydrolysis. *Proc. Natl. Acad. Sci. U.S.A.* **89**, 8472–8476 (1992). [doi:10.1073/pnas.89.18.8472](https://doi.org/10.1073/pnas.89.18.8472) [Medline](#)

41. K. M. Kerr, Z. E. Sauna, S. V. Ambudkar, Correlation between steady-state ATP hydrolysis and vanadate-induced ADP trapping in human P-glycoprotein. Evidence for ADP release as the rate-limiting step in the catalytic cycle and its modulation by substrates. *J. Biol. Chem.* **276**, 8657–8664 (2001). [doi:10.1074/jbc.M010044200](https://doi.org/10.1074/jbc.M010044200) [Medline](#)

42. I. L. Urbatsch, K. Gim, S. Wilke-Mounts, A. E. Senior, Investigation of the role of glutamine-471 and glutamine-1114 in the two catalytic sites of P-glycoprotein. *Biochemistry* **39**, 11921–11927 (2000). [doi:10.1021/bi001220s](https://doi.org/10.1021/bi001220s) [Medline](#)

43. J. K. Zolnerciks, C. Wooding, K. J. Linton, Evidence for a Sav1866-like architecture for the human multidrug transporter P-glycoprotein. *FASEB J.* **21**, 3937–3948

(2007). [doi:10.1096/fj.07-8610com](https://doi.org/10.1096/fj.07-8610com) Medline

44. J. K. Zolnerciks, B. G. Akkaya, M. Snippe, P. Chiba, A. Seelig, K. J. Linton, The Q loops of the human multidrug resistance transporter ABCB1 are necessary to couple drug binding to the ATP catalytic cycle. *FASEB J.* **28**, 4335–4346 (2014). [doi:10.1096/fj.13-245639](https://doi.org/10.1096/fj.13-245639) Medline

45. T. W. Loo, D. M. Clarke, Attachment of a ‘molecular spring’ restores drug-stimulated ATPase activity to P-glycoprotein lacking both Q loop glutamines. *Biochem. Biophys. Res. Commun.* **483**, 366–370 (2017). [doi:10.1016/j.bbrc.2016.12.137](https://doi.org/10.1016/j.bbrc.2016.12.137) Medline

46. C. F. Higgins, K. J. Linton, The ATP switch model for ABC transporters. *Nat. Struct. Mol. Biol.* **11**, 918–926 (2004). [doi:10.1038/nsmb836](https://doi.org/10.1038/nsmb836) Medline

47. C. Martin, G. Berridge, P. Mistry, C. Higgins, P. Charlton, R. Callaghan, Drug binding sites on P-glycoprotein are altered by ATP binding prior to nucleotide hydrolysis. *Biochemistry* **39**, 11901–11906 (2000). [doi:10.1021/bi000559b](https://doi.org/10.1021/bi000559b) Medline

48. M. F. Rosenberg, G. Velarde, R. C. Ford, C. Martin, G. Berridge, I. D. Kerr, R. Callaghan, A. Schmidlin, C. Wooding, K. J. Linton, C. F. Higgins, Repacking of the transmembrane domains of P-glycoprotein during the transport ATPase cycle. *EMBO J.* **20**, 5615–5625 (2001). [doi:10.1093/emboj/20.20.5615](https://doi.org/10.1093/emboj/20.20.5615) Medline

49. C. Martin, C. F. Higgins, R. Callaghan, The vinblastine binding site adopts high- and low-affinity conformations during a transport cycle of P-glycoprotein. *Biochemistry* **40**, 15733–15742 (2001). [doi:10.1021/bi01211z](https://doi.org/10.1021/bi01211z) Medline

50. Z. E. Sauna, I.-W. Kim, K. Nandigama, S. Kopp, P. Chiba, S. V. Ambudkar, Catalytic cycle of ATP hydrolysis by P-glycoprotein: Evidence for formation of the E-S reaction intermediate with ATP-γ-S, a nonhydrolyzable analogue of ATP. *Biochemistry* **46**, 13787–13799 (2007). [doi:10.1021/bi071385f](https://doi.org/10.1021/bi071385f) Medline

51. O. Bársony, G. Szalóki, D. Türk, S. Tarapcsák, Z. Gutay-Tóth, Z. Bacsó, I. J. Holb, L. Székvölgyi, G. Szabó, L. Csanády, G. Szakács, K. Goda, A single active catalytic site is sufficient to promote transport in P-glycoprotein. *Sci. Rep.* **6**, 24810 (2016). [doi:10.1038/srep24810](https://doi.org/10.1038/srep24810) Medline

52. D. Khare, M. L. Oldham, C. Orelle, A. L. Davidson, J. Chen, Alternating access in maltose transporter mediated by rigid-body rotations. *Mol. Cell* **33**, 528–536 (2009). [doi:10.1016/j.molcel.2009.01.035](https://doi.org/10.1016/j.molcel.2009.01.035) Medline

53. B. F. Scharschmidt, E. B. Keefe, N. M. Blankenship, R. K. Ockner, Validation of a recording spectrophotometric method for measurement of membrane-associated Mg- and NaK-ATPase activity. *J. Lab. Clin. Med.* **93**, 790–799 (1979). Medline

54. A. Rohou, N. Grigorieff, CTFFIND4: Fast and accurate defocus estimation from electron micrographs. *J. Struct. Biol.* **192**, 216–221 (2015). [doi:10.1016/j.jsb.2015.08.008](https://doi.org/10.1016/j.jsb.2015.08.008) Medline

55. T. Grant, N. Grigorieff, Measuring the optimal exposure for single particle cryo-EM using a 2.6 Å reconstruction of rotavirus VP6. *eLife* **4**, e06980 (2015). [doi:10.7554/eLife.06980](https://doi.org/10.7554/eLife.06980) Medline

56. J. L. Rubinstein, M. A. Brubaker, Alignment of cryo-EM movies of individual particles by optimization of image translations. *J. Struct. Biol.* **192**, 188–195 (2015). [doi:10.1016/j.jsb.2015.08.007](https://doi.org/10.1016/j.jsb.2015.08.007) Medline

57. A. Punjani, J. L. Rubinstein, D. J. Fleet, M. A. Brubaker, cryoSPARC: Algorithms for rapid unsupervised cryo-EM structure determination. *Nat. Methods* **14**, 290–296 (2017). [doi:10.1038/nmeth.4169](https://doi.org/10.1038/nmeth.4169) Medline

58. N. Grigorieff, Frealign: An exploratory tool for single-particle cryo-EM. *Methods Enzymol.* **579**, 191–226 (2016). [doi:10.1016/bs.mie.2016.04.013](https://doi.org/10.1016/bs.mie.2016.04.013) Medline

59. P. Emsley, K. Cowtan, Coot: Model-building tools for molecular graphics. *Acta Crystallogr. D Biol. Crystallogr.* **60**, 2126–2132 (2004). [doi:10.1107/S0907444904019158](https://doi.org/10.1107/S0907444904019158) Medline

60. M. D. Winn, C. C. Ballard, K. D. Cowtan, E. J. Dodson, P. Emsley, P. R. Evans, R. M. Keegan, E. B. Krissinel, A. G. W. Leslie, A. McCoy, S. J. McNicholas, G. N. Murshudov, N. S. Pannu, E. A. Potterton, H. R. Powell, R. J. Read, A. Vagin, K. S. Wilson, Overview of the CCP4 suite and current developments. *Acta Crystallogr. D Biol. Crystallogr.* **67**, 235–242 (2011). [doi:10.1107/S0907444910045749](https://doi.org/10.1107/S0907444910045749) Medline

61. P. E. Stein, A. Boodhoo, G. D. Armstrong, S. A. Cockle, M. H. Klein, R. J. Read, The crystal structure of pertussis toxin. *Structure* **2**, 45–57 (1994). [doi:10.1016/S0969-2126\(00\)00007-1](https://doi.org/10.1016/S0969-2126(00)00007-1) Medline

62. L. F. Ten Eyck, Efficient structure-factor calculation for large molecules by the fast Fourier transform. *Acta Crystallogr. A* **33**, 486–492 (1977). [doi:10.1107/S0567739477001211](https://doi.org/10.1107/S0567739477001211)

63. A. Brown, F. Long, R. A. Nicholls, J. Toots, P. Emsley, G. Murshudov, Tools for macromolecular model building and refinement into electron cryo-microscopy reconstructions. *Acta Crystallogr. D Biol. Crystallogr.* **71**, 136–153 (2015). [doi:10.1107/S1399004714021683](https://doi.org/10.1107/S1399004714021683) Medline

64. G. N. Murshudov, A. A. Vagin, E. J. Dodson, Refinement of macromolecular structures by the maximum-likelihood method. *Acta Crystallogr. D Biol. Crystallogr.* **53**, 240–255 (1997). [doi:10.1107/S090744496012255](https://doi.org/10.1107/S090744496012255) Medline

65. R. A. Nicholls, M. Fischer, S. McNicholas, G. N. Murshudov, Conformation-independent structural comparison of macromolecules with ProSMART. *Acta Crystallogr. D Biol. Crystallogr.* **70**, 2487–2499 (2014). [doi:10.1107/S1399004714016241](https://doi.org/10.1107/S1399004714016241) Medline

66. V. B. Chen, W. B. Arendall III, J. J. Headd, D. A. Keedy, R. M. Immormino, G. J. Kapral, L. W. Murray, J. S. Richardson, D. C. Richardson, MolProbity: All-atom structure validation for macromolecular crystallography. *Acta Crystallogr. D Biol. Crystallogr.* **66**, 12–21 (2010). [doi:10.1107/S0907444909042073](https://doi.org/10.1107/S0907444909042073) Medline

67. J. Frank, M. Radermacher, P. Penczek, J. Zhu, Y. Li, M. Ladjadj, A. Leith, SPIDER and WEB: Processing and visualization of images in 3D electron microscopy and related fields. *J. Struct. Biol.* **116**, 190–199 (1996). [doi:10.1006/jsb.1996.0030](https://doi.org/10.1006/jsb.1996.0030) Medline

68. C. V. Sindelar, N. Grigorieff, Optimal noise reduction in 3D reconstructions of single particles using a volume-normalized filter. *J. Struct. Biol.* **180**, 26–38 (2012). [doi:10.1016/j.jsb.2012.05.005](https://doi.org/10.1016/j.jsb.2012.05.005) Medline

69. E. F. Pettersen, T. D. Goddard, C. C. Huang, G. S. Couch, D. M. Greenblatt, E. C. Meng, T. E. Ferrin, UCSF Chimera—a visualization system for exploratory research and analysis. *J. Comput. Chem.* **25**, 1605–1612 (2004). [doi:10.1002/jcc.20084](https://doi.org/10.1002/jcc.20084) Medline

70. J. B. Heymann, D. M. Belnap, Bsoft: Image processing and molecular modeling for electron microscopy. *J. Struct. Biol.* **157**, 3–18 (2007). [doi:10.1016/j.jsb.2006.06.006](https://doi.org/10.1016/j.jsb.2006.06.006) Medline

ACKNOWLEDGMENTS

We would like to thank M. Ebrahim and J. Sotiris at Rockefeller’s Evelyn Gruss Lipper Cryo-Electron Microscopy Resource Center and Zhiheng Yu, Chuan Hong, and Rick Huang at the Janelia Farms Howard Hughes Medical Institute cryo-EM facility for assistance in data collection. We also thank Dr. Alan Senior for discussion and comments, Sarah McCarry for editing this manuscript, and Michael Oldham for helping with figures. **Funding:** J.C. is an investigator in the Howard Hughes Medical Institute. **Author contributions:** Y.K. performed all experiments. Y.K. and J.C. analyzed the structure and wrote the manuscript. **Competing interests:** The authors declare there are no competing interests. **Data and materials availability:** The cryo-EM density map and the atomic coordinates have been deposited in the EMDDataBank and the Protein Data Bank under accession codes EMD-7325 and 6COV, respectively. The expression vector, pEG BacMam, was provided by Dr. Eric Gouaux under a material transfer agreement with the Oregon Health & Science University. All other data are available in the manuscript or the Supplementary Materials.

SUPPLEMENTARY MATERIALS

www.scienmag.org/cgi/content/full/science.aar7389/DC1

Materials and Methods

Figs. S1 to S5

Table S1

References (53–70)

12 December 2017; accepted 16 January 2018

Published online 25 January 2018

10.1126/science.aar7389

Fig. 1. Characterization of recombinant human Pgp. (A) Topology diagram of Pgp. Residues not resolved in the structure are shown as dashed lines. (B) Vinblastine stimulates the ATPase activity of the wild type (WT) protein, but not the E556Q/E1201Q mutant (EQ). Data points represent the means \pm standard deviation of 3-9 measurements at 29°C. By nonlinear regression of the Michaelis-Menten equation, wt Pgp in DDM/CHS solution has a K_m of $30 \pm 3 \mu\text{M}$ for vinblastine and a maximal ATPase activity of $195 \pm 8 \text{ nmol/mg/min}$. (C) The ATPase activity as a function of ATP concentration. In the presence of 100 μM vinblastine, the wt protein has a K_m of $0.179 \pm 0.05 \text{ mM}$ for ATP and a maximal ATPase activity of $260 \pm 16 \text{ nmol/mg/min}$. (D) The overall structure of the E556Q/E1201Q Pgp in complex with ATP. The N-terminal half (TMD1 and NBD1) is colored in yellow and the C-terminal half (TMD2 and NBD2) in blue. ATP is shown in ball-and-stick format (yellow) and Mg^{2+} is shown as a sphere (magenta).

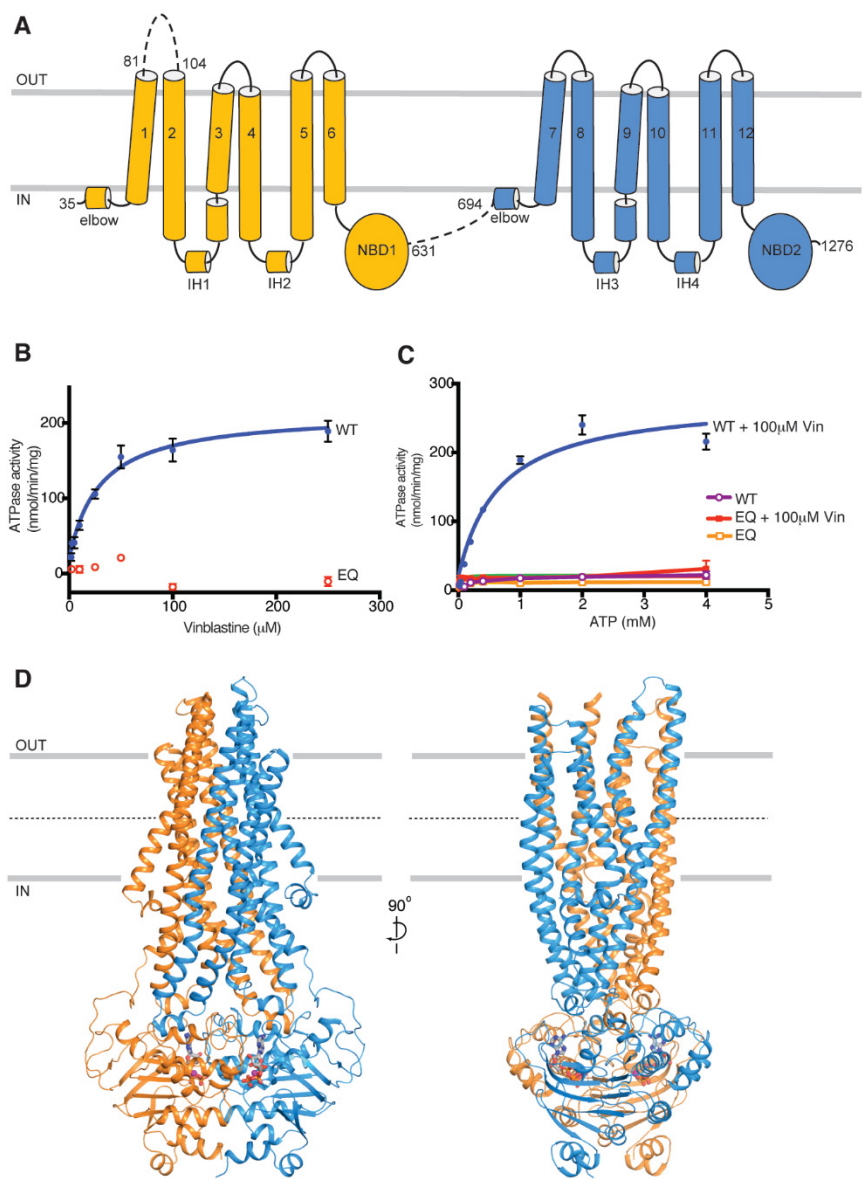


Fig. 2. Two symmetrical ATPase sites. (A) The Q loops (shown in blue) in the NBD dimer are positioned to interact with Mg^{2+} /ATP (magenta and yellow) and the TMDs through the two intracellular helices IH2 and IH4 (orange). The highly conserved glutamine residues (Q475 and Q1118) in the Q loops are indicated. (B) Molecular interactions at each ATPase site, together with density of Mg^{2+} -ATP (green mesh). (C) Zoom-in views of the Q loops. Interactions between the Q loop Q and Mg^{2+} /ATP are indicated by dashed lines.

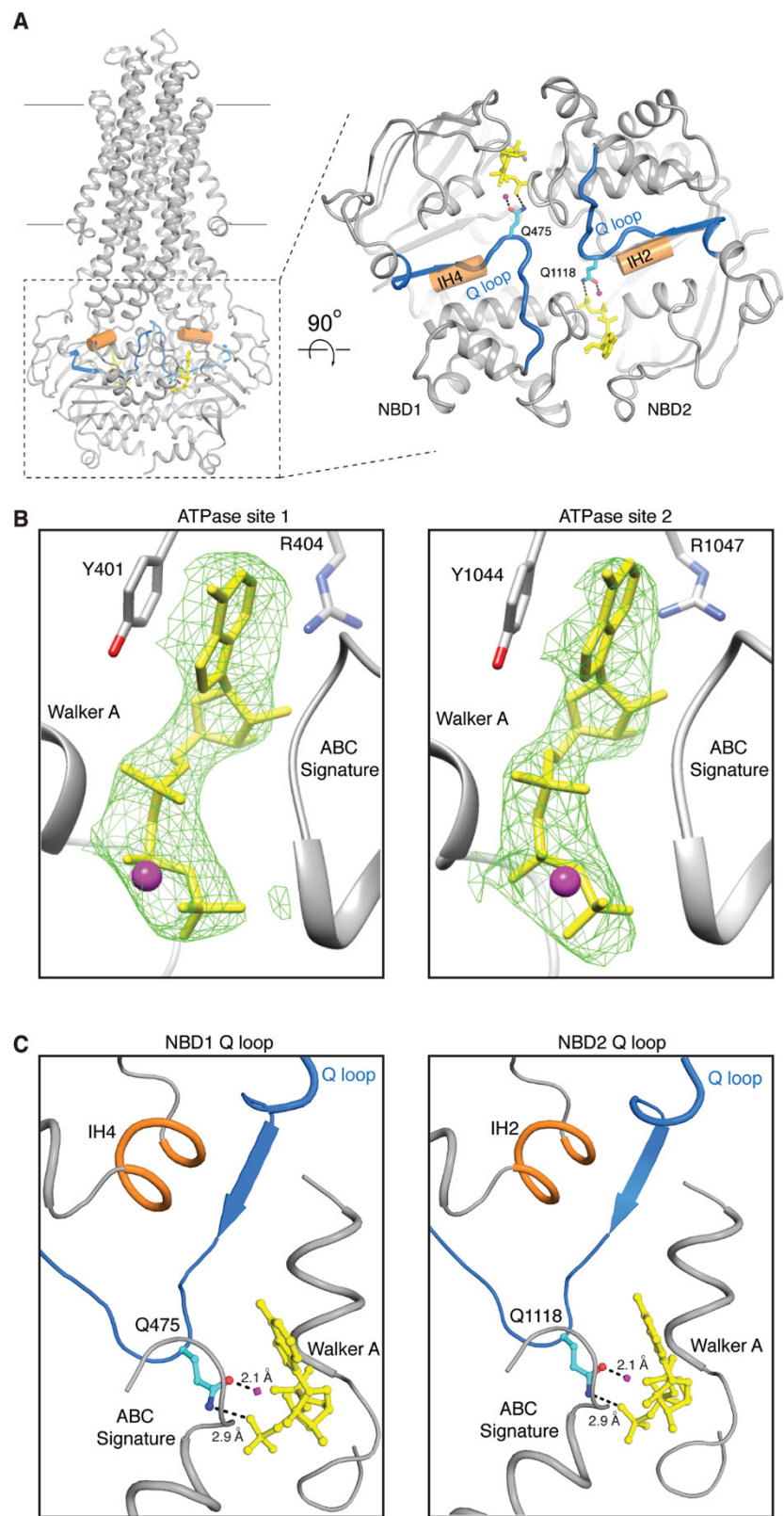


Fig. 3. The translocation pathway. (A) The inward-facing (PDB code 4F4C) and (B) the outward-facing (this study) conformations. The TM cavity is shown as a blue mesh. Drug-interacting residues, which were protected from inhibition in the presence of drugs, are labeled and shown as magenta balls. (C) B-factor distribution of human Pgp colored in rainbow. The extracellular region is relatively more flexible.

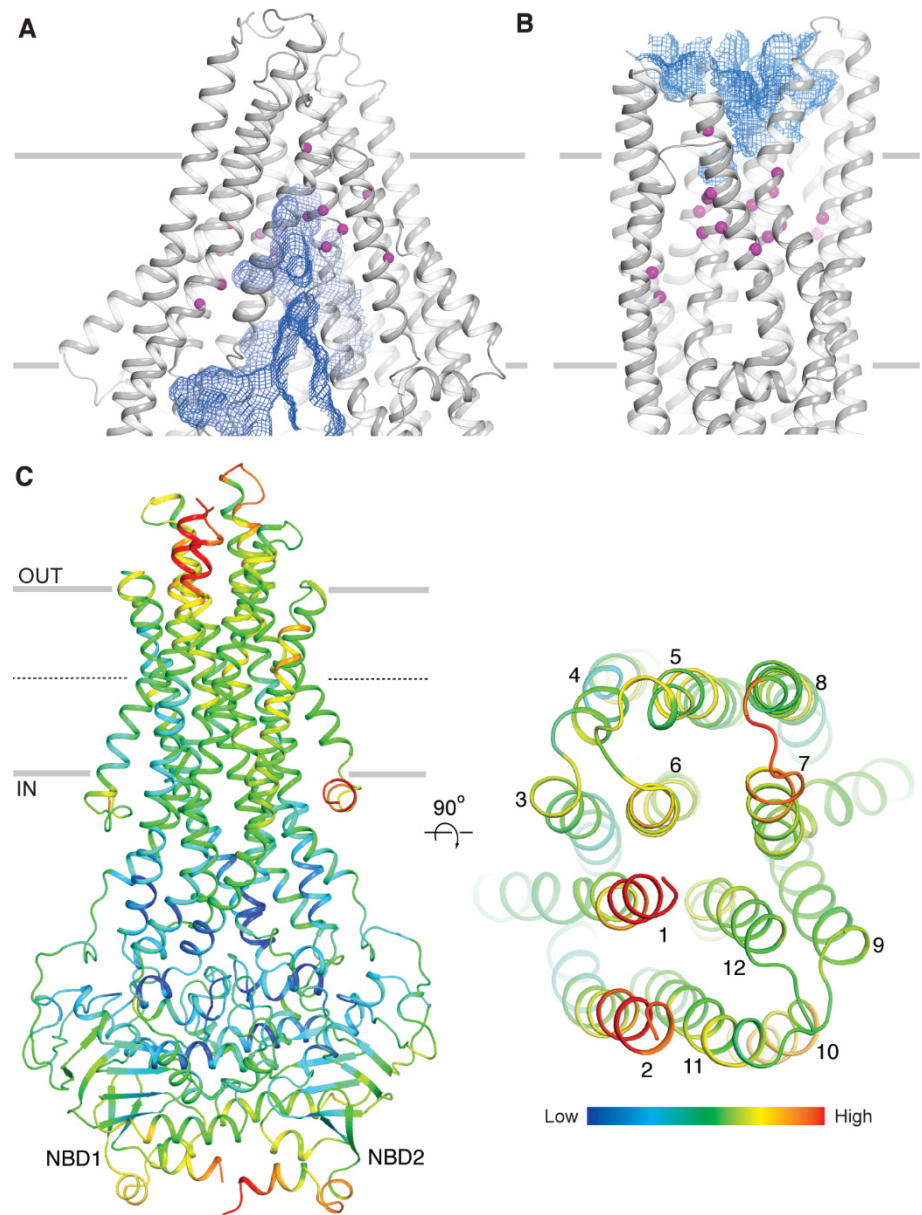
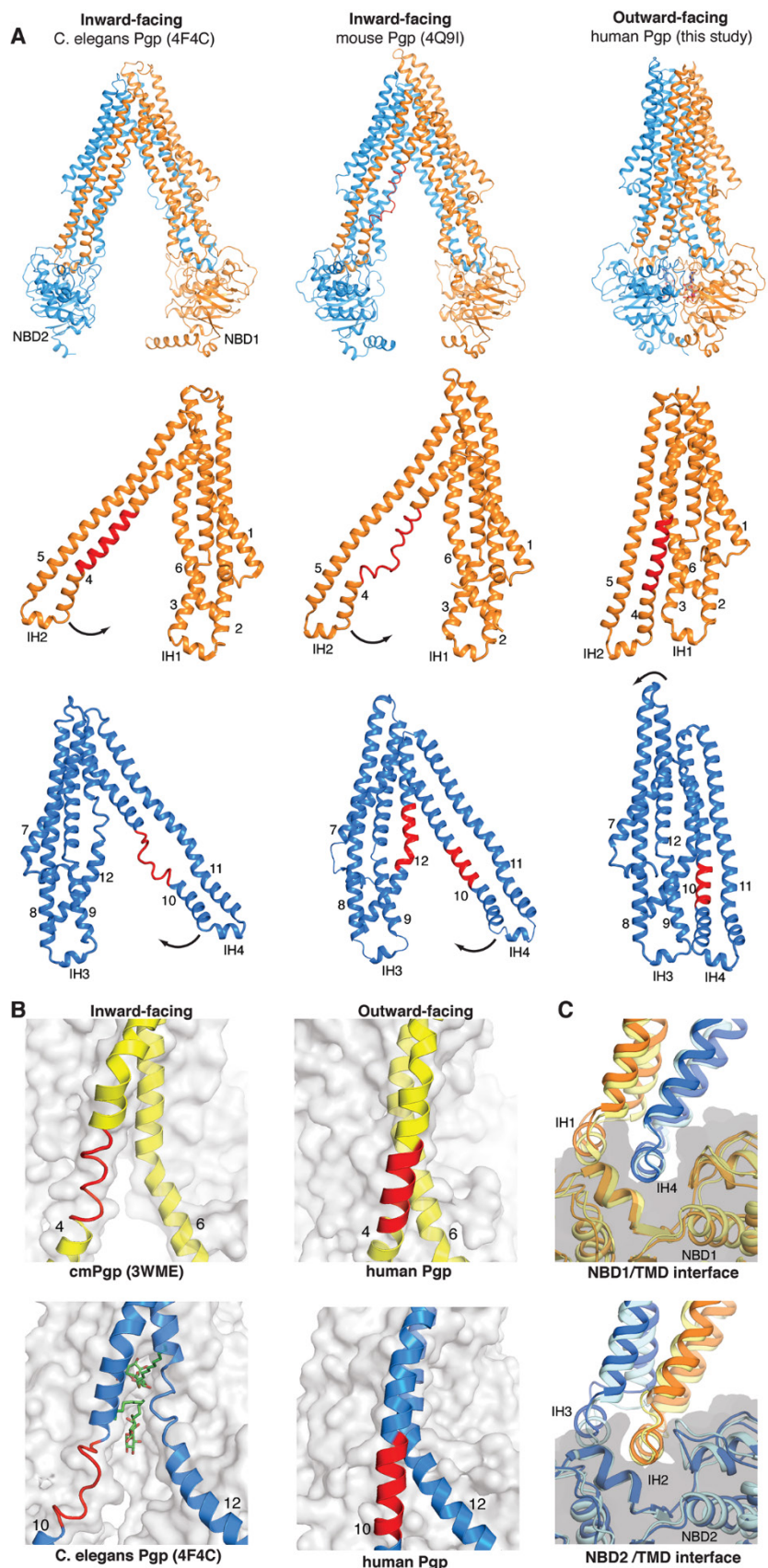


Fig. 4. Conformational changes of Pgp from inward- to outward-facing states. (A) Structures of two representative inward-facing Pgp and the outward-facing Pgp. The flexible regions in TM4 and TM1 are colored in red. Rotations of TM4-5 (yellow) and TM10-11 (blue) necessary for the transitions are indicated by black arrows. (B) Closure of the lateral opening and conformational changes of the flanking helices. Surface presentation of the TM region showing that loops in TM4 of cmPgp and TM10 of *C. elegans* Pgp are continuous helices in the outward-facing structure of human Pgp. Detergent molecules are shown as green/red sticks. (C) Few changes observed at the TMD/NBD interface. Structures of the inward-facing mouse Pgp (PDB code 5KPD) and the outward-facing human Pgp are superpositioned based on the NBDs. The two structures are differentiated by the shades (inward-facing, lighter; outward-facing, darker). The surface clefts into which the intracellular helices (IH2 and IH4) docked into are outlined in grey.



ORGANOID

Patient-derived organoids model treatment response of metastatic gastrointestinal cancers

Georgios Vlachogiannis,¹ Somaieh Hedayat,¹ Alexandra Vatsiou,² Yann Jamin,³ Javier Fernández-Mateos,^{1,2} Khurum Khan,^{1,4} Andrea Lampis,¹ Katherine Eason,¹ Ian Huntingford,¹ Rosemary Burke,⁵ Mihaela Rata,³ Dow-Mu Koh,^{3,6} Nina Tunariu,^{3,6} David Collins,³ Sanna Hulkki-Wilson,¹ Chanthirika Ragulan,¹ Inmaculada Spiteri,² Sing Yu Moorcraft,⁴ Ian Chau,⁴ Sheela Rao,⁴ David Watkins,⁴ Nicos Fotiadis,⁶ Maria Bali,^{3,6} Mahnaz Darvish-Damavandi,¹ Hazel Lote,^{1,4} Zakaria Eltahir,¹ Elizabeth C. Smyth,⁴ Ruwaida Begum,⁴ Paul A. Clarke,⁵ Jens C. Hahne,¹ Mitchell Dowsett,⁷ Johann de Bono,⁸ Paul Workman,⁵ Anguraj Sadanandam,¹ Matteo Fassan,⁹ Owen J. Sansom,¹⁰ Suzanne Eccles,⁵ Naureen Starling,⁴ Chiara Bracconi,^{4,5} Andrea Sottoriva,² Simon P. Robinson,³ David Cunningham,⁴ Nicola Valeri^{1,4*}

Patient-derived organoids (PDOs) have recently emerged as robust preclinical models; however, their potential to predict clinical outcomes in patients has remained unclear. We report on a living biobank of PDOs from metastatic, heavily pretreated colorectal and gastroesophageal cancer patients recruited in phase 1/2 clinical trials. Phenotypic and genotypic profiling of PDOs showed a high degree of similarity to the original patient tumors. Molecular profiling of tumor organoids was matched to drug-screening results, suggesting that PDOs could complement existing approaches in defining cancer vulnerabilities and improving treatment responses. We compared responses to anticancer agents *ex vivo* in organoids and PDO-based orthotopic mouse tumor xenograft models with the responses of the patients in clinical trials. Our data suggest that PDOs can recapitulate patient responses in the clinic and could be implemented in personalized medicine programs.

High-throughput sequencing has been extensively used in precision medicine to identify somatic mutations that can be exploited for cancer treatment and drug development (1). However, the limited role of genomic profiling in predicting response to targeted therapies and the limitations of pre-clinical models used for drug validation are important obstacles hampering the success of personalized medicine (2). Co-clinical trials are parallel studies in which drug responses in patients are matched to laboratory pre-clinical models to personalize treatment and understand mechanisms of chemosensitivity through functional genomics and reverse translation (3). Most co-clinical trials rely on the use of genetically

engineered mouse models or patient-derived xenografts, posing logistic, ethical, and economic issues (4).

LGR5⁺ stem cells can be isolated from a number of organs and propagated as epithelial organoids *in vitro* to study physiology and neoplastic transformation (5). Most studies on human colorectal cancer (CRC) organoids have been conducted on cultures derived from primary tumors (6). In contrast, examples of PDOs from metastatic cancer sites remain sparse (7–9). Furthermore, very limited evidence is available on the ability of PDOs to predict response to treatment in the clinic (10). Here we present a living biobank of PDOs from heavily pretreated metastatic gastrointestinal cancer patients and show examples of how the drug responses of these cancer organoids can be compared with those of the actual patient.

A total of 110 fresh biopsies from 71 patients enrolled in four prospective phase 1/2 clinical trials were processed between October 2014 and February 2017. In line with previous data (7), PDOs were grown from 70% of biopsies with a cellularity of 2+ and above, and their establishment rate strongly correlated with tumor cellularity in the parental biopsy (χ^2 test, $P < 0.0001$). No inverse correlation was observed between PDO establishment rate and presence of necrosis (cutoff $\geq 20\%$). Tumor percentage is a key limiting factor for genomic and transcriptomic analyses. When the 60% threshold used in large

sequencing studies of primary CRC (11) or gastroesophageal cancer (GOC) (12) was applied in our cohort, we found no correlation between PDO take-up rate and tumor percentage, suggesting that PDOs can also be established in cases of a low tumor/stroma ratio, thus allowing the *ex vivo* expansion of the cancer population in samples that would have otherwise failed quality-control tests for next-generation sequencing (NGS).

PDOs presented in this study were derived from ultrasound ($n = 20$), computed tomography (CT)-guided ($n = 7$), or endoscopic ($n = 2$) biopsies of metastatic CRC (mCRC; $n = 16$), metastatic GOC (mGOC; $n = 4$), and metastatic cholangiocarcinoma ($n = 1$) patients (fig. S1). Liver, pelvic, peritoneal, and nodal metastases of chemorefractory patients were used to establish PDOs. In several cases, PDOs were established from sequential biopsies at baseline (BL), at the time of best response [partial response (PR) or stable disease (SD)], and at the time of disease progression (PD), as well as from multiregion biopsies (table S1).

Histological evaluation revealed notable morphological similarities between PDOs and the patient biopsies from which they were originally derived (Fig. 1, A and B, and figs. S2A and S2B). Immunohistochemistry markers routinely used in the diagnosis of CRC (CDX-2 and CK7) showed that the parental tumor's expression pattern was maintained in PDOs, even when derived from sequential biopsies during treatment (fig. S2, C to E). Similarly, amplification of oncogenic drivers such as *ERBB2* (Fig. 1C and fig. S2F) and rearrangements in *FGFR2* (fig. S2G) were retained in PDOs from mGOC and metastatic cholangiocarcinoma, respectively.

NGS was used to profile 151 cancer-related genes in both PDOs ($n = 23$) and their parental biopsies; archival material from primary cancer or pretreatment diagnostic biopsies was also sequenced for eight patients, and whole-genome sequencing (WGS) was performed for one PDO (tables S2 and S3). The molecular landscape of our PDOs (Fig. 1D) largely overlapped with that reported for mCRC and mGOC in the MSK-IMPACT study (1), with the exception of *SRC* and *EGFR* amplifications and *ATM* and *BRCA2* mutations that were more frequent in our mCRC PDO cohort (table S4). Overall, a 96% overlap in mutational spectrum was observed between PDOs and their parental biopsies (Fig. 1D), whereas intratumor heterogeneity was observed between archival material (primary cancer) and metastatic deposits (biopsies or PDOs) (fig. S3A and table S2). PDOs were able to capture spatiotemporal intratumor heterogeneity when established from multiple biopsies at the time of disease progression and when compared with PDOs established at the beginning of treatment (Fig. 1D, fig. S3A, and table S2). Similar results were observed for copy number alterations (CNAs) in PDOs and biopsies collected at different time points during treatment (figs. S3B and S4). WGS confirmed CNAs extrapolated from targeted NGS of PDOs or PDO-derived orthotopic tumors (PDO-xenografts) (figs. S3B and S4); CNAs detected in key oncogenic

¹Division of Molecular Pathology, The Institute of Cancer Research, London, UK. ²Centre for Evolution and Cancer, The Institute of Cancer Research, London, UK. ³Cancer Research UK Cancer Imaging Centre, Division of Radiotherapy and Imaging, The Institute of Cancer Research and Royal Marsden Hospital, London, UK. ⁴Department of Medicine, The Royal Marsden NHS Trust, London, UK. ⁵Cancer Research UK Cancer Therapeutics Unit, The Institute of Cancer Research, London, UK. ⁶Department of Radiology, The Royal Marsden NHS Trust, London, UK. ⁷Ralph Lauren Centre for Breast Cancer Research, Royal Marsden Hospital NHS Trust, London, UK. ⁸Division of Clinical Studies, The Institute of Cancer Research, London, UK. ⁹Department of Medicine, Surgical Pathology and Cytopathology Unit, University of Padua, Padua, Italy. ¹⁰Cancer Research UK Beatson Institute, Glasgow, UK.

*Corresponding author. Email: nicola.valeri@icr.ac.uk

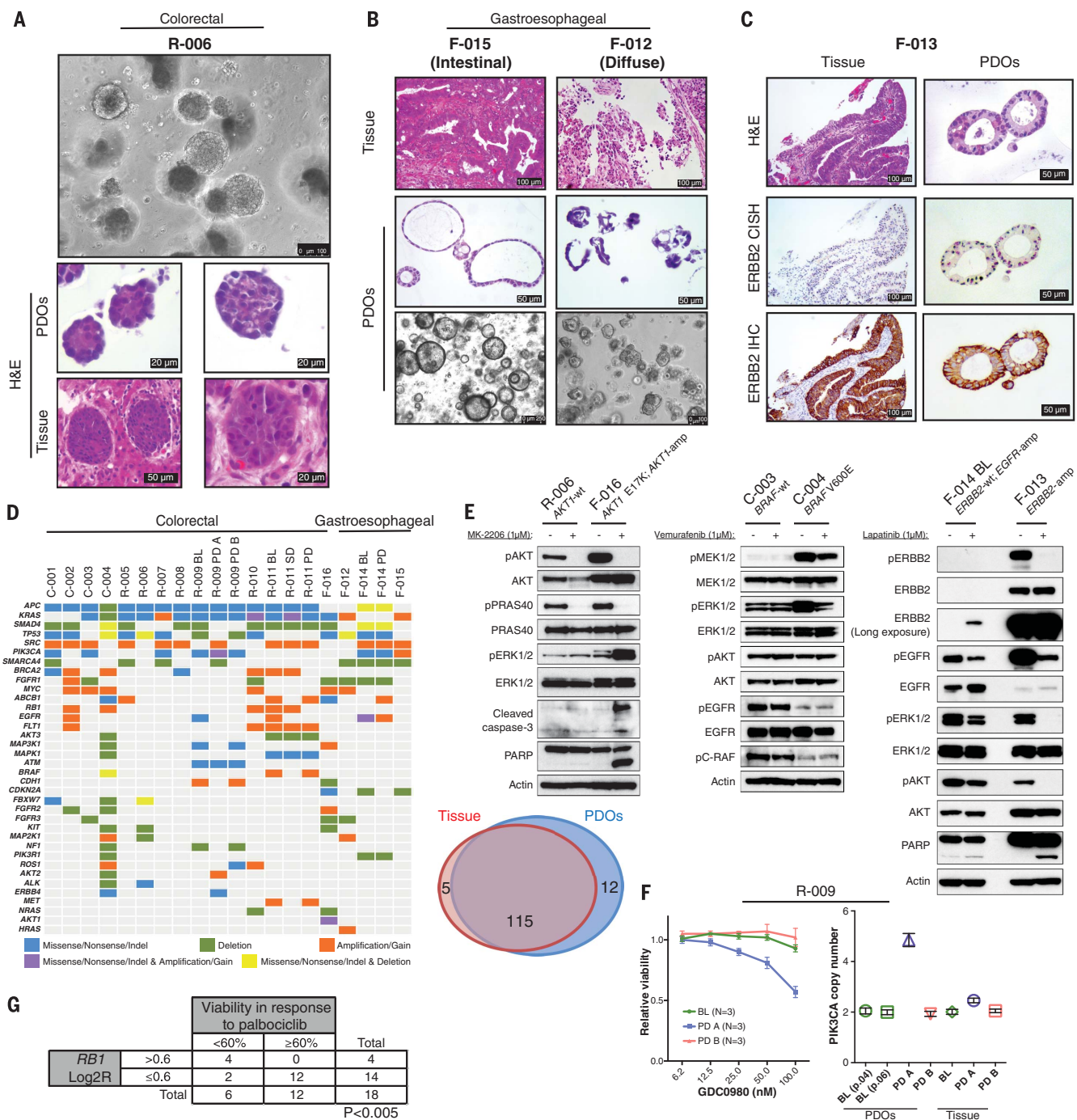


Fig. 1. Histopathological, molecular, and functional characterization of patient-derived organoids (PDOs). (A) Phase-contrast image of a mCRC PDO culture (top) and hematoxylin and eosin staining comparing organoids to their matching patient biopsy (bottom). (B) Intestinal and diffuse growth patterns are retained in mGOC PDOs. (C) *ERBB2* amplification and overexpression in mGOC PDOs and parental tissue biopsy (CISH, chromogenic *in situ* hybridization; IHC, immunohistochemistry). (D) Heatmap showing the most frequently mutated and/or copy number-altered genes in PDOs (left) and Venn diagram demonstrating 96% mutational overlap between PDOs and parental tissue biopsies (right). (E) Target engagement in genotype–drug phenotype combinations: pathway analysis downstream of ERBB2 in *ERBB2*-amplified and nonamplified PDOs treated with lapatinib (24 hours) (right), BRAF inhibition (24 hours) (center), and AKT inhibition (4 hours) (left). wt, wild type. (F) Concentration-dependent effect of the dual PI3K/mTOR inhibitor GDC-0980 in three PDOs from patient R-009, all carrying an acquired PIK3CA mutation (H1047R). PDOs established from a liver metastasis biopsied at disease progression (R-009 PD-A) that also harbored PIK3CA amplification showed concentration-dependent response to GDC-0980. *PIK3CA*-mutant but nonamplified PDOs established before regorafenib treatment (R-009 BL) or from a different liver metastasis biopsied at disease progression (R-009 PD-B) did not respond to GDC-0980. Viability data shown are means \pm SEM of indicated independent experiments. (G) Correlation (Fisher's exact test) between presence of *RB1* amplification in PDOs (D) and response to the CDK4/CDK6 inhibitor palbociclib in the reported drug screen (fig. S9A). BL, baseline; SD, stable disease; PD, posttreatment/progressive disease.

drivers were further validated by digital-droplet polymerase chain reaction (fig. S5). High concordance was observed in mutational, CNA, and transcriptomic profiling over successive passages when PDOs were tested before and after several months of continuous culture [passage range, 5 to 13; mutations, coefficient of determination (R^2) = 0.96, $P < 0.0001$; CNA, $R^2 = 0.97$, $P < 0.0001$; gene expression (RNA sequencing), $R^2 = 0.7$, $P < 0.001$] (fig. S6).

Next we tested the feasibility of using PDOs derived from metastatic cancers as drug-screening tools and validated the robustness of our approach by identifying several genotype–drug phenotype

correlations across the PDO panel. We ran three-dimensional (3D) screening assays over a period of 2 weeks (figs. S7 and S8), using a library of 55 drugs now in phase 1 to 3 clinical trials or in clinical practice (table S5). The heatmap shown in fig. S9A summarizes the screening data; hit validation at lower drug concentrations is reported in fig. S9B. For all 19 screens, a very high correlation was observed among each screen's three replicate assays and controls (fig. S10).

F-013 was the only *ERBB2*-amplified PDO in our cohort (Fig. 1C), and it exhibited the strongest response to lapatinib [dual *ERBB2*/epidermal growth factor receptor (EGFR) inhibitor]; lapatinib

potently inhibited the mitogen-activated protein kinase (MAPK) and phosphatidylinositol 3-kinase (PI3K)/AKT signaling downstream of EGFR/ERBB2, inducing apoptosis in the F-013 PDO (Fig. 1E and fig. S9A). In a PDO (F-014) in which *EGFR* was amplified but *ERBB2* was not, lapatinib had no effect on viability and only modestly reduced MAPK and PI3K/AKT signaling (Fig. 1E and fig. S9A).

Similarly, across all PDOs, F-016 was the only tumor carrying an *AKT1* amplification and E17K mutation (E, glutamic acid; K, lysine) (Fig. 1D) and was the only one to respond strongly to both AKT inhibitors present in the drug library (MK-2206

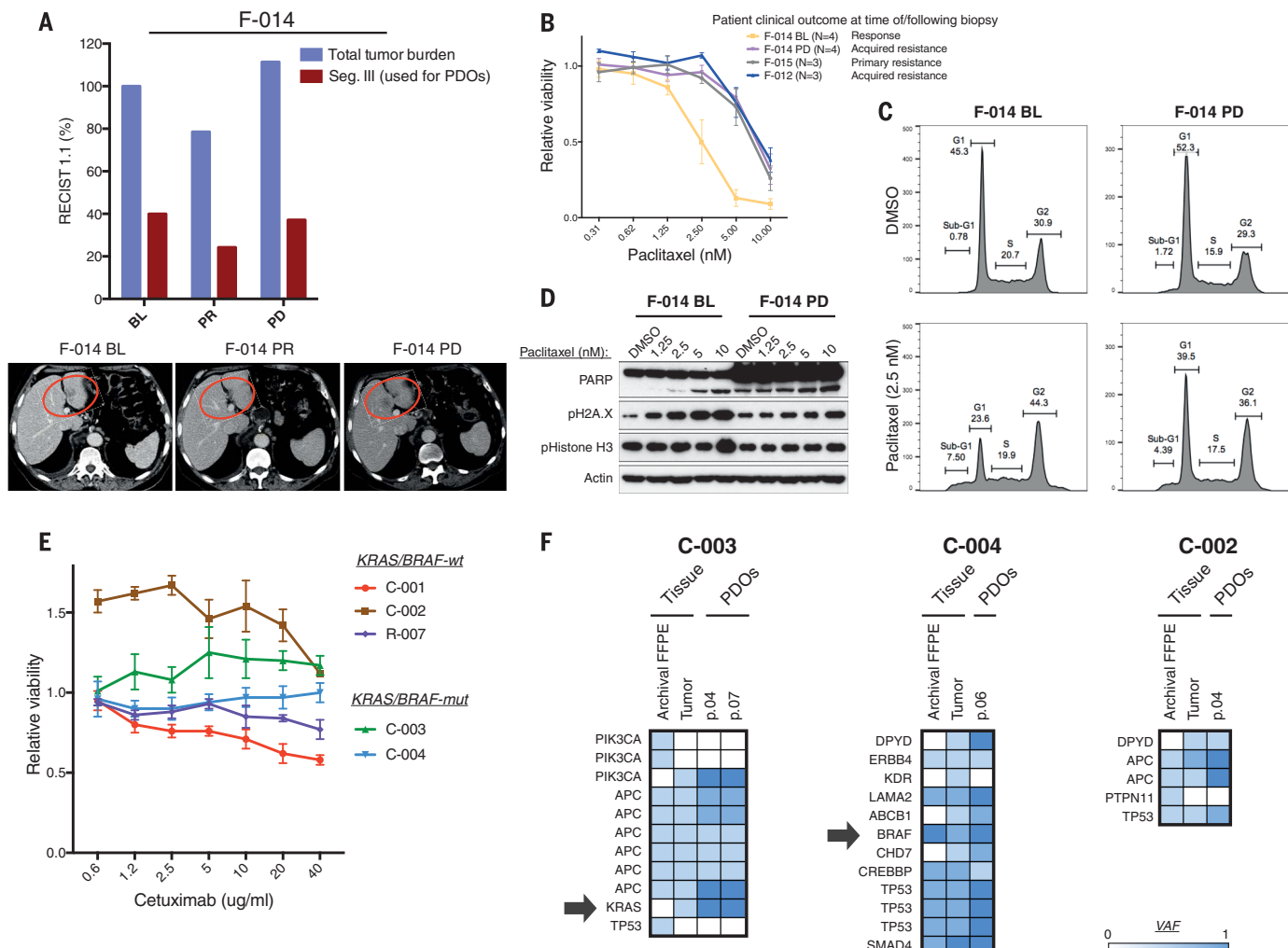


Fig. 2. PDO-based ex vivo co-clinical trials in mGOC and mCRC.

(A) PDOs were generated from sequential biopsies of a liver metastasis (red circles in the bottom panel) of mGOC patient F-014 that showed initial response to paclitaxel (F-014 BL) and subsequently progressed (F-014 PD). Violet bars indicate overall tumor volume [according to RECIST (Response Evaluation Criteria in Solid Tumors) 1.1], and red bars indicate volume of the target metastasis used to generate PDOs. (B) Cell viability upon paclitaxel treatment was compared in BL and PD PDOs from patient F-014 and PDOs from patients that exhibited primary (F-015) or acquired (F-012) resistance to paclitaxel in the clinic. Viability data shown are means \pm SEM of indicated independent experiments. (C) Cell cycle analysis upon paclitaxel treatment in the

F-014 BL PDO compared with the F-014 PD PDO. DMSO, dimethyl sulfoxide. (D) Concentration-dependent DNA damage was observed in the F-014 BL PDO in response to paclitaxel but not in PDOs from the same patient established at PD. (E) PDOs were established from BL (C-003 and C-004) and PD (C-001 and C-002) biopsies from patients treated with the anti-EGFR monoclonal antibody cetuximab. PDOs were treated with cetuximab in vitro; data shown are means \pm SD from independent experiments performed in triplicate. (F) Molecular analysis of BL and PD PDOs, matching biopsy (tumor), and primary bowel cancer (archival); arrows indicate the presence of clonal or subclonal mutations in *BRAF* or *KRAS*, respectively, in two patients. VAF, variant allele frequency; FFPE, formalin-fixed paraffin-embedded.

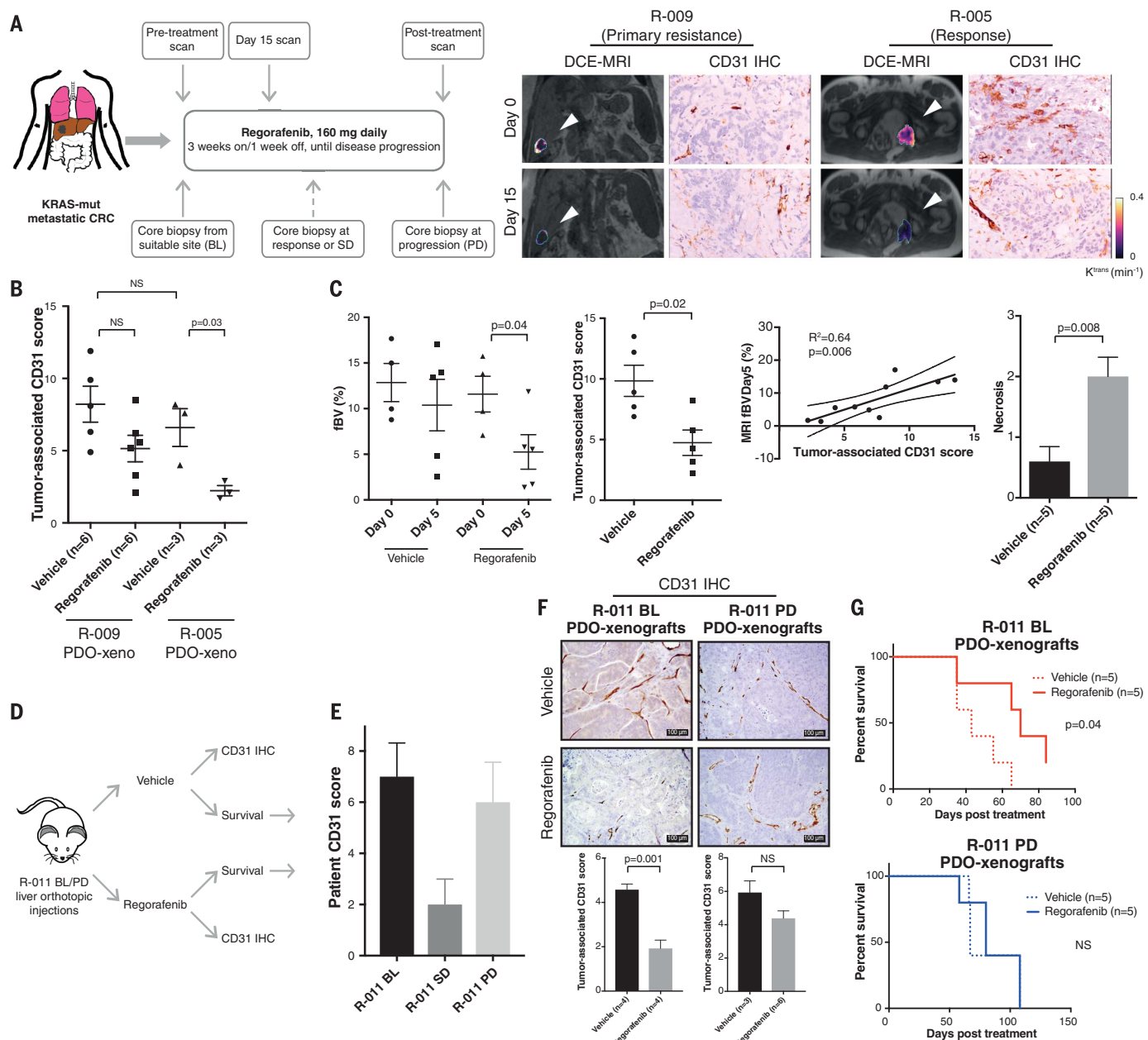


Fig. 3. PDO-based co-clinical trials mimic primary and acquired resistance to regorafenib in mice. (A) mCRC patients on regorafenib treatment underwent biopsies at BL, SD, or PD. An early reduction (15 days) in functional imaging (DCE-MRI) parameters correlated with changes in microvasculature assessed by CD31 staining and clinical benefit from regorafenib (right). Arrowheads indicate CRC metastases; K^{trans} , volume transfer constant. **(B)** Changes in microvasculature in response to regorafenib were assessed in PDO-xenografts in mice by quantification of tumor-associated CD31-positive vessels. Data show PDO-xenografts from a primary resistant patient (R-009) and a long-term responder (R-005) to regorafenib. Means \pm SD from the indicated number of mice (n) in a representative experiment are shown; significance was determined using Student's unpaired t test. **(C)** Reduction in fractional blood volume (fBV) in regorafenib-treated mice carrying long-term regorafenib responder (R-005) PDO-xenografts. A total of 10 animals were analyzed (five in each arm); shown are the means \pm SD of an individual experiment. Day 0 fBV values could not be obtained for two animals owing to respiratory movement. Significance was determined using Student's paired t test for fBV and unpaired t test for CD31 and necrosis.

(D) Schematic representation of the animal experiment using PDOs from patient R-011, established pre- and posttreatment with regorafenib. Mice carrying liver orthotopic R-011 pretreatment (BL) and posttreatment (PD) PDO-xenografts were randomized to control and treatment arms and treated with vehicle or regorafenib for 10 days. After treatment, each arm was further randomized to a cohort culled for histopathological analysis and a survival cohort, which was monitored over time. **(E)** CD31 immunostaining in the parental patient BL, SD, and PD biopsies, demonstrating an initial reduction in tumor microvasculature in response to regorafenib. Shown are means \pm SD calculated by scoring 10 high-power-field tumor areas. **(F)** Representative images (top) and analysis (bottom) of CD31 immunostaining in the BL and PD R-011 PDO-xenografts. Shown are means \pm SD calculated by scoring at least 10 high-power-field tumor areas per animal in an individual experiment; n , number of animals analyzed in each group. Significance was determined using Student's unpaired t test. **(G)** Kaplan-Mayer curves for regorafenib- or vehicle-treated mice bearing BL and PD PDO-xenografts from patient R-011 from an individual experiment (n , number of mice analyzed). Significance was determined using the Mantel-Cox log-rank test.

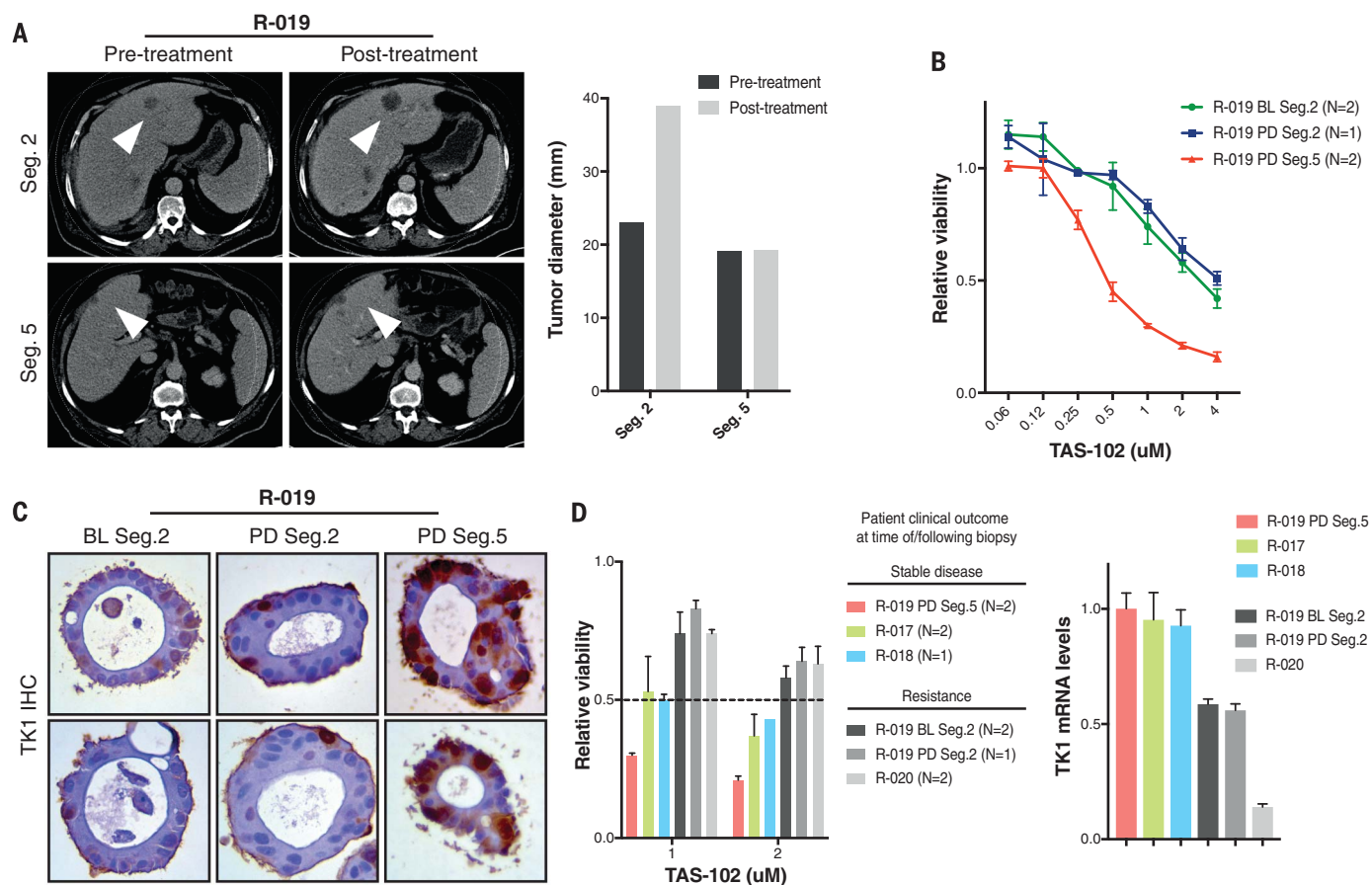


Fig. 4. PDOs recapitulate intra- and interpatient heterogeneity in response to TAS-102. (A) PDOs were established from a patient (R-019) with mixed response to TAS-102. Whereas the segment 2 metastasis rapidly progressed, the segment 5 metastasis remained stable upon TAS-102 treatment (white arrowheads in the CT scan indicate metastases; bars represent pre- and posttreatment measurements of the indicated metastases). **(B)** Ex vivo

concentration-response curves in BL and PD multiregion PDOs from patient R-019 (with mixed response to TAS-102). **(C)** TK1 IHC expression in TAS-102-refractory (segment 2) and -sensitive (segment 5) PDOs. **(D)** Cell viability (left) and TK1 mRNA expression (right) in PDOs from TAS-102-responsive and -refractory patients. In (B) and (D), *N* indicates the number of independent experiments, and viability values are expressed as means \pm SEM.

and GSK690693) (Fig. 1E and fig. S9A). One mCRC PDO (C-004) harbored a BRAF V600E mutation (V, valine) (Fig. 1D) and was the only PDO that showed significantly decreased viability after treatment with the BRAF inhibitor vemurafenib (fig. S9A). Consistent with this, vemurafenib selectively inhibited MEK/ERK (MAPK kinase/extracellular signal-regulated kinase) signaling in the C-004 PDO (Fig. 1E) but failed to induce apoptosis, in keeping with the lack of efficacy of single-agent BRAF inhibitors in mCRC (13).

Overall, *PIK3CA* mutations were not predictive of response to GDC-0980 (a dual PI3K/mTOR inhibitor) in the PDOs panel (Fig. 1D and fig. S9A). In line with this observation, in a patient from whom pre- and posttreatment PDOs were established from multiple metastases (R-009 BL, PD-A, and PD-B), a *PIK3CA* H1047R mutation (H, histidine; R, arginine) common to all the PDOs was not associated with any response to GDC-0980. However, PDOs carrying a synchronous *PIK3CA* amplification (R-009 PD-A) showed a concentration-dependent reduction in cell viability in response to GDC-0980 (Fig. 1F and fig. S3A). Last, in keeping with

published data (14), a significant correlation was observed between *RBI* amplification and sensitivity of PDOs to palbociclib [cyclin-dependent kinase 4 (CDK4)/CDK6 inhibitor] (Fig. 1G).

After extensive molecular and functional characterization of our PDOs, we examined their clinical predictive value in 21 comparisons of clinical responses observed in patients with ex vivo response data gathered in organoids (table S6). Taxanes are a standard second-line treatment option for metastatic gastric cancer; however, efficacy is modest, and no predictive biomarkers are available to inform clinical decisions (15). We compared response to paclitaxel in sequential PDOs established before and after treatment in a paclitaxel-sensitive patient (F-014) with that in PDOs established from liver metastases of two paclitaxel-resistant patients (Fig. 2, A and B). PDOs derived from the responsive metastasis showed a GI_{50} (concentration that inhibits growth of cancer cells by 50%) for clinically relevant paclitaxel concentrations (16) that was about one-fourth that for PDOs from the same patient derived at progression; these resistant PDOs dem-

onstrated an identical paclitaxel concentration-response profile to the two PDOs established from paclitaxel-refractory patients (Fig. 2B). Cell cycle analysis showed marked apoptosis and G_2 arrest upon taxane treatment in the pretreatment F-014 PDOs, whereas no significant difference was observed in PDOs established at progression (Fig. 2C and fig. S11A). Similarly, paclitaxel induced concentration-dependent DNA damage, mitotic arrest, and apoptosis in the pretreatment F-014 PDOs but had a much weaker impact on the progression (and thus resistant) PDOs (Fig. 2D). Consistent with data observed for second-line treatment, a \sim 10-fold difference in GI_{50} was observed in response to the combination of 5-fluorouracil and cisplatin in PDOs collected from chemosensitive and chemorefractory MGOC patients receiving first-line treatment (fig. S11B), highlighting the clinical potential of PDOs for treatment selection in cancers of unmet need.

Anti-EGFR monoclonal antibodies, regorafenib, and TAS-102 are U.S. Food and Drug Administration-approved options for treatment of chemorefractory mCRC; however, with the exception of RAS pathway

mutations for anti-EGFR therapy, there are no validated clinical biomarkers for patient selection in this setting. We initially tested the predictive value of PDOs in mCRC by comparing response to anti-EGFR treatment (cetuximab) in five PDOs and their respective patients (Fig. 2E). Two PDOs established from BL biopsies before anti-EGFR treatment in the PROSPECT-C trial showed no response to cetuximab, in keeping with the primary resistance observed in these two patients in the clinic. Unsurprisingly (17), both PDOs and their respective patient biopsies harbored either *KRAS* G12D (subclonal) (G, glycine; D, aspartic acid) or *BRAF*V600E (clonal) mutations (Fig. 2F). The third cetuximab-resistant PDO (C-002) was established from the progression biopsy of a patient who initially responded to cetuximab, and it harbored an *EGFR* amplification (Fig. 1D and fig. S5), no RAS pathway mutational aberrations (Fig. 2F), and high amphiregulin mRNA levels. Despite these molecular markers being suggestive of responsiveness to cetuximab, the C-002 PDO showed no response (and, in fact, paradoxically showed enhanced proliferation) upon cetuximab treatment, in line with the respective patient's clinical outcome, thus highlighting the potential of PDOs to predict clinical outcomes better than molecular pathology alone. Another *KRAS* wild-type PDO derived from a slow-growing progressing metastasis in a patient with otherwise stable disease (C-001) (fig. S11C) showed a marginal response to cetuximab. Last, the *KRAS* wild-type PDO established from a BL biopsy of a patient enrolled in the PROSPECT-R trial (R-007) (fig. S11C) showed response to cetuximab at concentrations higher than 5 μ g/ml; this, however, could not be compared with clinical response, because the patient did not receive anti-EGFR monoclonal antibodies.

Next we tested the ability of PDOs to recapitulate response to regorafenib, a multiple tyrosine kinase inhibitor blocking oncogenic and angiogenic signaling pathways. No response to regorafenib was observed in our 3D ex vivo screening assays (fig. S9A), an observation in keeping with our recently reported clinical results from the PROSPECT-R trial (18), suggesting that response to regorafenib is mainly driven by its anti-angiogenic effect (Fig. 3A).

To match responses to regorafenib in the clinic and in aligned PDOs, we established an orthotopic human tumor xenograft model by implanting luciferase-expressing (Luc^+) PDOs in the liver of NSG mice (PDO-xenografts) (fig. S12A). We initially compared response to regorafenib in PDO-xenografts from a patient with primary resistance (R-009; $n = 11$) and from a patient who achieved a durable (10-month) response (R-005; $n = 6$) to regorafenib (fig. S12, B and C). In keeping with the clinical responses (Fig. 3A), PDO-xenografts from the regorafenib-sensitive patient displayed a significant ($P = 0.03$) reduction in their microvasculature in response to regorafenib, as revealed by CD31 immunostaining; in contrast, no significant changes were observed in PDO-xenografts from the regorafenib-resistant patient (Fig. 3B). To mimic our clinical obser-

vations, we performed functional susceptibility contrast magnetic resonance imaging (MRI) of PDO-xenografts of the responding patient (R-005; $n = 10$) before and after treatment (fig. S12D). In line with dynamic contrast-enhanced MRI (DCE-MRI) results in patients (Fig. 3A), susceptibility contrast MRI revealed a significant reduction in tumor fractional blood volume (fBV) in regorafenib-treated mice (Fig. 3C). These changes were associated with a reduction in CD31 staining and increased necrosis (Fig. 3C). Notably, across all animals, a robust correlation was observed between the fBV values obtained from susceptibility contrast MRI and the microvasculature assessment (CD31) of the same samples ($R^2 = 0.64$, $P = 0.006$) (Fig. 3C). Consistent with our clinical data, changes in microvasculature indicative of response appeared to be independent of changes in tumor volume (fig. S12E) (18). Three different histopathological growth patterns (HGP)—desmoplastic HGP, pushing HGP, and replacement HGP—have been associated with different degrees of response to anti-angiogenic drugs, with the replacement HGP being frequently associated with vessel co-option and primary resistance (19). In our experiments, a predominance of replacement HGP, and thus vessel co-option, was observed in PDO-xenografts from the resistant patient, whereas tumors established from the PDOs of the sensitive patient showed a prevalence of desmoplastic and pushing HGP (fig. S12F), suggesting that vessel co-option might be the mechanism underpinning primary resistance to regorafenib. When the responder to regorafenib (R-005) progressed and received subsequent treatment, he was enrolled in a phase 1 trial of the ATR inhibitor VX-970. No response was observed in this patient with VX-970 monotherapy, and this was in keeping with the lack of response to ATM/ATR inhibitors observed in his PDOs in the drug screening reported in fig. S9A.

To test the PDOs' ability to capture tumor evolution and acquired resistance to treatment, we generated xenografts using PDOs from the same liver metastasis before (BL) and after (PD) treatment in mCRC patient R-011 that exhibited initial response to regorafenib and subsequently progressed (fig. S13A). Mice were randomized to treatment and control arms, and, after treatment, each arm was further randomized for survival or functional analysis (Fig. 3D). In line with clinical findings (Fig. 3E) (18), CD31 immunostaining revealed a ~60% reduction in microvasculature in response to regorafenib in BL PDO-xenografts ($P = 0.001$), whereas no significant change was observed in PD PDO-xenografts (Fig. 3F). More importantly, regorafenib treatment offered a selective survival benefit in mice carrying BL PDO-xenografts (Fig. 3G and fig. S13B), confirming the predictive value of PDOs and their ability to reflect cancer evolution upon treatment.

TAS-102, a combination of the nucleoside analog trifluridine and the thymidine phosphorylase inhibitor tipiracil, is approved for the treatment of chemorefractory mCRC, but no validated biomarkers are available (20). We compared clinical and preclinical response to TAS-102 in six organ-

oids from four different patients treated with TAS-102. Initially, we tested response to TAS-102 in PDOs from a patient (R-019) who had a mixed response, with stability of disease in one of the liver metastases (segment 5) and rapid progression in another (segment 2) (Fig. 4A). Ex vivo concentration-response data showed about an eightfold difference in GI_{50} between PDOs derived from the TAS-102-sensitive metastasis and those derived from pre- and posttreatment biopsy of the rapidly progressing metastasis (Fig. 4B), highlighting the ability of PDOs to recapitulate intrapatient heterogeneity. TK1 has been proposed as a potential biomarker of response to TAS-102 (21); TK1 protein expression was indeed higher in PDOs from the responding metastasis than in those from the nonresponding site (Fig. 4C). When we extended the TAS-102 sensitivity analysis to PDOs from three other patients, we confirmed that PDOs from patients who achieved disease control were sensitive to low micromolar concentrations of TAS-102, whereas no significant effect on cell viability was observed in PDOs from resistant (primary or acquired) patients (Fig. 4D, left); consistent with previous data, TK1 mRNA expression was higher in PDOs from patients that achieved stable disease in response to TAS-102 (Fig. 4D, right).

Overall, for the PDOs that we analyzed, we found 100% sensitivity, 93% specificity, 88% positive predictive value, and 100% negative predictive value in forecasting response to targeted agents or chemotherapy in patients (Fisher's exact test, $P < 0.0001$) (table S7). Our data suggest that PDOs can be exploited for functional genomics to simulate cancer behavior ex vivo and integrate molecular pathology into the decision-making process of early-phase clinical trials.

REFERENCES AND NOTES

1. A. Zehir *et al.*, *Nat. Med.* **23**, 703–713 (2017).
2. E. E. Voest, R. Bernards, *Cancer Discov.* **6**, 130–132 (2016).
3. A. T. Byrne *et al.*, *Nat. Rev. Cancer* **17**, 254–268 (2017).
4. J. G. Clohessy, P. P. Pandolfi, *Nat. Rev. Clin. Oncol.* **12**, 491–498 (2015).
5. A. L. Bredenoord, H. Clevers, J. A. Knoblich, *Science* **355**, eaaf9414 (2017).
6. M. van de Wetering *et al.*, *Cell* **161**, 933–945 (2015).
7. F. Weeber *et al.*, *Proc. Natl. Acad. Sci. U.S.A.* **112**, 13308–13311 (2015).
8. M. Fujii *et al.*, *Cell Stem Cell* **18**, 827–838 (2016).
9. C. Pauli *et al.*, *Cancer Discov.* **7**, 462–477 (2017).
10. J. F. Dekkers *et al.*, *Sci. Transl. Med.* **8**, 344ra84 (2016).
11. Cancer Genome Atlas Network, *Nature* **487**, 330–337 (2012).
12. Cancer Genome Atlas Research Network, *Nature* **513**, 202–209 (2014).
13. D. M. Hyman *et al.*, *N. Engl. J. Med.* **373**, 726–736 (2015).
14. C. J. Sherr, D. Beach, G. I. Shapiro, *Cancer Discov.* **6**, 353–367 (2016).
15. E. C. Smyth *et al.*, *Ann. Oncol.* **27**, v38–v49 (2016).
16. L. M. Zasadil *et al.*, *Sci. Transl. Med.* **6**, 229ra43 (2014).
17. C. S. Verissimo *et al.*, *eLife* **5**, e18489 (2016).
18. K. Khan *et al.*, *Gut* **10**.1136/gutjnl-2017-314178 (2017).
19. S. Frentzas *et al.*, *Nat. Med.* **22**, 1294–1302 (2016).
20. R. J. Mayer *et al.*, *N. Engl. J. Med.* **372**, 1909–1919 (2015).
21. Y. Kuboki *et al.*, *Lancet Oncol.* **18**, 1172–1181 (2017).

ACKNOWLEDGMENTS

This work was supported by Cancer Research UK (grant number CEA A18052), the National Institute for Health Research (NIHR) Biomedical Research Centre (BRC) at The Royal Marsden NHS Foundation Trust and The Institute of Cancer Research

(grant numbers A62, A100, A101, and A159), and the European Union Seventh Framework Programme (grant number CIG 334261) to N.V.; by Cancer Research UK (C52506/A22909) to A.So.; by a Wellcome Trust grant (105104/Z/14/Z) to the Centre for Evolution and Cancer; by Cancer Research UK Cancer Imaging Centre funding (C1060/A16464) to The Institute of Cancer Research; by Cancer Research UK Programme Grants C309/A11566 and C2739/A22897 to the Cancer Therapeutics Unit of The Institute of Cancer Research; and by a Bayer Oncology Group Research Grant to D.Cu. A.So. is supported by The Chris Rokos Fellowship in Evolution and Cancer. I.C. has had advisory roles with Merck Serono, Roche,

Sanofi Oncology, Bristol Myers Squibb, Eli Lilly, Novartis, and Gilead Science; has received research funding from Merck-Serono, Novartis, Roche, and Sanofi Oncology; and has received honoraria from Roche, Sanofi-Oncology, Eli Lilly, and Taiho. D.Cu. has received research funding from Roche, Amgen, Celgene, Sanofi, Merck Serono, Novartis, AstraZeneca, Bayer, Merrimack, and MedImmune. All other authors declare no conflicts of interest. The data presented in this paper are tabulated in the main text and supplementary materials. Sharing of materials is subject to a material transfer agreement with The Institute of Cancer Research, London (please direct requests to N.V.).

SUPPLEMENTARY MATERIALS

www.sciencemag.org/content/359/6378/920/suppl/DC1
Materials and Methods
Supplementary Text
Figs. S1 to S13
Tables S1 to S8
References (22–34)

4 July 2017; resubmitted 26 October 2017
Accepted 11 January 2018
10.1126/science.aoa2774

CANCER

Detection and localization of surgically resectable cancers with a multi-analyte blood test

Joshua D. Cohen,^{1,2,3,4,5} Lu Li,⁶ Yuxuan Wang,^{1,2,3,4} Christopher Thoburn,³ Bahman Afsari,⁷ Ludmila Danilova,⁷ Christopher Douville,^{1,2,3,4} Ammar A. Javed,⁸ Fay Wong,^{1,3,4} Austin Mattox,^{1,2,3,4} Ralph. H. Hruban,^{3,4,9} Christopher L. Wolfgang,⁸ Michael G. Goggins,^{3,4,9,10,11} Marco Dal Molin,⁴ Tian-Li Wang,^{3,9} Richard Roden,^{3,9} Alison P. Klein,^{3,4,12} Janine Ptak,^{1,2,3,4} Lisa Dobbyn,^{1,3,4} Joy Schaefer,^{1,3,4} Natalie Silliman,^{1,2,3,4} Maria Popoli,^{1,3,4} Joshua T. Vogelstein,¹³ James D. Browne,¹⁴ Robert E. Schoen,^{15,16} Randall E. Brand,¹⁵ Jeanne Tie,^{17,18,19,20} Peter Gibbs,^{17,18,19,20} Hui-Li Wong,¹⁷ Aaron S. Mansfield,²¹ Jin Jen,²² Samir M. Hanash,²³ Massimo Falconi,²⁴ Peter J. Allen,²⁵ Shabin Zhou,^{1,3,4} Chetan Bettegowda,^{1,3,4} Luis A. Diaz Jr.,^{1,3,4*} Cristian Tomasetti,^{3,6,7†} Kenneth W. Kinzler,^{1,3,4†} Bert Vogelstein,^{1,2,3,4†} Anne Marie Lennon,^{3,4,8,10,11†} Nickolas Papadopoulos^{1,3,4†}

Earlier detection is key to reducing cancer deaths. Here, we describe a blood test that can detect eight common cancer types through assessment of the levels of circulating proteins and mutations in cell-free DNA. We applied this test, called CancerSEEK, to 1005 patients with nonmetastatic, clinically detected cancers of the ovary, liver, stomach, pancreas, esophagus, colorectum, lung, or breast. CancerSEEK tests were positive in a median of 70% of the eight cancer types. The sensitivities ranged from 69 to 98% for the detection of five cancer types (ovary, liver, stomach, pancreas, and esophagus) for which there are no screening tests available for average-risk individuals. The specificity of CancerSEEK was greater than 99%; only 7 of 812 healthy controls scored positive. In addition, CancerSEEK localized the cancer to a small number of anatomic sites in a median of 83% of the patients.

The majority of localized cancers can be cured by surgery alone, without any systemic therapy (1). Once distant metastasis has occurred, however, surgical excision is rarely curative. One major goal in cancer research is therefore the detection of cancers before they metastasize to distant sites. For many adult cancers, it takes 20 to 30 years for incipient neoplastic lesions to progress to late-stage disease (2–4). Only in the past few years of this long process do neoplastic cells appear to successfully seed and give rise to metastatic lesions (2–5). Thus, there is a wide window of opportunity to detect cancers before the onset of metastasis. Even when metastasis has initiated but is not yet evident radiologically, cancers can be cured in up to 50% of cases with systemic therapies, such as cytotoxic drugs and immunotherapy

(6–9). Once large, metastatic tumors are formed, however, current therapies are rarely effective (6–9).

The only widely used blood test for earlier cancer detection is based on measurement of prostate-specific antigen, and the proper use of this test is still being debated (10). The approved tests for cancer detection are not blood-based and include colonoscopy, mammography, and cervical cytology. New blood tests for cancer must have very high specificity; otherwise, too many healthy individuals will receive positive test results, leading to unnecessary follow-up procedures and anxiety. Blood tests that detect somatic mutations ("liquid biopsies") offer the promise of exquisite specificity because they are based on driver gene mutations that are expected to be found only in abnormal clonal proliferations of

cells, such as cancers (11–18). To date, the vast majority of cancer patients evaluated with mutation-based liquid biopsies have advanced-stage disease. In addition, no studies have examined a large number of healthy control individuals, which is essential for evaluation of the specificity of such tests (19). Diagnostic sensitivity is also an issue for liquid biopsies. Available evidence indicates that patients with early-stage cancers can harbor less than one mutant template molecule per milliliter of plasma (11, 20), which is often beyond the limit of detection of previously reported technologies that assess multiple mutations simultaneously (19, 21). Yet another issue with liquid biopsies is the identification of the underlying tissue of origin. Because the same gene mutations drive multiple tumor types, liquid biopsies based on genomic analysis alone generally cannot identify the anatomical location of the primary tumor.

We describe here a new blood test, called CancerSEEK, that addresses the issues described above. The test uses combined assays for genetic alterations and protein biomarkers and has the capacity not only to identify the presence of relatively early cancers but also to localize the organ of origin of these cancers.

Initial studies demonstrated that the maximum sensitivity of plasma DNA-based tests—liquid biopsies—was limited for localized cancers (11). A subsequent study suggested that the combination of four protein biomarkers with one genetic marker (*KRAS*) could enhance sensitivity for the detection of pancreatic cancers (20). We sought to generalize this approach by evaluating a panel of protein and gene markers that might be used to detect many solid tumors at a stage before the emergence of distant metastases. We began by designing a polymerase chain reaction (PCR)-based assay that could simultaneously assess multiple regions of driver genes that are commonly mutated in a variety of cancer types. In designing this test, we were confronted by four competing challenges. First, the test must query a sufficient number of bases to allow detection of a large number of cancers. Second, each base queried in the test must be sequenced thousands of times to detect low-prevalence mutations (11, 19, 21, 22). Third, there must be a limit on the number of bases queried in the test because the more bases queried, the more likely that artifactual mutations would be identified, reducing the signal-to-noise ratio. And

¹Ludwig Center for Cancer Genetics and Therapeutics, Johns Hopkins University School of Medicine, Baltimore, MD 21205, USA. ²Howard Hughes Medical Institute, Johns Hopkins University School of Medicine, Baltimore, MD 21205, USA. ³Sidney Kimmel Cancer Center, Johns Hopkins University School of Medicine, Baltimore, MD 21205, USA. ⁴Sol Goldman Pancreatic Cancer Research Center, Johns Hopkins University School of Medicine, Baltimore, MD 21205, USA. ⁵Department of Biomedical Engineering, Johns Hopkins University School of Medicine, Baltimore, MD 21205, USA. ⁶Department of Biostatistics, Johns Hopkins Bloomberg School of Public Health, Baltimore, MD 21205, USA. ⁷Division of Biostatistics and Bioinformatics, Department of Oncology, Johns Hopkins Medical Institutions, Baltimore, MD 21287, USA. ⁸Department of Surgery, Johns Hopkins Medical Institutions, Baltimore, MD 21287, USA. ⁹Department of Pathology, Johns Hopkins Medical Institutions, Baltimore, MD 21287, USA. ¹⁰Department of Medicine, Johns Hopkins Medical Institutions, Baltimore, MD 21287, USA. ¹¹Department of Oncology, Johns Hopkins Medical Institutions, Baltimore, MD 21287, USA. ¹²Department of Epidemiology, Johns Hopkins Bloomberg School of Public Health, Baltimore, MD 21205, USA. ¹³Institute for Computational Medicine, Johns Hopkins University School of Medicine, Baltimore, MD 21205, USA. ¹⁴Department of Computer Science, Johns Hopkins University Whiting School of Engineering, Baltimore, MD 21218, USA. ¹⁵Department of Medicine, University of Pittsburgh, Pittsburgh, PA 15260, USA. ¹⁶Department of Epidemiology, University of Pittsburgh, Pittsburgh, PA 15260, USA. ¹⁷Division of Systems Biology and Personalized Medicine, Walter and Eliza Hall Institute of Medical Research, Parkville, VIC 3021, Australia. ¹⁸Faculty of Medicine, Dentistry and Health Sciences, University of Melbourne, Melbourne, VIC 3010, Australia. ¹⁹Department of Medical Oncology, Western Health, Melbourne, VIC 3021, Australia. ²⁰Department of Medical Oncology, Peter MacCallum Cancer Center, Melbourne, VIC 3000, Australia. ²¹Division of Medical Oncology, Department of Oncology, Mayo Clinic, Rochester, MN 55902, USA. ²²Division of Experimental Pathology, Department of Laboratory Medicine and Pathology, Mayo Clinic, Rochester, MN 55902, USA. ²³Sheikh Ahmed Center for Pancreatic Cancer Research, University of Texas MD Anderson Cancer Center, Houston, TX 77030, USA. ²⁴Division of Pancreatic Surgery, Department of Surgery, San Raffaele Scientific Institute Research Hospital, 20132 Milan, Italy. ²⁵Department of Surgery, Memorial Sloan-Kettering Cancer Center, New York, NY 10065, USA.

*Present address: Division of Solid Tumor Oncology, Memorial Sloan-Kettering Cancer Center, New York, NY 10065, USA.

†Corresponding author. Email: ctomasetti@jhmi.edu (C.T.); amlennon@jhmi.edu (A.M.L.); kinzle@jhmi.edu (K.W.K.); bertvog@gmail.com (B.V.); npapado1@jhmi.edu (N.P.)

fourth, for implementation in a screening setting, the test must be cost effective and amenable to high throughput, factors that limit the amount of sequencing that can be performed. To overcome these challenges, we searched for the minimum number of short amplicons that would allow us to detect at least one driver gene mutation in each of the eight tumor types evaluated. Using publicly available sequencing data, we found that there was a fractional power law relationship between the number of amplicons required and the sensitivity of detection, with a plateau at ~60 amplicons (Fig. 1). Once this plateau was reached, raising the number of amplicons would not detect substantially more cancers but would increase the probability of false-positive results. This decreasing marginal utility defined the optimal number of amplicons.

On the basis of these data, we designed a 61-amplicon panel, with each amplicon querying an average of 33 base pairs (bp) within one of 16 genes (table S1). As shown in Fig. 1, this panel would theoretically detect 41% (liver) to 95% (pancreas) of the cancers in the Catalog of Somatic Mutations in Cancer (COSMIC) data set (23). In practice, the panel performed considerably better, detecting at least one mutation in 82%, two mutations in 47%, and more than two mutations in 8% of the 805 cancers evaluated in our study (Fig. 1, colored dots; fig. S1; and table S2). We were able to detect a larger fraction of tumors than predicted by the COSMIC data set because the PCR-based sequencing assay we used was more sensitive for detecting mutations than conventional genome-wide sequencing. On the basis of this analysis of the DNA from primary tumors, the predicted maximum detection capability of circulating tumor DNA (ctDNA) in our study varied by tumor type, ranging from 60% for liver cancers to 100% for ovarian cancers (Fig. 1).

Armed with this small but robust panel of amplicons, we developed two approaches that enabled the detection of the rare mutations expected to be present in plasma ctDNA. First, we used multiplex-PCR to directly and uniquely label each original template molecule with a DNA barcode. This design minimizes the errors inherent to massively parallel sequencing (24) and makes efficient use of the small amount of cell-free DNA present in plasma. Additionally, we divided the total amount of DNA recovered from plasma into multiple aliquots and performed independent assays on each replicate. In effect, this decreases the number of DNA molecules per well; however, it increases the fraction of each mutant molecule per well, making the mutants easier to detect. Because the sensitivity of detection is often limited by the fraction of mutant alleles in each replicate, this partitioning strategy allowed us to increase the signal-to-noise ratio and identify mutations present at lower prevalence than possible if all of the plasma DNA was evaluated at once.

The second component of CancerSEEK is based on protein biomarkers. Previous studies have demonstrated that a major fraction of early-

stage tumors do not release detectable amounts of ctDNA, even when extremely sensitive techniques are used to identify them (11, 20). Many proteins potentially useful for early detection and diagnosis of cancer have been described in the literature (25–27). We searched this literature to find proteins that had previously been shown to detect at least one of the eight cancer types described above with sensitivities >10% and specificities >99%. We identified 41 potential protein biomarkers (table S3) and evaluated them in preliminary studies on plasma samples from normal individuals as well as from cancer patients. We found that 39 of these proteins could be reproducibly evaluated through a single immunoassay platform, and we then used this platform to assay all plasma samples (table S3). Eight of the 39 proteins proved to be particularly useful for discriminating cancer patients from healthy controls (table S3).

We then used CancerSEEK to study 1005 patients who had been diagnosed with stage I to III cancers of the ovary, liver, stomach, pancreas,

esophagus, colorectum, lung, or breast. No patient received neo-adjuvant chemotherapy before blood sample collection, and none had evident distant metastasis at the time of study entry. The median age at diagnosis was 64 (range 22 to 93). The eight cancer types were chosen because they are common in western populations and because no blood-based tests for their earlier detection are in common clinical use. The histopathological and clinical characteristics of the patients are summarized in table S4. The most common stage at presentation was American Joint Commission on Cancer (AJCC) stage II, accounting for 49% of patients, with the remaining patients harboring stage I (20%) or stage III (31%) disease. The number of samples per stage for each of the eight tumor types is summarized in table S1. The healthy control cohort consisted of 812 individuals of median age 55 (range 17 to 88) with no known history of cancer, high-grade dysplasia, autoimmune disease, or chronic kidney disease.

CancerSEEK evaluates levels of eight proteins and the presence of mutations in 1933 distinct

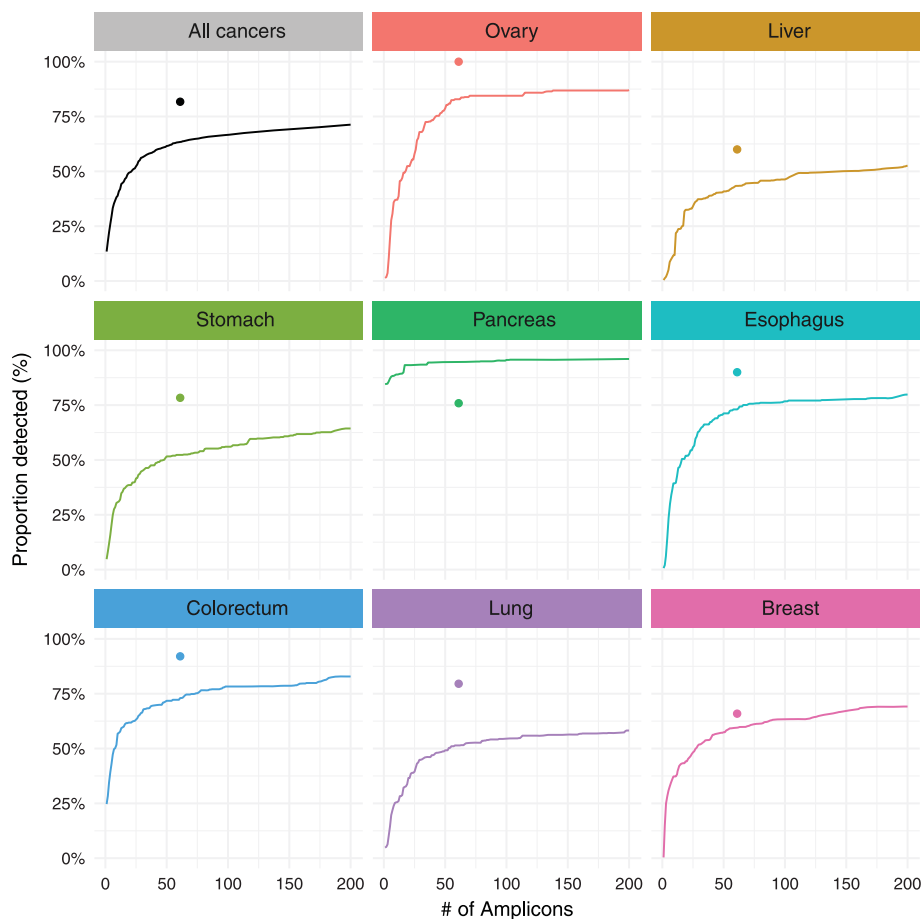


Fig. 1. Development of a PCR-based assay to identify tumor-specific mutations in plasma samples. Colored curves indicate the proportion of cancers of the eight types evaluated in this study that can be detected with an increasing number of short (<40 bp) amplicons. The sensitivity of detection increases with the number of amplicons but plateaus at ~60 amplicons. Colored dots indicate the fraction of cancers detected by using the 61-amplicon panel used in 805 cancers evaluated in our study, which averaged 82%. Publicly available sequencing data were obtained from the COSMIC repository.

genomic positions; each genomic position could be mutated in several ways (single base substitutions, insertions, or deletions). The presence of a mutation in an assayed gene or an elevation in the level of any of these proteins would classify a patient as positive. It was therefore imperative to use rigorous statistical methods to ensure the accuracy of the test. We used log ratios to evaluate mutations and incorporated them into a logistic regression algorithm that took into account both mutation data and protein biomarker levels to score CancerSEEK test results (supplementary materials). The mean sensitivities and specificities were determined by 10 iterations of 10-fold cross-validations. The receiver operating characteristic (ROC) curves for the entire cohort of cancer patients and controls in one representative iteration is shown in Fig. 2A.

The median sensitivity of CancerSEEK among the eight cancer types evaluated was 70% ($P < 10^{-96}$ one-sided binomial test) and ranged from 98% in ovarian cancers to 33% in breast cancers (Fig. 2C). At this sensitivity, the specificity was

>99%; only 7 of the 812 individuals without known cancers scored positive. We could not be certain that the few false positive–testing individuals identified among the healthy cohort did not actually have an as-yet undetected cancer, but classifying them as false positives provided the most conservative approach to classification and interpretation of the data.

The features of the test that were most important to the algorithm were the presence of a ctDNA mutation followed by elevations of cancer antigen 125 (CA-125), carcinoembryonic antigen (CEA), cancer antigen 19-9 (CA19-9), prolactin (PRL), hepatocyte growth factor (HGF), osteopontin (OPN), myeloperoxidase (MPO), and tissue inhibitor of metalloproteinases 1 (TIMP-1) protein levels (table S9). Waterfall plots for each of the ctDNA and protein features used in CancerSEEK illustrate their distribution among individuals with and without cancer (fig. S2). The importance ranking of the ctDNA and protein features used in CancerSEEK are provided in table S9, and a principal component analysis

displaying the clustering of individuals with and without cancer is shown in fig. S3. The complete data set, including the levels of all proteins studied and the mutations identified in the plasma samples, are provided in tables S5 and S6. The probabilistic rather than deterministic nature of the approach used here to call a sample positive is evident from fig. S4; each panel represents the sensitivity of CancerSEEK when one specific feature was excluded from the analysis.

One of the most important attributes of a screening test is the ability to detect cancers at relatively early stages. The median sensitivity of CancerSEEK was 73% for the most common stage evaluated (stage II), similar (78%) for stage III cancers, and lower (43%) for stage I cancers (Fig. 2B). The sensitivity for the earliest-stage cancers (stage I) was highest for liver cancer (100%) and lowest for esophageal cancer (20%).

The basis of liquid biopsy is that mutant DNA templates in plasma are derived from dying cancer cells and thus serve as exquisitely specific markers for neoplasia. To investigate whether CancerSEEK meets this expectation, we evaluated tumor tissue from 153 patients in whom ctDNA could be detected at statistically significant levels (supplementary materials) and for whom primary tumors were available. We found that the mutation in the plasma was identical to a mutation found in the primary tumor of the same individual in 138 (90%) of these 153 cases (table S7). This concordance between plasma and primary tumor was evident in all eight cancer types, and ranged from 100% in ovarian and pancreatic cancers to 82% in stomach cancers.

One limitation of liquid biopsies is their inability to determine the cancer type in patients who test positive, which poses challenges for clinical follow-up. To examine whether the CancerSEEK test can help identify a cancer's tissue of origin, we used supervised machine learning to predict the underlying cancer type in patients with positive CancerSEEK tests. The input algorithm took into account the ctDNA and protein biomarker levels as well as the gender of the patient (supplementary materials). One of the main purposes of such predictions is to determine the most appropriate follow-up test for cancer diagnosis or monitoring after a positive CancerSEEK test. We therefore grouped together patients with esophageal and gastric cancers because endoscopy would be the optimal follow-up in both instances. We then used this algorithm (supplementary materials) to study the 626 cancer patients with positive CancerSEEK tests. Without any clinical information about the patients, we were able to localize the source of the cancer to two anatomic sites in a median of 83% of these patients ($P < 10^{-77}$ one-sided binomial test) (Fig. 3 and table S8). Furthermore, we were able to localize the source of the positive test to a single organ in a median of 63% of these patients ($P < 10^{-47}$ one-sided binomial test) (Fig. 3 and table S8). Given that driver gene mutations are usually not tissue-specific, the vast majority of the localization information was derived from protein markers. The accuracy of prediction varied

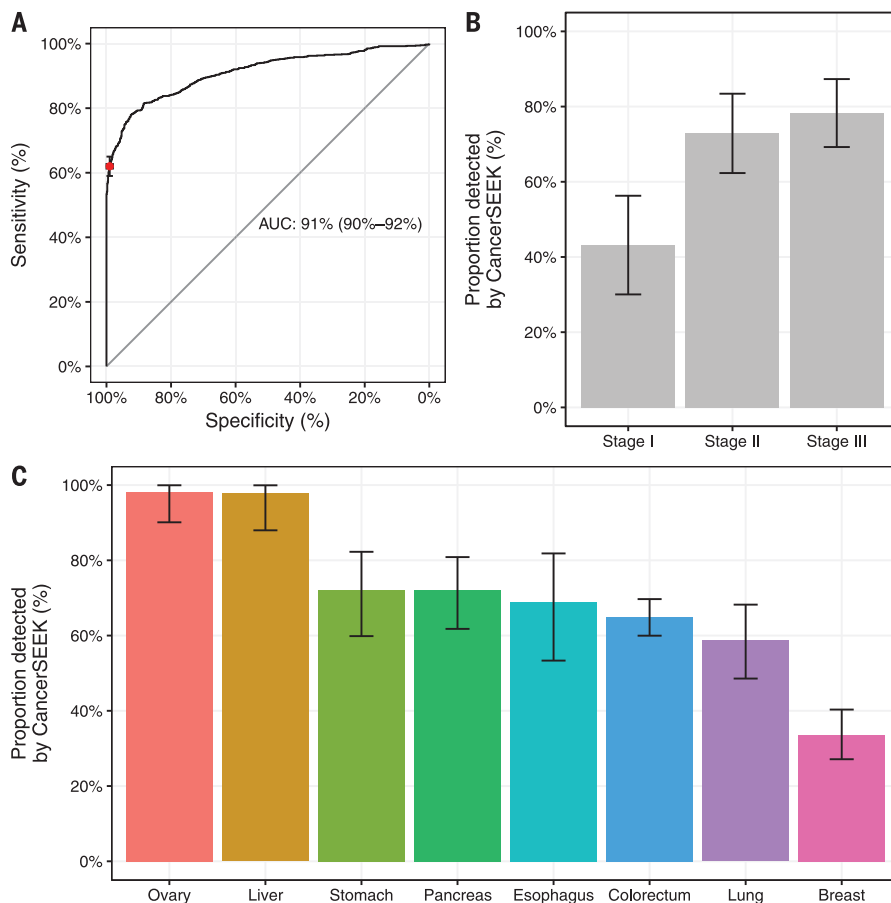


Fig. 2. Performance of CancerSEEK. (A) ROC curve for CancerSEEK. The red point on the curve indicates the test's average performance (62%) at >99% specificity. Error bars represent 95% confidence intervals for sensitivity and specificity at this particular point. The median performance among the eight cancer types assessed was 70%. (B) Sensitivity of CancerSEEK by stage. Bars represent the median sensitivity of the eight cancer types, and error bars represent standard errors of the median. (C) Sensitivity of CancerSEEK by tumor type. Error bars represent 95% confidence intervals.

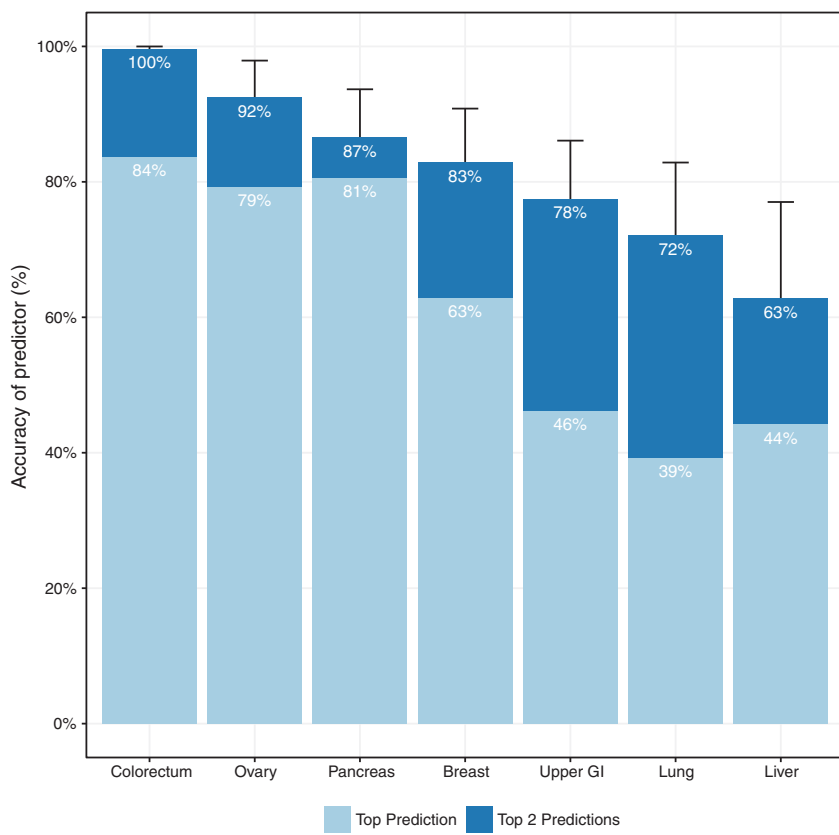


Fig. 3. Identification of cancer type by supervised machine learning for patients classified as positive by CancerSEEK. Percentages correspond to the proportion of patients correctly classified by one of the two most likely types (sum of light and dark blue bars) or the most likely type (light blue bar). Predictions for all patients for all cancer types are provided in table S8. Error bars represent 95% confidence intervals.

with tumor type; it was highest for colorectal cancers and lowest for lung cancers (Fig. 3 and table S10).

We have designed a multi-analyte blood test that can detect the presence of eight common solid tumor types. The advantage of combining completely different agents, with distinct mechanisms of action, is widely recognized in therapeutics (28–30) but has not been routinely applied to diagnostics. We combined protein biomarkers with genetic biomarkers to increase sensitivity without substantially decreasing specificity. Other cancer biomarkers—such as metabolites, mRNA transcripts, miRNAs, or methylated DNA sequences—could be similarly combined to increase sensitivity and localization of cancer site. Such multi-analyte tests are not meant to replace other non-blood-based screening tests, such as those for breast or colorectal cancers, but to provide additional information that could help identify those patients most likely to harbor a malignancy.

Several limitations of our study should be acknowledged. First, the patient cohort in our study was composed of individuals with known cancers, most diagnosed on the basis of symptoms of disease. Although none of our patients had clinically evident metastatic disease at the

time of study entry, most individuals in a true screening setting would have less advanced disease, and the sensitivity of detection is likely to be less than reported here. Second, our controls were limited to healthy individuals, whereas in a true cancer screening setting, some individuals might have inflammatory or other diseases, which could result in a greater proportion of false-positive results than observed in our study. Third, although multiple-fold cross-validation is a powerful and widely used technique for demonstrating robust sensitivity and specificity on a cohort of this study's scale, we were not able to use a completely independent set of cases for testing, which would have been optimal. Last, the proportion of cancers of each type in our cohort was purposefully not representative of those in the United States as a whole because we wanted to evaluate at least 50 examples of each cancer type with the resources available to us. When weighted for actual incidence in the United States, we estimate the sensitivity of CancerSEEK to be 55% among all eight cancer types. This weighting would not affect the high sensitivities of CancerSEEK (69 to 98%) to detect five cancer types (ovary, liver, stomach, pancreas, and esophagus) for which there are no screening tests available for average-risk individuals.

Our study lays the conceptual and practical foundation for a single, multi-analyte blood test for cancers of many types. We estimate the cost of the test to be less than \$500, which is comparable or lower than other screening tests for single cancers, such as colonoscopy. The eight cancer types studied here account for 360,000 (60%) of the estimated cancer deaths in the United States in 2017, and their earlier detection could conceivably reduce deaths from these diseases. To actually establish the clinical utility of CancerSEEK and to demonstrate that it can save lives, prospective studies of all incident cancer types in a large population will be required.

REFERENCES AND NOTES

1. R. L. Siegel, K. D. Miller, A. Jemal, *CA Cancer J. Clin.* **67**, 7–30 (2017).
2. B. Vogelstein *et al.*, *Science* **339**, 1546–1558 (2013).
3. S. Jones *et al.*, *Proc. Natl. Acad. Sci. U.S.A.* **105**, 4283–4288 (2008).
4. S. Yachida *et al.*, *Clin. Cancer Res.* **18**, 6339–6347 (2012).
5. B. Vogelstein, K. W. Kinzler, *N. Engl. J. Med.* **373**, 1895–1898 (2015).
6. I. Bozic *et al.*, *eLife* **2**, e00747 (2013).
7. T. J. Semrad, A. R. Fahri, I. Y. Gong, V. P. Khatri, *Ann. Surg. Oncol.* **22** (suppl. 3), S855–S862 (2015).
8. C. G. Moertel *et al.*, *Ann. Intern. Med.* **122**, 321–326 (1995).
9. A. C. Huang *et al.*, *Nature* **545**, 60–65 (2017).
10. P. F. Pinsky, P. C. Prorok, B. S. Kramer, *N. Engl. J. Med.* **376**, 1285–1289 (2017).
11. C. Bettigowda *et al.*, *Sci. Transl. Med.* **6**, 224ra24 (2014).
12. D. A. Haber, V. E. Velculescu, *Cancer Discov.* **4**, 650–661 (2014).
13. S. J. Dawson *et al.*, *N. Engl. J. Med.* **368**, 1199–1209 (2013).
14. Y. Wang *et al.*, *Sci. Transl. Med.* **7**, 293ra104 (2015).
15. T. Forshaw *et al.*, *Sci. Transl. Med.* **4**, 136ra68 (2012).
16. C. Abbott *et al.*, *Nature* **545**, 446–451 (2017).
17. E. Beddoe, S. J. Sammut, M. Gao, C. Caldas, *Breast* **34** (suppl. 1), S31–S35 (2017).
18. J. Phallen *et al.*, *Sci. Transl. Med.* **9**, eaan2415 (2017).
19. I. A. Cree *et al.*, *BMC Cancer* **17**, 697 (2017).
20. J. D. Cohen *et al.*, *Proc. Natl. Acad. Sci. U.S.A.* **114**, 10202–10207 (2017).
21. A. Bardelli, K. Pantel, *Cancer Cell* **31**, 172–179 (2017).
22. F. Diehl *et al.*, *Proc. Natl. Acad. Sci. U.S.A.* **102**, 16368–16373 (2005).
23. S. A. Forbes *et al.*, *Nucleic Acids Res.* **45** (D1), D777–D783 (2017).
24. I. Kinde, J. Wu, N. Papadopoulos, K. W. Kinzler, B. Vogelstein, *Proc. Natl. Acad. Sci. U.S.A.* **108**, 9530–9535 (2011).
25. L. A. Liotta, E. F. Petricoin 3rd, *Clin. Adv. Hematol. Oncol.* **1**, 460–462 (2003).
26. H. Wang *et al.*, *Expert Rev. Proteomics* **13**, 99–114 (2016).
27. E. F. Patz Jr. *et al.*, *J. Clin. Oncol.* **25**, 5578–5583 (2007).
28. World Health Organization, *Treatment of Tuberculosis: Guidelines* (World Health Organization, 2010).
29. World Health Organization, *Consolidated Guidelines on the Use of Antiretroviral Drugs for Treating and Preventing HIV Infection: Recommendations for a Public Health Approach* (World Health Organization, 2016).
30. A. B. Benson 3rd *et al.*, *J. Natl. Compr. Canc. Netw.* **15**, 370–398 (2017).

ACKNOWLEDGMENTS

We thank our patients for their courage and generosity. We are grateful to C. Blair and K. Judge for expert technical and administrative assistance. We thank H. Ren, J. Olson, M. Hathcock, H. Zeh, A. Singh, S. Crippa, M. Ryan, and L. Ryan for their assistance with this study. This work was supported by the Lustgarten Foundation for Pancreatic Cancer Research; The Virginia and D. K. Ludwig Fund for Cancer Research; The Conrad N. Hilton Foundation; The Commonwealth Fund; The John Templeton Foundation; the Clinomics Program; Mayo Clinic Center for Individualized Medicine; the Mayo Clinic Biobank; The Sol Goldman Center for Pancreatic Cancer Research; The Michael Rolfe Pancreatic Cancer Research Foundation; The Benjamin Baker Scholarship; The Gray Foundation; S. Wojcicki and D. Troper; The Marcus Foundation; The Honorable Tina Brozman Foundation; The Burroughs Wellcome

Career Award for Medical Scientists; The Doris Duke Charitable Foundation (201407); and National Institutes of Health grants P50-CA62924, P50-CA102701, CA06973, CA152753, GM-07309, U01CA200469, and U01CA152753. N.P., S.Z., K.W.K., L.D., and B.V. are founders of Personal Genome Diagnostics and PapGene. B.V. and K.W.K. are on the Scientific Advisory Board of Sysmex-Inostics. B.V. is also on the Scientific Advisory Boards of Exelixis GP. R.H.H. is on the Board of Directors of MiDiagnostics. These companies and others have licensed technologies from Johns Hopkins, and N.P., K.W.K., L.D., B.V., and R.H.H. receive equity or royalties from these licenses. The terms of these arrangements are being managed by Johns Hopkins University in accordance with its conflict of interest policies. L.D. is on the Board of Directors of

Jounce Therapeutics and is a Scientific Advisor for Gencea, Cell Design Labs, and Merck. A.S.M. is a consultant for Abbvie, Genentech, Bristol-Myers Squibb, and Trogogene. B.V., N.P., and K.W.K. are inventors on a patent (U.S. 20140227705 A1) held by Johns Hopkins University that covers basic aspects of the SafeSeqS technology used in this paper. B.V., K.W.K., N.P., J.D.C., C.T., and A.M.L. are inventors on a patent application to be submitted by Johns Hopkins University that covers other aspects of SafeSeqS as well as the multi-analyte approach described in this paper. All data needed to evaluate the conclusions in the paper are present in the paper and/or the supplementary materials. Contact C.T. for questions about the algorithms; A.M.L. for questions about clinically related issues; K.W.K. about the

sequencing analyses; B.V. about experimental procedures; and N.P. about the overall design of the study.

SUPPLEMENTARY MATERIALS

www.science.org/content/359/6378/926/suppl/DC1

Material and Methods

Figs. S1 to S4

Tables S1 to S11

References (31–37)

31 October 2017; accepted 8 January 2018

Published online 18 January 2018

10.1126/science.aar3247

PROTEIN EVOLUTION

Structural principles that enable oligomeric small heat-shock protein paralogs to evolve distinct functions

Georg K. A. Hochberg,^{1*}† Dale A. Shepherd,^{1*‡} Erik G. Marklund,^{1*§} Indu Santhanagopalan,^{2||} Matteo T. Degiacomi,^{1¶} Arthur Laganowsky,^{1#***††} Timothy M. Allison,¹ Eman Basha,^{2‡‡} Michael T. Marty,^{1‡‡} Martin R. Galpin,¹ Weston B. Struwe,¹ Andrew J. Baldwin,¹ Elizabeth Vierling,² Justin L. P. Benesch^{1§§}

Oligomeric proteins assemble with exceptional selectivity, even in the presence of closely related proteins, to perform their cellular roles. We show that most proteins related by gene duplication of an oligomeric ancestor have evolved to avoid hetero-oligomerization and that this correlates with their acquisition of distinct functions. We report how coassembly is avoided by two oligomeric small heat-shock protein paralogs. A hierarchy of assembly, involving intermediates that are populated only fleetingly at equilibrium, ensures selective oligomerization. Conformational flexibility at noninterfacial regions in the monomers prevents coassembly, allowing interfaces to remain largely conserved. Homomeric oligomers must overcome the entropic benefit of coassembly and, accordingly, homomeric paralogs comprise fewer subunits than homomers that have no paralogs.

Many proteins associate into selective homo- or heteromers in order to function (1). New assemblies are most often created by gene duplication of a preexisting homomer (2). The resulting oligomeric paralogs initially coassemble because both have the same sequence (and hence structure and interfaces) as their ancestor (Fig. 1A) (3). This coassembly can easily become entrenched if evolution of the two resulting duplicates is functionally constrained to maintain the interaction (4, 5), implying that heteromerization should be the most likely fate of oligomeric paralogs. However, when we analyzed the human, *Arabidopsis*, yeast, and *Escherichia coli* interactomes (supplementary materials and data file S1), we found that most oligomeric paralogs do not form heteromers (i.e., do not coassemble)

(Fig. 1B), despite overlapping localization and expression profiles (fig. S1, A and B). Moreover, we found that those paralogs that cannot coassemble share lower sequence identity and fewer common functions than paralogs that can (Fig. 1, C and D). This suggests that heteromerization acts as a constraint on the functional divergence of oligomeric paralogs (6). Relieving this constraint is therefore a key step in the evolutionary trajectories of oligomeric proteins toward evolving new functions.

To investigate how this occurs, we examined the selective assembly of two paralogous small heat-shock proteins (sHSPs), molecular chaperones found across the tree of life that are key to the cell's ability to respond to stress (7, 8). A duplication event led to land plants having two classes of cytosolic sHSPs (class 1 and 2; Fig. 1E and fig. S2) that both assemble as dodecamers but cannot form heteromers between classes (9). Both are required for thermotolerance in vivo (10) and have different mechanisms of action (11, 12). We chose one paralog of each class from *Pisum sativum*: HSP18.1 and HSP17.7 (hereafter WT-1 and WT-2, respectively). Both proteins comprise an N-terminal region, an α -crystallin domain, and a C-terminal tail, and both form homo-12mers (12) using three independent interfaces: The α -crystallin domain mediates the formation of an isologous α - α dimer; these dimers assemble into oligomers through heterologous contacts between the α -crystallin domain and the C-terminal tails from neighboring dimers (α -C), and interactions between the N-terminal regions (N-N) (Fig. 1F) (13). Their complex, multi-interface architecture makes these proteins an ideal system to investigate how evolution acts to regulate the biophysical

properties of oligomers to develop a set of selective interfaces that allows them to diverge functionally.

Small-angle x-ray scattering experiments indicated that both proteins form tetrahedral oligomers (fig. S3), implying that there are no major differences in quaternary structure that prevent coassembly. Nonetheless, when we obtained native mass spectra of a mixture of WT-1 and WT-2 after prolonged incubation (Fig. 1G, upper) or initiating reassembly from their subunits (fig. S4A), we could not detect any hetero-12-mers in either case. However, both homo-12-mers underwent continual dissociation and reassociation, although WT-1 did so >10 times faster than WT-2 (fig. S4). These facile quaternary dynamics show that heteromers are in principle kinetically accessible and so, despite the similarity in quaternary architectures of WT-1 and WT-2, must be thermodynamically unfavorable.

To identify the sequence determinants of selective assembly, we aligned class 1 and 2 sHSPs and noted conserved differences in their C-terminal tails (fig. S5). We then engineered a chimera with the class 1 N-terminal region and α -crystallin domain linked to the class 2 C-terminal tail ($N_1\alpha_1C_2$; see table S1) and incubated it with WT-2. This small change in sequence produced a series of hetero-12-mers formed between WT-2 and $N_1\alpha_1C_2$ (Fig. 1G, lower). These represent a proxy for class 1 and 2 coassembly and allowed us to interrogate the functional consequences of heteromerization. We incubated purified sHSPs with pea leaf lysate under heat-shock conditions to form reversible aggregates (14), mimicking their action in vivo (10, 11). WT-2 partitioned significantly faster into the insoluble fraction than WT-1 (Fig. 1H and fig. S6). The rate measured for the heteromers of $N_1\alpha_1C_2$ and WT-2, however, was intermediate between that of WT-1 and WT-2 homomers. The functional differentiation of the two proteins therefore depends on their selective homomerization, demonstrating the operational necessity of avoiding coassembly.

The hetero-12-mers formed by swapping C-terminal tails comprised only even numbers of each type of subunit (Fig. 1G, lower), implying that either the α - α or the N-N interface must also be selective. To determine which, we engineered an N-terminal chimera, $N_2\alpha_1C_1$, and incubated it with WT-1. This produced a series of hetero-12-mers comprising odd and even numbers of each subunit (fig. S7A). Although N-N contacts therefore are not thermodynamically selective (and hence the α - α interface must be), we noticed that dissociation of $N_1\alpha_1C_2$ oligomers was as fast as that of WT-1 (fig. S7B), whereas dissociation of $N_2\alpha_1C_1$ was slower (fig. S7A). This means that the promiscuous N-N contacts, not the thermodynamically selective α -C and α - α interfaces, control the kinetic stability of the 12-mers.

Our subunit-exchange data indicate that, over the functional temperature range, hetero-12-mers formed via N-N contacts during assembly would decompose into homomers on the time scale of minutes to hours (fig. S4E). Yet, we had observed no long-lived heteromers in our assembly experiment, even at low temperatures (fig. S4A). To

*Physical and Theoretical Chemistry Laboratory, Department of Chemistry, University of Oxford, Oxford OX1 3QZ, UK.

†Department of Biochemistry and Molecular Biology, University of Massachusetts, Amherst, MA 01003, USA.

‡These authors contributed equally to this work. †Present address: Department of Ecology and Evolution, University of Chicago, Chicago, IL 60637, USA. ¶Present address: Waters Corporation, Stamford Avenue, Wilmslow SK9 4AX, UK. §Present address:

Department of Chemistry-BMC, Uppsala University, Box 576, 75123, Uppsala, Sweden. ||Present address: Department of Plant Sciences, University of Cambridge, Cambridge CB2 3EA, UK. ¶¶Present address:

Department of Chemistry, Durham University, South Road, Durham DH1 3LE, UK. #Present address: Center for Infectious and Inflammatory Diseases, Institute of Biosciences and Technology, Texas A&M Health Science Center, Houston, TX 77030, USA. **Present address:

Department of Chemistry, Texas A&M University, College Station, TX 77842, USA. ¶¶Present address: Department of Microbial Pathogenesis and Immunology, College of Medicine, Texas A&M Health Science Center, Bryan, TX 77807, USA. ¶¶¶Present address:

Department of Chemistry and Biochemistry, University of Arizona, 1306 East University Boulevard, Tucson, AZ 85721, USA.

§§Corresponding author. Email: justin.benesch@chem.ox.ac.uk

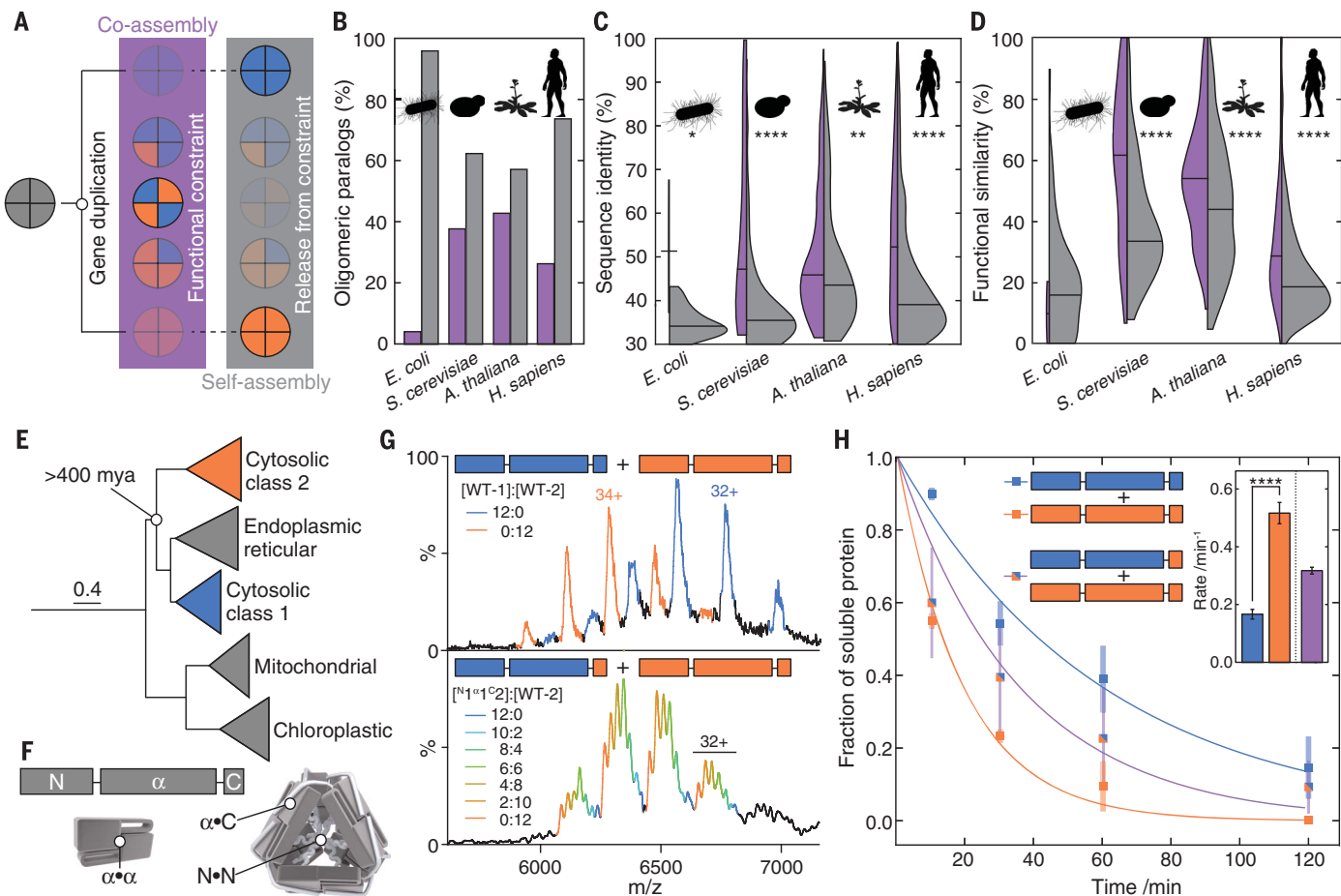


Fig. 1. Self-selective assembly allows oligomeric paralogs to evolve distinct functions. (A) After gene duplication, oligomeric paralogs coassemble into and predominantly populate heteromers, constraining their functions to be compatible with coassembly. If they subsequently evolve the ability to assemble self-selectively into homomers, their functions are free to diverge. (B) Percentage of pairs of oligomeric paralogs that either coassemble into heteromers (purple) or only self-assemble into homomers (gray) in *E. coli* (73 pairs in data set), *Saccharomyces cerevisiae* (215 pairs), *Arabidopsis thaliana* (742 pairs), and *Homo sapiens* (1086 pairs). (C) Pairwise sequence identity is higher between coassembling paralogs (purple) than between self-assembling paralogs (gray). Horizontal lines denote medians. * $P < 0.05$, ** $P < 0.01$, *** $P < 0.0005$, Mann-Whitney rank sums test. (D) Pairwise functional similarity of coassembling (purple) and self-assembling (gray) pairs of paralogs as measured by the intersection over the union of their Gene Ontology annotations. Horizontal lines denote medians. *** $P < 0.0005$, Mann-Whitney rank sums test. (E) Maximum-

likelihood phylogeny of select clades of plant shSPs. Scale bar indicates average number of substitutions per site. Mya, millions of years ago. (F) Schematic of the three different interfaces used by shSP to assemble into oligomers. (G) Mass spectrum of WT-1 and WT-2 after prolonged incubation plotted in the mass-to-charge (m/z) dimension. WT-1 (blue) and WT-2 (orange) 12-mers are observed, with varying numbers of charges. No peaks corresponding to heteromers are detected (upper). Hetero-12-mers are formed via exchange of dimers if WT-2 is mixed with $^{14}\text{N}^{14}\text{C}2$, resulting in additional peaks for each charge state (lower). One charge state is labeled for each 12-mer. (H) When mixed before incubation with pea-leaf lysate at 42°C, WT-1 and WT-2 partition into aggregates at different rates (**** $P < 0.0005$). When WT-2 is incubated with $^{14}\text{N}^{14}\text{C}2$, subunits from both proteins partition at the same, intermediate rate (inset). Heteromers thus function differently from segregated WT oligomers. Error bars in the raw data are standard deviations from three independent experiments; error bars in the inset are standard deviations calculated from 1000 bootstrap replicates of the fit.

resolve this apparent conflict, we generated constructs of WT-1 and WT-2 lacking the N-terminal region and measured their stoichiometries using native ion mobility mass spectrometry (IM-MS). Both were polydisperse, spanning dimers to 12-mers (Fig. 2A and fig. S8A). Constructs instead lacking the C terminus only formed monomers and dimers (Fig. 2B and fig. S8B). α -C contacts therefore likely form early and ensure rapid self-selective oligomerization, whereas N-N contacts subsequently stabilize the 12-meric fraction (fig. S8C and supplementary text). This hierarchy ob-

viates the need for kinetically stable N-N contacts to be selective and avoids long-lived heteromers that would compromise the rapid stress response of shSPs in the cell.

To understand the thermodynamic basis of selectivity at the α -C interface, we examined chimeric versions of the N-terminal truncations. $^{14}\text{C}2$ formed polydisperse oligomers, but $^{14}\text{C}1$ did not assemble beyond a dimer (Fig. 2C and fig. S8, D to F). Selectivity in the α -C interface is therefore directional, arising from an unfavorable association between the WT-1 C-terminal tail and

WT-2. We quantified this effect directly by excising the core domains of both proteins ($^{14}\text{C}1$ and $^{14}\text{C}2$, table S1) and measuring their affinity for each other's C-terminal tails. Whereas $^{14}\text{C}1$ bound peptides mimicking each tail equally well, $^{14}\text{C}2$ had a much lower affinity for a WT-1 than WT-2 peptide ($\Delta\Delta G > 6$ kJ mol⁻¹, fig. S9).

We next turned our attention to the α - α interface, which is selective (fig. S10A) despite high sequence conservation (fig. S5B). Crystal structures revealed $^{14}\text{C}1$ and $^{14}\text{C}2$ to be extremely alike (Fig. 3, A and B, and table S2). The dimer interface

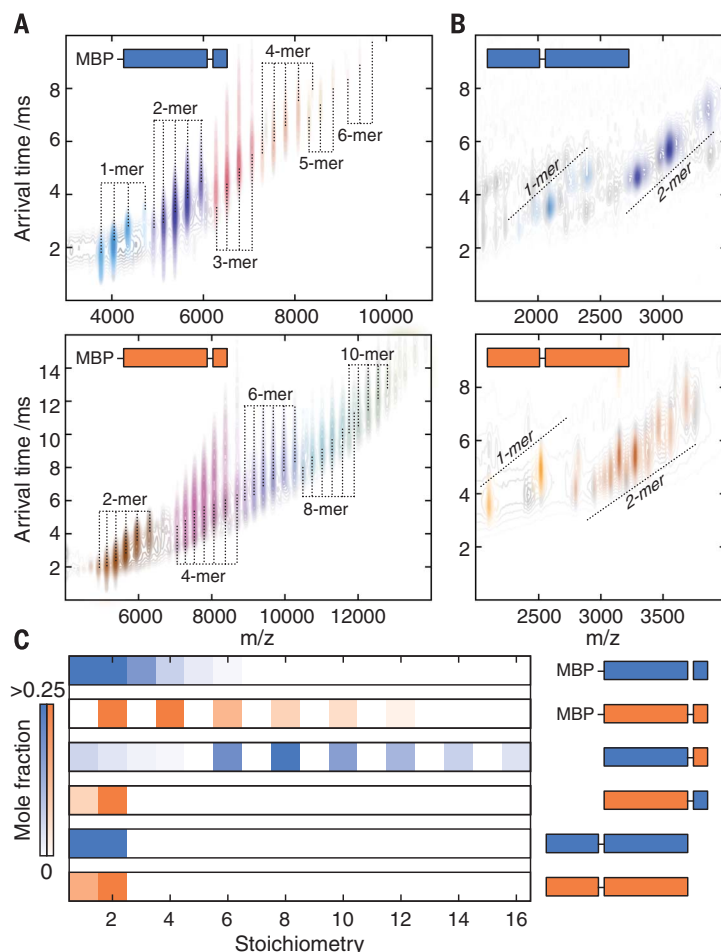


Fig. 2. Oligomeric interfaces form in a hierarchical order. (A) IM-MS spectra of truncated constructs of WT-1 (upper) and WT-2 (lower) lacking the N-terminal region. The two dimensions of separation (m/z and arrival time, which depends on collision cross section) separate charge-state series corresponding to a series of stoichiometries (colored individually). Both truncated proteins assemble into polydisperse ensembles. MBP, maltose binding protein. (B) IM-MS spectra of truncated constructs of WT-1 (upper) and WT-2 (lower) lacking the C-terminal tail. Both proteins do not assemble beyond dimers. Truncations in the exposed N-terminal region result in several charge series for monomers and dimers that are separated in the arrival-time dimension (see fig. S8 for detailed assignments). (C) Distribution of stoichiometries populated by truncated constructs extracted from spectra in (A), (B), and fig. S6. The C-terminal tail is required for assembly beyond dimers, whereas the N terminus is required for monodisperse 12-mers. The ${}^{\alpha}2{}^{\alpha}1$ construct (fig. S8E) does not oligomerize, indicating an unfavorable α -C interaction.

is formed in both homodimers by salt bridges centered on the β_8 - β_9 loop (L8/9) that are fully conserved between the two proteins, and by reciprocal strand-exchange between β_6 and β_2 . The latter involves only one obvious class-specific contact: between the π systems of a histidine on β_6 and a tryptophan on β_2 in WT-1 that is absent in WT-2 (Fig. 3, C and D). In 2- μ s molecular dynamics (MD) simulations, both homodimers and a modeled heterodimer were stable. The interfaces of the heterodimer featured equivalent overall numbers of interacting side chains, hydrogen bonds, and level of structural flexibility compared to both homodimers (figs. S10, B to E, and S11). The α -crystallin domain is therefore selective,

with only minimal differences in the number or type of contacts at its interface.

To investigate the origin of this selectivity, we performed calorimetric measurements and found that there are differences in the relative contributions from entropy and enthalpy to the favorable free energy of dimerization in ${}^{\alpha}1$ and ${}^{\alpha}2$ (fig. S12, A to C). This suggests subtle differences in their association mechanisms that may impart selectivity. To quantify which parts of the dimer are responsible for selectivity, we divided the core domain into three segments (Fig. 3E and table S1): the β -sandwich (S), which includes the L8/9 interface and β_2 from the β_6 - β_2 interface; β_6 (B); and the loop (L) connecting β_6 to the β -sandwich.

We shuffled these segments between ${}^{\alpha}1$ and ${}^{\alpha}2$ (Fig. 3E) and, for the 36 pairwise combinations of chimeric and wild-type constructs, determined the corresponding free energy of dimerization, $\Delta G_{\alpha\alpha}$, by performing quantitative IM-MS titration experiments (fig. S12, D to G). From the overall data set, we identified statistically significant intermolecular interactions between β_6 and the β -sandwich (B-S) and between the loop and the β -sandwich (L-S). Summed (B+L-S, Fig. 3F), these interactions contribute ≈ 11 kJ mol $^{-1}$ to the stability of the dimer, except when ${}^{\alpha}2$ encounters ${}^{\alpha}1$, which unilaterally destabilizes the dimer by ≈ 7 kJ mol $^{-1}$ (Fig. 3F, left). The L-S and B-S components contribute nearly equally to dimer stability (Fig. 3F, middle and right), a surprising observation considering that the loop is not part of the interface.

Because the ${}^{\alpha}1$ and ${}^{\alpha}2$ dimer structures did not reveal differences that account for our experimental thermodynamic data, we performed steered MD simulations in which we gradually detached β_6 from β_2 and estimated the resulting free-energy profile (Fig. 3G). As predicted by our thermodynamic data, we found that the heteromeric ${}^{\alpha}B+L-S-{}^{\alpha}2$ interface was significantly easier to break than the other combinations. We also noticed that in unconstrained simulations of the ${}^{\alpha}1$ monomer (performed in triplicate), the β -sandwich remained rigid (Fig. 3H and fig. S13, A, C, and D), whereas the loop distorted and formed intramolecular contacts (fig. S13D). In the ${}^{\alpha}2$ monomer, the loop more closely retained its conformation from the dimer (Fig. 3I and fig. S13, B to D), but β_2 detached from the β -sandwich and became highly flexible (fig. S13, C to E).

Our data imply that the loop in ${}^{\alpha}1$, and β_2 in ${}^{\alpha}2$, have a propensity to sample conformations in the monomers that are limited upon formation of a dimer interface (fig. S13D). In both homodimers, only one side of each B+L-S interface is restrained in this way, whereas in the heterodimer, both sides of the ${}^{\alpha}B+L-S-{}^{\alpha}2$ interface are restrained (Fig. 4), making it easier to break apart. Conversely, to dimerize, dynamic regions must undergo a structural transition from their monomeric conformations. In homodimers, only one side of each interface would have to do this, with the other being pre-ordered for dimerization. In a heterodimer, this conformational complementarity would be absent for the ${}^{\alpha}B+L-S-{}^{\alpha}2$ interface, also leading to a slow association rate. These effects would therefore combine to discourage the formation of heterodimers and instead ensure self-selection.

If this mechanism is correct, with the loop making a large contribution to the instability of the heterodimer (Fig. 3E), it should be a major regulator of the monomeric structure. Indeed, the conformations of simulated chimeric monomers lie between the extremes occupied by ${}^{\alpha}1$ and ${}^{\alpha}2$, and the segment that shifts the structure the most is the loop, not the interfacial segments (fig. S13F). Similarly, chimeric dimers incorporating segments that do not change conformations in our simulations (${}^{\alpha}S_1$, ${}^{\alpha}B_2$, and ${}^{\alpha}L_2$; Fig. 3E) should be more stable than both ${}^{\alpha}1$ and ${}^{\alpha}2$. This prediction is borne out in their experimental melting temperature being $\approx 5^{\circ}\text{C}$ higher (fig. S13G).

We mined our MD trajectories for specific contacts that were more abundant in one class over the other and identified 11 and 3 that involved residues that displayed class-specific evolutionary conservation in “1 and “2, respectively. Notably, we found that most of these are outside of the dimer interface: In “1, 7 out of 11 conserved sites either attach β 2 to the sandwich or promote curling of the loop, whereas in “2, one maintains an extended loop conformation (fig. S14), and another makes β 2 prone to detach in the monomer. Thus, noninterfacial regions, and their effects on the structure of dissociated monomers, determine selectivity in the α -crystallin domain of class 1 and 2 sHSPs across land plants. This is consistent with the observation that noninterfacial residues can affect interface stabilities (15).

To homomerize, paralogs must overcome a substantial entropic benefit of coassembly arising

from the number of ways distinguishable subunits can be arranged. This mixing entropy increases with the number of subunits in the oligomer such that the energetic cost of homomerization rises logarithmically (Fig. 4A) (supplementary text). Combining this contribution with the strength of interactions that we quantified experimentally allowed us to generate a model predicting the stability of all possible combinations of the two sHSPs and their chimeras, dependent only on their stoichiometry and constituent α -C and α - α interfaces (supplementary text and fig. S15). We used this model to calculate the difference in stability between every possible heteromer and the corresponding homomers along the assembly pathway (Fig. 4B). The selective interactions in the α -C and α - α interfaces narrowly overcome the entropic benefit of coassembly for all stoichiometries (Fig. 4C), result-

ing in a predicted population of hetero-12-mers at equilibrium that is just below detectable levels (Fig. 4C, right).

Homomers are therefore only marginally more stable than heteromers, even though the paralogs have diverged for >400 million years (16). The number and type of selective interactions that we found are the minimum required for a tetrahedron (17), with half of the oligomeric interfaces (N-N and those involving α -2) remaining promiscuous. These observations imply that selectivity is difficult to evolve, perhaps because most substitutions that disfavor coassembly also disfavor self-assembly (18).

Our model predicts that this would be more problematic for oligomers with more subunits, for which the entropic barrier to self-assembly is higher (Fig. 4A). Using a data set of oligomeric architectures based on curated crystal structures

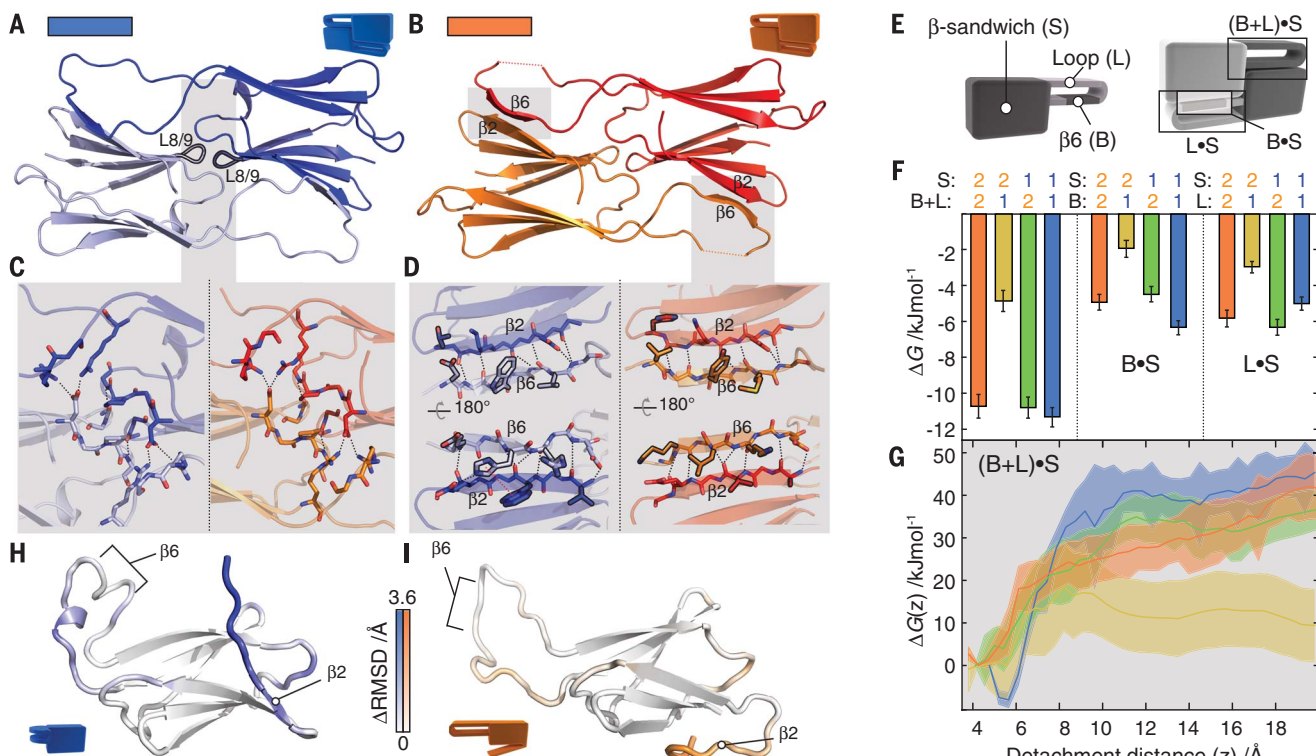


Fig. 3. Selectivity in the structurally conserved α -crystallin domain.

(A and B) “1 and “2 dimers have an identical fold [backbone root mean square deviation (RMSD) = 1.2 Å] in which two highly similar interfaces (labeled L8/9 and β 6- β 2) connect monomers. (C) The L8/9 interface is centered on the loop between β 8 and β 9 (black outline) and is indistinguishable in the two proteins. Interchain hydrogen bonds are shown as dashed lines. (D) The two β 6- β 2 interfaces in the dimer are formed by exchange between the β 6 and β 2 strands. Side chains that differ between “1 and “2 at homologous positions are outlined in black. The π -stacking interaction specific to “1 is shown as a dotted red line. (E) Constructs were designed by swapping the β -sandwich, loop, and β 6 strand (left). These were used to assess the strength of the β 6- β 2 interface and deconvolve the contribution from the loop and β 6 strand (right). (F) Global thermodynamic model of dimerization based on experimentally determined $\Delta G_{\alpha\alpha}$ values in fig. S12G. The combined loop and β 6 from “1 interact less favorably with β 2 than all other combinations (left).

“2 and “1 partition contributions to $\Delta G_{\alpha\alpha}$ differently (shaded). Error bars are standard deviations from 1000 bootstrap replicates of the model fit.

(G) In a simulated heterodimer, the free-energy barrier is significantly reduced for the “2-“1 pair (yellow), but indistinguishable from the homodimers in the case of “1-“2 (green) when the β 6- β 2 interface is disrupted along a reaction coordinate that separates them. Shaded area corresponds to the standard error of the mean. (H and I) Median monomeric conformations determined by principal-component analysis colored according to structural difference. This is calculated at each residue from the α -RMSD between “1 and “2 monomers, minus the RMSD between repeats for each monomer. Positive Δ RMSD values indicate conformational differences between proteins that cannot be explained by the variations intrinsic to each protein, and only those with $P < 0.05$ (after Bonferroni correction, permutation test) are colored. Differences are apparent in the loop surrounding β 6 and in β 2. In “1 the loop curls up, whereas in “2 the β 2 strand detaches readily from the remainder of the β -sandwich.

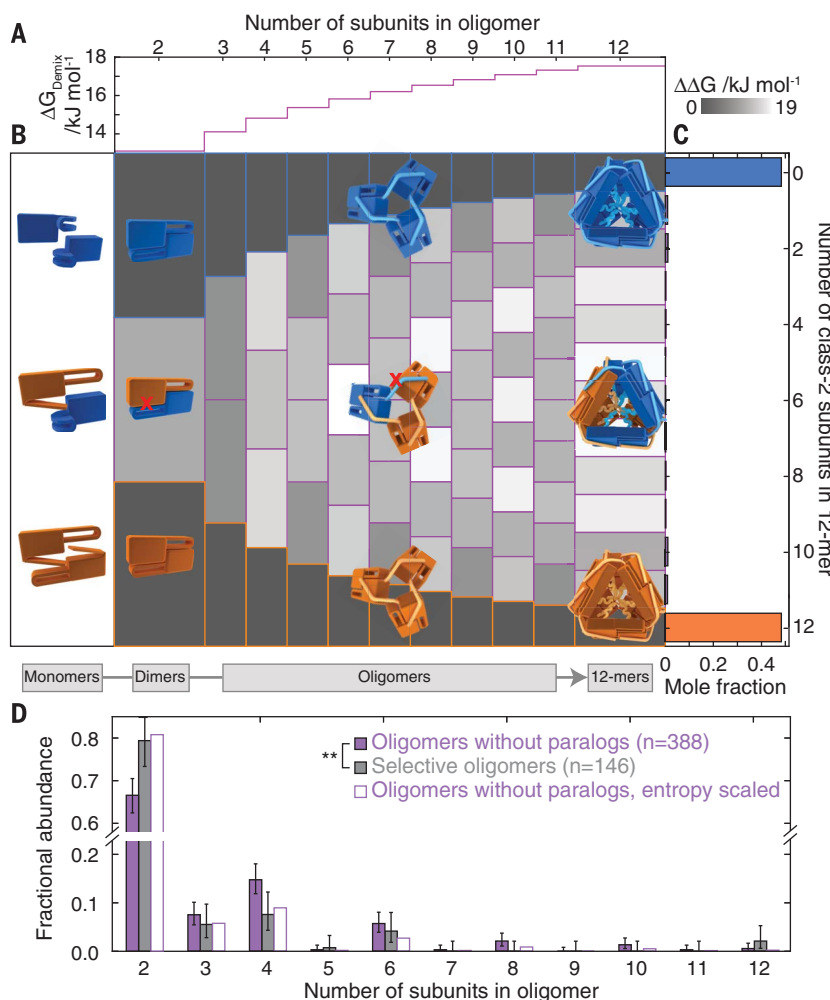


Fig. 4. Selective interfaces overcome unfavorable entropy of homomerization. (A) Selective homomerization is entropically unfavorable and requires an energetic penalty upon forming heteromeric contacts to suppress heteromerization. Shown is the theoretical magnitude of this penalty per subunit (ΔG_{Demix}) required to populate heteromers at only 2% of all oligomers. It increases logarithmically with the size of the oligomer, making it more challenging for larger oligomers to be selective. (B) Empirically derived stabilities of all possible heteromers along the assembly pathway compared to homomers of the same size ($\Delta \Delta G = \Delta G_{\text{heteromer}} - \Delta G_{\text{homomer}}$). The upper and lower tiles of each column correspond to homomers of WT-1 and WT-2, respectively. Those in between represent heteromers, with increasing numbers of WT-2 subunits (downward). The $\Delta \Delta G$ values are positive for all heteromers, meaning that the energetic penalty to coassembly that we quantified in selective interactions is larger than the positive entropy of heteromerization. (C) The equilibrium population of homo- and hetero-12-mers calculated based on the values in (B) results in mole fractions of hetero-12-mers just below detectable levels. More than 96% of subunits partition into homomers, compared to only 0.05% based on the binomial distribution of hetero-oligomers that would arise in the absence of selective interfaces. (D) The oligomeric stoichiometries populated by selective oligomeric paralogs (gray fill) are smaller with a particular excess of dimers than for a control set of oligomers that have no paralogs (purple). $**P < 0.005$, Mann-Whitney rank sums test. Error bars represent 90% Clopper-Person confidence interval, n denotes sample size. Applying a scaling according to ΔG_{Demix} to the control set reproduces closely the observed selective distribution (purple outline, $P = 0.0005$, Akaike information criterion).

(17) and combining it with our list of paralogs (Fig. 1B and data file S2), we found that self-selective paralogs comprise fewer subunits than homomers that have no paralogs (Fig. 4D). The data are well explained by the probability that

selectivity evolves after duplication being inversely proportional to the mixing entropy (supplementary text). Applying this relationship to scale the stoichiometry distribution of oligomers without paralogs renders it indistinguishable from

the self-selective set (Fig. 4D). This indicates that this fundamental thermodynamic bias acts as an evolutionary constraint across oligomeric proteins. The mechanisms for selectivity that we have uncovered for the sHSPs studied here are some of possibly many ways in which proteins have evolved to escape coassembly.

REFERENCES AND NOTES

1. J. A. Marsh, S. A. Teichmann, *Annu. Rev. Biochem.* **84**, 551–575 (2015).
2. J. B. Pereira-Leal, E. D. Levy, C. Kamp, S. A. Teichmann, *Genome Biol.* **8**, R51 (2007).
3. E. Kaltenegger, D. Ober, *Trends Plant Sci.* **20**, 814–821 (2015).
4. G. Diss *et al.*, *Science* **355**, 630–634 (2017).
5. G. C. Finnigan, V. Hanson-Smith, T. H. Stevens, J. W. Thornton, *Nature* **481**, 360–364 (2012).
6. C. R. Baker, V. Hanson-Smith, A. D. Johnson, *Science* **342**, 104–108 (2013).
7. W. E. Balch, R. I. Morimoto, A. Dillin, J. W. Kelly, *Science* **319**, 916–919 (2008).
8. K. Richter, M. Haslbeck, J. Buchner, *Mol. Cell* **40**, 253–266 (2010).
9. K. W. Helm, G. J. Lee, E. Vierling, *Plant Physiol.* **114**, 1477–1485 (1997).
10. F. McLoughlin *et al.*, *Plant Physiol.* **172**, 1221–1236 (2016).
11. M. Kirschner, S. Winkelhaus, J. M. Thierfelder, L. Nover, *Plant J.* **24**, 397–412 (2000).
12. E. Basha, C. Jones, V. Wysocki, E. Vierling, *J. Biol. Chem.* **285**, 11489–11497 (2010).
13. G. R. Hilton, H. Lioe, F. Stengel, A. J. Baldwin, J. L. P. Benesch, *Top. Curr. Chem.* **328**, 69–98 (2013).
14. E. W. Wallace *et al.*, *Cell* **162**, 1286–1298 (2015).
15. T. Perica *et al.*, *Science* **346**, 1254346 (2014).
16. E. R. Waters, E. Vierling, *Mol. Biol. Evol.* **16**, 127–139 (1999).
17. S. E. Ahnert, J. A. Marsh, H. Hernández, C. V. Robinson, S. A. Teichmann, *Science* **350**, aaa2245 (2015).
18. C. D. Aakre *et al.*, *Cell* **163**, 594–606 (2015).

ACKNOWLEDGMENTS

We thank C. Robinson, J. Schnell, P. Kukura, D. Staunton (all at University of Oxford), and B. Metzger (University of Chicago) for helpful discussions. We acknowledge access to B2I and help from M. Tully and J. Douthat at the Diamond Synchrotron (J.L.P.B. for SM9384-2); and the ARCUS cluster at Advanced Research Computing, Oxford. We thank the following funding sources: Engineering and Physical Sciences Research Council (G.K.A.H. for a studentship, J.L.P.B. for EP/J01835X/1); Carl Trygger's Foundation (E.G.M.); Swiss National Science Foundation (M.T.D. for P2ELP3_155339) and Biotechnology and Biological Sciences Research Council (A.J.B. for BB/J014346/1, J.L.P.B. for BB/K004247/1 and BB/J018082/1); National Institutes of Health (E.V. for R01 GM42761); Massachusetts Life Sciences Center (E.V. for a New Faculty Research Award); and the Royal Society (J.L.P.B. for a University Research Fellowship). All data necessary to support the conclusions are available in the manuscript or supplementary materials and are deposited with DOI 10.5287/bioRxiv:54jBVeAzw.

SUPPLEMENTARY MATERIALS

www.science.org/content/359/6378/930/suppl/DC1
 Materials and Methods
 Supplementary Text
 Figs. S1 to S15
 Tables S1 and S2
 References (19–77)
 Data Files S1 and S2

8 January 2017; resubmitted 25 September 2017
 Accepted 8 January 2018
 10.1126/science.aam7229

IMAGING

Single-cell bioluminescence imaging of deep tissue in freely moving animals

Satoshi Iwano,¹ Mayu Sugiyama,¹ Hiroshi Hama,¹ Akiya Watakabe,² Naomi Hasegawa,² Takahiro Kuchimaru,³ Kazumasa Z. Tanaka,⁴ Megumu Takahashi,⁵ Yoko Ishida,⁵ Junichi Hata,⁶ Satoshi Shimozono,¹ Kana Namiki,¹ Takashi Fukano,¹ Masahiro Kiyama,⁷ Hideyuki Okano,⁶ Shinae Kizaka-Kondoh,³ Thomas J. McHugh,⁴ Tetsuo Yamamori,² Hiroyuki Hioki,⁵ Shojiro Maki,⁷ Atsushi Miyawaki^{1,8*}

Bioluminescence is a natural light source based on luciferase catalysis of its substrate luciferin. We performed directed evolution on firefly luciferase using a red-shifted and highly deliverable luciferin analog to establish AkaBLI, an all-engineered bioluminescence *in vivo* imaging system. AkaBLI produced emissions *in vivo* that were brighter by a factor of 100 to 1000 than conventional systems, allowing noninvasive visualization of single cells deep inside freely moving animals. Single tumorigenic cells trapped in the mouse lung vasculature could be visualized. In the mouse brain, genetic labeling with neural activity sensors allowed tracking of small clusters of hippocampal neurons activated by novel environments. In a marmoset, we recorded video-rate bioluminescence from neurons in the striatum, a deep brain area, for more than 1 year. AkaBLI is therefore a bioengineered light source to spur unprecedented scientific, medical, and industrial applications.

Bioluminescence imaging (BLI) is based on the detection of light produced by the enzyme (luciferase)-catalyzed oxidation reaction of a substrate (luciferin) (1, 2). *In vivo* BLI is a noninvasive method for measuring light output from luciferase-expressing cells after luciferin administration in living animals (3), and this method typically employs firefly luciferase (Fluc) and the natural substrate D-luciferin (Fig. 1A, left) that produces longer-wavelength (green-yellow) light and is more stable for enzymatic reaction after administration than the other commonly used luciferase substrate, coelenterazine (4–7). However, due to its relatively low tissue permeability, D-luciferin has a heterogeneous biodistribution in the body (8). The low affinity (high Michaelis constant, K_M) of D-luciferin for Fluc also suggests uneven saturation of the Fluc reporter enzyme with

substrate *in vivo*. In particular, *in vivo* BLI in the brain has been hampered due to low passage of D-luciferin through the blood-brain barrier (BBB) (8). In recent years, synthetic analogs of D-luciferin were reported (9–11), including AkaLumine (Fig. 1A, right), that when catalyzed by Fluc produces near-infrared emission peaking at 677 nm, which can penetrate most animal tissues and bodies. We previously demonstrated that AkaLumine hydrochloride (AkaLumine-HCl) has favorable biodistribution to access Fluc-expressing cells in deep organs such as the lung and can saturate Fluc more effectively than D-luciferin (12).

We hypothesized that Fluc is not enzymatically optimal for AkaLumine-HCl; therefore, we performed directed evolution on the luciferase gene through successive rounds of mutagenesis, screening, and validation to develop an enzyme that could strongly pair with AkaLumine-HCl. We constructed gene libraries encoding variants of three luciferases (13)—Fluc, emerald luciferase (Eluc), and cricket beetle red luciferase (CBRluc)—and screened them by selecting for bacterial colonies with brighter emission in the presence of AkaLumine (fig. S1A). Candidates in the Fluc-based library were iteratively screened with multiple cycles of random mutagenesis (fig. S1B) to produce Akaluc, which has 28 amino acid substitutions relative to Fluc (fig. S1C). Application of D-luciferin and AkaLumine on bacterial colonies expressing Akaluc or Fluc enabled bright near-infrared emission with AkaLumine/Akaluc and very weak emission with the other combinations (fig. S2). *In vitro* experiments with purified luciferases (Fig. 1B) showed that Akaluc catalyzed AkaLumine ~7 times more efficiently

than Fluc to produce emissions with a maximum at 650 nm (fig. S3). Their catalytic activity was equally pH-sensitive (fig. S4) and, in addition, Akaluc exhibited higher thermostability than Fluc (fig. S5).

Akaluc-expressing HeLa cells (HeLa/Akaluc cells) were constructed after transfection with a cDNA encoding Venus-Akaluc and purification by flow cytometry for Venus fluorescence. Likewise, HeLa/Fluc cells were also prepared. We examined the comparative BLI performance of the four luciferin/luciferase combinations (Fig. 1C). To compare the performance of Akaluc and Fluc for AkaLumine in cultured cells, we additionally performed a comparative experiment using HeLa/Akaluc cells and HeLa/Fluc cells exposed to 500 μ M AkaLumine (fig. S6A). The cellular BLI signal ratio of Venus-Akaluc to Venus-Fluc was ~52. In addition, we analyzed Venus-luciferase-expressing HeLa cells by flow cytometry and quantified the expression level ratio of Venus-Akaluc to Venus-Fluc to be ~4. Accordingly, we assigned the ~13-fold improvement of Akaluc over Fluc to an improvement intrinsic to luciferase's catalytic activity. Akaluc showed a 3.79 ± 0.20 ($n = 58$) times higher expression level compared with Fluc (fig. S6B) despite the same speed of folding/degradation (fig. S7). Based on these results, we conclude that in cultured cells, Akaluc performs better than Fluc due to a 7- to 13-fold enhancement of its catalytic activity and a roughly 4-fold improvement in the expression level.

We next compared the *in vivo* BLI performance of AkaLumine-HCl/Akaluc and D-luciferin/Fluc in deep tissues of mice. Whereas *in vitro* and cellular BLI employs AkaLumine, *in vivo* BLI uses AkaLumine-HCl (see the supplementary materials). Care was taken in this study regarding the route, timing, and dose of systemic administration of the substrates (fig. S8). Considering the high K_M value for Fluc and the poor tissue delivery of D-luciferin, a relatively high dose of the substrate was injected (500 nmol/g body weight, comparable to a 100 μ l volume of 100 mM D-luciferin for an average-sized mouse). In contrast, a 100 μ l solution of 30 mM AkaLumine-HCl was injected into mice, a dose previously shown to provide a saturating concentration *in vivo* of AkaLumine-HCl (12).

We localized luciferase expression deep inside the mouse body by two approaches, (i) cell implantation in the vasculature and (ii) viral transduction in the brain. In the former approach, HeLa/Akaluc or HeLa/Fluc cells were transplanted. We injected 10^3 cells into the tail vein. Using this protocol, the majority of intravenously injected cells are initially trapped in the small capillaries of the lung (14, 15); thus, we imaged the upper part of an anesthetized animal 10 min after cell injection and immediately after intraperitoneal substrate administration. Under these conditions, the AkaLumine-HCl/Akaluc combination yielded a 52 ± 9.5 -fold stronger signal than D-luciferin/Fluc (Fig. 1D).

¹Laboratory for Cell Function and Dynamics, Brain Science Institute, RIKEN, 2-1 Hirosawa, Wako-city, Saitama 351-0198, Japan. ²Laboratory for Molecular Analysis of Higher Brain Function, Brain Science Institute, RIKEN, 2-1 Hirosawa, Wako-city, Saitama 351-0198, Japan. ³School of Life Science and Technology, Tokyo Institute of Technology, 4259 Nagatsuta, Midori-ku, Yokohama 226-8501, Japan.

⁴Laboratory for Circuit and Behavioral Physiology, Brain Science Institute, RIKEN, 2-1 Hirosawa, Wako-city, Saitama 351-0198, Japan. ⁵Department of Morphological Brain Science, Graduate School of Medicine, Kyoto University, Yoshida-Konoe-Cho, Sakyo-ku, Kyoto 606-8501, Japan.

⁶Laboratory for Marmoset Neural Architecture, Brain Science Institute, RIKEN, 2-1 Hirosawa, Wako-city, Saitama 351-0198, Japan. ⁷Graduate School of Informatics and Engineering, The University of Electro-Communications, 1-5-1 Chofugaoka, Chofu-city, Tokyo 182-8585, Japan. ⁸Biotechnological Optics Research Team, Center for Advanced Photonics, RIKEN, 2-1 Hirosawa, Wako-city, Saitama 351-0198, Japan.

*Corresponding author. Email: matsushi@brain.riken.jp

In the second approach, we imaged bioluminescence from the striatum, a group of contiguous subcortical structures deep in the brain involved in motor control and other functions. Because access of D-luciferin to the brain is lim-

ited by the BBB (8) but AkaLumine-HCl is tissue-permeant (12), we expected that brain imaging should benefit from AkaLumine-HCl/Akaluc. We used an adeno-associated virus (AAV)-based tetracycline (TET)-inducible system (16) for ex-

pression of Akaluc or Fluc (fig. S9) in the striatum. Two weeks after viral infection, mouse heads were comparatively imaged after substrate administration (intraperitoneal). First, the activity of striatally expressed Fluc was examined with different substrates, indicating that AkaLumine-HCl was more accessible to the brain than another reported synthetic analog CycLuc1 (10), as well as D-luciferin (fig. S10). In a pair of mice, strong and faint bioluminescence signals were observed for the AkaLumine-HCl/Akaluc and D-luciferin/Fluc combinations, respectively (Fig. 1E, top). We verified that a 100- μ l solution of 30-mM AkaLumine-HCl was sufficient for saturating striatally expressed Akaluc (fig. S11) and that both the AkaLumine-HCl/Akaluc and D-luciferin/Fluc signals developed in a similar sustained pattern, peaking around 10 to 20 min after substrate administration (intraperitoneal) (fig. S12). Statistical analysis revealed that AkaLumine-HCl/Akaluc yielded a 1408 ± 375 -fold stronger signal than D-luciferin/Fluc (Fig. 1E, middle, fig. S10), which is a more prominent improvement than that observed for pulmonary localization (Fig. 1D).

The all-engineered BLI system composed of AkaLumine-HCl and Akaluc is hereafter referred to as AkaBLI. AkaBLI with intravenous administration allowed the monitoring of brain striatal bioluminescence at video rate in a freely moving mouse for >1 hour (Fig. 1E, bottom right; fig. S13; and movie S1), demonstrating the practical applicability of AkaBLI for studying naturally behaving animals. The same measurement was not possible with D-luciferin/Fluc (Fig. 1E, bottom left). We also monitored the signal development of striatal AkaBLI via three major systemic administration routes (fig. S8). We found that the maximal intensity was higher in the order of intravenous, intraperitoneal, and oral administration and that intravenous gave the same temporal profile as intraperitoneal, whereas oral gave the most persistent bioluminescence (fig. S14). In a trial experiment, after 1 day of water deprivation we gave the mouse ad libitum oral access to an AkaLumine-HCl solution and recorded striatal AkaBLI. About 5 min after several fluid intakes, a substantial amount of bioluminescence became apparent on the head and was monitored at video rate for more than 1 hour (fig. S15 and movie S2). Such painless and voluntary self-administration of substrate to awake animals will be useful for BLI experiments under natural conditions and to assess sensitive behavioral changes.

Based on the bright bioluminescence signals from HeLa/Akaluc cells in the mouse lung (Fig. 1D), we examined the cell sensitivity of AkaBLI as a quantitative method to examine pulmonary cell trapping by titrating down the number of injected HeLa/Akaluc cells. By observation of Venus fluorescence, we prepared solutions that contained 1, 2, 3, or 10 HeLa/Akaluc cells (fig. S16). Twelve mice were injected with a 1-cell-containing solution (nos. 1 to 12). A focal bioluminescent signal was observed over the upper back of mice 6 and 9 (Fig. 2, 1 cell), presumably derived from the one HeLa/Akaluc cell trapped

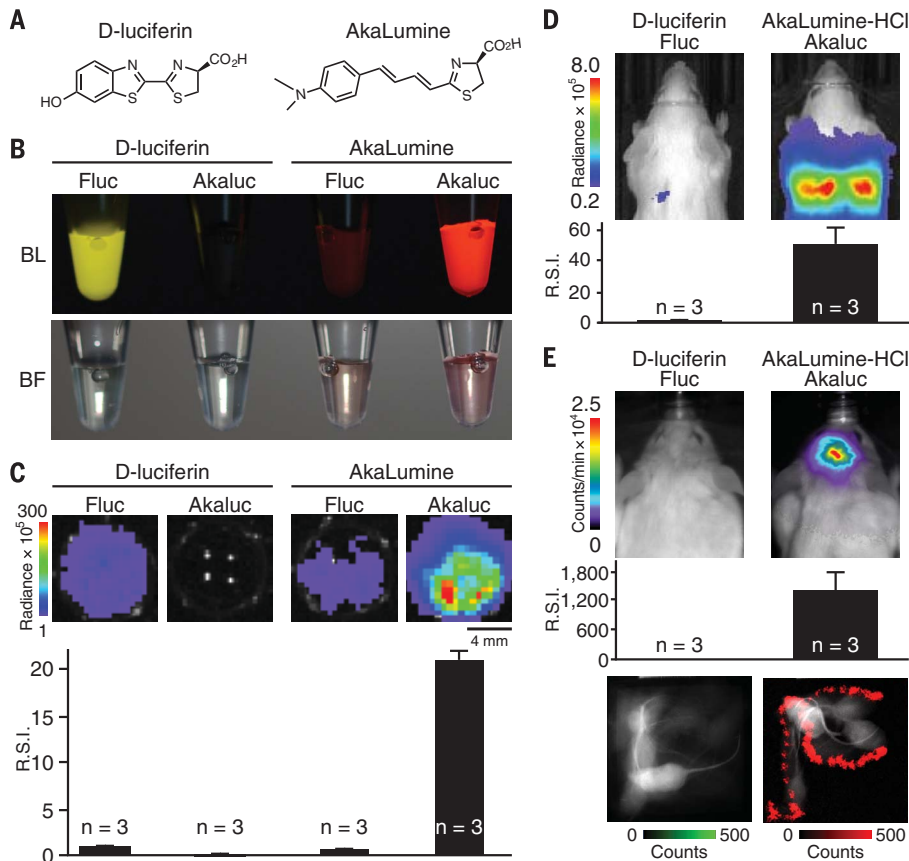
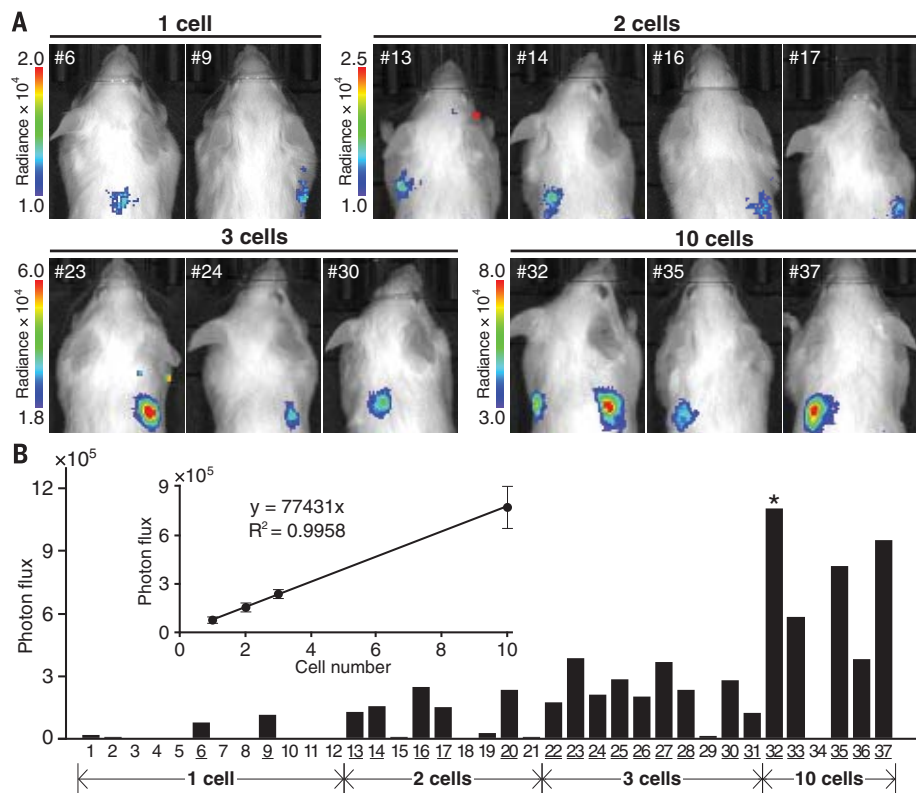


Fig. 1. Performance of engineered AkaLumine/Akaluc versus natural D-luciferin/Fluc for in vitro and in vivo bioluminescence imaging. (A) Chemical structures of D-luciferin (left) and AkaLumine (right). (B) BLI of four mixtures of the substrate (100 μ M) and enzyme (2 mg/ml). Color images of solutions containing (from left to right) D-luciferin/Fluc, D-luciferin/Akaluc, AkaLumine/Fluc, and AkaLumine/Akaluc. BL, bioluminescence (top). BF, bright-field (bottom). (C) Comparative BLI of cultured cells with the four substrate/enzyme combinations described in (B). HeLa cells expressing Fluc or Akaluc were treated with 250 μ M D-luciferin (left) or 250 μ M AkaLumine (right) and imaged using a cooled charge-coupled device (CCD) camera (1-min exposure time). Similar results were obtained from two other experiments. Bioluminescence signals were quantified and normalized to that of the D-luciferin/Fluc system. Data are presented as mean \pm SEM of three independent experiments. (D) Bioluminescence images of mice intravenously injected with 10^3 HeLa cells expressing Fluc (left) or Akaluc (right). Substrate administration was performed intraperitoneally. Images were acquired using a cooled CCD camera (1-min exposure time). The AkaLumine-HCl/Akaluc signals were statistically compared to D-luciferin/Fluc signals. Data are presented as mean \pm SEM of $n = 3$ mice. (E) Bioluminescence images of mice 2 weeks after viral infection for expression of Fluc (left) and Akaluc (right) in the right striatum. Immediately after substrate administration (intraperitoneal), anesthetized mice were imaged using a cooled CCD camera (top). The AkaLumine-HCl/Akaluc signals were statistically compared to D-luciferin/Fluc signals (middle). Data are presented as mean \pm SEM of $n = 3$ mice. After intravenous injection with their respective substrates, mice were allowed to behave naturally in the arena (bottom) were alternately acquired using an electron-multiplying CCD (EM-CCD) camera. An integrated image spanning 5 s is shown. Bioluminescence signals are shown in green (D-luciferin/Fluc) and red (AkaLumine-HCl/Akaluc). Bright-field signals are shown in black and white. Mice were injected with 100 to 200 μ l of D-luciferin (100 mM) or AkaLumine-HCl (30 mM) [(D) and (E)]. The color bars indicate the total bioluminescence radiance (photons/sec/cm²/sr) [(C) and (D)] and counts/min [(E)]. R.S.I., relative signal intensity [(C) to (E)].

Fig. 2. Analysis of single-cell and sparse-cell AkaBLI of implanted tumorigenic cells trapped in the mouse lung. Detection (all-or-nothing) of bioluminescence from a small number of Akaluc-expressing HeLa cultured cells trapped in the mouse lung. An anesthetized mouse was intravenously injected with the indicated number of cells and 10 min later with 100 μ l of AkaLumine-HCl (30 mM). Bioluminescence images were acquired using a cooled CCD camera (1-min exposure time). Mouse samples nos. 1 to 12, 13 to 21, 22 to 31, and 32 to 37 were injected with 1, 2, 3, and 10 cells, respectively. (A) Representative images with substantial bioluminescent signals. Mouse sample numbers are indicated inside. The color bars indicate the total bioluminescence radiance (photons/sec/ cm^2/sr). (B) Bioluminescence was quantified for each mouse and plotted. Numbers of samples with a significant amount of signal are underlined. The bioluminescent signals (mean \pm SEM) of the underlined samples are plotted as a function of cell number (inset).



in the lung. No signal was detected from the other 10 mice, suggesting efficient pulmonary passage of single cells. Likewise, mice injected with 2, 3, and 10 cells were imaged. Bioluminescence signals were observed in 5 of 9 mice given the 2-cell injection (Fig. 2, 2 cells) and in 9 of 10 mice given the 3-cell injection (Fig. 2, 3 cells), and all of them appeared as single foci. The 10-cell injection produced a focal fission in mouse 32 and single foci in mice 33, 35, 36, and 37 (Fig. 2, 10 cells). Because the bioluminescent foci mostly occurred singly on the body surface, and because the total bioluminescence intensity was linearly correlated with the number of injected cells (Fig. 2B, inset), it is likely that multiple circulating HeLa/Akaluc cells were clustered before being trapped in the lung. It is also noted that larger clusters were trapped in the lung more frequently; the bioluminescence detection rates were 2 of 12, 5 of 9, 9 of 10, and 5 of 6 for 1-, 2-, 3-, and 10-cell injections, respectively. This result agrees with a previous finding that pulmonary trapping depends on the size of infused cell clumps (14, 15). Although single-cell transplantation of fluorescent protein-labeled bone marrow cells was previously performed (17, 18), their repopulating activity was analyzed retrospectively by flow cytometry. In contrast, AkaBLI will allow real-time long-term monitoring of transplanted stem cells at the single-cell level.

We examined the capability of functional AkaBLI to detect behaviorally induced longitudinal changes in deep brain structures. We used neuronal-activity-dependent expression of im-

mediate early genes (IEGs), including c-Fos and c-Arc, to genetically mark neurons responsible for encoding learned experiences (19–21). Previous studies identified neurons activated by experiences occurring within a limited time window before sacrifice using postmortem histological techniques for the detection of IEG expression in fixed tissue (22, 23). Here, to noninvasively monitor active ensembles in the hippocampus during spatial learning and adaptation in a single living mouse, we designed an experimental system (Fig. 3A), in which Venus-Akaluc was expressed under the control of the *c-fos* promoter. The coupling between activity-dependent transcription and reporter gene expression was controlled by doxycycline (Dox) in the diet. A recombinant AAV expressing TRE-Venus-Akaluc was targeted unilaterally (right) to the CA1 area of hippocampus in a transgenic mouse line expressing *c-fos-tTA* (Fig. 3B). The experimental protocol using a single virus-infected mouse was composed of three consecutive observation epochs (1, 2, and 3) (Fig. 3C). In each epoch, three BLIs were carried out under anesthesia. The first BLI provided the background signal after Dox was withheld from the mouse for 48 hours (Fig. 3D, gray circles). Then, about 17 hours later, the mouse was allowed to explore a novel context (red cross) or a familiar context (blue cross) for 15 min \times 2. Exactly 7 hours after the exploration, the second BLI gave an exploration-dependent change in the signal (Fig. 3D, red circles). Finally, the mouse was maintained on a Dox diet for a long time (>4 days) for

the complete removal of TRE-Venus-Akaluc signal, which was confirmed by a background-level signal of the third BLI (Fig. 3D, black circles). These data serve as a practical indication of the sufficient degradation of the Akaluc reporter in multiple observations 1, 2, and 3, involving a novel environment, a return to the familiar home cage, and another novel environment, respectively (Fig. 3C). The temporal profile of the bioluminescence (Fig. 3D and fig. S17) validates the capability of AkaBLI to reliably track the response history of the same neurons to multiple stimuli over many days. Photographs of the first, second, and third BLIs during observation 1 (i, ii, and iii, respectively) (Fig. 3E) show the focal occurrence of the bioluminescence signal, indicating that the infection was confined to the injection site. About 8 hours after a treatment with kainic acid for the full activation of the infected neurons, we fixed the brain for tissue clarification with the ScaleS technique (24) and focused on the region containing the cortex and hippocampus for a three-dimensional reconstruction of Venus-expressing neurons (Fig. 3, F and G). Unexpectedly, only 49 neurons were identified as fluorescent and presumed bioluminescent emitters (Fig. 3G). We statistically validated the novelty-dependent increase in the neuronal activation signals over the background (Fig. 3H) and home-cage signals (Fig. 3I). The results demonstrate that AkaBLI can be used to directly monitor the activation patterns of much fewer numbers of neurons than any existing noninvasive optical

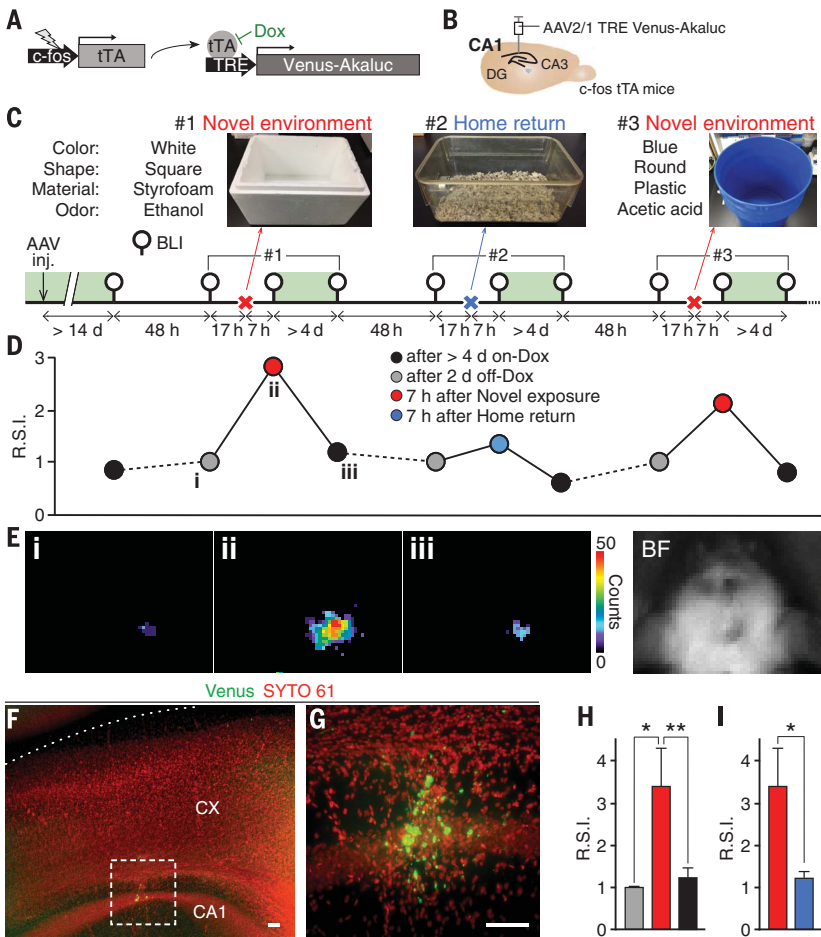


Fig. 3. Noninvasive monitoring of neuronal ensemble responses to novel environments in mouse hippocampal CA1 using AkaBLI. (A and B) c-fos-tTA mice were injected with AAV-TRE-Venus-Akaluc (A) targeting the right hippocampal CA1 region. (B) While off-Dox, exposure to a novel environment induces c-fos-dependent expression of tTA, which binds to the TRE and drives the expression of Venus-Akaluc, labeling a subpopulation of activated neurons. (C) Experimental setup to study brain responses to two novel environments: a white, square styrofoam box with an alcohol odor (#1), and a blue, round plastic bucket with an acetic acid odor (#3). The familiar context was a home cage (#2). Shown below is the experimental scheme containing three consecutive observation epochs: 1 to 3. BLI: Mice were anesthetized, administered (intraperitoneally) with AkaLumine-HCl (75 nmol/g body weight), and then imaged using a cooled CCD camera (5-min exposure time). Depilation was performed during the on-Dox period (green shade). (D and E) BLI data of a representative mouse, which showed a novel-context dependent increase in the bioluminescence signal. R.S.I., relative signal intensity. BLI time points correspond to BLI symbols shown in (C). Photographs of the first, second, and third BLIs during observation 1 [i, ii, and iii, respectively (D)] with bright-field image (BF) are shown (E). The color bar indicates the total bioluminescence counts/5 min. (F and G) Three-dimensional reconstructions of infected neurons with Venus expression (green) in a cleared brain sample stained for nucleic acid with SYTO 61 (red). Maximum projection images of the region containing the cortex (CX) and the hippocampal CA1. A magnified micrograph (G) (80- μ m volume, 0.5- μ m step size) corresponding to the box shown in (F) (910- μ m volume, 6.1- μ m step size). Scale bars, 100 μ m. (H and I) Statistical analysis of BLI data. Bioluminescence signals after novel exposure (red) compared with those taken 1 day earlier (gray) and >4 day later with Dox (black) (H). Bioluminescence signals after novel exposure (red) compared with those after home cage return (blue) (I). Data are presented as mean \pm SEM ($n = 6$ mice). * $P < 0.05$. ** $P < 0.01$. Significance was calculated by means of two-sided paired *t* tests.

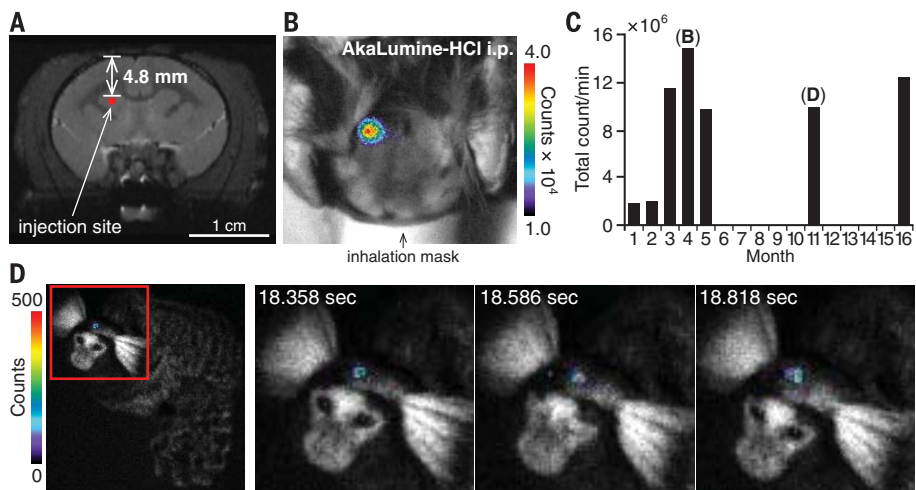
technique (25), therefore allowing the visualization of genetically defined small neural ensembles.

We examined AkaBLI as a method for the long-term noninvasive monitoring of the brain in a higher-order species by performing AkaBLI in the marmoset, a small New World monkey (26). A 4-year-old female marmoset was introduced with recombinant AAVs for expression of Akaluc. The injection was precisely guided by magnetic resonance imaging (MRI) (27) of the right striatum located 4.8 mm from the brain surface (Fig. 4A). The depilated head was imaged under anesthesia after AkaLumine-HCl administration (intraperitoneal), and AkaBLI was repeated every month at minimum. The bioluminescence emitted from the striatum was detected through the intact head, with an intensity peaking at 20 to 30 min after substrate administration (fig. S18). The BLI signal greatly increased over the 3 months after injection (Fig. 4B) and then lasted for many months (Fig. 4C), suggesting stable integration of the transgene in the transduced neurons. At 1 year after injection, we used a fast mode of BLI without anesthesia, and we were able to follow striatal bioluminescence with a 100-msec exposure time for over 1 hour while the 5-year-old female marmoset was freely moving (Fig. 4D, fig. S19, and movie S3). Her behavior was normal, suggesting that the dose of AkaLumine-HCl administration had no overt side effects (fig. S20). Such video-rate long-lasting and noninvasive BLI will have many applications in neuroscience for mapping and probing neural circuitry in behaving animals under natural conditions (28, 29).

In this study, the directed evolution of firefly luciferase with an artificial substrate allowed a major improvement for *in vivo* deep bioluminescence imaging. The AkaBLI system, composed of AkaLumine-HCl and Akaluc, enabled the improved performance by optimized Akaluc yield and catalysis of AkaLumine-HCl compared with Fluc. In accord, AkaBLI displayed superior sensitivity for *in vivo* noninvasive BLI in long-lasting video-rate monitoring of a few cells in freely moving animals. Importantly, we chose to demonstrate the AkaBLI in deep tissue areas to highlight the strength of the light source to penetrate body walls while retaining accurate spatial and temporal specificity. In contrast, current coelenterazine-based BLI systems are useful in dissociated cell- and slice-based *in vitro* applications but do not have adequate substrate biodistribution in animals *in vivo* (4, 5, 30, 31) (figs. S21 and S22), and there is no reliable evidence to date of the practical applicability of coelenterazine substrates for *in vivo* physiological studies. In contrast, AkaLumine-HCl has high permeability and stability for homogeneous substrate distribution inside the body, including the ability to cross the BBB into the brain. Thus, AkaBLI is expected to accurately map reporter enzyme expression as opposed to substrate distribution. Further coevolution of BLI enzymes and substrates will be a promising approach to synthetic biological light

Fig. 4. Chronic video-rate AkaBLI of brain striatal neurons in a common marmoset.

(A) Brain MRI picture (T2 weighted image) showing guided AAV injection into the right striatum of a 4-year-old female marmoset for expression of Venus-Akaluc. (B) A bioluminescence image 4 months after injection. After the AkaLumine-HCl (75 nmol/g body weight) administration (intraperitoneal), the head of the anesthetized marmoset was imaged using an EM-CCD camera (30-s exposure time). (C) Bioluminescence signals were quantified and plotted against time after injection. Due to growth with various degrees of depilation during the long time period, the efficiency of bioluminescence collection varied, and the data are displayed by a bar graph. (D) Bioluminescence images 12 months after injection. After AkaLumine-HCl administration (intraperitoneal), the entire marmoset (naturally behaving) was imaged using an EM-CCD camera (100-msec exposure time). An eye blink was recorded in three consecutive, expanded images. The color bars indicate the total bioluminescence counts/30 s (B) and counts/100 msec (D).



production for research, industry, and medical applications.

REFERENCES AND NOTES

1. T. Wilson, J. W. Hastings, *Annu. Rev. Cell Dev. Biol.* **14**, 197–230 (1998).
2. C. H. Contag, M. H. Bachmann, *Annu. Rev. Biomed. Eng.* **4**, 235–260 (2002).
3. A. Sacco, R. Dayonnas, P. Kraft, S. Vitorovic, H. M. Blau, *Nature* **456**, 502–506 (2008).
4. A. Pichler, J. L. Prior, D. Piwnica-Worms, *Proc. Natl. Acad. Sci. U.S.A.* **101**, 1702–1707 (2004).
5. N. Vassel et al., *Luminescence* **27**, 234–241 (2012).
6. L. Mezzanotte et al., *Contrast Media Mol. Imaging* **8**, 505–513 (2013).
7. A. C. Stacer et al., *Mol. Imaging* **12**, 457–469 (2013).
8. K.-H. Lee et al., *Nucl. Med. Commun.* **24**, 1003–1009 (2003).
9. S. Iwano et al., *Tetrahedron* **69**, 3847–3856 (2013).
10. M. S. Evans et al., *Nat. Methods* **11**, 393–395 (2014).
11. A. P. Jathoul, H. Grounds, J. C. Anderson, M. A. Pule, *Angew. Chem. Int. Ed. Engl.* **53**, 13059–13063 (2014).
12. T. Kuchimaru et al., *Nat. Commun.* **7**, 11856 (2016).
13. Z. M. Kaskova, A. S. Tsarkova, I. V. Yampolsky, *Chem. Soc. Rev.* **45**, 6048–6077 (2016).
14. S. Schrepfer et al., *Transplant. Proc.* **39**, 573–576 (2007).
15. U. M. Fischer et al., *Stem Cells Dev.* **18**, 683–692 (2009).
16. J. Sohn et al., *PLOS ONE* **12**, e0169611 (2017).
17. H. Ema et al., *Dev. Cell* **8**, 907–914 (2005).
18. R. Yamamoto et al., *Cell* **154**, 1112–1126 (2013).
19. L. G. Reijmers, B. L. Perkins, N. Matsuo, M. Mayford, *Science* **317**, 1230–1233 (2007).
20. S. Kubik, T. Miyashita, J. F. Guzowski, *Learn. Mem.* **14**, 758–770 (2007).
21. K. J. Kovács, *J. Neuroendocrinol.* **20**, 665–672 (2008).
22. C. J. Guenthner, K. Miyamichi, H. H. Yang, H. C. Heller, L. Luo, *Neuron* **78**, 773–784 (2013).
23. Y. Kim et al., *Cell Reports* **10**, 292–305 (2015).
24. H. Hama et al., *Nat. Neurosci.* **18**, 1518–1529 (2015).
25. M. Eguchi, S. Yamaguchi, *Neuroimage* **44**, 1274–1283 (2009).
26. K. Mansfield, *Comp. Med.* **53**, 383–392 (2003).
27. T. Hashikawa, R. Nakatomi, A. Iriki, *Neurosci. Res.* **93**, 116–127 (2015).
28. O. Sadakane et al., *Cell Reports* **13**, 1989–1999 (2015).
29. H. Okano et al., *Neuron* **92**, 582–590 (2016).
30. J. Chu et al., *Nat. Biotechnol.* **34**, 760–767 (2016).
31. H.-W. Yeh et al., *Nat. Methods* **14**, 971–974 (2017).

ACKNOWLEDGMENTS

The authors thank K. Ohtawa and R. Takahashi for technical assistance; S. Okabe for advice; Kurogane Kasei Co., Ltd., for providing AkaLumine and AkaLumine-HCl; Summit Pharmaceuticals International Corporation for granting the temporary use of IVIS Lumina III; and C. Yokoyama for manuscript editing. **Funding:** This work was supported in part by grants from the Japan Ministry of Education, Culture, Sports, Science, and Technology Grant-in-Aid for Scientific Research on Innovative Areas: Resonance Bio (15H05948 to A.M.; 16H01426 to H. Hioki); Scientific Research (16H04663 to H. Hioki); Exploratory Research (17K19451 to H. Hioki; 24650633 to S.M.); Adaptive, Seamless Technology Transfer Program through target-driven R&D JST (AS2614119N to S.M.); and the Brain Mapping by Integrated Neurotechnologies for Disease Studies (Brain/MINDS) and Japan Agency for Medical Research and Development-Core Research for Evolutional Science and Technology (AMED-CREST), the Uehara Memorial Foundation, and Special Postdoctoral Researchers Program from RIKEN (S.I.). **Author contributions:** S.I. and A.M. conceived and designed the

whole study. S.I. performed all the experiments and analyzed the data. M.S. analyzed Fluc mutants in cultured cells. S.S. performed gene construction. H. Hama designed and performed histological experiments. K.N. acquired light-sheet microscopy images. T.F. studied the thermostability of luciferases. A.W., N.H., J.H., H.O., and T.Y. performed AkaBLI experiments with the marmoset. T.K. and S.K. K. performed AkaBLI experiments of pulmonary trapping of transplanted tumor cells. M.T., Y.I., and H. Hioki prepared AAVs. K.Z.T., H. Hioki, and T.J.M. designed AkaBLI experiments for observing novelty-dependent neuronal activation. M.K. and S.M. performed quantum yield measurement and diphenylterazine synthesis. A.M. wrote the manuscript and supervised the project. **Competing interests:** S.I. and A.M. are inventors on patent application PCT/JP2017/030491 submitted by RIKEN that covers the creation and use of Akaluc. **Data and materials availability:** The data reported in this paper are presented in the main text and supplemental materials. The Akaluc genes (pcDNA3/Venus-Akaluc, pAAV2 SynTetOff Venus-Akaluc, pAAV2 TRE Venus-Akaluc) will be available from the RIKEN Bio-Resource Center (BRC) (<http://en.brc.riken.jp>) under a material transfer agreement with RIKEN. The accession number in the DDBJ/EMBL/GenBank database is LC320664 for Akaluc.

SUPPLEMENTARY MATERIALS

www.sciencemag.org/content/359/9378/suppl/DC1
 Materials and Methods
 Figs. S1 to S22
 Table S1
 Movies S1 to S3
 References (32–39)
 3 October 2017; accepted 31 December 2017
 10.1126/science.aaq1067

Cite as: V. Kasinath *et al.*, *Science* 10.1126/science.aar5700 (2018).

Structures of human PRC2 with its cofactors AEBP2 and JARID2

Vignesh Kasinath,^{1,2} Marco Faini,^{3*} Simon Poepzel,^{1,2*} Dvir Reif,¹ Xinyu Ashlee Feng,⁴ Goran Stjepanovic,^{1,2} Ruedi Aebersold,^{3,5} Eva Nogales^{1,2,6†}

¹QB3 Institute, Department of Molecular and Cell Biology, University of California, Berkeley, CA 94720, USA. ²Molecular Biophysics and Integrated Bioimaging Division, Lawrence Berkeley National Laboratory, Berkeley, CA, USA. ³Department of Biology, Institute of Molecular Systems Biology, ETH Zurich, 8093 Zurich, Switzerland.

⁴Department of Chemistry, University of California, Berkeley, CA, USA. ⁵Faculty of Science, University of Zurich, Zurich, Switzerland. ⁶Howard Hughes Medical Institute, University of California, Berkeley, CA 94720, USA.

*These authors contributed equally to this work.

†Corresponding author. Email: enogales@lbl.gov

Transcriptionally repressive histone H3K27 methylation by PRC2 (Polycomb repressive complex 2) is essential for cellular differentiation and development. Here we report cryo-EM structures of human PRC2 in two distinct, active states, while in complex with its cofactors JARID2 and AEBP2. Both cofactors mimic the binding of histone H3 tails. JARID2, methylated by PRC2, mimics a methylated H3 tail to stimulate PRC2 activity, while AEBP2 interacts with the RBAP48 subunit mimicking an unmodified H3 tail. SUZ12 interacts with all other subunits within the assembly and thus contributes to the stability of the complex. Our analysis defines the complete architecture of a functionally relevant PRC2 and provides a structural framework to understand its regulation by cofactors, histone tails and RNA.

Polycomb repressive complex 2 (PRC2) is responsible for introducing and maintaining heterochromatin regions and for spreading of a transcriptionally repressive state locally (1, 2). PRC2 consists of four core proteins: EZH2, EED, SUZ12 and RBAP46/RBAP48 (3). EZH2 catalyzes the trimethylation of histone H3 at lysine 27 (H3K27me3), a repressive marker ultimately resulting in transcriptional silencing via chromatin compaction (1). EED binding of H3K27me3 allosterically activates EZH2 (4, 5). PRC2 associates with several cofactors that may modulate its activity and aid in its recruitment to chromatin (3, 6–9). The best characterized cofactors are AEBP2 and JARID2, which coexist in PRC2 complexes (6, 10, 11).

A structure of human PRC2 with AEBP2, using negative-stain electron microscopy (EM), elucidated the overall architecture and subunit organization of the complex (12). More recently, crystal structures of the catalytic lobe, consisting of EZH2, EED, and the VEFS domain of SUZ12 (refer to Fig. 1A for proteins and domains), with either trimethylated H3 or a trimethylated JARID2 peptide bound to EED, hinted at a potential mechanism for allosteric activation of EZH2 (4, 5, 13–15). The binding of methylated JARID2 to EED, mimicking that of a methylated histone H3 tail, to EED has been suggested to play an important role in promoting PRC2 methyltransferase activity toward nucleosomes in the absence of pre-existing H3K27me3 (14). In both cases, binding of the methylated peptide stabilized a Stimulatory Responsive Mo-

tif (SRM) that is otherwise disordered and which subsequently interacts with the catalytic SET domain in EZH2 (4, 13, 15). Additionally, the crystal structure of RBAP48 bound to a histone peptide described its preference for unmodified H3 over H3K4me3, which is known to inhibit PRC2 (16). However, the mechanisms by which different histone substrates and cofactors regulate the activity of the complete complex are unknown. Since cofactors are thought to be integral parts of PRC2 complexes *in vivo* (10, 17–19), how they affect PRC2 structure and function remains a crucially important question.

Here, we report three high-resolution cryo-EM structures of the complete human PRC2 with the cofactors AEBP2 and JARID2, two corresponding to two distinct active states, and one corresponding to a basal state bound to a shorter JARID2 construct. The structures show that both JARID2 and AEBP2 mimic histone tails binding to PRC2 and that SUZ12 interacts with all other subunits and the cofactors. SUZ12 and AEBP2, with the help of JARID2, bridge the catalytic lobe with the rest of PRC2 and play a pivotal role in maintaining its structural integrity. Collectively, these structures elucidate the synergistic effect of AEBP2 and JARID2 on PRC2 activity.

To maximize the resolution of our cryo-EM analysis, we purified PRC2 with truncations in the core subunits EED and SUZ12 in order to eliminate large unstructured regions without known functional role (see Methods). We also used a minimal construct of JARID2 (aa 106–450) that has been shown to be sufficient for binding nucleosomes and stimulating

PRC2 activity (6, 7, 18). We refer to this 330 kDa complex as PRC2-AJ₁₀₆. Both cross-linking mass spectrometry (XL-MS) (Fig. 1B) and cryo-EM studies (fig. S1A) confirmed that the truncations did not affect the overall architecture of the complex. JARID2 has been shown to be a substrate of PRC2 and to bind to EED when methylated at K116 (13, 14). We obtained reconstructions at 3.5 Å and 3.9 Å for two coexisting conformational states of PRC2-AJ₁₀₆ (Fig. 1C and figs. S1B and S2), both containing a substrate JARID2 at the EZH2 active site, as well as a stimulatory, methylated JARID2 bound to EED (Fig. 2, A and B; fig. S3; and table S1). Therefore, we consider both states “active”, and refer to them as Compact Active and Extended Active states. While there is no significant difference in the conformation of the catalytic SET domain (fig. S4, A and B), the two states differ in the conformations of the SRM, which is stably bound in the Compact Active state, but disordered in the Extended Active state, as well as in the conformation of the SBD-SANT1 module, where SBD stands for SANT1-Binding Domain. While in the Compact Active state the SBD is bent and the SANT1 is packed against the SBD, in the Extended Active state the SBD is straight and the SBD-SANT1 module stands tall over the EED (Fig. 1C).

Figure 1D shows the overall structure of PRC2, in this case for the Compact Active state, bound to its two cofactors. In addition to the previously described catalytic half comprising the top lobe, which includes EZH2, EED and the SUZ12 VEFS domain, our study now describes the bottom lobe that includes the rest of the SUZ12, RBAP48 and stably bound segments of AEBP2 and JARID2. The resolution of our cryo-EM structures, together with XL-MS data, allowed us to generate an atomic model of this complete, functional relevant, six-subunit human complex (movie S1).

The previous crystal structure of the human catalytic subcomplex containing an activating peptide bound to EED corresponds closely to the Compact Active state described here (4, 13), likely because it was trapped in the more compact state. In our study the JARID2 segment bound to EED has fewer interactions with the SRM in the Extended Active state (Fig. 2A). In the Compact Active state, the interactions of methylated JARID2 with the EED aromatic cage (F97, Y148, Y365) and the side chain of D136 from the EZH2 SRM mirror those previously reported (Fig. 2A) (13). To probe further the role of JARID2 K116me2/3 in the conformational partitioning of PRC2, we also visualized a ternary complex of PRC2 bound to AEBP2 and a shorter JARID2 construct (aa 119–450) lacking K116, which we refer to as PRC2-AJ₁₁₉ (fig. S5). As expected, there is no JARID2 bound to either EED or the EZH2 active site (Fig. 2C), further supporting our assignments of the JARID2 segments in these regions for the active states of PRC2-AJ₁₀₆. The PRC2-AJ₁₁₉ structure overall resembles the Extended Active state (i.e., disordered SRM and straight

SBD), but differs from it in the relative position of the methyltransferase catalytic SET domain with respect to EED (fig. S4, B and C). Thus, the absence of JARID2 aa 106–118 results in a PRC2 structure that lacks the conformational landmarks associated with activation, and we refer to the structure of PRC2-AJ₁₁₉ as the Extended Basal state.

Our PRC2 structures validate biochemical experiments demonstrating that JARID2 is a substrate of PRC2 (14) through the direct visualization of two JARID2 molecules simultaneously bound to the allosteric and active sites of the complex. Such structures lend strong support to a model in which PRC2 initially acts on unmethylated JARID2 and methylates it at K116, and this methylated JARID2 then binds EED resulting in allosteric stimulation of PRC2 and a cascade of PRC2 activity toward additional unmethylated JARID2 substrate. Additionally, our observations emphasize the conformational versatility of PRC2, wherein the binding of a methylated peptide to EED is not strictly coupled to EZH2 (SRM) stabilization. The existence of two distinct “active” PRC2 states suggest that additional signals could exploit the conformational complexity of PRC2 in order to fine tune PRC2 methyltransferase activity, its interaction with nucleosomes, and/or other functional aspects of the complex. Furthermore, although we observe density for both cofactors in our structure (see below), both AEBP2 and JARID2 contain large disordered regions that are unresolved in our reconstructions. This flexibility of these cofactors, together with the coexistence of multiple conformational states, further reflect the intrinsic conformational variability that may be exploited in order to integrate diverse cues critical for the complex regulation of PRC2 in different biological contexts.

Our MS analysis of PRC2-AJ₁₀₆ revealed JARID2 to be mono-, di- and trimethylated at K116 and phosphorylated on neighboring Ser residues (S120, S124 or S126) (fig. S3, A and B). A similar MS analysis of PRC2-AJ₁₁₉ showed no differences in the phosphorylation of these residues in JARID2 (fig. S3B), suggesting that JARID2 K116 methylation by PRC2 is unlikely to be required for this phosphorylation. It is possible that phosphorylation facilitates processivity of JARID2 methylation by PRC2, perhaps by decreasing the off-rate of the K116me1 peptide at the active site. It is tempting to speculate that JARID2 phosphorylation could be part of a control mechanism of PRC2 methyltransferase activity toward JARID2, and thus of its activity on other targets as well. Further studies aiming at elucidating the relationship between serine phosphorylation and different methylation states of JARID2, as well as the conformational states of PRC2 hold promise of enhancing our mechanistic understanding of PRC2 regulation and function.

AEBP2, like JARID2, plays a role in stimulation of PRC2 methyltransferase activity (17, 20), but the structural basis for such stimulation is still unknown. AEBP2 contains three

C2H2-type zinc fingers (17) and previous labeling studies localized these domains by the top lobe of PRC2 near the EED/EZH2 (SET) domains (12). In our cryo-EM reconstructions, the N-terminal region of AEBP2 containing the three zinc-fingers is disordered, while part of the C-terminal region is clearly visible and appears to have a stabilizing effect on the complex (Fig. 2D and fig. S6A). The fold of AEBP2 is mostly dictated by its interactions with SUZ12. Residues 269–283 of AEBP2 interacts with the “foot” of the complex that is part of SUZ12 (Fig. 2D, see below), while a preceding helical segment (aa 246–266) forms extensive hydrophobic interactions with a helix near the N terminus of SUZ12 (referred to as ABH in Figs. 1D and 2D and fig. S7A). Most significantly, our structures reveal that K294 and R295, at the C terminus of AEBP2, mimic the binding of R2 and K4 of histone H3 to RBAP48 (16) (Fig. 2, D to F). This finding suggests a potential interplay between AEBP2 and unmodified H3K4 when PRC2 is recruited to nucleosomes.

Though unmodified H3K4 has been proposed to stimulate PRC2 through its binding to RBAP48 (16), a functional explanation for this allosteric effect was hard to envision, especially since RBAP48 is located 60 Å away from the EZH2-SET domain (fig. S6B). Our structures now suggest that the interactions of the C-terminal region of AEBP2 with RBAP48 and SUZ12 help position the more N-terminal flexible elements of AEBP2, including the three zinc-fingers, near the EZH2-SET domain (fig. S6C). This proposal is supported by our XL-MS analysis, which shows that residues 160–200 of AEBP2, a region rich in Lys and Arg, extends toward and likely interacts with the SET domain (fig. S6, A and C). Thus, AEBP2 appears to have the potential to establish a structural bridge between RBAP48 and the SET domain, which we propose contributes to the allosteric coupling of these distant sites (fig. S6C and S7C).

Our work directly shows that both cofactors, AEBP2 and JARID2, contain segments that simultaneously engage histone tail binding sites on PRC2. The observation that both cofactors mimic histone H3 tails suggests that they could function to regulate PRC2 activity in diverse chromatin environments by selectively overriding the effects of existing histone marks. JARID2 K116me2/3 can dispense with the need for H3K27me3 to stimulate PRC2, while AEBP2 interacts with RBAP48 at a site that is engaged by unmethylated H3K4, but not by the inhibitory H3K4me3 (16), potentially allowing PRC2 to remain active even in the presence of the H3K4me3 mark.

Structural and functional information on the role played by SUZ12 has so far been limited to the C-terminal VEFS domain (4, 13, 15, 20). Our structures now show that SUZ12 is critical for maintaining the integrity of the full complex and for the synergistic effect of AEBP2 and JARID2 on PRC2 activity. SUZ12 follows a complicated path through the complex

and interacts with all other core components as well as the two cofactors (Fig. 3A and fig. S8A). SUZ12 contains a C2H2-type zinc-finger domain (aa 448–472) (20) (Fig. 3D) that provides a platform for the folding of regions extending both N- and C-terminal (aa 426–548) that we collectively refer to as the “neck” region (referred to as “NR” in Fig. 3, A and B, and fig. S8A). The SUZ12 neck region interacts both with a AEBP2 helical segment (aa. 246–266) and a Lys and Arg rich region of AEBP2 (aa 160–200) and thereby helps AEBP2 establish a bridge between RBAP48 and the EZH2-SET domain. (Fig. 3B and 4C and fig. S6C). In addition, the SUZ12 neck region forms extensive hydrophobic interactions with catalytically important regions of EZH2 (the so-called SAL motif), EED and the SUZ12 VEFS domain. Mutations in residues of the SUZ12 neck region (R508C) and SUZ12 VEFS (N562S) seen in adenocarcinoma and myeloproliferative neoplasms (21, 22) map to the contacts with the EZH2 (SAL) and SUZ12 neck region, respectively. While the VEFS domain of SUZ12 has been known to be important for the proper folding and activity of EZH2 (4, 16), we now find that the interaction of the SUZ12 neck region with the VEFS domain is important for the stability of SUZ12 within the PRC2 complex (Fig. 3E). We also find that the region of SUZ12 corresponding to residues 109–136 wraps around RBAP48 in a manner similar to the folding of EZH2 around EED and is solely responsible for the incorporation of RBAP48 in the PRC2 complex (4, 13, 15) (fig. S7B).

The SUZ12 neck region serves as a scaffold for interaction with both cofactors. In addition to its critical role in the folding of AEBP2, as described above, the SUZ12 neck is also the region of stable interaction with JARID2 (Fig. 4). Previous studies showed that a JARID2 construct containing aa 147–165 is important for interaction with SUZ12 (19). Comparison of our structure of PRC2-AJ₁₀₆ with a 4.6 Å resolution cryo-EM structure of PRC2-AEBP2 (i.e., lacking JARID2;) (23) shows the presence of an additional density in the vicinity of the SUZ12 zinc-finger domain that we assigned to a JARID2 segment corresponding to aa 140–166 (Fig. 4, A and B). This assignment agrees with our XL-MS data, which shows the presence of cross-links between this region of JARID2 and the SUZ12 zinc-finger domain within the neck region (Fig. 4C). The JARID2 segment forms a helix-turn-helix motif (HTH) that wedges in between AEBP2 and a beta sheet region within the SUZ12 neck (Fig. 4D). The three-way junction between SUZ12, AEBP2 and JARID2 is important for stability, as a core PRC2 complex in the absence of JARID2 and AEBP2 becomes dramatically more flexible and its overall stability is decreased (Fig. 4D) (12). Our structures show how JARID2 stabilizes the interaction between AEBP2 and SUZ12 to maintain the integrity of the complex by stapling the top, catalytic, and bottom lobes together (Fig. 1D and 4D).

Finally, we observed a SUZ12 domain rich in beta-sheet

forming the “foot” of the complex (referred to as beta-sheet domain (BSD) in Fig. 3C and fig. S8, A and B). Because of its flexibility (fig. S2), we were only able to build this region as a poly-alanine chain (Fig. 3C). A domain search across the PDB database indicated that it resembles an RNA recognition motif (RRM)-like fold (24) (fig. S7B). SUZ12, as well as EZH2, have been implicated in RNA binding (25–27). Long non-coding RNAs (lncRNAs) have been proposed to play a role in PRC2 recruitment to nucleosomes (28) or affect its activity on nucleosome substrates (29). We carried out hydrogen-deuterium exchange experiments in the presence and absence of the lncRNA XIST A-repeat that showed that this domain contributes to RNA binding (fig. S8, C and D). Additional roles, such as binding to nucleosomes/DNA, are also conceivable for the flexible, RRM-like beta-sheet rich domain located at the foot of the complex.

Our structures of the full human PRC2 in complex with two critical cofactors AEBP2 and JARID2, include regions of AEBP2, JARID2 and SUZ12 for which there was no prior structural information (fig. S9). While the catalytic lobe of PRC2, containing EZH2, EED and part of SUZ12 has been shown to be sufficient for methyltransferase activity, the bottom lobe of PRC2 described here is likely to play additional regulatory functions for the activity and recruitment of the complex. Our structures highlight the critical role played by SUZ12 in maintain the integrity of the full complex. The interactions of both cofactors AEBP2 and JARID2 with PRC2 mimicking those of histone H3 tails result in two active states and contribute not only to the global stabilization of PRC2 (fig. S9) but also potentially aids in the synergistic stimulation of PRC2 activity and regulated recruitment to chromatin.

REFERENCES AND NOTES

1. R. Cao, L. Wang, H. Wang, L. Xia, H. Erdjument-Bromage, P. Tempst, R. S. Jones, Y. Zhang, Role of histone H3 lysine 27 methylation in Polycomb-group silencing. *Science* **298**, 1039–1043 (2002). [doi:10.1126/science.1076997](https://doi.org/10.1126/science.1076997) Medline
2. P. B. Talbert, S. Henikoff, Spreading of silent chromatin: Inaction at a distance. *Nat. Rev. Genet.* **7**, 793–803 (2006). [doi:10.1038/nrg1920](https://doi.org/10.1038/nrg1920) Medline
3. R. Margueron, D. Reinberg, The Polycomb complex PRC2 and its mark in life. *Nature* **469**, 343–349 (2011). [doi:10.1038/nature09784](https://doi.org/10.1038/nature09784) Medline
4. L. Jiao, X. Liu, Structural basis of histone H3K27 trimethylation by an active polycomb repressive complex 2. *Science* **350**, aac4383 (2015). [doi:10.1126/science.aac4383](https://doi.org/10.1126/science.aac4383) Medline
5. R. Margueron, N. Justin, K. Ohno, M. L. Sharpe, J. Son, W. J. Drury 3rd, P. Voigt, S. R. Martin, W. R. Taylor, V. De Marco, V. Pirrotta, D. Reinberg, S. J. Gamblin, Role of the polycomb protein EED in the propagation of repressive histone marks. *Nature* **461**, 762–767 (2009). [doi:10.1038/nature08398](https://doi.org/10.1038/nature08398) Medline
6. J. Son, S. S. Shen, R. Margueron, D. Reinberg, Nucleosome-binding activities within JARID2 and EZH1 regulate the function of PRC2 on chromatin. *Genes Dev.* **27**, 2663–2677 (2013). [doi:10.1101/gad.225888.113](https://doi.org/10.1101/gad.225888.113) Medline
7. S. Kaneko, R. Bonasio, R. Saldaña-Meyer, T. Yoshida, J. Son, K. Nishino, A. Umezawa, D. Reinberg, Interactions between JARID2 and noncoding RNAs regulate PRC2 recruitment to chromatin. *Mol. Cell* **53**, 290–300 (2014). [doi:10.1016/j.molcel.2013.11.012](https://doi.org/10.1016/j.molcel.2013.11.012) Medline
8. E. Walker, W. Y. Chang, J. Hunkapiller, G. Cagney, K. Garcha, J. Torchia, N. J. Krogan, J. F. Reiter, W. L. Stanford, Polycomb-like 2 associates with PRC2 and regulates transcriptional networks during mouse embryonic stem cell self-renewal and differentiation. *Cell Stem Cell* **6**, 153–166 (2010). [doi:10.1016/j.stem.2009.12.014](https://doi.org/10.1016/j.stem.2009.12.014)
9. Z. Zhang, A. Jones, C.-W. Sun, C. Li, C.-W. Chang, H.-Y. Joo, Q. Dai, M. R. Mysliwiec, L.-C. Wu, Y. Guo, W. Yang, K. Liu, K. M. Pawlik, H. Erdjument-Bromage, P. Tempst, Y. Lee, J. Min, T. M. Townes, H. Wang, PRC2 complexes with JARID2, MTF2, and esPRC2p48 in ES cells to modulate ES cell pluripotency and somatic cell reprogramming. *Stem Cells* **29**, 229–240 (2011). [doi:10.1002/stem.578](https://doi.org/10.1002/stem.578) Medline
10. A. Grijenhout, J. Godwin, H. Koseki, M. R. Gdula, D. Szumska, J. F. McGouran, S. Bhattacharya, B. M. Kessler, N. Brockdorff, S. Cooper, Functional analysis of AEBP2, a PRC2 Polycomb protein, reveals a Trithorax phenotype in embryonic development and in ESCs. *Development* **143**, 2716–2723 (2016). [doi:10.1242/dev.123935](https://doi.org/10.1242/dev.123935) Medline
11. S. Hauri, F. Comoglio, M. Seimiya, M. Gerstung, T. Glatter, K. Hansen, R. Aebersold, R. Paro, M. Gstaiger, C. Beisel, A high-density map for navigating the human Polycomb complexome. *Cell Rep.* **17**, 583–595 (2016). [doi:10.1016/j.celrep.2016.08.096](https://doi.org/10.1016/j.celrep.2016.08.096) Medline
12. C. Ciferri, G. C. Lander, A. Maiolica, F. Herzog, R. Aebersold, E. Nogales, Molecular architecture of human polycomb repressive complex 2. *eLife* **1**, e00005 (2012). [doi:10.7554/eLife.00005](https://doi.org/10.7554/eLife.00005) Medline
13. N. Justin, Y. Zhang, C. Tarricone, S. R. Martin, S. Chen, E. Underwood, V. De Marco, L. F. Haire, P. A. Walker, D. Reinberg, J. R. Wilson, S. J. Gamblin, Structural basis of oncogenic histone H3K27M inhibition of human polycomb repressive complex 2. *Nat. Commun.* **7**, 11316 (2016). [doi:10.1038/ncomms11316](https://doi.org/10.1038/ncomms11316) Medline
14. S. Sanulli, N. Justin, A. Teissandier, K. Ancelin, M. Portoso, M. Caron, A. Michaud, B. Lombard, S. T. da Rocha, J. Offer, D. Loew, N. Servant, M. Wassef, F. Burlina, S. J. Gamblin, E. Hard, R. Margueron, Jarid2 methylation via the PRC2 complex regulates H3K27me3 deposition during cell differentiation. *Mol. Cell* **57**, 769–783 (2015). [doi:10.1016/j.molcel.2014.12.020](https://doi.org/10.1016/j.molcel.2014.12.020) Medline
15. A. Brooun, K. S. Gajiwala, Y.-L. Deng, W. Liu, B. Bolaños, P. Bingham, Y.-A. He, W. Diehl, N. Grable, P.-P. Kung, S. Sutton, K. A. Maegley, X. Yu, A. E. Stewart, Polycomb repressive complex 2 structure with inhibitor reveals a mechanism of activation and drug resistance. *Nat. Commun.* **7**, 11384 (2016). [doi:10.1038/ncomms11384](https://doi.org/10.1038/ncomms11384) Medline
16. F. W. Schmitges, A. B. Prusty, M. Faty, A. Stützer, G. M. Lingaraju, J. Aiawazian, R. Sack, D. Hess, L. Li, S. Zhou, R. D. Bunker, U. Wirth, T. Bouwmeester, A. Bauer, N. Ly-Hartig, K. Zhao, H. Chan, J. Gu, H. Gut, W. Fischle, J. Müller, N. H. Thomä, Histone methylation by PRC2 is inhibited by active chromatin marks. *Mol. Cell* **42**, 330–341 (2011). [doi:10.1016/j.molcel.2011.03.025](https://doi.org/10.1016/j.molcel.2011.03.025) Medline
17. H. Kim, K. Kang, J. Kim, AEBP2 as a potential targeting protein for Polycomb Repression Complex PRC2. *Nucleic Acids Res.* **37**, 2940–2950 (2009). [doi:10.1093/nar/gkp149](https://doi.org/10.1093/nar/gkp149) Medline
18. G. Li, R. Margueron, M. Ku, P. Chambon, B. E. Bernstein, D. Reinberg, Jarid2 and PRC2, partners in regulating gene expression. *Genes Dev.* **24**, 368–380 (2010). [doi:10.1101/gad.1886410](https://doi.org/10.1101/gad.1886410) Medline
19. D. Pasini, P. A. C. Cloos, J. Walfridsson, L. Olsson, J.-P. Bukowski, J. V. Johansen, M. Bak, N. Tommerup, J. Rappaport, K. Helin, JARID2 regulates binding of the Polycomb repressive complex 2 to target genes in ES cells. *Nature* **464**, 306–310 (2010). [doi:10.1038/nature08788](https://doi.org/10.1038/nature08788) Medline
20. R. Cao, Y. Zhang, SUZ12 is required for both the histone methyltransferase activity and the silencing function of the EED-EZH2 complex. *Mol. Cell* **15**, 57–67 (2004). [doi:10.1016/j.molcel.2004.06.020](https://doi.org/10.1016/j.molcel.2004.06.020) Medline
21. M. Brecqueville, N. Cervera, J. Adélaïde, J. Rey, N. Carbuccia, M. Chaffanet, M. J. Mozziconacci, N. Vey, D. Birnbaum, V. Gelsi-Boyer, A. Murati, Mutations and deletions of the SUZ12 polycomb gene in myeloproliferative neoplasms. *Blood Cancer J.* **1**, e33 (2011). [doi:10.1038/bcj.2011.31](https://doi.org/10.1038/bcj.2011.31) Medline
22. D. Mouradov, C. Sloggett, R. N. Jorissen, C. G. Love, S. Li, A. W. Burgess, D. Arango, R. L. Strausberg, D. Buchanan, S. Wormald, L. O'Connor, J. L. Wilding, D. Bicknell, I. P. M. Tomlinson, W. F. Bodmer, J. M. Mariadason, O. M. Sieber, Colorectal cancer cell lines are representative models of the main molecular subtypes of primary cancer. *Cancer Res.* **74**, 3238–3247 (2014). [doi:10.1158/0008-5472.CAN-14-0013](https://doi.org/10.1158/0008-5472.CAN-14-0013) Medline
23. S. Poepsel, V. Kasinath, E. Nogales, Visualization of PRC2-dinucleosome interactions leading to epigenetic repression. *bioRxiv* (2018). [10.1101/245134](https://doi.org/10.1101/245134)
24. C. Maris, C. Dominguez, F. H. Allain, The RNA recognition motif, a plastic RNA-binding platform to regulate post-transcriptional gene expression. *FEBS J.* **272**, 2118–2131 (2005). [doi:10.1111/j.1742-4658.2005.04653.x](https://doi.org/10.1111/j.1742-4658.2005.04653.x) Medline

25. J. G. Betancur, Y. Tomari, Cryptic RNA-binding by PRC2 components EZH2 and SUZ12. *RNA Biol.* **12**, 959–965 (2015). [doi:10.1080/15476286.2015.1069463](https://doi.org/10.1080/15476286.2015.1069463) Medline

26. S. Kaneko, G. Li, J. Son, C.-F. Xu, R. Margueron, T. A. Neubert, D. Reinberg, Phosphorylation of the PRC2 component Ezh2 is cell cycle-regulated and up-regulates its binding to ncRNA. *Genes Dev.* **24**, 2615–2620 (2010). [doi:10.1101/gad.1983810](https://doi.org/10.1101/gad.1983810) Medline

27. A. Kanhere, K. Viiri, C. C. Araújo, J. Rasaiyah, R. D. Bouwman, W. A. Whyte, C. F. Pereira, E. Brookes, K. Walker, G. W. Bell, A. Pombo, A. G. Fisher, R. A. Young, R. G. Jenner, Short RNAs are transcribed from repressed polycomb target genes and interact with polycomb repressive complex-2. *Mol. Cell* **38**, 675–688 (2010). [doi:10.1016/j.molcel.2010.03.019](https://doi.org/10.1016/j.molcel.2010.03.019) Medline

28. C. Davidovich, T. R. Cech, The recruitment of chromatin modifiers by long noncoding RNAs: Lessons from PRC2. *RNA* **21**, 2007–2022 (2015). [doi:10.1261/rna.053918.115](https://doi.org/10.1261/rna.053918.115) Medline

29. X. Wang, R. D. Paucek, A. R. Gooding, Z. Z. Brown, E. J. Ge, T. W. Muir, T. R. Cech, Molecular analysis of PRC2 recruitment to DNA in chromatin and its inhibition by RNA. *Nat. Struct. Mol. Biol.* **24**, 1028–1038 (2017). [doi:10.1038/nsmb.3487](https://doi.org/10.1038/nsmb.3487) Medline

30. A. Leitner, T. Walzthoeni, R. Aebersold, Lysine-specific chemical cross-linking of protein complexes and identification of cross-linking sites using LC-MS/MS and the xQuest/xProphet software pipeline. *Nat. Protoc.* **9**, 120–137 (2014). [doi:10.1038/nprot.2013.168](https://doi.org/10.1038/nprot.2013.168) Medline

31. M. C. Chambers, B. Maclean, R. Burke, D. Amodei, D. L. Ruderman, S. Neumann, L. Gatto, B. Fischer, B. Pratt, J. Egertson, K. Hoff, D. Kessner, N. Tasman, N. Shulman, B. Frewen, T. A. Baker, M.-Y. Brusniak, C. Paulse, D. Creasy, L. Flashner, K. Kani, C. Moulding, S. L. Seymour, L. M. Nuwaysir, B. Lefebvre, F. Kuhlmann, J. Roark, P. Rainer, S. Detlev, T. Hemenway, A. Huhmer, J. Langridge, B. Connolly, T. Chadick, K. Holly, J. Eckels, E. W. Deutscher, R. L. Moritz, J. E. Katz, D. B. Agus, M. MacCoss, D. L. Tabb, P. Mallick, A cross-platform toolkit for mass spectrometry and proteomics. *Nat. Biotechnol.* **30**, 918–920 (2012). [doi:10.1038/nbt.2377](https://doi.org/10.1038/nbt.2377) Medline

32. T. Walzthoeni, M. Claassen, A. Leitner, F. Herzog, S. Bohn, F. Förster, M. Beck, R. Aebersold, False discovery rate estimation for cross-linked peptides identified by mass spectrometry. *Nat. Methods* **9**, 901–903 (2012). [doi:10.1038/nmeth.2103](https://doi.org/10.1038/nmeth.2103) Medline

33. C. W. Combe, L. Fischer, J. Rappaport, xiNET: Cross-link network maps with residue resolution. *Mol. Cell. Proteomics* **14**, 1137–1147 (2015). [doi:10.1074/mcp.O114.042259](https://doi.org/10.1074/mcp.O114.042259) Medline

34. T. Walzthoeni, L. A. Joachimiak, G. Rosenberger, H. L. Röst, L. Malmström, A. Leitner, J. Frydman, R. Aebersold, xTract: Software for characterizing conformational changes of protein complexes by quantitative cross-linking mass spectrometry. *Nat. Methods* **12**, 1185–1190 (2015). [doi:10.1038/nmeth.3631](https://doi.org/10.1038/nmeth.3631) Medline

35. B. MacLean, D. M. Tomazela, N. Shulman, M. Chambers, G. L. Finney, B. Frewen, R. Kern, D. L. Tabb, D. C. Liebler, M. J. MacCoss, Skyline: An open source document editor for creating and analyzing targeted proteomics experiments. *Bioinformatics* **26**, 966–968 (2010). [doi:10.1093/bioinformatics/btp054](https://doi.org/10.1093/bioinformatics/btp054) Medline

36. K. Bertram, D. E. Agafonov, W.-T. Liu, O. Dybkov, C. L. Will, K. Hartmuth, H. Urlaub, B. Kastner, H. Stark, R. Lührmann, Cryo-EM structure of a human spliceosome activated for step 2 of splicing. *Nature* **542**, 318–323 (2017). [doi:10.1038/nature21079](https://doi.org/10.1038/nature21079) Medline

37. Y. He, C. Yan, J. Fang, C. Inouye, R. Tjian, I. Ivanov, E. Nogales, Near-atomic resolution visualization of human transcription promoter opening. *Nature* **533**, 359–365 (2016). [doi:10.1038/nature17970](https://doi.org/10.1038/nature17970) Medline

38. B. Carragher, N. Kisseberth, D. Kriegman, R. A. Milligan, C. S. Potter, J. Pulokas, A. Reilein, Legion: An automated system for acquisition of images from vitreous ice specimens. *J. Struct. Biol.* **132**, 33–45 (2000). [doi:10.1006/jsb.2000.4314](https://doi.org/10.1006/jsb.2000.4314) Medline

39. G. C. Lander, S. M. Stagg, N. R. Voss, A. Cheng, D. Fellmann, J. Pulokas, C. Yoshioka, C. Irving, A. Mulder, P.-W. Lau, D. Lyumkis, C. S. Potter, B. Carragher, Appion: An integrated, database-driven pipeline to facilitate EM image processing. *J. Struct. Biol.* **166**, 95–102 (2009). [doi:10.1016/j.jsb.2009.01.002](https://doi.org/10.1016/j.jsb.2009.01.002) Medline

40. S. Q. Zheng, E. Palovcak, J.-P. Armache, K. A. Verba, Y. Cheng, D. A. Agard, MotionCor2: Anisotropic correction of beam-induced motion for improved cryo-electron microscopy. *Nat. Methods* **14**, 331–332 (2017). [doi:10.1038/nmeth.4193](https://doi.org/10.1038/nmeth.4193) Medline

41. K. Zhang, Gctf: Real-time CTF determination and correction. *J. Struct. Biol.* **193**, 1–12 (2016). [doi:10.1016/j.jsb.2015.11.003](https://doi.org/10.1016/j.jsb.2015.11.003) Medline

42. S. H. W. Scheres, RELION: Implementation of a Bayesian approach to cryo-EM structure determination. *J. Struct. Biol.* **180**, 519–530 (2012). [doi:10.1016/j.jsb.2012.09.006](https://doi.org/10.1016/j.jsb.2012.09.006) Medline

43. D. Kimanius, B. O. Forsberg, S. H. W. Scheres, E. Lindahl, Accelerated cryo-EM structure determination with parallelisation using GPUs in RELION-2. *eLife* **5**, e18722 (2016). [doi:10.7554/elife.18722](https://doi.org/10.7554/elife.18722) Medline

44. X. C. Bai, E. Rajendra, G. Yang, Y. Shi, S. H. W. Scheres, Sampling the conformational space of the catalytic subunit of human γ -secretase. *eLife* **4**, e11182 (2015). [doi:10.7554/elife.11182](https://doi.org/10.7554/elife.11182) Medline

45. J. B. Heymann, Bsoft: Image and molecular processing in electron microscopy. *J. Struct. Biol.* **133**, 156–169 (2001). [doi:10.1006/jsb.2001.4339](https://doi.org/10.1006/jsb.2001.4339) Medline

46. F. Sievers, A. Wilm, D. Dineen, T. J. Gibson, K. Karplus, W. Li, R. Lopez, H. McWilliam, M. Remmert, J. Söding, J. D. Thompson, D. G. Higgins, Fast, scalable generation of high-quality protein multiple sequence alignments using Clustal Omega. *Mol. Syst. Biol.* **7**, 539 (2011). [doi:10.1186/1744-6080-7-539](https://doi.org/10.1186/1744-6080-7-539) Medline

47. L. A. Kelley, S. Mezulis, C. M. Yates, M. N. Wass, M. J. E. Sternberg, The Phyre2 web portal for protein modeling, prediction and analysis. *Nat. Protoc.* **10**, 845–858 (2015). [doi:10.1038/nprot.2015.053](https://doi.org/10.1038/nprot.2015.053) Medline

48. E. F. Pettersen, T. D. Goddard, C. C. Huang, G. S. Couch, D. M. Greenblatt, E. C. Meng, T. E. Ferrin, UCSF Chimera—a visualization system for exploratory research and analysis. *J. Comput. Chem.* **25**, 1605–1612 (2004). [doi:10.1002/jcc.20084](https://doi.org/10.1002/jcc.20084) Medline

49. P. Emsley, K. Cowtan, Coot: Model-building tools for molecular graphics. *Acta Crystallogr. D Biol. Crystallogr.* **60**, 2126–2132 (2004). [doi:10.1107/S0907444904019158](https://doi.org/10.1107/S0907444904019158) Medline

50. J. R. López-Blanco, P. Chacón, iMODFIT: Efficient and robust flexible fitting based on vibrational analysis in internal coordinates. *J. Struct. Biol.* **184**, 261–270 (2013). [doi:10.1016/j.jsb.2013.08.010](https://doi.org/10.1016/j.jsb.2013.08.010) Medline

51. P. D. Adams, R. W. Grosse-Kunstleve, L.-W. Hung, T. R. Ioerger, A. J. McCoy, N. W. Moriarty, R. J. Read, J. C. Sacchettini, N. K. Sauter, T. C. Terwilliger, PHENIX: Building new software for automated crystallographic structure determination. *Acta Crystallogr. D Biol. Crystallogr.* **58**, 1948–1954 (2002). [doi:10.1107/S0907444902016657](https://doi.org/10.1107/S0907444902016657) Medline

52. G. N. Murshudov, A. A. Vagin, E. J. Dodson, Refinement of macromolecular structures by the maximum-likelihood method. *Acta Crystallogr. D Biol. Crystallogr.* **53**, 240–255 (1997). [doi:10.1107/S090744496012255](https://doi.org/10.1107/S090744496012255) Medline

53. C. S. Nagano, J. J. Calvete, D. Baretto, A. Pérez, B. S. Cavada, L. Sanz, Insights into the structural basis of the pH-dependent dimer-tetramer equilibrium through crystallographic analysis of recombinant *Diocleinae lectins*. *Biochem. J.* **409**, 417–428 (2008). [doi:10.1042/BJ20070942](https://doi.org/10.1042/BJ20070942) Medline

54. K. Brown, K. Djinovic-Carugo, T. Haltia, I. Cabrito, M. Saraste, J. J. G. Moura, I. Moura, M. Tegoni, C. Cambillau, Revisiting the catalytic CuZ cluster of nitrous oxide (NO) reductase. Evidence of a bridging inorganic sulfur. *J. Biol. Chem.* **275**, 41133–41136 (2000). [doi:10.1074/jbc.M008617200](https://doi.org/10.1074/jbc.M008617200) Medline

ACKNOWLEDGMENTS

We thank D. Toso (Bay Area Cryo-EM consortium) as well as C. Hong, R. Huang and Z. Yu (Janelia CryoEM Facility) for help with microscope operation and data collection, P. Grob, J. Fang and Y. Liu for technical support, and T. Houweling, A. Chintangal and P. Tobias for computer support. We thank R. Danev for his help with the operation of the Volta Phase plate. Computational resources were provided in part by the National Energy Research Scientific Computing Center (DE-AC02-05CH11231) and LAWRENCIUM computing cluster at Lawrence Berkeley National Laboratory. Funding: This work was in part funded by Eli Lilly through the Lilly Research Award Program. V.K. was supported by a postdoctoral fellowship from Helen Hay Whitney. S.P. was supported by the Alexander von Humboldt foundation (Germany) as a Feodor-Lynen postdoctoral fellow. M.F. was supported by a Long-Term Fellowship from the European Molecular Biology Organization (EMBO). R.A. was supported by the European Union 7th Framework Program (PROSPECTS, HEALTH-F4-2008-201648), the European Research Council (ERC Advanced Grants no. 233226 and no. 670821).

and the Innovative Medicines Initiative Joint Undertaking (ULTRA-DD, grant no. 115766). E.N. is a Howard Hughes Medical Institute Investigator. Author contributions: V.K. established experimental procedures, expressed and purified the different complexes, prepared the sample and cryo-grids, collected and processed all EM data, and carried out model building and refinement. D.R. and X.A.F. assisted with molecular cloning, protein purification and negative-stain electron microscopy sample screening. S.P. helped with input and discussion during the course of the work and provided critical feedback and help for manuscript preparation. M.F. and R.A. performed the mass spectrometry experiments. M.F. performed the mass spectrometry experiments and analyzed the targeted MS data. V.K. and M.F. analyzed the XL-MS data. V.K. and G.S. performed the H/D-exchange experiments and analyzed the data. V.K. and E.N. analyzed all the data. E.N. and R.A. supervised the work. V.K. and E.N. wrote the manuscript with input from all authors. Data and materials availability: Cryo-EM density maps and fitted models have been deposited in the Electron Microscopy Data Bank (EMDB) for the complete PRC2-AJ₁₀₆ – Compact active state (EMD-7334 and PDB:6C23), PRC2-AJ₁₀₆ – Extended active state (EMD-7335 and PDB:6C24), and PRC2-AJ₁₁₉ (EMD-7337). All the primary MS data are available to the public through PRIDE archive and can be accessed via ProteomeXchange (ID: PXD008605).

SUPPLEMENTARY MATERIALS

www.science.org/cgi/content/full/science.aar5700/DC1

Materials and Methods

Figs. S1 to S10

Table S1

References (30–54)

Movie S1

22 November 2017; accepted 9 January 2018

Published online 18 January 2018

10.1126/science.aar5700

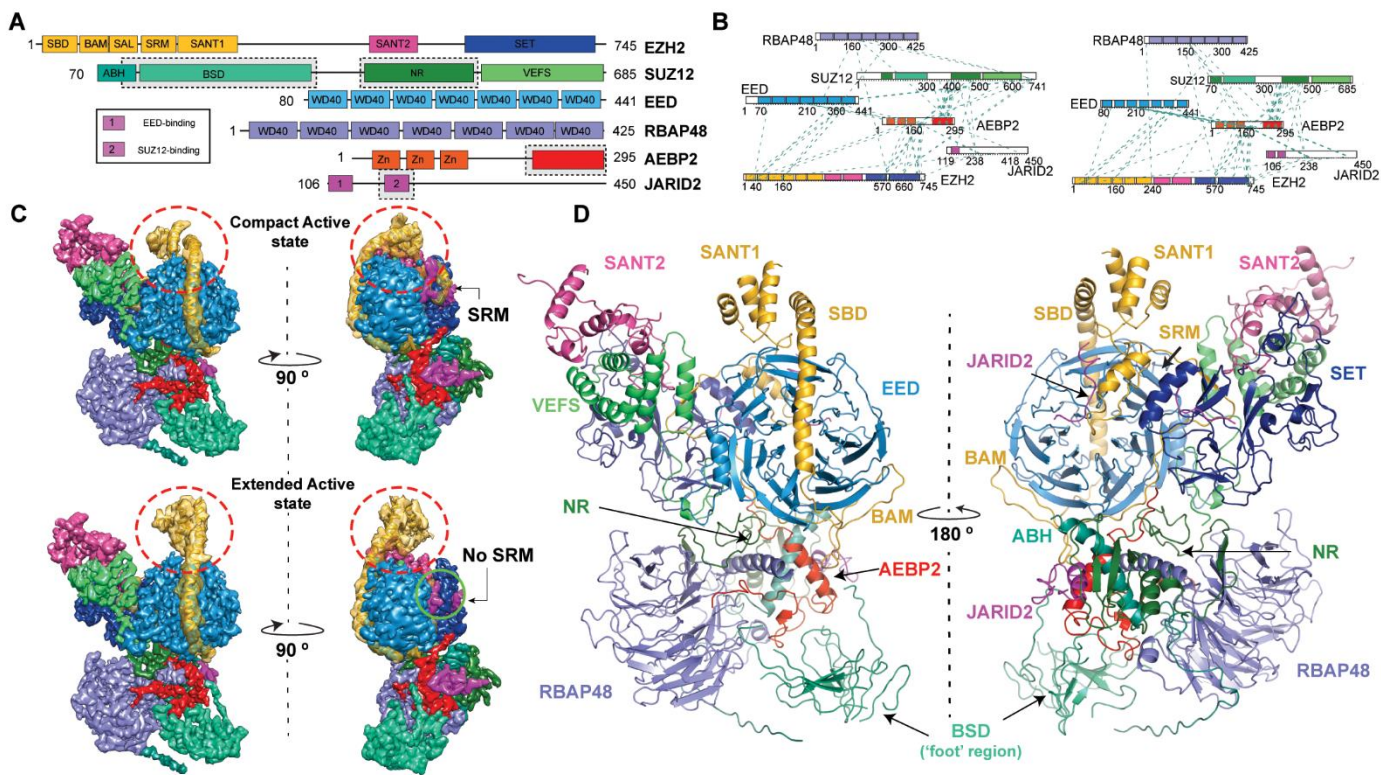


Fig. 1. Cryo-EM structure of PRC2-JARID2-AEBP2. (A) Schematic representation of the proteins in PRC2-JARID2-AEBP2 complex. Dashed boxes highlight regions for which structural information was previously unknown and that are now described in our study. (B) Cross-linking mass spectrometry results for PRC2-AJ₁₁₉ (left) and PRC2-AJ₁₀₆ (right). (C) Cryo-EM densities for the two conformational states (Compact active and Extended active) of PRC2-AJ₁₀₆, with differences in SBD and SANT1 indicated by the red, dashed circles. SRM is ordered and visible only in the Compact active state (top panel). JARID2 K116me3 fragment is bound in both states. (D) Atomic model of the Compact active state, with EZH2 (SANT1, SBD, SRM) in gold, EZH2 (SET, CXC) in dark blue, EZH2 (MCSS, SANT2) in pink, with EED in light blue, RBAP48 in violet, AEBP2 in red, JARID2 in magenta and SUZ12 (ABH, BSD) in light green, SUZ12 (NR) in dark green and SUZ12 (VEFS) in fluorescent green.

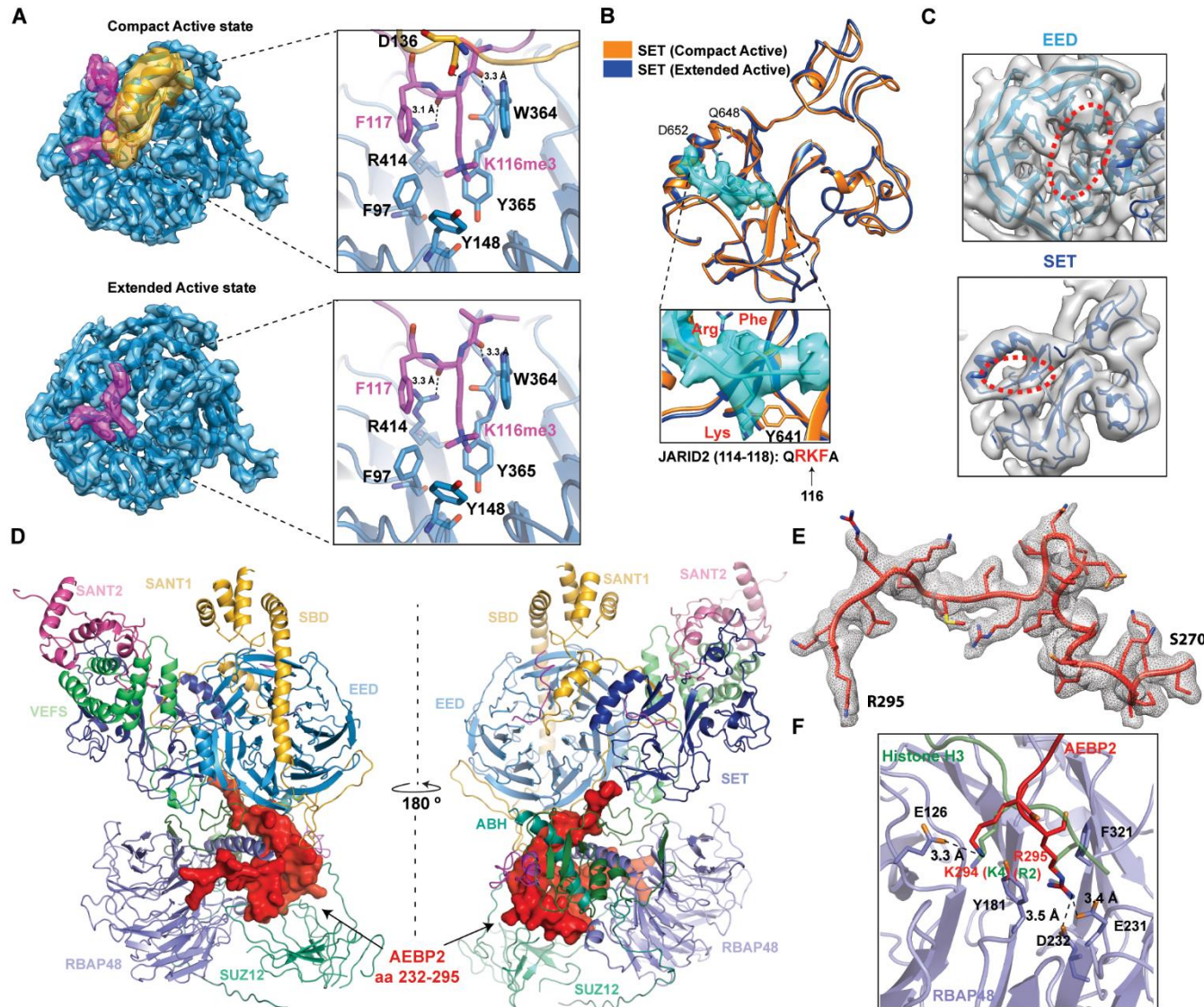


Fig. 2. Cofactors AEBP2 and JARID2 mimic histone H3 tail. (A) Interaction of JARID2 K116me3 with EED in the two conformational states sampled by PRC2-AJ₁₀₆. JARID2 K116me3 sits in the middle of an aromatic cage (F97, Y148, Y365) with hydrogen bond interactions (R414:F117, W364:R115) that stabilize the JARID2 peptide backbone. In the Compact Active state, additional interaction between EZH2 D136 and the backbone amide of JARID2 K116 helps position the EZH2 SRM helix next to the EZH2 SET domain. (B) EZH2 SET domain of PRC2-AJ₁₀₆ is in a similar conformation in both states (Compact Active, orange and Extended Active, blue; C_α r.m.s.d = 0.74 Å; see also fig. S4B) and is bound to a substrate peptide (shown in cyan). Inset: density of substrate observed in our cryo-EM reconstruction along with a model for JARID2 aa 114-118 (C) Cryo-EM density of PRC2-AJ₁₁₉ EED/EZH2-SET region with ribbon representations of EED (light blue) and SET (dark blue) showing the absence of both the stimulatory fragment bound to EED and the substrate bound to the SET domain (red, dashed circles). (D) AEBP2 (aa 232-295, red), shown in surface representation connects RBAP48, the SUZ12 N-terminal region and the EZH2 SET domain. (E) Map vs model of AEBP2 region that binds RBAP48 at the histone H3 binding site. (F) View of the RBAP48 WD40 domain showing in stick representation the conserved amino acids in RBAP48 (violet) interacting with K294 and R295 of AEBP2 (red). Overlay of the crystal structure of Drosophila homolog of RBAP48 (NURF55) bound to unmodified histone H3 peptide (PDB: 2YBA (16), green) highlights the similarity of the binding mode between AEBP2 and histone H3, with all key residues in identical conformations (only the AEBP2/H3 residues R295/R2 and K294/K4 are shown for clarity).

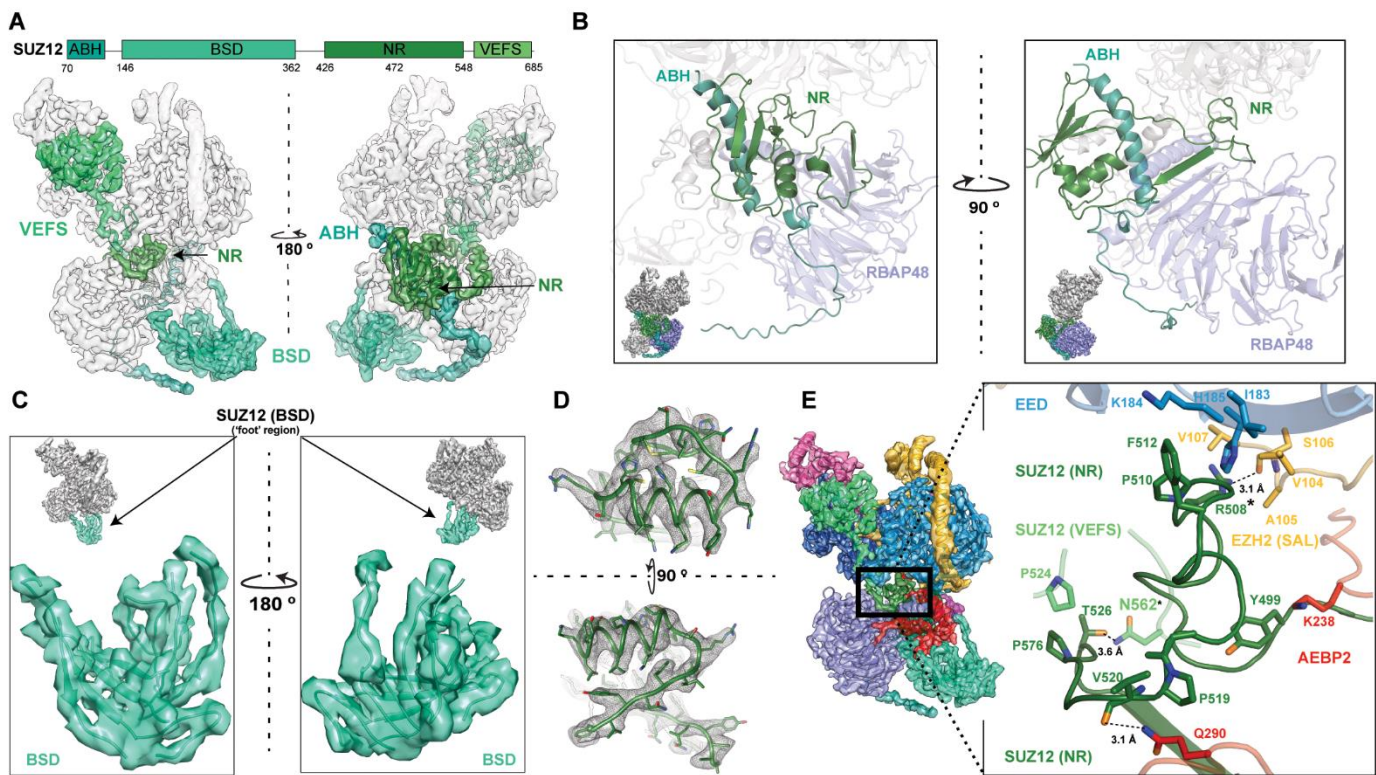


Fig. 3. SUZ12 interacts with all subunits of PRC2. (A) (Top) Schematic representation of the different domains. (Bottom) Cryo-EM density of SUZ12 (green) showing the location of each domain within PRC2. (B) Orthogonal views of the SUZ12 AEBP2-binding helix (ABH), and neck region (NR), defining the region of SUZ12 at the center of the complex. Inset shows the relative location of these regions within the full PRC2 complex. (C) Cryo-EM density of the beta-sheet rich domain (BSD) comprising the “foot” of the complex with fitted poly-Ala model. Top inset: position of BSD within PRC2. (D) Map vs model for the SUZ12 zinc-finger domain, which interacts with the AEBP2 (aa 246-266), the helix-turn-helix of JARID2 (see below) and the ABH of SUZ12. (E) Close up of the neck region of PRC2 showing in stick representation the amino acids contributing to the hydrophobic interactions between the SUZ12 NR, the SAL of EZH2, EED and the SUZ12 VEFS. Dotted lines indicate potential hydrogen bonds. Mutations in R508 and N562 (asterisk) have been observed in a number of cancers.

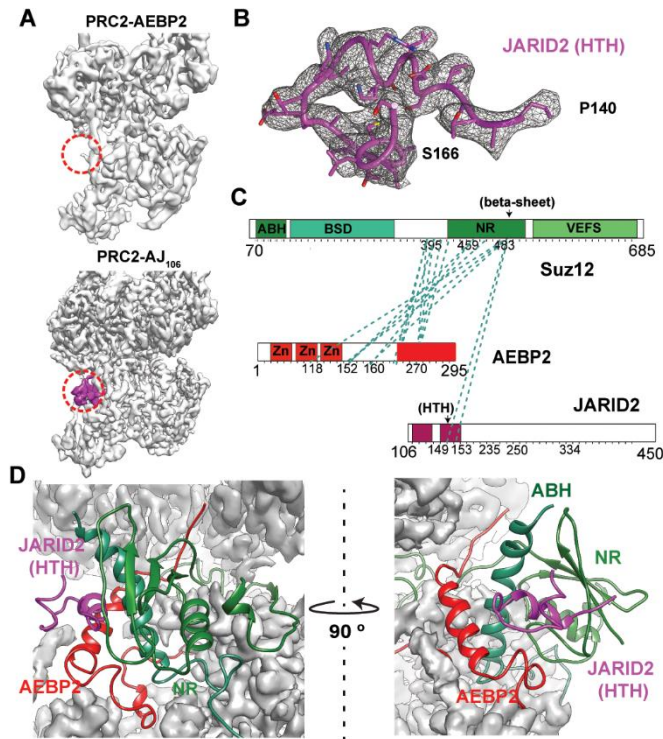


Fig. 4. JARID2-AEBP2-SUZ12 interactions contribute to the stability of PRC2. (A) The density region marked by the red-dashed circle is only present in JARID2-containing complexes (both PRC2-AJ₁₀₆ and PRC2-AJ₁₁₉, the former displayed at the bottom with JARID2 segment in magenta). (B) Map versus model for JARID2 aa 140-166. The model built into the density agrees well with the helix-turn-helix (HTH) secondary structure prediction for this region. (C) Cross-links of the SUZ12 NR with AEBP2 and JARID2 (aa 140-166) confirm the relative localization of each of these regions in the cryo-EM map. (D) The JARID2 HTH (magenta) is wedged between AEBP2 (red) and the SUZ12 ABH (light green), NR (green).

TECHNICAL COMMENT

CARBON CYCLE

Comment on “The whole-soil carbon flux in response to warming”

Jing Xiao,¹ Fangjian Yu,¹ Wanying Zhu,¹ Chenchao Xu,¹ Kaihang Zhang,¹ Yiqi Luo,² James M. Tiedje,³ Jizhong Zhou,^{2,4} Lei Cheng^{1*}

In a compelling study, Hicks Pries *et al.* (Reports, 31 March 2017, p. 1420) showed that 4°C warming enhanced soil CO₂ production in the 1-meter soil profile, with all soil depths displaying similar temperature sensitivity (Q_{10}). We argue that some caveats can be identified in their experimental approach and analysis, and that these critically undermine their conclusions and hence their claim that the strength of feedback between the whole-soil carbon and climate has been underestimated in terrestrial models.

Hicks Pries *et al.* (1) used a deep soil warming experiment to examine CO₂ production in response to warming across the soil profile in a coniferous temperate forest. They found that a 2-year *in situ* warming of 4°C significantly enhanced the whole-soil CO₂ production by 34 to 37%, and that all soil layers exhibited similar temperature sensitivity with a mean apparent Q_{10} of 2.7 ± 0.3 . We argue that although the idea of subsoil carbon dynamics in response to warming is worth testing (2, 3), their conclusions are critically undermined by the experimental approach and analysis.

Hicks Pries *et al.* buried heating rods at a depth of 2.4 m (with additional circular heating cables near the surface at radii of 0.5 and 1 m) to warm the 1-m soil profile evenly by 4°C. This method differed from the majority of previous studies, in which soil temperature was elevated through heating surface air and/or topsoil layers to simulate the magnitude of rise in surface air temperature (2, 3). Although it is expected that ongoing and future air warming would increase the temperature of the soil profile, the magnitude of temperature elevation likely attenuates with depth. This happens because net energy inputs from air and subsequent heat conduction driven by a thermal gradient would inevitably invoke temperature variation in deep soils lagging behind that of surface soils under a dynamic climate system. Such a thermal lag effect is also ascribed to low thermal diffusivity and thickness of the soil profile (4). In an alpine meadow with clipping to simulate animal grazing under 4°C surface air warming, for instance, the magnitude of temperature elevation decreased by 88% and 77%, respectively, at 60- and 100-cm soil depths (5). In a boreal forest under 3.4°C soil warming at

a depth of 10 cm, the magnitude of temperature elevation declined by 40% and 53%, respectively, at 75- and 100-cm soil depths (6). These previous findings imply that Hicks Pries *et al.*'s experimental warming approach may cause higher temperature elevations in deeper soil layers (e.g., <50 cm) than expected under air warming, thus overestimating the whole-soil CO₂ production.

To examine temperature sensitivity of CO₂ production across the soil profile, Hicks Pries *et al.* used the following equation to calculate the apparent Q_{10} , a factor by which the CO₂ production rate increases with a 10°C rise, of each soil layer:

$$Q_{10} = \left(\frac{R_H}{R_C} \right)^{\frac{10}{T_H - T_C}} \quad (1)$$

where R_C and R_H are the CO₂ production rates of each control and heated plot pair, respectively, and T_C and T_H are the soil temperatures of the corresponding control and heated plots, respectively. By directly comparing CO₂ production between each treatment plot pair on every sampling date, however, a large number of anomalous Q_{10} values appeared (for example, 33% of them <1.0 and 20% of them >5). Hicks Pries *et al.* included Q_{10} values less than 1.0 but excluded those greater than 6.4 (45 of 281) as “unrealistic values” ($Q_{10} > 30$) or “outliers” ($6.4 < Q_{10} < 30$) in their analysis. At 7.5-cm soil depth, for instance, nearly one-third of the data points were not included in computing the mean apparent Q_{10} . Although many Q_{10} values were ignored in Hicks Pries *et al.*, they did not propose a different mechanism (other than the warming treatment) underlying the emergence of these anomalous data points. We believe that the analysis of Hicks Pries *et al.* is inappropriate, leading to the biased conclusion that all soil depths responded to warming with very similar temperature sensitivity.

In a seminal work, Hawkins defined an outlier as “an observation which deviates so much from other observations as to arouse suspicions that it was generated by a different mechanism” (7). Evidently, the apparent Q_{10} was not a direct observation but was calculated from the paired soil CO₂ in their study. As such, the exclusion of any Q_{10} must be based on the statistical analysis of soil CO₂ measurements rather than the Q_{10} itself. If any Q_{10} value could be considered an outlier or even unrealistic, the corresponding paired soil CO₂ data should also be excluded in analyzing the mean soil CO₂ production (figure 2A of Hicks Pries *et al.*). To reach a fair conclusion about the whole-soil response to warming, we

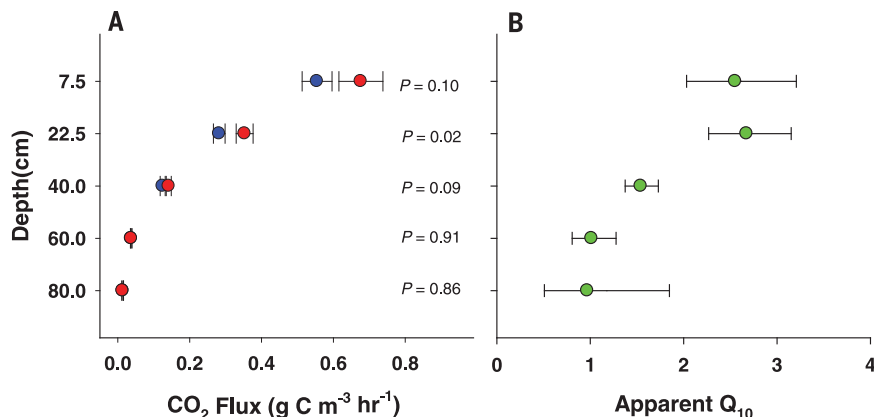


Fig. 1. Soil CO₂ production of different soil depths in response to warming. (A) Soil CO₂ production (mean \pm SE, $n = 3$) at different soil layers in control plots (blue circles) and heated plots (red circles). $P < 0.05$ denotes a significant effect of warming. Data are from soil CO₂ measurements of Hicks Pries *et al.* but excluding the “outliers” and “unrealistic high values” in their Q_{10} analysis. (B) The mean apparent Q_{10} of each soil layer according to a linear regression model. Hicks Pries *et al.* estimated the mean apparent Q_{10} by averaging the Q_{10} values of each sampling point but excluded many data points because of high variation. Our method allows for a more accurate calculation of temperature sensitivity through an unbiased estimation of $\ln(Q_{10})$ with low deviation. Error bars were computed from SE of the fitted parameters. The apparent Q_{10} of the two upper depths ($2.62^{+0.38}_{-0.33}$) is significantly higher than that of the three deeper depths ($1.20^{+0.21}_{-0.18}$). $P < 0.001$. Data are from the Hicks Pries *et al.* analysis of soil CO₂ production. All paired soil CO₂ data except for those equal to zero are included in the current analysis.

¹College of Life Sciences, Zhejiang University, Hangzhou 310058, China. ²Department of Microbiology and Plant Biology, University of Oklahoma, Norman, OK 73019, USA.

³Center for Microbial Ecology, Michigan State University, East Lansing, MI 48824, USA. ⁴Institute for Environmental Genomics, University of Oklahoma, Norman, OK 73019, USA.

*Corresponding author. Email: lcheng@zju.edu.cn

reanalyzed the mean soil CO₂ production using the original data sets by omitting those not included in the estimation of the mean apparent Q₁₀ in figure 2B of Hicks Pries *et al.* In contrast to Hicks Pries *et al.*, results from the current analysis show that CO₂ flux from the whole-soil profile remained unchanged under warming (Fig. 1A, $P = 0.15$). This result indicates that the omission of many data points in the Hicks Pries *et al.* analysis could lead to inconsistent conclusions about the response of the whole soil to warming.

We argue that the exclusion of many data points in the Hicks Pries *et al.* analysis could be problematic because their data were collected from a time-series experiment. In their study, soil CO₂ measurements had been conducted repeatedly on the same object (i.e., each soil layer) over 2 years; thus, measurements at different time points were not independent of each other (8). Actually, soil CO₂ production decreased significantly over time in the whole-soil profile ($P < 0.001$). Moreover, two CO₂ measurements taken at adjacent time points were more highly correlated than two taken several time points apart [the fittest covariance structure: first-order autoregressive with heterogeneous variance ARH(1), $\phi = 0.994$]. If such repeated and self-correlated CO₂ measurements were treated erroneously as if they were random samples, as in the analysis of Hicks Pries *et al.*, the exclusion of a large number of data points could lead to serious power loss in statistical analysis (7).

To avoid the occurrence of many “abnormal” Q₁₀ values, we propose a different method to estimate the mean apparent Q₁₀ of each soil depth. In the Hicks Pries *et al.* analysis, many anomalous Q₁₀ values appeared because any variation in soil CO₂ data collection would be amplified exponentially by a power of $10/(T_H - T_C)$. To ameliorate error propagation, we use a least-squares regression model to estimate the apparent Q₁₀ (9) by reformatting Eq. 1 as follows:

$$\ln \frac{R_H}{R_C} = \frac{\ln(Q_{10})}{10} \cdot (T_H - T_C) \quad (2)$$

Using Eq. 2, the apparent Q₁₀ for each soil layer can be estimated through performing a linear regression between $\ln(R_H/R_C)$ and $(T_H - T_C)$. Meanwhile, the potentially confounding effects of seasonal changes, emphasized in Hicks Pries *et al.*, could be minimized because the same paired data are used. In our analysis, only those data points with CO₂ production equal to zero were not included. Tests of difference in Q₁₀ between soil depths were conducted based on a generalized linear model by introducing a dumb variable of depth. Interestingly, we found that the mean apparent Q₁₀ of the two surface soil layers (mean Q₁₀ = 2.62) was significantly higher than that of the three deeper soil layers (mean Q₁₀ = 1.20) (Fig. 1B, $P < 0.001$). These results are in conflict with those of Hicks Pries *et al.* and suggest that the surface soil layers were more responsive to

warming, with a much higher temperature sensitivity relative to the deep layers.

Hicks Pries *et al.* concluded their analysis with a claim that the strength of the carbon-climate feedback in terrestrial models has been underestimated because these models have ignored the warming effects on subsoil (e.g., >50 cm) and usually include relatively low apparent Q₁₀ values of soil CO₂ production. Given the above caveats with respect to how this experiment was carried out and how the data were interpreted, we believe that their recommendation lacks a solid foundation.

REFERENCES AND NOTES

1. C. E. Hicks Pries, C. Castanha, R. C. Porras, M. S. Torn, *Science* **355**, 1420–1423 (2017).
2. L. Cheng *et al.*, *ISME J.* **11**, 1825–1835 (2017).
3. T. W. Crowther *et al.*, *Nature* **540**, 104–108 (2016).
4. T. Mimouni, L. Lei, L. Laloui, *Acta Geotech.* **10**, 197–208 (2015).
5. M. Xu *et al.*, *J. Arid Land* **7**, 189–204 (2015).
6. R. L. Rich *et al.*, *Glob. Change Biol.* **21**, 2334–2348 (2015).
7. D. M. Hawkins, *Identification of Outliers* (Springer, 1980).
8. R. C. Littell, G. A. Milliken, W. W. Stroup, R. D. Wolfinger, O. Schabenberger, *SAS for Mixed Models* (SAS Institute, Cary, NC, ed. 2, 2006).
9. M. D. Mahecha *et al.*, *Science* **329**, 838–840 (2010).

ACKNOWLEDGMENTS

We thank M. S. Torn for stimulating discussions. Supported by National Natural Science Foundation of China (NSFC) grants 31670501, 31422010, and 31370487 and by Zhejiang Provincial NSFC grant LR14C030001.

6 June 2017; accepted 21 December 2017
10.1126/science.aa00218

TECHNICAL RESPONSE

CARBON CYCLE

Response to Comment on “The whole-soil carbon flux in response to warming”

Caitlin E. Hicks Pries,^{1,2*} C. Castanha,¹ R. Porras,¹ Claire Phillips,³ M. S. Torn^{1*}

Temperature records and model predictions demonstrate that deep soils warm at the same rate as surface soils, contrary to Xiao *et al.*'s assertions. In response to Xiao *et al.*'s critique of our Q_{10} analysis, we present the results with all data points included, which show Q_{10} values of >2 throughout the soil profile, indicating that all soil depths responded to warming.

In their comment, Xiao *et al.* (1) raise several questions about our whole-soil warming experiment and results (2), which we address in this response. We agree that this is an important topic and appreciate the opportunity to clarify points that perhaps were not sufficiently clear in our original report.

Xiao *et al.* question the relevance of heating the whole profile because they assert that deep soil will not warm as much as surface soil due to low thermal diffusivity. Although the exact rates of warming in any location will depend on a host of factors, both direct observations and soil thermal modeling find that nearly synchronous warming of the subsurface is a realistic climate change scenario. Analyses of temperature records for 38 stations across North America showed no difference in average warming trends at 10 cm and 100 cm depth between 1967 and 2002 [0.31° and 0.31°C decade⁻¹, respectively (3)]. Analyses of soil temperature predictions from IPCC models (Coupled Model Intercomparison Project; CMIP5) show that both surface soils (0 to 2 cm) and deep soils (80 to 140 cm) will warm at roughly the same rate throughout this century, closely following air warming trends under scenario RCP 8.5 (Fig. 1), except in permafrost regions. The thermal diffusivity of soils does not impose meaningful lags to warming at 1 m depth over climatic time scales.

In addition, the lack of deep soil warming in most warming experiments is not evidence that deep soils will exhibit reduced warming relative to the surface under future climates. The attenuation of warming with depth measured in the top-down warming (i.e., warming applied at or near the surface only) experiments cited by Xiao *et al.* (4, 5)

was caused not by the low thermal diffusivity of the soil but as a result of lateral heat transfer. In top-down warming experiments, the area being warmed is adjacent to areas of ambient temperature to which heat is lost. Thus, many top-down warming experiments have soil heating profiles that attenuate much more steeply with depth than would be predicted in climate change scenarios in which the entire surface is warmed. Our warming design corrects for this experimental artifact that occurs when surface warming is implemented over a limited soil volume. Our study,

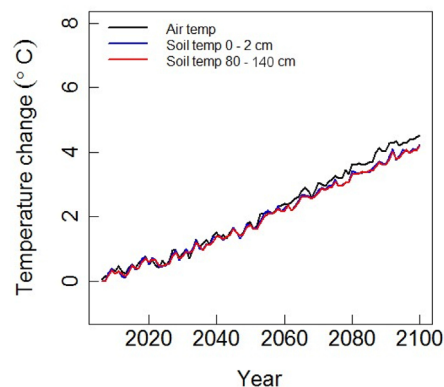


Fig. 1. Surface and deep soil temperatures are predicted to rise in synchrony. Within the next century, global air temperatures over land are projected to increase 4°C according to Community Earth System Model Version 1–Biogeochimistry (CESM1-BGC) scenario RCP 8.5. Globally, soil temperature at the surface and at depth will lag slightly behind air temperature in the later part of the century, as a result of permafrost/snow feedbacks at high latitudes, but will also warm by approximately 4°C by 2100. Temperature change is reported as the difference between average 2081–2100 global temperatures for scenario RCP 8.5 and average 1986–2005 global temperatures simulated under a historical scenario.

wherein the entire profile to 1 m was warmed by +4°C while allowing for natural differences in diurnal and seasonal temperature fluctuations among depths, is a more realistic scenario of future soil warming. Warming by a similar amount at all depths not only approximates future climate change scenarios, it also facilitated quantification of the temperature response of the whole profile.

Moreover, Xiao *et al.* critiqued our soil profile Q_{10} analysis on the basis of an apparent misunderstanding of data treatment and a lack of clarity on our part regarding mechanisms. In setting up our analysis, we tried many ways of calculating Q_{10} , including curve fitting, before deciding on a comparison between the heated and control plots of each plot pair. This method avoided confounding seasonal effects that can arise when warmer and cooler temperatures from the same site are used to fit a curve. We dropped unrealistically high Q_{10} values (>30) from our analysis because these values were likely caused by differences in substrate availability and microbial communities among paired samples and were not a response to the warming manipulation. Unlike laboratory incubation experiments that calculate Q_{10} , we could not measure the temperature response of the same soil sample. In most laboratory incubations, either the soil is homogenized, split, and subjected to different temperatures in parallel (6) or the same soil sample is subjected to different temperatures in series (7). In such experiments, the effects of natural spatial heterogeneity in substrate availability and microbial communities are reduced. Furthermore, in contrast to the description provided by Xiao *et al.*, we did not exclude Q_{10} values greater than 6.4 and less than 30, and we took into account the nonindependence of repeated measures.

Rather than removing data points as Xiao *et al.* did, we present the Q_{10} analysis with all data (Fig. 2). Q_{10} values calculated using all data are

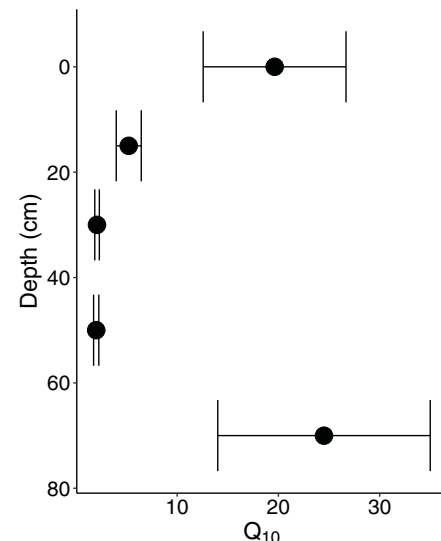


Fig. 2. The soil profile of mean Q_{10} (\pm SE) with values of >30 retained. All depths have Q_{10} values of >2 , showing that all soil depths are responding to warming.

¹Climate Sciences Department, Climate and Ecosystem Sciences Division, Lawrence Berkeley National Laboratory, MS 74R316C, Berkeley, CA 94720, USA. ²Biological Sciences Department, Dartmouth College, Hanover, NH 03755, USA. ³Department of Crops and Soil Science, Oregon State University, Corvallis, OR 97331, USA. *Corresponding author. Email: caitlin.e.h.pries@dartmouth.edu (C.E.H.P.); mstorn@lbl.gov (M.S.T.)

still >2 throughout the soil profile, with more extreme variability at the shallowest and deepest depths. Furthermore, although the Q_{10} results of Xiao *et al.* differ in magnitude from ours, their analysis shows a pattern similar to the pattern we originally published (2), with a tendency toward stronger Q_{10} responses in the shallower soil at depths of 0 to 15 cm and 15 to 30 cm.

Putting aside the different ways to calculate Q_{10} , our conclusions are also supported by the CO_2 production data. All depths responded to

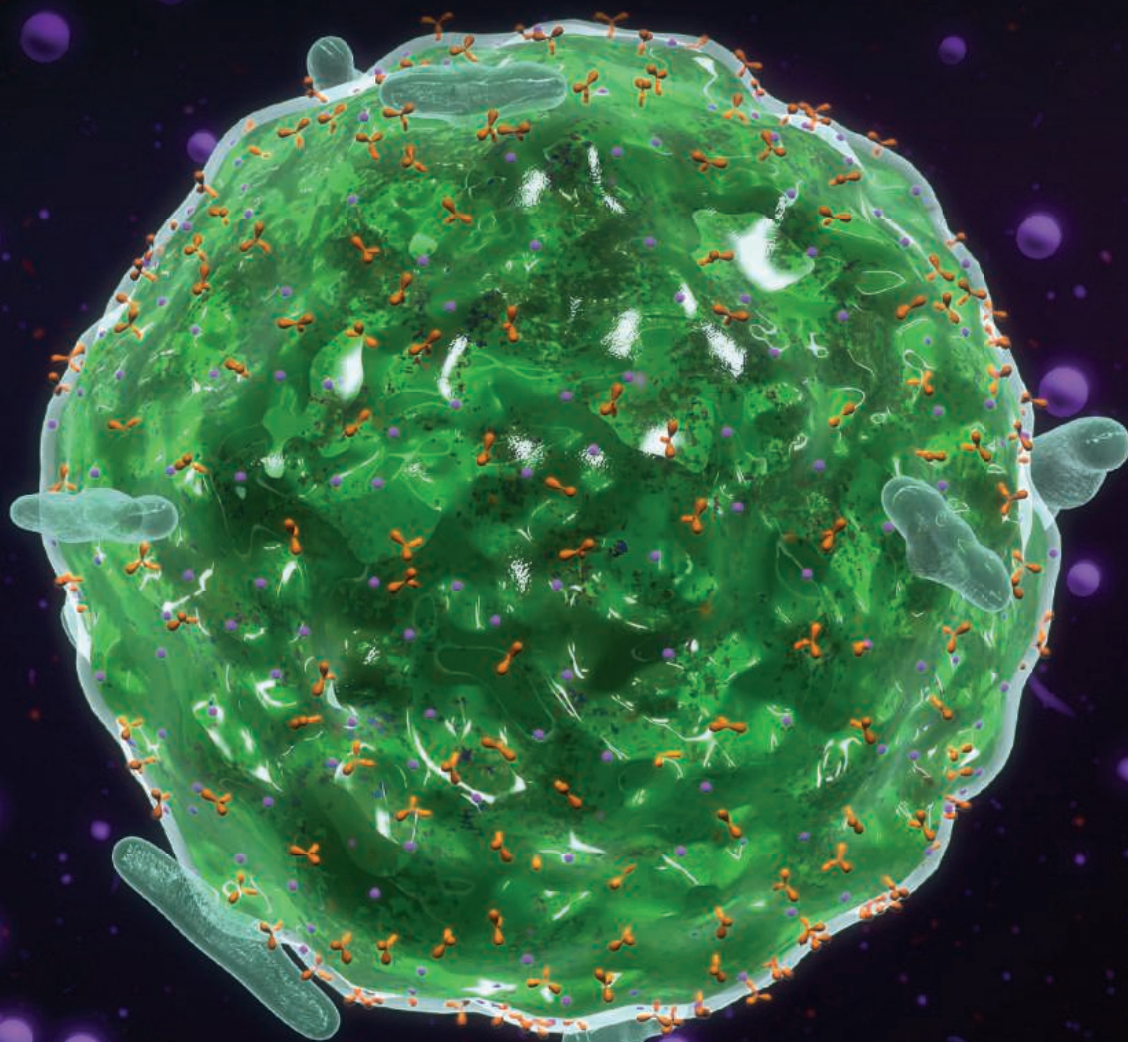
warming with an increase in CO_2 production. As stated in the original article, the warming response was greater (on an absolute basis) toward the surface, but it was an unexpected finding that the deeper soils responded at all. Although deeper soils (>30 cm) only contributed 10% of the total warming response, neglecting their contributions, as has been standard in most experiments, has major implications when scaling up soil carbon feedbacks to climate change from the site level to the global scale.

REFERENCES

1. J. Xiao *et al.*, *Science* **359**, eaao0218 (2018).
2. C. E. Hicks Pries, C. Castanha, R. C. Porras, M. S. Torn, *Science* **355**, 1420–1423 (2017).
3. Q. Hu, S. Feng, *J. Appl. Meteorol.* **42**, 1139–1156 (2003).
4. M. Xu *et al.*, *J. Arid Land* **7**, 189–204 (2015).
5. R. L. Rich *et al.*, *Glob. Change Biol.* **21**, 2334–2348 (2015).
6. C. Fissore *et al.*, *Glob. Change Biol.* **14**, 193–205 (2008).
7. J. M. Craine, N. Fierer, K. K. McLauchlan, *Nat. Geosci.* **3**, 854–857 (2010).

28 July 2017; accepted 21 December 2017
10.1126/science.aao0457

Submit your high-impact research to *Science Immunology*



Science Immunology publishes original, peer-reviewed, science-based research articles that report critical advances in all areas of immunological research, including important new tools and techniques. Share your research with *Science Immunology* global readership and submit your manuscript today!

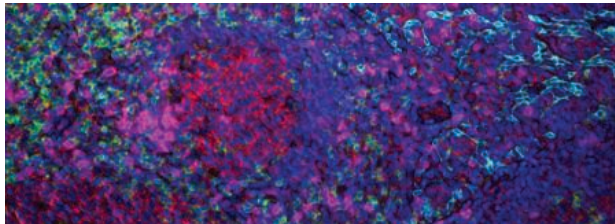
What will your discovery be?

Submit your manuscript today at
ScienceImmunology.org

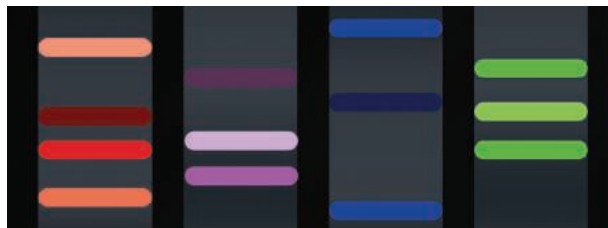
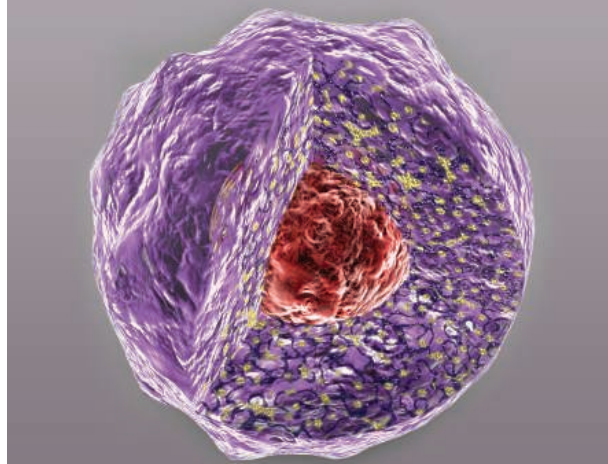
Science Immunology

AAAS

want new technologies?



antibodies
apoptosis
biomarkers
cancer
cytometry
data
diseases
DNA
epigenetics
genomics
immunotherapies
medicine
microbiomics
microfluidics
microscopy
neuroscience
proteomics
sequencing
toxicology
transcriptomics



watch our webinars

Learn about the latest breakthroughs, new technologies, and ground-breaking research in a variety of fields. Our expert speakers explain their quality research to you and answer questions submitted by live viewers.

VIEW NOW!
webinar.
sciencemag.org

Science
AAAS

Brought to you by the Science/AAAS
Custom Publishing Office

eppendorf
& Science

PRIZE FOR NEURO BIOLOGY

2017 Winner

Flavio Donato, Ph.D.
Kavli Institute
Norwegian University of
Science and Technology

For research on how neural
networks mature during
development to represent
space in the brain



Call for Entries

Eppendorf & Science Prize for Neurobiology

The annual Eppendorf & Science Prize for Neurobiology is an international award which honors young scientists for their outstanding contributions to neurobiological research based on methods of molecular and cell biology. The winner and finalists are selected by a committee of independent scientists, chaired by *Science's* Senior Editor, Dr. Peter Stern. To be eligible, you must be 35 years of age or younger.

Application Deadline
June 15, 2018

As the Grand Prize Winner, you could be next to receive

- > Prize money of US\$25,000
- > Publication of your work in *Science*
- > Full support to attend the Prize Ceremony held in conjunction with the Annual Meeting of the Society for Neuroscience in the USA
- > 10-year AAAS membership and online subscription to *Science*
- > Complimentary products worth US\$1,000 from Eppendorf
- > An invitation to visit Eppendorf in Hamburg, Germany

It's easy to apply! Learn more at:

www.eppendorf.com/prize

eppendorf

Science
AAAS



Glass-Bottom Slide

Lower costs and flawless imaging make the new ibidi μ -Slide VI 0.5 Glass Bottom an interesting option for researchers who are working with glass-bottom slides or dishes for immunofluorescence assays, flow experiments, total

internal reflection fluorescence (TIRF) microscopy, or superresolution (e.g., PALM, STORM, or SIM) applications. This slide is ideally suited for applications using six channels in parallel. Experiments are cost-effective because they require only a small number of cells and a low volume of reagents. The cell seeding results in a homogeneous cell distribution over the channel surface, regardless of handling practices. Plus, fewer steps are needed in immunofluorescence assays because of the slide's all-in-one chamber, resulting in simplified protocols. Achieving flawless cell imaging in assays is also possible thanks to the low thickness variability of the coverslip glass (#1.5H = $170 \pm 5 \mu\text{m}$).

ibidi

For info: 844-276-6363
www.ibidi.com

Sample Preservation System

The DriBank System preserves, maintains, and organizes dozens of small ($\leq 3 \text{ g}$ or $50 \mu\text{L}$) laboratory biological samples at room temperature (20°C) for months without the need for electrical power, toxic fixatives, coatings, or matrices. It is a compact unit made of ruggedized materials that is environmentally sealed when closed, effectively separating the interior from outside conditions. Specimens are preserved within hours, using evaporative dehydration via powerful dessicants contained inside a unique replaceable and rechargeable cartridge. This patented, all-in-one solution accepts samples in a variety of media, including microscope slides, microcentrifuge tubes, cell culture dishes, swabs, and more. Its layout allows for easy cleaning and sterilization for reuse. DriBank can also be used to ship samples under ambient conditions, without the expense associated with refrigerants such as dry ice, and includes an external locking port that maintains chain-of-custody for critical specimens.

DriBank Labs

For info: 844-599-1472
www.dribanklabs.com

Histone H3 and H4 Multiplex Assays

EpiGentek offers a complete series of kits available for the quantification of methylation, acetylation, and phosphorylation

of H3 and H4 histones at all sites. Histones are primary protein components of eukaryotic chromatin and play a role in gene regulation. H3 and H4 histones have tails that protrude from the nucleosome and can be modified posttranslationally to alter the histones' interactions with DNA and nuclear proteins, leading to epigenetic changes that regulate many normal and disease-related processes. We offer the most comprehensive selection of histone-modification research products, to cover every step of your experiment workflow from upstream to downstream. Getting started is easy with H3 and H4 Multiplex Assays—you can screen and measure up to 21 different histone-H3 or 10 different histone-H4 modification patterns in a single ELISA-like kit.

EpiGentek

For info: 877-374-4368
www.epigentek.com

Multispecies Kit for Pharmacokinetic Studies

The new Gyrolab Generic PK Kit is optimized for use in automated, nanoliter-scale Gyrolab xP and Gyrolab xPlore systems, enabling quantification of human therapeutic antibodies. It is designed for use with several species of preclinical animal models, including mouse and cynomolgus monkey. While most immunoassays for pharmacokinetic (PK) applications can take up to a full day to get results, the Gyrolab Generic PK Kit generates results in just one hour. This generic kit reduces the need for researchers to develop assays using costly, analyte-specific reagents. The kit's broad dynamic range minimizes the need for dilutions and repeats that can introduce errors, enabling researchers to deliver high-quality results. Moreover, Gyrolab assays consume nanoliter volumes, providing major preclinical benefits by allowing serial sampling of fewer mice, thus generating better data for more analyses while using less material.

Gyros Protein Technologies

For info: +46-(0)-18-566-300
www.gyrosproteintech.com

Thermal Cameras

FLIR Systems' high-speed, longwave thermal cameras—FLIR X6900sc SLS and FLIR X8500sc SLS—feature strained-layer superlattice (SLS) detectors filtered for longwave infrared. These detectors produce high frame rates, wide temperature ranges, and integration times more than 12-fold faster than their midwave counterparts. FLIR combined this advanced technology with popular features of high-speed visible cameras, such as remote triggering and precise synchronization, to produce high-performance cameras that can capture meaningful data for anything from aerospace research to composite materials testing. The FLIR X6900sc SLS captures full-frame 640×512 thermal images at 1,004 fps. The FLIR X8500sc SLS records up to 181 fps of full 1280×1024 high-definition thermal imagery. Both cameras feature the FLIR digital video recorder, which saves up to 36 s of data to on-camera RAM without dropping frames, and can measure temperatures up to $3,000^\circ\text{C}$.

FLIR Systems

For info: +32-(0)-3665-5100
www.flir.com/science

Electronically submit your new product description or product literature information! Go to www.sciencemag.org/about/new-products-section for more information.

Newly offered instrumentation, apparatus, and laboratory materials of interest to researchers in all disciplines in academic, industrial, and governmental organizations are featured in this space. Emphasis is given to purpose, chief characteristics, and availability of products and materials. Endorsement by *Science* or AAAS of any products or materials mentioned is not implied. Additional information may be obtained from the manufacturer or supplier.

Science Career Fair at Harvard University

March 14, 2018
11:00 AM - 5:00 PM EST



A Day of Job Opportunities and Career Seminars

JOB SEEKERS! *Science Careers* has partnered with Harvard University to produce a unique career fair open to all. Join us for a chance to meet with top scientific organizations and get important advice from career experts. The combination of valuable career development seminars, company presentations, and exciting career opportunities makes this a free “must-attend” event for scientists.



**Northwest Science Building,
Harvard Campus**
B100
Cambridge, MA

*For more details and
to register, visit
sciencemag.org/careers/jobfair*

Science **Careers**

FROM THE JOURNAL SCIENCE 

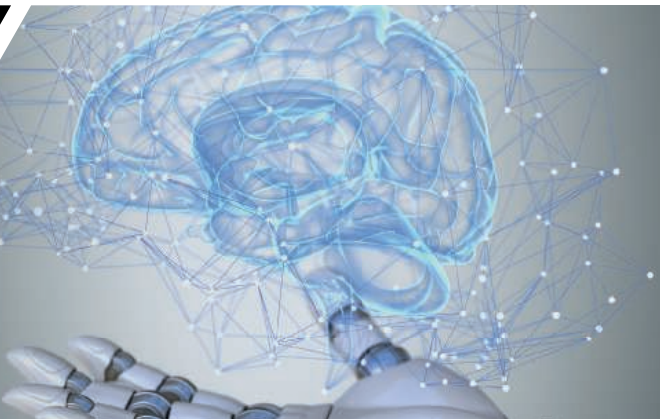
SCIENCECAREERS.ORG

The First Journal of Interdisciplinary Robotics Research

UPCOMING SPECIAL ISSUES IN 2018



Social Robotics: Summer 2018



Learning—Beyond Imitation: Fall 2018



Submit Your Article for Publication in *Science Robotics*:

- Rapid review, scoop protection, and no article page limits.
- Exposure to an international audience, including 11,000 science journalists.
- Supportive and knowledgeable editorial staff.
- Promotion on the *Science Robotics* website and the potential for accompanying commentary or podcasts.
- AAAS social media and media relations support.

Learn more at robotics.sciencemag.org.

Send pre-submission inquiries to sciroboteditors@aaas.org.

Science Careers

SCIENCE CAREERS ADVERTISING

For full advertising details, go to ScienceCareers.org and click For Employers, or call one of our representatives.



AMERICAS

+1 202 326-6577

+1 202 326-6578

advertise@sciencecareers.org

EUROPE, INDIA, AUSTRALIA, NEW ZEALAND, REST OF WORLD

+44 (0) 1223 326527

advertise@sciencecareers.org

CHINA, KOREA, SINGAPORE, TAIWAN, THAILAND

+86 131 4114 0012

advertise@sciencecareers.org

JAPAN

+81 3-6459-4174

advertise@sciencecareers.org

CUSTOMER SERVICE

AMERICAS

+1 202 326-6577

REST OF WORLD

+44 (0) 1223 326528

advertise@sciencecareers.org

All ads submitted for publication must comply with applicable U.S. and non-U.S. laws. *Science* reserves the right to refuse any advertisement at its sole discretion for any reason, including without limitation for offensive language or inappropriate content, and all advertising is subject to publisher approval. *Science* encourages our readers to alert us to any ads that they feel may be discriminatory or offensive.

Science Careers

FROM THE JOURNAL SCIENCE AAAS

ScienceCareers.org

ScienceCareers

FROM THE JOURNAL SCIENCE AAAS

Step up your job search with *Science* Careers



- Access thousands of job postings
- Sign up for job alerts
- Explore career development tools and resources



Search jobs on **ScienceCareers.org** today



MAX-PLANCK-GESELLSCHAFT

The Max Planck Society and the Max Planck Institutes for

Astrophysik (Garching), **Biochemie** (Martinsried), **biophysikalische Chemie** (Göttingen), **chemische Ökologie** (Jena), **Chemische Physik fester Stoffe** (Dresden), **die Physik des Lichts** (Erlangen), **Eisenforschung** (Düsseldorf), **Intelligente Systeme** (Stuttgart, Tübingen), **Kernphysik** (Heidelberg), **Kolloid- und Grenzflächenforschung** (Potsdam-Golm), **Marine Mikrobiologie** (Bremen), **Mathematik** (Bonn), **Meteorologie** (Hamburg), **Molekulare Pflanzenphysiologie** (Potsdam-Golm), **Psychiatrie** (München), **Softwaresysteme** (Saarbrücken, Kaiserslautern), **terrestrische Mikrobiologie** (Marburg), and the **Fritz-Haber-Institut der Max-Planck-Gesellschaft** (Berlin)

are seeking nominations for the position of

Max Planck Director

in any exciting field of science and, in particular, including the following:

artificial intelligence, bio-hybrid intelligent systems, biochemistry, biological/biophysical technologies (incl. cryo-EM tomography), biology (cellular, computational, mechanistic, molecular, structural), chemical ecology, chemistry/physics/theory of materials, clinical neuromodeling, cognition, collective and multi-agent systems, computational climate physics, corrosion, computational psychiatry or psychosomatics and computational neuroimaging, computer science, developmental robotics, electrochemistry, electronic structure theory, machine learning, materials science and engineering, microbial interactions, marine microbiology (microbial physiology, ecology, evolution, interactions, or other related disciplines), molecular machines, optical sciences, physics and chemistry approaches in life science, plant biology (physiology, molecular biology, biochemistry or molecular ecology), multiscale modelling, pure mathematics, quantum chemistry, single cell genomics, soft robotics, theoretical/numerical astrophysics relevant to stellar, planetary, high-energy or transient phenomena, theoretical and experimental biophysics, theoretical astrophysics or astroparticle physics.

Directors pursue a bold research agenda and lead the institute jointly with their fellow directors.

Nominees should have achieved distinction in their fields. Chief criteria for a directorship are scientific or scholarly excellence and an innovative research program, rather than seniority or publication rankings. The committees of the Max Planck Society will read and evaluate the three to five best publications provided for the nominee. We are looking for the strongest and most creative scientists worldwide, and offer an international, excellent research environment, outstanding infrastructure and long-term scientific funding.

Written nominations will be treated with strictest confidentiality.

The Max Planck Society strives for gender equity and welcomes nominations from all backgrounds. We actively encourage nominations of persons with disabilities.

Nominations should include a letter in support of nomination, a curriculum vitae, a list of publications, three to five selected publications and a brief description of the research program and should be uploaded at the following page:

<https://www.mpg.de/career/commoncall>

Nominations should be submitted by April 30, 2018

Later nominations may also be considered.

Special Job Focus:
Biology

Issue date: March 30
Book ad by March 15

Ads accepted until March 23 if space allows



129,562

subscribers in print
every week

70,202

unique active job seekers
searching for biology
positions in 2017

57,556

applications submitted
for biology position
in 2017

To book your ad:
advertise@sciencecareers.org

The Americas

+ 202 326 6577

Europe

+44 (0) 1223 326527

Japan

+81 3 6459 4174

China/Korea/Singapore/
Taiwan

+86 131 4114 0012

Produced by the Science/AAAS
Custom Publishing Office.

What makes *Science* the best choice for recruiting?

- Read and respected by 400,000 readers around the globe
- 80% of readers read *Science* more often than any other journal
- Your ad dollars support AAAS and its programs, which strengthens the global scientific community.

Why choose this issue for your advertisement?

- Relevant ads lead off the career section with a special biology banner
- Bonus distribution to Experimental Biology:
April 21–25, San Diego, CA.

Expand your exposure.

Post your print ad online to benefit from:

- Link on the job board homepage directly to a landing page for biology jobs
- Additional marketing driving relevant job seekers to the job board.



ScienceCareers

FROM THE JOURNAL SCIENCE AAAS

SCIENCECAREERS.ORG

FOR RECRUITMENT IN SCIENCE, THERE'S ONLY ONE SCIENCE.



UNIVERSITY OF GEORGIA

College of Public Health
Department of Environmental Health Science

A Tenure-Track Assistant/Associate Professors in Environmental Health Science

The Department of Environmental Health Science in the College of Public Health, at The University of Georgia, invites applications for a tenure-track position at assistant/associate professor level. The appointment is academic year appointment with an opportunity to supplement salary through external funding. We primarily are interested in the individual with strong academic record in research, teaching, and service in the area of environmental chemistry with focus on studying adverse health effects of environmental chemical toxicants on animals and humans with advanced analytical instruments. Qualifications include: doctoral degree in a discipline related to analytical chemistry, biochemistry, molecular toxicology with minimal postdoctoral training for one year. Preferred qualifications include the strong evidence of ability to submit extramural grants proposals, produce and communicate research, excellence in teaching and working with students, and a commitment to cultural diversity are expected. For associate professor position, strong evidence for acquiring and administering external funding is expected, and the current principal investigator with existing grants is preferred.

Review of applications will begin immediately until filled. Application materials should include a cover letter, current curriculum vitae, statement of research and teaching experience, and the names and contact information of three references (name, address, e-mail address, and phone number), and should send via the quick link for posting: <http://facultyjobs.uga.edu/postings/3436>.

The University of Georgia is an Equal Opportunity/Affirmative Action Employer. All qualified applicants will receive consideration for employment without regard to race, color, religion, sex, national origin, ethnicity, age, genetic information, disability, gender identity, sexual orientation or protected veteran status. Persons needing accommodations or assistance with the accessibility of materials related to this search are encouraged to contact Central HR (facultyjobs@uga.edu). Please do not contact the department or search committee with such requests.



W.M. Keck Science Department

Clemont McKenna College • Pitzer College • Scripps College

TENURE-TRACK POSITION IN NEUROSCIENCE W.M. KECK SCIENCE DEPARTMENT OF CLAREMONT MCKENNA, PITZER, AND SCRIPPS COLLEGES

The W.M. Keck Science Department of Claremont McKenna College, Pitzer College and Scripps College invites applications for a tenure-track appointment in **Neuroscience** at the Assistant Professor level to begin July 2018. The department, which houses a wide spectrum of faculty members from the physical and life sciences, including neuroscience, for three of the five undergraduate Claremont Colleges, offers innovative and interdisciplinary programs in the natural sciences. The neuroscience program extends across the five undergraduate Claremont Colleges. Many faculty members participate in collaborative research projects, both within the department and with research groups at nearby colleges and universities. We seek a broadly trained neuroscientist who is committed to excellence in teaching and who will develop a vibrant research program using quantitative methods that fully engages undergraduate students. We are interested in all aspects of neuroscience, excluding cognitive neuroscience. The position offers opportunities to teach both cell/molecular and systems neuroscience courses, introductory biology, non-majors courses, and a course in the candidate's field. Candidates will be asked to discuss their ability to teach a diverse student body and contribute to fostering diversity in the department. A Ph.D. degree, post-doctoral experience, and a record of scholarly publication are required.

Please apply online at https://webapps.cmc.edu/kecksci/faculty/faculty_opening_detail.php?PostingID=16034. Upload a cover letter, a curriculum vitae, a diversity statement (of no more than one page), a statement of teaching philosophy, a description of proposed research with equipment needs, and the names and e-mail addresses of three references. Any inquiries may be addressed to Professor Melissa Coleman at mcoleman@kecksci.claremont.edu. Additional information about the department may be found at www.kecksci.claremont.edu. Review of applications will begin **March 12, 2018**, and the position will remain open until filled.

The Keck Science Department of Claremont McKenna, Pitzer, and Scripps Colleges is an Equal Opportunity Employer. In a continuing effort to enrich its academic environment and provide equal educational and employment opportunities, the department actively encourage applications from women and members of historically under-represented social groups in higher education.



DukeNUS
Medical School

SingHealth DukeNUS
ACADEMIC MEDICAL CENTRE

Tenure-Track Faculty Positions in Visual Sciences and Vision Disorders at the Duke-NUS Medical School (Assistant, Associate and Professor Levels)

The Duke-National University of Singapore Medical School (Duke-NUS) is unique in bringing post-baccalaureate, research-intensive medical education to Asia. It represents a truly global partnership and combines the expertise and resources of two leading universities: the National University of Singapore and Duke University, North Carolina, USA. Duke-NUS has established five Signature Research Programmes (SRPs) to raise the standard and quality of healthcare and to develop novel and better strategies for treatment of diseases. The five SRPs are in the area of Cancer and Stem Cell Biology, Cardiovascular and Metabolic Disorders, Emerging Infectious Diseases, Neuroscience and Behavioural Disorders and Health Services and Systems Research. As part of the SingHealth Duke-NUS Academic Medical Centre (AMC), Duke-NUS has its home in a modern facility adjacent to the Singapore General Hospital and maintains strong basic, translational and clinical research partnerships throughout Singapore, including the Singapore Eye Research Institute (SERI) and the Singapore National Eye Centre (SNEC).

Duke-NUS is recruiting outstanding candidates with MD, PhD or MD/PhD qualification and a strong, proven research track record in the area of **Visual Sciences and Vision Disorders**, at the Assistant, Associate and Professor levels. The recruited faculty will hold their primary appointment in Duke-NUS, specifically at the **Centre for Vision Research**, and a joint appointment with SERI/SNEC where the faculty's office and laboratory will be located. **Candidates with strong track record conducting internationally competitive fundamental and translational research in areas of stem cell and regenerative medicine, vascular and cell biology, functional genomics and animal models in major eye diseases such as age-related macular degeneration, diabetic retinopathy, glaucoma and myopia are strongly encouraged to apply.** The package for the faculty recruit will include full salary, start-up research funding as well as office and laboratory space. The successful candidate is expected to apply for competitive grants to sustain his/her research in the long term.

Interested candidates should submit a cover letter, curriculum vitae and summary of accomplishments via e-mail by **31 May 2018**. Candidates applying for the Assistant Professor position are requested to additionally arrange to have three letters of reference sent in support of their application.

Interested candidates who wish to know more about these positions will have the opportunity to meet up with senior SNEC/SERI/ Duke-NUS faculty at the Association for Research in Vision and Ophthalmology (ARVO) Annual meeting at the Hawaii Convention Centre (SERI Booth) between 29 April to 3 May 2018. Please contact zhou.ting@seri.com.sg to coordinate the meet-up.

Professor Tin Aung
Search Committee Chair
Duke-NUS Medical School
E-mail: hr@duke-nus.edu.sg
Website: www.duke-nus.edu.sg

By Nicole Forrester

Independent but not alone

Crowing up, I idealized independence. I always wanted my own efforts to be enough, whether it was completing school assignments without help from my parents or moving into a new apartment by myself. When I decided to pursue a graduate degree, I wanted to develop a novel research program and quickly establish myself as an independent scientist. I sought out an adviser who would give me complete agency over my doctoral work while also offering strong mentorship. But I was naïvely optimistic about what I could accomplish.

I figured that my adviser and labmates could help me learn to conduct sound experiments and become a successful researcher, and I could rely on published literature to learn the specific techniques I would need. As I began designing experiments to investigate the symbiotic relationship between legumes and nitrogen-fixing bacteria, my committee members applauded my ambition to pioneer a project far beyond the scope of my lab, which focuses on plant-pollinator interactions. They also warned me about the challenges I would face.

But my need for independence drove me to push forward with my research plan. As a result, the first 4 years of my graduate career were defined by a series of failures. My head spun with possible questions to explore, but I struggled to translate these ideas into feasible studies. Because my research interests were distinct from ongoing work in the lab, I rarely asked for help. When I did seek assistance, my labmates were often at a loss because they didn't have the expertise I needed.

During my second year, I solicited little feedback about the research proposal I was writing for my comprehensive exam—and I went on to fail part of the exam because it was unclear whether the experiments I proposed would lead to conclusive results. Unwilling to abandon my project, I spent the next 3 months rethinking, redesigning, and rewriting my proposal. I developed a clear vision for my research, but the setbacks weren't over. During my third year, I had grand ambitions to genetically manipulate plants, only to discover that after treating thousands of seeds, I obtained just one plant I could use for experiments.

By my fourth year, my desperation to succeed overshadowed my desire for independence. The only thing I cared about was generating publishable data. I was disappointed by my inability to conduct a successful experi-



"I ... embarked on a cross-country road trip to develop the expertise I needed."

ment on my own, but I knew that I needed to take a new approach.

A few months later, I packed my car and embarked on a cross-country road trip to develop the expertise I needed. My adviser and I had devised a somewhat unusual solution: I would spend a 3-month "sabbatical" in a collaborating lab to obtain specialized training. I worked extensively with other students, constantly asked questions, and offered to help with ongoing projects to learn everything I could. For the culmination of my sabbatical, I executed an elegant experiment that would not have been possible without the dedicated help of the principal investigator, three graduate students, and numerous undergrads.

But the experiment still failed. Thirty percent of my control plants

were contaminated with bacteria. My data were unpublishable. I drove back to Pennsylvania with the same feeling of desperation I had earlier in my graduate career. Even asking for help was not enough to produce a successful experiment.

My adviser, on the other hand, saw this experience as a groundbreaking success, emphasizing the extensive skill set I acquired. A few months later, when I repeated the experiment in my home lab, I produced publishable data. By learning when to ask for help, I had found the perfect balance of independence and assistance, which ultimately led to success.

Being an independent scientist doesn't require me to do everything on my own. I can address novel questions without feeling obligated to master every aspect of the scientific process. Now when I get stuck, I don't hesitate to ask others for help, whether they're across the country or in my own lab. ■

Nicole Forrester is a doctoral candidate at the University of Pittsburgh in Pennsylvania. Do you have an interesting career story? Send it to SciCareerEditor@aaas.org.